UNIVERSITY OF BIRMINGHAM

SURFACE AND FRAMEWORK MODIFICATION OF SILICA NANOPARTICLES FOR EFFICIENT DELIVERY OF ANTIBIOTICS

by

ASIER RODRIGUEZ MUGURUZA

A thesis submitted to the University of Birmingham for the degree of

DOCTOR OF PHYLOSOPHY

School of Chemistry

College of Engineering and Physical Sciences

University of Birmingham

December 2023

UNIVERSITY OF
BIRMINGHAM

University of Birmingham Research Archive

e-theses repository

This unpublished thesis/dissertation is copyright of the author and/or third parties. The intellectual property rights of the author or third parties in respect of this work are as defined by The Copyright Designs and Patents Act 1988 or as modified by any successor legislation.

Any use made of information contained in this thesis/dissertation must be in accordance with that legislation and must be properly acknowledged. Further distribution or reproduction in any format is prohibited without the permission of the copyright holder.

ABSTRACT

Antimicrobial resistance is a growing health concern being the cause of higher morbidity and mortality worldwide. Alongside the increased number of resistant bacterial strains identified and the reduced number of new antibiotics in the pipeline, the development of new antimicrobial therapies is crucial. Silica nanoparticles present unique properties for the design of novel drug delivery systems. The chemical versatility of their surface and framework proposes an advantage for the design of innovative antibiotic delivery systems.

Hereby, we present different approaches for the development of novel silica nanoparticles for the efficient delivery of antibiotics against Gram-negative bacteria. Firstly, surface functionalization of silica nanoparticles led to a novel drug delivery system able to deliver an antibiotic inside Gram-negative bacterial cells, that in its free form is not active due to the reduced permeability of Gram-negative bacteria. Furthermore, the simultaneous inclusion of a ruthenium(II) luminescent metal complex alongside an antibiotic allowed the tracking of the therapeutic nanoparticles. Further Fe^{3+} cation complexation to the ligand attached to the nanoparticle surface is determined to be an excellent approach to enhance the uptake of nanoparticles in bacterial cells driven by nutrient uptake systems expressed in the bacterial membrane. Another studied approach consisted of the modification of silica nanoparticles framework with spiropyran derivatives to achieve photoresponsive particles that displayed light triggered antibiotic release against urinary tract pathogenic bacterial cells.

Finally, two different approaches for the modification of nanoparticle's framework were investigated by development of polysilesquioxane nanoparticles and micelle-driven

encapsulation in order to enhance the loading and release of a model hydrophobic antibiotic resulting in nanoparticles with better antibiotic delivery performance than traditional non-porous and mesoporous silica nanoparticles.

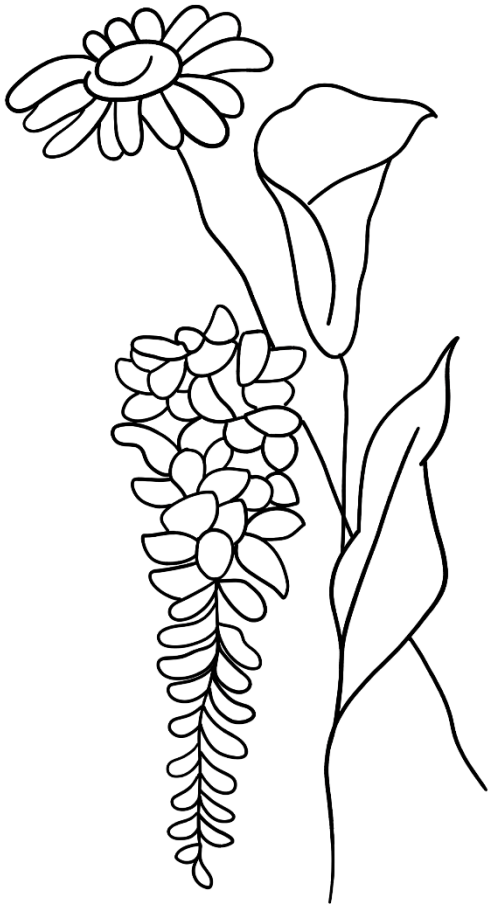

ACKNOWLEDGEMENTS

First of all, I would like to acknowledge my supervisors, Prof Zoe Pikramenou and Prof Jessica M. A. Blair for their constant guidance, support and scientific input along this experience. I would also like to thank all the collaborators that have made possible this work: Dr Alessandro di Maio, Dr Nikolas Hodges, Dr Cécile Le Duff, Theresa Morris, Dr Ludwig Schenide, Dr Knut Rurack and Dr Timothy Easun. Finally, I would like to acknowledge the Midlands Integrative Biosciences Training Partnership (MIBTP) and the Biotechnology and Biological Sciences Research Council (BBSRC) for funding my PhD.

I would also like to thank the members of the Pikramenou and Blair groups, for their support and patience with me. Starting with the first member of the Pikrameou group I met and who become my mentor during the first year, Menisha, because she always had the correct words to cheer me. To Maria and Grace, the best silica buddies, and friends I could ever had. To Patricia and Elena, the southerners, thanks for always bringing a little bit of the Mediterranean essence to bright our days. And obviously, to all the rest, Jamie, Joe, Sarah, Ana, Zaina, and Charley. Thanks to the Blair group members for letting a chemist step into your lab. Finally, to George and Alex, sharing office which such clever, and still funny, minds has been one of the best experiences.

Since I came to Birmingham, a lot of things happened and changed, including a global pandemic. It has not been the easiest time. That's why, at the end of this journey, I would like to thank my chosen family, those friends that have been always there, for a cry, for a wine, or for both at the same time. Thanks to Vicky and Candela, who would have thought that after seven years those Erasmus friends would be still there. Thanks to my friends in Barcelona, I would need another thesis to put all your names, you

have always been my safe place. Specially to Javi, Carol, and Sergio, you found me in my worst and picked me up, and that's something I will always treasure. And to the rest, to all of you, simply, thank you for being part of my family.

And now the brummies. To Cynthia, what to say to you that you do not know already. My best friend, we started this together and we finished it together. I could not have imagined a better travel buddy. To Tom, the best flatmate I would even dream about, thanks for the long conversations after work and for always have an opened bottle of wine after a bad day. To Edu, thanks for always being there, besides being far. Finally, to Marta, because when you need help you should always ask for it.

Gracias a mis padres y a mi hermana. Gracias por el apoyo constante durante estos años, por acompañarme en este camino y ayudarme a levantarme en los momentos más duros. Sé que tener a ambos hijos lejos de casa no ha sido fácil, y por ello os agradezco más el dejar que nos fuéramos del nido para crecer como personas y encontrar quienes éramos. Eskerrik asko.

Ahora es momento de celebrarlo con todos, de sacar el txakoli de la nevera y poner la tortilla de patatas en la mesa. Solo me queda decir: ¿Quién trae el patxaran?

TABLE OF CONTENTS

ABSTRACT II
ACKNOWLEDGEMENTS V
TABLE OF CONTENTS VII
LIST OF ABBREVIATIONS XII
1. GENERAL INTRODUCTION 1
1.1. Antimicrobial resistance 1
1.1.1. Mechanism of action of antibiotics 2
1.1.2. Resistance mechanisms 4
1.2. Nanoparticles for antibiotic delivery 7
1.2.1. Silica nanoparticles for antibiotic delivery 8
1.2.1.1. Non-porous silica nanoparticles 9
1.2.1.2. Porous silica nanoparticles 12
1.2.1.3. Organosilica and polysilesquioxane nanoparticles 15
1.2.1.4. Hybrid silica nanoparticles for therapy and imaging 17
1.2.2. Other nanoparticles for antibiotic delivery 20
1.2.2.1. Organic nanoparticles 20
1.2.2.2. Inorganic nanoparticles 22
1.3. Research aims 23
1.4. References 25
2. CHELATING SILICA NANOPARTICLES FOR THE EFFICIENT ANTIBIOTIC DELIVERY AND PARTICLE TRACKING IN GRAM-NEGATIVE BACTERIA 38
2.1. Introduction 38
2.1.1. Outer membrane impermeability to antibiotics 38
2.1.2. Outer membrane destabilisers 40
2.1.1.2. Antimicrobial peptides 41
2.1.1.3. Polymers 43
2.1.1.4. Chelators 44
2.1.2. Silica nanoparticles with membrane permeabilization functionalization 45
2.1.3. Chapter outline 48
2.2. Results and Discussion 49
2.2.1. Synthesis of DTPA@SiO_2⊃Ru-Van 49
2.2.1.1. Synthesis of hybrid SiO_2⊃Ru-Van 49
2.2.1.2. Synthesis of DTPA-Si_2 50

2.2.1.3. Coating of SiO_2⊃Ru-Van with DTPA-Si_2 ... 53
2.2.2. Characterization of DTPA@SiO_2⊃Ru-Van ... 55
2.2.2.1. Size and morphology ... 55
2.2.2.2. Composition analysis of DTPA@SiO_2⊃Ru-Van ... 58
2.2.2.3. Photophysical properties of DTPA@SiO_2⊃Ru-Van ... 60
2.2.2.4. Quantification of included cargos in DTPA@SiO_2⊃Ru-Van ... 62
2.2.2.5. Quantification of DTPA coating in DTPA@SiO_2⊃Ru-Van ... 64
2.2.3. Release studies of DTPA@SiO_2⊃Ru-Van ... 65
2.2.4. Biocompatibility of DTPA@SiO_2⊃Ru-Van ... 67
2.2.5. Antibacterial activity of DTPA@SiO_2⊃Ru-Van ... 68
2.2.5.1. Minimal Inhibitory Concentration (MIC) determination ... 68
2.2.5.2. DTPA@SiO_2⊃Ru-Van chelating abilities against cell membrane Ca^{2+} ... 73
2.2.5.3. Nanoparticle penetration in bacterial cells ... 75
2.3. Conclusions ... 81
2.4. Experimental section ... 83
2.4.1. Synthetic procedures ... 83
2.4.2. Methodologies ... 85
2.5. Appendix ... 88
2.6. References ... 131
3. IRON(III) AMINOCARBOXYLATE DECORATED NANOPARTICLES FOR ENHANCED NANOPARTICLE UPTAKE IN GRAM-NEGATIVE BACTERIAL CELLS ... 136
3.1. Introduction ... 136
3.1.1. Siderophore: Structure and biological importance ... 136
3.1.2. Siderophore uptake systems ... 138
3.1.3. Siderophore-antibiotic conjugates ... 140
3.1.4. Siderophore-coated silica nanoparticles ... 143
3.1.5. Chapter Outline ... 144
3.2. Results and discussion ... 145
3.2.1. Synthesis of Fe^{3+}DTPA@SiO_2⊃Ru-Van ... 145
3.2.1.1. Synthesis and characterization of Fe^{3+}DTPA-Si_2 ... 145
3.2.1.2. Coating of SiO_2⊃Ru-Van with Fe^{3+}DTPA-Si_2 ... 147
3.2.2. Characterization of Fe^{3+}DTPA@SiO_2⊃Ru-Van ... 148
3.2.2.1. Size and composition of Fe^{3+}DTPA@SiO_2⊃Ru-Van ... 148
3.2.2.2. Quantification of Fe^{3+}DTPA coating ... 150
3.2.3. Release studies ... 152
3.2.4. Biocompatibility of Fe^{3+}DTPA@SiO_2⊃Ru-Van ... 153

3.3. Antibacterial activity of Fe^{3+}DTPA@SiO_2⊃Ru-Van ... 154
3.3.1. Antimicrobial activity determination of Fe^{3+}DTPA@SiO_2⊃Ru-Van ... 154
3.3.1.1. Minimal Inhibitory Concentration (MIC) determination ... 154
3.3.1.2. Effect of medium Fe(III) concentration in nanoparticles antibacterial activity 158
3.3.2. Identification of siderophore uptake systems involved in the uptake of Fe^{3+}DTPA@SiO_2⊃Ru-Van ... 163
3.3.3. Internalization of Fe^{3+}DTPA@SiO_2⊃Ru-Van nanoparticles ... 170
3.3.3.1. Internalization of control nanoparticles ... 183
3.3.4. Molecular analogue of Fe^{3+}DTPA@SiO_2⊃Ru-Van: Fe^{3+}DTPA-$Amox_2$ ... 185
3.3.4.1. Synthesis and characterization of DTPA-$Amox_2$ and Fe^{3+}DTPA-$Amox_2$ .. 185
3.3.4.2. Antimicrobial activity of DTPA-$Amox_2$ and Fe^{3+}DTPA-$Amox_2$ ... 189
3.3.4.3. Effect of Fe(III) availability on antibacterial activity of conjugates ... 191
3.3.4.4. Identification of involved siderophore-uptake system in Fe^{3+}DTPA-$Amox_2$ activity. 193
3.4. Conclusion ... 195
3.5. Experimental section ... 197
3.5.1. Synthetic procedures ... 197
3.5.2. Methodology ... 200
3.6. Appendix ... 204
3.7. References ... 236
4. SPIROPYRAN-CONTAINING PHOTORESPONSIVE ORGANOSILICA NANOPARTICLES FOR ANTIBIOTICS DELIVERY IN URINARY TRACT INFECTIONS ... 241
4.1. Introduction ... 241
4.1.1. Catheter Associated Urinary Tract Infections ... 241
4.1.2. Nanotechnology against catheter-associated UTIs ... 242
4.1.3. Photoresponsive silica nanoparticles for drug delivery ... 244
4.1.4. Spiropyran-containing silica nanoparticles ... 247
4.1.5. Chapter outline ... 249
4.2. Results and discussion ... 250
4.2.1. Synthesis of the photoresponsive silica precursor ... 250
4.2.2. Optimization of SP-content in phoresponsive nanoparticles ... 251
4.2.3. Effect of hydrophobicity in SP ... 255
4.2.4. Synthesis and characterization of TMP-containing nanoparticles ... 258
4.2.4.1. Size and morphology ... 258
4.2.4.2. Composition of TMP-containing nanoparticles ... 260
4.2.4.3. Porous structure of TMP-containing nanoparticles ... 263

4.2.4.4. Quantification of TMP in SP-SiO_2⊃TMP and SP-$HSiO_2$⊃TMP 265
4.2.5. Responsive properties of nanoparticles 267
4.2.5.1. Solid-state photoswitching properties of nanoparticles 267
4.2.5.2. Solid-state reversible photoswitching 270
4.2.5.3. Stability of solid-state reversible photoswitching 271
4.2.6. Release studies 272
4.2.6.1. Light triggered antibiotic release 272
4.2.6.2. On-off TMP release from SP-containing nanoparticles 274
4.2.7. Antibacterial activity 276
4.2.7.1. Minimal inhibitory concentration (MIC) determination 276
4.2.7.2. Effect of light irradiation in nanoparticle activity 277
4.2.7.3. Effect of on-off release in bacterial cell viability 279
4.3. Conclusion 281
4.4. Experimental section 282
4.4.1. Synthesis procedures 282
4.4.2. Methodology 285
4.5. Appendix 288
4.6. References 317
5. NEW APPROACHES FOR CIPROFLOXACIN DELIVERY FROM SILICA NANOPARTICLES 322
5.1. Introduction 322
5.1.1. Delivery of hydrophobic molecules from silica nanoparticles 322
5.1.2. Antibiotic templated silica nanoparticles 324
5.1.3. Silica nanoparticles with organic bridges 328
5.1.4. Chapter outline 330
5.2. Results and discussion 332
5.2.1. Interactions between CPX and CPC micelles 332
5.2.1.1. Dynamic Light Scattering 332
5.2.1.2. Nuclear Magnetic Resonance 334
5.2.1.3. Optical spectroscopy 341
5.2.2. Synthesis of SiO_2⊃CPC-CPX 343
5.2.3. Characterization of SiO_2⊃CPC-CPX 344
5.2.3.1. Size and morphology of CPC-CPX micelles and SiO_2⊃CPC-CPX 344
5.2.3.2. Quantification of SiO_2⊃CPC-CPX loading 347
5.2.3.3. Porous structure of SiO_2⊃CPC-CPX 349
5.2.4. Release studies of SiO_2⊃CPC-CPX 353
5.2.5. Validation of encapsulation strategy with rifampicin 355

5.2.6. Synthesis and characterization of PSQ⊃CPX 355
5.2.6.1. Size and morphology of PSQ and PSQ⊃CPX 355
5.2.6.2. Quantification of PSQ⊃CPX loading 358
5.2.6.3. Porous structure of PSQ and PSQ⊃CPX 359
5.2.7. Release studies of PSQ⊃CPX 361
5.2.8. Comparative study of CPX release from novel nanoparticles 361
5.2.9. Biocompatibility of novel CPX delivery nanoparticles 365
5.3. Conclusion 367
5.4. Experimental section 368
5.4.1. Synthesis procedures 368
5.4.2. Methodologies 369
5.5. Appendix 371
5.6. References 395
6. GENERAL CONCLUSIONS AND FUTURE WORK 401
7. INSTRUMENTATION 405

LIST OF ABBREVIATIONS

^{1}MLCT	Singlet metal to ligand charge transfer electronic transition
^{3}MLCT	Triplet metal to ligand charge transfer electronic transition
AgNPs	Silver nanoparticles
Ala	Alanine
Amox	Amoxicillin
AMP	Antimicrobial peptide
AMR	Antimicrobial resistance
ANOVA	Analysis of variances
APTES	Aminopropyltriethoxysilane
ATP	Adenosine triphosphate
AuNPs	Gold nanoparticles
BET	Brunauer-Emmett-Teller
bpy	Bipyridine
BTEB	1,4-bis(triethoxysilyl)benzene
CAUTI	Catheter-associated urinary tract infection
CFU	Colony forming units
CHCA	α-Cyano-4-hydroxycinnamic acid
CMC	Critical micelle concentration
COK	Centrum voor Oppervlaktechemie en Katalyse
COSY	Correlation Spectroscopy
CPC	Cetylpyridinium chloride
CPX	Ciprofloxacin
CTAB	Cetyltrimethylammonium chloride
CuNPs	Copper nanoparticles
D_2O	Deuterated water
d_6-DMSO	Deuterated dimethylsulfoxide
DDS	Drug delivery system
DFT	Density functional theory
D_h	Hydrodynamic diameter
DIPA	Diisoporpylamine
DIPEA	*N,N*-diisopropylethylamine
DLS	Dynamic light scattering
DMAP	4-dimethylamonopyridine
DMDES	Dimethyldiethoxysilane
DTPA	Diethylenetriaminepentaacetic acid
DTPA-Bua_2	DTPA-bisbutylamide
DTPA-Si_2	DTPA-bis(amidepropyltriethoxysilane)
ε	Molar extinction coefficient
EDTA	Ethylenediaminetetraacetic acid
EE	Encapsulation efficiency

Ent	Enterobactin
ESI-MS	Electrospray ionization - mass spectrometry
EtOH	Ethanol
fcc	Face centred cubic
FDA	Food and drug administration
FDU	Fudan University
Fe_3O_4	Iron nanoparticles
FT-IR	Fournier transformed infrared spectroscopy
GHS	Glutathione
H^+MC	Protonated merocyanine
HMBC	Heteronuclear Multiple Bond Correlation
HSQC	Heteronuclear single quantum coherence
IC_{50}	Half-maximal inhibitory concentration
ITC	Isothermal titration calorimetry
JACoP	Just another co-localization plug in
K_D	Affinity constant
K_h	Higuchi constant
KIT	Korean Institute of Technology
K_{kp}	Korsmeyer-Peppas constant
LB	Lysogenic broth
LC-MS	Liquid Chromatography-Mass Spectrometry
λ_{em}	Emission wavelength
λ_{exc}	Excitation wavelength
LL-37	Cathelecin
λ_{max}	Maximum wavelength
M_∞	Fraction of cumulative release
MALDI-ToF	Matrix assisted laser desorption ionization-time of flight mass spectrometry
MC	Merocyanine
MCM	Mobile composite material
MECAM	1,3,5-Tris(2,3-dihydroxybenzamidomethyl) benzene
MIC	Minimal inhibitory concentration
MONs	Mesoporous organosilica nanoparticles
MOPS	3-(*N*-morpholino)propanesulfonic acid
MRI	Magnetic resonance imaging
MSNs	Mesoporous silica nanoparticles
M_t	Fraction of release at t time
MTNs	Mesoporous titanium oxide nanoparticles
MTT	3-[4,5-dimethylthiazol-2-yl]-2,5 diphenyl tetrazolium bromide
NaCl	Sodium chloride
NaOH	Sodium hydroxide
NHS	National Health System
NIPAM	*N*-isopropylacrylamide
NMR	Nuclear magnetic resonance

NOE	Nuclear overhauser effects
NOESY	Nuclear overhauser effect spectroscopy
OD600	Optical density at 600 nm
Ormosil	Organically modified silica
PBP	Penicillin binding protein
PBS	Phosphate buffer saline
PDI	Polydisperisty index
PEG	Polyethylene glycol
PEI	Poly(ethylene imine)
phen	1,10-phenantroline
PMO	Periodic mesoporous organosilica
ppy	2-phenylpyrydine
PSQ	Polysislesquioxane
R	Reflectance
RIF	Rifampicin
RND	Resistance-nodulation-division
ROS	Reactive oxygen species
rRNA	Ribosomal ribonucleic acid
rt	Room temperature
Ru	Dichlorotris(1,10-phenanthroline)ruthenium(II) chloride
SAC	Siderophore-antibiotic conjugate
SBA	Santa Barbara Amorphous materials
SD	Standard deviation
SEM	Scanning electron microscopy
SIM	Structural illumination microscopy
SiO_2	Silica nanoparticle
SP	Spiropyran
SPR	Surface plasmon resonance
τ	Emission lifetime
TBDT	TonB-Dependant Transporters
Tc-99m	Technecium-99m
TEM	Transmission electron microscopy
TEOS	Tetraethoxysilane
TGA	Thermogravimetric analysis
TiO_2	Titanium nanoparticles
TMP	Trimethoprim
tRNA	Transfer RNA
UTI	Urinary tract infections
UV	Ultraviolet
UV/Vis	Ultraviolet / Visible
Van	Vancomycin
ZnNPs	Zink nanoparticles

1. GENERAL INTRODUCTION

1.1. Antimicrobial resistance

Antimicrobial resistance (AMR) is a major health challenge worldwide, being the cause of significant morbidity and death globally. It has been estimated that in 2019 1.27 million deaths were directly attributed to AMR, while 4.95 million deaths were caused by conditions associated with resistant bacterial infections (Figure 1.1A).[1,2] It has been also argued by The Review on Antimicrobial Resistance, commissioned by the UK Government, that AMR could kill 10 million people per year by 2050 (Figure 1.1B).[3]

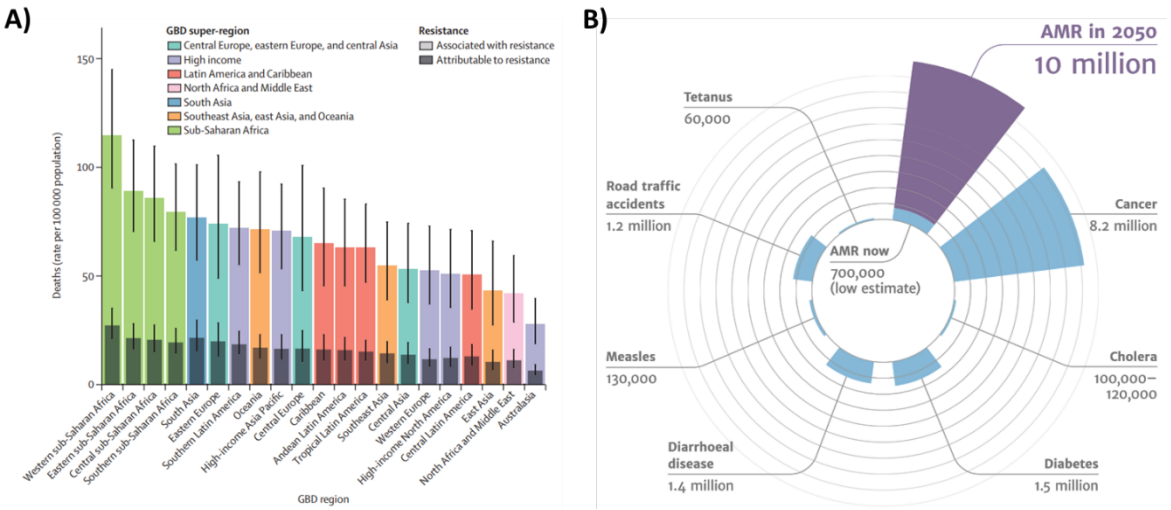

Figure 1.1. (A) All-age rate of deaths attributable to and associated with bacterial antimicrobial resistance by Global Burden of Diseases, Injuries, and Risk Factors Study (GBD) region in 2019. Estimates were aggregated across drugs, accounting for the co-occurrence of resistance to multiple drugs. Error bars show 95% uncertainty intervals.[1] (B) Estimated deaths attributed by cause of deaths from 2016 until 2050.[3]

ARM is the results of bacterial cells expressing resistance against the action of one of more antibiotics. Some bacteria are intrinsically resistant to certain antibiotics, but they can also acquire resistance to antibiotics through different mechanism. Among all the bacterial species, the so-called ESKAPEE pathogens (*Enterococcus faecium,*

Staphylococcus aureus, Klebsiella pneumoniae, Acinetobacter baumannii, Pseudomonas aeruginosa, Escherichia coli and *Enterobacter* spp.) represent the most concerning bacterial species due to their multidrug resistance and virulence.[4]

1.1.1. Mechanism of action of antibiotics

A substance able to inhibit bacterial growth or reduce bacterial viability is defined as an antibiotic. Even though a large number of antibacterial compounds have been identified only few of them have gone through clinical trials and a very limited number of them approved by official institutions for their applications in the clinic.[5]

Table 1.1. Classification and mechanism of actions of the main classes of antibiotics, adapted from Darby *et al*.[6]

Class	Examples	Mechanism of action
Aminoglycosides	Gentamicin, Streptomycin, Kanamycin	Protein translation inhibition by targeting 16S rRNA of the 30S ribosomal subunit[7] Pore formation in outer membrane[8]
β-lactams	Penicillins, Carbapenems, Cephamycins	Inhibition of cell wall peptide crosslinking by binding the penicillin-binding proteins[9]
Glycopeptides	Vancomycin	Cell wall inhibition by binding to peptide chain of peptidoglycans[10]
Macrolides	Erythromycin, Spiramicin, Azithromycin	Protein translation inhibition by targeting 23S rRNA of the 50S ribosomal subunit[11]
Fluoroquinolones	Ciprofloxacin, Trovafloxacin, Levofloxacin	Inhibition of DNA replication by binding the DNA gyrase and polymerase IV[12]
Ansamycins	Rifampicin, Geldanamicin, Strptovaricin	Transcription inhibition by binding RNA polymerase[13]
Sulfonamides	Sulfamethizole, Sulfadimide, Sulfademethoxime	Cell growth inhibition by binding dihydropteroate synthase[14]

Tetracyclines	Tigecycline, Tetracycline, Doxycycline	Protein translation inhibition by targeting 16S rRNA of the 30S ribosomal subunit[15]
Cationic peptides	Colistin	Membrane permeabilization by binding the lipid A in lipopolysaccharides[16]

Antibiotics can be classified based on their chemical structure (Table 1.1), by their mechanism or spectrum of action.

Some antibiotics target the bacterial cell membrane, inhibiting growth of bacteria directly disruption the membrane. β-lactams[9] and glycopeptides[10] are very well known and widely used cell wall synthesis inhibitors. β-lactams target the penicillin binding proteins (PBPs) located in the membrane of the bacterial cell.[9] PBPs are involved in the peptidoglycans crosslinking process, the main component of the bacterial cell wall. Upon binding of β-lactams to PBPs' active site, the active site of PBPs is blocked and the biosynthesis interrupted. Similarly, glycopeptides also inhibit the crosslinking of peptidoglycans in the cell wall. In this case, the inhibition takes place as the glycopeptide bind the terminal *D*-Ala-*D*-Ala of the peptidoglycan, blocking its recognition by the PBP.[10] Furthermore, another difference between β-lactams and glycopeptides is their spectrum of action, as glycopeptides display very low or even no activity against Gram-negative bacterial cells due to low membrane permeability.[10,17] However, some aminoglycosides are also able to increase cell membrane permeability by pore formation.[8] Nevertheless, all antibiotics that target the cell wall do not need to be internalised. Such a case are cationic antimicrobial peptides (AMP) such us colistin.[16] Their mechanism of action relies on membrane disruption by internalization between membrane lipopolysaccharides or by increasing

permeabilization due to charge unbalance after scavenging structurally important divalent cations from the cell membrane.

Protein translation is also a targeted process for several types of antibiotics. Aminoglycosides[7] and tetracyclines[15] are able to inhibit protein translation by binding to the 30S ribosomal subunit of the 16S rRNA (ribosomal RNA); while macrolides bind the 50S subunit. Fluoroquinolones, on the contrary, target DNA gyrase by inhibiting DNA replication.[11] Furthermore, fluoroquinolones also inhibit protein transcription by targeting DNA polymerase.[18] In case of ansamycin, they target RNA polymerase, inhibiting its activity.[10]

Nonetheless, antibiotics can also target other processes, such as folic acid biosynthesis. Sulphonamides act as a competitive inhibitor with *p*-aminobenzoic acid, which is involved in the metabolic cycle of folic acid.[14] Trimethoprim and its derivatives inhibit the reduction of dihydrofolate to tetrahydrofolate, a crucial step in the folic acid biosynthesis.[19,20]

1.1.2. Resistance mechanisms

Bacterial cells can present intrinsic and acquired resistance mechanisms against antibiotics (Figure 1.2). Intrinsic mechanisms rely on the genes that bacterial cells already possess and, hence, can be used by cells to protect themselves from antibiotic's effect.[6] Acquired resistance mechanism, however, takes place after a bacterial cell gains genetic material that provides further protection against antibiotics. These mechanisms can be acquired after mutations during cell replications or by horizontal gene transfer, which involves the acquisition of genetic material from another bacterial cell *via* different processes.

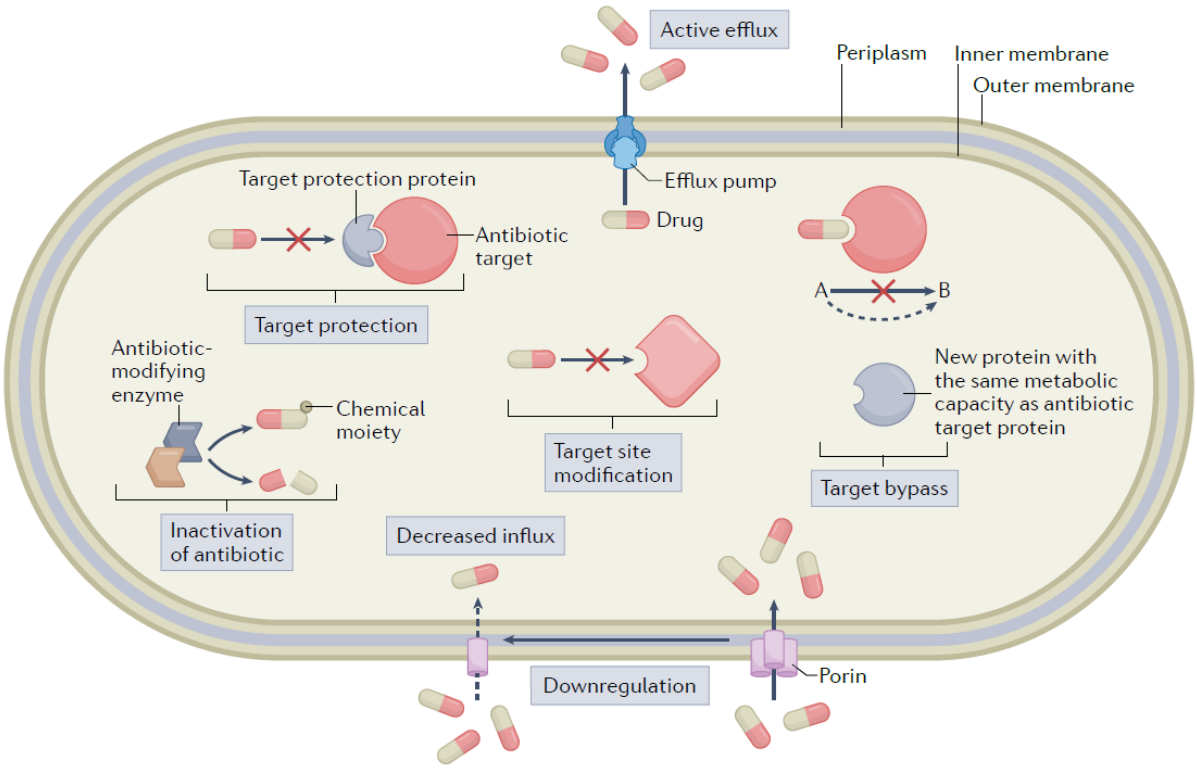

Figure 1.2. Overview of the molecular mechanisms of antibiotic resistance. Reproduced from Darby *et al*.[6]

Among the intrinsic resistance mechanisms, reduced cell permeability and efflux pumps are particularly important for resistance to antibiotics. The target of many antibiotics is located in the cytoplasm of bacterial cells, and thereby, the antibiotic needs to cross the cell membrane to reach it. Nevertheless, in case of Gram-negative bacterial cells, the impermeability of the double cell membrane prevents some antibiotics from crossing to the cytoplasm, and thereby reduces their activity.[21–23] Cell impermeably is, in fact, one of the most significant resistance factors in Gram-negative bacteria. Furthermore, changes in the membrane, such as loss of porins (β-barrel membrane proteins that act as pores for different substrates to penetrate the cell)[24] or alteration of phospholipids and fatty acids can also affect the ability of molecules to penetrate the cell.[21] Gram-positive bacterial cells, on the contrary, possess a simpler

cell membrane composed by a single cell membrane with no cell wall, that ease the transport of antibiotics inside the cell.

Efflux pumps are also one of the biggest AMR contributors alongside reduced cell permeability. Efflux pumps are transmembrane proteins that are able to transport a wide range of substrates, including antibiotics into the bacterial cell but also from the bacterial cell to the outside media. Efflux pumps are present in all bacterial cells but in Gram-negative species they are a major AMR contributor. Resistance-nodulation-division (RND) family of efflux pumps are those that specially confer the most clinically relevant resistance in Gram-negative species.[25,26] Furthermore, due to the ability of efflux pumps to transport a wide variety of antibiotics, their overexpression contributed to multidrug resistance.[27,28]

Furthermore, other AMR mechanisms are involved with the target structures of antibiotics. Target modification and protection also lead to resistance against those antibiotics that were meant to target those modified or protected structures. These modifications decrease the affinity between the antibiotic and the target structure, reducing, or even inhibiting the activity of the antibiotic.[7,29] For example, amino acids substitution in the target enzyme of quinolones reduced their affinity while not having any consequence for its activity of the abovementioned enzyme. Similarly, mutations in the PBP lead to decreased susceptibility to β-lactams.[30] Protection of binding sites can also be achieved by simple chemical modifications. Methylation of the target structure on the 16S rRNA results in protection against macrolides.[31] Addition of phosphoethanolamine groups to outer membrane lipopolysaccharides alters their structure and confers resistance against membrane disruptors like colistin.[32]

Finally, other AMR mechanisms directly tackle the antibiotic itself: antibiotic degradation of modification. The clearest example of antibiotic deactivation is β-lactam ring opening by β-lactamase enzymes. β-lactam deactivation is also the leading cause of carbapenem resistance, which has been listed as 'critical' priority by the World Health Organization.[33] Enzymatic oxidation of tetracyclines is also a common AMR mechanism.[34] Beside antibiotic degradation, affinity between antibiotic and its target structure can also be reduced by enzymatic modification of the antibiotic by acetyltransferases,[35] phosphotransferases,[36] nucleotidyltransferases,[37] glycosyltransferases,[38] ribosyltransferases[39] and monooxygenases,[40] among others.

1.2. Nanoparticles for antibiotic delivery

Due to the increase in AMR and its consequences, new approaches to combat resistant bacterial infections have been explored. One of the most explored approaches has been the design and synthesis of new antimicrobial agents able to overcome identified resistance mechanisms.[41] This approach consists of chemical modifications of current Food and Drug Administration (FDA)-approved antibacterial compounds, increasing their activity and overcoming resistance mechanism against them. However, this process is very time consuming.[5,42,43] In addition, due to the close resemblance of the new antibacterial agent to the parent molecule, resistance to the new antibiotic is identified shortly after its implementation in the clinic [44]

Thereby, nanotechnology has stood up as a promising toolbox for the development of new antibacterial therapies. In particular, nanoparticles have attracted the attention of the scientific community as drug delivery systems (DDS) due to their chemical versatility and promising results (Figure 1.3).[45,46] Nanoparticles are defined as

nanosized structures with dimensions between 1 and 100 nm. Nanoparticles can present different composition, structure, and morphology (Figure 1.3). Nanoparticles have been widely investigated as DDS.

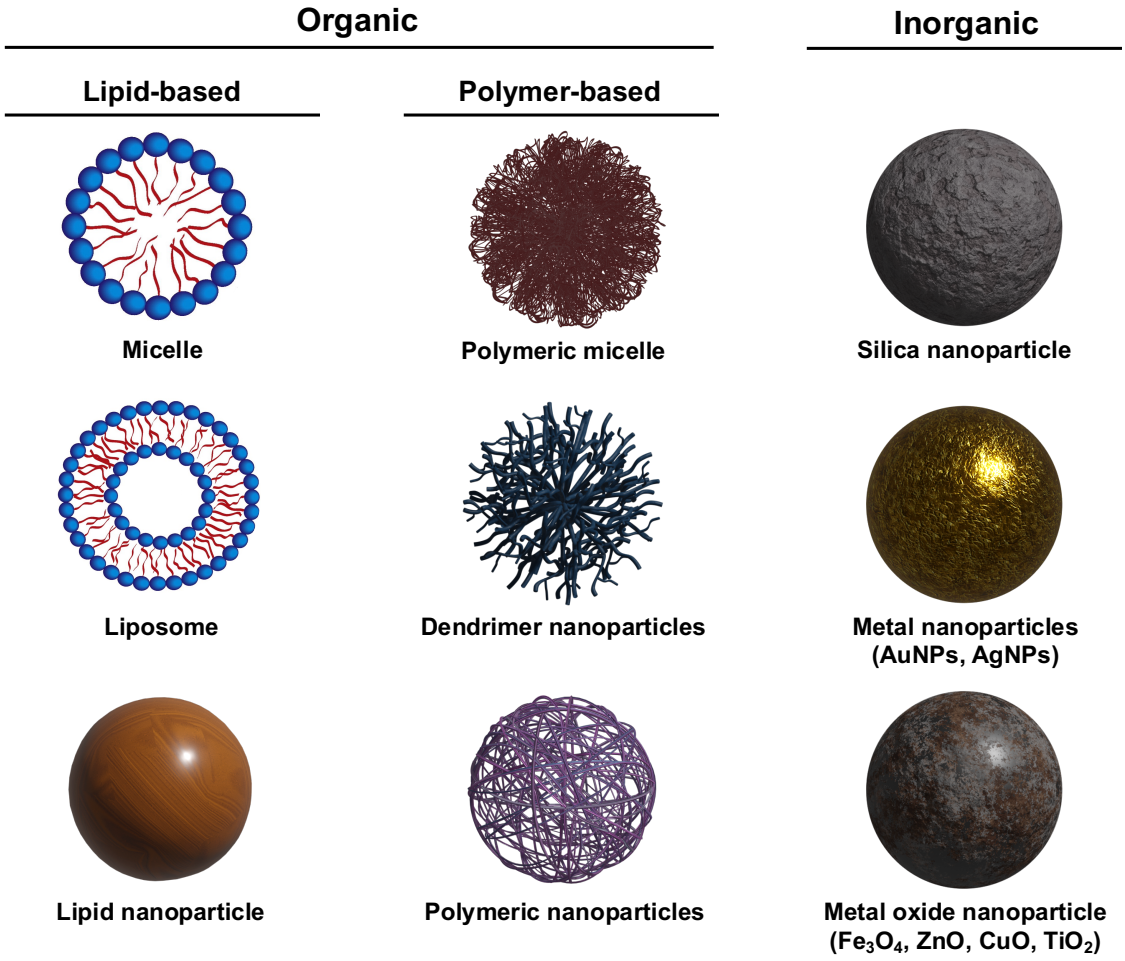

Figure 1.3. Classification of nanoparticles reported for antibiotic delivery. Micelle and liposome structure reproduced from Husseini *et al*.[47]

1.2.1. Silica nanoparticles for antibiotic delivery

Among the wide variety of nanoparticles investigated in the literature, silica nanoparticles (**SiO_2**) are a unique type of inorganic nanoparticles that have been extensively explored for antibacterial therapies with higher biocompatibility.[48–51] Due to their surface chemistry, **SiO_2** present a high colloidal stability and their facile synthesis allows the production of **SiO_2** with different sizes, morphologies and particle

structures (Figure 1.4).[50,52] Furthermore, the chemical versatility of the hydroxyl groups in nanoparticles surface allows surface functionalization of nanoparticles with a large library of moieties, leading to bespoke nanoparticles with unique properties.

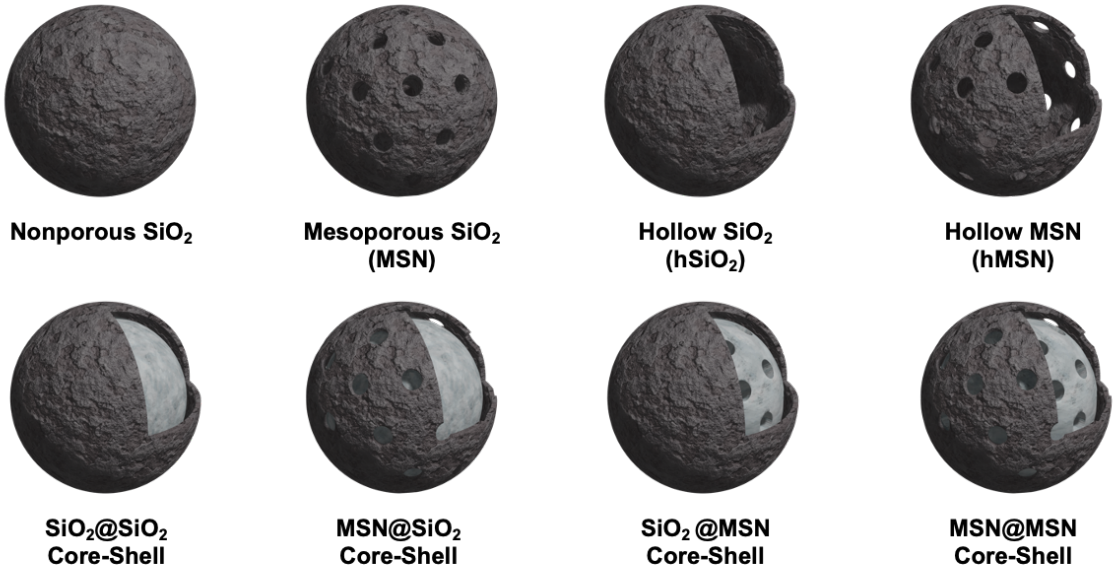

Figure 1.4. Representation of different **SiO_2** nanoparticles obtained following different synthetic methodologies.

1.2.1.1. Non-porous silica nanoparticles

The first described synthetic procedure for the production of **SiO_2** was reported by Stöber *et al.* in 1968; afterward named as 'Stöber synthesis'.[53] This methodology results in nonporous **SiO_2** with varying sizes between 50 nm and 2 μm. The silica framework formation has been widely investigated. The framework synthesis starts with the hydrolysis of the silane precursors, mostly tetraethoxysilane (TEOS) under basic or acidic conditions, leading to the silanol form of the precursor. Then, condensation between silanol groups creates siloxane species that keeps polymerizing to form a nucleus from which growth continues, forming the **SiO_2** particle (Figure 1.5).[53–55] Hydrolysis and condensation reaction take place simultaneously

during the **SiO_2** formation. The concentration of the catalyst, precursor, reaction time and temperature control the size and polydispersity of nanoparticles.[56,57]

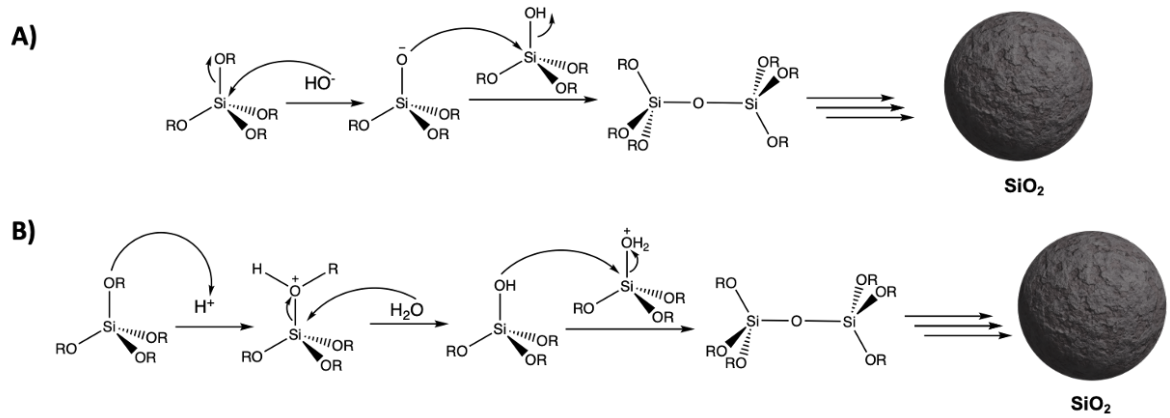

Figure 1.5. Mechanism of **SiO_2** framework synthesis under (A) basic or (B) acidic conditions.

The use of **SiO_2** as DDS has been widely investigated.[51,52,58–60] Due to the nanoparticle's non-porous structure, antibiotics cannot be adsorbed within nanoparticles framework once the particle has been formed. Thereby, two major strategies are followed for the development of antibiotic containing **SiO_2**: antibiotic inclusion within nanoparticles framework during synthesis and antibiotic conjugation onto nanoparticle surface (Figure 1.6).[61]

The most straightforward approach for the development of **SiO_2** containing antibiotics, is the antibiotic entrapment within the siliceous framework during particle formation. Briefly, nanoparticle synthesis takes place in an ethanolic solution that already contains the antibiotic of interest. The inclusion of the antibiotic is then driven by the interactions between the forming framework and the antibiotic. This is a crucial feature as the encapsulation efficiency (EE) of the antibiotic mainly relies on these interactions. This is one of the limiting factors for encapsulation if hydrophobic or negatively charged antibiotics.[61] Antibiotic such as tetracyclines,[62] gentamycin[63–65], rifampicin[63,66] or vancomycin[67] have been included into **SiO_2** nanoparticles and their

activity proven against Gram-negative bacterial cells. Furthermore, the major restriction of this approach is the low release efficiency of loaded nanoparticles, due to the low porosity of the network, diffusion of incorporated antibiotic is limited, leading to low release efficiency. However, the quantity of release could be enough for the intended application.[61]

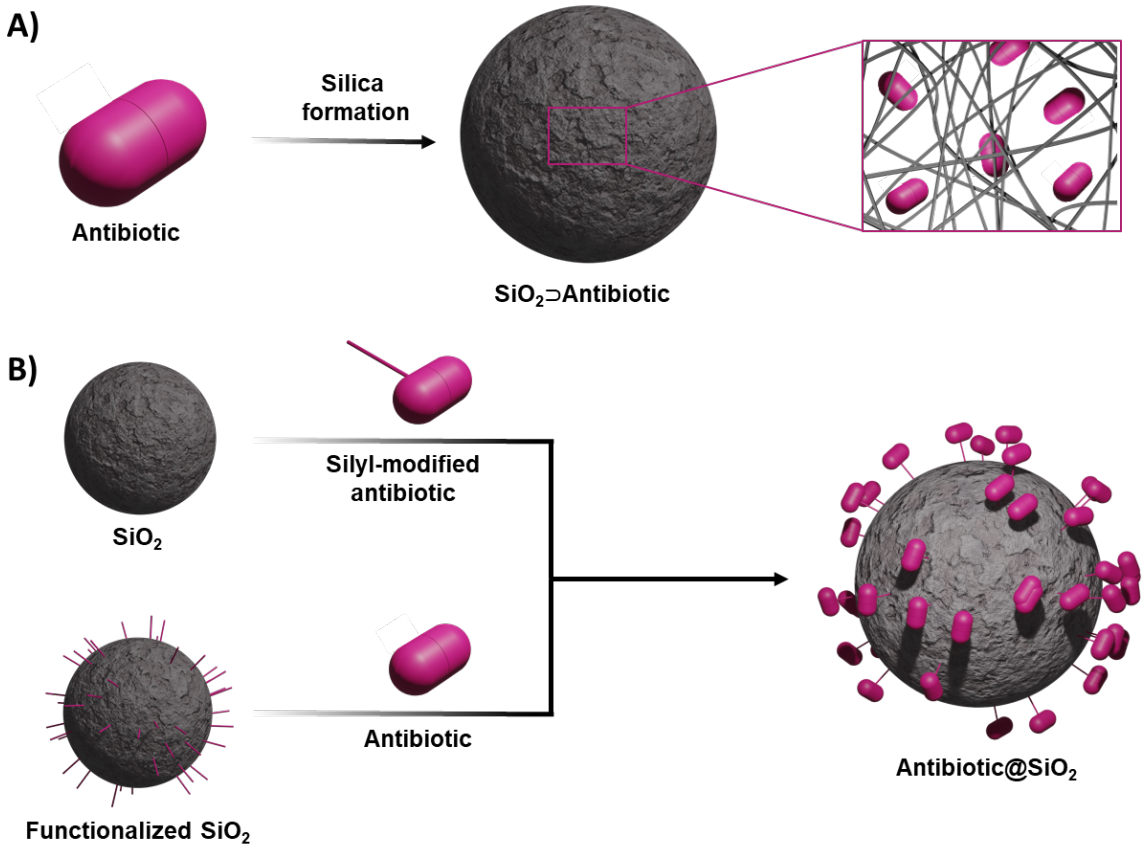

Figure 1.6. Strategies of nonporous **SiO_2** containing antibiotics production by (A) antibiotic inclusion during particle formation and (B) antibiotic conjugation onto nanoparticles surface.

Conjugation of antibiotic onto nanoparticles surface has been another explored strategy. The antibiotic conjugation can directly be achieved using a silyl-derivative antibiotic or can be achieved by reacting an antibiotic to an already conjugated functional group on the nanoparticle surface (Figure 1.6B). In this way antibiotics such as vancomycin[68–70] and fluoroquinolones[71–73] have been conjugated, among others,[74–

[76] and resulting nanoparticles have showed successful antibacterial activity. Nevertheless, the extra conjugation step or steps required for this approach limits its applications and the covalent modification of the antibiotic must be studied case by case not to affect the activity of the antibiotic.[77]

Beside low molecular weight antibiotics, antibacterial peptides have been also added onto **SiO_2** surface. Electrostatic interaction between cationic peptides and negatively charge **SiO_2** surface is the preferred strategy;[78,79] nevertheless, tailored approaches have been developed where covalent conjugation between the peptide and particle's surface has been achieved.[80]

1.2.1.2. Porous silica nanoparticles

The chemical versatility of the Stöber synthesis has also allowed the development of porous silica nanoparticles with pore sized within the meso (2 nm – 50 nm) or macro (> 50 nm) ranges. Materials with macropores usually present dimensions bigger than 1 μm and, thereby, they are not usually classified as nanomaterial. On the contrary, mesoporous silica nanoparticles (**MSNs**) have been widely employed as DDS for antibacterial purposes due to the possibility of using their mesopores as antibiotic reservoirs.[52,81]

Synthesis of **MSNs** is based on a modified Stöber synthesis were the presence of a liquid-phase tempted is required. The template is commonly a cationic surfactant able to form micellar aggregates at the beginning of the synthesis. After silica precursor addition, the siliceous framework is formed around the template driven by attractive electrostatic interaction between the cationic template and the negatively charge framework. Finally, and in order to make the formed porosity accessible to the

inclusion of antibiotics, the template must be fully removed or by calcination treatment of by acidic extraction (Figure 1.7). In fact, full removal of the templating agent is a crucial step in the development of **MSNs** as DDS due to the toxicity of the template.[48,82,83]

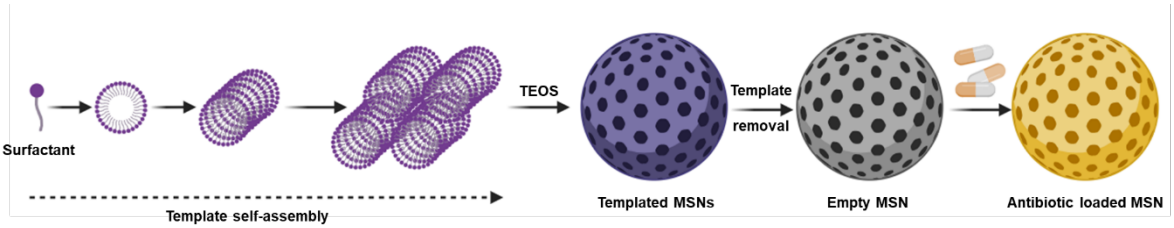

Figure 1.7. Scheme of the synthesis of MSNs using a liquid phase template, its removal after particle formation and antibiotic encapsulation.

The porous structure of **MSNs** is a result of the employed template during the synthesis. The most commonly reported **MSNs** topology MCM-41 (MCM = Mobile Composite Material), which consist on hexagonally arranged unidimensional periodic porosity formed using cetyltrimethylammonium chloride (CTAB) as templating agent.[84] Nevertheless, a large number of topologies have been achieved after changing the templating agent of the synthetic conditions (Figure 1.8).

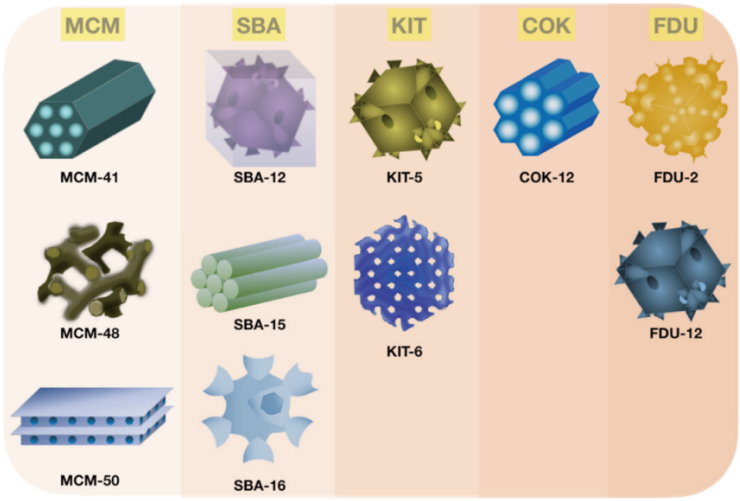

Figure 1.8. Structure of different **MSNs** reported as antibiotic DDS reproduced from Rastegari et al.[59] (SBA = Santa Barbara Amorphous materials, KIT = Korean Institute of Technology, COK = Centrum voor Oppervlaktechemie en Katalyse and FDU = Fudan University)

As previously mentioned, antibiotics can be encapsulated within the **MSNs** mesopores. Molecular antibiotic such us, aminoglycosides,[85–89] glycopeptides,[90,91] β-lactams,[86,92–96] fluoroquinolones,[87,97–103] macrolides,[104,105] tetracyclines[86,106] or ansamycins[87,107,108] have been encapsulated in **MSNs**. Nevertheless, due to the large pore size of **MSNs**, other bigger antimicrobial compounds, such us peptides, have been also encapsulated,[78,79,90,101,109,110] highlighting the versatility of these nanoparticles. Beside antibiotic encapsulation within the **MSNs** pores, antibacterial compounds have also been covalently anchored to **MSNs** surface, mostly antimicrobial peptides.[78,111,112]

Even though antibiotic loaded **MSNs** have resulted in promising nanomaterials against bacterial infections, they also suffer from uncontrollable leakage of included antibiotics as the pores are open to the outside media. This is one of their major limitations and surface modification and capping strategies has been investigated to prevent it.[60,113] Capping of loaded **MSNs** allows to better control the release of the antibiotic and prevent its leakage. Furthermore, with the right design of the capping stimuli responsive **MSNs** have been reported. antibiotic loaded **MSNs** responsive to light,[93] redox reactions,[114,115] temperature,[116] pH,[117–122] ultrasound[123–126] or enzymes[121,127] have been developed by choosing the right surface coating. Similarly, coating of **MSNs** with lipidic shells[107,128,129] or cationic polymers[122,130,131] has proven to increase nanoparticle internalization into bacterial cells while controlling the leakage of loaded antibiotic.

1.2.1.3. Organosilica and polysilesquioxane nanoparticles

Beyond **SiO_2** with frameworks purely composed by silicon and oxygen atoms, the chemical versatility of the Stöber synthesis has allowed the development of silica nanoparticles with high organic content incorporated within the framework. These new nanoparticles are obtained by simple addition of organosilane precursors (Figure 1.9A-B) to the previously explained synthesis, or by fully substituting TEOS with an organosilica precursor.[58,132] Organosilane precursor may contain one silane group, which would lead to **SiO_2** framework with organic pendant groups (Figure 1.9A and 1.9C); or with two or more silane functionalizations, resulting in amorphous frameworks where the organic moieties are part of the framework itself, bridging silicon atoms (Figure 1.9B and 1.9D). The first class of nanoparticles are known as Organically modified silica (**Ormosil**) and the second class are classified as polysilesquioxane (**PSQ**) nanoparticles. Similarly, if these frameworks are templated to achieve porosity, Mesoporous Organosilica Nanoparticles (**MONs**) or Periodic Mesoporous Organosilica (**PMOs**) namely particles can be obtained, respectively (Figure 1.9D).[58,133]

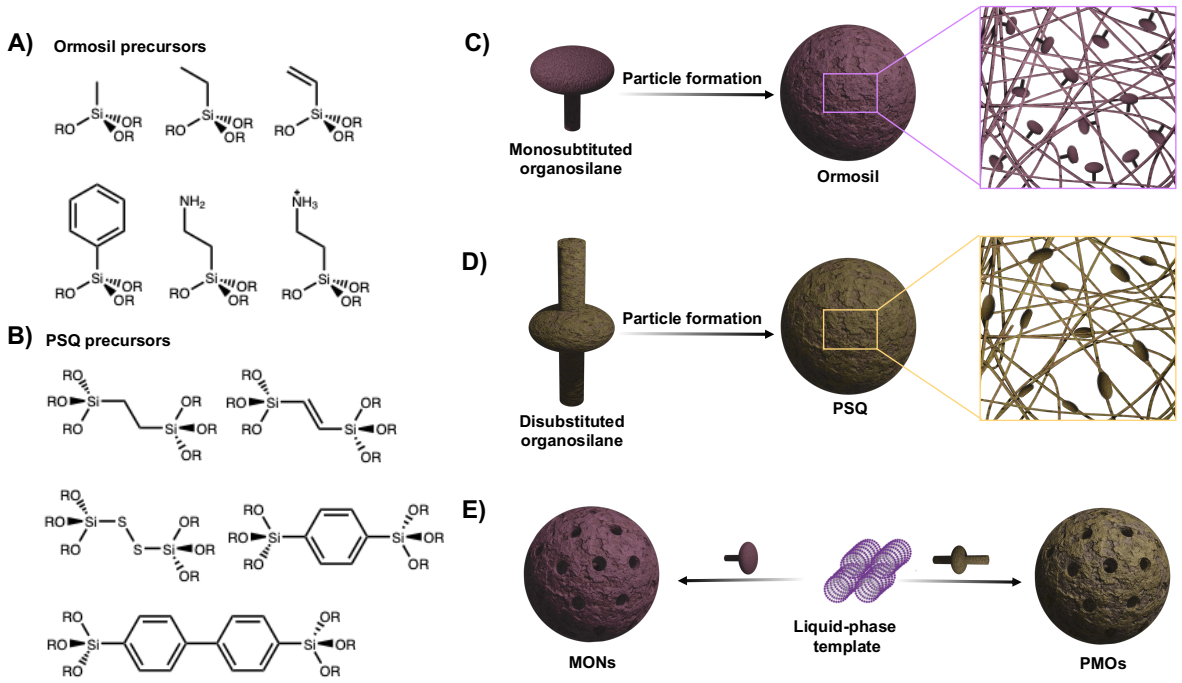

Figure 1.9. (A, B) Chemical structure of most commonly reported precursors (-OR = alkoxy group) and synthesis and illustrative scheme of the framework composition of (C) organosilica modified nanoparticles (**Ormosil**), (E) polysilesquioxane nanoparticles (**PSQ**) and (E) mesoporous organosilica nanoparticles (**MONs**) and periodic mesoporous organosilica (**PMOs**) nanoparticles.

Due to their high organic content and chemical versatility, these nanoparticles have attracted the attention of the scientific community. Their use has been explored for many applications including sensing,[134] pollutant removal,[135] membrane development,[136] catalysis[137] or precursor for carbon-based materials.[138] Their use as DDS in the literature is very limited, focusing more in the aforementioned applications.

The presence of organic moieties is, however, very attractive for the development of DDS as interaction between framework and included drug can be tuned by modifying the organosilica precursor.[86,139,140] Furthermore, upon direct comparison with the well-known **SiO_2**, introducing bulky organic groups within the nanoparticle's framework can also increase the porosity of the framework,[136,141] and thereby, enhance the diffusion of included cargos, leading to higher release efficiency.

Most studied cargos have been anticancer compounds such us doxorubicin,[142,143] metformin[144] and paclitaxel.[145,146] However, to our knowledge **Ormosil** or **PSQ** nanoparticles have not been explored for antibiotic delivery. **MONs** and **PMOs** nanoparticles have been increasingly explored as antibiotic DDS due to their porous structure, which lead to uncontrolled burst release of the cargo, as explained for **MSNs**. Antibiotic such us ciprofloxacin,[147] rifampicin[148] and gentamycin[149] have been adsorbed into the porous structure of these nanoparticles.

Another advantage of **PSQ** and **PMOs** nanoparticles relies on the reactivity of the organic bridges within the framework. Stimuli responsive nanostructures have been reported.[142,144,150,151] For instance, H. Mekaru *et al.* reported a **PSQ** nanoparticle with disulphide bridges within the framework that in presence of glutathione (GHS) the disulphide bridged are reduced, the framework degraded and thereby, included cargo (dye) release.[152]

1.2.1.4. Hybrid silica nanoparticles for therapy and imaging

As previously mentioned, silica nanoparticles have been widely explored as drug delivery system due to their ability to encapsulate a therapeutic agent for later targeted delivery. However, other molecules with properties useful for sensing and diagnostics have also been included within the siliceous framework of silica nanoparticles. Luminescent agents, such as, organic fluorophores, transition metals complexes or lanthanide complexes, are a clear example of this. Encapsulation of luminescent molecules lead to silica nanoparticles with emissive properties, with ability to be imaged by commonly used confocal microscopes. In this way, tracking of particles in

living systems by luminescence-based microscopy techniques has aided understanding of the interactions of nanoparticles with cells and tissues.

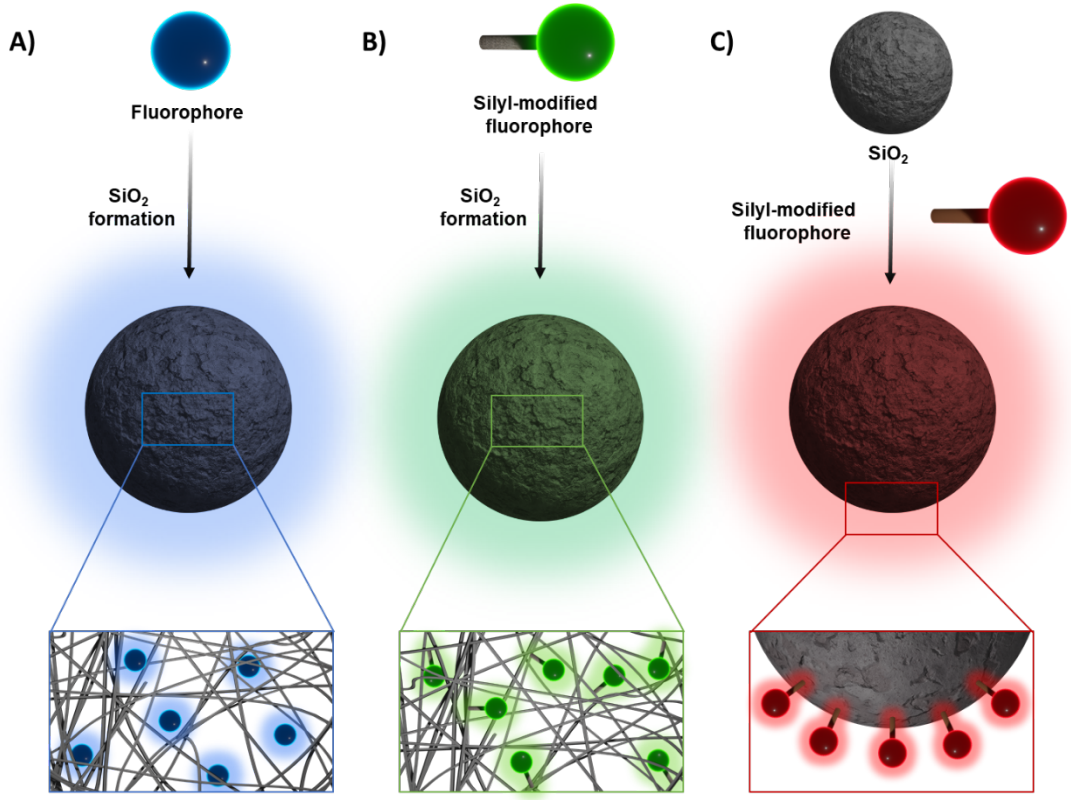

Figure 1.10. Scheme of emissive **SiO_2** formation by (A) fluorophore inclusion during particle formation and graphing of silyl-derivative fluorophores in nanoparticles (B) framework and (C) surface.

Similarly, as when silica nanoparticles are employed as drug delivery systems, luminescent agents can be directly included into the silica framework *via* silica formation in presence of the agent, or by adsorption of desired imaging agent into the pore of porous silica nanoparticles (Figure 1.10). Nevertheless, the release of the imaging agent is avoided due to their toxicity and to prevent staining of cells and tissues by released agents, which could interfere with nanoparticle's imaging.[153–156] In fact, covalent anchoring of the imaging agent to the frameworks is one of the most common approaches. In this way, organic fluorophores such as fluorescein[92,157–159] or

rhodamine B[158] (Figure 1.11)have been anchored to the framework, in porous and non-porous silica particles. Likewise, ruthenium(II)[160–164] or iridium(III)[165–168] complexes (Figure 1.11) have been chemically designed to contain at least one ligand that can be anchored to the silica surface or framework. Finally, in case of silica nanoparticles with embedded lanthanide complexes, the most followed strategy has been to decorate the pore walls of MSNs with a chelating ligand for the subsequent complexation of the lanthanide cation, in presence or not of an ancillary ligand.[169–173] Furthermore, nonporous silica nanoparticles with included positively charged imaging agents have shown minimal leakage of the included agent due to the electrostatic interactions with the negatively charged siliceous framework.[174–178]

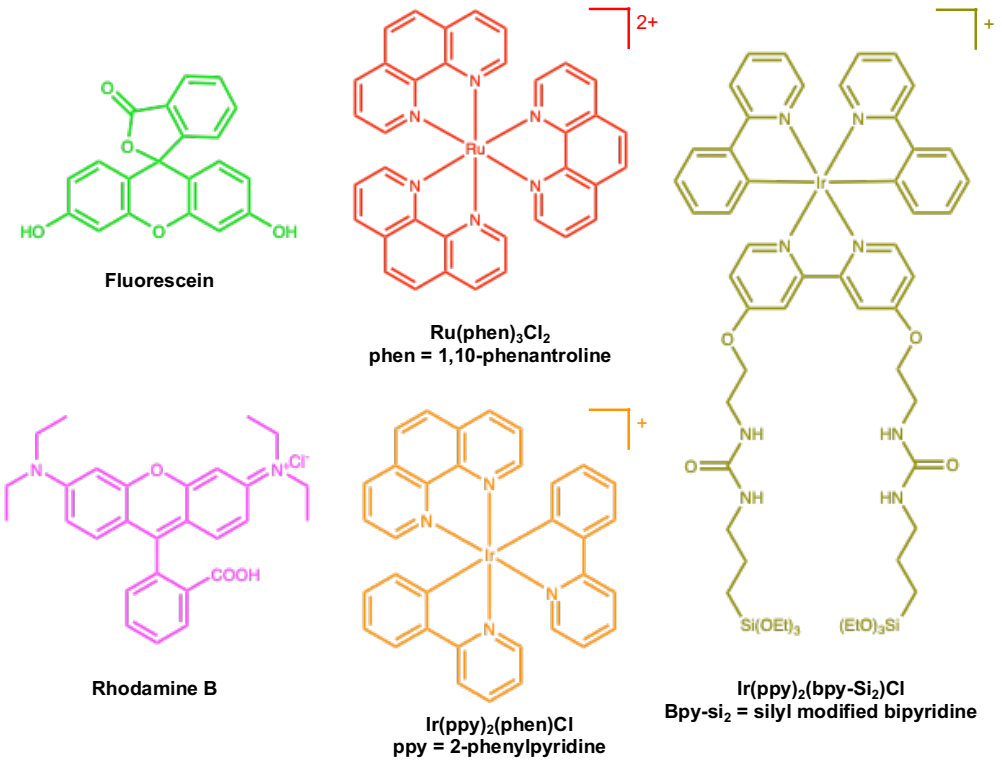

Figure 1.11. Chemical structure of most commonly explored fluorophores for development of emissive **SiO_2** for cell imaging.

Even though described emissive nanoparticles have been previously reported to study nanoparticle-cell interactions as analogue particles to those containing the therapeutic agent; the use of hybrid silica nanoparticles containing simultaneously an imaging and a therapeutic agent is less common in the literature. The advantage of a hybrid nanoparticle over a single-loaded emissive nanoparticle is that the use of these single loaded emissive nanoparticles assumes that emissive particles and particles containing the therapeutic agents would have the same behaviour, interaction and even uptake.

Reported hybrid nanoparticles for therapy and imaging have been mainly designed using an organic fluorophore as imaging agent for the delivery of anticancer drugs. To our knowledge, the only example of silica nanoparticle for antibiotic delivery also containing an imaging agent was reported by G. F. Andrade *et al.*[99], where they conjugated a Tc-99m complex to the surface of ciprofloxacin loaded SBA-16 MSNs, allowing radio imaging in bones during antibiotic release. Addition of antibiotic to fluorescent silica nanoparticles have been, however, previously explored but for detection purposes.[92,179,180]

1.2.2. Other nanoparticles for antibiotic delivery

Beside silica-based nanoparticles, other nanoparticles, inorganic and organic have been studied for the delivery of antibiotics. In this section we would like to give insight in their use as DDS, their advantages but also their limitations.

1.2.2.1. Organic nanoparticles

Organic nanoparticles can be subclassified in lipid-based and polymer-based nanoparticles. Lipid-based nanoparticles, such as, lipidic micelles, vesicles or

emulsion formulations were the first studied nanoparticle for the delivery of bioactive compounds due to their high biocompatibility.[181,182] Antibiotic such as β-lactams[183], glycopeptides,[184] and ansamycins[185] have been included in lipid-based nanoparticles. Furthermore, their composition and rheology properties can be easily modulated by altering the proportion of the lipid used. Surface functionalization of these nanoparticle also differs from the **SiO_2** surface chemistry, as functionalization is achieved through introduction of amphiphile groups with determined functionality rather than through direct chemical modification of existing surface.[186] Nevertheless, these nanoparticles are only stable in solution and are very susceptible in pH and temperature changes, resulting in a limitation for their production and distribution.[181]

Polymer-based nanoparticles have been also extensively explored.[182,187,188] Polymer-based nanoparticles include polymeric micelles, dendrimers, and polymer nanoparticles. The biggest advantage of polymer-based materials is their easy and diverse chemical versatility.[187] Polymer-based nanoparticles' properties can be tuned relatively easily by chemically modifying the monomer of interest or combining different monomer as in case of copolymeric nanoparticles. This chemical versatility also allows conjugation of antibiotics to the polymer chain via a pH- [189], light-[190,191] or enzyme-responsible[189] bond for their triggered release, rather than direct encapsulation of antibiotics inside the nanoparticles. Encapsulation of hydrophobic molecules can be also easily achieved in hydrophobic-core polymer nanoparticles or using amphiphile polymeric structures.[192] Nevertheless, polymer-based nanoparticles also present some limitations mostly associated with their scale-up processes and unknown toxicity.[193,194] In fact, while degradation of other nanoparticles is a well-known process, and their toxicity has been explored.[193,195] The large variety of developed polymer-

based nanoparticles has hindered the study of their degradation processes and the toxicity related to them.

1.2.2.2. Inorganic nanoparticles

The use of inorganic nanoparticles in the delivery of antibiotic is less extensive in the literature compared with **SiO_2** or organic particles due to their bulk, nonporous structure, in most of the cases. Nevertheless, advances in their application as antibiotic DDS have been achieved.[196–198]

Metal nanoparticles, such as gold or silver nanoparticles (**AuNPs** and **AgNPs**, respectively) have been reported for the delivery of antibiotics.[199–201] Due to their dense face cantered cubic (fcc) packing, antibiotics have been conjugated onto nanoparticle surface through bottom-up and top-down approaches yielding in metal nanoparticles coated with antibiotic containing ligands or polymers.[202–204] Similarly, direct conjugation through electrostatic or Au···N or Au···S bonding between amino or thiol-containing antibiotics such as β-lactams has been reported.[205,206] Another more one-step approach is the use of an antibiotic as capping and reducing agent, as it is the case of bromelain (antibacterial proteolytic enzyme).[207] On the contrary, this one-step reaction also requires for the oxidised product to be fully removed from the formulation. Metal nanoparticles such as **CuNPs** or **ZnNPs** present synergistic activity when loaded with antibiotic due to the slow release of metallic cations, that can produce reactive oxygen species (ROS).[208–210] The changes on the optical properties of metal nanoparticles, such as the surface plasmon resonance (SPR), have also been employed to confirm the loading of antibitoic.[211]

Unfortunately, most of metal nanoparticles also display high production cost in scale-up processes, their translation to the clinic has been hindered.[212]

Similar to metal nanoparticles, metal oxide nanoparticles, such as **Fe_3O_4**, **ZnO** or **TiO_2** have been reviewed in the literature as antibiotic DDS.[213] Antibiotics have also been conjugated to the surface of these nanoparticles through electrostatic or covalent interactions.[214–216] The main advantage of these nanoparticles is their chemical and physical properties. For instance, the magnetic properties of **Fe_3O_4** have been widely employed for the development of magnetic DDS that allow an easy recovery of nanoparticles. Magnetic resonance imaging has also been used with antibiotic-**Fe_3O_4** nanoparticles for their imaging in cells and tissues.[217,218] Furthermore, magnetic hyperthermia has been employed alongside antibiotic delivery for more efficient antibacterial treatments.[219] Synergy between delivered antibiotic and ROS production has been also another advantage of using metal oxide nanoparticles like **CeO_2** for antibiotic delivery upon UV irradiation.[208,220]

Even though metal oxide nanoparticles' structure is a dense packing, porous metal oxide nanoparticles can also be produced with a templating agent.[221] Porous **TiO_2** nanoparticles (**MTNs**) is one of the most well described systems. Antibiotic has been included in **MTNs** and similar strategies used in **MSNs** applied for their targeted delivery.[222,223]

1.3. Research aims

There is a need for new antibacterial therapies that are able to overcome the AMR mechanisms that bacteria have against current antibiotics. In this context nanoparticles present a very promising platform for the development of DDS able to tackle resistant infections.

The efficacy of nanoparticles as DDSs depends on their ability to interact with bacterial cells and on their release efficiency. Therefore, the overall aim of this thesis is to explore new surface and framework modifications in **SiO_2** nanoparticles for more efficient delivery of antibiotics. To achieve this, different approaches have been explored:

- **SiO_2** nanoparticles containing a cell non-permeable antibiotic were modified with a cell permeating agent to accomplish efficient antibiotic delivery inside the bacterial cell, and thereby, making this antibiotic active. Moreover, nanoparticles were developed to simultaneously bear a luminescent metal complex alongside the antibiotic, allowing nanoparticle tracking while drug release occurred.
- Modification of **SiO_2** nanoparticles was further explored by cation chelation in previously developed coating, leading to a cell-recognisable surface coating. Interactions between bacterial cells and novel nanoparticles were investigated and the involved cell surface receptors identified for the enhancement of **SiO_2** internalization in cells. Furthermore, a molecular analogue was designed and synthetized to evaluate if nanoparticles followed the same mechanism of internalization than their molecular analogue.
- Photoresponsive **SiO_2** nanoparticles were designed by framework modification with a photoswichable precursor for the light triggered release of a first line antibiotic against urinary tract infections. The effect of the antibiotic within the framework was investigated alongside its light triggered release. Furthermore, the activity of novel nanoparticle was evaluated against clinal isolates.
- Finally, different strategies based on framework modification were studied to enhance the inclusion of hydrophobic antibiotics in **SiO_2** nanoparticles.

Inclusion was enhanced by entrapment within antimicrobial micelles prior nanoparticle encapsulation and by using an organically-bridged precursor. The antibiotic release performance was explored and compared with more common **SiO_2** nanoparticles and encapsulation approaches.

1.4. References

1 C. J. Murray, K. S. Ikuta, F. Sharara, L. Swetschinski, G. Robles Aguilar, A. Gray, C. Han, C. Bisignano, P. Rao, E. Wool, S. C. Johnson, A. J. Browne, M. G. Chipeta, F. Fell, S. Hackett, G. Haines-Woodhouse, B. H. Kashef Hamadani, E. A. P. Kumaran, B. McManigal, R. Agarwal, S. Akech, S. Albertson, J. Amuasi, J. Andrews, A. Aravkin, E. Ashley, F. Bailey, S. Baker, B. Basnyat, A. Bekker, R. Bender, A. Bethou, J. Bielicki, S. Boonkasidecha, J. Bukosia, C. Carvalheiro, C. Castañeda-Orjuela, V. Chansamouth, S. Chaurasia, S. Chiurchiù, F. Chowdhury, A. J. Cook, B. Cooper, T. R. Cressey, E. Criollo-Mora, M. Cunningham, S. Darboe, N. P. J. Day, M. De Luca, K. Dokova, A. Dramowski, S. J. Dunachie, T. Eckmanns, D. Eibach, A. Emami, N. Feasey, N. Fisher-Pearson, K. Forrest, D. Garrett, P. Gastmeier, A. Z. Giref, R. C. Greer, V. Gupta, S. Haller, A. Haselbeck, S. I. Hay, M. Holm, S. Hopkins, K. C. Iregbu, J. Jacobs, D. Jarovsky, F. Javanmardi, M. Khorana, N. Kissoon, E. Kobeissi, T. Kostyanev, F. Krapp, R. Krumkamp, A. Kumar, H. H. Kyu, C. Lim, D. Limmathurotsakul, M. J. Loftus, M. Lunn, J. Ma, N. Mturi, T. Munera-Huertas, P. Musicha, M. M. Mussi-Pinhata, T. Nakamura, R. Nanavati, S. Nangia, P. Newton, C. Ngoun, A. Novotney, D. Nwakanma, C. W. Obiero, A. Olivas-Martinez, P. Olliaro, E. Ooko, E. Ortiz-Brizuela, A. Y. Peleg, C. Perrone, N. Plakkal, A. Ponce-de-Leon, M. Raad, T. Ramdin, A. Riddell, T. Roberts, J. V. Robotham, A. Roca, K. E. Rudd, N. Russell, J. Schnall, J. A. G. Scott, M. Shivamallappa, J. Sifuentes-Osornio, N. Steenkeste, A. J. Stewardson, T. Stoeva, N. Tasak, A. Thaiprakong, G. Thwaites, C. Turner, P. Turner, H. R. van Doorn, S. Velaphi, A. Vongpradith, H. Vu, T. Walsh, S. Waner, T. Wangrangsimakul, T. Wozniak, P. Zheng, B. Sartorius, A. D. Lopez, A. Stergachis, C. Moore, C. Dolecek and M. Naghavi, *Lancet*, 2022, **399**, 629–655.

2 V. Ratcheva, S. Zahidi, K. K. Pal, K. Piaget, S. Baller and W. E. Forum., *Global risk report 2023*, 2023.

3 J. O'Neill, *Rev. Antimicrob. Resist.*, 2016, **7**, 110.

4 D. M. P. De Oliveira, B. M. Forde, T. J. Kidd, P. N. A. Harris, M. A. Schembri, S. A. Beatson, D. L. Paterson and M. J. Walker, *Clin. Microbiol. Rev.*, 2020, **33**, e00181-19.

5 M. Hutchings, A. Truman and B. Wilkinson, *Curr. Opin. Microbiol.*, 2019, **51**, 72–80.

6 E. M. Darby, E. Trampari, P. Siasat, M. S. Gaya, I. Alav, M. A. Webber and J.

M. A. Blair, *Nat. Rev. Microbiol.*, 2022, **21**, 280–295.

7 F. Baquero and B. R. Levin, *Nat. Rev. Microbiol.*, 2021, **19**, 123–132.

8 B. D. Davis, L. Chen and P. C. Tai, *Proc. Natl. Acad. Sci. U. S. A.*, 1986, **83**, 6164–6168.

9 L. M. Lima, B. N. M. da Silva, G. Barbosa and E. J. Barreiro, *Eur. J. Med. Chem.*, 2020, **208**, 112829.

10 D. Zeng, D. Debabov, T. L. Hartsell, R. J. Cano, S. Adams, J. A. Schuyler, R. McMillan and J. L. Pace, *Cold Spring Harb. Perspect. Med.*, 2016, **6**, a026989.

11 N. Vázquez-Laslop and A. S. Mankin, *Trends Biochem. Sci.*, 2018, **43**, 668–684.

12 S. Correia, P. Poeta, M. Hébraud, J. L. Capelo and G. Igrejas, *J. Med. Microbiol.*, 2017, **66**, 551–559.

13 H. G. Floss and T. W. Yu, *Chem. Rev.*, 2005, **105**, 621–632.

14 O. Sköld, *Drug Resist. Updat.*, 2000, **3**, 155–160.

15 J. L. Markley and T. A. Wencewicz, *Front. Microbiol.*, 2018, **9**, 1–22.

16 F. F. Andrade, D. Silva, A. Rodrigues and C. Pina-Vaz, *Microorganisms*, 2020, **8**, 1–12.

17 W. R. Miller, J. M. Munita and C. A. Arias, *Expert Rev. Anti. Infect. Ther.*, 2014, **12**, 1221–1236.

18 L. S. Redgrave, S. B. Sutton, M. A. Webber and L. J. V. Piddock, *Trends Microbiol.*, 2014, **22**, 438–445.

19 G. H. Hitchings, *J. Infect. Dis.*, 1973, **128**, S433–S436.

20 B. Roth, E. A. Falco and G. H. Hitchings, *J. Med. Chem.*, 1962, **5**, 1103–1123.

21 L. Fernández and R. E. W. Hancock, *Clin. Microbiol. Rev.*, 2012, **25**, 661–681.

22 J. Ude, V. Tripathi, J. M. Buyck, S. Söderholm, O. Cunrath, J. Fanous, B. Claudi, A. Egli, C. Schleberger, S. Hiller and D. Bumann, *Proc. Natl. Acad. Sci. U. S. A.*, 2021, **118**, 1–8.

23 A. Kumar and H. P. Schweizer, *Adv. Drug Deliv. Rev.*, 2005, **57**, 1486–1513.

24 S. Acosta-Gutiérrez, L. Ferrara, M. Pathania, M. Masi, J. Wang, I. Bodrenko, M. Zahn, M. Winterhalter, R. A. Stavenger, J. M. Pagès, J. H. Naismith, B. Van Den Berg, M. G. P. Page and M. Ceccarelli, *ACS Infect. Dis.*, 2018, **4**, 1487–1498.

25 I. Alav, J. Kobylka, M. S. Kuth, K. M. Pos, M. Picard, J. M. A. Blair and V. N. Bavro, *Chem. Rev.*, 2021, **121**, 5479–5596.

26 K. Tsutsumi, R. Yonehara, E. Ishizaka-Ikeda, N. Miyazaki, S. Maeda, K. Iwasaki, A. Nakagawa and E. Yamashita, *Nat. Commun.*, 2019, **10**, 1520–1529.

27 K. Wang, J. Burban and E. Cusster, in *Responsive Gels: Volume Transitions*

II. Advances in Polymer Science, ed. K. Dusek, Springer Berlin, Heidelberg, 1993, pp. 67–79.

28 D. Du, X. Wang-Kan, A. Neuberger, H. W. van Veen, K. M. Pos, L. J. V. Piddock and B. F. Luisi, *Nat. Rev. Microbiol.*, 2018, **16**, 523–539.

29 N. G. Bush, I. Diez-Santos, L. R. Abbott and A. Maxwell, *Molecules*, 2020, **25**, 5662.

30 A. Zapun, C. Contreras-Martel and T. Vernet, *FEMS Microbiol. Rev.*, 2008, **32**, 361–385.

31 R. Bhujbalrao and R. Anand, *J. Am. Chem. Soc.*, 2019, **141**, 1425–1429.

32 R. Elias, A. Duarte and J. Perdigão, *Diagnostics*, 2021, **11**, 1165–1185.

33 C. L. Tooke, P. Hinchliffe, E. C. Bragginton, C. K. Colenso, V. H. A. Hirvonen, Y. Takebayashi and J. Spencer, *J. Mol. Biol.*, 2019, **431**, 3472–3500.

34 K. J. Forsberg, S. Patel, T. A. Wencewicz and G. Dantas, *Chem. Biol.*, 2015, **22**, 888–897.

35 C. G. Liu, S. I. Green, L. Min, J. R. Clark, K. C. Salazar, A. L. Terwilliger, H. B. Kaplan, B. W. Trautner, R. F. Ramig and A. W. Maresso, *MBio*, 2020, **11**, 1–19.

36 P. Spanogiannopoulos, N. Waglechner, K. Koteva and G. D. Wright, *Proc. Natl. Acad. Sci. U. S. A.*, 2014, **111**, 7102–7107.

37 M. S. Ramirez and M. E. Tolmasky, *Drug Resist. Updat.*, 2010, **13**, 151–171.

38 P. Spanogiannopoulos, M. Thaker, K. Koteva, N. Waglechner and G. D. Wright, *Antimicrob. Agents Chemother.*, 2012, **56**, 5061–5069.

39 A. Rominski, A. Roditscheff, P. Selchow, E. C. Böttger and P. Sander, *J. Antimicrob. Chemother.*, 2017, **72**, 376–384.

40 K. Koteva, G. Cox, J. K. Kelso, M. D. Surette, H. L. Zubyk, L. Ejim, P. Stogios, A. Savchenko, D. Sørensen and G. D. Wright, *Cell Chem. Biol.*, 2018, **25**, 403-412.e5.

41 M. Miethke, M. Pieroni, T. Weber, M. Brönstrup, P. Hammann, L. Halby, P. B. Arimondo, P. Glaser, B. Aigle, H. B. Bode, R. Moreira, Y. Li, A. Luzhetskyy, M. H. Medema, J. L. Pernodet, M. Stadler, J. R. Tormo, O. Genilloud, A. W. Truman, K. J. Weissman, E. Takano, S. Sabatini, E. Stegmann, H. Brötz-Oesterhelt, W. Wohlleben, M. Seemann, M. Empting, A. K. H. Hirsch, B. Loretz, C. M. Lehr, A. Titz, J. Herrmann, T. Jaeger, S. Alt, T. Hesterkamp, M. Winterhalter, A. Schiefer, K. Pfarr, A. Hoerauf, H. Graz, M. Graz, M. Lindvall, S. Ramurthy, A. Karlén, M. van Dongen, H. Petkovic, A. Keller, F. Peyrane, S. Donadio, L. Fraisse, L. J. V. Piddock, I. H. Gilbert, H. E. Moser and R. Müller, *Nat. Rev. Chem.*, 2021, **5**, 726–749.

42 A. Zorzet, *Ups. J. Med. Sci.*, 2014, **119**, 170–175.

43 L. L. Silver, *Clin. Microbiol. Rev.*, 2011, **24**, 71–109.

44 U. Theuretzbacher, *Curr. Opin. Pharmacol.*, 2011, **11**, 433–438.

45 J. M. V. Makabenta, A. Nabawy, C. H. Li, S. Schmidt-Malan, R. Patel and V. M. Rotello, *Nat. Rev. Microbiol.*, 2021, **19**, 23–36.

46 M. J. Mitchell, M. M. Billingsley, R. M. Haley, M. E. Wechsler, N. A. Peppas and R. Langer, *Nat. Rev. Drug Discov.*, 2021, **20**, 101–124.

47 G. A. Husseini and W. G. Pitt, *Adv. Drug Deliv. Rev.*, 2008, **60**, 1137–1152.

48 Y. Shi, M. L. Miller and A. J. Di Pasqua, *Comments Inorg. Chem.*, 2016, **36**, 61–80.

49 A. Ali, M. Ovais, X. Cui, Y. Rui and C. Chen, *Chem. Res. Toxicol.*, 2020, **33**, 1082–1109.

50 T. I. Janjua, Y. Cao, C. Yu and A. Popat, *Nat. Rev. Mater.*, 2021, **6**, 1072–1074.

51 A. Lérida-Viso, A. Estepa-Fernández, A. García-Fernández, V. Martí-Centelles and R. Martínez-Máñez, *Adv. Drug Deliv. Rev.*, 2023, **201**, 115049.

52 M. Vallet-Regí, F. Schüth, D. Lozano, M. Colilla and M. Manzano, *Chem. Soc. Rev.*, 2022, **51**, 5365–5451.

53 W. Stöber and A. Fink, *J. Colloid Interface Sci.*, 1968, **26**, 62–69.

54 V. K. LaMer and R. H. Dinergar, *J. Am.Chem.Soc.*, 1950, **72**, 4847–4854.

55 C. B. Whitehead, S. Özkar and R. G. Finke, *Mater. Adv.*, 2021, **2**, 186–235.

56 V. Candela-Noguera, M. Alfonso, P. Amoros, E. Aznar, M. Dolores Marco and R. Martines-Manez, *Microporous Mesoporous Mater.*, 2024, **363**, 112840.

57 L. F. Ferreira, G. F. Giordano, A. L. Gobbi, M. H. O. Piazzetta, G. R. Schlender and R. S. Lima, *ACS Sensors*, 2022, **7**, 1045–1057.

58 J. G. Croissant, X. Cattoën, M. Wong Chi Man, J. O. Durand and N. M. Khashab, *Nanoscale*, 2015, **7**, 20318–20334.

59 E. Rastegari, Y. J. Hsiao, W. Y. Lai, Y. H. Lai, T. C. Yang, S. J. Chen, P. I. Huang, S. H. Chiou, C. Y. Mou and Y. Chien, *Pharmaceutics*, 2021, **13**, 1–56.

60 P. Yang, S. Gai and J. Lin, *Chem. Soc. Rev.*, 2012, **41**, 3679–3698.

61 L. Tang and J. Cheng, *Nano Today*, 2013, **8**, 290–312.

62 L. Brentano Capeletti, L. F. de Oliveira, K. de Almeida Gonçalves, J. F. Affonso de Oliveira, Â. Saito, J. Kobarg, J. H. Zimnoch dos Santos and M. B. Cardoso, *Langmuir*, 2014, **30**, 7456–7464.

63 A. M. Mebert, C. Aimé, G. S. Alvarez, Y. Shi, S. A. Flor, S. E. Lucangioli, M. F. Desimone and T. Coradin, *J. Mater. Chem. B*, 2016, **4**, 3135–3144.

64 V. Purcar, V. Rădiţoiu, C. Nichita, A. Bălan, A. Rădiţoiu, S. Căprărescu, F. M. Raduly, R. Manea, R. Şomoghi, C. A. Nicolae, I. Raut and L. Jecu, *Materials (Basel).*, 2021, **14**, 2086–2098.

65 M. N. Seleem, P. Munusamy, A. Ranjan, H. Alqublan, G. Pickrell and N. Sriranganathan, *Antimicrob. Agents Chemother.*, 2009, **53**, 4270–4274.

66 G. S. Alvarez, C. Hélary, A. M. Mebert, X. Wang, T. Coradin and M. F. Desimone, *J. Mater. Chem. B*, 2014, **2**, 4660–4670.

67 V. Uskoković, S. Ghosh and V. M. Wu, *J. Mater. Chem. B*, 2017, **5**, 6065–6080.

68 V. Zarghami, M. Ghorbani, K. P. Bagheri and M. A. Shokrgozar, *Mater. Chem. Phys.*, 2020, **241**, 122423.

69 M. M. Abdelaziz, A. Hefnawy, A. Anter, M. M. Abdellatif, M. A. F. Khalil and I. A. Khalil, *ACS Omega*, 2022, **7**, 30161–30170.

70 A. J. Kell, G. Stewart, S. Ryan, R. Peytavi, M. Boissinot, A. Huletsky, M. G. Bergeron and B. Simard, 2008, **2**, 1777–1788.

71 M. Ugalde-Arbizu, J. J. Aguilera-Correa, E. San Sebastian, P. L. Páez, E. Nogales, J. Esteban and S. Gómez-Ruiz, *Pharmaceuticals*, 2023, **16**, 961–981.

72 B. de J. Mora, L. Filipe, A. Forte, M. M. Santos, C. Alves, F. Teodoro, R. Pedrosa, M. R. Carrott, L. C. Branco and S. Gago, *Pharmaceutics*, 2021, **13**, 1–16.

73 H. A. Fariba Abdollahi, Azadeh Pirisedigh, Mohammad Abbasinazari, Afshin Mohammad –Alizadeh, *Iran. J. Pharmacol. Ther.*, 2015, **14**, 50–58.

74 S. Perni, K. Martini-Gilching and P. Prokopovich, *Colloids Surfaces A Physicochem. Eng. Asp.*, 2018, **541**, 212–221.

75 J. F. A. De Oliveira, Â. Saito, A. T. Bido, J. Kobarg, H. K. Stassen and M. B. Cardoso, *Sci. Rep.*, 2017, **7**, 1326.

76 B. Yilmaz and O. Ozay, *Phosphorus, Sulfur Silicon Relat. Elem.*, 2022, **197**, 964–972.

77 Z. C. Wu, M. D. Cameron and D. L. Boger, *ACS Infect. Dis.*, 2020, **6**, 2169–2180.

78 K. Braun, A. Pochert, M. Lindén, M. Davoudi, A. Schmidtchen, R. Nordström and M. Malmsten, *J. Colloid Interface Sci.*, 2016, **475**, 161–170.

79 S. M. Häffner, E. Parra-Ortiz, K. L. Browning, E. Jørgensen, M. W. A. Skoda, C. Montis, X. Li, D. Berti, D. Zhao and M. Malmsten, *ACS Nano*, 2021, **15**, 6787–6800.

80 X. Wu, P. H. Wei, X. Zhu, M. J. Wirth, A. Bhunia and G. Narsimhan, *Colloids Surfaces B Biointerfaces*, 2017, **156**, 305–312.

81 A. Bernardos, E. Piacenza, F. Sancenón, M. Hamidi, A. Maleki, R. J. Turner and R. Martínez-Máñez, *Small*, 2019, **15**, 1900669.

82 G. C. Carvalho, G. D. Marena, J. C. F. Karnopp, J. Jorge, R. M. Sábio, M. A. U. Martines, T. M. Bauab and M. Chorilli, *Adv. Colloid Interface Sci.*, 2022, **307**, 102746.

83 J. Lu, M. Liong, Z. Li, J. I. Zink and F. Tamanoi, *Bone*, 2005, **23**, 1–7.

84 C. T. Kresge, M. E. Leonowicz, W. J. Roth, J. C. Vartuli and J. S. Beck,

Nature, 1992, **359**, 710–712.

85 T. Tamanna, J. B. Bulitta and A. Yu, *J. Mater. Sci. Mater. Med.*, 2015, **26**, 117–126.

86 K. Bouchmela, Q. Lion, C. Gervais and M. B. Cardoso, *ACS Omega*, 2023, **8**, 12154–12164.

87 A. Aguilar-Colomer, M. Colilla, I. Izquierdo-Barba, C. Jiménez-Jiménez, I. Mahillo, J. Esteban and M. Vallet-Regí, *Microporous Mesoporous Mater.*, 2021, **311**, 110681.

88 S. Lu, W. Bi, Q. Du, S. Sinha, X. Wu, A. Subrata, S. Bhattacharjya, B. Xing and E. K. L. Yeow, *Nat. Commun.*, 2018, **9**, 4277.

89 L. Tahmasbi, T. Sedaghat, H. Motamedi and M. Kooti, *J. Solid State Chem.*, 2018, **258**, 517–525.

90 Z. Gounani, M. A. Asadollahi, J. N. Pedersen, J. Lyngsø, J. Skov Pedersen, A. Arpanaei and R. L. Meyer, *Colloids Surfaces B Biointerfaces*, 2019, **175**, 498–508.

91 R. Chen, H. Qu, A. Agrawal, S. Guo and P. Ducheyne, *J. Mater. Sci. Mater. Med.*, 2013, **24**, 137–146.

92 S. Tummala, W. A. Huang, B. H. Wu, K. C. Chang and Y. P. Ho, *ChemistryOpen*, 2020, **9**, 1074–1081.

93 Y. Liu, X. Liu, Y. Xiao, F. Chen and F. Xiao, *RSC Adv.*, 2017, **7**, 31133–31141.

94 V. Nairi, L. Medda, M. Monduzzi and A. Salis, *J. Colloid Interface Sci.*, 2017, **497**, 217–225.

95 A. Najafi, P. Khosravian, M. Validi, M. Porgham Daryasari, F. Drees and A. Gholipour, *J. Drug Deliv. Sci. Technol.*, 2021, **65**, 102757.

96 K. Montiel-Centeno, D. Barrera, F. García-Villén, R. Sánchez-Espejo, A. Borrego-Sánchez, E. Rodríguez-Castellón, G. Sandri, C. Viseras and K. Sapag, *J. Drug Deliv. Sci. Technol.*, 2022, **72**, 103348.

97 R. J. Mudakavi, S. Vanamali, D. Chakravortty and A. M. Raichur, *RSC Adv.*, 2017, **7**, 7022–7032.

98 Q. Liu, Y. Zhang, J. Huang, Z. Xu, X. Li, J. Yang, H. Huang, S. Tang, Y. Chai, J. Lin, C. Yang, J. Liu and S. Lin, *J. Nanobiotechnology*, 2022, **20**, 386–402.

99 G. F. Andrade, J. A. Q. A. Faria, D. A. Gomes, A. L. B. de Barros, R. S. Fernandes, A. C. S. Coelho, J. A. Takahashi, A. da Silva Cunha and E. M. B. de Sousa, *J. Sol-Gel Sci. Technol.*, 2018, **85**, 369–381.

100 M. N. Alandiyjany, A. S. Abdelaziz, A. Abdelfattah-Hassan, W. A. H. Hegazy, A. A. Hassan, S. T. Elazab, E. A. A. Mohamed, E. S. El-Shetry, A. A. Saleh, N. A. Elsawy and D. Ibrahim, *Pharmaceuticals*, 2022, **15**, 357–374.

101 Q. Yu, D. Tian, F.-C. Lin, B. Zhang and J. I. Zink, *ACS Nano*, 2020, **14**, 5926–5937.

102 F. Liu, J. Wang, P. Huang, Q. Zhang, J. Deng, Q. Cao, J. Jia, J. Cheng, Y.

Fang, D. Y. B. Deng and W. Zhou, *J. Mater. Chem. B*, 2015, **3**, 2206–2214.

103 M. Deaconu, A. M. Brezoiu, R. A. Mitran, I. Nicu, B. Manolescu, C. Matei and D. Berger, *Microporous Mesoporous Mater.*, 2020, **305**, 110323.

104 A. Pourjavadi and Z. M. Tehrani, *Int. J. Polym. Mater. Polym. Biomater.*, 2014, **63**, 692–697.

105 J. J. Aguilera-Correa, M. Gisbert-Garzarán, A. Mediero, M. J. Fernández-Aceñero, D. de-Pablo-Velasco, D. Lozano, J. Esteban and M. Vallet-Regí, *Acta Biomater.*, 2022, **154**, 608–625.

106 B. Koneru, Y. Shi, Y. C. Wang, S. H. Chavala, M. L. Miller, B. Holbert, M. Conson, A. Ni and A. J. Di Pasqua, *Molecules*, 2015, **20**, 19690–19698.

107 S. Wu, Y. Huang, J. Yan, Y. Li, J. Wang, Y. Y. Yang, P. Yuan and X. Ding, *Adv. Funct. Mater.*, 2021, **31**, 210344.

108 S. Subramaniam, N. Thomas, H. Gustafsson, M. Jambhrunkar, S. P. Kidd and C. A. Prestidge, *Antibiotics*, 2019, **8**, 5–7.

109 K. Braun, A. Pochert, M. Gerber, H. F. Raber and M. Lindén, *Mol. Syst. Des. Eng.*, 2017, **2**, 393–400.

110 B. Beitzinger, F. Gerbl, T. Vomhof, R. Schmid, R. Noschka, A. Rodriguez, S. Wiese, G. Weidinger, L. Ständker, P. Walther, J. Michaelis, M. Lindén and S. Stenger, *Adv. Healthc. Mater.*, 2021, **10**, 2100453.

111 C. Li, K. Feng, N. Xie, W. Zhao, L. Ye, B. Chen, C. H. Tung and L. Z. Wu, *ACS Appl. Nano Mater.*, 2020, **3**, 5070–5078.

112 J. Li, F. Liu, Q. Shao, Y. Min, M. Costa, E. K. L. Yeow and B. Xing, *Adv. Healthc. Mater.*, 2014, **3**, 1230–1239.

113 A. Bakhshian Nik, H. Zare, S. Razavi, H. Mohammadi, P. Torab Ahmadi, N. Yazdani, M. Bayandori, N. Rabiee and J. Izadi Mobarakeh, *Microporous Mesoporous Mater.*, 2020, **299**, 110115.

114 B. Y. Lee, Z. Li, D. L. Clemens, B. J. Dillon, A. A. Hwang, J. I. Zink and M. A. Horwitz, *Small*, 2016, **12**, 3690–3702.

115 J. Li, Z. Ding, Y. Li, J. Miao, W. Wang, K. Nundlall and S. Chen, *Mater. Des.*, 2020, **195**, 109021.

116 E. Yu, I. Galiana, R. Martínez-Máñez, P. Stroeve, M. D. Marcos, E. Aznar, F. Sancenón, J. R. Murguía and P. Amorós, *Colloids Surfaces B Biointerfaces*, 2015, **135**, 652–660.

117 B. González, M. Colilla, J. Díez, D. Pedraza, M. Guembe, I. Izquierdo-Barba and M. Vallet-Regí, *Acta Biomater.*, 2018, **68**, 261–271.

118 A. A. Hwang, B. Y. Lee, D. L. Clemens, B. J. Dillon, J. I. Zink and M. A. Horwitz, *Small*, 2015, **11**, 5066–5078.

119 Z. Li, D. L. Clemens, B. Y. Lee, B. J. Dillon, M. A. Horwitz and J. I. Zink, *ACS Nano*, 2015, **9**, 10778–10789.

120 D. L. Clemens, B. Y. Lee, M. Xue, C. R. Thomas, H. Meng, D. Ferris, A. E.

Nel, J. I. Zink and M. A. Horwitz, *Antimicrob. Agents Chemother.*, 2012, **56**, 2535–2545.

121 M. M. Lu, Y. Ge, J. Qiu, D. Shao, Y. Zhang, J. Bai, X. Zheng, Z. M. Chang, Z. Wang, W. F. Dong and C. B. Tang, *Int. J. Nanomedicine*, 2018, **13**, 7697–7709.

122 R.-L. Zhang, F. Wijaya Pratiwi, B.-C. Chen, P. Chen, S.-H. Wu and C.-Y. Mou, *ACS Appl. Mater. Interfaces*, 2020, **12**, 42472–42482.

123 J. L. Paris, M. V. Cabanas, M. Manzano and M. Vallet-Regí, *ACS Nano*, 2015, **9**, 11023–11033.

124 S. F. Lee, X. M. Zhu, Y. X. J. Wang, S. H. Xuan, Q. You, W. H. Chan, C. H. Wong, F. Wang, J. C. Yu, C. H. K. Cheng and K. C. F. Leung, *ACS Appl. Mater. Interfaces*, 2013, **5**, 1566–1574.

125 M. Du, Y. Chen, J. Tu, C. Liufu, J. Yu, Z. Yuan, X. Gong and Z. Chen, *ACS Biomater. Sci. Eng.*, 2020, **6**, 2904–2912.

126 X. Li, C. Xie, H. Xia and Z. Wang, *Langmuir*, 2018, **34**, 9974–9981.

127 Y. Wu, Y. Long, Q.-L. Li, S. Han, J. Ma, Y.-W. Yang and H. Gao, *ACS Appl. Mater. Interfaces*, 2015, **7**, 17255–17263.

128 H. W. Lee, S. Kharel, S. Chye and J. Loo, *ACS Omega*, 2022, **7**, 35814–35824.

129 R. J. Mudakavi, A. M. Raichur and D. Chakravortty, *RSC Adv.*, 2014, **4**, 61160–61166.

130 Y. Jiang, W. Zheng, K. Tran, E. Kamilar, J. Bariwal, H. Ma and H. Liang, *Nat. Commun.*, 2022, **13**, 197–204.

131 A. Pamukçu, N. Erdoğan and D. Şen Karaman, *J. Biomed. Mater. Res. - Part B Appl. Biomater.*, 2022, **110**, 2506–2520.

132 J. Croissant, D. Salles, M. Maynadier, O. Mongin, V. Hugues, M. Blanchard-Desce, X. Cattoën, M. Wong Chi Man, A. Gallud, M. Garcia, M. Gary-Bobo, L. Raehm and J. O. Durand, *Chem. Mater.*, 2014, **26**, 7214–7220.

133 J. G. Croissant, Y. Fatieiev, A. Almalik and N. M. Khashab, *Adv. Healthc. Mater.*, 2018, **7**, 1700831.

134 C. Liu, A. M. Kaczmarek, H. S. Jena, Z. Yang, D. Poelman and P. Van Der Voort, *J. Mater. Chem. C*, 2023, **11**, 5634–5645.

135 A. Walcarius and L. Mercier, *J. Mater. Chem.*, 2010, **20**, 4478–4511.

136 M. Guo, J. Qian, R. Xu, X. Ren, J. Zhong and M. Kanezashi, *J. Memb. Sci.*, 2022, **643**, 120018.

137 Y. Liang, *Nanoscale Adv.*, 2021, **3**, 6827–6868.

138 D. Wu, Y. Liu, Y. Wu, B. Tan and Z. Xie, *Dalt. Trans.*, 2018, **47**, 5961–5967.

139 Z. Li, S. Zhu, B. Shao, X. Zeng, T. Wang and T. Y. Liu, *Brief. Bioinform.*, 2023, **24**, 1–12.

140 O. Osta, M. Bombled, D. Partouche, F. Gallier, N. Lubin-Germain, N. Brodie-Linder and C. Alba-Simionesco, *ACS Omega*, 2020, **5**, 18842–18848.

141 C. Zhang, F. Babonneau, C. Bonhomme, R. M. Laine, C. L. Soles, H. A. Hristov and A. F. Yee, *J. Am. Chem. Soc.*, 1998, **120**, 8380–8391.

142 Y. Xu, W. Shi, H. Li, X. Li and H. Ma, *ChemMedChem*, 2019, **14**, 1079–1085.

143 X. Feng, F. Li, L. Zhang, W. Liu, X. Wang, R. Zhu, Z. A. Qiao, B. Yu and X. Yu, *Acta Biomater.*, 2022, **143**, 392–405.

144 Y. Yu, J. Chen, S. Liu and D. Cheng, *J. Mater. Chem. B*, 2021, **9**, 6044–6055.

145 R. Xing, L. Ning, L. Li, L. He, H. Lin, C. You and F. Wang, *J. Drug Deliv. Sci. Technol.*, 2023, **86**, 104654.

146 W. Zhang, H. Ma, J. Hua, W. Zhang, C. Guo and J. Wang, *J. Solid State Chem.*, 2019, **277**, 761–768.

147 J. Gao, X. Zhang, S. Xu, F. Tan, X. Li, Y. Zhang, Z. Qu, X. Quan and J. Liu, *Chem. - A Eur. J.*, 2014, **20**, 1957–1963.

148 M. Jambhrunkar, S. Maghrebi, D. Doddakyathanahalli, A. Wignall, C. A. Prestidge and K. E. Bremmell, *Pharmaceutics*, 2023, **15**, 1037.

149 H. Li, D. Li, F. Chen, C. Yang, X. Li, Y. Zhang, C. Hua, X. Ma, X. Zhao, D. Shao, Y. Wang and L. Ming, *Int. J. Nanomedicine*, 2021, **16**, 4631–4642.

150 R. S. Guimarães, C. F. Rodrigues, A. F. Moreira and I. J. Correia, *Pharmacol. Res.*, 2020, **155**, 104742.

151 P. Picchetti, S. Volpi, M. Rossetti, M. D. Dore, T. Trinh, F. Biedermann, M. Neri, A. Bertucci, A. Porchetta, R. Corradini, H. Sleiman and L. De Cola, 2023, 22896–22902.

152 H. Mekaru, A. Yoshigoe, M. Nakamura, T. Doura and F. Tamanoi, *ACS Appl. Nano Mater.*, 2019, **2**, 479–488.

153 R. Nair, A. C. Poulose, Y. Nagaoka, Y. Yoshida, T. Maekawa and D. S. Kumar, *J. Fluoresc.*, 2011, **21**, 2057–2068.

154 J. B. Wacker, I. Lignos, V. K. Parashar and M. A. M. Gijs, *Lab Chip*, 2012, **12**, 3111–3116.

155 S. Santra, B. Liesenfeld, C. Bertolino, D. Dutta, Z. Cao, W. Tan, B. M. Moudgil and R. A. Mericle, *J. Lumin.*, 2006, **117**, 75–82.

156 S. Foglia, M. Ledda, D. Fioretti, G. Iucci, M. Papi, G. Capellini, M. G. Lolli, S. Grimaldi, M. Rinaldi and A. Lisi, *Sci. Rep.*, 2017, **7**, 46513.

157 T. Ribeiro, E. Coutinho, A. S. Rodrigues, C. Baleizão and J. P. S. Farinha, *Nanoscale*, 2017, **9**, 13485–13494.

158 N. Klippel, G. Jung and G. Kickelbick, *J. Sol-Gel Sci. Technol.*, 2021, **107**, 2–19.

159 E. Phillips, O. Penate-Medina, P. B. Zanzonico, R. D. Carvajal, P. Mohan, Y. Ye, J. Humm, M. Gönen, H. Kalaigian, H. Schöder, H. W. Strauss, S. M.

Larson, U. Wiesner and M. S. Bradbury, *Sci. Transl. Med.*, 2014, **6**, 149–157.

160 N. Knežević, B. G. Trewyn and V. S. Y. Lin, *Chem. Commun.*, 2011, **47**, 2817–2819.

161 N. Z. Knežević, *RSC Adv.*, 2013, **3**, 19388–19392.

162 M. Frasconi, Z. Liu, J. Lei, Y. Wu, E. Strekalova, D. Malin, M. W. Ambrogio, X. Chen, Y. Y. Botros, V. L. Cryns, J. P. Sauvage and J. Fraser Stoddart, *J. Am. Chem. Soc.*, 2013, **135**, 11603–11613.

163 Y. Salinas, O. Brüggemann, U. Monkowius and I. Teasdale, *Nanomaterials*, 2020, **10**, 1030.

164 S. Lechevallier, R. Mauricot, H. Gros-Dagnac, S. Chevreux, G. Lemercier, E. Phonesouk, M. Golzio and M. Verelst, *Chempluschem*, 2017, **82**, 770–777.

165 D. J. Lewis, V. Dore, N. J. Rogers, T. K. Mole, G. B. Nash, P. Angeli and Z. Pikramenou, *Langmuir*, 2013, **29**, 14701–14708.

166 C. Ezquerro, I. P. López, E. Serrano, E. Alfaro-Arnedo, E. Lalinde, I. M. Larráyoz, J. G. Pichel, J. García-Martínez and J. R. Berenguer, *Mater. Adv.*, 2022, **3**, 3582–3592.

167 Z. Chen, P. Yan, L. Zou, M. Zhao, J. Jiang, S. Liu, K. Y. Zhang, W. Huang and Q. Zhao, *Adv. Healthc. Mater.*, 2018, **7**, 1–14.

168 M. Cheng, L. Zhou, J. Ma, J. Mu, C. Yi and M. J. Li, *Mater. Sci. Eng. C*, 2019, **104**, 109972.

169 A. J. Amoroso and S. J. A. Pope, *Chem. Soc. Rev.*, 2015, **44**, 4723–4742.

170 M. Huang, L. Liu, S. Wang, H. Zhu, D. Wu, Z. Yu and S. Zhou, *Langmuir*, 2017, **33**, 519–526.

171 F. E. Maturi, R. M. Sábio, R. R. Silva, M. G. Lahoud, A. B. Meneguin, G. T. Valente, R. A. Caface, I. S. Leite, N. M. Inada and S. J. L. Ribeiro, *Materials (Basel).*, 2019, **16**, 933–944.

172 J. Liu, S. Liu, Y. Li, J. Xue, Y. He, F. Liu, L. Yang, J. Hu, Z. Xiong and L. Long, *RSC Adv.*, 2019, **9**, 40835–40844.

173 M. H. Chan and H. M. Lin, *Biomaterials*, 2015, **46**, 149–158.

174 S. Claire, A. D. Walmsley, S. Glinton, H. Floyd, R. Sammons and Z. Pikramenou, *J. Dent.*, 2015, **43**, 1242–1248.

175 D. Zhang, Z. Wu, J. Xu, J. Liang, J. Li and W. Yang, *Langmuir*, 2010, **26**, 6657–6662.

176 L. M. Rossi, L. Shi, F. H. Quina and Z. Rosenzweig, *Langmuir*, 2005, **21**, 4277–4280.

177 W. J. Rieter, J. S. Kim, K. M. L. Taylor, H. An, W. Lin, T. Tarrant and W. Lin, *Angew. Chemie - Int. Ed.*, 2007, **46**, 3680–3682.

178 E. Lipani, S. Laurent, M. Surin, L. Vander Elst, P. Lecleìre and R. N. Muller, *Langmuir*, 2013, **29**, 3419–3427.

179 S. Zhao, S. Sun, K. Jiang, Y. Wang, Y. Liu, S. Wu, Z. Li, Q. Shu and H. Lin, *Nano-Micro Lett.*, 2019, **11**, 1–13.

180 L. Liu, X. Fu, H. Zhang, W. Ma, L. Zhang, Y. Zhang, M. Liu, K. Liang, S. Hou and A. Chen, *J. Mater. Res.*, 2018, **33**, 1442–1448.

181 X. Hou, T. Zaks, R. Langer and Y. Dong, *Nat. Rev. Mater.*, 2021, **6**, 1078–1094.

182 S. A. Dilliard and D. J. Siegwart, *Nat. Rev. Mater.*, 2023, **8**, 282–300.

183 C. Zhang, W. Zhao, C. Bian, X. Hou, B. Deng, D. W. McComb, X. Chen and Y. Dong, *ACS Appl. Bio Mater.*, 2019, **2**, 1270–1277.

184 M. Mohammed, U. H. Ibrahim, A. Aljoundi, C. A. Omolo, N. Devnarain, M. A. Gafar, C. Mocktar and T. Govender, *Int. J. Pharm.*, 2023, **640**, 122967.

185 D. P. Gaspar, M. M. Gaspar, C. V. Eleutério, A. Grenha, M. Blanco, L. M. D. Gonçalves, P. Taboada, A. J. Almeida and C. Remunán-López, *Mol. Pharm.*, 2017, **14**, 2977–2990.

186 I. Menon, M. Zaroudi, Y. Zhang, E. Aisenbrey and L. Hui, *Mater. Today Adv.*, 2022, **16**, 100299.

187 S. E. Birk, A. Boisen and L. H. Nielsen, *Adv. Drug Deliv. Rev.*, 2021, **174**, 30–52.

188 C. I. C. Crucho and M. T. Barros, *Mater. Sci. Eng. C*, 2017, **80**, 771–784.

189 M. Chen, S. Xie, J. Wei, X. Song, Z. Ding and X. Li, *ACS Appl. Mater. Interfaces*, 2018, **10**, 36814–36823.

190 G. Gao, Y. W. Jiang, H. R. Jia and F. G. Wu, *Biomaterials*, 2019, **188**, 83–95.

191 K. He, Z. Shen, Z. Chen, B. Zheng, S. Cheng and J. Hu, *Polym. Chem.*, 2021, **12**, 6344–6354.

192 J. A. S. Ritsema, E. M. A. Herschberg, S. E. Borgos, C. Løvmo, R. Schmid, Y. M. te Welscher, G. Storm and C. F. van Nostrum, *Int. J. Pharm.*, 2018, **548**, 730–739.

193 A. B. Sairam, A. Sanmugam, A. Pushparaj, G. Mahesh Kumar, N. Sundarapandian, S. Balaji, M. Nallal and K. H. Park, *ACS Chem. Heal. Saf.*, 2023, **30**, 236–250.

194 N. Desai, *AAPS J.*, 2012, **14**, 282–295.

195 A. Suriya Prabha, R. Dorothy, S. Jancirani, S. Rajendran, G. Singh and S. Senthil Kumaran, *Recent advances in the study of toxicity of polymer-based nanomaterials*, INC, 2020.

196 V. Chandrakala, V. Aruna and G. Angajala, *Emergent Mater.*, 2022, **5**, 1593–1615.

197 V. Tsikourkitoudi, B. Henriques-Normark and G. A. Sotiriou, *Curr. Opin. Chem. Eng.*, 2022, **38**, 100872.

198 M. Liong, J. Lu, M. Kovochich, T. Xia, S. G. Ruehm, A. E. Nel, F. Tamanoi and

J. I. Zink, *ACS Nano*, 2008, **2**, 889–896.

199 M. Fuller, H. Whiley and I. Köper, *SN Appl. Sci.*, 2020, **2**, 1022.

200 M. Sengani, A. M. Grumezescu and V. D. Rajeswari, *OpenNano*, 2017, **2**, 37–46.

201 N. Tarannum, Divya and Y. K. Gautam, *RSC Adv.*, 2019, **9**, 34926–34948.

202 A. Rai, A. Prabhune and C. C. Perry, *J. Mater. Chem.*, 2010, **20**, 6789–6798.

203 X. Li, S. M. Robinson, A. Gupta, K. Saha, Z. Jiang, D. F. Moyano, A. Sahar, M. A. Riley and V. M. Rotello, *ACS Nano*, 2014, **8**, 10682–10686.

204 L. Wang, S. Li, J. Yin, J. Yang, Q. Li, W. Zheng, S. Liu and X. Jiang, *Nano Lett.*, 2020, **20**, 5036–5042.

205 M. C. Jazmín Silvero, D. M. Rocca, E. Artur de la Villarmois, K. Fournier, A. E. Lanterna, M. F. Perez, M. Cecilia Becerra and J. C. Scaiano, *ACS Omega*, 2018, **3**, 1220–1230.

206 P. Khandelwal, D. K. Singh and P. Poddar, *ChemistrySelect*, 2019, **4**, 6719–6738.

207 S. Iram, M. Zahera, I. Wahid, A. Baker, M. Raish, A. Khan, N. Ali, S. Ahmad and M. S. Khan, *Sci. Rep.*, 2019, **9**, 13826.

208 A. Kessler, J. Hedberg, E. Blomberg and I. Odnevall, *Nanomaterials*, 2022, **12**, 1922–1945.

209 Y. Li, W. Zhang, J. Niu and Y. Chen, *ACS Nano*, 2012, **6**, 5164–5173.

210 H. Zhao, M. Wang, Y. Cui and C. Zhang, *Environ. Sci. Technol.*, 2022, **56**, 5090–5101.

211 V. Amendola, R. Pilot, M. Frasconi, O. M. Maragò and M. A. Iatì, *J. Phys. Condens. Matter*, 2017, **29**, 203002.

212 H. L. Karlsson, M. S. Toprak and B. Fadeel, in *Handbook on the Toxicology of Metals: Fourth Edition*, Elsevier, 4th Ed., 2015, pp. 75–112.

213 S. Saha, M. R. Ali, M. A. Khaleque, M. S. Bacchu, M. Aly Saad Aly and M. Z. H. Khan, *J. Drug Deliv. Sci. Technol.*, 2023, **86**, 104728.

214 L. M. Armijo, S. J. Wawrzyniec, M. Kopciuch, Y. I. Brandt, A. C. Rivera, N. J. Withers, N. C. Cook, D. L. Huber, T. C. Monson, H. D. C. Smyth and M. Osiński, *J. Nanobiotechnology*, 2020, **18**, 1–27.

215 M. Rashid, M. A. Rabbi, T. Ara, M. M. Hossain, M. S. Islam, A. Elaissari, H. Ahmad and M. M. Rahman, *RSC Adv.*, 2021, **11**, 36319–36328.

216 G. Luongo, P. Campagnolo, J. E. Perez, J. Kosel, T. K. Georgiou, A. Regoutz, D. J. Payne, M. M. Stevens, M. P. Ryan, A. E. Porter and I. E. Dunlop, *ACS Appl. Mater. Interfaces*, 2017, **9**, 40059–40069.

217 C. N. Lee, Y. M. Wang, W. F. T. Lai, T. J. Chen, M. C. Yu, C. L. Fang, F. L. Yu, Y. H. Tsai, W. H. S. Chang, C. S. Zuo and P. F. Renshaw, *Clin. Microbiol. Infect.*, 2012, **18**, E149–E157.

218 S. Lefevre, D. Ruimy, F. Jehl, A. Neuville, P. Robert, C. Sordet, M. Ehlinger, J. L. Dietemann and G. Bierry, *Radiology*, 2011, **258**, 722–728.

219 L. A. Almutairi, B. Yu, E. Dyne, A. A. Ojaym and M. H. Kim, *Int. J. Hyperth.*, 2023, **40**.

220 P. Bellio, C. Luzi, A. Mancini, S. Cracchiolo, M. Passacantando, L. Di Pietro, M. Perilli, G. Amicosante, S. Santucci and G. Celenza, *Biochim. Biophys. Acta - Biomembr.*, 2018, **1860**, 2428–2435.

221 H. Mao, F. Zhang, M. Du, L. Dai, Y. Qian and H. Pang, *Ceram. Int.*, 2021, **47**, 25177–25200.

222 C. M. Han, E. J. Lee, H. E. Kim, Y. H. Koh and J. H. Jang, *Thin Solid Films*, 2011, **519**, 8074–8076.

223 S. Bakhshandeh, Z. Gorgin Karaji, K. Lietaert, A. C. Fluit, C. H. E. Boel, H. C. Vogely, T. Vermonden, W. E. Hennink, H. Weinans, A. A. Zadpoor and S. Amin Yavari, *ACS Appl. Mater. Interfaces*, 2017, **9**, 25691–25699.

2. CHELATING SILICA NANOPARTICLES FOR THE EFFICIENT ANTIBIOTIC DELIVERY AND PARTICLE TRACKING IN GRAM-NEGATIVE BACTERIA

2.1. Introduction

2.1.1. Outer membrane impermeability to antibiotics

The vast majority of currently employed and newly designed antibacterial agents target bacterial cell processes *via* binding to targeted structures located in the cell cytoplasm.[1–4] Herein, the antibacterial agent must cross the outer bacterial membrane to reach its target. This process is relatively simple in case of Gram-positive bacterial cells due to their simple cell wall structure, mainly composed by lipids and peptidoglycans. However, Gram-negative bacterial cells possess a double, more rigid, cell membrane (Figure 2.1B). This membrane is organised in an outer and inner membrane, bearing a compartment, the periplasm, between them. Some antibiotics are able to access the bacterial cytoplasm through pore-forming β-barrel-shaped membrane proteins named porins, such us, β-lactams or fluoroquinolones.[5,6] Other molecules, like macrolides, are able to diffuse across the lipid bilayer.[7,8] Unfortunately, the rigidity of the outer cell membrane prevents the crossing of hydrophobic and high

molecular weight antibacterial agents, such us, vancomycin. Vancomycin is a highly active cell wall-synthesis inhibitor against Gram-positive bacteria, but non-active against Gram-negative species. For these reasons, outer membrane impermeability to antibiotics is one of the major intrinsic antibacterial resistant mechanisms.[1,8,9]

Gram-negative bacteria outer cell membrane is an asymmetric bilayer composed by lipopolysaccharides in the outer leaflet and by phospholipids in the inner leaflet. The integrity of the outer membrane, relies, in fact, in the lipopolysaccharides. Lipopolysaccharides are composed by a hydrophobic fatty acid chain linked to lipid A (a glucosamine saccharide phosphorylated at the 1 and 4' positions and acetylated at the 2, 2', 3 and 3' position), a core of oligosaccharides and the O-antigen (an immunogenic oligosaccharide with remarkable variability across bacterial species). Furthermore, lipid A contains negatively charged phosphate groups that strongly interacts with divalent cations (Ca^{2+} and Mg^{2+}) through electrostatic interactions (Figure 2.1.A).[10–12] Such cations are structurally essential components of the outer membrane as they compensate the overall negative charge of the outer membrane, allowing high packing of lipopolysaccharides.[3] However, these cations, are simultaneously, a very common target for antibacterial therapies as their removal would lead to destabilization of the outer membrane and thereby, to an increase in permeability.[8,11,13] Consequently, allowing the internalization of molecules that would not be able to cross the undamaged outer membrane.

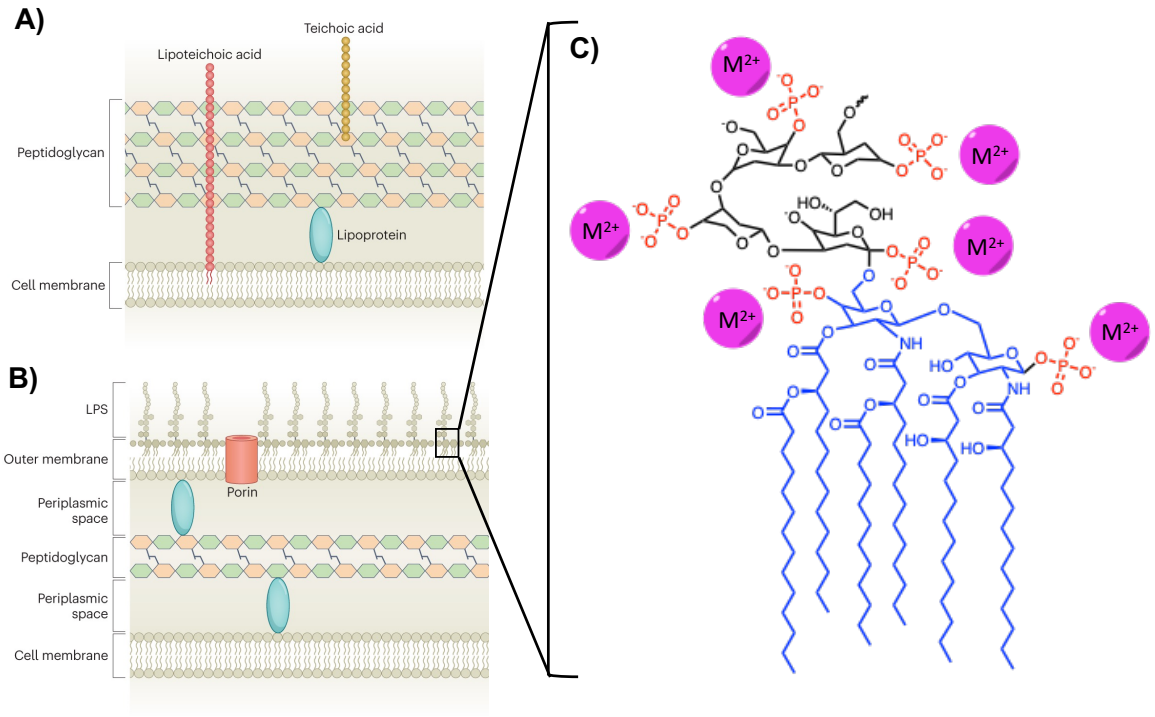

Figure 2.1. Simplified scheme of the (A) Gram-positive and (B) Gram-negative bacterial cell membrane structure reproduced from T. Lithgow *et al.*[14] and (C) scheme of the basic structure of lipopolysaccharide's lipid A structure (in blue) bearing phosphate groups (in red) interacting with divalent cations (pink spheres).

2.1.2. Outer membrane destabilisers

New antibacterial therapies targeting the Gram-negative bacterial cell outer membrane have attracted attention from the scientific community as it represents the first barrier for antibiotics that cannot reach the target structure in the Gram-negative bacterial cytoplasm. Destabilization of outer membrane barrier could facilitate the entry of Gram-positive active antibiotic into Gram-negative pathogens, expanding the pipeline against this bacterial species.[15]

Destabilization of outer membrane has been previously explored through different approaches including, inhibition of lipopolysaccharide biosynthesis, targeting lipopolysaccharide transport to the outer membrane and physical disruption of the

already formed outer membrane.[16] Physical disruption of the outer membrane can happen by insertion of foreign molecules within the lipid bilayer, creating artificial pores or by removal of structurally essential components.[15]

2.1.1.2. Antimicrobial peptides

Antimicrobial peptides (AMP) comprise a large variety of peptides with antimicrobial activity. Their mechanism of action mainly relies on their ability to disrupt the outer membrane through difference processes; from pore-formation in the outer membrane, to divalent cations displacements. Cathelicin (LL-37) human peptide is one of the most studied AMPs. LL-37 is a 37 amino acid containing cationic peptide which mechanism of actions involves the electrostatic interaction with the negatively charge lipopolysaccharides, intercalating in the outer membrane, when LL-37 reaches optimal concentration, LL-37 peptide can rearrange forming β-barrel pores, enhancing the permeability of the membrane (Figure 2.2).[17] Nevertheless, LL-37 has several limitations including low activity in physiological conditions, high cytotoxicity in human cells and high production cost.[18]

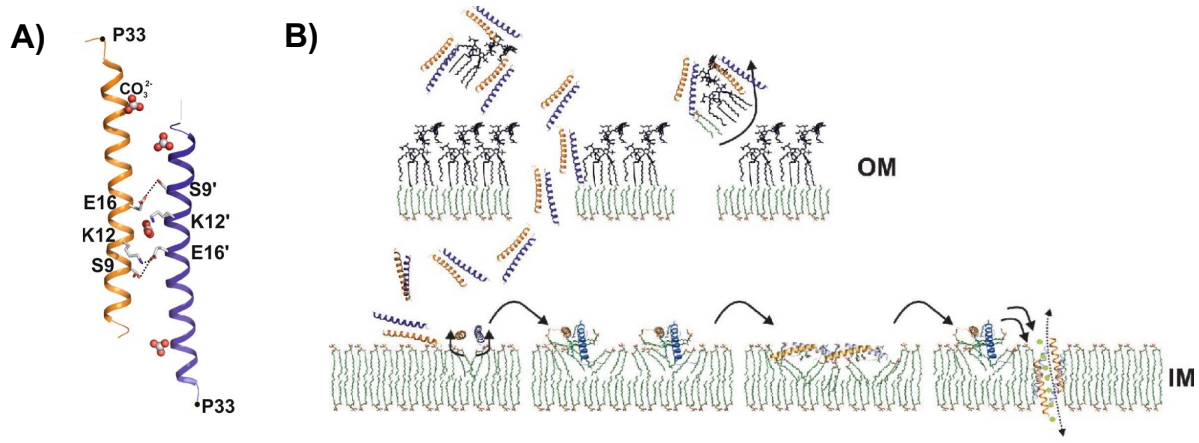

Figure 2.2. (A) Structure of LL-37 AMP and (B) scheme of the antimicrobial mechanism of LL-37 AMPs, which exemplifies the general mechanism of AMPs. Figures reproduced from E. Sancho-Vaello *et al*.[17,19]

Polymyxins, also, are a very well-known AMP family. Polymyxins are positively charged low molecular weight peptides (< 1000 Da) that permeabilize the outer membrane via competitive bidding with lipopolysaccharides, displacing the native Ca^{2+} and Mg^{2+} cations and, thereby, decompensating the overall charge of the membrane.[20,21] Moreover, the fatty acid chain of polymyxin assists on its solubilisation in the hydrophobic region of the membrane. Furthermore, it has been previously reported that the combined administration of polymyxin B with low penetration abilities antibiotics has enhanced the activity of the antibiotics, indicating that membrane destabilization by polymyxin B also facilitates the entry of antibiotics to the cytoplasm, where they reach their targets.[22] Another widely used polymyxin is polymyxin E, also known as colistin. The bactericidal action of colistin is also based on the displacement of the divalent cations present on the outer membrane. Unfortunately, the use of polymyxin has been restricted due to their nephrotoxic effect, as is has been identified that prolonged exposure to polymyxins can potentially lead to kidney deterioration.[22]

2.1.1.3. Polymers

Similarly to AMPs, cationic polymers are able to associate with lipopolysaccharides and competitively interaction with the lipid A, displacing the cationic ions, and thereby, destabilizing the outer membrane.[23] Moreover, insertion of ampicillin polymers into the lipid bilayer also lead to increase membrane permeability through pore forming, similar to well-known surfactants.

Cationic polymers were the first studied antimicrobial polymers.[24] Their activity relies on electrostatic interaction between the overall negatively charged membrane polymers. Nevertheless, these interactions also take place in mammalian cells, leading to higher cytotoxicity. Further modification of chemical composition of cationic polymers lead to quaternary ammonium polymers, which increased biocompatibility and electivity against bacterial cells over mammalian cells, even in derivative materials.[25] Cationic polymers based on amino acid, like ε-poly-*L*-lysine, display a higher biocompatibility, while their antibacterial activity is more modest that other polymers.[26]

Poly(ethylene imine) (PEI) is another widely explored cationic polymer with promising antibacterial properties. Whereas previous polymers had a linear structure, PEI polymers have presented a linear or branched structure. Even PEI polymers display selectivity to bacterial over mammalian cells their activity against Gram-negative bacteria is still not comparable to more toxic cationic polymers.[27]

Finally, antibiotic-polymer conjugates are also cindered antimicrobial polymers. Nevertheless their activity relies on the antibiotic conjugated to the polymer backbone, which served a carrier for the active molecule and their mechanism of action does not usually relies on membrane disruption.[28–30]

2.1.1.4. Chelators

As previously mentioned, removal of divalent metal cations Ca^{2+} and Mg^{2+} leads to membrane destabilization, and, hence, increased permeability.[10–12] Small polydentate molecules able to tightly bind metal cations are known as chelators. The affinity of metal chelators to different metals depend on the number of binding moieties (carboxylate, amine, hydroxyl, hydroxamate, etc) and their affinity for soft or hard metals cations.[31] Chelators, such us, ethylenediaminetetraacetic acid (EDTA) or diethylenetriaminepentaacetic acid (DTPA) are some of the most employed and studied metal chelators (Figure 2.3). Even if metal chelators are also able to bind to other metals present in the bacterial growth media, such as, Fe^{3+}, Mn^{2+} or Zn^{2+}; G. J. Sharples and co-workers concluded that the main antibacterial mechanism of polyaminocaboxylate metal cations relies of the destabilization of outer membrane after Ca^{2+} and Mg^{2+} sequestering. Even though sequestering of the other cations was also observed, the reduction of free cation species was not significant in order to be translated into bacterial cell growth inhibition.[31]

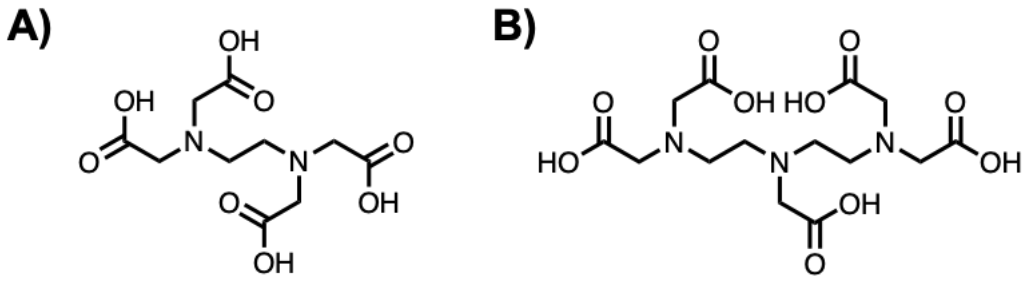

Figure 2.3. Chemical structure of (A) EDTA and (B) DTPA.

Due to their ability to sequester metal cations, antimicrobial therapies based on chelators have been previously explored. The main example in literature is the case of EDTA.[32] Interactions between EDTA and divalent cations have led to destabilization of the outer membrane of a wide range of Gram-negative bacterial species, such us*, E. coli*, *S. enterica, K. pneumoniae* or *S. thyphimurium*.[33,34] Similarly, DTPA, has shown higher antibacterial activity against several gram-negative bacterial species as it contains more chelating groups that its analogue EDTA.[31] Nevertheless, other metal chelators, like, *meso*-2,3-dimercaptosuccinic acid[35], bis-(2-ethylhexyl)sulfosuccinate[36] or nitrilotriacetic acid[37] (simpler version than EDTA) have shown membrane destabilization abilities. Combinational therapies with chelating agents and antibiotics have also been reported as potential strategy to enhance activity of antibiotic with reduce cell penetration abilities.[34]

2.1.2. Silica nanoparticles with membrane permeabilization functionalization

Silica nanoparticles with no further surface modification are not able to be internalised in Gram-negative bacteria due to outer membrane rigidity. Hence, and due to the promising results of membrane permeabilization agents in the enhancement of antibiotics activity, surface functionalization with membrane permeabilizers has been explored as a promising strategy to overcome this impermeability and allow delivery of antibiotic inside Gram-negative bacterial cells.

Conjugation of AMP onto silica nanoparticle surface has been widely explored. Surface modification is, in the majority of examples, based on electrostatic interaction between he negatively charged nanoparticle surface and the positively charged

peptides. AMP such as LL-37[38,39], Deferin 5[40] and Polymyxin B[41] have been electrostatically deposited on the surface on silica nanoparticles. However, due to the weak interactions between AMP and nanoparticles, AMP leakage has been reported as one of the main disadvantages. For instance, Gounani *et al*.[41] reported the development of MSNs loaded with vancomycin and with the AMP polymyxin adsorbed on the surface. The resulted DDS showed enhanced activity compared with particles only with vancomycin or the AMP. However, and due to the release of AMP authors could not conclude if the observed activity was due to the enhanced uptake of particles due to the AMP coating or due to the synergistic activity of the AMP along with vancomycin. AMP leakage could be prevented by covalent grafting of the peptide onto the silica surface. Unfortunately, due to the complexity of peptide structure and the importance of its structure to remain active, grafting of proteins on silica nanoparticles surface is a very complex process.

Grafting of cationic polymers, on the other hand, is an easier process as they do not have a defined structure that needs to be preserved and they can be conjugated to nanoparticles surface via *grafting-from* (polymerization of monomer from an already conjugated activator) or *grafting-to* (covalent attachment of already synthetized polymer).[25,42] Moreover, polymer surface functionalization has also been achieved by electrostatic interaction between negative surface groups and positively charged polymers.[43–45] Other polymers, such as, PEI have been widely conjugated onto the surface of MSNs to enhance cell penetration but also to cap nanoparticle's pores, avoiding burst release.[46–49] Antibiotics like tetracycline[48], levofloxacin[46] or ciprofloxacin[49] have been delivered using theses nanoparticles. Enthought the advanced in development of biocompatible polymer coatings, the majority of examples also displays moderate to low biocompatibility.

Interestingly, the only example of silica nanoparticles with surface aminocarboxylates for antibiotic delivery was reported by P. Amorós and co-workers.[43,44] They took advantage of the electrostatic interaction between the surface negatively charged *n*-[(3-trimethoxysilyl)propyl]ethylendiamine triacetic acid and the positively charged ε-poly-*L*-lysine polymer to cap antibiotic loaded MSNs (Figure 2.4). The resulting increased activity of nanoparticles was associated with the permeabilization effect of the cationic polymer, and not with the chelating abilities of the surface aminocarboxylate. Nevertheless, the use of aminocarboxylate coating, such as EDTA, DTPA for extended chelators have been widely explored for metal removal[50–53] or formation of metal complexes for lanthanide-based luminescent[54–56], gadolinium-mediated magnetic resonance imaging[56–61] or technecium-99m (Tc-99m)-mediated radio imaging[13].

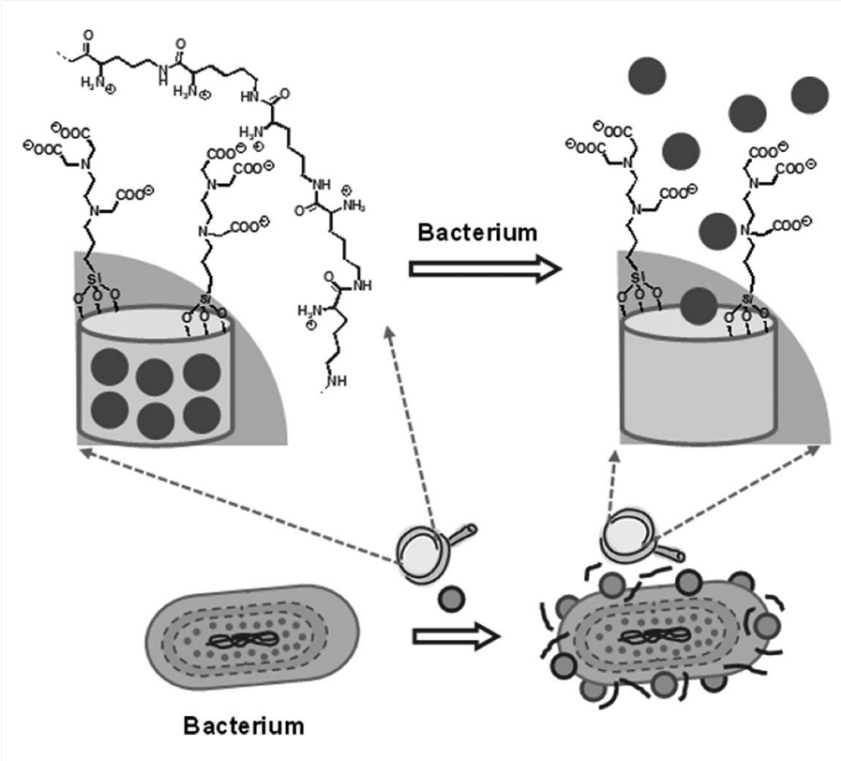

Figure 2.4. Surface functionalization of nanoparticles developed by P. Amorós and co-workers based on electrostatic interactions between surface anchored aminocarboxylates and ε-poly-*L*-lysine polymer.[43,44]

2.1.3. Chapter outline

The design, synthesis, antibacterial activity and bacterial cell penetration abilities of aminocarboxylate-coated hybrid nonporous silica nanoparticles (**DTPA@SiO_2⊃Ru-Van**) is reported as a new approach for the development of silica-based antibiotic delivery systems into Gram-negative bacterial cells. The theragnostic design of the nanoparticle, due to the simultaneous presence of the luminescent complex $Ru(phen)_3Cl_2$ (**Ru,** where phen = 1,10-phenantroline), and an antibiotic, can be employed for imaging purposes and, hence, tracking of the nanoparticles within the bacterial cell while the included antibiotic is being released (Figure 2.5). The developed coating also allows the penetration of nanoparticles in Gram-negative bacterial cells and the delivery of the antibiotic Vancomycin (**Van**), that in its free form, it is not able to cross the double cell membrane, being non-active. Hereby, the presented nanoparticle contributes toward the development of more efficient delivery systems for the use of antibiotics that are not active due cell impermeability.

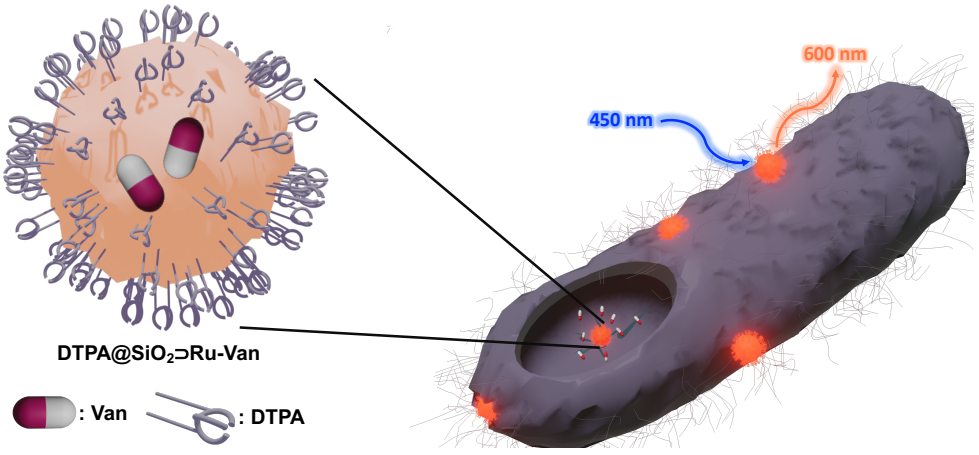

Figure2.5. Schematic representation of developed **DTPA@SiO_2⊃Ru-Van** and internalization of coated nanoparticles and antibiotic release inside Gram-negative bacterial cells.

The work presented in this chapter resulted in the following publication: A. R. Muguruza, A. di Maio, N. J. Hodges, J. M. A. Blair, Z. Pikramenou. *Nanoscale Adv.,* **2023***, 5*, 2453-2461.[62]

2.2. Results and Discussion

2.2.1. Synthesis of DTPA@SiO_2⊃Ru-Van

2.2.1.1. Synthesis of hybrid SiO_2⊃Ru-Van

To develop hybrid nonporous silica nanoparticles, a previously reported procedure based on the Stöber synthesis was followed,[63] where the silica nanoparticles was formed in presence of **Ru** and **Van** was followed in order to yield **SiO_2⊃Ru-Van** (Figure 2.6). Following similar methodology, control particles with just one cargo (**SiO_2⊃Ru** and **SiO_2⊃Van**) and with no included cargo (**SiO_2**) were prepared. Inclusion of **Ru** in the silica frameworks is driven by the electrostatic interaction between the positively charged metal complex and the negatively charged hydroxyl groups of the framework.[64,65] Inclusion of **Van**, however, it is presumably achieved *via* hydrogen bonding between the antibiotic and the framework. The ability of **Van** to stablish hydrogen bonds is well-reported as its interaction with the target moieties (*D*-Ala-*D*-Ala terminated peptidoglycans) is based on interactions of this nature.[66]

Into an ethanolic solution of NH_4OH, aqueous solutions of **Ru** and **Van** were added, and the solution stirred for 5 min. Then, an ethanolic solution of the silica precursor tetraethoxysilane (TEOS) was added dropwise and the reaction stirred at room temperature for 2 h, followed by 15 min of sonication treatment (200 W, 50 Hz) before another hour of stirring at room temperature. Formed orange suspension was then centrifuged, and isolated nanoparticles washed with water to ensure removal of

unreacted TEOS and non-included cargos. Finally, **SiO_2⊃Ru-Van** were dried under vacuum.

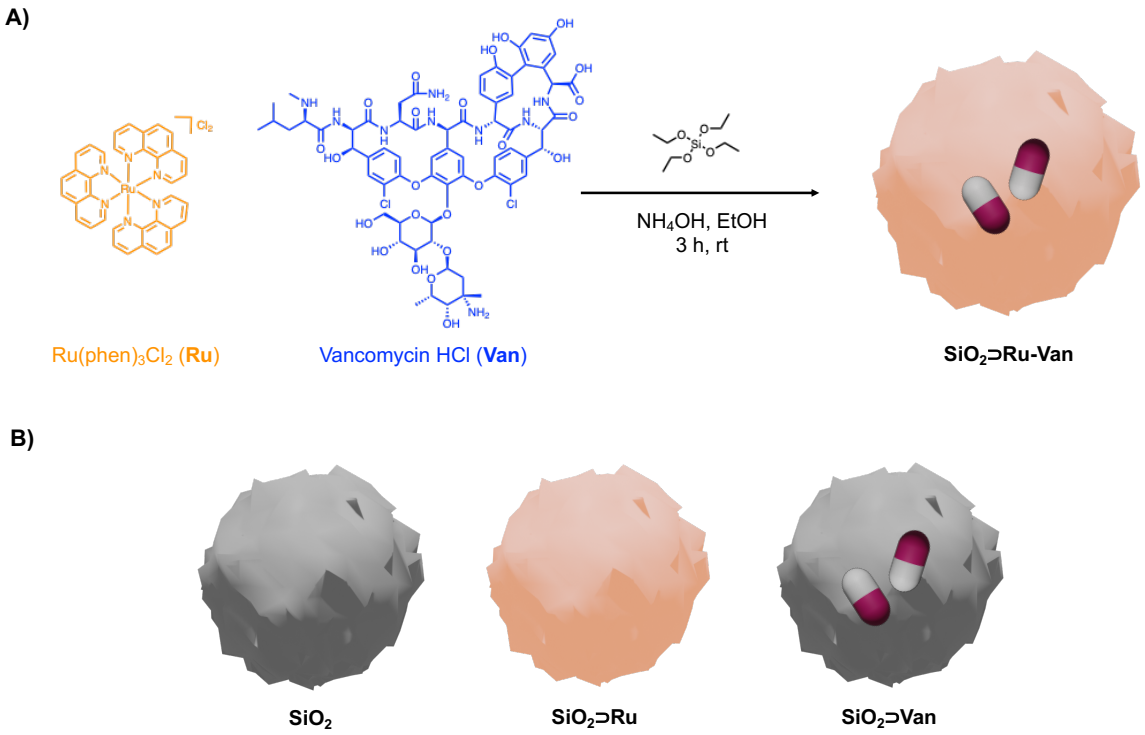

Figure 2.6. (A) Scheme of the formation of **SiO_2⊃Ru-Van** and (B) graphical illustration of the control nanoparticles produced via the same methodology.

The synthesis of the control particles (**SiO_2**, **SiO_2⊃Ru** and **SiO_2⊃Van**) was done following the same procedure but only adding the single cargo to the synthesis media, or in case of **SiO_2** the reaction was performed without addition of cargos.

2.2.1.2. Synthesis of DTPA-Si_2

The ligand **DTPA-Si_2** was chosen as nanoparticle coating due to the previous reports on the membrane disruption abilities of diethylenetriamino pentaacetic acid (DTPA).[12,31,67] In fact, **DTPA-Si_2** is a DTPA derivative that possess two triethoxysilyl groups can be conjugated with the hydroxy groups of the silica nanoparticle surface,

acting as coating (Figure 2.7). The synthesis of **DTPA-Si$_2$** was achieved in a one-step reaction using DTPA bis anhydride as stating material, which would lead to the desired product *via* a nucleophilic ring opening by the silyl-containing reagent (3-aminopropyltriethoxysilane, APTES) (Figure 2.8).[54]

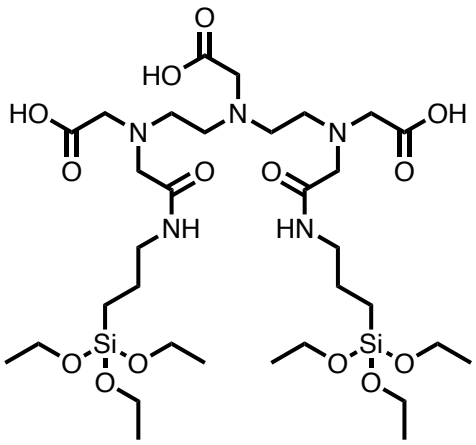

Figure 2.7. Chemical structure of **DTPA-Si$_2$**.

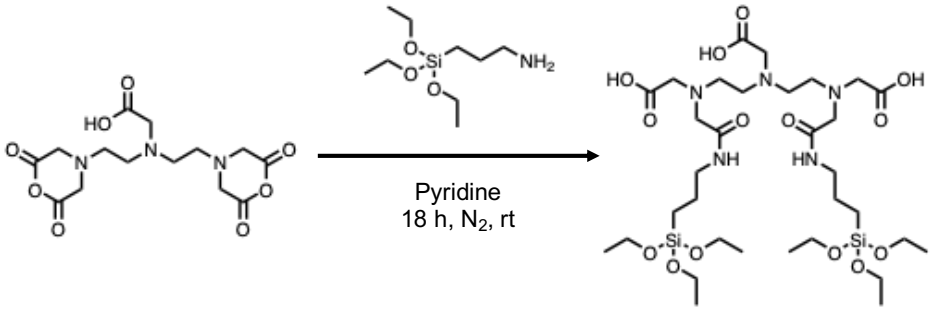

DTPA-Si$_2$

Figure 2.8. Scheme of the synthesis of **DTPA-Si$_2$.**

DTPA bis anhydride was dissolved in anhydrous pyridine before the slow addition of APTES. The reaction was stirred under N_2 atmosphere overnight to ensure completion

before the precipitation of **DTPA-Si$_2$** in cold anhydrous hexane as a white solid. Overnight refrigeration of the formed suspension ensured the full precipitation of the product. Finally, **DTPA-Si$_2$** was isolated *via* filtration and copious amounts of anhydrous hexane was used to wash the product to guarantee full removal of pyridine. Final product was characterised by ^{1}H-NMR (Figure 2.9), ^{13}C-NMR (Figure 2.S2) mass spectrometry (Figure 2.S3) and FT-IR (Figure 2.S4).

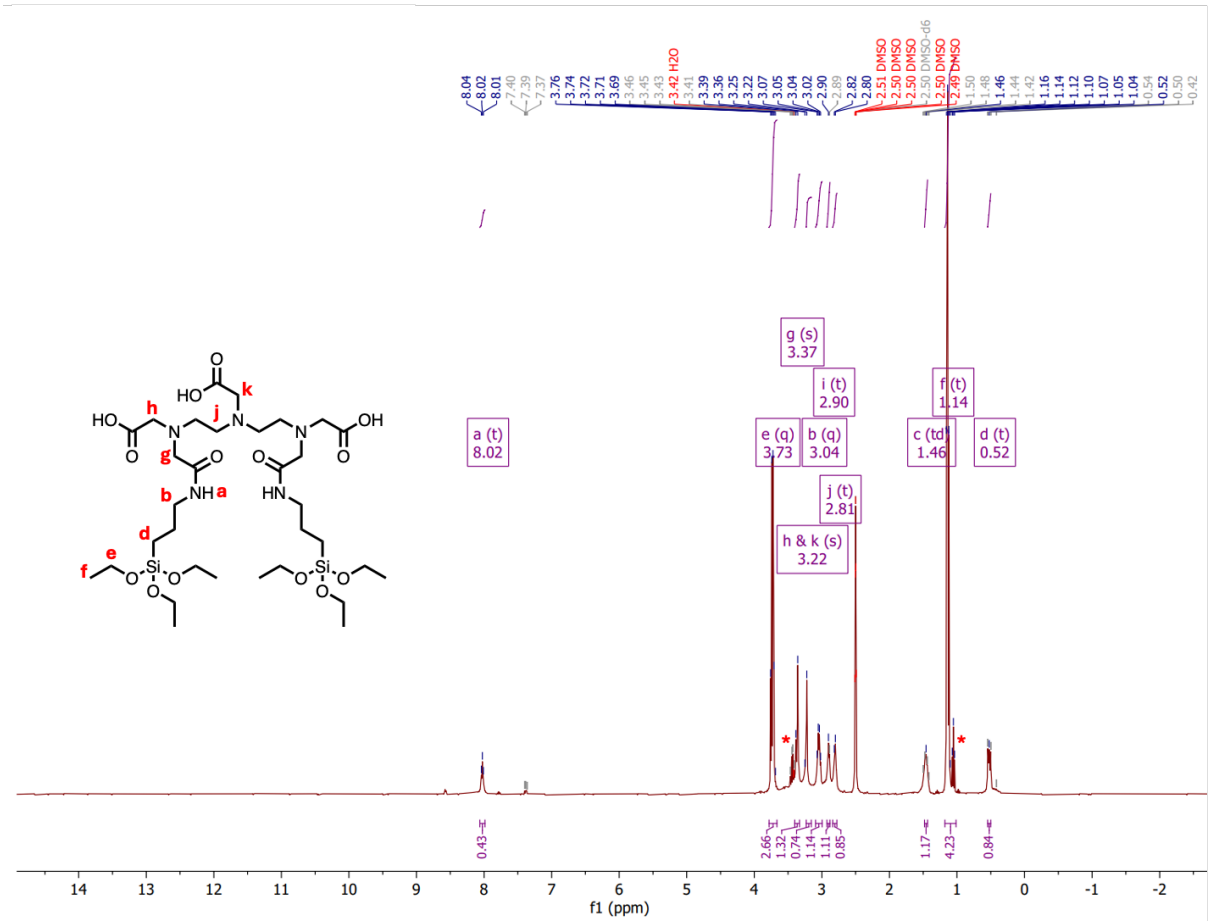

Figure 2.9. ^{1}H-NMR (400 Hz, d_6-DMSO) spectrum of **DTPA-Si$_2$**. * indicates residual solvent (EtOH) peaks.

^{1}H-NMR spectra in d_6-DMSO (Figure 2.9) showed 11 proton environments (excluding the 2 environments of the hydroxyl -OH groups, H_1 and H_5). Synthesis of **DTPA-Si$_2$** was firstly confirmed by the presence of a triplet NMR shift at 8.08 ppm which was assigned to the N*H*CO (H_8) proton of the amide bond. Triplets NMR shifts were also

identified in the aliphatic region at 2.94 ppm and 2.81 ppm, assigned to protons H_3 and H_4. The singlet at 3.33 ppm was assigned to protons H_2 and H_6. The loss of symmetry from the starting materials led to the superimposition of both signals, arising into a single peak with integration of 6 H. Moreover, the formation of amide bond and carboxylic groups also changed the electronic properties of the molecule, being H_2, H_6 and H_7 the most affected and, hence, shifted in respect to DTPA bis anhydride (Figure 2.S1), which also indicates the successful formation of **DTPA-Si$_2$**. Finally, in the ^{1}H-NMR spectrum, the signals associated with the silyl chains at 3.04 ppm (H_9) , 1.45 ppm (H_{10}), 1.14 ppm (H_{13}) and 0.52 ppm (H_{11}) were also observed. ESI-MS (negative mode) also confirmed the formation of **DTPA-Si$_2$** detecting a single specie with m/z of 798.3988 which was assigned to [DTPA-Si_2 – H]$^-$ with a calculated m/z of 798.4008. Thereby, along with ^{13}C-NMR (Figure 2.S2) and FT-IR (Figure 2.S4), the successful synthesis of **DTPA-Si$_2$** was confirmed.

2.2.1.3. Coating of SiO_2⊃Ru-Van with DTPA-Si_2

Furthermore, produced nanoparticles were surface coated by a condensation reaction between the synthesised **DTPA-Si$_2$** and the hydroxyl groups present on the nanoparticles surface. The methodology followed was previously reported for the formation of DTPA-coated silica nanoparticles.[50]

Dried nanoparticles were redispersed in anhydrous toluene to which **DTPA-Si$_2$** was added in a weight ratio of 1:2 nanoparticles:**DTPA-Si$_2$** (Figure 2.10). The suspension was heated in reflux overnight under N_2 atmosphere. Yielded coated hybrid nanoparticles (**DTPA@SiO_2⊃Ru-Van**) were isolated by centrifugation and washed with water to remove unreacted **DTPA-Si$_2$**. Same procedure was followed for the

control nanoparticles leading to **DTPA@SiO$_2$**, **DTPA@SiO$_2$⊃Ru** and **DTPA@SiO$_2$⊃Van**. Followed condensation mechanism of DTPA-Si$_2$ onto the surface of silica nanoparticles has been previously described as *thermal silanol condensation*.[68] This mechanism takes place in anhydrous conditions in a non-polar organic solvent (cyclohexane, xylene or toluene).[68] In the condensation process, the alkoxy groups of the silane coupling agent, **DTPA-Si$_2$** in this case, directly condensate with the hydroxyl groups on the nanoparticle surface, releasing the correspondent alcohol molecule.[69]

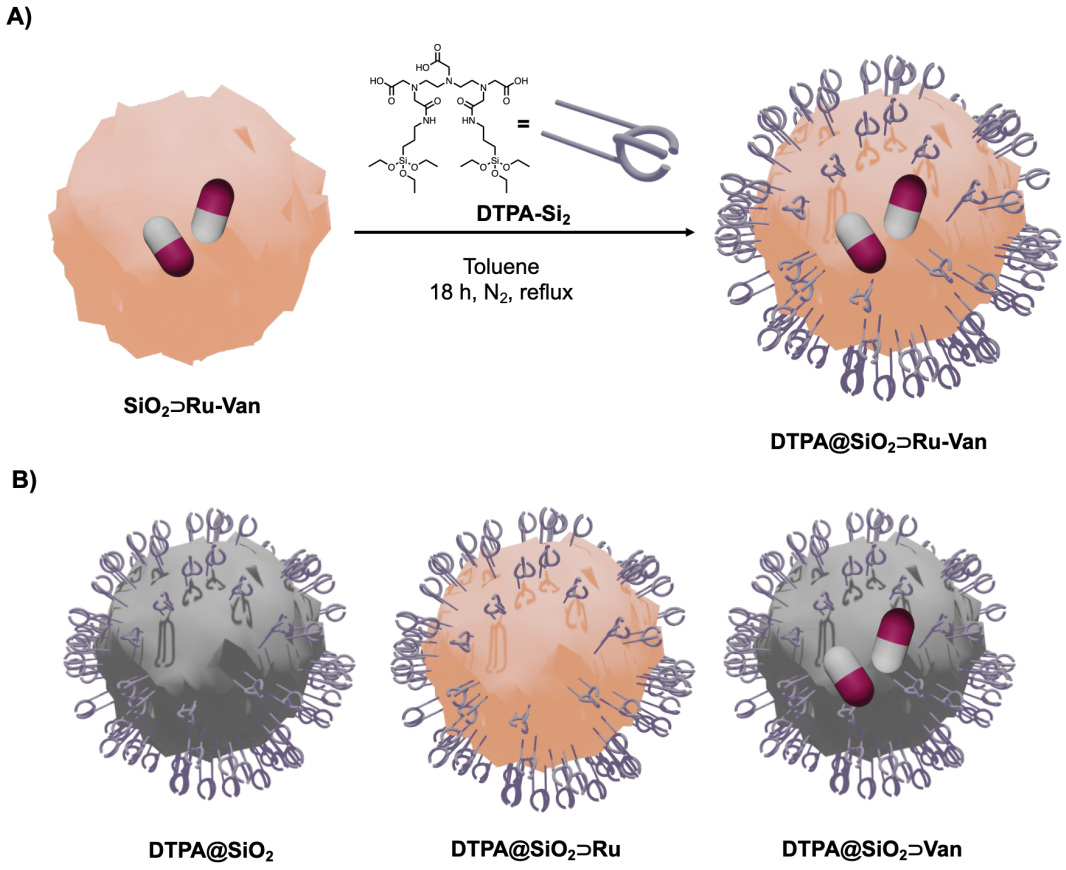

Figure 2.10. (A) Scheme of the coating procedure of **SiO$_2$⊃Ru-Van** and (B) graphical illustration of coated control nanoparticles.

2.2.2. Characterization of DTPA@SiO_2⊃Ru-Van

2.2.2.1. Size and morphology

Produced nanoparticles were firstly analysed by Dynamic Light Scattering (DLS). DLS employs the light scattered by a nanoparticles suspension to estimate the size distribution of the particles, based on the Brownian motion theory.[70] The DLS analysis provided the nanoparticles sizes by intensity (how much light is scattered by the particles in the different size bins), volume (total volume of particles in different size bins) and number (distribution of particles in the different size bins), based on the Stokes Einstein equation.[70] Furthermore, DLS calculated the polydispersity index (PDI) of the particle suspension, which shows the homogeneity or heterogeneity of nanoparticles sizes in the measured sample. Same principle makes also possible to measure the surface charge distribution of particles in solution. After applying an electric current, the Brownian movement of particles is investigated from where the electrophoretic mobility of particles is determined and, hence, the surface charge (ζ-potential) is calculated. ζ-potential measurements can be used to study the colloidal stability of the sample as, in aqueous solutions, particles with higher absolute surface charge would display higher stability, while those with surface charge closer to 0 mv will display lower stability, leading to aggregation and/or precipitation of particles.[71]

Table 2.1. shows the DLS sizes, PDI and ζ-potential values of hybrid nanoparticles before (**SiO_2⊃Ru-Van**) and after (**DTPA@SiO_2⊃Ru-Van**) surface coating. Rest of DLS characterization of control nanoparticles can be found in Figure 2.S5-S8 and Table 2.S1. In water, there is no significance difference between particle before (89 ± 29 nm by intensity) and after (94 ± 10 nm) surface coating, as expected as DTPA is a small molecule that should not affect the size of the nanoparticles. Both nanoparticles showed low PDI values which highlight the high monodispersity of the samples.

Moreover, hydrodynamic diameter of nanoparticles was also recorded in PBS (0.1 M, pH 7.4) in order to mimic the conditions of microbiological studies. In this case, **DTPA@SiO_2⊃Ru-Van** displayed a bigger hydrodynamic size by intensity (113 ± 28 nm) compared with uncoated **SiO_2⊃Ru-Van** (98 ± 29 nm) but the polydispersity is not affected, still measuring a low PDI values (0.21), which excludes formation of aggregates in PBS. Furthermore, this result was further supported by the surface ζ-potential value of particles in PBS, suggesting colloidal stability of the coated particles (-24 ± 5 mV).

Table 2.1. Dynamic Light Scattering (DLS) analysis (n = 5) and ζ-potential measurements (n = 3) of **SiO_2⊃Ru-Van** and **DTPA@SiO_2⊃Ru-Van**. Measurements were performed in at 25 ºC in MiliQ water and in PBS buffer (0.1 M, pH 7.4) with a nanoparticles concentration of 0.1 mg/mL.

		Hydrodynamic size / nm				ζ-potential / mV
		Intensity	Volume	Number	PDI	
SiO_2⊃Ru-Van	**Water**	89 ± 29	86 ± 12	84 ± 22	0.16	- 16 ± 2
	PBS	98 ± 29	82 ± 26	67 ± 18	0.15	-18 ± 6
DTPA@SiO_2⊃Ru-Van	**Water**	94 ± 10	92 ± 15	89 ± 14	0.24	-20 ± 3
	PBS	113 ± 28	105 ± 25	94 ± 20	0.21	-24 ± 5

The disagreement between hydrodynamic diameters in water and in PBS buffer (0.1 M, pH 7.4) is more prominent in case of coated nanoparticles. The presence of higher density of carboxylate groups in case of coated nanoparticles lead to more interactions between nanoparticles and solvent molecules,[72–74] This was further observed when the ionic strength of the PBS suspension was increased by addition of NaCl (Figure 2.S7-S8 and Table 2.S1). Upon addition of NaCl, an increase in the hydrodynamic size of all nanoparticles was observed, with more significant increase in case of coated nanoparticles. These results suggested that the hydrodynamic diameter of the

nanoparticles by DLS is subjected to the ionic strength of the dispersing medium, explaining the discrepancy between the DLS measurement in MilliQ water and in PBS.

Successful DTPA-coating was confirmed as evidenced by the decrease of the surface ζ-potential after coating (-20 ± 3 mV in water and -24 ± 5 mV in PBS) compared with uncoated particles (-16 ± 2 mV in water -18 ± 6 mV in PBS) due to the increased number of negatively charged carboxylate groups in nanoparticle's surface after coating. The overall negative charge of the nanoparticles suggested that the included cargos are within the silica framework, as if they were located on the surface higher values would have been recorded due to the cationic nature of **Ru**.

Scanning Electron Microscopy (SEM) and Transmission Electron Microscopy (TEM) were employed to investigate the morphology and size distribution of developed nanoparticles. The SEM and TEM micrographs (Figure 2.11) of **SiO_2⊃Ru-Van** and **DTPA@SiO_2⊃Ru-Van** confirmed the highly monodisperse nature of nanoparticles with predominant spherical morphology. No significant difference between particles before and after coating was observed, neither in the morphology or the surface texture. Nanoparticles, however, did not show a smooth surface, which has been previously associated with the short synthetic methodology followed for their synthesis.[75] Moreover, independent particle measurements in TEM micrographs (n = 20) led to an estimated size of 85 ± 3 nm for **SiO_2⊃Ru-Van** and 87 ± 3 nm for **DTPA@SiO_2⊃Ru-Van**. TEM analysis resulted in a smaller particle size distribution than previous DLS analysis, which is expected, and previously reported. DLS measurement take into account the solvation layer of the particles in suspension, and this is not reflected in electron microscopy images.[76] The rest of control nanoparticles showed similar size distributions between 50 and 90 nm, as can be found in Figure 2.S10-S12.

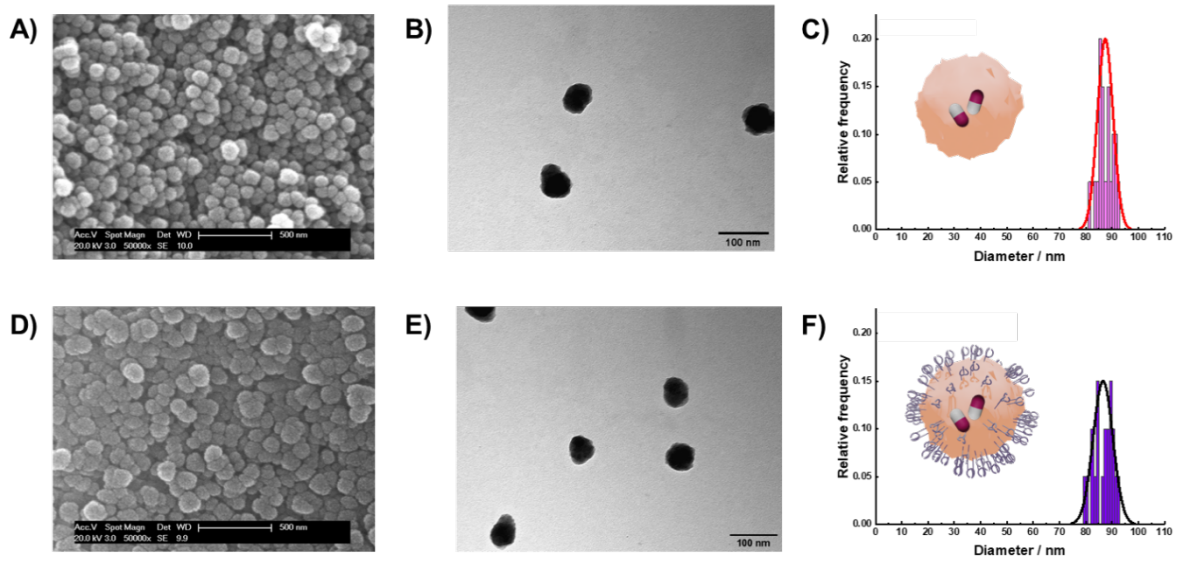

Figure 2.11. (A, D) Scanning Electron Microscopy (SEM) and (B, E) Transmission Electron microscopy (TEM) micrographs of (A-C) **SiO_2⊃Ru-Van** and (D-F) **DTPA@SiO_2⊃Ru-Van.** (C and F) Size disruptions were calculated based on 20 independent nanoparticles from TEM images by ImageJ software. SEM images were recorded with a 50k x magnification and a 20.0 eV electron beam and TEM images with a 250k x magnification.

2.2.2.2. Composition analysis of DTPA@SiO_2⊃Ru-Van

Further analysis of **DTPA@SiO_2⊃Ru-Van** was carried out in order to confirm the presence of the cargos and the DTPA-coating. This section contains the composition characterization of **DTPA@SiO_2⊃Ru-Van**. Full characterization of control nanoparticles can be found in **Appendix section XX.** Firstly, FT-IR and Raman spectroscopy were employed in order to explore the composition of **DTPA@SiO_2⊃Ru-Van**. FT-IR spectra of coated nanoparticles (Figure 2.12C-D) was dominated by the Si-O-Si and Si-OH stretches at 1050 cm^{-1}, 950 cm^{-1} and 795 cm^{-1} and the characteristics stretched of the cargos were too weak to be able to be identified. Nevertheless, characteristics IR stretched of DTPA could be observed in all coated nanoparticles. IR stretches attributed to C-H and N-H bonds as well as to the carbonyl (C=O) bond were observed, confirming the presence of DTPA in coated nanoparticles.

In addition, raman spectroscopy was employed to confirm the presence of included cargos. raman spectroscopy was chosen as suitable technique due to its higher sensitivity and the possibility of using a 633 nm red laser to avoid scattering from the silica framework, and hence, be able to observe the Raman shifts of the cargos. As shown in Figure 2.12B, Raman shifts attributed to **Ru** and **Van** were identified in **SiO_2⊃Ru-Van**. In this case, **SiO_2⊃Ru-Van** was analysed by Raman spectroscopy instead of **DTPA@SiO_2⊃Ru-Van** to avoid any misleading Raman shift from the coating that could be understood as a Raman shift from one of the cargos.

Similarly, solid-state UV/Vis spectroscopy of **SiO_2⊃Ru-Van** (Figure 2.S15A) showed a broad band centred at 425 nm, characteristic of the singlet metal to ligand charge transfer electronic transition (^{1}MLCT) of included **Ru**, as well another band with maximum absorption at 261 nm attributed to the $\pi-\pi^*$ intramolecular transition of 1,10-phenatroline ligands of **Ru.** The last band also showed a shoulder at 281 nm that was assigned to **Van.**

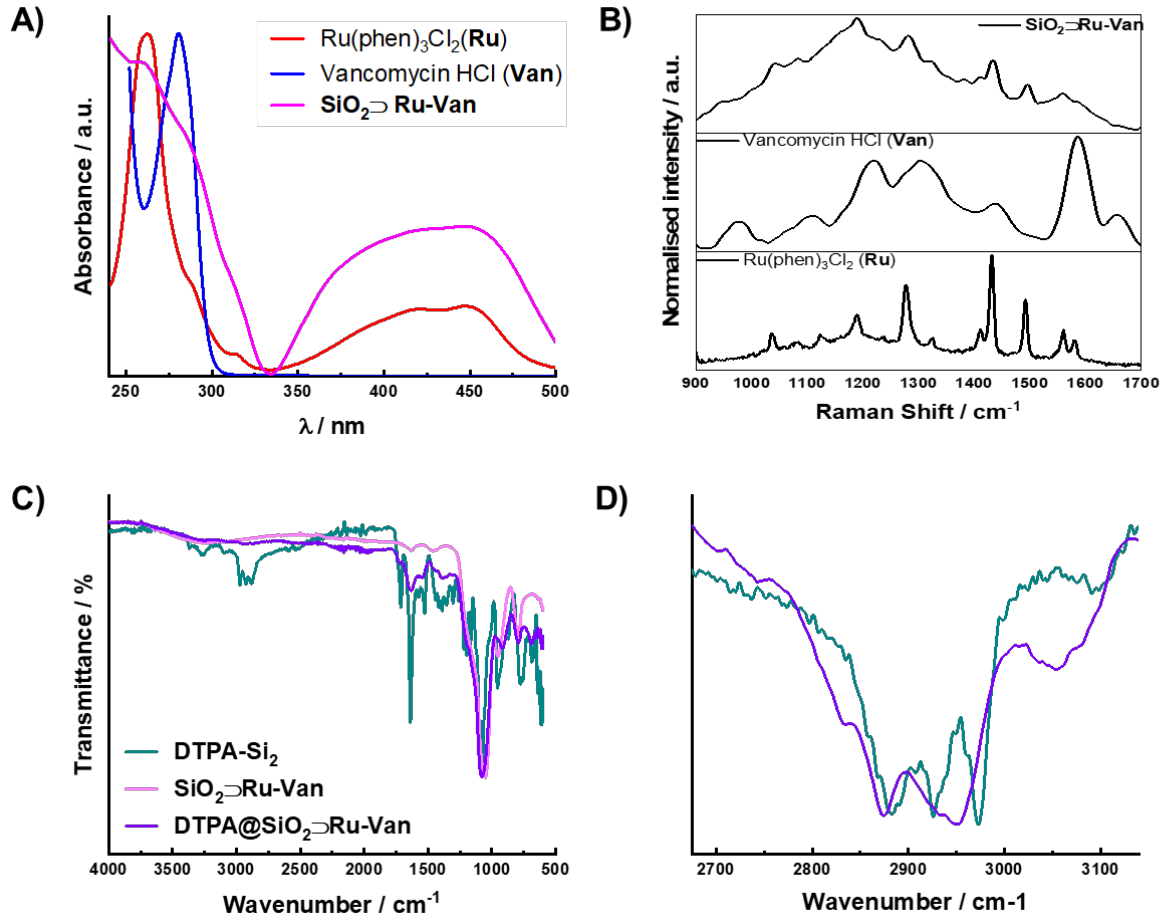

Figure 2.12. Initial composition analysis of **DTPA@SiO₂⊃Ru-Van** was carried out by (A) solid-state UV/Vis, (B) Raman (λ_{exc} = 633 nm) and (C) FT-IR spectroscopy. (D) shows the enlarged range where C-H stretching are present in the FT-IR spectra. Inclusion of cargos was confirmed by UV/Vis and Raman spectroscopy and the successful coating by FT-IR spectroscopy.

2.2.2.3. Photophysical properties of DTPA@SiO₂⊃Ru-Van

Because the application of developed nanoparticles includes imaging in bacterial cells, the photophysical properties of the nanoparticle were explored. All results shown below were recorded in solid-state.

Upon excitation at 450 nm (^{1}MLCT maxima), **SiO_2⊃Ru-Van** and **DTPA@SiO_2⊃Ru-Van** displayed a broad red luminescence peak, characteristic of the triplet MLCT (^{3}MLCT) transition (Figure 2.13A). The recorded spectrum of **SiO_2⊃Ru-Van** showed an emission maximum at 613 nm (Figure 2.13A)**,** in good agreement with recorded emission of **SiO_2⊃Ru** (Figure 2.S16), which displayed an emission maximum at 612 nm; indicating that the presence of **Van** did not influence the emission of **Ru**. Also, both emissions showed a small red shift respect to the solid-state emission of **Ru** complex upon excitation at 450 nm (λ_{max} = 595 nm). This phenomenon has been previously described in the literature, being assigned to the change in the environment of the **Ru** complex, once it is included in the silica framework, which also confirmed the successful inclusion of **Ru**.[64,65,77] Furthermore, a small increase in the **Ru**-based luminescence lifetime was observed in the presence of **Van**. Interestingly **SiO_2⊃Ru-Van** and **SiO_2⊃Ru** showed a longer luminescence lifetime comparing with the **Ru** complex. The protection of **Ru** inside the framework from luminescence quenchers such as oxygen has been attributed as the main reason for lifetime lengthening, as also reported in the literature.[64,65,78]

Furthermore, upon coating, **DTPA@SiO_2⊃Ru-Van** displayed an emission band with maximum at 595 nm, 17 nm blue-shifted compared with uncoated nanoparticles. This is further observed for **DTPA@SiO_2⊃Ru**, which showed a 19 nm blue-shifted emission upon excitation at 450 nm in comparison with **SiO_2⊃Ru**. Interestingly, upon coating, the **Ru**-based luminescence lifetime of resulting nanoparticles increased from 1.69 μs for **SiO_2⊃Ru-Van** to 2.52 μs for **DTPA@SiO_2⊃Ru-Van** (Figure 2.13B) and from 1.45 μs for **SiO_2⊃Ru** to 3.31 μs for **DTPA@SiO_2⊃Ru** (Figure 2.S16B). The further protection from oxygen quenchers due to the presence of the coating may be the cause of the lifetime lengthening.

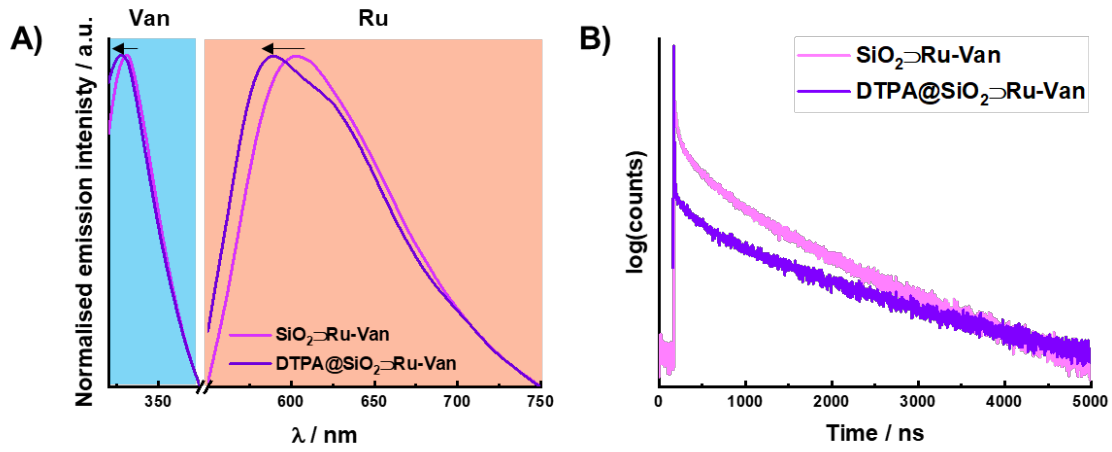

Figure 2.13. Solid-state photophysical study of **SiO_2⊃Van** and **DTPA@SiO_2⊃Van.** (A) Emission of **Van** (λ_{exc} = 270 nm) and **Ru** (λ_{exc} = 450 nm) and (B) **Ru**'s luminescence lifetime decay (λ_{exc} = 455 nm, λ_{em} = 600 nm).

Equally, the presence of **Van** was confirmed by observing its characteristic fluorescence signal at 330 nm upon excitation at 270 nm (Figure 2.13A), which suffered a 3 nm blue shift upon coating for **DTPA@SiO_2⊃Ru-Van** and a 5 nm blue-shift for **DTPA@SiO_2⊃Van** (Figure 2.S17). The dual emission properties of designed nanoparticles confirmed the presence of both cargos, and the attractive long-lifetime red-luminescence of included **Ru** made them ideal for imaging purposes.

2.2.2.4. Quantification of included cargos in DTPA@SiO_2⊃Ru-Van

After confirmation of inclusion of **Ru** and **Van** in **DTPA@SiO_2⊃Ru-Van**, quantification of the cargos was calculated by Thermogravimetric Analysis (TGA) and optical spectroscopy.

TGA relies on the monitoring of the weight loss of a sample upon heating in a controlled atmosphere. From the thermal degradation it is possible to quantify the weight percentage of, in this case, organic content. Quantification of cargos was calculated by comparing the thermal degradation profiles of nanoparticles without cargo inclusion (**SiO_2**) and those particles with one of both cargos. Thermal degradation profile of **SiO_2** only showed one thermal degradation step at 150 ºC attributed to the elimination of adsorbed water molecules, as previously described (Figure 2.14A).[79] **SiO_2⊃Ru-Van** also showed the degradation step at 150 ºC, but it showed a further weight loss between 200 ºC and 900 ºC, which was associated with the included cargos, the cumulative cargo amount was calculated to be 58 $\mu g/mg_{NPs}$. The small content of **Ru** and the broad thermal degradation profile of **Van** made impossible to differentiate between both cargos, hence, determining the cumulative mass that was association to **Ru+Van.** Similarly, **SiO_2⊃Ru** showed a weight loss of 0.3% (7 $\mu g_{Ru}/mg_{NPs}$) and **SiO_2⊃Van** of 8.9 % (89 $\mu g_{Van}/mg_{NPs}$).

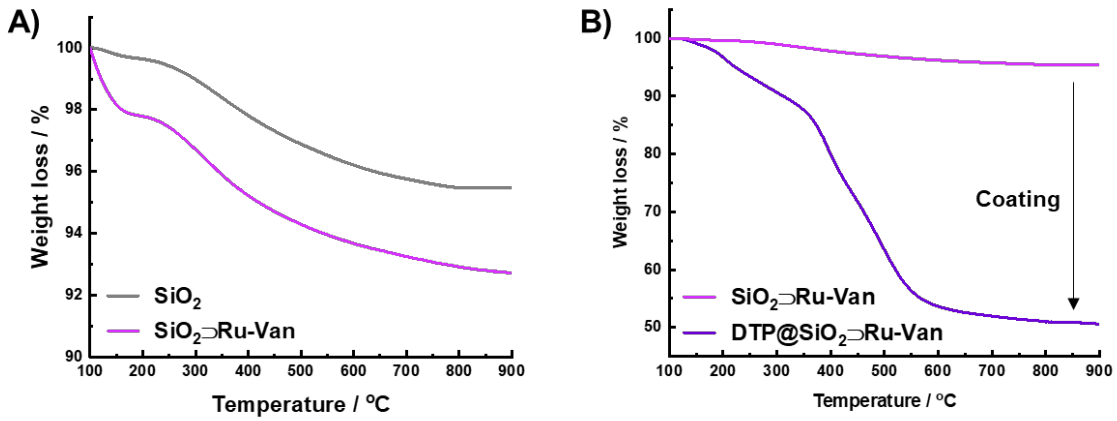

Figure 2.14. Quantification of (A) included cargo in **SiO_2⊃Ru-Van** and (B) DTPA quantification for **DTPA@SiO_2⊃Ru-Van** by Thermogravimetric Analysis (TGA). Samples were heated from 30 ºC to 900 ºC at 1 ºC /min rate with a 10 min isothermal step at 100 ºC to ensure water removal. All degradation curves are set at 100 % for clarity.

In order to obtain more specific quantification for each included cargo separately, UV/Vis spectroscopy was used. The remaining **Van** and **Ru** in the synthesis solution and washing was quantified using the absorptivity value at 271 nm for **Van** (ε = 6200 M^{-1}) and the absorptivity at the ^{1}MLCT band of **Ru** (ε(450 nm) = 16000 M^{-1}). Concentration of remaining **Ru** and **Van** was then calculated and it was estimated, for **SiO_2⊃Ru-Van**, 5 $\mu g_{Ru}/mg_{NPs}$ and 54 $\mu g_{Van}/mg_{NPs,}$ in good agreement with the estimated overall agent content by TGA. The cargo content of **SiO_2⊃Ru** was estimated to be 25 $\mu g_{Ru}/mg_{NPs}$ and 92 $\mu g_{Van}/mg_{NPs}$ for **SiO_2⊃Van** (Figure 2.S20).

2.2.2.5. Quantification of DTPA coating in DTPA@SiO_2⊃Ru-Van

For coating quantification, luminescence Tb^{3+} titrations and TGA. Thermal degradation graph of coated nanoparticles showed, as expected, the weight loss of coated nanoparticles was much higher, reaching in all cases an average weight loss of 53 % (Figure 2.14B and Figure 2.S20). In coated particles, the thermal degradation profile of **DTPA-Si_2** was very dominating, confirming its presence in the particles. From them, an estimated content of 0.55 mg_{DTPA}/mg_{NPs} was calculated. For the rest of coated control particles, a DTPA content between 0.49 mg_{DTPA}/mg_{NPs} and 0.55 mg_{DTPA}/mg_{NPs} was calculated, highlighting the coating homogeneity between all studied nanoparticles (Table 2.S4).

Beside TGA, luminescence titrations were also employed as a secondary coating quantification procedure. Tb^{3+} titrations for quantification of surface DTPA molecules are based on the emission properties of chelated Tb^{3+} in comparison to free solvated Tb^{3+} (Figure 2.S18A). In solution, lanthanide's emission is quenched by the O-H oscillation of the solvent molecules in the coordination sphere, however, upon

chelation, solvent molecules are displaced from the coordination sphere and lanthanide's emission is increased.[80] Moreover, the 1:1 stoichiometry between Tb^{3+} and DTPA-bisamide derivatives is well known.[81] The 1:1 stoichiometry was further confirmed by titration of a methanolic solution of $TbCl_3 \cdot 6H_2O$ to a methanolic solution of **DTPA-Si$_2$** (Figure 2.S18B). Hence, by titration of Tb^{3+} to a suspension of **DTPA@SiO$_2$⊃Ru-Van**, the luminescent signal of Tb^{3+} increased until reaching a plateau. From the plateau, the concentration of DTPA was correlated with the concentration of nanoparticles in the experiment and 0.53 mg_{DTPA}/mg_{NPs} was estimated, in goo agreement with the TGA quantification (0.55 mg_{DTPA}/mg_{NPs}). Similar results for the quantification of DTPA were calculated for the rest of coated nanoparticles (Figure 2.S19**,** Table 2.S4).

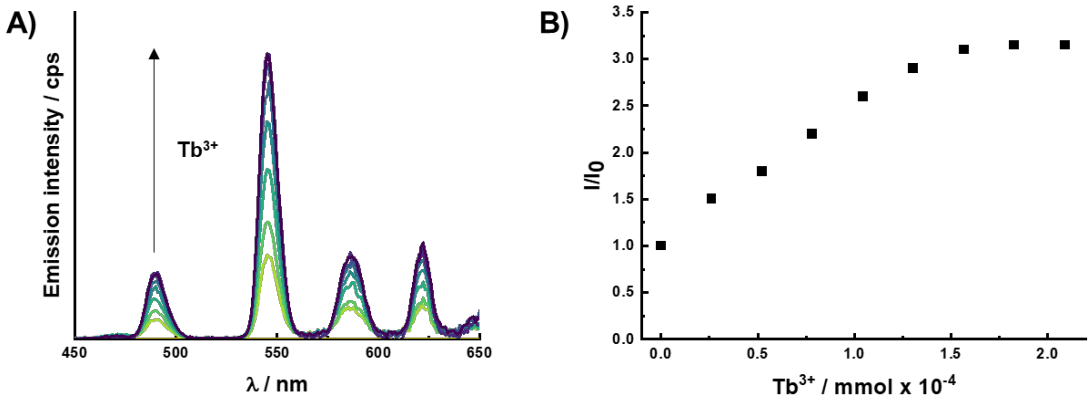

Figure 2.15. Recorded emission spectra (λ_{exc} = 273 nm) and Tb^{3+} titration curve of **DTPA@SiO$_2$⊃Ru-Van**. Nanoparticles titrations were performed using a 1 mg/mL methanolic suspension and a methanol Tb^{3+} solution of 3.3 mM.

2.2.3. Release studies of DTPA@SiO$_2$⊃Ru-Van

Release studied of **Van** from **DTPA@SiO$_2$⊃Ru-Van** were monitored by fluorescence spectroscopy based on calibration of **Van**'s fluorescence signal at 330 nm upon

excitation at 270 nm. Release experiments were performed with aqueous nanoparticles dispersions with a nanoparticle concentration of 2.5 mg/mL. Nanoparticles suspensions in MiliQ water were subjected to continuous shaking at 150 rpm at 37 ºC. Release studied upon shaking of **Van** from **DTPA@SiO$_2$⊃Ru-Van** showed a cumulative release of the antibiotic up to 18 h, with a cumulative estimated release of 3.3 ± 0.5 $\mu g_{Van}/mg_{NPs}$ (Figure 2.16). **DTPA@SiO$_2$⊃Van** (Figure 2.S24), similarly, showed a cumulative release of 3.3 ± 0.3 $\mu g_{Van}/mg_{NPs}$ after 18 h upon shaking (150 rpm) at 37 ºC (Figure 2.S24).

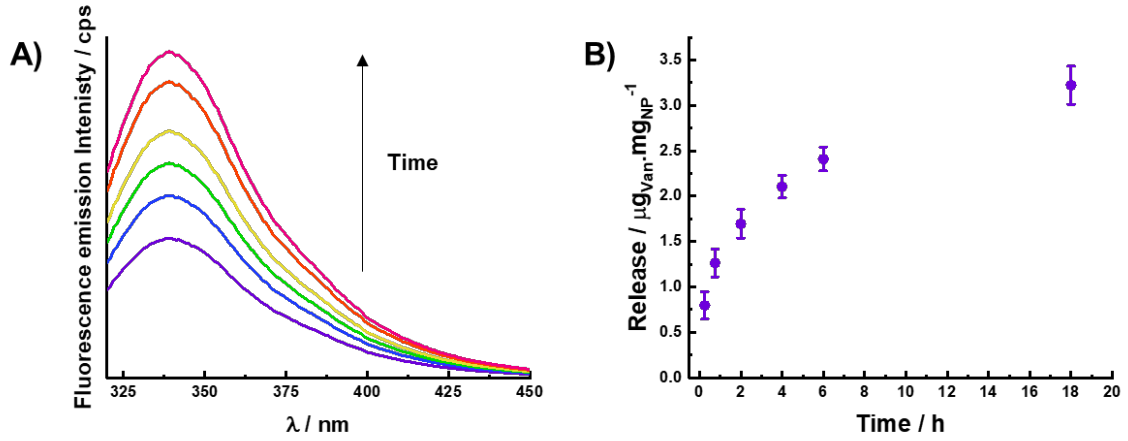

Figure 2.16. (A) Representative fluorescence monitoring release of **Van** from **DTPA@SiO$_2$⊃Ru-Van** (λ_{exc} = 270 nm, λ_{em} = 330 nm) at 37 ºC and 150 rpm and (B) cumulative **Van** release graph (n = 3).

Moreover as, triggered nature of Van release was explored. For that, nanoparticle suspension was kept undisturbed at 37 ºC were also carried out, defining these conditions as “static release”. The static release was performed for 90 min and the results directly compared with **Van**’s release upon continuous shaking (150 rpm, 37 ºC) for 90 min (Figure 2.S25). Interestingly, the cumulative release of **Van** under static conditions was only estimated to be 0.9 ± 0.2 $\mu g_{Van}/mg_{NPs}$ for **DTPA@SiO$_2$⊃Ru-Van**

and 0.6 ± 0.1 $\mu g_{Van}/mg_{NPs}$ for **DTPA@SiO$_2$⊃Van**, while **Van** releases of 3.2 ± 0.3 $\mu g_{Van}/mg_{NPs}$ and 3.7 ± 0.2 $\mu g_{Van}/mg_{NPs}$ were estimated upon continuous shaking for **DTPA@SiO$_2$⊃Ru-Van** and **DTPA@SiO$_2$⊃Van**, respectively. Release experiments of **Ru**, also monitored by luminescence spectroscopy (λ_{exc} = 450 nm, λ_{em} = 600 nm) revealed a very low leakage of the complex under both release conditions (Figure 2.S25). These results showed the potential of designed coated hybrid nanoparticles to act as triggered drug delivery systems for the delivery of **Van**, and still possess the vast majority of **Ru**, also making them ideal for luminescence imaging purposes.

2.2.4. Biocompatibility of DTPA@SiO$_2$⊃Ru-Van

Biocompatibility of designed nanoparticles was assessed through MTT assays using A549 cell line (lung cancer cell line) as model cell line. The MTT assay is a colorimetric assay for assessing cell metabolic activity. After treatment of cells with the studied compounds or nanoparticles, 3-(4,5-dimethylthiazol-2-yl)-2,5-diphenyl-2H-tetrazolium bromide (MTT) is added to the cells and incubated. The MTT reagent, with a yellow colour, will be metabolised into formazan, which possess a purple colour. Cell viability is, hereby, assessed by determining the concentration of produced formazan by optical spectroscopy (λ = 595 nm) to respect a negative (DMSO) and positive (Triton-X) controls.[82]

MTT assay of **SiO$_2$** did not show any cytotoxicity even up to concentration of 10 mg/mL, emphasizing the high biocompatibility of SiO_2, as previously reported.[83–85] Upon coating, **DTPA@SiO$_2$** only showed statistically significance cytotoxicity, as assessed by a 1-way ANOVA followed by a post-hoc Dunnett's T-test, at concentration of 10 mg/mL. Similarly, **SiO$_2$⊃Ru-Van** did not show significant

cytotoxicity even up to concentrations of 10 mg/mL. After coating, **DTPA@SiO_2⊃Ru-Van** only showed statistically significance toxicity at concentrations of 10 mg/mL (Figure 2.17). The rest of control particles described similar trend that **SiO_2⊃Ru-Van** and **DTPA@SiO_2⊃Ru-Van** (Figure 2.S26), beside **SiO_2⊃Van**, where cytotoxicity was observed from concentration of 0.37 mg/mL and above.

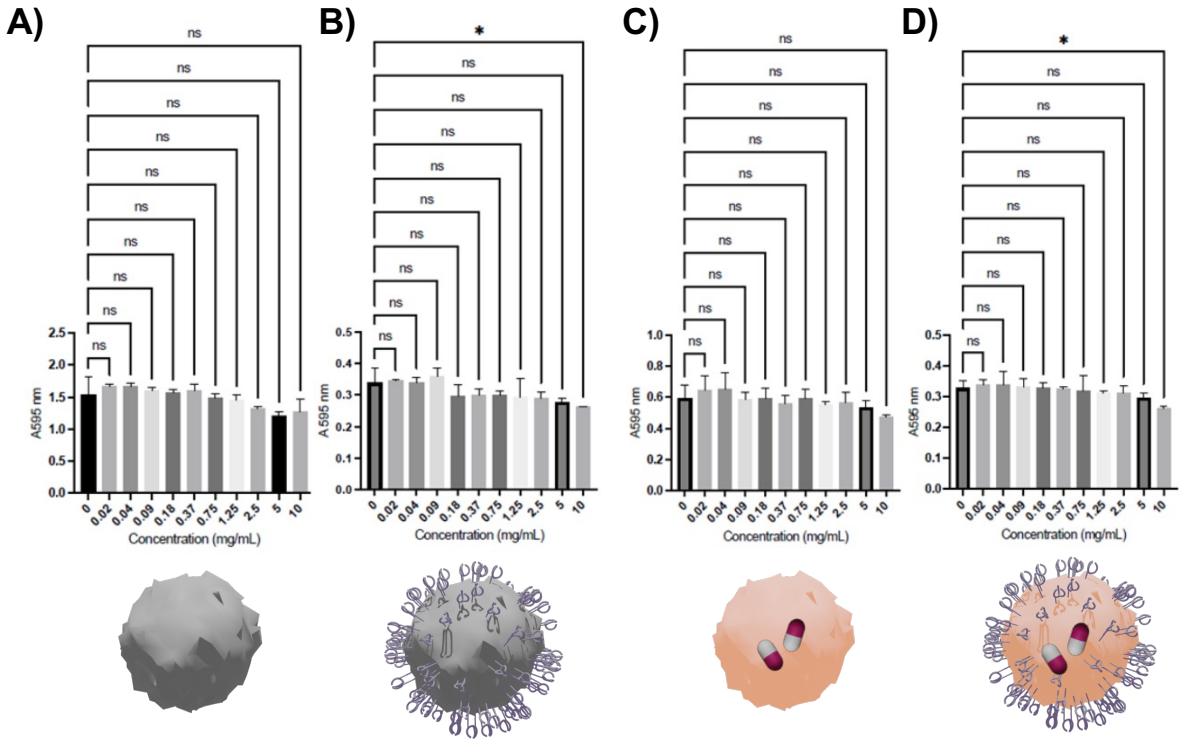

Figure 2.17. MTT cell viability assays of A549 cell line incubated with studied nanoparticles for 18 hours with (A) **SiO_2**, (B) **DTPA@SiO_2**, (C) **SiO_2⊃Ru-Van** and (D) **DTPA@SiO_2⊃Ru-Van** 1-way ANOVA followed by a Dunnett's t-test corrected for multiple comparisons was performed, * = P<0.05, ** = P<0.01 and *** = P< 0.001 n = 3.

2.2.5. Antibacterial activity of DTPA@SiO_2⊃Ru-Van

2.2.5.1. Minimal Inhibitory Concentration (MIC) determination

In order to assess the antibacterial activity of designed hybrid coated silica nanoparticles, a Gram-positive representative specie (*S. aureus,* ATTC23841) and a library of Gram-negative species (*Escherichia coli*, MG1655; *Acinetobacter baumanii*,

AYE; *Klebsiella pneumoniae*, ATTC43816R; *Klebsiella oxytoca*, 080-KPC CHD; *Citrobacter freundii*, NCTC9750, *Salmonella enterica*, SL1344; *Pseudomonas aeruginosa*, PA14 and *Burkhoderia cenocepacia*, K57-2, CF isolate) were chosen. The main difference between Gram-positive and -negative species relies on the structure of the cell membrane. Gram-negative bacterial cells possess a double cell membrane that includes a rigid and impermeable outer membrane; while Gram-positive species only have one cell membrane, easy to be crossed by molecules. The impermeability of Gram-negative outer membrane gives bacterial cells intrinsic resistant against many antibiotics, including **Van**. However, the susceptibility of *S. aureus* and Gram-positive bacterial cells in general to **Van** is very well-known, as **Van** is able to cross the simple cell-membrane of *S. aureus* and reach the target structure.[1]

The antibacterial activity of designed nanoparticles and individual cargos was evaluated by determining the minimal inhibitory concentration (MIC) in Lysogenic Broth (LB). MIC is, hereby, defined as the minimum concentration of nanoparticles or cargos where no growth of bacteria is detected.[86] Hence, nanoparticles antibacterial activity was evaluated in a concentration range between 10 mg_{NPs}/mL and 0.02 mg_{NPs}/mL under shaking conditions (150 rpm, 37 ^{o}C) and calculated MIC values are summarised in Table 2.2.

Table 2.2. Minimal Inhibitory Concentrations (MIC, mg/mL) of **Van**, **SiO_2**, **DTPA@SiO_2**, **SiO_2⊃Ru-Van** and **DTPA@SiO_2⊃Ru-Van** for *S. aureus* (ATCC23851), *E. coli* (MG1655), *A. baumannii* (AYE), *K. pneumoniae* (ATCC43816R), *K. oxytoca* (080-KPC CHD), *C. feundii* (NCTC9750) and *S. enterica* (SL1344) determined by the 2-fold dilution method upon shaking at 150 rpm at 37 °C in LB media. Depicted results are based on three biological replicas.

*Estimated **Van** released based on release studies *in vitro* (in μg/mL, ± 16 %)

	E. coli	***A. baumannii***	***K. pneumoniae***	***K. oxytoca***	***C. feundii***	***S. enterica***	***S. aureus***
Van	> 0.25	> 0.25	> 0.25	> 0.25	> 0.25	> 0.25	0.001
SiO_2	> 10	> 10	> 10	> 10	> 10	> 10	> 10
DTPA@SiO_2	> 10	10	10	10	10	10	2.50
SiO_2⊃Ru-Van	5.00	2.50	2.50	5.00	5.00	2.50	1.25
DTPA@SiO_2⊃Ru-Van	1.25 (4.1)*	1.25 (4.1)*	0.75 (2.5)*	1.25 (4.1)*	1.25 (4.1)*	0.75 (2.5)*	0.37 (1.2)*

The antibiotic **Van** showed high activity against *S. aureus* with an MIC of 0.001 mg/mL, while no activity was observed for *E. coli* up to concentrations of 0.25 mg/mL. The aforementioned impermeability of Gram-negative bacterial cell's outer cell membrane to **Van** is the reason for its lack of activity.[1,66,87] The luminescent agent **Ru** also showed moderate activity against *S. aureus* (MIC = 0.312 mg/mL) and no significant activity against the Gram-negative species. Ruthenium(II) complexes' antibacterial activity has been previously reported.[88] Nevertheless, the modest antibacterial activity of

employed **Ru** has been associated with its low lipophilicity, in comparison with other ruthenium(II) polypyridyl complex.[89,90]

Plain **SiO_2**, moreover, showed no antibacterial activity up to concentrations of 10 mg/mL in all bacteria espies studied, as previously also reported in the literature.[91] Interestingly, once the plain nanoparticles are coated, **DTPA@SiO_2**, their activity increased slightly in Gram-positive bacterial cells, resulting on a MIC of 2.5 mg/mL while no significance increase was observed for the Gram-negative species. The membrane-disrupting abilities of DTPA has been previously reported and this is more evident in simple cell membranes as in the case of *S. aureus,* supporting these results.[31] Nevertheless, the disruption abilities of surface DTPA may not be enough in case of Gram-negative species to be translated into a significant antibacterial activity. **SiO_2⊃Ru-Van** displayed a moderate antibacterial activity compared with plain **SiO_2** with MIC of 1.25 mg/mL for *S. aureus* and MIC values between 2.50 and 5.00 mg/mL for Gram-negative species. This activity is significantly increased after coating. **DTPA@SiO_2⊃Ru-Van** nanoparticles showed a higher antibacterial activity with MIC values of 0.37 mg/mL for *S. aureus* and between 0.75 and 1.25 mg/mL for the Gram-negative species. The increase in the antibacterial activity of coated nanoparticles evidences the importance of the coating on the nanoparticle penetration into cells as only when **Van** is released within the Gram-negative cells it will be active.

Moreover, note that the estimated release of **Van** in the MIC concentrations was much lower that the MIC values determined for free **Van**. It is worth to highlight that in case of Gram-negative bacterial species, an estimated **Van** release between 4.1 and 2.5 μg/mL (± 16 %) was enough to inhibit the growth of bacterial cells, when free **Van** is not able to inhibit bacterial growth **Van** in concentration up to 250 μg/mL.

Equally, **SiO_2⊃Ru** and **SiO_2⊃Van** showed moderate to null antibacterial activity depending on the bacterial specie studied, but their activity increased upon coating, highlighting again the role of the coating in particle activity.

Finally, same experiment was reproduced under static conditions at 37 ^oC to further explore the triggered nature of **Van** release (Table 2.S5). Determined MIC values under static conditions were much higher than those determined upon shaking (150 rpm, 37 ^oC), emphasising the importance of triggered release and in good agreement with *in vitro* release studies.

Nevertheless, two of exanimated Gram-negative bacterial species (*P. aeruginosa* and *B. cenocepacia*) did not show the same susceptibility to explored nanoparticles compared with the rest of Gram-negative species. In case of these two species, the presence of DTPA-coating did not enhance the antibacterial activity of nanoparticles as it can be seen in Table 2.S5. These results have been associated to the aminoarabinosylation of Lipid A component of the outer membrane lipopolysaccharides. Through this modification, a phosphoethylamine or 4-amino-4-deoxy-L-arabinose molecule is covalently conjugated to the Lipid A next to the divalent cations, protecting them from chelating agents.[92–94] Aminoarabinosylation has been identified across a large range of *P. aeruginosa* strains,[95] including PA14 as well as in several Burkholderia genre species.[96]

2.2.5.2. DTPA@SiO_2⊃Ru-Van chelating abilities against cell membrane Ca^{2+}

As previously mentioned, the increased antibacterial activity of coated nanoparticles was attributed to their ability to penetrate the cell membrane and, hence, release **Van** inside the cell. In fact, the activity of was **DTPA@SiO_2⊃Ru-Van** attributed to being able to chelate structurally essential Ca^{2+} and Mg^{2+} cations in the membrane, destabilizing them and , hereby, allowing nanoparticle penetration.[10,11] It is reported the ability of poly-aminocarboxylate chelators to interact with bacterial cell membranes and damage its structural stability by sequestering crucial Ca^{2+} and Mg^{2+} cations, destabilizing it.[31,97] This effect has been further supported by simulation studied that revealed that when ethylenediaminotetraacetic acid (EDTA) sequesters the divalent cations the density of phospholipids increased in the outer membrane, along with a decrease in the density of lipopolysaccharides; resulting in membrane destabilization.[12] Furthermore, the binding constant (*K*) of cations to DTPA-bisamide derivatives have been reported to be in the range of 10^5-10^9 (log*K* = 5-9).[98]

Hence, firstly, the binding affinity of **DTPA@SiO_2⊃Ru-Van** against Ca^{2+} was explored by Isothermal Titration Calorimetry (ITC). ITC enables the measurement of the heat released or absorbed during a chemical reaction, in this case, the heat released or absorbed when the metal cation is chelated by the aminocarboxylate. From it, the affinity between the cation and chelator can be calculated (log*K*) as well as the thermodynamic parameters (ΔH, -TΔS and ΔG) of the chemical event. The titration of a PBS buffer (0.1 M, pH 7.4) solution of Ca^{2+} ($CaCl_2$) into a PBS buffer.

suspension of **DTPA@SiO_2⊃Ru-Van** concluded a log*K* value of 7.5 ± 0.6, in good agreement with reported values (Figure 2.18). Moreover, thermodynamic parameters calculated from the binding curve also indicated that the chelation of Ca^{2+} by

DTPA@SiO_2⊃Ru-Van is a thermodynamically favourable event. Finally, *in-situ* formation of the Ca^{2+}DTPA-Si_2 complex was further confirmed by mass spectrometry (Figure 2.S28) supported the viability of the Ca^{2+}DTPA complex on the nanoparticles' surface.

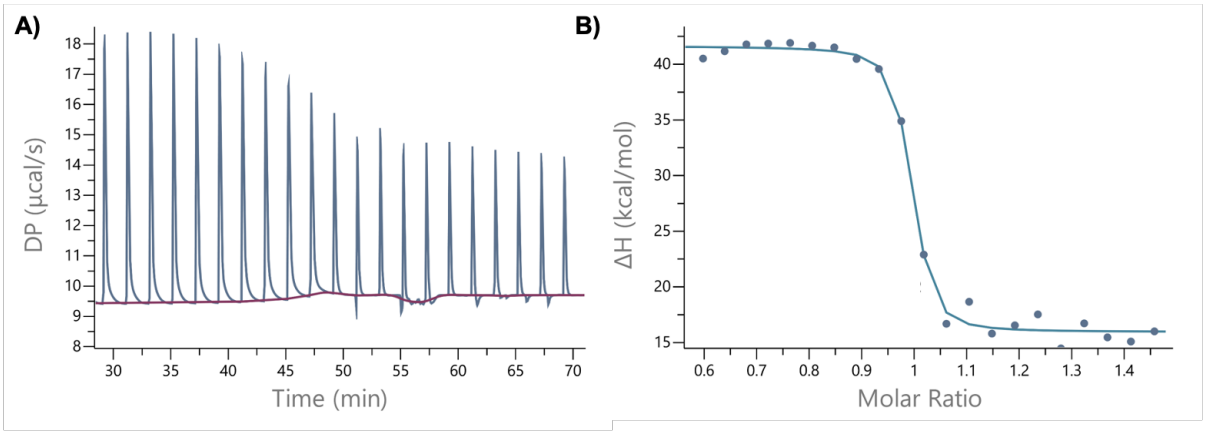

Figure 2.18. Isothermal Titration Calorimetry (ITC) graph and fitted data of Ca^{2+} (2.5 mM) into a suspension of **DTPA@SiO2⊃Ru-Van** ([DTPA] = 0.32 mM) in PBS (0.1 M, pH 7.4) at 25 °C.

Subsequently, **DTPA@SiO_2⊃Ru-Van** nanoparticles with DTPA chelating sites already blocked with Ca^{2+} were developed, denoted **Ca^{2+}DTPA@SiO_2⊃Ru-Van**. Briefly, incubation of **DTPA@SiO_2⊃Ru-Van** in a Ca^{2+}-rich aqueous solution yielded to **Ca^{2+}DTPA@SiO_2⊃Ru-Van** (full nanoparticle characterization in Figure 2.S27-S28 and Table 2.S6-S7). Antibacterial activity of chelated nanoparticles, assessed by MIC determination, showed lower antibacterial activity, with similar values to those MIC values determined for uncoated **SiO_2⊃Ru-Van** (Table 2.3). These results showed the importance of free carboxylate groups in the particle surface. These carboxylic group would be then able to remove divalent cations from the membrane and allow particle penetration.

Table 2.3. Minimal Inhibitory Concentrations (MIC, mg/mL) of **Ca^{2+} DTPA@SiO_2⊃Ru-Van** for *S. aureus* (ATCC23851), *E. coli* (MG1655), *A. baumannii* (AYE), *K. pneumoniae* (ATCC43816R), *K. oxytoca* (080-KPC CHD), *C. feundii* (NCTC9750) and *S. enterica* (SL1344) determined by the 2-fold dilution method upon shaking at 150 rpm at 37 °C in LB media. Depicted results are based on three biological replicas.

	E. coli	***A. baumannii***	***K. pneumoniae***	***K. oxytoca***	***C. feundii***	***S. enterica***	***S. aureus***
Ca^{2+}DTPA@SiO_2⊃Ru-Van	5.00	10	5.00	5.00	5.00	5.00	2.50

2.2.5.3. Nanoparticle penetration in bacterial cells

In order to further confirm that the observed increased antibacterial activity of coated nanoparticles is due to their abilities to penetrate the bacterial cells, Structured Illumination Microscopy (SIM) was employed to monitor the nanoparticle uptake, taking advantage of the emissive properties of the nanoparticles. SIM, opposite to conventional confocal luminescence microscopy, uses patterned illumination, usually stripes, to excite the sample. The emitted luminescence signal is recorded for each of those positions and then, reconstructed to achieve luminescence imaging with a resolution effectively double respect to traditional confocal microscopy. Furthermore, the gentler illumination set-up of SIM prevents organic dyes from photobleaching, allowing linger imaging experiments.[99]

S. aureus (ATCC23851) and *E. coli* (MG1655) were chosen as representative Gram-positive and Gram-negative species for the imaging studies. Bacterial cells were

incubated with coated and uncoated hybrid nanoparticles and live imaging of cells with uptaken nanoparticles was recorded. SIM showed the uptake of red emissive nanoparticle by tracking the signal of included **Ru** complex. Spherical S*. aureus* and rod-shaped *E. coli* cells were also co-stained with nucleic-acid stain Hoechst H33342. Investigation of particle penetration in cells was further explored by z-stack imaging, that allowed the localization of particles inside cells. Z-stacks were additionally processed by building intensity profile graphs of **Ru** signal in comparison with Hoechst H33342 to confirm the presence of the particles inside the bacterial cells.

After 2 h incubation at 37 ºC and mild shaking (150 rpm) in LB, nanoparticle penetration in *S. aureus*, based on **Ru** signal, was observed for **SiO_2⊃Ru-Van** (Figure 19A,B) and **DTPA@SiO_2⊃Ru-Van** (Figure 2.19C,D). This was expected due to the simple cell membrane structure of Gram-positive bacterial cells, which allows easer particle penetration, and it is also in good agreement with the determined MIC values of hybrid nanoparticles for *S. aureus*. However, no nanoparticle uptake, based on **Ru** signal, was observed for *E. coli* when it was incubated with uncoated **SiO_2⊃Ru-Van** nanoparticles (Figure 2.20A). Nevertheless, when incubated with coated **DTPA@SiO_2⊃Ru-Van**, **Ru** signal was observed inside *E. coli* cells (Figure 2.20B). Particle penetration was confirmed by z-stack reconstruction (Figure 2.20B1-B2) of selected cells and orthogonal projections (Figure 2.20C). However, in case of *P. aeruginosa*, did not show any internalised nanoparticles even after 18 h incubation (Figure 2.S31), associated with the aminorabinosylation of lipopolysaccharides as previously explained.

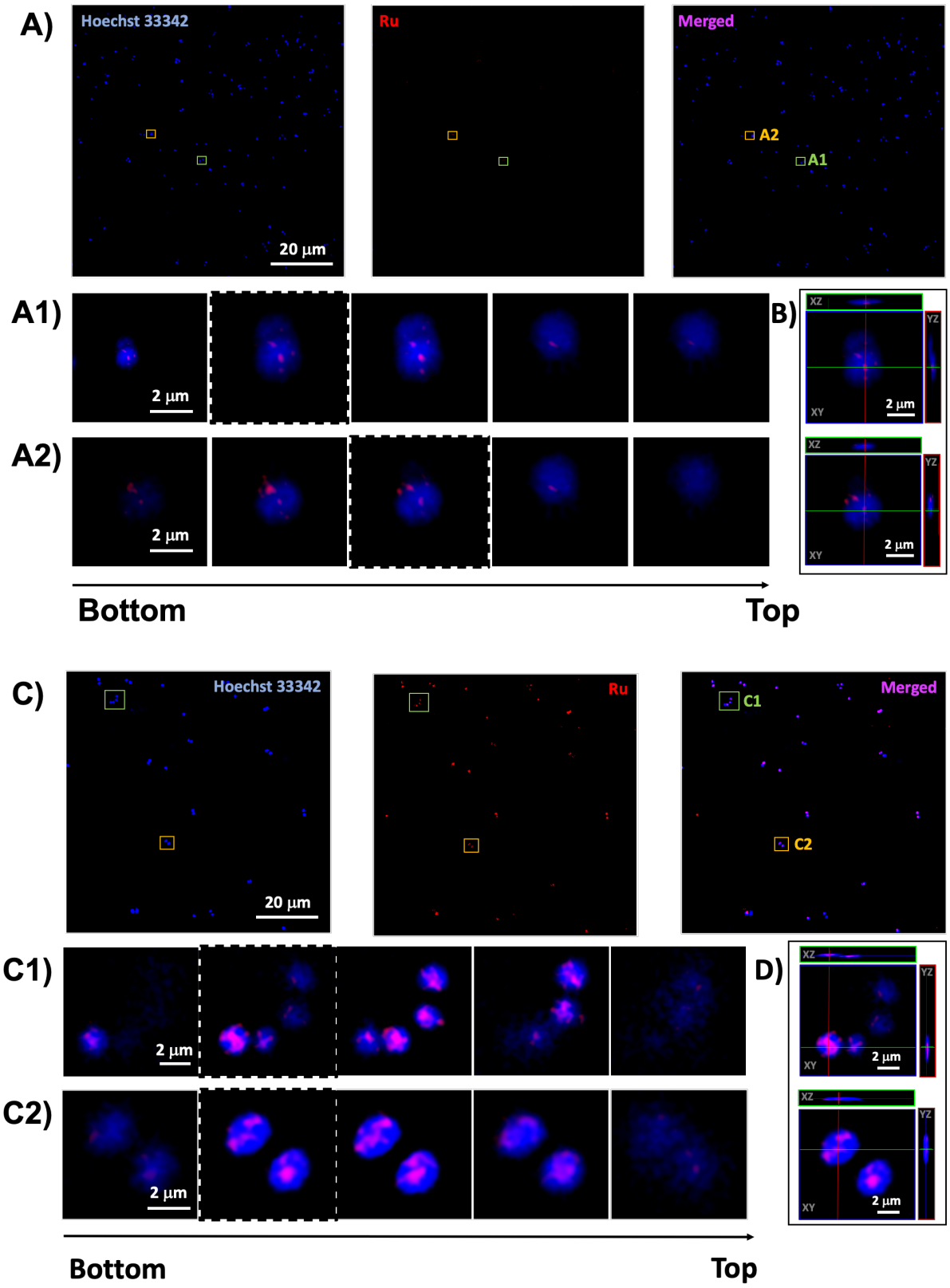

Figure 2.19. Representative live bacterial cell imaging (n = 5) by structural illumination microscopy showing red luminescent particle uptake in *S. aureus* with (A) **SiO_2⊃Ru-Van** and (C) **DTPA@SiO_2⊃Ru-Van**. Overnight grown bacteria are treated with the nanoparticles (2.5 mg/mL) for 2 h at 37 °C under mild shaking (150 rpm). Images show

each channel for the outline of bacterial cells (blue) and particle luminescence (red) as well as merged channels. 3-D reconstruction: image sequence extracted from the z-stack of two *S. aureus* incubated with (A1 and A2) **SiO_2⊃Ru-Van** and (C1 and C2) **DTPA@SiO_2⊃Ru-Van** and orthogonal reconstruction of (C) A1 and A2 and of (D) C1 and C2. Orthogonal reconstructions display central plane image (highlighted with dashed line) showing red luminescence from nanoparticles inside the cells. Red channel, ruthenium emission (λ_{exc} = 488 nm, λ_{em} = 580 – 620 nm); blue channel, Hoechst H33342 emission (λ_{exc} = 405 nm, λ_{em} = 410 – 455 nm).

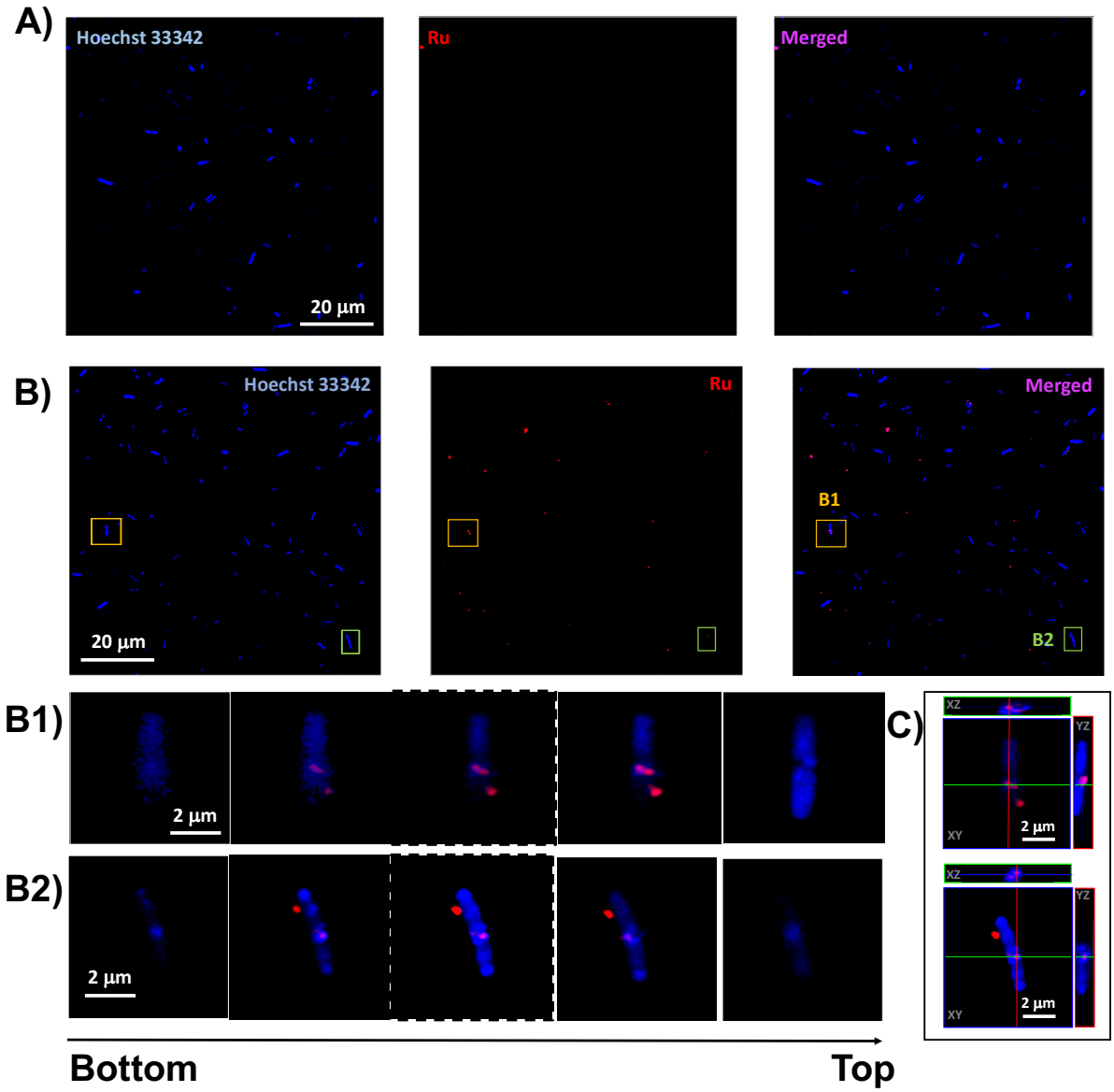

Figure 2.20. Representative live bacterial cell imaging (n = 5) by structural illumination microscopy showing red luminescent particle uptake in *E.coli* with (A) **SiO_2⊃Ru-Van** and (B) **DTPA@SiO_2⊃Ru-Van**. Overnight grown bacteria are treated with the nanoparticles (2.5 mg/mL) for 2 h at 37 °C under mild shaking (150 rpm). Images show each channel for the outline of bacterial cells (blue) and particle luminescence (red) as well as merged channels. 3-D reconstruction: image sequence extracted from the z-stack of two *S. aureus* incubated with (B1 and B2) **DTPA@SiO_2⊃Ru-Van** and orthogonal reconstruction of (C) B1 and B2. Orthogonal reconstructions display central plane image (highlighted with dashed line) showing red luminescence from nanoparticles inside the cells. Red channel, ruthenium emission (λ_{exc} = 488 nm, λ_{em} = 560 – 620 nm); blue channel, Hoechst H33342 emission (λ_{exc} = 405 nm, λ_{em} = 410 – 455 nm).

Furthermore, quantification of internalised nanoparticles was assessed through two different methodologies: (A) by determining the percentage of bacterial cells that display **Ru** signal colocalised with Hoechst H33342 using ImageJ software based on previously reported method[100]; and (B) calculating the Manders' colocalization coefficient (M1) using the JACoP plug-in[101] in ImageJ, which reflects the percentage of Hoechst H33342 signal is colocalized with **Ru** signal. SIM image analysis revealed that 34 ± 8 % (M1 = 45 ± 12) of *S. aureus* cells showed **Ru** signal after incubation for 2 h with **SiO_2⊃Ru-Van**, which increased to 88 ± 12 % (M1 = 78 ± 2 %) with **DTPA@SiO_2⊃Ru-Van**. More interestingly, no *E. coli* cells were observed with **Ru** signal after 2 h incubation with **SiO_2⊃Ru-Van** (M1 = 3 ± 2 %). However, **Ru** signal arising from **DTPA@SiO_2⊃Ru-Van** was found in 45 ± 10 % (M1 = 55 ± 16 %) of *E. coli* cells. Analysis of the same live cell imaging after 18 h incubation with **DTPA@SiO_2⊃Ru-Van** increased that percentage of cells with **DTPA@SiO_2⊃Ru-Van** to 70 ± 7 % (M1 = 75 ± 11 %); while no nanoparticles were detected after 18 h with **SiO_2⊃Ru-Van** (M1 = 8 ± 5 %). These results confirmed the effect of DTPA coating in the penetration abilities of nanoparticles supported the results of the antibacterial activity of nanoparticles against Gram-negative bacterial cells.

In case of those species displaying lipid A aminoarabinosylation, SIM imaging of *P. aeruginosa* incubated with DTPA-coated nanoparticles did not reveal any particle internalization after 18 h incubation. Nevertheless, particle interaction with bacterial membrane was observed (Figure 2.S32). Lack of particle internalization supported the MIC results.

SIM images analysis of *S. aureus* and *E. coli* bacterial cells incubated with **Ca^{2+}DTPA@SiO_2⊃Ru-Van** for 2 h (Figure 2.S33) revealed internalisation quantifications, by Manders' colocalization coefficient, similar to **SiO_2⊃Ru-Van**, further

supporting the MIC data of chelated **Ca^{2+}DTPA@SiO_2⊃Ru-Van** and the proposed mechanism of internalization.

2.3. Conclusions

In this study, a novel theragnostic antibiotic delivery system, **DTPA@SiO_2⊃Ru-Van**, has been developed by inclusion of the glycopeptide **Van** and the red-luminescent metal complex **Ru.** Both cargos were included within the silica framework in a one-pot process. Furthermore, this platform was modified *via* surface modification with **DTPA-Si_2.** A plethora of material characterization techniques were employed to obtain sufficient evidence of the successful presence of both cargos and coating. The nanoparticles also exhibited long red luminescence lifetime, ideal for tracking purposes. Furthermore, complimentary techniques revealed that formed spherical particles possessed a highly monodispersed sub-100 nm size. *In vitro* release studies revealed that release of **Van** was triggered upon shaking, showing minimal release of the antibiotic under static conditions. Moreover, minimal leakage of **Ru** was observed under any conditions. Finally, particles showed good biocompatibility properties based on MTT assays.

Antibacterial activity studies of nanoparticles by determining the MIC values revealed the importance of the DTPA coating. Against Gram-negative species, antibacterial activity of nanoparticles highly increased upon coating, while uncoated nanoparticles resulted in low antibacterial activity. Against the Gram-positive representative *S. aureus*, uncoated nanoparticles showed modest activity, even though, it increased upon coating. Luminescent red-signal of encapsulated **Ru** allowed the tracking of nanoparticles in cells by SIM microscopy, revealing that in case of the Gram-negative

representative *E. coli,* particle penetration was only observed with coated nanoparticles, in good agreement with the antibacterial activity experiments.

The suggested mechanism of cell penetration was investigated and the scavenging abilities of **DTPA@SiO_2⊃Ru-Van** against structurally required divalent cations (Ca^{2+}) was assessed by ITC, resulting in a strong affinity. Moreover, blocking of surface DTPA molecules with Ca^{2+} resulted in antibacterial activity comparable with uncoated **SiO_2⊃Ru-Van**. Confirming its chelating mechanism

Hereby, **DTPA@SiO_2⊃Ru-Van** represent the first example of the use of the aminocarboxylate DTPA as cell permeation surface modification for the enhancement of silica nanoparticles into Gram-negative bacterial cells. Finally, **DTPA@SiO_2⊃Ru-Van** supposes a step forward for the use of nanoparticle for the treatment of Gram-negative bacterial infections, allowing the use of antibiotics, such as **Van**, that are not active due to the cell membrane impermeability. Additionally, the emissive properties of the particles make them ideal for imaging and tracking, opening the door to further experimentation for the understanding of nanoparticle-cell interactions.

2.4. Experimental section

2.4.1. Synthetic procedures

$Ru(phen)_3Cl_2 \cdot 6H_2O$ (**Ru**) and tetraethoxysilane (TEOS) were purchase from Sigma-Aldrich and Vancomycin·HCl (**Van**) from Alfa Aesar. Rest of chemicals and consumables were purchased from Sigma-Aldrich and were of the highest quality available.

SiO_2⊃Ru-Van. $Ru(phen)_3Cl_2$ (**Ru**) and Vancomycin HCl (**Van**) loaded silica nanoparticles (**SiO_2**) were synthetized following a modified methodology reported by D. J. Lewis *et al*.[63] Briefly, a solution containing 25 mL of EtOH, 1.5 mL of 28% NH_4OH and 125 μL of a 13 mM aqueous solution of **Ru** and 125 μL of a 67 mM aqueous solution of **Van** was stirred at room temperature. To this, a solution containing 5 mL of EtOH and 2 mL of TEOS was slowly added, and the resulting solution was stirred for 2 h at room temperature, followed by 15 min of sonication treatment (200 W, 50 Hz) before another hour of stirring. Finally, obtained yellow suspension was centrifuged (7450 rpm, 15 min) and the supernatant removed. **SiO_2⊃Ru-Van** were washed with water (3 x 20 mL) and dried overnight under vacuum.

SiO_2⊃Van. **Van** loaded **SiO_2** were synthesised following the same procedure by using 125 μL of a 67 mM aqueous solution of **Van**.

SiO_2⊃Ru. **Ru** loaded **SiO_2** were synthesised following the same procedure by using 125 μL of a 13 mM aqueous solution of **Ru**.

DTPA-Si_2, silyl-derivative bisamide diethyelenetriaminepentaacetic acid. Diethylenetriaminepentaacetic acid dianhydride (0.5 g, 1.4 mmol) was dissolved in anhydrous pyridine (20 mL) under nitrogen. To the stirred solution, 3-aminopropyl triethoxysilane (APTES, 0.7 mL, 2.8 mmol) was added. The solution was left to stir under nitrogen for 24 h at room temperature. The resulting solution was reduced to 5 mL upon rotary evaporation. The product was precipitated using anhydrous hexane (200 mL), stirred in an ice bath under nitrogen. The product was left to further precipitate overnight at 4 °C. Resulting white precipitate was isolated via filtration, washed with anhydrous hexane (4 x 40 mL) and dry under vacuum (1 g, 95%). ^{1}H-NMR (300 MHz, d_6-DMSO, ppm): 8.08 (2H, s, NHCO), 3.73 (12H, q, *J = 6.96 Hz*, OCH_2CH_3), 3.33 (6H, s, CH_2COOH), 3.22 (4H, s, NH_2CON), 3.04 (4H, m, *J = 7.11 Hz*, NCH_2Et), 2.94 (4H, t, *J = 6.16 Hz*, NCH_2CH_2N), 2.81 (4H, t, *J = 6.16 Hz*, NCH_2CH_2N), 1.45 (4H, m, *J = 7.11 Hz*, $NCH_2CH_2CH_2$), 1.14 (18H, t, *J* = 6.96, CH_3), 0.52 (4H, t, *J = 7.50 Hz*, $NCH_2CH_2CH_2$). ^{13}C-NMR (400 MHz, d_6-DMSO, ppm): 167.9, 165.4, 53.1, 52.8, 51.4, 50.5, 47.5, 35.6, 19.8, 18.1, 14.6, 14.4, 2.8. ESI-MS: m/z 798.4008 ($[M-H]^-$, calcd. 798.3989). FTIR (cm^{-1}) = 3215 (w, N-H), 2965 (m, C-H_2), 2920 (m, C-H_2), 2875 (m, N-H), 1653 (s, C=O), 1355 (m, C-OCH_2CH_3), and 1073 (s, C-O).

DTPA@SiO_2. The **SiO_2** nanoparticles (30 mg) and silyl-derivative bisamide **DTPA-Si_2** (70 mg) were mixed in anhydrous toluene (10 mL) and sonicated for 5 min to give a homogenous suspension which was heated in reflux at 125 °C under nitrogen overnight. The **DTPA@SiO_2** nanoparticles were isolated by centrifugation and

washed with ethanol (1 x 20 mL) and MiliQ water (3 x 20 mL) to remove unreacted **DTPA-Si$_2$** and dried under vacuum. FTIR (cm^{-1}) = 3215 (w, N-H), 2965 (m, C-H_2), 2920 (m, C-H_2), 2875 (m, N-H), 1653 (s, C=O), and 1073 (s, C-O).

Ca^{2+} complexation to DTPA@SiO_2⊃Ru-Van. **DTPA@SiO_2⊃Ru-Van** (25 mg) was added into a saturated aqueous solution of $CaCl_2$ and sonicated for 5 min to give a homogenous suspension. The resulted suspension was stirred at room temperature for 1 h. **Ca^{2+}DTPA@SiO_2⊃Ru-Van** were isolated by centrifugation and washed with ethanol (1 x 20 mL), MiliQ water (3 x 20 mL) and dried under vacuum.

2.4.2. Methodologies

Quantification of DTPA on SiO_2 by Tb(III) titration on DTPA@SiO_2. In order to quantify surface conjugated DTPA molecules, a methanolic solution of $TbCl_3 \cdot 6H_2O$ (0.33 mM) was added in 5 μl aliquots to a suspension of **DTPA@SiO_2** (1 mg in 2 mL of MeOH) and the Tb(III) luminescence signal (λ_{exc} = 236 nm, λem = 450 – 750 nm) was monitored.

Antibiotic release studies. Release studies were performed using loaded **SiO_2** suspension (2.5 mg/mL) in Milli-Q water at 37 °C under mild shaking (150 rpm) at 37 °C. Aliquots were removed at different time points, centrifuged (5 min at 14000 rpm) to remove nanoparticles and released **Ru** and/or **Van** in the supernatant determined by fluorescence spectroscopy using a Horiba Fluorolog-3 spectrometer (for **Ru** λ_{exc} = 450 nm and λ_{em} = 600 nm and **Van** λ_{exc} = 270 nm and λ_{em} = 330 nm).

Minimal Inhibitory Concentration (MIC) **determination**. MIC values of studied nanoparticles, **Ru** and **Van** were determined for *S. aureus* (ATCC29213) *E. coli* (MG1655), *A. baumannii* (AYE), *K. pneumoniae* (ATCC43816R), *K. oxytoca* (080-KPC CHD), *C. feundii (*NCTC9750), *S. enterica* (SL1344), *P. aeruginosa* (PA14) and **B.** *cenocepacia* (CFI) via the standard broth-dilution method in 96-well microlitre plates in Lysogeny Broth (LB). The MIC of each compound was evaluated using a 2-fold decreasing concentration of each sample between 500 – 0.5 μg/mL for **Ru** and **Van** and between 10.00 – 0.04 mg/mL for the **SiO_2** nanoparticles against a bacterial inoculum of 10^7 - 10^9 colony forming units per mL (CFU/mL). Plates were incubated at 37 °C for 18 h under mild shaking (150 rpm). MIC values were determined as the lowest concentration where no turbidity is observed.

Isothermal Titration Calorimetry (ITC). Binding constant of Ca^{2+} with **DTPA@SiO_2⊃Ru-Van** was determined by ITC in PBS (0.1 M, pH = 7.4) at 25 °C titrating a solution of $CaCl_2$ (2.5 mM) into a **DTPA@SiO_2⊃Ru-Van** suspension with a DTPA concentration of 0.32 mM. Recorded data was fitted using the Malvern MicroCal PEAQ-ITC V1.41 software.

Structured illumination microscopy (SIM) imaging. In order to study the cell-uptake of nanoparticles, overnight inocula (2 mL) were mixed with **SiO_2⊃Ru-Van** and **DTPA@ SiO_2⊃Ru-Van** with a final nanoparticle concentration of 2.5 mg/mL and incubated at 37 ºC and 150 rpm for 2 h or 18 h. 1 mL of incubated cells were stained with Hoechst H33342 (10 μL, 1 mM) for 30 min, followed with washing with PBS (0.1 M, pH 7.4, 1

mL). Stained bacteria were placed on microscope slides and imaged. In each experiment five images were obtained from five independent biological replicates (n=5). Colocalization analysis between channels was carried out using the Fiji image software plugin JACoP[101], from which the Pearson and Manders' Overlapping correlation parameters were calculated over five different images per treatment

MTT (3-(4,5-dimethylthiazol-2-yl)-2,5-diphenyltetrazolium bromide) cell viability assays. Cytotoxicity of studied nanoparticles was assessed by MTT cell viability assays using A459 lung cancer cell line. Cells were seeded at 6500 cells per plate in 96-well plates and left overnight for attachment to occur. The next day the media was removed and fresh media (100 μL) containing nanoparticles added. Following treatment for 18 h the media was removed, and cells incubated with 200 μL of media containing 0.5 mg/mL MTT solution for 3 hours. The media was removed and reduced MTT was solubilized by addition of DMSO (200 μL) and absorbance at 590 nm measured in a plate reader (Tecan Infinite 200Pro) as an indicator of mitochondrial reductive activity and cellular viability. All samples were normalized to a solvent (DMSO) blank, and the results represent the mean of three experiments carried out in triplicate (n= 3 ± SEM).

2.5. Appendix

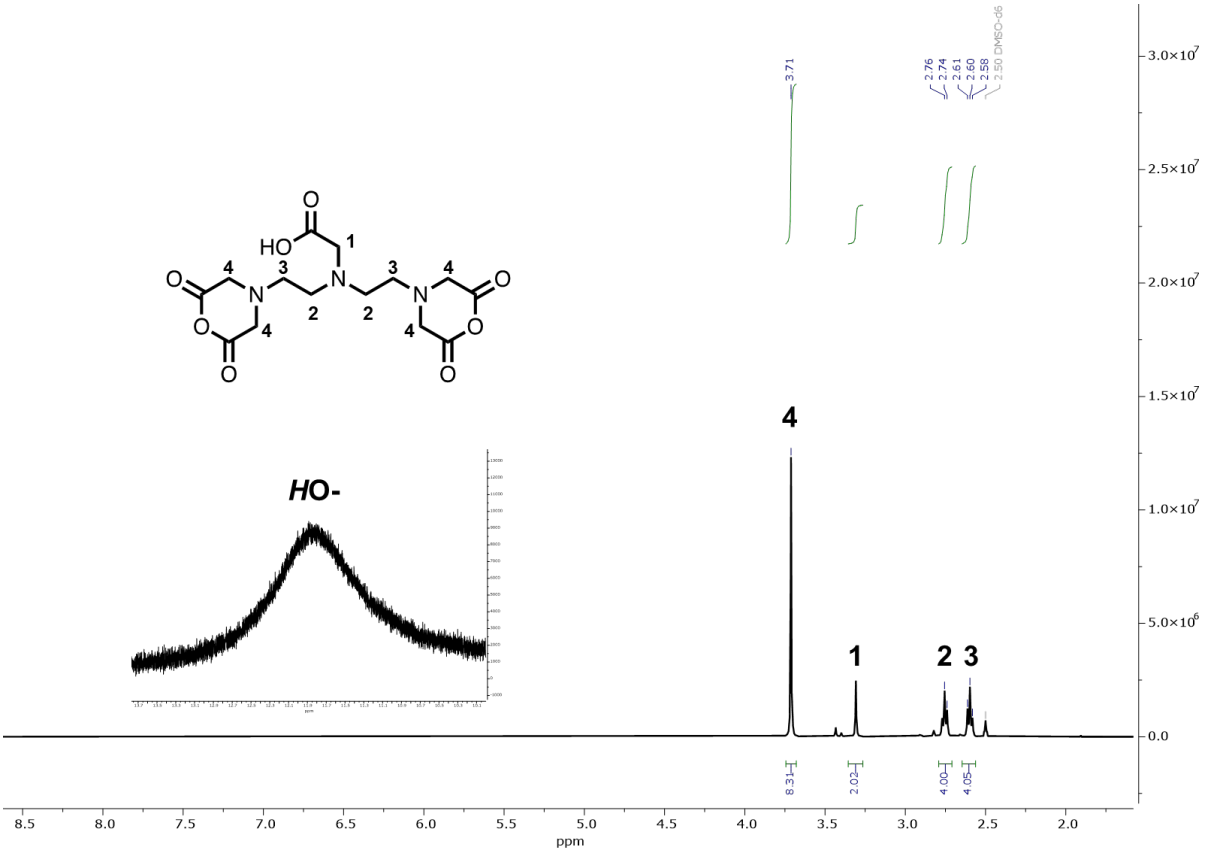

Figure 2.S1. ^{1}H-NMR (400 MHz, d_6-DMSO) spectra for DTPA bis anhydride

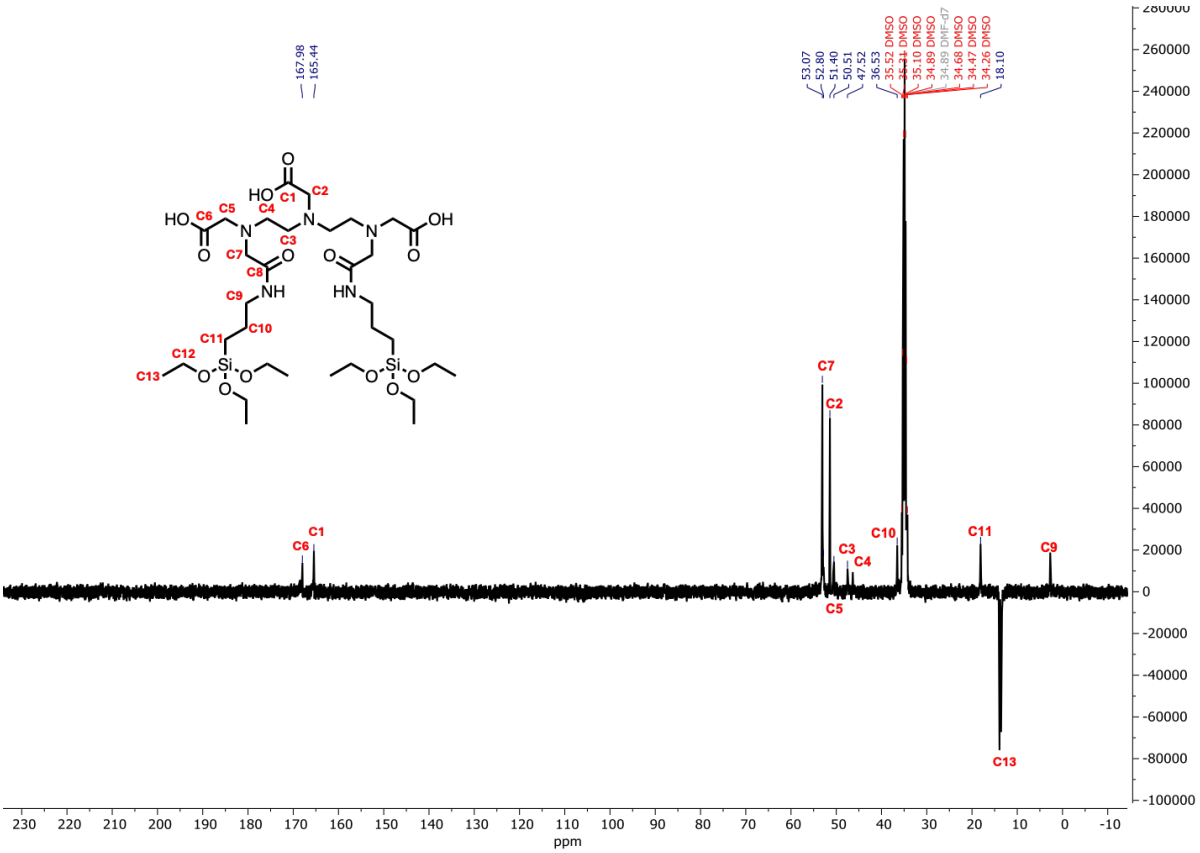

Figure 2.S2. ^{13}C-NMR (400 MHz, d_6-DMSO) spectra of **DTPA-Si$_2$**

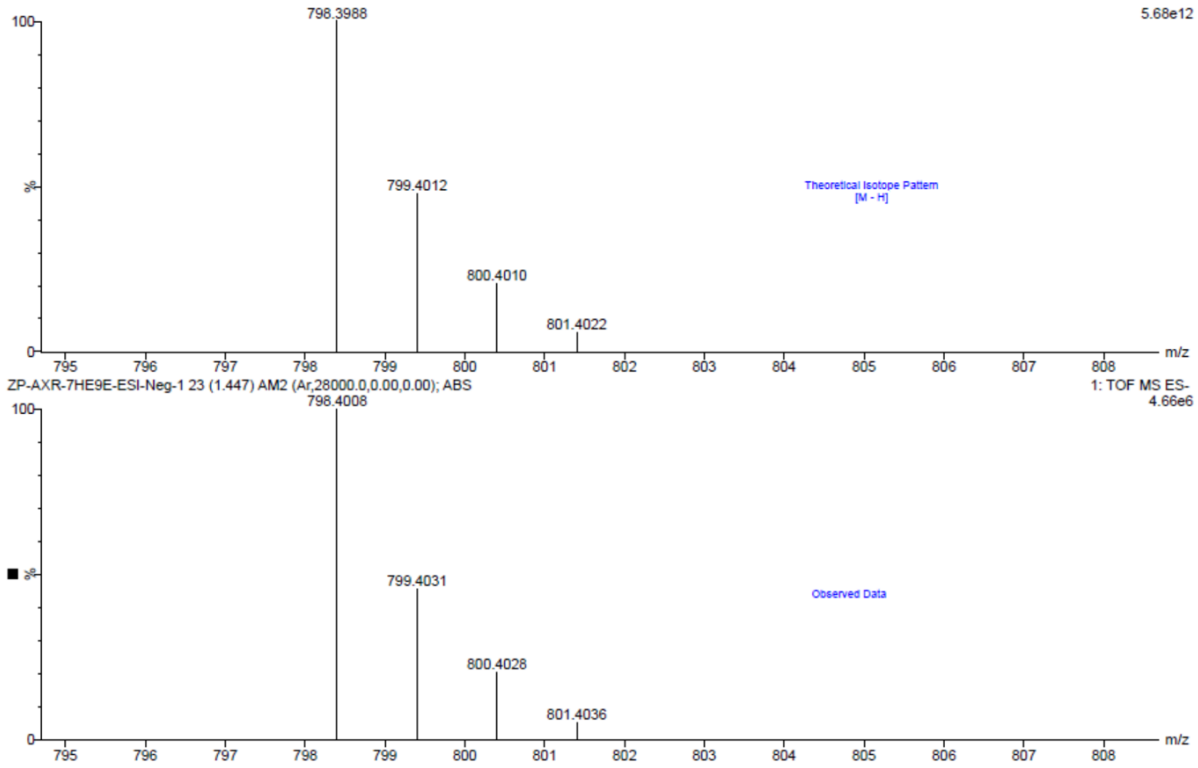

Figure 2.S3. Observed and Calculated (-)ESI-ToF mass spectrum of **DTPA-Si$_2$**.

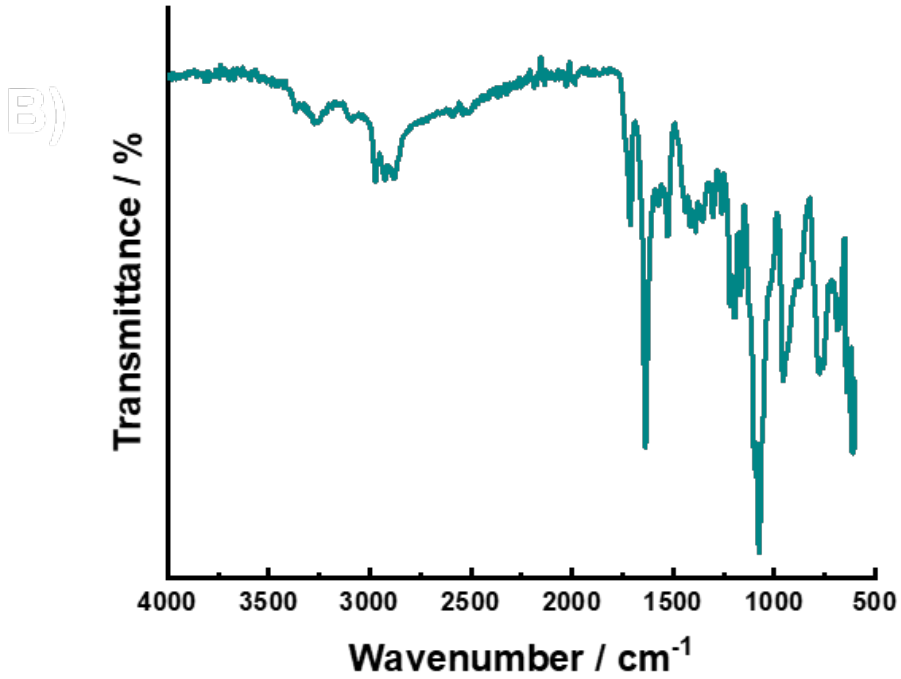

Figure 2.S4. FT-IR spectra of **DTPA-Si$_2$**.

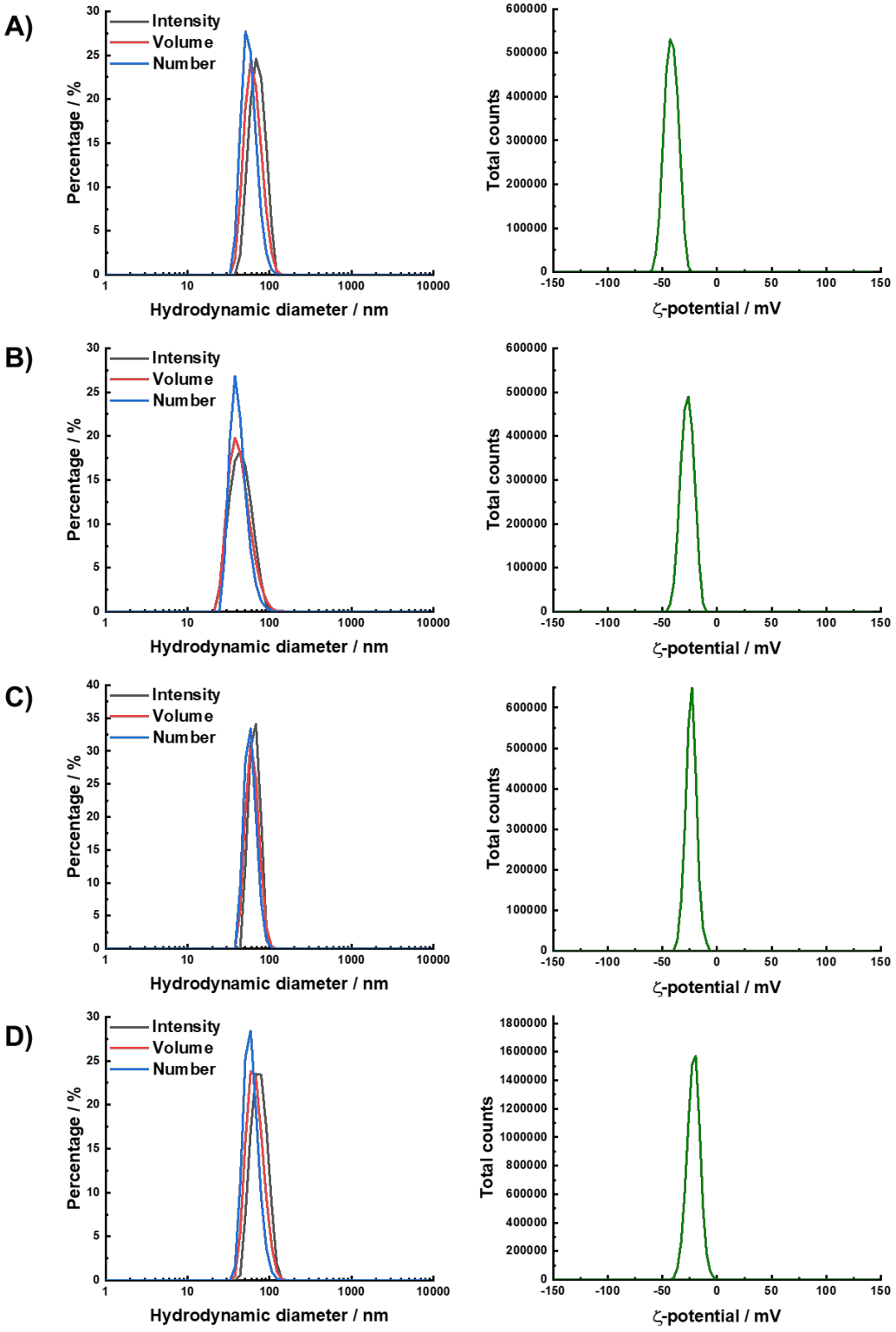

Figure 2.S5. Dynamic Light Scattering (DLS) analysis (n = 5) and surface ζ-potential (n = 3) distribution in PBS of (A) **SiO_2**, (B) **SiO_2⊃Ru**, (C)**SiO_2⊃Van**, and (D) **SiO_2⊃Ru-Van** in PBS buffer (0.1 M, pH 7.4).

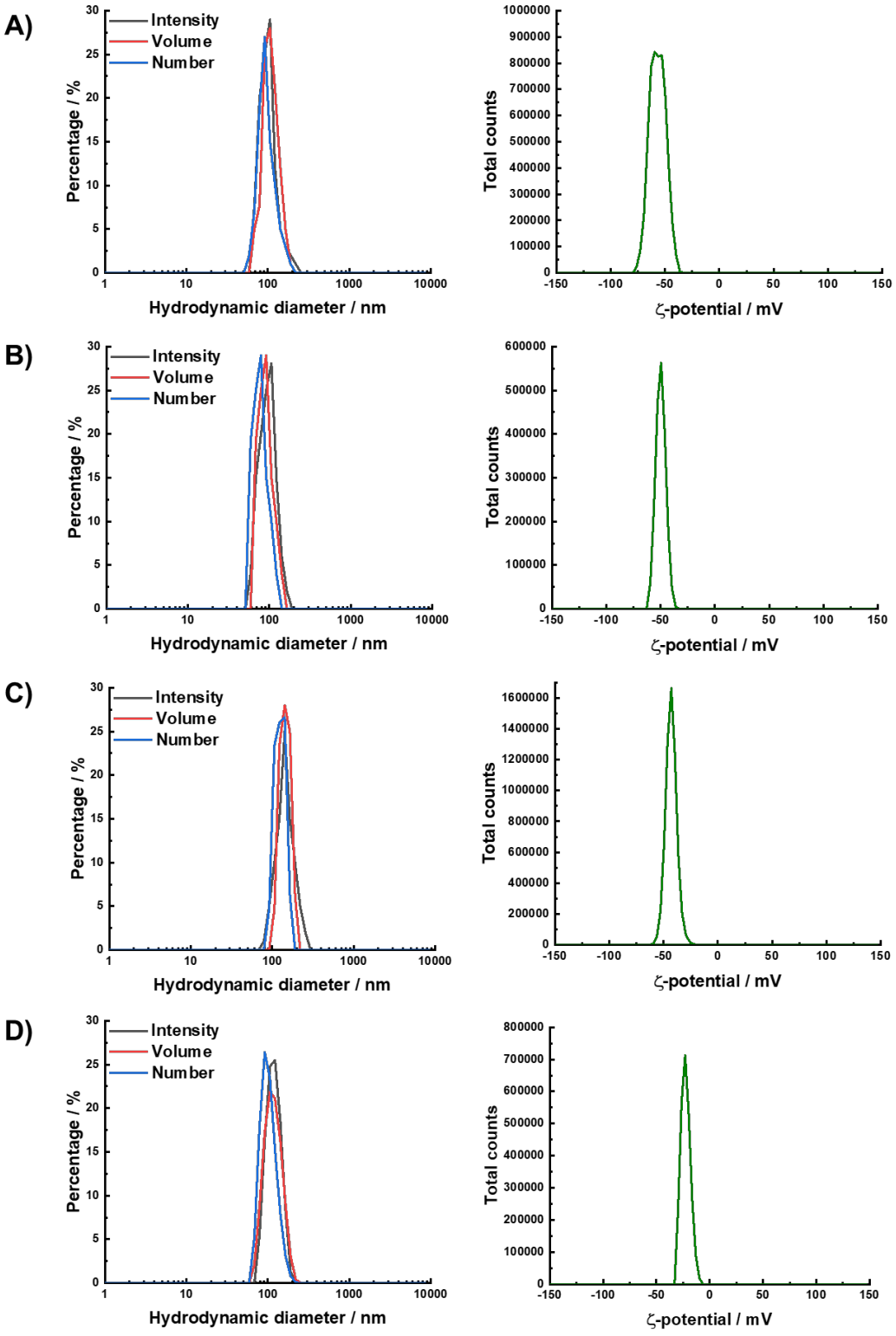

Figure 2.S6. Dynamic Light Scattering (DLS) analysis (n = 5) and surface ζ-potential (n = 3) distribution in PBS of (A) **DTPA@SiO$_2$,** (B) **DTPA@SiO$_2$⊃Ru**, (C) **DTPA@SiO$_2$⊃Van** and (D) **DTPA@SiO$_2$⊃Ru-Van** in PBS (0.1 M, pH 7.4)

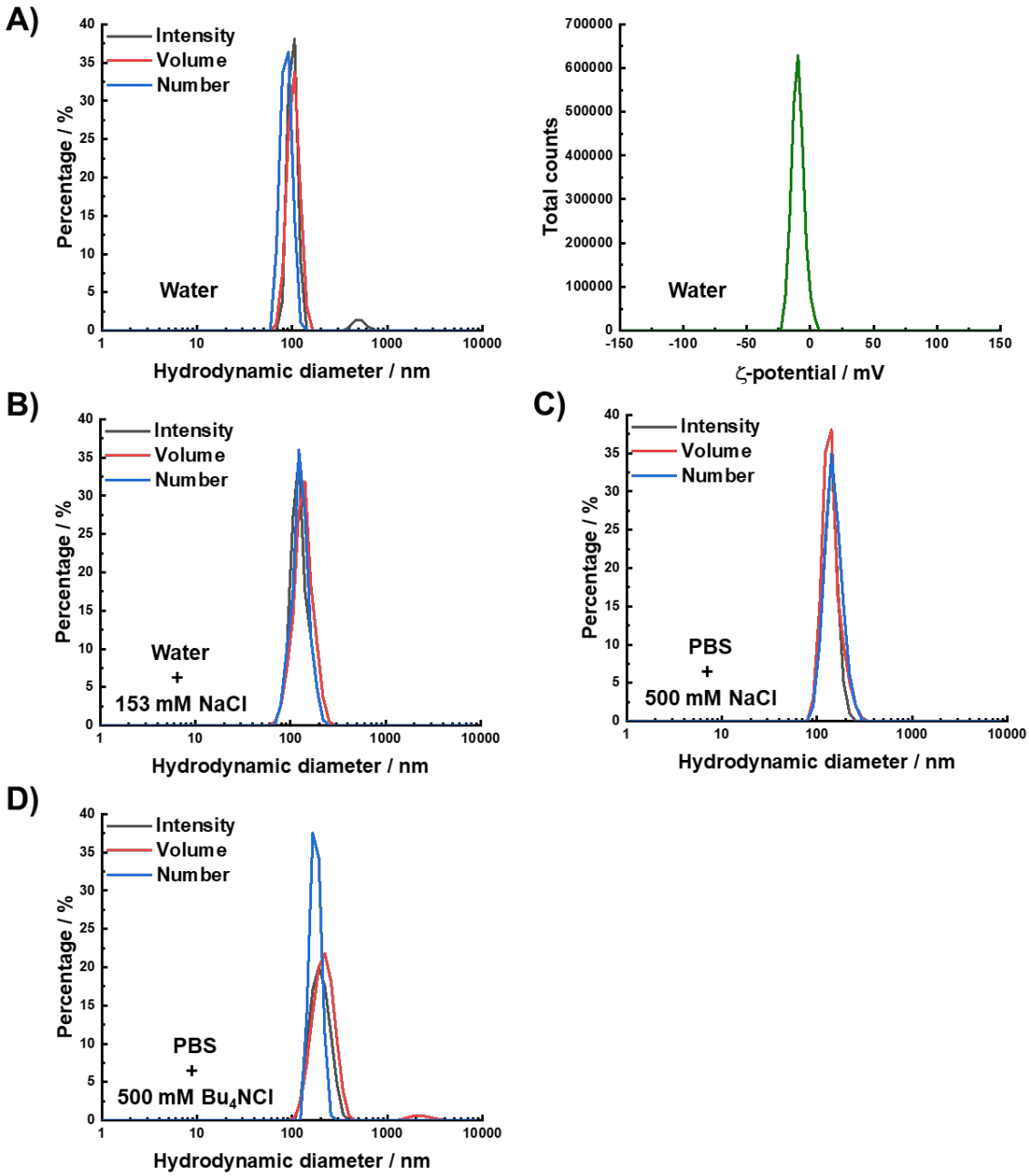

Figure 2.S7. Dynamic Light Scattering (DLS) analysis (n = 5) and surface ζ-potential (n = 3) distribution of **SiO_2⊃Ru-Van** in (A) water, (B) water + 153 mM NaCl, (C) PBS (0.1 M, pH 7.4) + 500 mM NaCl and (D) PBS + 500 mM Bu_4NCl.

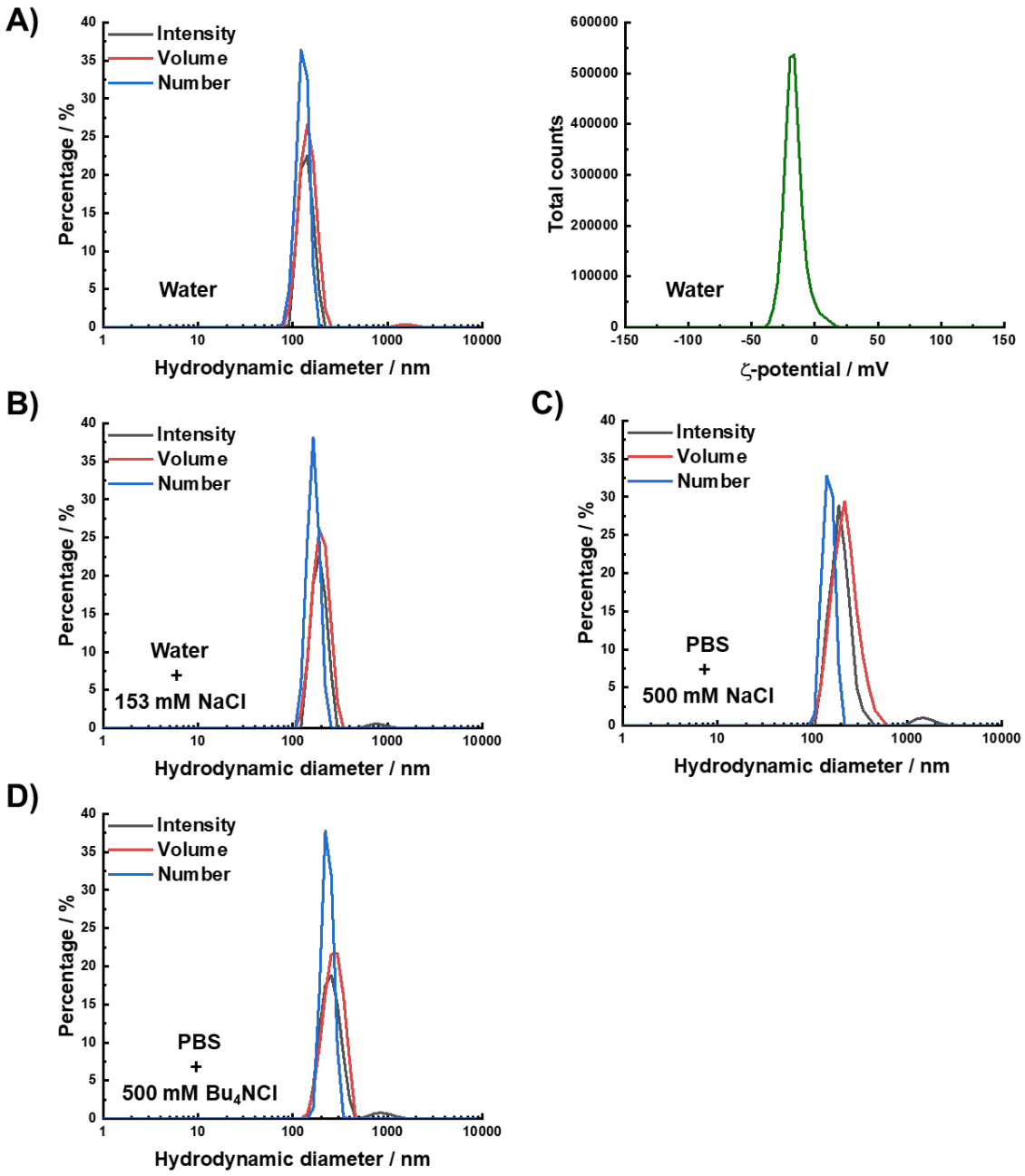

Figure 2.S8. Dynamic Light Scattering (DLS) analysis (n = 5) and surface ζ-potential (n = 3) distribution of **DTPA@SiO_2⊃Ru-Van** in (A) water, (B) water + 153 mM NaCl, (C) PBS (0.1 M, pH 7.4) + 500 mM NaCl and (D) PBS + 500 mM Bu_4NCl.

Table 2.S1. Dynamic Light Scattering (DLS, n = 5) and surface ζ-potential (n = 3) measurements of **SiO_2**, **SiO_2⊃Ru**, **SiO_2⊃Van**, **SiO_2⊃Ru-Van** and respective coated nanoparticles. Measurements were performed at 25 ºC in PBS buffer (0.1 M, pH 7.4, [Na^+] = 153 mM) with nanoparticle concentration of 1 mg/mL. Additional data was recorded in water and in PBS with addition of NaCl and tetrabutylammonium chloride (Bu_4NCl) to explore the effect of the ionic strength of the media in the hydrodynamic size of the hybrid nanoparticles.

		Hydrodynamic size / nm				ζ-potential /mV
	Dispersant	Intensity	Volume	Number	PDI	
SiO_2		68 ± 8	65 ± 5	57 ± 2	0.02	-37 ± 6
DTPA@SiO_2		89 ± 33	67 ± 26	52 ± 15	0.17	-45 ± 7
SiO_2⊃Ru		74 ± 20	61 ± 26	52 ± 15	0.17	-25 ± 5
DTPA@SiO_2⊃Ru		121 ± 26	113 ± 28	100 ± 22	0.24	-37 ± 6
SiO_2⊃Van		94 ± 22	64 ± 18	47 ± 17	0.07	-24 ± 9
DTPA@SiO_2⊃Van		103 ± 30	92 ± 30	81 ± 15	0.17	-40 ± 7
SiO_2⊃Ru-Van	Water	89 ± 29	86 ± 12	84 ± 22	0.16	-16 ± 2
	Water + 153 mM NaCl	100 ± 21	89 ± 15	72 ± 23	0.17	
	PBS	98 ± 29	82 ± 26	67 ± 18	0.15	-18 ± 6
	PBS + 500 mM NaCl	168 ± 22	148 ± 21	115 ± 15	0.18	
	PBS+ 500 mM Bu_4NCl	148 ± 22	138 ± 15	148 ± 20	0.20	
DTPA@SiO_2⊃Ru-Van	Water	94 ± 10	92 ± 15	89 ± 14	0.24	-20 ± 3
	Water + 153 mM NaCl	118 ± 15	110 ± 21	98 ± 23	0.19	

PBS	113 ± 28	105 ± 25	94 ± 20	0.21	-24 ± 5
PBS + 500 mM NaCl	185 ± 14	175 ± 31	170 ± 30	0.32	
PBS+ 500 mM Bu_4NCl	165 ± 17	155 ± 23	151 ± 22	0.25	

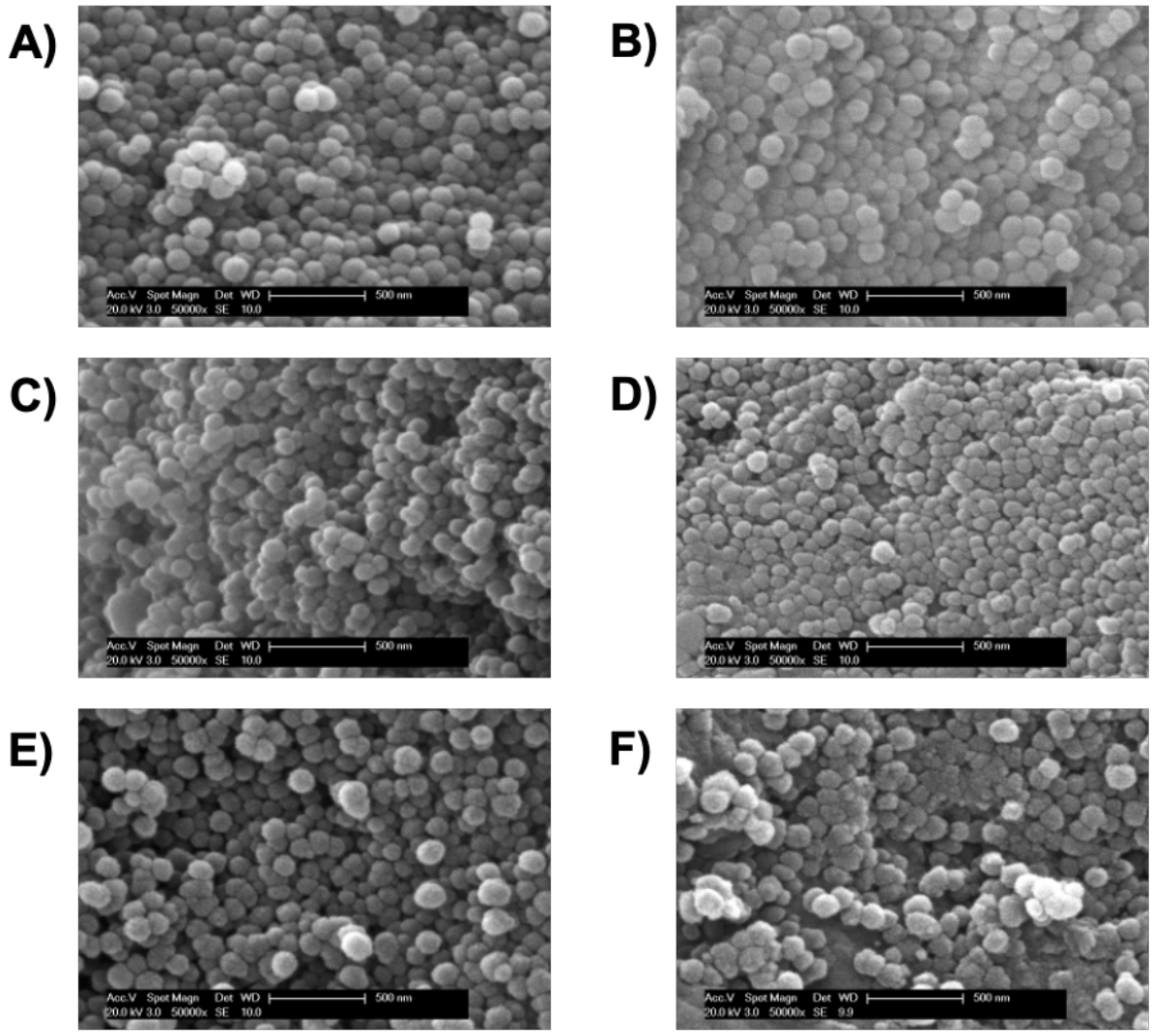

Figure 2.S9. Scanning Electron Microscopy (SEM) images of A) **SiO_2**, (B) **DTPA@SiO_2,** (C) **SiO_2⊃Ru**, (D) **DTPA@SiO_2⊃Ru**, (E) **SiO_2⊃Van**, (F) **DTPA@SiO_2⊃Van.** Magnification 50k x, 20.0 kV electron beam.

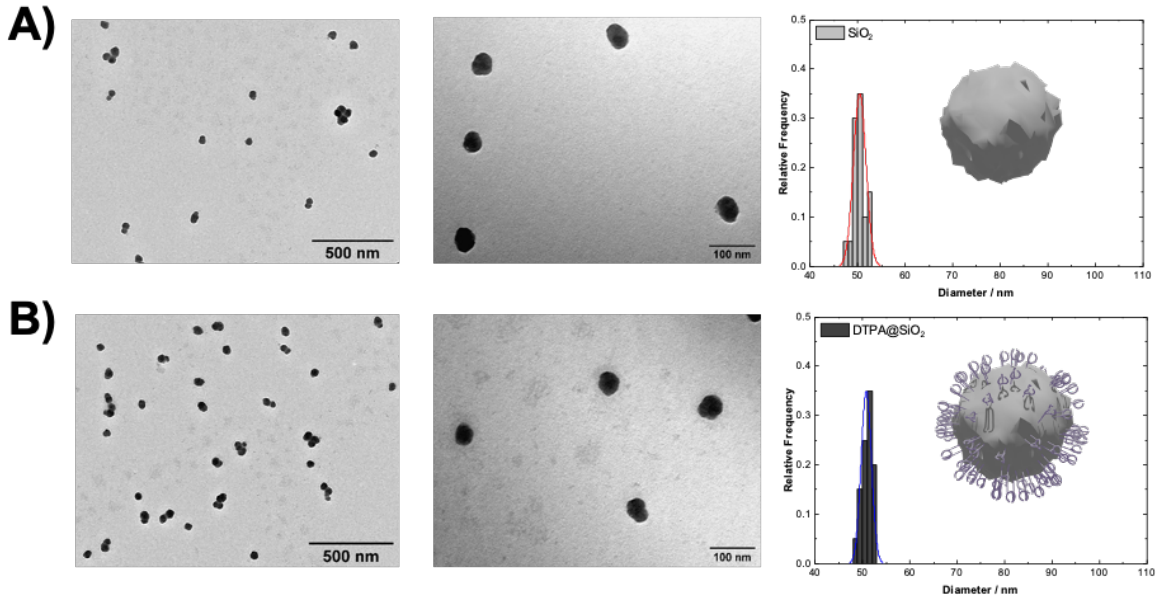

Figure 2.S10. Transmission Electron Microscopy images and particle size distribution of (A) **SiO_2** and (B) **DTPA@SiO_2**. Size-distribution was calculated using a Gaussian distribution function based on 20 diameter measurements.

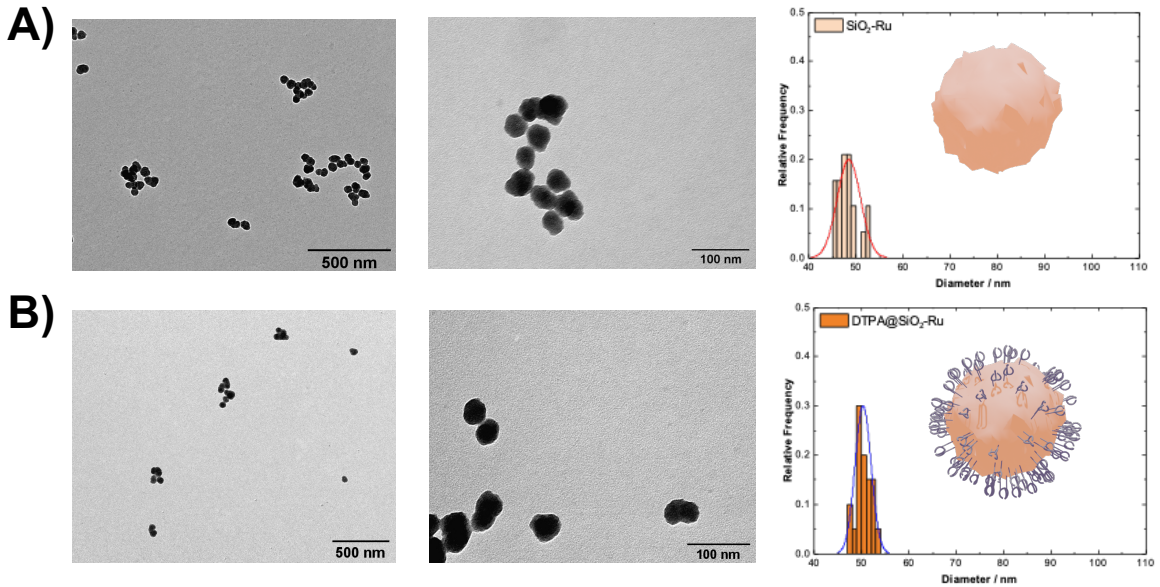

Figure S2.11. Transmission Electron Microscopy images and particle size distribution of (A) **SiO_2⊃Ru** and (B) **DTPA@SiO_2⊃Ru**. Size-distribution was calculated using a Gaussian distribution function based on 20 diameter measurements.

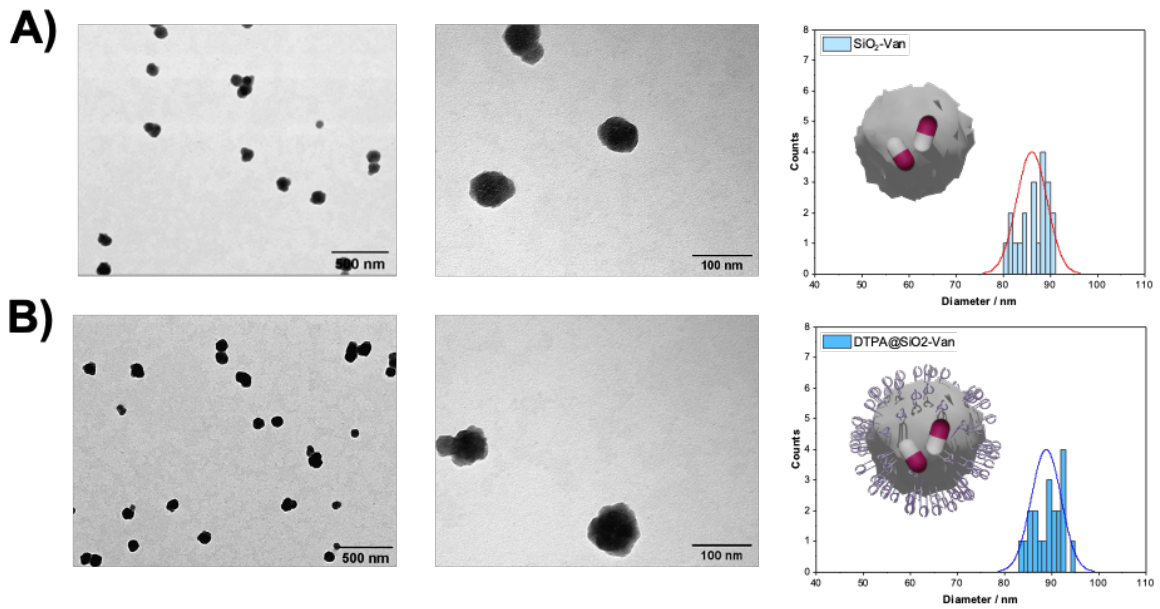

Figure 2.S12. Transmission Electron Microscopy images and particle size distribution of (A) **SiO_2⊃Van** and (B) **DTPA@SiO_2⊃Van**. Size-distribution was calculated using a Gaussian distribution function based on 20 diameter measurements.

Table 2.S2. Size-distribution was calculated using a Gaussian distribution function based on 20 nanoparticle measurements from TEM images.

	Size / nm	**PDI**
SiO_2	50 ± 1	0.02
DTPA@SiO_2	51 ± 1	0.02
SiO_2⊃Ru	48 ± 3	0.03
DTPA@SiO_2⊃Ru	50 ± 2	0.03
SiO_2⊃Van	84 ± 5	0.02
DTPA@SiO_2⊃Van	88 ± 6	0.02
SiO_2⊃Ru-Van	85 ± 3	0.02
DTPA@SiO_2⊃Ru-Van	87± 4	0.02

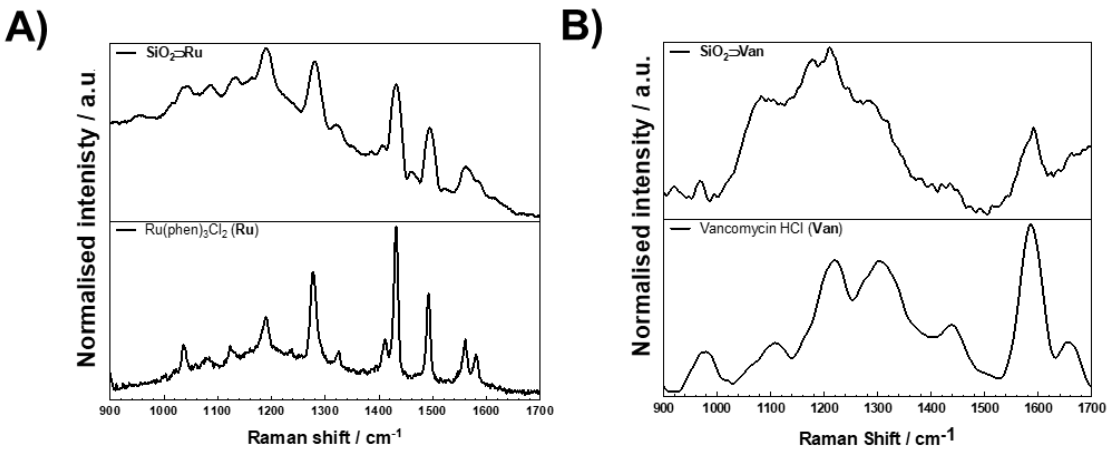

Figure 2.S13. Raman spectra (λ_{exc} = 633 nm) of (A) **SiO_2⊃Ru** and (B) **SiO_2⊃Van**.

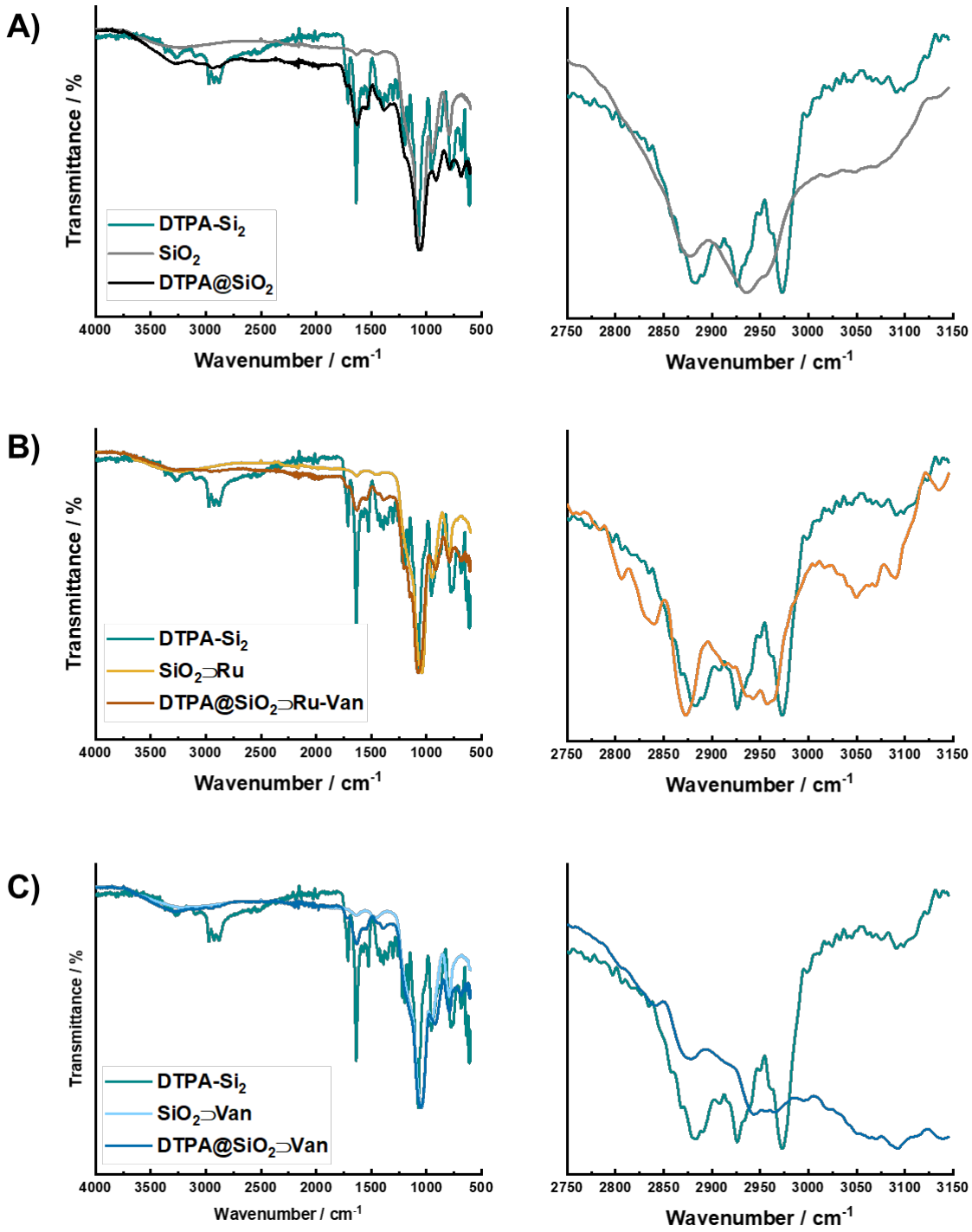

Figure 2.S14. FT-IR spectra of (A) **DTPA@SiO₂**, (B) **DTPA@SiO₂⊃Ru** and (C) **DTPA@SiO₂⊃Van**.

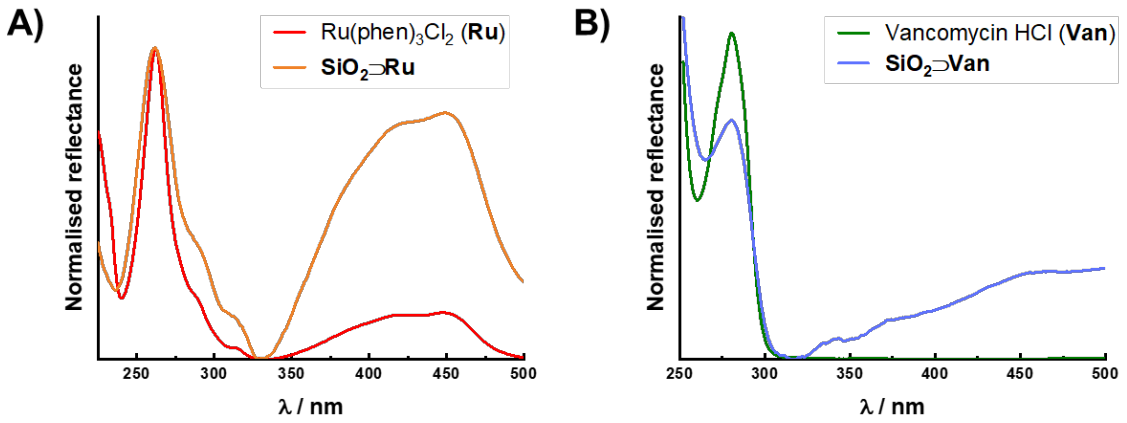

Figure 2.S15. Solid-state UV/Vis spectra of (A) **SiO_2⊃Ru** and (B) **SiO_2⊃Van**.

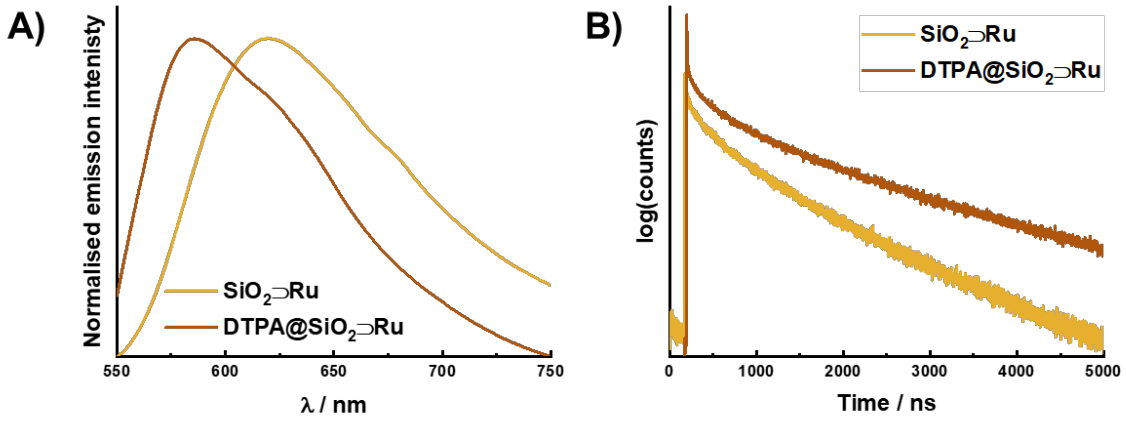

Figure 2.S16. Solid-state **Ru** emission spectra (λ_{exc} = 450 nm) and luminescence lifetime decays (λ_{exc} = 455 nm, λ_{em} = 600 nm) of **SiO_2⊃Ru** and **DTPA@ SiO_2⊃Ru**

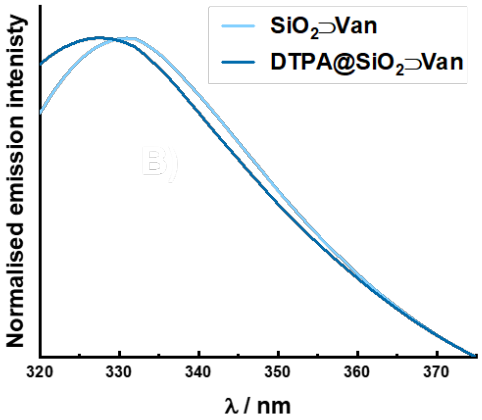

Figure 2.S17. Solid-state **Van** emission spectra (λ_{exc} = 270 nm) of (A) **SiO_2⊃Van** and **DTPA@ SiO_2⊃Ru** and (B) **SiO_2⊃Ru-Van** and **DTPA@ SiO_2⊃Ru-Van**.

Table 2.S3. Solid-state photophysical parameters of **Ru** complex and **Ru**-containing nanoparticles (λ_{max} and Φ λ_{exc} = 450 nm, τ λ_{exc} = 455 nm and λ_{em} = 600 nm)

	λ_{max} / nm	τ_1 / μs (%)	τ_2 / μs (%)	χ^2
$Ru(phen)_3Cl_2$ (**Ru**)	495	1.1 (100)[a]		
SiO_2⊃Ru	612	1.45 (89)	0.38 (11)	1.019
DTPA@SiO_2⊃Ru	593	3.31 (90)	0.84 (10)	1.004
SiO_2⊃Ru-Van	613	1.69 (90)	0.33 (10)	1.021
DTPA@SiO_2⊃Ru-Van	595	2.52 (91)	0.34 (10)	1.049

[a]Reported from ref ([102]) for comparison.

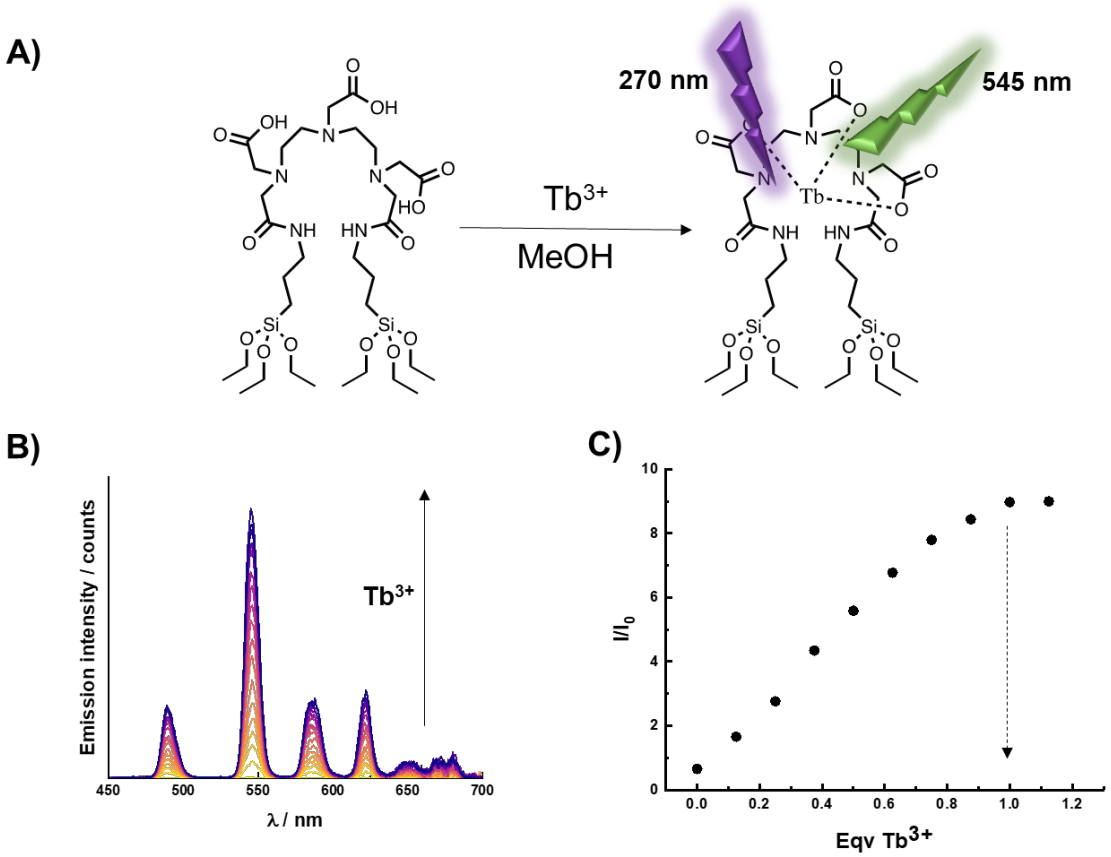

Figure 2.S18. (A)Scheme, showing the principles of the principles of luminescence Tb^{3+} titrations with **DTPA-Si$_2$** and (B) Recorded emission spectra (λ_{exc} = 273 nm) and titration curves of **DTPA-Si$_2$** in methanol (4 mM) showing 1:1 stoichiometry between Tb^{3+} and **DTPA-Si$_2$**.

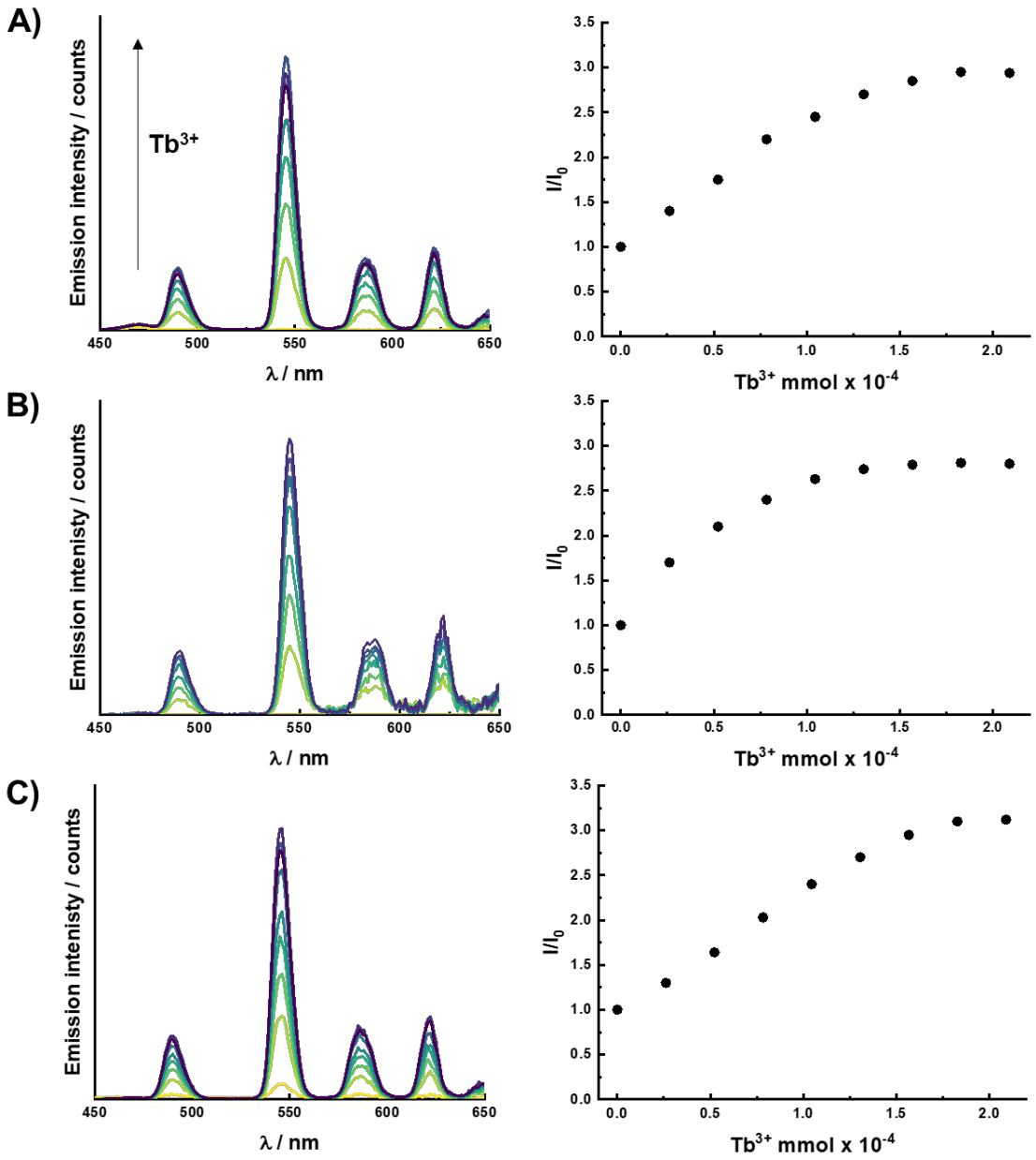

Figure 2.S19. Recorded emission spectra (λ_{exc} = 273 nm) and titration curves of (A) **DTPA@SiO$_2$,** (B) **DTPA@SiO$_2$⊃Ru** and (C) **DTPA@SiO$_2$⊃Van**. Nanoparticles titrations were performed using a 1 mg/mL methanolic suspension and a methanol Tb^{3+} solution of 3.3 mM.

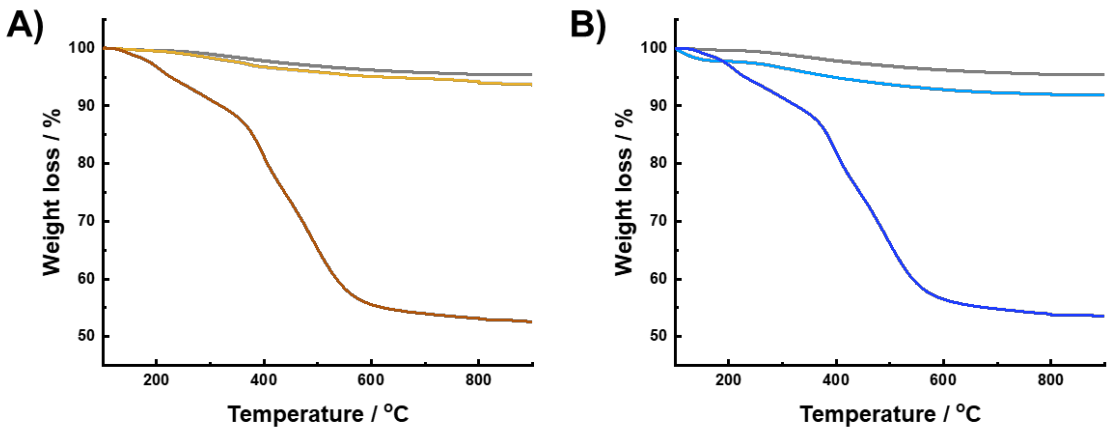

Figure 2.S20. Quantification of included cargo and DTPA quantification in (A) **DTPA@SiO_2⊃Ru** and (B) **DTPA@SiO_2⊃Van**. Samples were heated from 30 °C to 900 °C at 1 °C /min rate with a 10 min isothermal step at 100 °C to ensure water removal. All degradation curves are set at 100 % for clarity.

Table 2.S4. Quantification of loading and DTPA content in control nanoparticles by different quantification techniques.

	Loading / μg·mg_{NPs}^{-1}		**Coating / mg_{DTPA}·mg_{NPs}^{-1}**	
	Fluorescence	**TGA**	**TGA**	**Tb^{3+}**
DTPA@SiO_2	N/A		0.55	0.50
DTPA@SiO_2⊃Ru	25	26	0.50	0.54
DTPA@SiO_2⊃Van	92	89	0.49	0.53

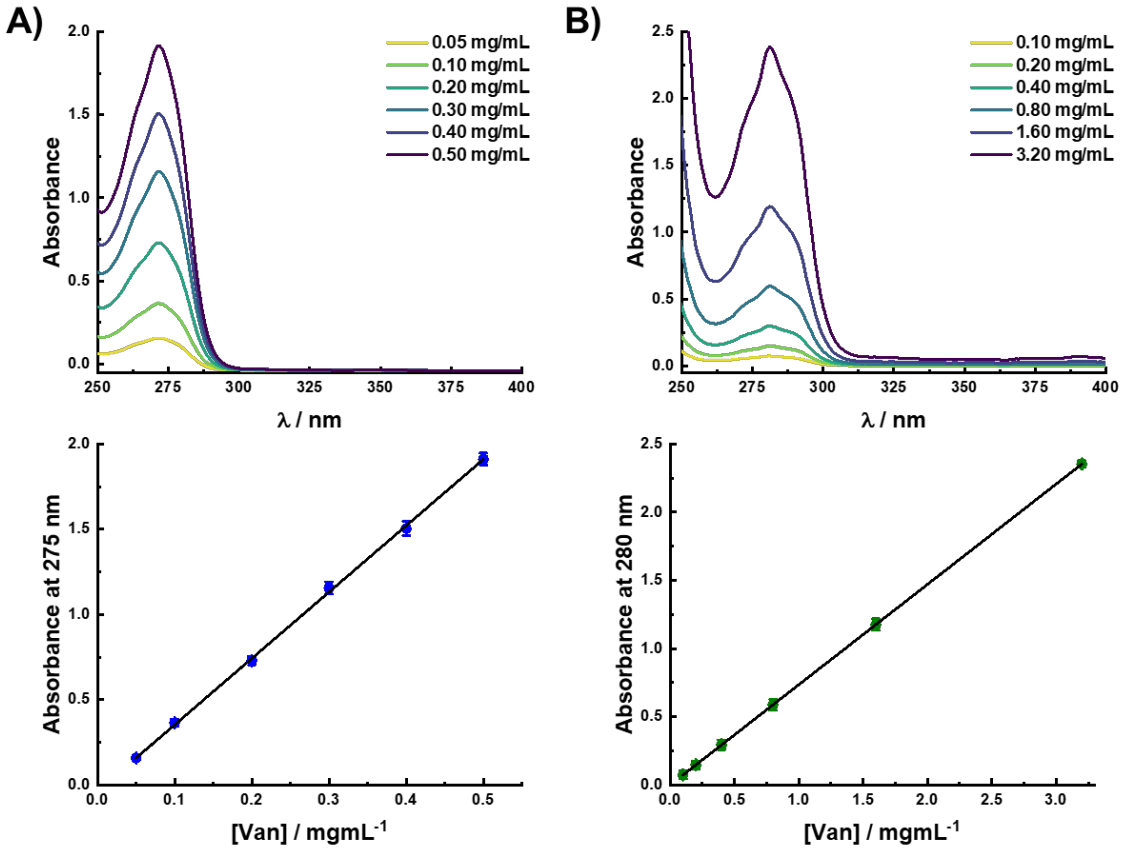

Equation	y = a + b*x
Weight	Instrumental (=1/ei^2)
Intercept	-0.03378 ± 0.0026
Slope	2.90636 ± 0.02307
Residual Sum of Squares	0.63453
Pearson's r	0.99987
R-Square (COD)	0.99975
Adj. R-Square	0.99969

Equation	y = a + b*x
Weight	Instrumental (=1/ei^2)
Intercept	-0.06231 ± 0.00776
Slope	0.7354 ± 0.0524
Residual Sum of Squares	30.40073
Pearson's r	0.99659
R-Square (COD)	0.99319
Adj. R-Square	0.99148

Figure 2.S21. UV/Vis calibration of **Van** in (A) water and (B) EtOH (0.4 μM NH_4OH). n = 3

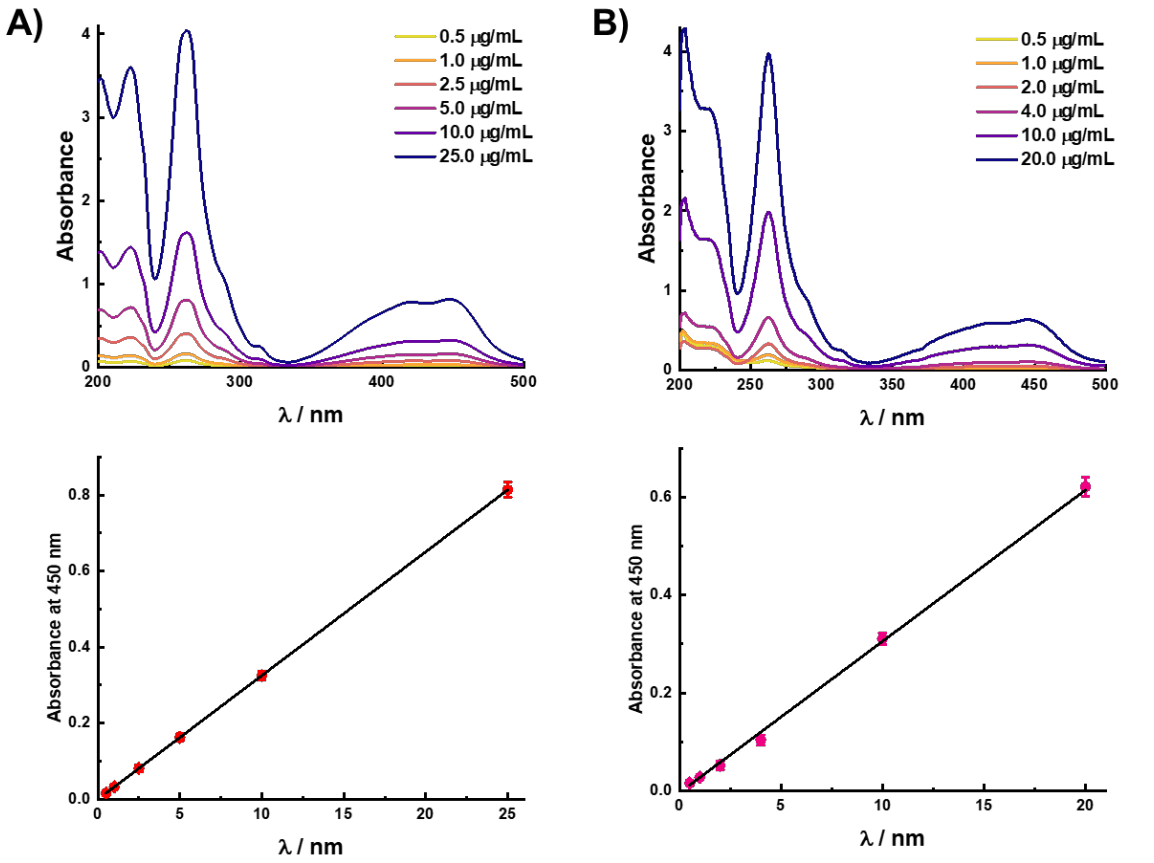

Equation	y = a + b*x
Weight	Instrumental (=1/ei^2)
Intercept	-0.02524 ± 0.00025
Slope	0.03254 ± 2.26363E-18
Residual Sum of Squares	4.114E-29
Pearson's r	0.99854
R-Square (COD)	0.99985
Adj. R-Square	0.99989

Equation	y = a + b*x
Weight	Instrumental (=1/ei^2)
Intercept	-0.00395 ± 0.00322
Slope	0.03093 ± 8.40287E-4
Residual Sum of Squares	4.08657
Pearson's r	0.99853
R-Square (COD)	0.99706
Adj. R-Square	0.99632

Figure 2.S22. UV/Vis calibration of **Ru** in (A) water and (B) EtOH (0.4 μM NH_4OH). n = 3

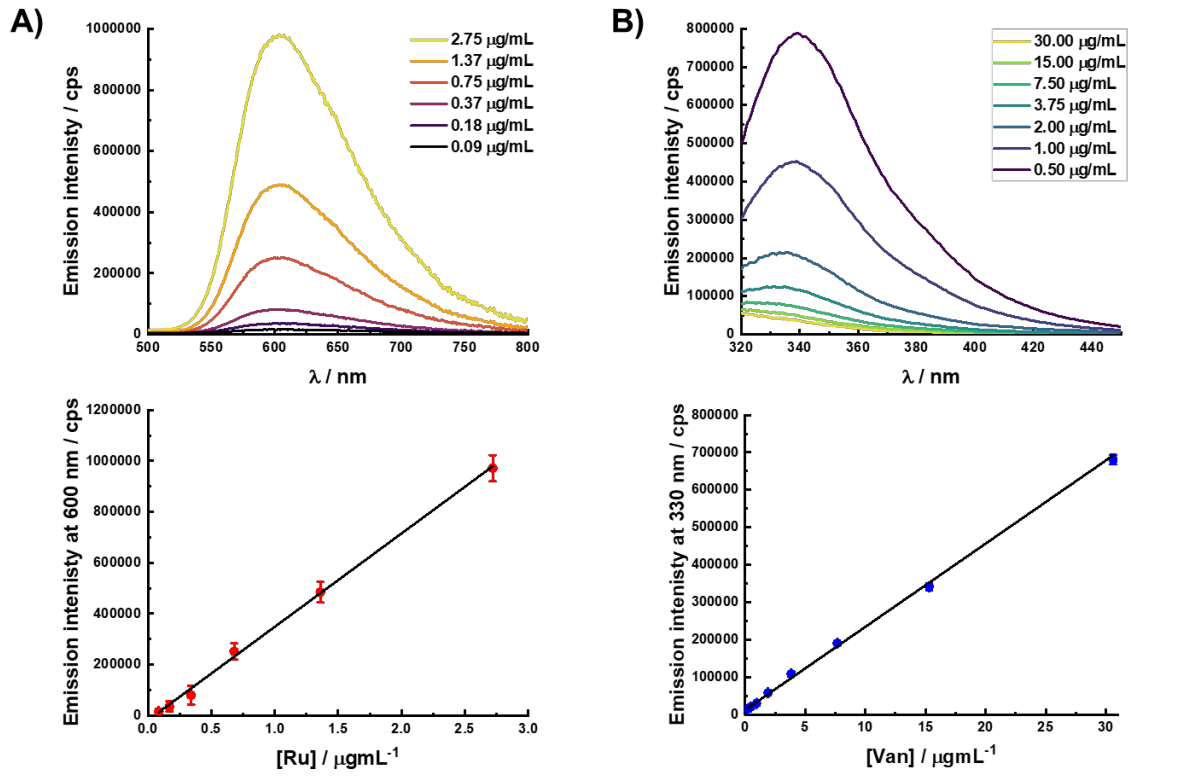

Equation	y = a + b*x
Plot	Luminescence emission
Weight	Instrumental (=1/ei^2)
Intercept	-17918.48713 ± 5141.68835
Slope	366626.69672 ± 9293.82334
Residual Sum of Squares	1.22878
Pearson's r	0.99872
R-Square (COD)	0.99744
Adj. R-Square	0.9968

Equation	y = a + b*x
Plot	Fluorescence emission
Weight	Instrumental (=1/ei^2)
Intercept	21092.25342 ± 6941.70927
Slope	24804.46377 ± 796.75898
Residual Sum of Squares	57.66855
Pearson's r	0.99743
R-Square (COD)	0.99487
Adj. R-Square	0.99384

Figure 2.S23. Fluorescence emission calibrations of (A) **Ru** (λ_{exc} = 450 nm) and (B) **Van** (λ_{exc} = 270 nm) in water. n = 3

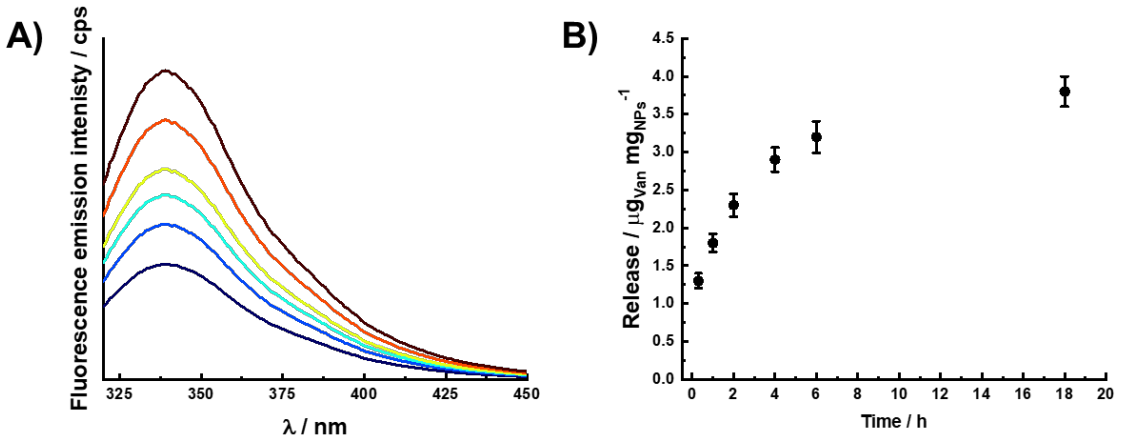

Figure 2.S24. (A) Representative fluorescence monitoring release of **Van** from **DTPA@SiO$_2$⊃Van** (λ_{exc} = 270 nm, λ_{em} = 330 nm) at 37 ºC and 150 rpm and (B) cumulative **Van** release graph (n = 3).

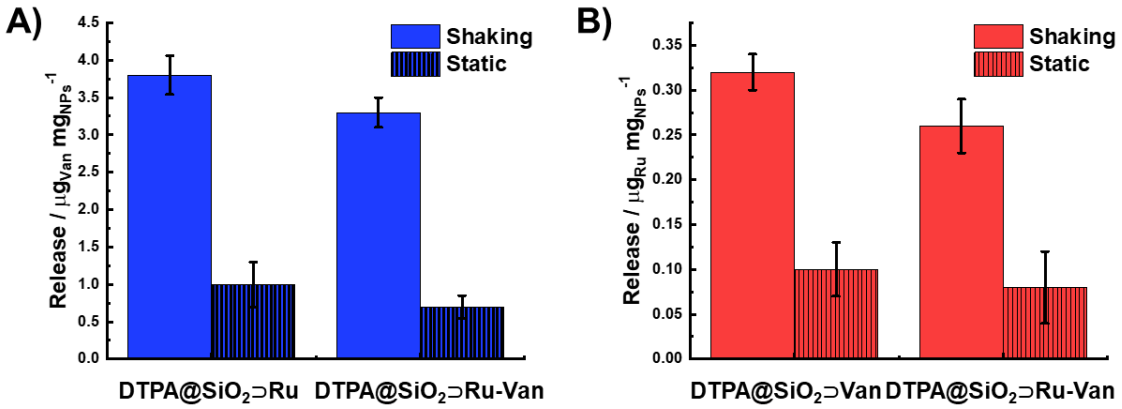

Figure 2.S25. Quantification of (A) released **Van** from **DTPA@SiO$_2$⊃Van** and **DTPA@SiO$_2$⊃Ru-Van** and (B) **Ru** leakage from **DTPA@SiO$_2$⊃Ru** and **DTPA@SiO$_2$⊃Ru-Van** under stirring (150 rpm) or static conditions at 37 ºC after 90 min by luminescence spectroscopy (λ_{exc} = 270 nm, λ_{em} = 330 nm for **Van** and λ_{exc} = 450 nm, λ_{em} = 600 nm for **Ru**, n = 3).

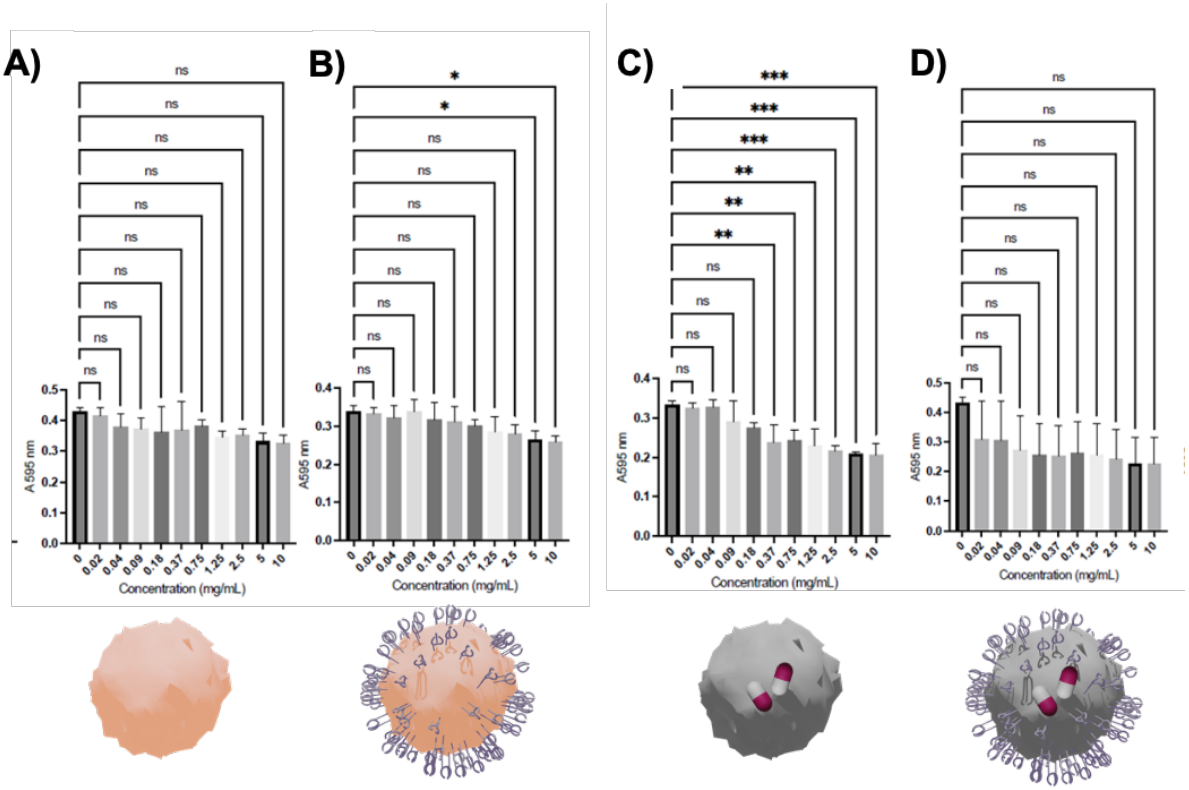

Figure 2.S26. MTT cell viability assays of A549 cell line incubated with studied nanoparticles for 18 hours with (A) **SiO_2⊃Ru**, (B) **DTPA@SiO_2⊃Ru**, (C) **SiO_2⊃Van** and (D) **DTPA@SiO_2⊃Van**. 1-way ANOVA followed by a Dunnett's t-test corrected for multiple comparisons was performed, ns = $p>0.05$, * = $p<0.05$, ** = $p<0.01$ and *** = $p< 0.001$, n = 3.

Table 2.S5. Minimal inhibitory concentration (MIC, mg/mL) of Ru(phen)3Cl2 (**Ru**) and Vancomycin HCl (**Van**) active compounds and synthetized nanoparticle library for *S. aureus* (ATCC23851), *E. coli* (MG1655), *A. baumannii* (AYE), *K. pneumoniae* (ATCC43816R), *K. oxytoca* (080-KPC CHD), *C. feundii* (NCTC9750), *S. enterica* (SL1344), *P. aeruginosa* (PA14) and *B. cenocepacia* (K57-2, CF isolate) determined by the 2-fold dilution method upon shaking at 150 rpm (red) and under static conditions (black) at 37 ^{o}C in LB media. Depicted results are based on 3 biological replicas.

	E. coli	***A. baumannii***	***K. pneumoniae***	***K. oxytoca***	***C. freundii***	***S. enterica***	***P. aeruginosa***	***B. cenocepacia***	***S. aureus***
$Ru(phen)_3Cl_2$ (**Ru**)	1.25		>2.50	>	>	>	> 2.50	> 2.50	0.32
Vancomycin HCl (**Van**)	>	>	> 0.25	>	>	>	> 0.25	> 0.25	0.00
SiO_2	> 10	> 10	> 10	> 10	> 10	> 10	> 10	> 10	> 10
	> 10	> 10	> 10	> 10	> 10	> 10	> 10	> 10	> 10
DTPA@SiO_2	> 10	10	10	10	10	10	> 10	> 10	2.50
	> 10	10	10	10	10	10	> 10	> 10	2.50
SiO_2⊃Ru	> 10	> 10	> 10	> 10	> 10	> 10	> 10	> 10	5.00
	> 10	> 10	> 10	> 10	> 10	> 10	> 10	> 10	1.25
DTPA@SiO_2⊃Ru	> 10	> 10	> 10	> 10	> 10	> 10	> 10	> 10	1.25
	5.00	5.00	5.00	5.00	10	5.00	10	10	0.75
SiO_2⊃Van	5.00	10	5.00	10	5.00	10	10	10	0.75
	5.00	10	10	10	5.00	10	10	5.00	0.75
DTPA@SiO_2⊃Vam	5.00	5.00	10	5.00	5.00	5.00	10	10	0.37
	2.50	2.50	2.50	1.25	1.25	1.25	5.00	5.00	0.37
SiO_2⊃Ru-Vam	10	10	> 10	10	10	10	10	10	2.50
	5.00	2.50	2.50	5.00	5.00	2.50	5.00	5.00	1.25
DTPA@SiO_2⊃Ru-Vam	5.00	2.50	2.50	10	10	5.00	10	10	0.37
	1.25	1.25	0.75	1.25	1.25	0.75	5.00	5.00	0.37

Table 2.S6. Thermodynamic parameters (kcal/mol) determined by Isothermal Titration Calorimetry (ITC) of Ca^{2+} (2.5 mM) into a suspension of **DTPA@SiO$_2$⊃Ru-Van** ([DTPA] = 0.32 mM) in PBS (0.1 M, pH 7.4) at 25 °C.

ΔH	-TΔS	ΔG
25.6 ± 0.5	- 9.6	- 35.3

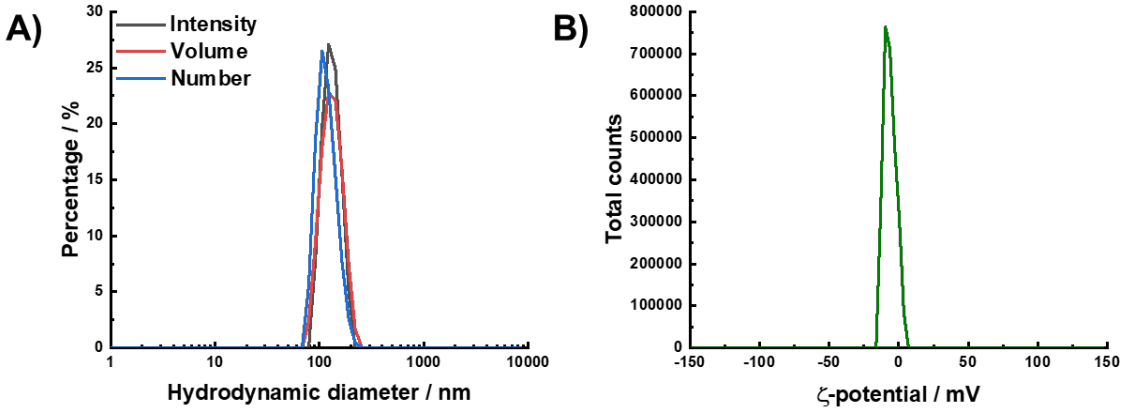

Figure 2.S27. Dynamic Light Scattering (DLS) analysis (n = 5) and surface ζ-potential distribution (n = 3) in PBS (0.1 M, pH 7.4) of **Ca^{2+}DTPA@SiO$_2$⊃Ru-Van**.

Table 2.S7. Dynamic Light Scattering (DLS, n = 5) and surface ζ-potential (n = 3) measurements of **Ca^{2+}DTPA@SiO$_2$⊃Ru-Van**. Measurements were performed at 25 °C in PBS buffer (0.1 M, pH 7.4) with nanoparticle concentration of 1 mg/mL.

Hydrodynamic size / nm				ζ-potential /mV
Intensity	Volume	Number	PDI	
112 ± 21	128 ± 15	98 ± 5	0.21	-10 ± 4

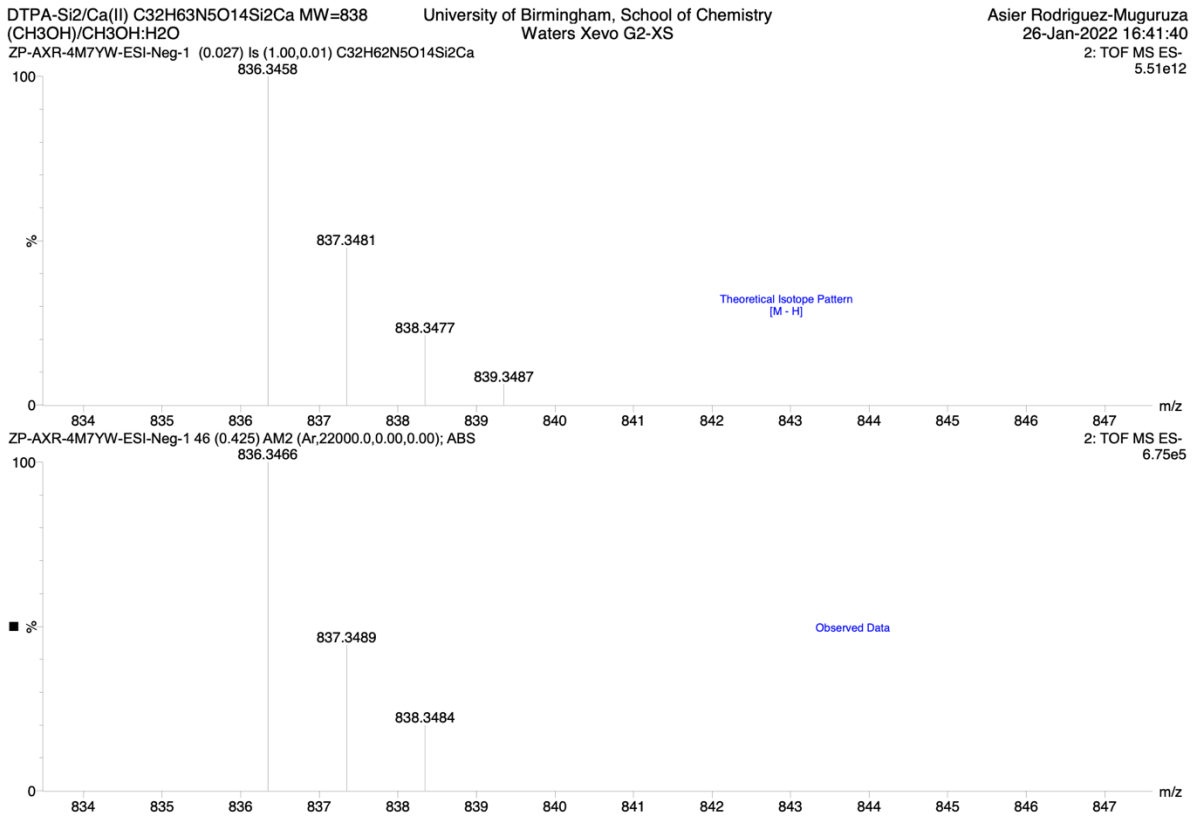

Figure 2.S28. Theoretical and observed (-)ESI-ToF spectrum of **Ca^{2+}DTPA-Si_2**.

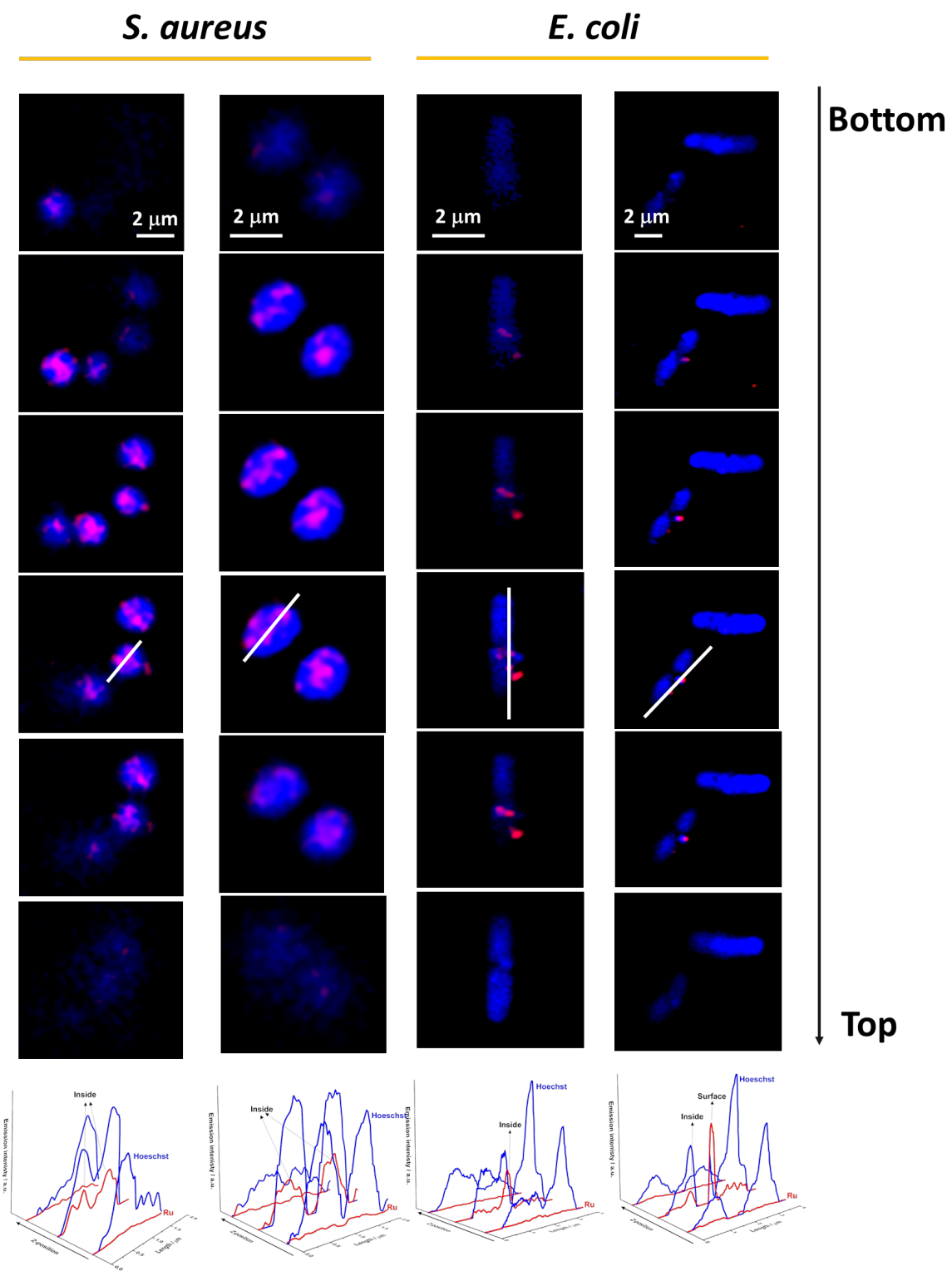

Figure 2.S29. Emission profiles generated from z-stack analysis (Figure 2.X) for selected stained *S. aureus* (ATCC23851) and *E. coli* (MG1655) cells incubated with **DTPA@SiO$_2$⊃Ru-Van** with a final nanoparticle concentration of 2.5 mg/mL for 2 h at 37 ^{o}C under mild shaking (150 rpm). Red channel, **Ru** emission (λ_{exc} = 488 nm, λ_{em} = 560 – 620 nm); blue channel Hoechst H33342 emission (λ_{exc} = 405 nm, λ_{em} = 410 – 450 nm).

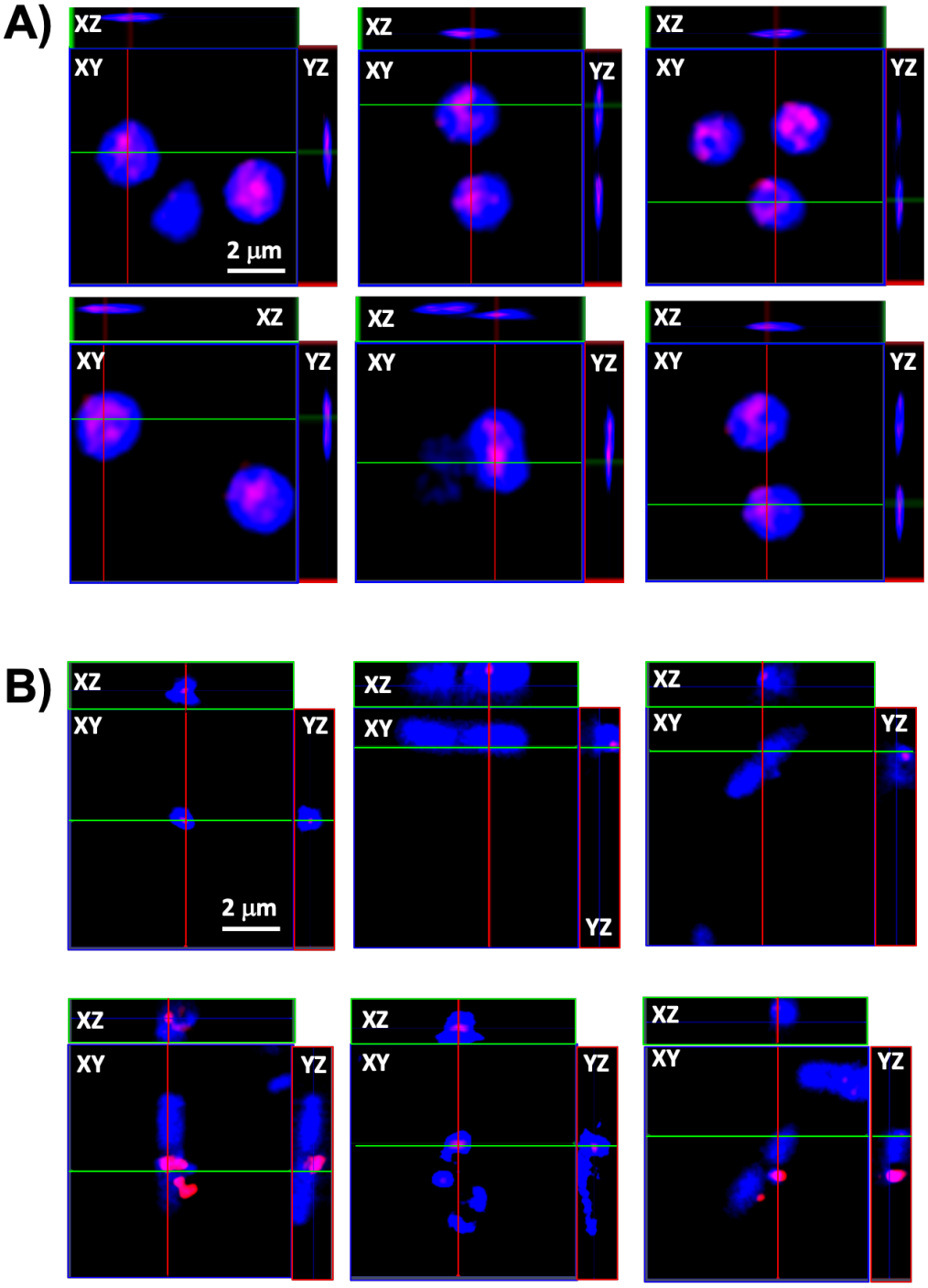

Figure 2.S30. Orthogonal reconstruction of selected central plane from z-stack images of further biological replicates from (A) *S. aureus* (ATCC23851) and (B) *E.coli* (MG1655) cells showing ruthenium signal inside cells after incubation with **DTPA@SiO$_2$⊃Ru-Van**. Overnight grown bacteria were incubated with **DTPA@SiO$_2$⊃Ru-Van** with a final nanoparticle concentration of 2.5 mg/mL for 2 h at 37 ^{o}C under mild shaking (150 rpm). Red channel, **Ru** (λ_{exc} = 488 nm, λ_{em} = 560 – 620 nm); blue channel Hoechst H33342 emission (λ_{exc} = 405 nm, λ_{em} = 410 – 450 nm).

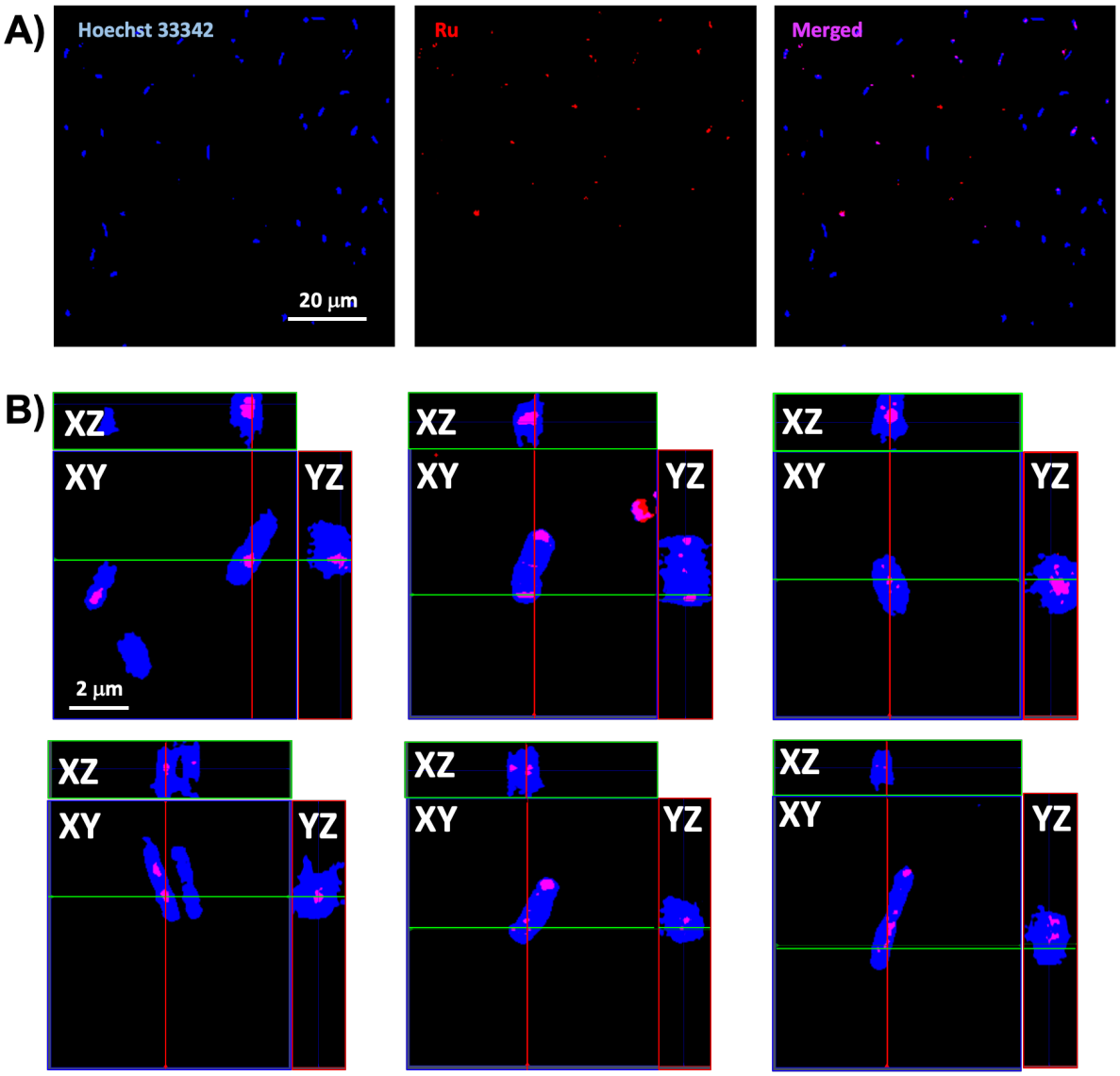

Figure 2.S31. Representative live cell structural illumination microscopy of bacterial cells with 18 h incubation time of **DTPA@SiO$_2$⊃Ru-Van** in *E. coli* (MG1655) (n = 5). Images show each channel for the outline of bacterial cells (blue) and particle luminescence (red) as well as merged channels (A) and orthogonal reconstruction of 3D z-stack images (B). Overnight grown bacteria were incubated with **DTPA@SiO$_2$⊃Ru-Van** with a final nanoparticle concentration of 2.5 mg/mL at 37 ^{o}C under mild shaking (150 rpm). Red channel, **Ru** emission (λ_{exc} = 488 nm, λ_{em} = 520 – 620 nm); blue channel Hoechst H33342 emission (λ_{exc} = 405 nm, λ_{em} = 410 – 450 nm).

Table 2.S8. Colocalization between blue and red signal in *S. aureus* (ATCC23851) cells after incubation with **SiO_2⊃Ru-Van** and **DTPA@SiO_2⊃Ru-Van** (2.5 mg/mL) at 150 rpm and 37 ºC for 2 h and was analysed by the Fiji plug in JACoP[101] calculating the Pearson and Manders' Overlap coefficient (n = 5) after different incubation times. M1 corresponds to the relative blue signal (Hoechst, bacterium cell) overlapping with the red channel (**Ru**, nanoparticles). M2 corresponds to the relative red signal overlapping with the blue one.

	JACoP	
	Manders' overlapping coefficient	
	M1	**M2**
SiO_2⊃Ru-Van	0.45 ± 0.12	0.55 ± 0.09
DTPA@SiO_2⊃Ru-Van	0.78 ± 0.06	0.87 ± 0.12

Table 2.S9. Colocalization between blue and red signal in *E. coli* (MG1655) cells after incubation with **SiO_2⊃Ru-Van** and **DTPA@SiO_2⊃Ru-Van** (2.5 mg/mL) at 150 rpm and 37 ºC for 2 h and 18 h was analysed by the Fiji plug in JACoP,[101] calculating the Pearson and Manders' Overlap coefficient (n = 5) after different incubation times. M1 corresponds to the relative blue signal (Hoechst, bacterium cell) overlapping with the red channel (**Ru**, nanoparticles). M2 corresponds to the relative red signal overlapping with the blue one.

		JACoP	
		Manders' overlapping coefficient	
	Incubation time	**M1**	**M2**
SiO_2⊃Ru-Van	2 h	0.03 ± 0.02	0.10 ± 0.04
	18 h	0.08 ± 0.05	0.20 ± 0.07
DTPA@SiO_2⊃Ru-Van	2 h	0.55 ± 0.16	0.61 ± 0.13
	18 h	0.75 ± 0.11	0.87 ± 0.07

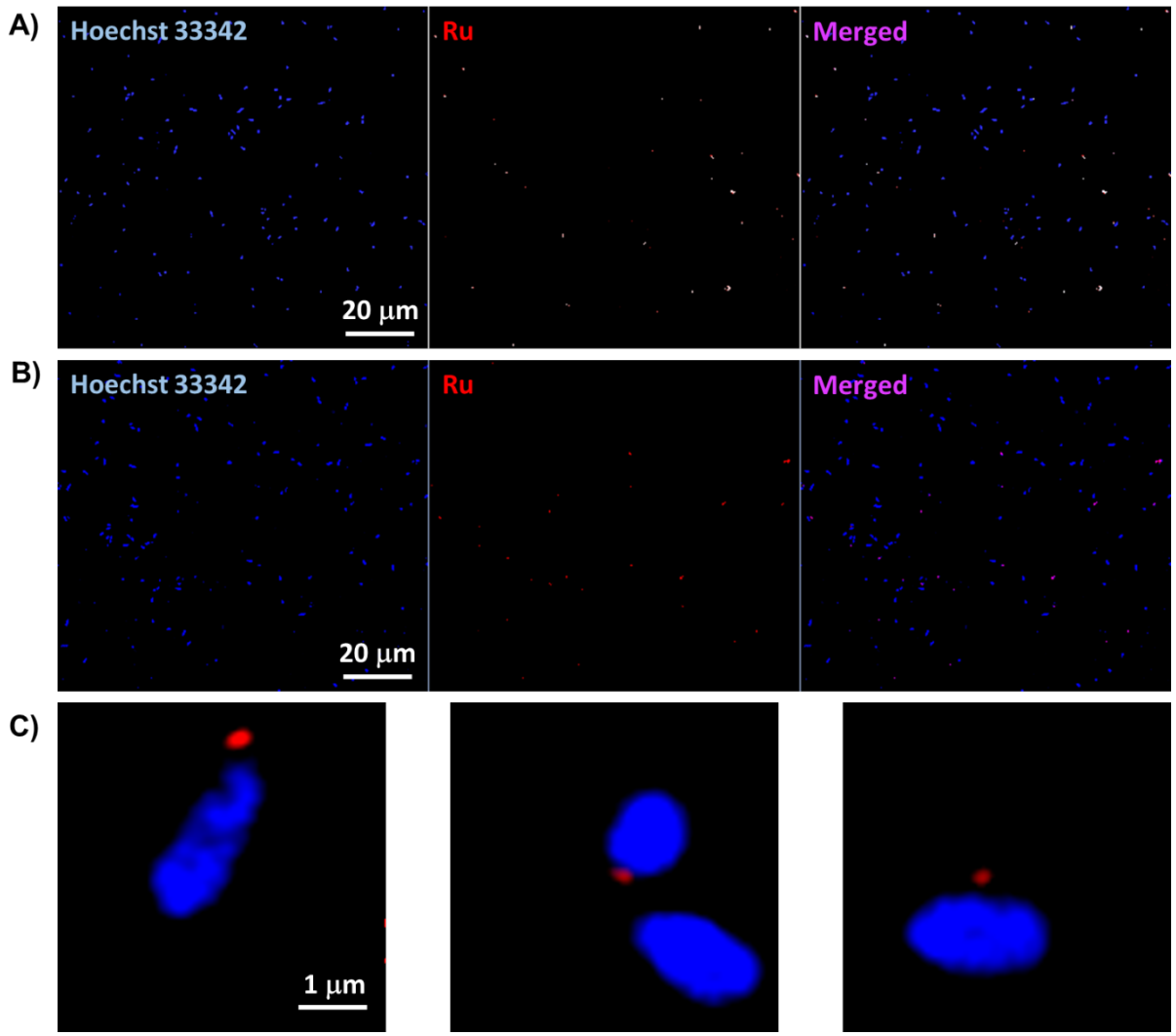

Figure 2.S32. Representative live cell structural illumination microscopy of bacterial cells with (A) 2 h and (B) 18 h incubation time with **DTPA@SiO$_2$⊃Ru-Van** in *P. aeruginosa* (PA14) (n = 5). Images show each channel for the outline of bacterial cells (blue) and particle luminescence (red) as well as merged channels. (C) shows nanoparticles close to the membrane of *P. aeruginosa* cells after 18 h incubation, but no **Ru** signal inside cells was observed. Overnight grown bacteria were incubated with **DTPA@SiO$_2$⊃Ru-Van** with a final nanoparticle concentration of 2.5 mg/mL at 37 ^{O}C under mild shaking (150 rpm). Red channel, **Ru** emission (λ_{exc} = 488 nm, λ_{em} = 520 – 620 nm); blue channel Hoechst H33342 emission (λ_{exc} = 405 nm, λ_{em} = 410 – 450 nm).

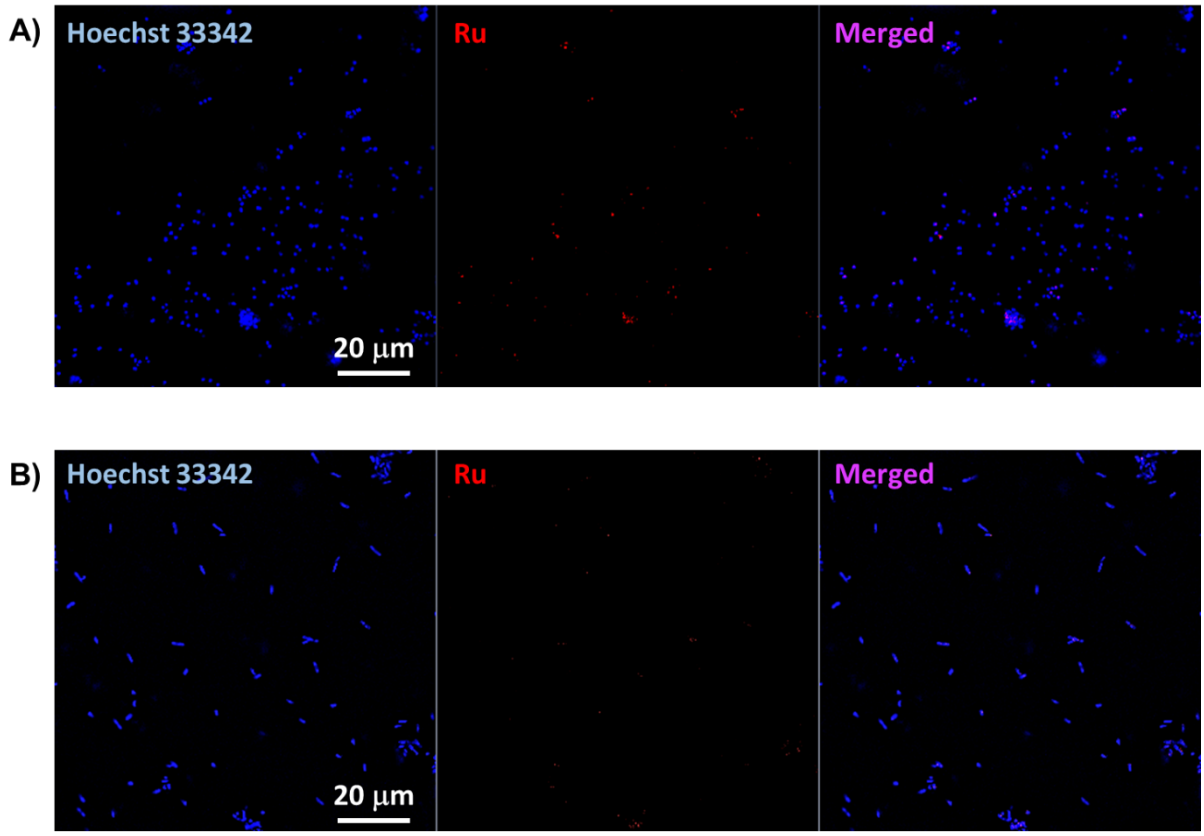

Figure 2.S33. Representative live cell structural illumination microscopy of bacterial cells with 2 h incubation time of **Ca^{2+}DTPA@SiO_2⊃Ru-Van** in (A) *S. aureus* (ATCC23851) and (B) *E. coli* (MG1655) (n = 5). Images show each channel for the outline of bacterial cells (blue) and particle luminescence (red) as well as merged channels. Overnight grown bacteria were incubated with **Ca^{2+}DTPA@SiO_2⊃Ru-Van** with a final nanoparticle concentration of 2.5 mg/mL at 37 ^{O}C under mild shaking (150 rpm). Red channel, **Ru** emission (λ_{exc} = 488 nm, λ_{em} = 520 – 620 nm); blue channel Hoechst H33342 emission (λ_{exc} = 405 nm, λ_{em} = 410 – 450 nm).

Table 2.S10. Colocalization between blue and red signal in *S. aureus (ATCC23851) E. coli* (MG1655) cells after incubation with **Ca^{2+}DTPA@SiO_2⊃Ru** (2.5 mg/mL) at 150 rpm and 37 ºC for 2 h was analysed by the Fiji plug in JACoP[101] calculating the Pearson and Manders' Overlap coefficient (n = 5) after different incubation times. M1 corresponds to the relative blue signal (Hoechst, bacterium cell) overlapping with the red channel (**Ru**, nanoparticles). M2 corresponds to the relative red signal overlapping with the blue one.

	JACoP	
	Manders' overlapping coefficient	
	M1	**M2**
S. aureus	0.35 ± 0.09	0.65 ± 0.16
E. coli	0.09 ± 0.03	0.55 ± 0.07

Showcasing research from Professor Pikramenou and Dr. Blair's laboratories, School of Chemistry and Institute of Microbiology and Infection at University of Birmingham, Edgbaston, UK.

Chelating silica nanoparticles for efficient antibiotic delivery and particle imaging in Gram-negative bacteria

Nanoparticles with encapsulated antibiotics are delivered in Gram-negative bacteria using surface modification of the nanoparticles. Aminocarboxylate ligands are used to decorate the nanoparticle surface and allow penetration of nanoparticles into Gram-negative bacteria, with demonstrated activity of vancomycin which is inactive on its own. The particles are detected in bacteria by structural illumination microscopy monitoring the red luminescence of a ruthenium co-encapsulated probe.

As featured in:

See Jessica M. A. Blair, Zoe Pikramenou *et al.*, *Nanoscale Adv.*, 2023, **5**, 2453.

ROYAL SOCIETY OF CHEMISTRY

rsc.li/nanoscale-advances

Registered charity number: 207890

Nanoscale Advances

ROYAL SOCIETY OF CHEMISTRY

PAPER

View Article Online
View Journal

Check for updates

Cite this: DOI: 10.1039/d2na00884j

Chelating silica nanoparticles for efficient antibiotic delivery and particle imaging in Gram-negative bacteria†

Asier R. Muguruza, [a] Alessandro di Maio, [b] Nikolas J. Hodges, [c] Jessica M. A. Blair *[d] and Zoe Pikramenou *[a]

The inefficacy of antibiotics against Gram-negative bacteria is a major challenge for treatment of many clinically important bacterial infections. The complex structure of the double cell membrane of Gram-negative bacteria makes it inaccessible to many key antibiotics such as vancomycin and also presents a major challenge for drug development. In this study we design of a novel hybrid silica nanoparticle system bearing membrane targeting groups with the antibiotic encapsulated together with a ruthenium luminescent tracking agent, for optical detection of the nanoparticle delivery in the bacterial cell. The hybrid system shows delivery of vancomycin and efficacy against a library of Gram negative bacterial species. Evidence of penetration of nanoparticles in bacteria cells is achieved *via* luminescence of the ruthenium signal. Our studies show that nanoparticles modified with aminopolycarboxylate chelating groups are an effective delivery system in bacterial growth inhibition in species whereas the molecular antibiotic is ineffective. This design provides a new platform for delivery of antibiotics that cannot alone penetrate the bacterial membrane.

Received 2nd December 2022
Accepted 15th February 2023

DOI: 10.1039/d2na00884j

rsc.li/nanoscale-advances

Open Access Article. Published on 20 February 2023. Downloaded on 4/8/2023 4:18:53 PM.
This article is licensed under a Creative Commons Attribution 3.0 Unported Licence.

Introduction

Gram-negative bacterial species, including *E. coli*, are major causes of infectious diseases worldwide and account for all organisms in the "critical" category of the WHO list of antibiotic-resistant "priority pathogens".[1] These bacteria are intrinsically drug-resistant due to the presence of an impermeable outer membrane.[2,3] The design of novel antibiotics with activity against Gram-negative bacteria can be challenging due to the drug's size and hydrophobicity properties in order for the drug to cross the membrane and access intracellular targets. Nanoscale materials are attractive vehicles for the delivery of therapeutic agents with wide chemical versatility which provides potential to overcome multi-drug resistance mechanisms.[4]

Silica nanoparticles are attractive vehicles due to their excellent biocompatibility, facile synthesis with tunability of their size and surface chemistry for functionalisation. The most popular approach using silica nanoparticles for drug delivery is the formation of mesoporous particles. Indeed, such approach leads to high loading capacity with a plethora of agents, from nucleic acids to cancer drugs and several antibiotics.[5–7] However, there are two drawbacks which limit their translation to the clinic: the porosity of the particle is induced by the use of a surfactant such as cetyl trimethyl bromide which is cytotoxic and needs to be fully removed from the particle;[6] secondly, the high porosity leads to uncontrolled, "burst" release of the adsorbed agent in fluid delivery conditions which limits their application in targeted delivery. Approaches to limit the leakage of the drug usually involve functionalization of the particle's outer surface with a range of macromolecular structures to block the pores such as polymers,[8,9] peptides[10] or lipids.[11]

To tackle the challenge of both membrane permeation and controlled antibiotic delivery we chose to develop a hybrid, non-mesoporous silica nanoparticle system with surface functionalization to enhance penetration of the bacterial cell and inclusion of a metal complex to allow optical tracking of the nanoparticle's fate inside the cell. Hybrid nanoparticles have been previously developed with designs involving covalent modification of particle surface with organic fluorophores,[12] or condensation of silyl-modified organic fluorophores in the silica network[13] or by covalently linking quantum dots to the silica framework of porous nanoparticles.[14] We have previously explored tracking of nanoparticles using metal complexes as photostable luminescent agents with characteristic emission properties which offer optical imaging modalities based on

[a]School of Chemistry, College of Engineering and Physical Sciences, University of Birmingham, Edgbaston, B15 2TT, UK. E-mail: z.pikramenou@bham.ac.uk; Tel: +44 (0)121 4142290

[b]Birmingham Advanced Light Microscopy Facility, University of Birmingham, Edgbaston, B15 2TT, UK

[c]School of Biosciences, University of Birmingham, Edgbaston, B15 2TT, UK

[d]Institute of Microbiology and Infection, College of Medical and Dental Sciences, University of Birmingham, Edgbaston, B15 2TT, UK. E-mail: J.M.A.Blair@bham.ac.uk; Tel: +44 (0)121 4147606

† Electronic supplementary information (ESI) available. See DOI: https://doi.org/10.1039/d2na00884j

© 2023 The Author(s). Published by the Royal Society of Chemistry

Open Access Article. Published on 20 February 2023. Downloaded on 4/8/2023 4:18:53 PM.
This article is licensed under a Creative Commons Attribution 3.0 Unported Licence.

their distinct signal, away from any scattering, with long luminescent lifetimes, to probe their localisation in tissues,[15,16] under flow conditions[17,18] and in drug delivery.[19] In this study we chose to use ruthenium tris phenanthroline, **Ru**, as a luminescent photostable probe which is much more resistant to photobleaching than organic dyes. In addition, its encapsulation in the silica framework is well established,[20] leading to highly luminescence nanoparticles that can be tracked by imaging.[21]

Vancomycin, **Van**, was chosen as it is a well-studied antibiotic, effective against many Gram-positive species but not Gram-negative bacteria which are intrinsically resistant to it due to the low permeability.[2] This has been attributed to the bulky glycopeptide structure which does not cross the Gram-negative bacteria cell outer membrane. By encapsulation of vancomycin in the silica particle it is envisaged that the interaction with the outer membrane will be governed by the particle properties rather than the properties of the antibiotic. Inclusion of vancomycin in silica nanoparticles has been previously reported through two different methodologies: surface covalent anchoring[22] or absorption into the porous network of mesoporous silica nanoparticles,[23] which would not be effective in our case as it would only allow the treatment of those bacterial cells that are in contact with the nanoparticle leading to the aforementioned limitations of usage. In our approach we would use encapsulation of the vancomycin together with the positively charged ruthenium agent during the growth of the silica network.

To modulate the particle's surface properties and interaction with the bacterial membrane we have incorporated a bis(amide) derivative of diethylene triamine pentaacetic acid (noted as **DTPA**) to attach covalently onto the silica nanoparticle outer surface. Diethylene triamine pentaacetic acid has been shown previously to destabilize the Gram-negative bacterial cell wall, based on its chelating properties to calcium in the bacterial outer membrane.[19–21] Our hybrid silica design was based on using the surface properties of the particle to induce uptake and the encapsulated antibiotic to act following particle uptake. The hybrid nanoparticle was formed in two steps: firstly, **Van** was encapsulated together with **Ru** luminescent agent during the silica nanoparticle formation, followed by the attachment of the surface active **DTPA** to the isolated nanoparticles to give **DTPA@SiO$_2$⊃Ru-Van** (Fig. 1). To assess the influence of the surface-active ligand and the encapsulation, control nanoparticles were also examined without the surface coating, or with a single agent. All particles were tested against *S. aureus* and a selection of Gram-negative bacterial species and luminescence microscopy was also used to demonstrate tracking of the particles.

Results and discussion

Particle formation and characterization

Our synthetic methodology was based on the formation of the silica nanoparticles in the presence of the antibiotic, **Van**, and

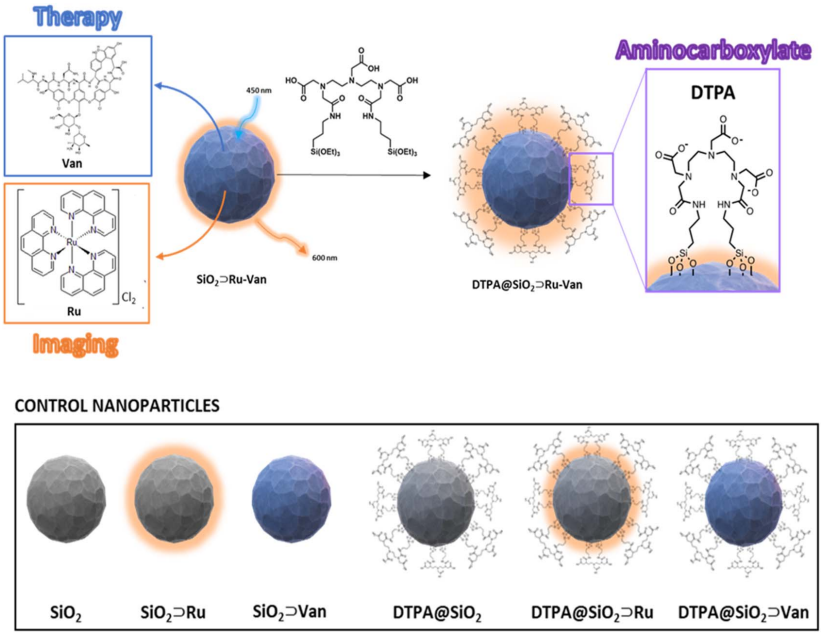

Fig. 1 Schematic representation of hybrid DTPA@SiO$_2$⊃Ru-Van and nanoparticles with single agents with and without DTPA coating for control experiments.

© 2023 The Author(s). Published by the Royal Society of Chemistry

Open Access Article. Published on 20 February 2023. Downloaded on 6/10/2023 2:30:22 PM.
This article is licensed under a Creative Commons Attribution 3.0 Unported Licence.

the luminescent tracking agent, **Ru** under controlled conditions[24] to yield **SiO_2⊃Ru-Van** particles (Fig. 1). Although **SiO_2⊃Ru** have been previously reported[20,24] with the ruthenium complex as encapsulated agent, hybrid particles with antibiotic have not been previously developed. It was envisaged that the addition of vancomycin at the same time of the ruthenium agent will allow growth of silica around them as it occurs with single agents. Encapsulation of both agents may have been driven by the electrostatic properties of the positively charged ruthenium and the hydrogen-bonding of vancomycin with the silica framework. Particles with single agent were also prepared, **SiO_2⊃Ru** and **SiO_2⊃Van**, under the same conditions for comparisons. Following isolation and purification of the particles with the encapsulated agents, the surface of the particles was modified upon reaction with the silyl surface active bis(amide) derivative (Fig. 1).[23] The final particles were purified by washing and centrifugation. Size and properties of all nanoparticles were analyzed by a suite of characterization techniques, including Dynamic Light Scattering (DLS) and electron microscopy techniques. A summary of the two hybrid nanoparticle systems is presented in Table 1 and the rest of the nanoparticle systems in Tables S1 and S2.† DLS results provide the hydrodynamic diameter of the particles. In water there is not a significant difference of the coated **DTPA@SiO_2⊃Ru-Van** and uncoated **SiO_2⊃Ru-Van** particles as it is expected. However, in PBS **DTPA@SiO_2⊃Ru-Van** show larger sizes on intensity values without increase of polydispersity which excludes aggregation. The effect is more pronounced with the coated particles which have free carboxylate groups and it is also evidenced upon addition of excess NaCl (Table S1†). The change of the surface coating was also evidenced by the ζ-potential measurements with a higher negative potential of **DTPA@SiO_2⊃Ru-Van**, −24 mV compared to **SiO_2⊃Ru-Van** from −18 mV (Table 1), attributed to the negatively charged carboxylate moieties. This trend in the ζ-potential measurements is also supported for the nanoparticles with the single agent **Ru** or **Van** upon coating (ESI†). Scanning electron microscopy (SEM) and transmission electron microscopy (TEM) (Fig. 2 and ESI†) images confirmed the uniform, spherical morphology and good monodispersity of **SiO_2⊃Ru-Van** and **DTPA@SiO_2⊃Ru-Van** (ESI†). Independent particle measurements of the nanoparticles from the microscopy images led to estimated average sizes of 85 ± 3 nm and 87 ± 4 nm for **SiO_2⊃Ru-Van** and **DTPA@SiO_2⊃Ru-Van**, respectively. The smaller sizes from the microscopy studies were anticipated as the images do not reflect the outer surface of the particle accounted in the hydrodynamic measurements. The same trend for the size and shape of the particles was observed for the particles including the single agents with sizes of 50–90 nm. FT-IR and Raman spectroscopy were employed to provide signatures of the agents in the particles. FT-IR spectra are dominated by the Si–O–Si and Si–O stretches and the individual cargo peaks are too weak to be observed. However, the **DTPA** stretches are observed in all coated particles with peaks attributed to C–H and N–H bands, as well as characteristic C=O stretches (SI†). The characteristic cargo peaks are observed by Raman spectroscopy. In cargo-loaded **SiO_2** nanoparticles, Raman shifts assigned to the C–C stretching and C–H of both cargos were observed in the 1000–1700 cm^{-1} range (ESI†), confirming their presence in the silica framework.

To evaluate their properties for detection in bacterial cells, optical spectroscopy was employed. Solid-state UV/vis spectroscopy of SiO_2⊃Ru-Van showed a broad band centred at 425 nm, characteristic of the singlet metal to ligand charge transfer transition (^{1}MLCT) of the **Ru** complex along with a broad band with shoulder at 281 nm and a 261 nm attributed to the **Van** antibiotic π–π* transitions and phenanthroline transitions, respectively (Fig. 2). Excitation of both coated and uncoated particles, **DTPA@SiO_2⊂Ru-Van** and **SiO_2⊃Ru-Van**, at the ^{1}MLCT band at 450 nm showed a broad luminescence peak in the red of the spectrum which is characteristic of the ^{3}MLCT transition. The peak is observed at 613 and 612 nm in **SiO_2⊃Ru-Van** and **SiO_2⊃Ru** showing no effect from the presence of Van with a small lifetime increase (ESI†). However, the coated particles **DTPA@SiO_2⊂Ru-Van** showed a blue shift to 595 nm. This was further supported by the 19 nm shift of the emission in **DTPA@SiO_2⊃Ru** in comparison with **SiO_2⊃Ru**. Interestingly, the luminescence lifetime of the **Ru**-based emission was increased from 1.69 μs in **SiO_2⊃Ru-Van** to 2.52 μs in **DTPA@SiO_2⊂Ru-Van** and from 1.45 μs in **SiO_2⊃Ru** to 3.31 μs **DTPA@SiO_2⊃Ru**. The increase of the lifetime may be attributed to the surface functionalisation with **DTPA** which decreases oxygen access, responsible for quenching the ruthenium luminescence. Upon excitation at 270 nm, a fluorescence signal at 330 nm indicated the presence of **Van** in **SiO_2⊃Ru-Van**, a 3 nm blue sift was observed for **Van**'s emission after coating with **DTPA**. **SiO_2⊃Van** also displayed a 5 nm blue shift upon **DTPA** coating (ESI†). The hybrid particles display dual emission in the

Table 1 Summary of nanoparticle properties for SiO_2⊃Ru-Van and DTPA@SiO_2⊃Ru-Van. Dynamic Light Scattering measurements are performed at 25 °C in MiliQ water and phosphate buffer solution (PBS, 0.1 M, pH 7.4), PDI = Polydispersity Index. Size by TEM is determined based on 20 nanoparticle measurements

		Mean $size_{DLS}$/nm					
		Intensity	Volume	Number	PDI	Mean $size_{TEM}$/nm	ζ-Potential/mV
SiO_2⊃Ru-Van	Water	89 ± 29	86 ± 12	84 ± 22	0.16	85 ± 3	−16 ± 2
	PBS	98 ± 29	82 ± 26	67 ± 18	0.15		−18 ± 6
DTPA@SiO_2⊂Ru-Van	Water	94 ± 10	92 ± 15	89 ± 14	0.24	87 ± 4	−20 ± 3
	PBS	113 ± 28	105 ± 25	94 ± 20	0.21		−24 ± 5

© 2023 The Author(s). Published by the Royal Society of Chemistry

Open Access Article. Published on 20 February 2023. Downloaded on 4/8/2023 4:18:53 PM.
This article is licensed under a Creative Commons Attribution 3.0 Unported Licence.

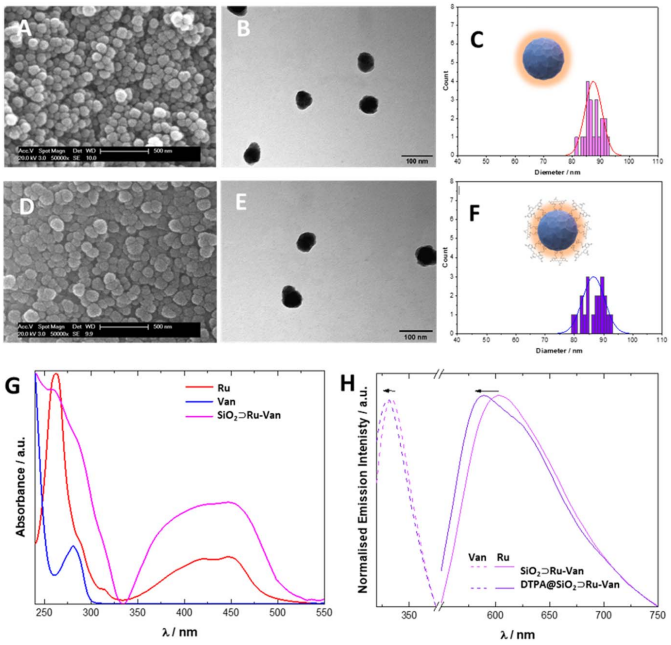

Fig. 2 Characterisation and analysis of size and optical properties of hybrid particles with cargo agents Scanning Electron Microscopy (A and D) and Transmission Electron Microscopy (B and E) images of hybrid particles $SiO_2 \supset$ Ru-Van (A and B) and DTPA@$SiO_2 \supset$ Ru-Van (D and E). Size distributions are calculated based on 20 measurements and distribution is fitting according to a Gaussian distribution (C and F). Optical properties of DTPA@$SiO_2 \supset$ Ru-Van and $SiO_2 \supset$ Ru-Van confirming the presence of Van and Ru by solid state UV/vis spectroscopy (G) and solid-state luminescence (H) of Van (λ_{exc} = 270 nm) and Ru (λ_{exc} = 450 nm).

blue from vancomycin and the red from the ruthenium agent with the latter making them attractive for detection in bacterial cells. To quantify the surface coating, we used the **DTPA** ligand's property to bind to lanthanide ions to form 1 : 1 stable complexes.[26] By titration of a solution of Tb^{3+} to a solution of **DTPA@$SiO_2 \supset$ Ru-Van** the luminescence signal of terbium was increased, reaching a plateau. The coordination of terbium to he **DTPA** moiety on **DTPA@$SiO_2 \supset$ Ru-Van**, forming a 1 : 1 complex with **DTPA**, led to replacement of water molecules in the terbium coordination sphere which quench the terbium signal, hence leading to a luminescence signal increase. From the titration, the concentration of **DTPA** was correlated to the nanoparticle concentration and it was estimated to be 0.53 mg_{DTPA}/mg_{NP}.

Loading of the agents in nanoparticles and antibiotic release

Loading of the agents in **$SiO_2 \supset$ Ru-Van** were determined by (a) thermogravimetric analysis (TGA) and (b) optical spectroscopy of the remaining supernatant following centrifugation (Fig. 3). TGA is a widely used technique for material characterization and determination of the loading of drugs in silica nanoparticles, based on the continuous monitoring of sample's weight loss upon heating at a defined rate under a controlled atmosphere. In the plain **SiO_2** particles the first loss of weight of 15 $\mu g/mg_{NP}$ is observed at 150 °C and it is attributed to adsorbed water as previously observed[21] where the hybrid **$SiO_2 \supset$ Ru-Van** particles showed a loss of weight from 200–900 °C of 58 $\mu g/mg_{NP}$ (Fig. 3A); in comparison, the **$SiO_2 \supset$ Ru** particles showed a weight loss of 0.3% and **$SiO_2 \supset$ Van** a loss of 8.9%, although the latter did not show distinct steps as the other particles, attributed to Van thermal degradation.

Interestingly, the TGA graphs of the particles coated with **DTPA**, **DTPA@SiO2 $\supset$ Ru-Van**, **DTPA@SiO2 $\supset$ Ru** and **DTPA@$SiO_2 \supset$ Van** were dominated by the degradation of the **DTPA** with an estimated content of 0.55 mg_{DTPA}/mg_{NP} (Fig. 3B) in agreement with the independent optical analysis by coordination of Tb^{3+} which was 0.53 mg_{DTPA}/mg_{NP}. For the control nanoparticles, the **DTPA** content by TGA was calculated also to be between 0.49 to 0.55 mg_{DTPA}/mg_{NP} (ESI†). In order to define the amount of **Ru** and **Van** separately in **$SiO_2 \supset$ Ru-Van** we studied the luminescence signal of the supernatant **Ru** and **Van** agents, following centrifugation after their preparation. It was estimated that in **$SiO_2 \supset$ Ru-Van** there were 5 $\mu g_{Ru}/mg_{NP}$ and 54 $\mu g_{Van}/mg_{NP}$.

These were in good agreement with the overall agent content determined by TGA (0.6 $\mu g_{Agent}/mg_{NP}$).

© 2023 The Author(s). Published by the Royal Society of Chemistry

Asier Rodriguez Muguruza – December 2023

Open Access Article. Published on 20 February 2023. Downloaded on 4/8/2023 4:18:53 PM.
This article is licensed under a Creative Commons Attribution 3.0 Unported Licence.

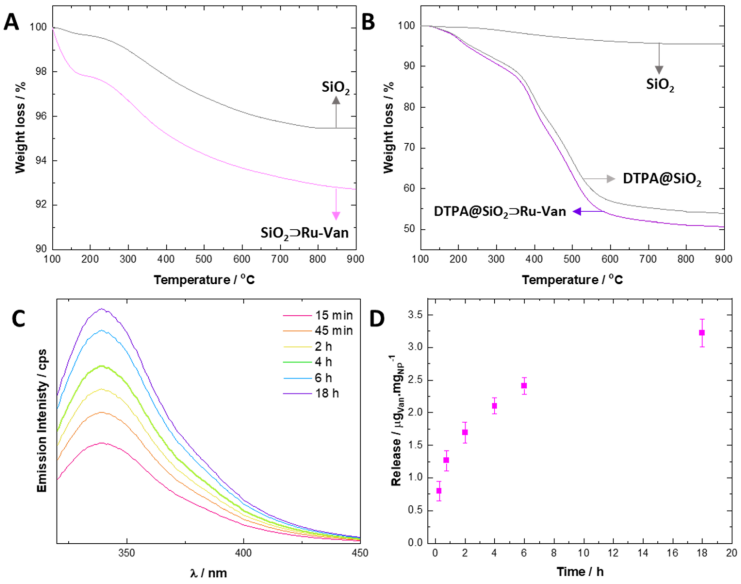

Fig. 3 Quantification of included cargo by Thermal Gravimetric Analysis and optical spectroscopy studies showing cargo loading. TGA profiles showing **Ru** and **Van** loading (A) and **DTPA** coating (B) in **SiO_2⊃Ru-Van** and **DTPA@SiO_2⊃Ru-Van**, respectively. Samples are heated from 30 °C to 900 °C at 1 °C per min rate with a 10 min isothermal step at 100 °C to ensure water removal. All degradation curves are set at 100% for clarity. Fluorescence monitoring of release of **Van** from hybrid **DTPA@SiO_2⊃Ru-Van** nanoparticles and cumulative release graph (C and D) at 37 °C, 150 rpm, in water (λ_{exc} = 270 nm and λ_{em} = 330 nm) (n = 3).

Release of the antibiotic **Van** from the hybrid nanoparticles was monitored by fluorescence spectroscopy when the particle dispersion was subjected to shaking (150 rpm) at 37 °C. It was calculated that up to 3.3 ± 0.5 $\mu g_{Van}/mg_{NP}$ of the antibiotic can be released from **DTPA@SiO_2⊃Ru-Van** with a continuous cumulative release (Fig. 3C and D), up to 18 h, determined based on calibration of **Van**'s fluorescence signal upon excitation at 270 nm. **DTPA@SiO_2⊃Van** showed a cumulative release of 3.8 ± 0.3 $\mu g_{Van}/mg_{NP}$ upon continuous shaking. Minimal release of the antibiotic **Van** was observed under static conditions (ESI†). Furthermore, the luminescent agent's release **Ru** under shaking or static conditions led also to minimal leakage.

Antibacterial activity

In order to assess the antibacterial properties of the designed luminescent hybrid nanoparticles in the first instance, *S. aureus* (ATTC23841) and *E. coli* (MG1665) were chosen as representative Gram-positive and Gram-negative bacterial species, respectively. Gram-negative bacteria have a double membrane structure that includes a rigid, impermeable outer membrane making them intrinsically resistant to many antibiotics including vancomycin. Gram-positive bacteria, however, possess a much simpler single cell membrane through which many more antibiotics can pass.[1,2,28]

The antibacterial activity of all the nanoparticles and individual agents was evaluated by measuring the Minimum Inhibitory Concentration (MIC) in Lysogeny Broth (LB) with mild shaking. MIC values were determined as the minimum nanoparticle concentration (mg mL^{-1}) where no bacterial growth was observed (Table 2).

Chelating nanoparticles with the cargos, **DTPA@SiO_2⊃Ru-Van**, displayed significantly increased antimicrobial activity (decreased MIC values) in both *S. aureus* (MIC = 0.37 mg mL^{-1}) and *E. coli* (1.25 mg mL^{-1}) compared to **SiO_2⊃Ru-Van** suggesting that these functionalised nanoparticles had increased uptake into *E. coli*. It is worth noting that the estimated concentration of the released antibiotic is only by **DTPA@SiO_2⊃Ru-Van**, is in the μg ml^{-1} region (Table 2), showing the efficiency of the delivery system. As expected, the antibiotic **Van** only had antimicrobial activity against *S. aureus*, (MIC = 1 μg mL^{-1}), but not *E. coli* reflecting the intrinsic low permeability of the Gram-negative outer membrane. Similarly, the luminescent tracking agent, **Ru**, had moderate antimicrobial activity against *S. aureus* (MIC = 312 μg mL^{-1}, Table S5†) but not *E. coli* or the other Gram-negative species. The plain **SiO_2** nanoparticles were also not found with antibacterial activity up to a concentration of 10 mg mL^{-1} (Table S5†). Inclusion of the cargos in the nanoparticles to give **SiO_2⊃Ru-Van**, **SiO_2⊃Ru** or **SiO_2⊃Van**, show only moderately increased bacterial susceptibility, suggesting that encapsulating within

© 2023 The Author(s). Published by the Royal Society of Chemistry

Table 2 Minimal Inhibitory Concentrations (MIC, mg mL^{-1}) of **Van**, SiO_2, **DTPA@SiO$_2$**, SiO_2⊃**Ru-Van** and **DTPA@SiO$_2$⊃Ru-Van** for *S. aureus* (ATTC23851), *E. coli* (MG1665), *A. baumannii* (AC05), *K. pneumoniae* (ATCC43816R), *K. oxytoca* (080-KPC CHD), *C. feundii* (NCTC9750) and *S. enterica* (SL1344) determined by the 2-fold dilution method upon shaking at 150 rpm at 37 °C in LB media. Depicted results are based on three biological replicas

	E. coli	*A. baumannii*	*K. pneumoniae*	*K. oxytoca*	*C. freundii*	*S. enterica*	*S. aureus*
Chelating particles **DTPA@SiO$_2$⊃Ru-Van**	1.25 (4.1)[a]	1.25 (4.1)[a]	0.75 (2.5)[a]	1.25 (4.1)[a]	1.25 (4.1)[a]	0.75 (2.5)[a]	0.37 (1.2)[a]
Plain antibiotic **Van**	> 0.25	> 0.25	> 0.25	> 0.25	> 0.25	> 0.25	0.001
Non-chelating particles **SiO$_2$⊃Ru-Van**	5.00	2.50	2.50	5.00	5.00	2.50	1.25

[a] Estimated Van released based on release studies of **DTPA@SiO$_2$⊃Ru-Van** *in vitro* (in μg mL^{-1}, ± 16%).

Open Access Article. Published on 20 February 2023. Downloaded on 4/8/2023 4:18:53 PM.
This article is licensed under a Creative Commons Attribution 3.0 Unported Licence.

the nanoparticle had not sufficiently increased penetration of the antimicrobial agent. The particles with no cargo, **DTPA@SiO$_2$**, had no antimicrobial activity against *E. coli*. Antimicrobial activity of antibiotic containing nanoparticles was greater when particles were shaken compared with static incubation which was in good agreement with the release studies under static conditions (ESI†). A range of other clinically relevant Gram-negative bacterial species were also analysed (Table 2) to examine the effect of the aminocarboxylate coating. The results show that functionalisation of nanoparticle surface greatly increased susceptibility in all Gram-negative species tested: *A. baumannii* (AC05), *K. pneumoniae* (ATCC43816R), *K. oxytoca* (080-KPC CHD), *C. feundii* (NCTC9750) and *S. enterica* (SL1344). In these Gram-negative bacterial species, the antibiotic had no effect if delivered without the nanoparticle system even when delivered at concentrations of 0.25 mg mL^{-1}. Overall **DTPA@SiO$_2$⊃Ru-Van** shows greater antibacterial activity than previously achieved with vancomycin encapsulated in porous networks.[23] Moreover, all functionalised nanoparticles showed low overall cytotoxicity against A549 lung cancer cells as assessed by the MTT assay. Cell viability was above 85% at concentrations used in MIC experiments and this was not statistically significant as assessed by a 1-way ANOVA followed by a post-hoc Tukey *T*-test (Fig. S12†).

We attribute the activity of the hybrid nanoparticles **DTPA@SiO$_2$⊃Ru-Van** to the **DTPA** chelating ability against Ca^{2+} and Mg^{2+}. It has been previously reported that polyaminocarboxylate chelators interact with bacterial membranes and damage its structural stability by removing crucial Ca^{2+} and Mg^{2+} cations.[27,28] Recent simulation studies by L. A. Clifton *et al.*[29] on the effect of ethylene diamino tetraacetic acid in Gram-negative bacteria cell membrane revealed that cation removal leads to an increasing presence of phospholipids in the outer membrane structure, along with a decreasing concentration of lipopolysaccharides. Furthermore, the binding of cations to bisamides of diethylene triamino pentaacetic acid is known to be in the range of 10^5–10^9.[30] Isothermal titration calorimetry (ITC) experiments allowed the evaluation of the binding of **DTPA@SiO$_2$⊃Ru-Van** particles to Ca^{2+} which showed a log *K* value of 7.5 ± 0.6 (ESI†), in good agreement with reported values. The chelating effect of **DTPA@SiO$_2$⊃Ru-Van** was further confirmed by MIC studies of the particles **DTPA@SiO$_2$⊃Ru-Van** in the presence of Ca^{2+}. The chelated particles (**Ca^{2+}DTPA@SiO$_2$⊃Ru-Van**) showed a lower efficacy of the nanoparticles with values similar to the uncoated **SiO$_2$⊃Ru-Van** (Table S7†). These results confirmed the blocking the chelating ability of the nanoparticles, did not lead to efficient antibiotic delivery.

Imaging in bacterial cells

In order to confirm that increased antimicrobial activity of the particles was due to increased penetration, luminescence microscopy was used to monitor the uptake of the emissive particles into bacterial cells based on the detection of the ruthenium signal. The **DTPA@SiO$_2$⊃Ru-Van** and **SiO$_2$⊃Ru-Van** were incubated with *S. aureus* or *E. coli* and images were collected of the live bacteria cells (Fig. 4). Structural illumination microscopy images showed the uptake of the red luminescent particles by tracking the signal of the **Ru** encapsulated cargo in spherical, *S. aureus*, and rod-shaped, *E. coli*., bacterial cells co-stained with nucleic acid dye, Hoechst H33342. Investigation of the penetration of the particles into the bacteria was studied by z-stack imaging. An intensity profile graph of the ruthenium signal in comparison with Hoechst H33342 as a bacterial cell stain indicated particle presence inside the bacterial cells. *S. aureus* bacteria cells show particle uptake based on the **Ru** luminescence signal for both **DTPA** uncoated- and coated-particles, namely **SiO$_2$⊃Ru-Van** (ESI†) and **DTPA@SiO$_2$⊃Ru-Van** (Fig. 4). This is expected due to their simpler cell membrane which allows particle penetration. This result is also in agreement with the MIC assays which show activity of both set of particles.

However, *E. coli* bacterial cells, show that only the **DTPA** coated particles, **DTPA@SiO$_2$⊃Ru-Van**, were visualised inside the stained cells, by monitoring of the ruthenium signal (Fig. 4). Penetration was confirmed by z-stack 3D image reconstruction of selected cells and orthogonal views (Fig. 4 and S8 and S9†). Absence of **DTPA** surface functionalization resulted in no particle penetration in *E. coli* (Fig. S10†). Quantification of the proportion of bacterial cells with internalised **DTPA@SiO$_2$⊃Ru-Van** was performed by determining the colocalization of the red luminescent particles and blue-stained bacterial cells using ImageJ software based on previous methods.[31] This analysis showed that un-coated/non-functionalised nanoparticles (**SiO$_2$⊃Ru-Van**) did not enter any *E. coli* cells while **DTPA@SiO$_2$⊃Ru-Van** were found in 45% of *E. coli.* Analysis of the same live cell imaging of *E. coli* treated with **DTPA@SiO$_2$⊃Ru-Van** for 18 h (Fig. S11†) show that nanoparticle penetration is increased to 70 ± 7% of the bacteria cells. These

© 2023 The Author(s). Published by the Royal Society of Chemistry

Asier Rodriguez Muguruza – December 2023

Open Access Article. Published on 20 February 2023. Downloaded on 4/8/2023 4:18:53 PM.
This article is licensed under a Creative Commons Attribution 3.0 Unported Licence.

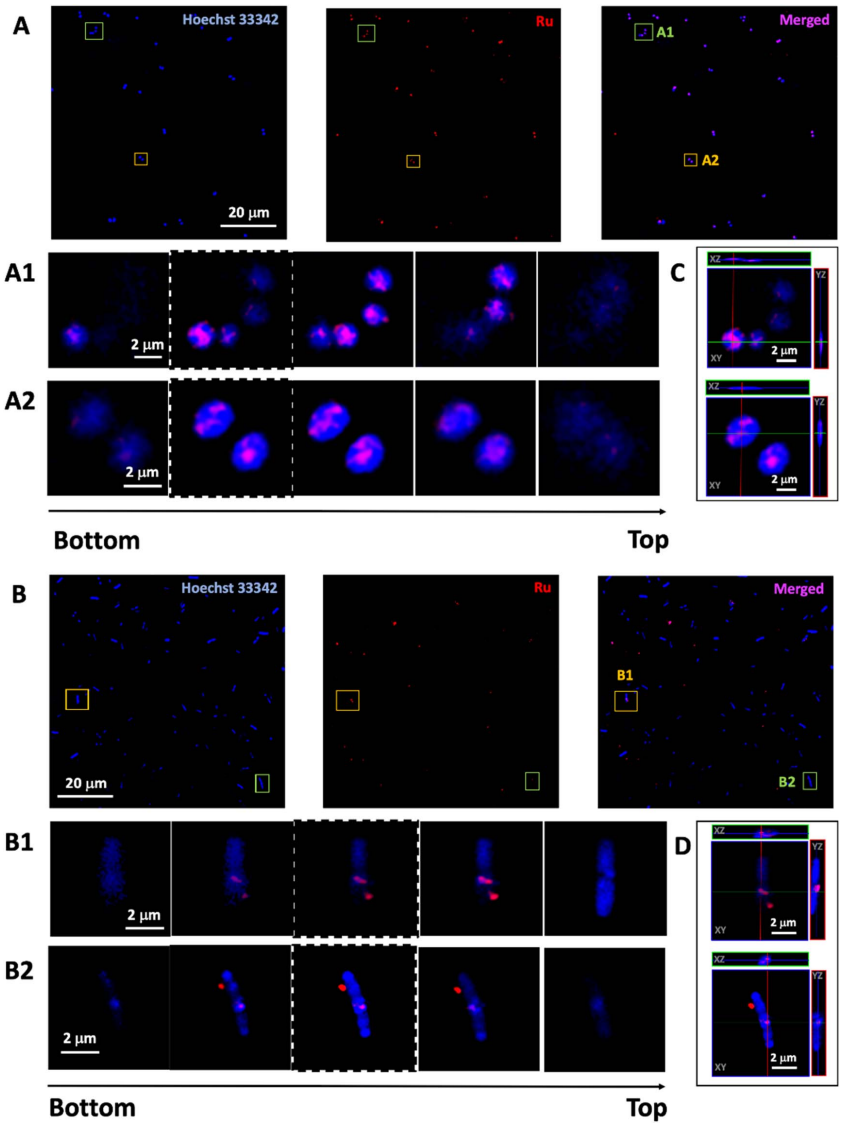

Fig. 4 Live bacteria cell imaging ($n = 5$) by structural illumination microscopy showing red luminescent particle uptake in *S. aureus* (A) and *E. coli* (B). Overnight grown bacteria are treated with **DTPA@SiO$_2$⊃Ru-Van** (2.5 mg mL^{-1}) for 2 h at 37 °C under mild shaking (150 rpm). Images show each channel for the outline of bacteria cells (blue) and particle luminescence (red) as well as merged channels. 3-D reconstruction: image sequence extracted from the z-stack of two cells in *S. aureus* (A1 and A2) and in *E. coli* (B1 and B2) and orthogonal reconstruction *S. aureus* (C) and *E. coli* (D) of central plane image (highlighted with dashed line) showing red luminescence from **DTPA@SiO$_2$⊃Ru-Van** inside the cells. Red channel, ruthenium emission ($\lambda_{exc} = 488$ nm, $\lambda_{em} = 580–620$ nm); blue channel, Hoechst H33342 emission ($\lambda_{exc} = 405$ nm, $\lambda_{em} = 410–455$ nm).

conclusions are further supported by the JACoP analysis (Table S6†) showing accuracy of the colocalization analysis between both channels, indicating presence of the particles within the bacteria cells which is increased after longer incubation time. This supports the results of the higher antibacterial activity of **DTPA@SiO$_2$⊃Ru-Van** which are used as vehicles to transport

© 2023 The Author(s). Published by the Royal Society of Chemistry

Open Access Article. Published on 20 February 2023. Downloaded on 4/8/2023 4:18:53 PM.
This article is licensed under a Creative Commons Attribution 3.0 Unported Licence.

Van across the Gram-negative bacterial membrane and release the antibiotic inside the bacterial cells.

Conclusions

The dual encapsulation of a glycopeptide antibiotic and a ruthenium complex was successful, allowing nanoparticles to be tracked in the bacterial cells by the ruthenium-based red signal. This nanoparticle platform was ideal for the modification of the outer surface with a membrane permeating agent, such as **DTPA**, which allowed the **DTPA@SiO$_2$⊃Ru-Van** nanoparticles to be internalized in the Gram-negative bacterial species and release a therapeutic agent, which was otherwise not able to permeate Gram-negative bacterial cells. The permeability of the nanoparticles is attributed to the chelating properties of the aminocarboxylate surface group, **DTPA**, which is known to bind to calcium and magnesium ions. These results suggest that encapsulation of antibiotics into a nanoparticle coated with chelating ligands shows strong potential for increasing the spectrum of activity of existing or novel drugs that are not able to permeate Gram-negative bacterial cells. Indeed, **DTPA@SiO$_2$⊃Ru-Van** shows greater antibacterial activity than any previously reported platforms for vancomycin delivery. Our results represent a step forward against Gram-negative bacterial infections to allow nanoparticle designs with imaging and therapeutic agents to be internalized in cells, overcoming membrane impermeability challenges and tracking drug delivery in cells.

Author contributions

A. R. M. performed all experimental work with A.di M. contributing in imaging analysis and NJH in MTT assays, J. M. A. B. and Z. P. originally designed the project with A. R. M. providing input; all authors contributed to versions of the manuscript.

Conflicts of interest

The authors declare no conflict of interest.

Acknowledgements

The BBRSC-funded MIBTP program (BB/M01116X/1) is acknowledged for the studentship of A. R. M. The BBSRC David Philips Fellowship (BB/M02623X/1) is thanked for the funding of JMAB.

References

1 J. B. Kasper, J. P. Nataro and H. L. T. Mobley, *Nat. Rev. Microbiol.*, 2004, **2**, 123–140.
2 J. M. A. Blair, M. A. Webber, A. J. Baylay, O. D. Ogbolu and L. J. V. Piddock, *Nat. Rev. Microbiol.*, 2015, **13**, 42–51.
3 H. I. Zgurskaya, C. A. Lopez and S. Gnanakaran, *ACS Infect. Dis.*, 2015, **11**, 512–522.
4 J. M. V. Makabenta, A. Nabawy, C. H. Li, S. Schemidt-Malan, R. Pater and V. M. Rotello, *Nat. Rev. Microbiol.*, 2021, **19**, 23–36.
5 J. G. Croissant, Y. Fatieiev, A. Almalik and N. M. Khashab, *Adv. Healthcare Mater.*, 2018, **7**, 1700831.
6 J. G. Croissant, K. S. Butler, J. I. Zink and C. J. Brinker, *Nat. Rev. Mater.*, 2020, **5**, 886–909.
7 M. Materinez-Carmona, K. Y. Gun'kuo and M. Vallet-Regí, *Pharmaceutics*, 2018, **10**, 279–307.
8 D. L. Clemens, B. Y. Lee, M. Xue, C. R. Thomas, H. Meng, D. Ferrins, S. E. Nel, J. I. Zink and M. A. Horwitz, *Antimicrob. Agents Chemother.*, 2012, **56**, 2535–2545.
9 B. González, M. Colilla, J. Díez, D. Pedraza, M. Guembe, I. Izaquierdo-Barba and M. Vallet-Regí, *Acta Biomater.*, 2018, **68**, 261–271.
10 B. Ma, Y. Chem, G. Hu, Q. Zeng, X. Lv, D. H. Oh, Z. Fu and Y. Jin, *ACS Biomater. Sci. Eng.*, 2022, **8**, 109–118.
11 S. Wu, Y. Huang, J. Yan, Y. Li, J. Wang, Y. Y. Tang, P. Yuan and X. Ding, *Adv. Funct. Mater.*, 2021, **31**, 2103442–2103451.
12 P. Zhang and J. Kong, *Talanta*, 2015, **134**, 501–507.
13 T. Ribeiro, E. Coutihno, A. S. Rodrigues, C. Baleizao and J. P. S. Farihna, *Nanoscale*, 2017, **9**, 13485–13494.
14 M. Hembury, C. Chiappini, S. Bertazzo, T. L. Kalber, G. L. Drisko, O. Ogunlade, S. Walker-Samuel, K. S Krushna, C. Jumeaux, P. Beard, C. S. S. R. Kumar, A. E. Porter, M. F. Lynthgoe, C. Boissiére, C. Sanchez and M. M. Stevens, *Proc. Natl. Acad. Sci. U. S. A.*, 2015, **112**, 1959–1964.
15 S. M. King, S. Claire, R. I. Teixeria, A. N. Dosumu, A. J. Carrod, H. Deghani, M. J. Hannon, A. D. Ward, R. Bicknell, S. W. Botchway, N. J. Hodges and Z. Pikramenou, *J. Am. Chem. Soc.*, 2018, **140**, 10242–10249.
16 N. J. Rogers, S. Claire, R. M. Harris, S. Farabi, G. Zikeli, I. A. Styles, N. J. Hodges and Z. Pikramenou, *Chem. Commun.*, 2014, **50**, 617–619.
17 N. J. Rogers, H. C. Jeffery, S. Claire, D. L. Lewis, G. Zikeli, N. J. Hodges, S. Egginton, G. B. Nash and Z. Pikramenou, *Nanomedicine*, 2017, **12**, 2725–2740.
18 D. J. Lewis, V. Sore, N. J. Rogers, T. K. Mole, G. B. Nash, P. Angeli and Z. Pikramenou, *Langmuir*, 2013, **29**, 14701–14709.
19 A. B. Caballer, L. Cardo, S. Claire, J. S. Criag, N. J. Hodges, A. Vladyka, T. Albrecht, L. Rochford and Z. Pikramnou, *Chem. Sci.*, 2019, **10**, 9244–9256.
20 D. Zhang, Z. Wu, J. Xu, J. Liang, J. Li and W. Yang, *Langmuir*, 2010, **26**, 6657–6662.
21 D. J. Lewis, V. Dove, M. J. Goodwin, A. C. Savage, G. B. Nash, P. Angeli and Z. Pikramenou, *Meas. Sci. Technol.*, 2012, **23**, 084004–084012.
22 G. Qi, L. Li and F. Tu, *ACS Appl. Mater. Interfaces*, 2015, **3**, 10874–10881.
23 V. Uskoković and S. Ghosh, *J. Mater. Chem. B*, 2017, **5**, 6065–6080.
24 L. M. Rossi, L. Shi, F. H. Quina and Z. Rosenzweig, *Langmuir*, 2005, **21**, 4277–4280.
25 R. M. Ashour, M. Samouhos, E. Polido Legaria, M. Svärd, J. Högblom, K. Forsberg, M. Palmlöf, V. G. Kessler,

 © 2023 The Author(s). Published by the Royal Society of Chemistry

Asier Rodriguez Muguruza – December 2023

G. A. Seisenbaeva and Å. Rasmuson, *ACS Sustainable Chem. Eng.*, 2018, **6**, 6889–6900.
26 L. L. Ruston, G. M. Robertson and Z. Pikramenou, *Chem.–Asian J.*, 2010, **5**, 571–580.
27 C. A. López, H. Zgurskaya and S. Gnanakaran, *Biochim. Biophys. Acta, Biomembr.*, 2020, **1862**, 183151–183162.
28 K. J. Thomas and C. V. Rice, *BioMetals*, 2014, **27**, 1361–1370.
29 L. A. Clifton, M. W. A. Skoda, A. P. Le Brun, F. Ciesileski, I. Kuzmenko, S. A. Holt and J. H. Lakey, *Langmuir*, 2015, **31**, 404–412.
30 Y. M. Wang, T. H. Cheng, G. C. Liu and R. S. Sheu, *Dalton Trans.*, 1997, **1**, 833–837.
31 A. N. Dosumu, S. Claire, L. S. Watson, P. M. Girio, S. A. M. Osborne, Z. Pikramenou and N. J. Hodges, *JACS Au*, 2021, **1**, 174–186.

Open Access Article. Published on 20 February 2023. Downloaded on 4/8/2023 4:18:53 PM.
This article is licensed under a Creative Commons Attribution 3.0 Unported Licence.

© 2023 The Author(s). Published by the Royal Society of Chemistry

2.6. References

1 E. M. Darby, E. Trampari, P. Siasat, M. S. Gaya, I. Alav, M. A. Webber and J. M. A. Blair, *Nat. Rev. Microbiol.*, 2022, **21**, 280–295.

2 N. C. Rosas and T. Lithgow, *Trends Microbiol.*, 2022, **30**, 544–552.

3 J. Sun, S. T. Rutherford, T. J. Silhavy and K. C. Huang, *Nat. Rev. Microbiol.*, 2022, **20**, 236–248.

4 J. M. Pagès, C. E. James and M. Winterhalter, *Nat. Rev. Microbiol.*, 2008, **6**, 893–903.

5 A. Rocker, J. A. Lacey, M. J. Belousoff, J. J. Wilksch, R. A. Strugnell, M. R. Davies and T. Lithgow, *MBio*, 2020, **11**, e00603-20.

6 R. Jasim, M. A. Baker, Y. Zhu, M. Han, E. K. Schneider-Futschik, M. Hussein, D. Hoyer, J. Li and T. Velkov, *ACS Infect. Dis.*, 2018, **4**, 1692–1704.

7 A. H. Delcour, *Biochim. Biophys. Acta - Proteins Proteomics*, 2009, **1794**, 808–816.

8 M. Vaara, *Microbiol. Rev.*, 1992, **56**, 395–411.

9 C. R. Macnair and E. D. Brown, *MBio*, 2020, **11**, e01615-20.

10 K. J. Thomas and C. V. Rice, *BioMetals*, 2014, **27**, 1361–1370.

11 L. A. Clifton, M. W. A. Skoda, A. P. Le Brun, F. Ciesielski, I. Kuzmenko, S. A. Holt and J. H. Lakey, *Langmuir*, 2015, **31**, 404–412.

12 C. A. López, H. Zgurskaya and S. Gnanakaran, *Biochim. Biophys. Acta - Biomembr.*, 2020, **1862**, 183151.

13 G. F. Andrade, J. A. Q. A. Faria, D. A. Gomes, A. L. B. de Barros, R. S. Fernandes, A. C. S. Coelho, J. A. Takahashi, A. da Silva Cunha and E. M. B. de Sousa, *J. Sol-Gel Sci. Technol.*, 2018, **85**, 369–381.

14 T. Lithgow, C. J. Stubenrauch and M. P. H. Stumpf, *Nat. Rev. Microbiol.*, , DOI:10.1038/s41579-023-00862-w.

15 S. L. Regen, *JACS Au*, 2021, **1**, 3–7.

16 C. R. MacNair, C. N. Tsai and E. D. Brown, *Ann. N. Y. Acad. Sci.*, 2020, **1459**, 69–85.

17 E. Sancho-Vaello, D. Gil-Carton, P. François, E. J. Bonetti, M. Kreir, K. R. Pothula, U. Kleinekathöfer and K. Zeth, *Sci. Rep.*, 2020, **10**, 1–16.

18 K. E. Ridyard and J. Overhage, *Antibiotics*, , DOI:10.3390/antibiotics10060650.

19 E. Sancho-Vaello, P. François, E. J. Bonetti, H. Lilie, S. Finger, F. Gil-Ortiz, D. Gil-Carton and K. Zeth, *Sci. Rep.*, 2017, **7**, 15371.

20 S. French, M. Farha, M. J. Ellis, Z. Sameer, J. P. Côté, N. Cotroneo, T. Lister, A. Rubio and E. D. Brown, *ACS Infect. Dis.*, 2020, **6**, 1405–1412.

21 L. Poirel, A. Jayol and P. Nordmann, *Clin. Microbiol. Rev.*, 2017, **30**, 557–596.

22 J. R. Lenhard, R. L. Nation and B. T. Tsuji, *Int. J. Antimicrob. Agents*, 2016, **48**, 607–613.

23 Z. Si, W. Zheng, D. Prananty, J. Li, C. H. Koh, E. Kang, K. Pethe and M. B. Chan-park, *Chem. Sci.*, 2022, **13**, 345–364.

24 T. Ikeda, A. Ledwith, C. H. Bamford and R. A. Hann, *BBA - Biomembr.*, 1984, **769**, 57–66.

25 Y. Jiang, W. Zheng, K. Tran, E. Kamilar, J. Bariwal, H. Ma and H. Liang, *Nat. Commun.*, 2022, **13**, 197–204.

26 M. Zheng, M. Pan, W. Zhang, H. Lin, S. Wu, C. Lu, S. Tang, D. Liu and J. Cai, *Bioact. Mater.*, 2021, **6**, 1878–1909.

27 K. A. Gibney, I. Sovadinova, A. I. Lopez, M. Urban, Z. Ridgway, G. A. Caputo and K. Kuroda, *Macromol. Biosci.*, 2012, **12**, 1279–1289.

28 R. Zhang, M. M. Jones, H. Moussa, M. Keskar, N. Huo, Z. Zhang, M. B. Visser, C. Sabatini, M. T. Swihart and C. Cheng, *Biomater. Sci.*, 2019, **7**, 287–295.

29 Z. Zhang, M. M. Jones, C. Sabatini, S. T. Vanyo, M. Yang, A. Kumar, Y. Jiang, M. T. Swihart, M. B. Visser and C. Cheng, *Biomater. Sci.*, 2021, **9**, 2043–2052.

30 N. D. Stebbins, M. A. Ouimet and K. E. Uhrich, *Adv. Drug Deliv. Rev.*, 2014, **78**, 77–87.

31 J. R. Paterson, M. S. Beecroft, R. S. Mulla, D. Osman, N. L. Reeder, J. A. Caserta, T. R. Young, C. A. Pettigrew, G. E. Davies, J. A. G. Williams and G. J. Sharples, *Appl. Environ. Microbiol.*, 2022, **88**, 1–38.

32 V. Prachayasittikul, C. Isarankura-Na-Ayudhya, T. Tantimongcolwat, C. Nantasenamat and H. J. Galla, *Acta Biochim. Biophys. Sin. (Shanghai).*, 2007, **39**, 901–913.

33 H. L. Alakomi, M. Saarela and I. M. Helander, *Microbiology*, 2003, **149**, 2015–2021.

34 A. M. Aboelenin, R. Hassan and E. S. Abdelmegeed, *Microb. Pathog.*, 2021, **154**, 104840.

35 S. J. S. Flora, M. Pande and A. Mehta, *Chem. Biol. Interact.*, 2003, **145**, 267–280.

36 R. Bansal-Mutalik and V. G. Gaikar, *Enzyme Microb. Technol.*, 2003, **32**, 14–26.

37 H. M. Ayres, D. N. Payne, J. R. Furr and A. D. Russell, *Lett. Appl. Microbiol.*, 1998, **26**, 422–426.

38 S. M. Häffner, E. Parra-Ortiz, K. L. Browning, E. Jørgensen, M. W. A. Skoda, C. Montis, X. Li, D. Berti, D. Zhao and M. Malmsten, *ACS Nano*, 2021, **15**, 6787–6800.

39 K. Braun, A. Pochert, M. Lindén, M. Davoudi, A. Schmidtchen, R. Nordström and M. Malmsten, *J. Colloid Interface Sci.*, 2016, **475**, 161–170.

40 G. Zhao, Y. Chen, Y. He, F. Chen, Y. Gong, S. Chen, Y. Xu, Y. Su, C. Wang and J. Wang, *Biomater. Sci.*, 2019, **7**, 2440–2451.

41 Z. Gounani, M. A. Asadollahi, J. N. Pedersen, J. Lyngsø, J. Skov Pedersen, A. Arpanaei and R. L. Meyer, *Colloids Surfaces B Biointerfaces*, 2019, **175**, 498–508.

42 A. Quarta, A. Curcio, H. Kakwere and T. Pellegrino, *Nanoscale*, 2012, **4**, 3319–3334.

43 N. Velikova, N. Mas, L. Miguel-Romero, L. Polo, E. Stolte, E. Zaccaria, R. Cao, N. Taverne, J. R. Murguía, R. Martinez-Manez, A. Marina and J. Wells, *Nanomedicine Nanotechnology, Biol. Med.*, 2017, **13**, 569–581.

44 N. Mas, I. Galiana, L. Mondragõn, E. Aznar, E. Climent, N. Cabedo, F. Sancenõn, J. R. Murguía, R. Martínez-Máñez, M. D. Marcos and P. Amorõs, *Chem. - A Eur. J.*, 2013, **19**, 11167–11171.

45 D. L. Clemens, B. Y. Lee, M. Xue, C. R. Thomas, H. Meng, D. Ferris, A. E. Nel, J. I.

Zink and M. A. Horwitz, *Antimicrob. Agents Chemother.*, 2012, **56**, 2535–2545.

46 B. González, M. Colilla, J. Díez, D. Pedraza, M. Guembe, I. Izquierdo-Barba and M. Vallet-Regí, *Acta Biomater.*, 2018, **68**, 261–271.

47 A. Pamukçu, N. Erdoğan and D. Şen Karaman, *J. Biomed. Mater. Res. - Part B Appl. Biomater.*, 2022, **110**, 2506–2520.

48 R. K. Kankala, W. Z. Lin and C. H. Lee, *Nanomaterials*, 2020, **10**, 597–612.

49 Q. Liu, Y. Zhang, J. Huang, Z. Xu, X. Li, J. Yang, H. Huang, S. Tang, Y. Chai, J. Lin, C. Yang, J. Liu and S. Lin, *J. Nanobiotechnology*, 2022, **20**, 386–402.

50 R. M. Ashour, M. Samouhos, E. Polido Legaria, M. Svärd, J. Högblom, K. Forsberg, M. Palmlöf, V. G. Kessler, G. A. Seisenbaeva and Å. C. Rasmuson, *ACS Sustain. Chem. Eng.*, 2018, **6**, 6889–6900.

51 M. Laprise-Pelletier, M. Bouchoucha, J. Lagueux, P. Chevallier, R. Lecomte, Y. Gossuin, F. Kleitz and M. A. Fortin, *J. Mater. Chem. B*, 2015, **3**, 748–758.

52 E. Polido Legaria, M. Samouhos, V. G. Kessler and G. A. Seisenbaeva, *Inorg. Chem.*, 2017, **56**, 13938–13948.

53 A. R. Rastinehad, H. Anastos, E. Wajswol, J. S. Winoker, J. P. Sfakianos, S. K. Doppalapudi, M. R. Carrick, C. J. Knauer, B. Taouli, S. C. Lewis, A. K. Tewari, J. A. Schwartz, S. E. Canfield, A. K. George, J. L. West and N. J. Halas, *Proc. Natl. Acad. Sci. U. S. A.*, 2019, **116**, 18590–18596.

54 S. L. C. Pinho, H. Faneca, C. F. G. C. Geraldes, M. H. Delville, L. D. Carlos and J. Rocha, *Biomaterials*, 2012, **33**, 925–935.

55 E. Fadeyev, S. Smola, O. Snurnikova, O. Korovin and N. Rusakova, *J. Sol-Gel Sci. Technol.*, 2013, **68**, 479–487.

56 C. Wu, J. Hong, X. Guo, C. Huang, J. Lai, J. Zheng, J. Chen, X. Mu and Y. Zhao, *Chem. Commun.*, 2008, 750–752.

57 W. J. Rieter, J. S. Kim, K. M. L. Taylor, H. An, W. Lin, T. Tarrant and W. Lin, *Angew. Chemie - Int. Ed.*, 2007, **46**, 3680–3682.

58 S. Lechevallier, R. Mauricot, H. Gros-Dagnac, S. Chevreux, G. Lemercier, E. Phonesouk, M. Golzio and M. Verelst, *Chempluschem*, 2017, **82**, 770–777.

59 S. Santra, R. P. Bagwe, D. Dutta, J. T. Stanley, G. A. Walter, W. Tan, B. M. Moudgil and R. A. Mericle, *Adv. Mater.*, 2005, **17**, 2165–2169.

60 E. Lipani, S. Laurent, M. Surin, L. Vander Elst, P. Lecleìre and R. N. Muller, *Langmuir*, 2013, **29**, 3419–3427.

61 L. An, H. Hu, J. Du, J. Wei, L. Wang, H. Yang, D. Wu, H. Shi, F. Li and S. Yang, *Biomaterials*, 2014, **35**, 5381–5392.

62 A. R. Muguruza, A. di Maio, N. J. Hodges, J. M. A. Blair and Z. Pikramenou, *Nanoscale Adv.*, , DOI:10.1039/d2na00884j.

63 D. J. Lewis, V. Dore, N. J. Rogers, T. K. Mole, G. B. Nash, P. Angeli and Z. Pikramenou, *Langmuir*, 2013, **29**, 14701–14708.

64 L. M. Rossi, L. Shi, F. H. Quina and Z. Rosenzweig, *Langmuir*, 2005, **21**, 4277–4280.

65 D. Zhang, Z. Wu, J. Xu, J. Liang, J. Li and W. Yang, *Langmuir*, 2010, **26**, 6657–6662.

66 D. Zeng, D. Debabov, T. L. Hartsell, R. J. Cano, S. Adams, J. A. Schuyler, R. McMillan and J. L. Pace, *Cold Spring Harb. Perspect. Med.*, 2016, **6**, a026989.

67 D. H. Qiu, Z. L. Huang, T. Zhou, C. Shen and R. C. Hider, *FEMS Microbiol. Lett.*, 2011, **314**, 107–111.

68 F. Ahangaran and A. H. Navarchian, *Adv. Colloid Interface Sci.*, 2020, **286**, 102298.

69 W. Posthumus, P. C. M. M. Magusin, J. C. M. Brokken-Zijp, A. H. A. Tinnemans and R. Van Der Linde, *J. Colloid Interface Sci.*, 2004, **269**, 109–116.

70 J. Stetefeld, S. A. McKenna and T. R. Patel, *Biophys. Rev.*, 2016, **8**, 409–427.

71 S. Bhattacharjee, *J. Control. Release*, 2016, **235**, 337–351.

72 C. Pfeiffer, C. Rehbock, D. Hühn, C. Carrillo-Carrion, D. J. De Aberasturi, V. Merk, S. Barcikowski and W. J. Parak, *J. R. Soc. Interface*, 2014, **11**, 20130931.

73 A. M. El Badawy, T. P. Luxton, R. G. Silva, K. G. Scheckel, M. T. Suidan and T. M. Tolaymat, *Environ. Sci. Technol.*, 2010, **44**, 1260–1266.

74 B. Bharti, J. Meissner, S. H. L. Klapp and G. H. Findenegg, *Soft Matter*, 2014, **10**, 718–728.

75 B. O. Alan, M. Barisik and H. G. Ozcelik, *J. Phys. Chem. C*, 2020, **124**, 7274–7286.

76 M. Kaasalainen, V. Aseyev, E. von Haartman, D. Ş. Karaman, E. Mäkilä, H. Tenhu, J. Rosenholm and J. Salonen, *Nanoscale Res. Lett.*, 2017, **12**, 74.

77 M. Mirenda, V. Levi, M. L. Bossi, L. Bruno, A. V. Bordoni, A. E. Regazzoni and A. Wolosiuk, *J. Colloid Interface Sci.*, 2013, **392**, 96–101.

78 D. Wencel, C. Dolan, M. Barczak, T. E. Keyes and C. McDonagh, *Nanotechnology*, 2013, **24**, 365705.

79 F. Kunc, V. Balhara, Y. Sun, M. Daroszewska, Z. J. Jakubek, M. Hill, A. Brinkmann and L. J. Johnston, *Analyst*, 2019, **144**, 5589–5599.

80 N. Kofod and T. J. Sørensen, *J. Phys. Chem. Lett.*, 2022, **13**, 11968–11973.

81 L. L. Ruston, G. M. Robertson and Z. Pikramenou, *Chem. - An Asian J.*, 2010, **5**, 571–580.

82 T. Mosmann, *J. oflmmunologicalMethods*, 1983, **65**, 55–63.

83 Y. Shi, M. L. Miller and A. J. Di Pasqua, *Comments Inorg. Chem.*, 2016, **36**, 61–80.

84 J. Lu, M. Liong, Z. Li, J. I. Zink and F. Tamanoi, *Bone*, 2005, **23**, 1–7.

85 T. Asefa and Z. Tao, *Chem. Res. Toxicol.*, 2012, **25**, 2265–2284.

86 J. H. Jorgensen and M. J. Ferraro, *Clin. Infect. Dis.*, 2009, **49**, 1749–1755.

87 W. R. Miller, J. M. Munita and C. A. Arias, *Expert Rev. Anti. Infect. Ther.*, 2014, **12**, 1221–1236.

88 F. Li, J. G. Collins and F. R. Keene, *Chem. Soc. Rev.*, 2015, **44**, 2529–2542.

89 S. V. Kumar, S. O. Scottwell, E. Waugh, C. J. McAdam, L. R. Hanton, H. J. L. Brooks and J. D. Crowley, *Inorg. Chem.*, 2016, **55**, 9767–9777.

90 F. Li, Y. Mulyana, M. Feterl, J. M. Warner, J. G. Collins and F. R. Keene, *Dalt. Trans.*, 2011, **40**, 5032–5038.

91 A. Ali, M. Ovais, X. Cui, Y. Rui and C. Chen, *Chem. Res. Toxicol.*, 2020, **33**, 1082–1109.

92 J. B. McPhee, M. Bains, G. Winsor, S. Lewenza, A. Kwasnicka, M. D. Brazas, F. S. L. Brinkman and R. E. W. Hancock, *J. Bacteriol.*, 2006, **188**, 3995–4006.

93 A. Lo Sciuto and F. Imperi, *Antimicrob. Agents Chemother.*, 2018, **62**, 4–7.

94 K. Jeannot, A. Bolard and P. Plésiat, *Int. J. Antimicrob. Agents*, 2017, **49**, 526–535.

95 A. Lo Sciuto, M. Cervoni, R. Stefanelli, C. Mancone and F. Imperi, *Int. J. Antimicrob. Agents*, 2020, **55**, 105957.

96 J. Ghimire, S. Guha, B. J. Nelson, L. A. Morici and W. C. Wimley, *J. Membr. Biol.*, 2022, **255**, 503–511.

97 T. Onoda, J. Enokizono, H. Kaya, A. Oshima and P. Freestone, 2000, **182**, 1419–1422.

98 Y.-M. Wang, T.-H. Cheng, G.-C. Liu and R.-C. Sheu, *J. Chem. Soc., Dalt. Trans.*, 1997, 833–837.

99 R. Heintzmann and T. Huser, *Chem. Rev.*, 2017, **117**, 13890–13908.

100 A. N. Dosumu, S. Claire, L. S. Watson, P. M. Girio, S. A. M. Osborne, Z. Pikramenou and N. J. Hodges, *JACS Au*, 2021, **1**, 174–186.

101 S. Bolte and F. P. Cordelieres, *J. Microsc.*, 2006, **224**, 213–232.

102 N. Kobayashi, H. Minami and K. Nakamura, *Nanophotonics*, 2018, **7**, 1373–1385.

3. IRON(III) AMINOCARBOXYLATE DECORATED NANOPARTICLES FOR ENHANCED NANOPARTICLE UPTAKE IN GRAM-NEGATIVE BACTERIAL CELLS

3.1. Introduction

3.1.1. Siderophore: Structure and biological importance

Among all metabolites that bacterial cells require, iron is one of the essential trace metals for most organisms. Iron acts a global metabolic regulator for a wide range of biological processes including DNA and adenosine triphosphate (ATP) biosynthesis, electron transport and nitrite reduction in nitrogen cycle.[1–4] Microorganisms like bacteria need 10^{-5}-10^{-7} M of iron(III) for their optimal growth. However, iron(III) solubility at physiological pH is around 10^{-17} M and most of it is converted into insoluble oxyhydroxide species.[4] In order to access available iron, bacterial cells are able to produce and secrete secondary metabolites with higher affinity for ferric cations called siderophores (Figure 3.1). Siderophores are biosynthesised Fe(III) chelators that are classified based on the chelating units that they possess: catecholates, hydroxamates, carboxylates or mixed siderophores (Figure 3.2).

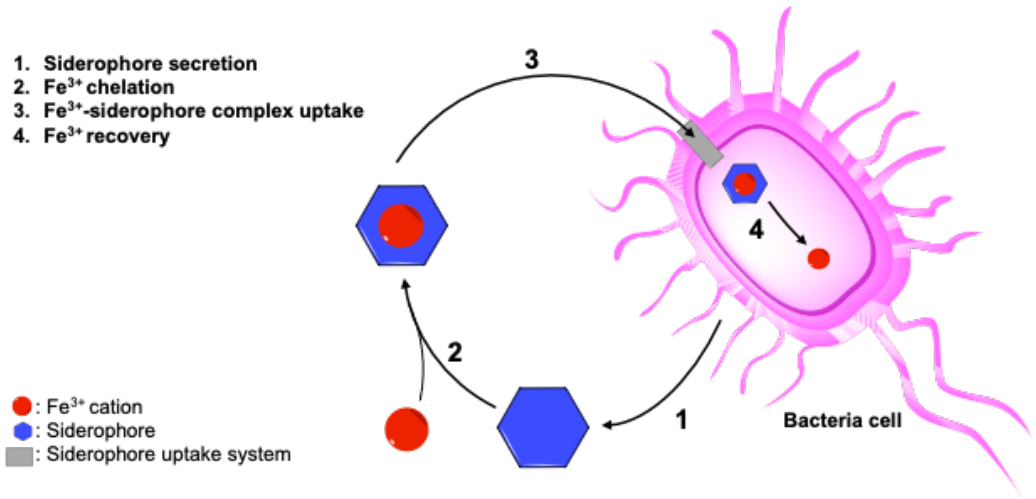

Figure 3.1. General scheme of Fe(III) acquisition by bacterial cells through siderophore-mediated Fe(III) uptake.

Catecholate-based siderophores are only found in bacterial cells and ferric ions can be chelated to these siderophores by dihydroxybenzoic acid chelating units. Most of catecholate siderophores form hexadentate octahedral Fe(III) complexes with high chemical and pH stability with binding constant close to 10^{52} M^{-1}, at physiological pH, in case of enterobactin.[5] Hydroxamate-based siderophores, on the contrary, are composed by acetylated and hydroxylated alkylamines. These siderophores also form octahedral Fe(III) complexes with binding constants in the range of 10^{22} – 10^{32} M^{-1}.[6] Finally, carboxylate-based siderophores facilitate iron acquisition via formation of Fe(III) octahedral complexes with carboxylate groups. Most carboxylate-based siderophores are produced by Gram-positive bacteria and they possess binding constants in the range of 10^{24} – 10^{28} M.[7] Citrates are not considered siderophores but Fe^{3+}-citrate complexes (binding constants between 10^{13} - 10^{15} M^{-1})[8] are also employed by bacterial cells for Fe(III) acquisition, and many have specific membrane receptors for recognition.

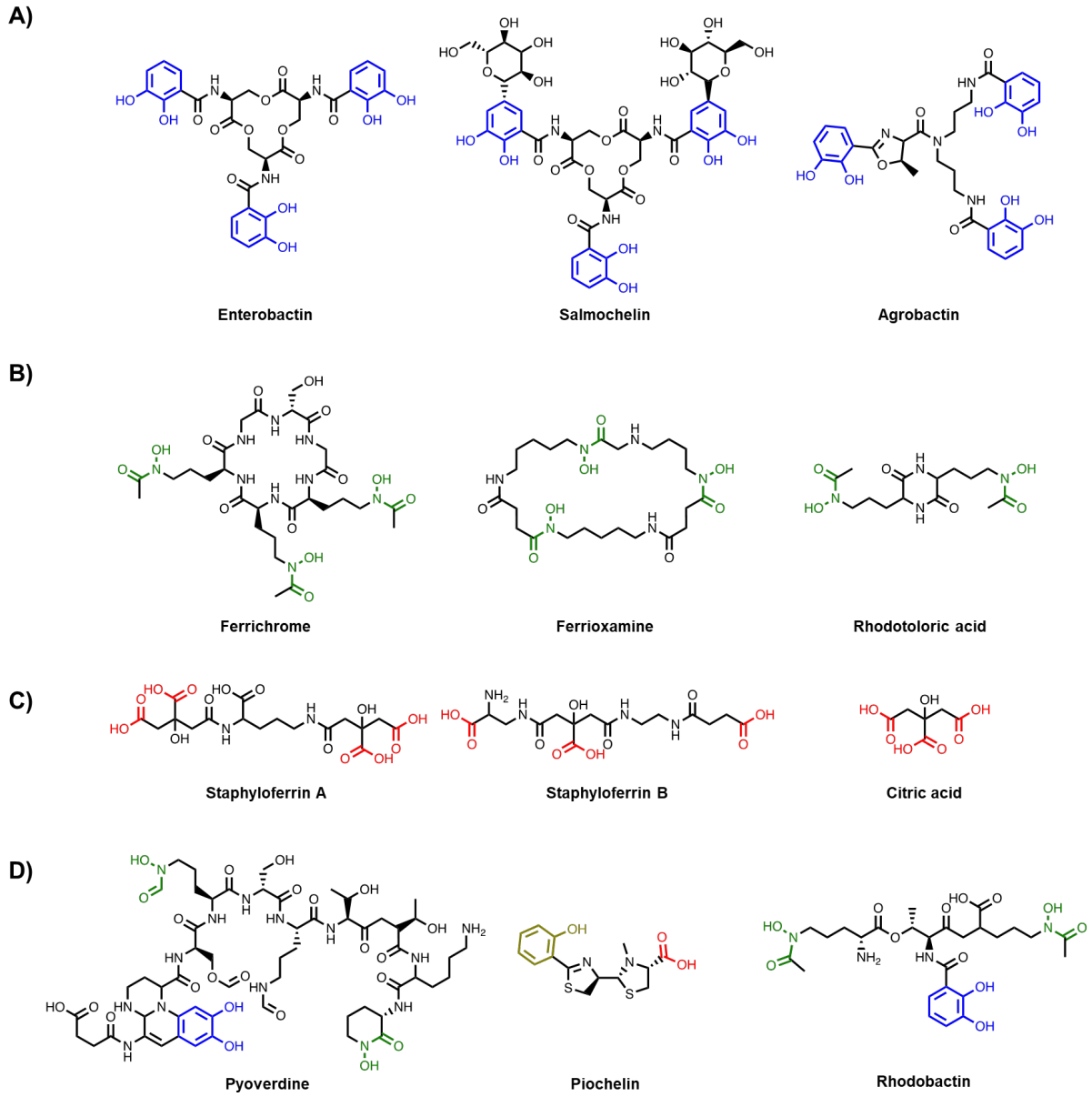

Figure 3.2. Examples of (A) catechol-based, (B) hydroxamate-based (C) carboxylate-based and (D) mixed siderophores with highlighted binding sites to Fe(III).

3.1.2. Siderophore uptake systems

Once Fe^{3+}-siderophore has been formed, the resulting complex is internalised into bacterial cells through specific TonB-Dependant Transporters (TBDT), commonly known as siderophore uptake systems.[9] TBDT are characterized by their stringent siderophore selectivity and the number of siderophores that a bacterial species is able to recognize is tightly correlated with the number of genes encodings the TBDTs.[10]

TBDTs consist of a 22-stranted antiparallel transmembrane β-barrel protein. Specific residues and chiral centres in the inside of the surface receptor β-barrel confer them with high siderophore-specificity.

After surface recognition, the Fe^{3+}-siderophore complex is transported to the cytoplasm. In case of Gram-positive bacteria, a set of permease proteins aid this process.[11] In Gram-negative species, Fe^{3+}-siderophore transport involves several proteins that first, transport the complex to the periplasm, bound complex is then transported through the periplasm, and finally internalised into the cytoplasm through inner membrane permease complex.[12] Pyoverdine is a peculiar case as the Fe^{3+} acquisition also involved another chelator in that scavenges Fe^{3+} from the Fe^{3+}-siderophore complex, FpvC. Then the formed Fe^{3+}-FpvC complex is transported through the FpvGHJK complex into the cytoplasm.[13]

Once internalised, Fe^{3+} is recovered from the Fe^{3+}siderophore. In most of the cases, Fe^{3+} is reduced to Fe^{2+} by an ATP binding cassette protein. Reduction of metal centre decreases the affinity with the siderophore, releasing Fe^{2+} to the cytoplasm. Fe^{2+} is then oxidised back to Fe^{3+}. Fe^{3+} is then employed in different metabolic processes or storaged in ferritins, haem-containing bacterioferritins and the Dps proteins.[14] Resulting free siderophore is degraded or reused and secreted back to the medium (Figure 3.3).[15]

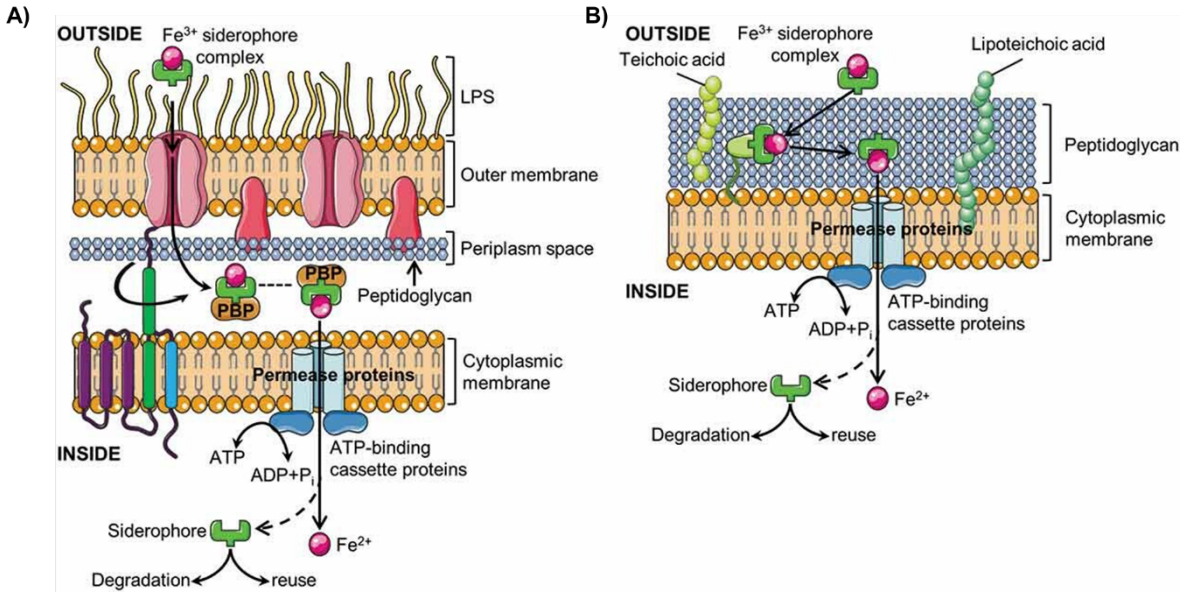

Figure 3.3. Schematic representation of bacterial siderophore-mediated iron uptake in (A) Gram-negative and (B) Gram-positive bacteria. Periplasmic binding protein (PBP). Reproduced from Y. Seyoum *et al*. [15]

3.1.3. Siderophore-antibiotic conjugates

Due to the ability of bacterial cells to uptake Fe^{3+}-siderophore complexes, and inspired by the natural occurring albomycin siderophores (Figure 3.5A), new approaches to design antibacterial therapies based on siderophores have been developed. Albomycins are natural occurring antibacterial compounds that bear a hydroxamate-based siderophore that can be uptaken up by the Fhu system and inhibit seryl-tRNA synthetase.[16,17] The principle of the strategy relies on the increase of uptake of the siderophore-antibiotic conjugate (SAC) compared with the free antibiotic; as the conjugation to the siderophore does not alter the mechanism of action of the antibiotic (Figure 3.4).

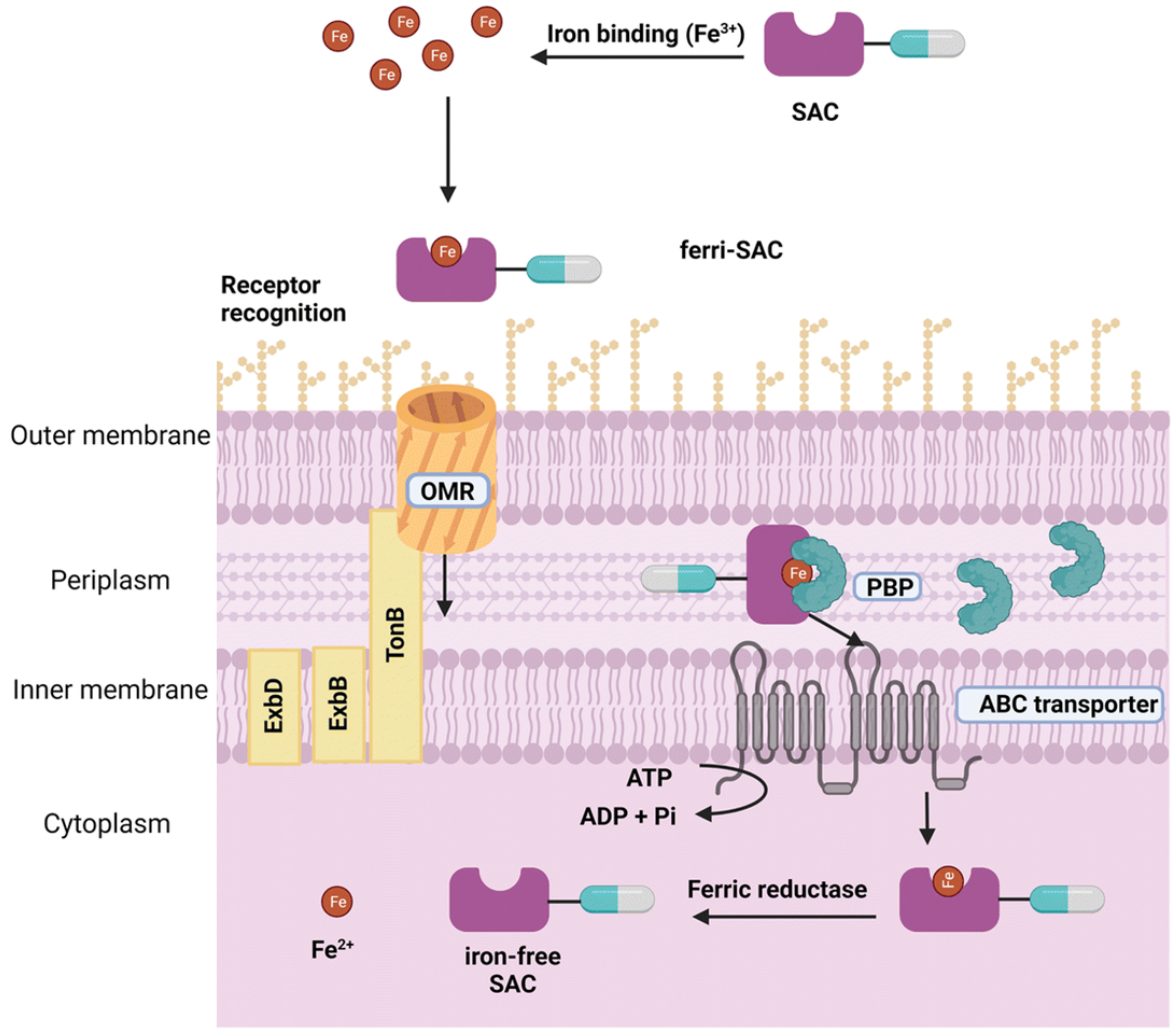

Figure 3.4. Uptake pathway of Fe^{3+}-SAC complexes in Gram-negative bacterial cells. OMR; outer membrane receptor, PBP; periplasmic binding protein, ATP; adenosine triphosphate, ADP; adenosine diphosphate, ABC transporter; ATP binding cassette. Reproduced from B. Rayner *et al.*[18]

The first developed SACs were designed by chemical modification of simple antibiotics such us β-lactam or fluoroquinolones with iron chelating moieties (dihydroxybenzoic acid or hydroxamate derivatives) (Figure 3.5B).[19] Reported SACs were able to interact with non-specific siderophore receptors and were internalised into cell's cytoplasm. Later approaches showcased the possibility to conjugate antibiotics to natural siderophores such us enterobactin[20] (Figure 3.5C) or

deferroxamine[21]. The design of these SACs is more challenging due to the complex structure of natural siderophores and most of the times they need multistep synthetic routes to achieve them. Finally, in recent years, researchers have managed to design synthetic siderophores and their corresponding SACs as seen in Figure 3.5D which depicts amoxicillin conjugation to a MCAM-based siderophore (MECAM = 1,3,5-Tris(2,3-dihydroxybenzamidomethyl) benzene).[22] The only FDA approved SAC, to this date, has been cefiderocol (Figure 3.5B) which has been applied to treat resistant UTI infection and a wide range of aerobic bacterial species. Nevertheless, its safety during pregnancy is still under investigation.[23]

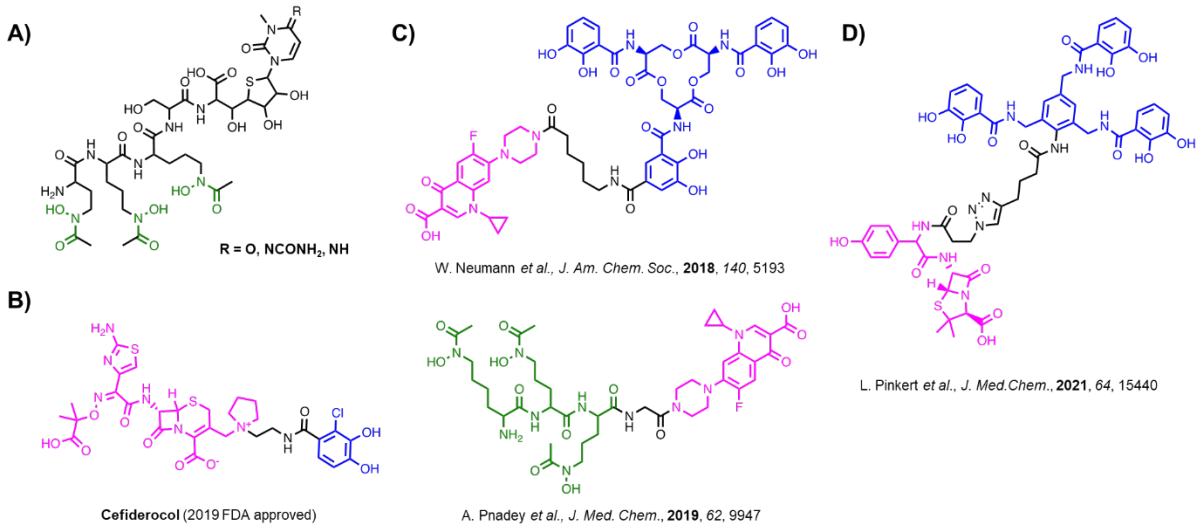

Figure 3.5. Chemical structures of (A) albomycin and (B-D) representative SAC compounds. Conjugated antibiotic is highlighted in pink. Structures can be reproduced from references 16-22.

A very important aspect in the design of SACs is the linker between the antibiotic and the siderophore. Covalent modification of antibiotics may affect their activity.[24,25] Modification of structurally crucial groups in antibiotics may result in decreased interaction with the target structure, reducing their activity. Hence, precise

functionalization of antibiotics is crucial to remain their activity. Furthermore, enzyme[20,26] cleavable linkers have been also developed for antibiotic release once the SAC arrives to the cytoplasm.

Beside antibiotics, other bioactive molecules such us antimicrobial peptides[27], imaging agents[28–30] (fluorophores or MRI agents) or metal complexes[31] have been conjugated to natural and synthetic siderophores, enhancing their uptake and hence, improving their performance.

3.1.4. Siderophore-coated silica nanoparticles

The conjugation of siderophores on silica nanoparticle's surface is very limited in the literature. Due to the complex structure of siderophores, the selective conjugation onto silica nanoparticle's surface can be very challenging. Thereby, the few examples in the literature are limited to the conjugation of linear siderophores with a terminal amine group.[32,33] To our knowledge, deferoxamine is the most common siderophore that has been covalently conjugated to silica nanoparticles.[33–35] Resulting nanoparticles have been employed for metal recovery from different media[34,36,37] or for bacteria detection[32]. Deferoxamine-coated **SiO_2**[36] and silica-coated iron oxide nanoparticles (**$SiO_2@Fe_3O_4$**)[32] nanoparticles have been reported as excellent materials for removal of metal ions from water or biological media. Moreover, due to their higher affinity and selectivity for iron over other (III) or (IV) metals, produced nanoparticles have been employed for quantification of Fe(III) in biological media.[33,35] Finally, Fe^{3+}-deferoxamine has been conjugated to **$SiO_2@Fe_3O_4$** nanoparticles for bacterial detection.[34] Siderophore-coated **$SiO_2@Fe_3O_4$** nanoparticles incubated with unknown samples to achieve nanoparticle attachment to bacterial cells. Nanoparticles were then

magnetically recovered, attached bacterial cells grown and identified by genomic procedures. Nevertheless, other nanoparticles, such as magnetic nanoparticles (Fe_3O_4)[38] or gold nanoparticles[39] have been also reported for metal cation (Fe^{3+}, Co^{3+}, Cr^{3+} and Ln^{3+}, Ln: Lanthanide) removal or sensing applications.

To our knowledge, there are no examples in the literature of siderophore-conjugated nanoparticles for antibiotic delivery into bacterial cells.

3.1.5. Chapter Outline

In the current chapter the ability of Fe^{3+} chelation in previously reported aminocarboxylate-coated nonporous hybrid silica nanoparticles' (**Fe^{3+}DTPA@SiO_2⊃Ru-Van**) cell internalization is explored. We explored the antimicrobial activity of the hybrid nanoparticles and we investigated the effect of siderophore-receptor overexpression in the activity of the nanoparticles. Moreover, microscopy techniques were employed to study cell-nanoparticle interactions. Furthermore, the capacity of bis-amide Fe^{3+}DTPA complex to be recognized by siderophore-uptake systems was further evidence through the design of a DTPA-based SAC containing amoxicillin (**DTPA-$Amox_2$**). Hereby, the presented new coating represents a step forward towards the development of bioinspired nanomaterials for antibiotic delivery.

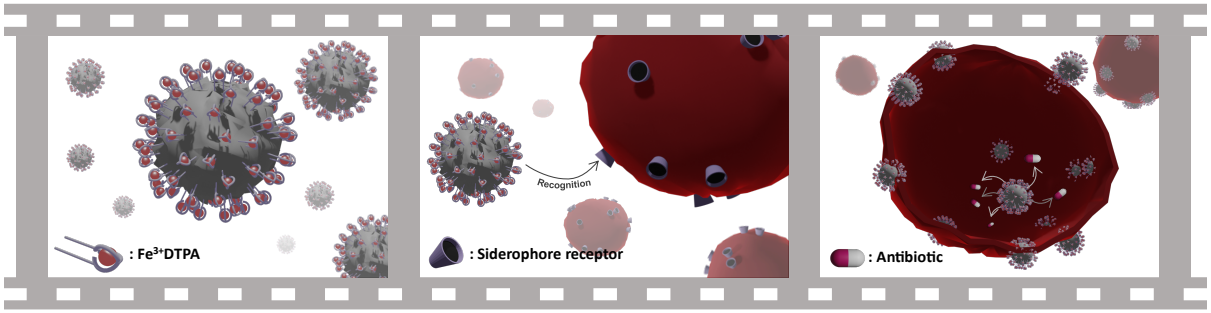

Figure 3.6. Schematic representation of developed **Fe^{3+}DTPA@SiO_2⊃Ru-Van** and internalization into bacterial cells through siderophore-uptake systems.

3.2. Results and discussion

3.2.1. Synthesis of Fe^{3+}DTPA@SiO_2⊃Ru-Van

For the synthesis of **Fe^{3+}DTPA@SiO_2⊃Ru-Van** nanoparticles, the coating procedure reported in Chapter 2 was modified. Previously, **DTPA-Si_2** was conjugated onto the nanoparticle surface, leading to **DTPA@SiO_2⊃Ru-Van**, under heating in anhydrous toluene. If Fe(III) was to be titrated to) to **DTPA@SiO_2⊃Ru-Van** in the pH range where DTPA is deprotonated, it could lead to **Fe^{3+}DTPA@SiO_2⊃Ru-Van** nanoparticles. Nevertheless, this approach would not ensure that all DTPA sites would be chelated to Fe(III) and that free Fe(III) would not be interecting with the hydroxyl groups of the silica surface. Therefore, we decided to *in situ* synthetize the **Fe^{3+}DTPA-Si_2** complex and functionalise **SiO_2⊃Ru-Van** nanoparticles with it (Figure 3.7 and Figure 3.8).

3.2.1.1. Synthesis and characterization of Fe^{3+}DTPA-Si_2

We firstly synthesised the **Fe^{3+}DTPA-Si_2** complex in situ based on previously reported methodologies by our group (Figure 3.7A). Briefly, **DTPA-Si_2** precursors, DTPA-A and APTES were combined in anhydrous pyridine with *N,N*-diisopropylethylamine (DIPEA) as base and 4-dimethylaminopyridine (DMAP) as catalyst. The solution was stirred at room temperature overnight and an equimolar amount of anhydrous $FeCl_3$ was added

to the solution. The formed yellow solution was stirred at room temperature. The formed **Fe^{3+}DTPA-Si_2** complex was isolated as a yellow powder.

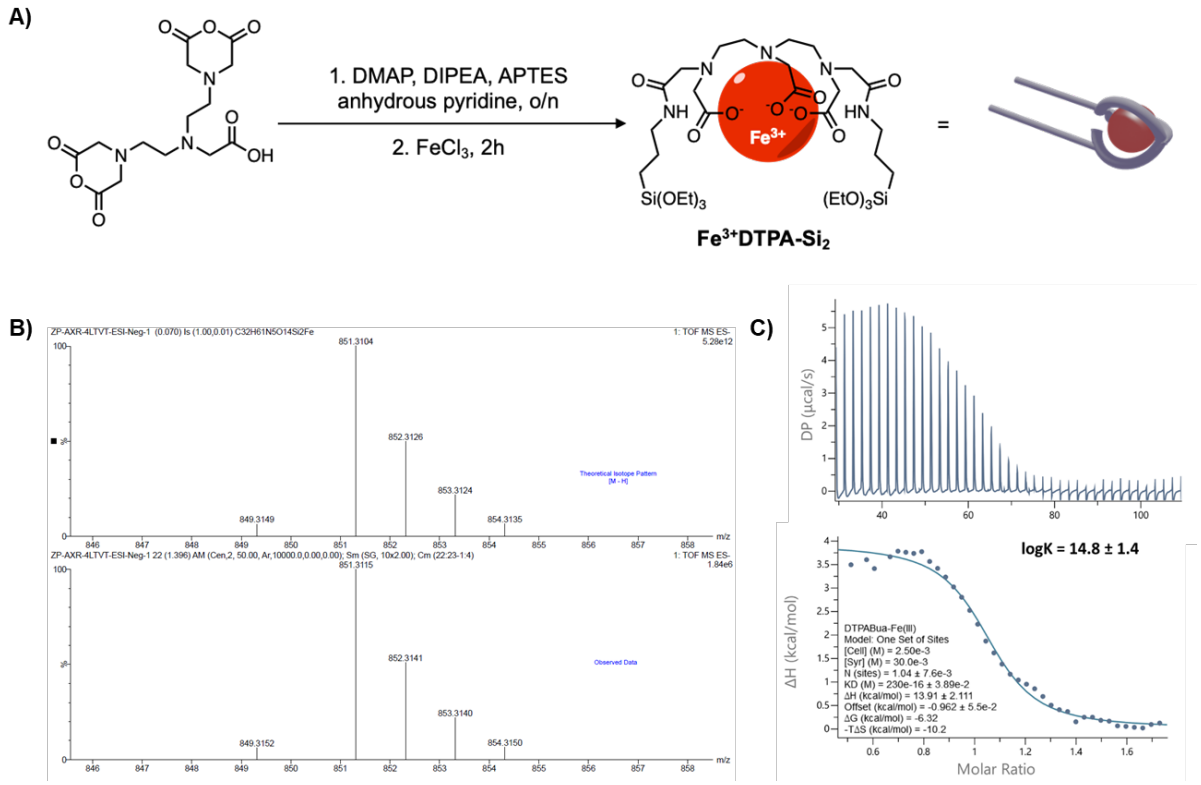

Figure 3.7. (A)Synthesis scheme of **Fe^{3+}DTPA-Si_2** complex. (B) (-)ESI-MS (top) experimental and (bottom) theoretical spectra of **Fe^{3+}DTPA-Si_2**. (C) Isothermal Titration Calorimetry (ITC) and fitted data of **Fe^{3+}DTPA-Bua_2** in PBS buffer (0.1 M, pH 7.4).

The isolated complex was characterised by (-)ESI-MS which showed a peak m/z of 851.3115 assigned to $[Fe^{3+}DTPA\text{-}Si_2\text{ -H}]^-$ (calculated m/z = 851.3104) (Figure 3.S1).

Furthermore, the affinity between the DTPA bis-amide chelator and Fe(III) was studied by ITC. Due to the lack of solubility of **DTPA-Si_2**, the water soluble butylamine-modified DTPA bisamide analogue (**DTPA-Bua_2**) was employed (Full characterization in Figure 3.S2-S6). Upon titration of a PBS buffer (0.1 M, pH 7.4) solution of Fe(III) to a solution of **DTPA-Bua_2** in the same buffer a logK value of 14.8 ± 1.4 was estimated for a 1:1 stoichiometry (Figure 3.7C). The value is in good agreement with previously reported

affinity constant between DTPA bi-amide derivatives with trivalent cations (10^{11}-10^{15}).[40]

3.2.1.2. Coating of SiO_2⊃Ru-Van with Fe^{3+}DTPA-Si_2

Uncoated hybrid (**SiO_2⊃Ru-Van**) and control (**SiO_2**, **SiO_2⊃Ru** and **SiO_2⊃Van**) particles were synthetized and characterized as previously reported.[41] Coating of hybrid nanoparticles, to achieve **Fe^{3+}DTPA@SiO_2⊃Ru-Van**, was performed in anhydrous pyridine (Figure 3.8), at room temperature, to avoid any leakage of chelated Fe(III) upon heating. Due to the milder conditions employed, a 3:1 mass ratio of **Fe^{3+}DTPA-Si_2**:**SiO_2⊃Ru-Van** was used.

Control particles bearing only one cargo (**SiO_2⊃Ru** and **SiO_2⊃Van**) or no cargo (**SiO_2**) were coating following the same methodology to achieve **Fe^{3+}DTPA@SiO_2⊃Ru**, **Fe^{3+}DTPA@SiO_2⊃Van** and **Fe^{3+}DTPA@SiO_2**, respectively.

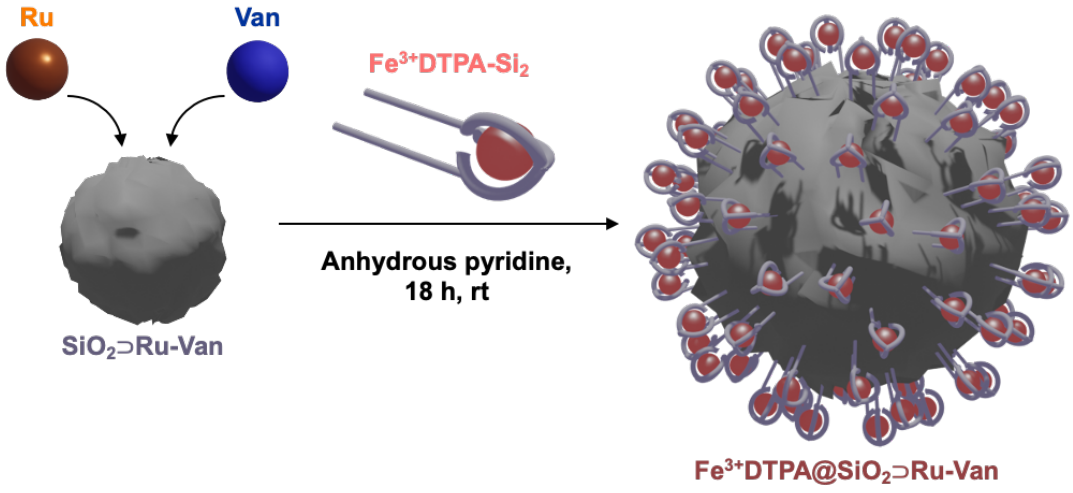

Figure 3.8. Scheme of **SiO_2⊃Ru-Van** coating with **Fe^{3+}DTPA-Si_2**

3.2.2. Characterization of Fe^{3+}DTPA@SiO_2⊃Ru-Van

3.2.2.1. Size and composition of Fe^{3+}DTPA@SiO_2⊃Ru-Van

Coated nanoparticles were characterized by a series of surface analysis and spectroscopy techniques to confirm the presence of the Fe^{3+}DTPA coating. Firstly, coated nanoparticles were analysed by Dynamic Light Scattering (DLS) (Figure 3.9A, Table 3.9X) and ζ-potential measurements (Figure 3.9B) in PBS buffer (0.1 M, pH 7.4). DLS of **Fe^{3+}DTPA@SiO_2⊃Ru-Van** particles revealed a slight increase in the hydrodynamic size by number from 90 ± 5 nm (PDI = 0.19) to 95 ± 9 nm (PDI = 0.21). An increase in the ζ-potential of **Fe^{3+}DTPA@SiO_2⊃Ru-Van** nanoparticles, compared with **SiO_2⊃Ru-Van** particles, also confirmed the successful coated on nanoparticles. While **SiO_2⊃Ru-Van** particles displayed a surface charge of -28 ± 5 mV, upon coating the surface charge decreased up to -14 ± 4 mV due to the neutral charge of the **Fe^{3+}DTPA-Si_2** complex. Transmission Electron Microscopy (TEM) images (Figure 3.9C) showed no significant change in nanoparticle size before (85 ± 3 nm, n = 50) and after coating (86 ± 5 nm, n = 50).

FT-IR spectroscopy (Figure 3.9D) further confirmed the presence of the coating as stretching assigned to N-H (3050 cm^{-1} and 870 cm^{-1}), C-H (2690 cm^{-1}), C=O (1633 cm^{-1}) and C-N (1580 cm^{-1}) bonds from the DTPA complex were observed in coated particles (Figure 3.9D). Similarly, MALDI-ToF mass spectrometry analysis (Figure 3.9F) of **Fe^{3+}DTPA@SiO_2⊃Ru-Van** samples revealed peaks assigned to Fe^{3+}DTPA species after coating.

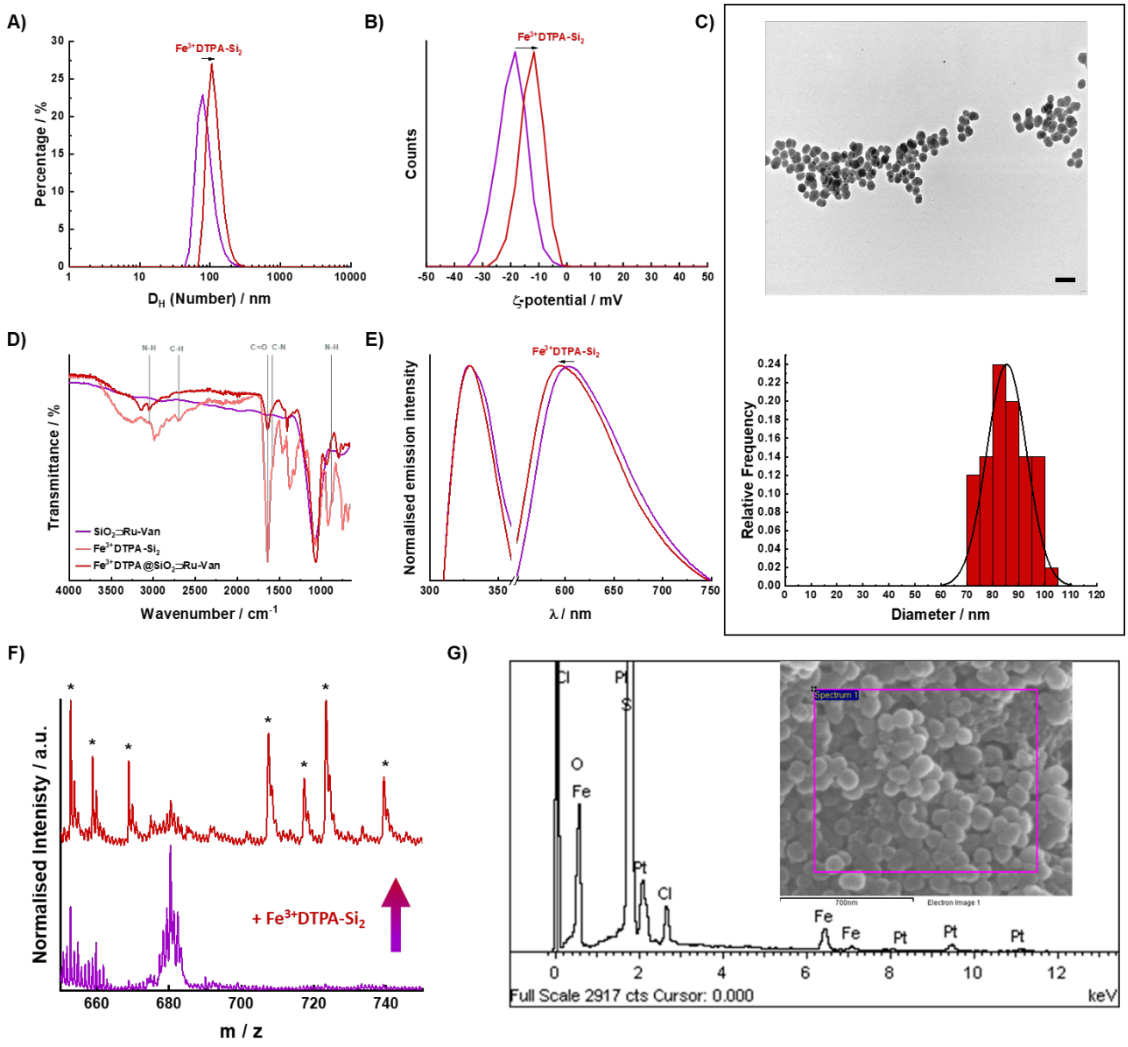

Figure 3.9. Characterization of **Fe^{3+}DTPA@SiO_2⊃Ru-Van.** (A) Dynamic Light scattering and (B) ζ-potential measurements of **SiO_2⊃Ru-Van** (purple) and **Fe^{3+}DTPA@SiO_2⊃Ru-Van** (red) particles in PBS buffer (0.1 M, pH 7.4). (C) Transmission Electron Microscopy (TEM) micrograph of **Fe^{3+}DTPA@SiO_2⊃Ru-Van** (scale bar = 200 nm) and particle size distribution (n = 50). Solid-state (D) FT-IR and (E) luminescence spectroscopy of **SiO_2⊃Ru-Van** (purple) and **Fe^{3+}DTPA@SiO_2⊃Ru-Van** (red) particles. (F) (+)MALDI-ToF mass spectrometry (positive mode) of **SiO_2⊃Ru-Van** before and after coating, peaks assigned to Fe^{3+}DTPA-coating are indicated with *. α-Cyano-4-hydroxycinnamic acid (CHCA) was employed as MADI-ToF matrix. (G) Representative Scanning electron Microscopy (SEM) and Energy Disperse X-Ray Scattering (EDS) and elemental quantification of Pt-coated **Fe^{3+}DTPA@SiO_2⊃Ru-Van**.

Energy-Dispersed Spectroscopy (EDS) also confirmed the presence of the complex on nanoparticles surface as Fe Kα and Lα energies at 0.705 and 6.398 were observed

in coated nanoparticles whole Fe signal was not detected before coating (Figure 3.S10).

The emissive properties of **Fe^{3+}DTPA@SiO_2⊃Ru-Van** were investigated in the solid state. Upon excitation at 450 nm, the characteristic **Ru** broad red luminescence signal with emission maximum at 595 nm was recoded, which was 18 nm blue shifted compared with **SiO_2⊃Ru-Van** nanoparticles (λ_{max} = 613 nm). Similarly, **Van**'s emission from hybrid nanoparticles shifted a 5 nm upon coating (λ_{exc} = 270 nm). Observed shifts further evidenced the successful coating of the nanoparticles, as previously reported **DTPA@SiO_2⊃Ru-Van** nanoparticles.[41] Finally, as observed upon DTPA-coating, a lengthening of **Ru**'s lifetimes (λ_{exc} = 455 nm, λ_{em} = 600 nm) was observed to 2.52 μs (85 %) and 0.27 μs (15 %) from 1.69 μs (90 %) and 0.33 μs (10 %) before coating (Figure S13). Similar lengthening was observed for **DTPA@SiO_2⊃Ru-Van** nanoparticles upon coating, which suggest that the presence of Fe^{3+} on the coating does not quench the emissive properties of **Ru**, which would be due to the distance between he coated and included **Ru** molecules.

Successful coating for control particles (**Fe^{3+}DTPA@SiO_2⊃Ru**, **Fe^{3+}DTPA@SiO_2⊃Van** and **Fe^{3+}DTPA@SiO_2**,) was also confirmed by the same set of characterization techniques and all data can be found in the appendix (Figure 3. S8-S13 and Table 3.S1-S3)

3.2.2.2. Quantification of Fe^{3+}DTPA coating

Thermogravimetric analysis (TGA) was employed as quantification method for the quantification of conjugated **Fe^{3+}DTPA**-coating (Figure 3.10) in **Fe^{3+}DTPA@SiO_2⊃Ru-Van** nanoparticles. TGA profile of coated nanoparticles

exhibited a greater weight loss compared with uncoated nanoparticles with main thermal degradation steps at 350 °C and 800 °C. Similarly, **Fe^{3+}DTPA-Si_2** exhibited thermal degradation steps at 250 °C, 350 °C and 800 °C. A total weight loss of 41 % was calculated between coated and uncoated **SiO_2⊃Ru-Van** nanoparticles, which was estimated in a coating of 57 mg_{FeDTPA}/g_{NPs} (0.12 $mmol_{FeDTPA}/g_{NPs}$). Due to the high coating content compared with the cargo, the degradation profile was dominated by the coating degradation and we could not distinguish cargo thermal degradation. Moreover, DTPA-coated nanoparticles' coating was previously estimated to be 54 mg_{DTPA}/g_{NPs} (0.13 $mmol_{DTPA}/g_{NPs}$). Thereby, both sets of particles presented a very similar coating degree.

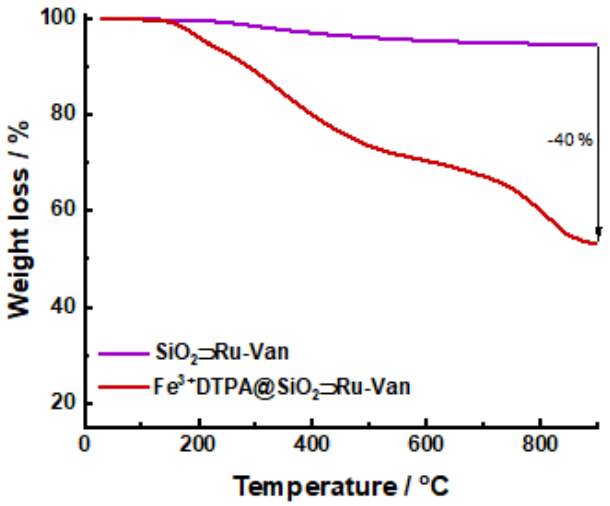

Figure 3.10. Thermogravimetric analysis (TGA) of **SiO_2⊃Ru-Van**, **Fe^{3+}DTPA-Si_2** and **Fe^{3+}DTPA@SiO_2⊃Ru-Van**. Samples were dried for 1 h at 120 °C before the analysis. Samples were heating at 5 °C/min under nitrogen atmosphere.

Control Fe^{3+}DTPA-coated nanoparticles (**Fe^{3+}DTPA@SiO_2⊃Ru**, **Fe^{3+}DTPA@SiO_2⊃Van** and **Fe^{3+}DTPA@SiO_2**,) TGA estimated similar amount of coatings between 0.53 mg_{FeDTPA}/g_{NPs} and 0.59 mg_{FeDTPA}/g_{NPs} (Figure 3.S14 and Table 3.S4).

3.2.3. Release studies

Release of **Van** from coated **Fe^{3+}DTPA@SiO_2⊃Ru-Van** was investigated. Particles were subjected to mild stirring conditions at 150 rpm at 37ºC to mimic the bacteria incubation conditions. Release of **Van** was quantified by monitoring **Van**'s fluorescence (Figure 3.11A-11B). Particles displayed a cumulative Van release up to 3.2 ± 0.6 μg/mg_{NPs} after 18 h of stirring. Furthermore, particle also showcased a triggered released as only of 0.8 ± 0.3 μg/mg_{NPs} **Van** release was observed if particles were not stirred at 37ºC (Figure 3.11C). Furthermore, **Fe^{3+}DTPA@SiO_2⊃Van** also displayed a cumulative release upon stirring with maximum release after 18 h of 3.6 ± 0.3 μg/mg_{NPs} (Figure 3.S15). Under stirring conditions **Ru**'s leakage is minimal (Figure 3.S16) for any **Ru**-containing coated nanoparticles.

Fe^{3+}DTPA@SiO_2⊃Ru-Van nanoparticles' release is comparable to previously reported **DTPA@SiO_2⊃Ru-Van**, which released 3.3 ± 0.5 μg/mg_{NPs} after 18 h of stirring at 150 rpm and 37 ºC. Suggesting that the presence of Fe^{3+} does not altered the release abilities of the nanoparticles.

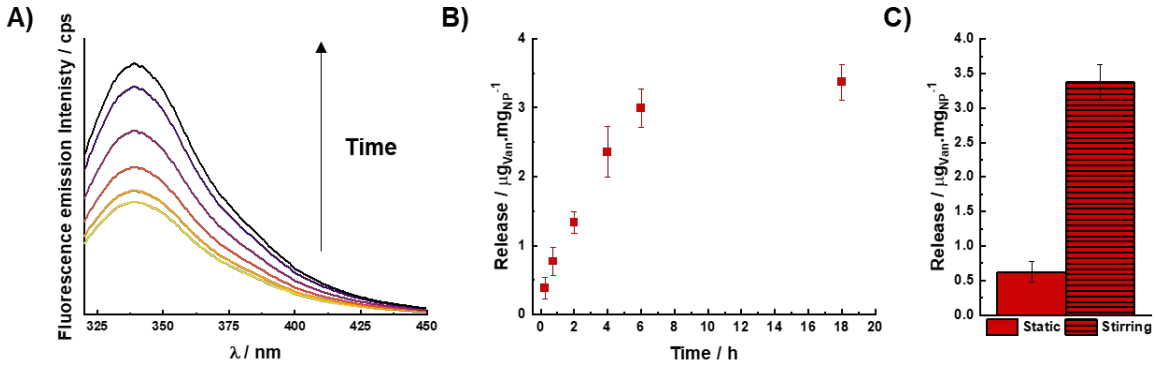

Figure 3.11. Van release studied from **Fe^{3+}DTPA@SiO_2⊃Ru-Van**. (A) Representative fluorescence monitoring release of **Van** (λ_{exc} = 270 nm, λ_{em} = 330 nm) at 37 ºC and 150 rpm and (B) cumulative **Van** release graph (n = 3). (C) Comparative Van release after 18 h at 37 ºC upon static conditions or stirring at 150 rpm (n = 3).

3.2.4. Biocompatibility of Fe^{3+}DTPA@SiO_2⊃Ru-Van

Cytotoxicity of designed Fe^{3+}DTPA-coated nanoparticles was assessed with MTT assays (Figure 3.12) as previously reported for uncoated and **DTPA@SiO_2⊃Ru-Van** nanoparticles. A549 lung cancer cell line was chosen as the model cell line. Obtained results revealed no significant toxicity of **Fe^{3+}DTPA@SiO_2** nanoparticles up to 10 mg/mL. Presence of both cargos resulted in cell toxicity in concentration higher than 5.00 mg/mL. Control particle **Fe^{3+}DTPA@SiO_2⊃Ru** did not show any toxicity even up to 10 mg/mL and control **Fe^{3+}DTPA@SiO_2⊃Van** only displayed significant cytotoxicity in concentrations of 5.00 mg/mL and higher (Figure 3.S19).

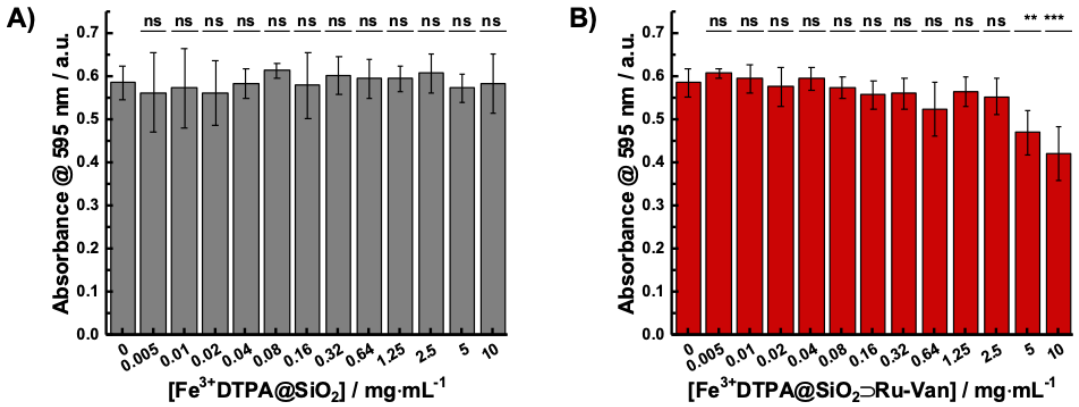

Figure 3.12. MTT cell viability assays of A549 cell line incubated with (A) **Fe^{3+}DTPA@SiO_2** and (B) **Fe^{3+}DTPA@SiO_2⊃Ru-Van** nanoparticles for 18 h. (Average ± SD, n = 3). Significance was calculated based on 1-way ANOVA followed by Dunnett's t-test corrected for multiple comparisons, ns = no significance * = $p<0.05$, ** $p<0.01$ and *** $p<0.0001$.

3.3. Antibacterial activity of Fe^{3+}DTPA@SiO_2⊃Ru-Van

3.3.1. Antimicrobial activity determination of Fe^{3+}DTPA@SiO_2⊃Ru-Van

3.3.1.1. Minimal Inhibitory Concentration (MIC) determination

The antibacterial activity of Fe^{3+}DTPA-coated nanoparticles was measured by determining their Minimal Inhibitory Concentration (MIC) against a Gram-positive representative, *S. aureus* (ATCC23851), and a library of Gram-negative bacterial species (Table 3.5). The activity with uncoated and DTPA-coated nanoparticles was compared.

As previously mentioned in Chapter 2, **Van** is not active against investigated Gram-negative bacterial species due to outer membrane impermeability. Similarly, **SiO_2** nanoparticles do not show any antibacterial ability in concentration up to 10 mg/mL, which slightly increased upon DTPA coating in case of *S. aureus* (2.50 mg/mL) due to its simpler cell membrane. Nevertheless, no increase in activity was observed in case of Gram-negative species. Interestingly, upon coating with the Fe(III) complex, the antibacterial activity of **Fe^{3+}DTPA@SiO_2** increased compared with **DTPA@SiO_2** in all studied species. An MIC of 1.25 mg/mL was determined for *S. aureus*, while a MIC of 2.50 mg/mL was observed in case of DTPA-coated nanoparticles. However, the biggest increase in antibacterial activity was observed for Gram-negative bacterial species. Upon Fe(III) chelation, MIC values of **Fe^{3+}DTPA@SiO_2** decreased to 2.50 mg/mL for Gram-negative bacterial species. The activity of these nanoparticles, despite not bearing any antimicrobial compound, may be attributed to physical disruption of bacterial membrane upon increased nanoparticle-cell interactions, as previously shown for silica nanoparticle after surface functionalization.[43,44] Moreover, the **Fe^{3+}DTPA-Bua_2** complex, analogue of **Fe^{3+}DTPA-Si_2** with higher water solubility,

did not show any significant antibacterial activity up to concentrations of 20 mg/mL in Gram-negative species and a MIC of 1.25 mg/mL for *S. aureus* (Table 3.S1).

Subsequently, the activity of **Fe^{3+}DTPA@SiO_2⊃Ru-Van** was investigated. Uncoated hybrid nanoparticles, **SiO_2⊃Ru-Van**, as previously mentioned, only displayed moderate antibacterial activity against studied bacterial species, with MIC values between 5.00 mg/mL and 2.50 mg/mL for Gram-negative species and a MIC of 1.25 mg/mL for *S. aureus* (Table 2.2). Protection of membrane divalent cations by lipid-A aminoarabinosylation could be attributed to the lower activity of DTPA-coated nanoparticles, as previously reported.[45–47]

Fe^{3+}DTPA@SiO_2⊃Ru-Van nanoparticles displayed an increased activity compared with **DTPA@SiO_2⊃Ru-Van** in all studied bacterial species. MIC values between 1.6 mg/mL and 0.40 mg/mL were determined for Gram-negative bacterial species while a MIC value of 0.20 mg/mL was determined for *S. aureus*. While the increase in the antibacterial activity of novel Fe^{3+}DTPA-coated nanoparticles is very significant, it is more remarkable the low MIC values (1.6 mg/mL and 0.40 mg/mL) determined for *P. aeruginosa* and *B. cenocepacia*.

These results indicate that the presence of the metal cation chelated to the surface aminocarboxylate moieties enhances the activity of the particles, and furthermore, may represent a novel strategy to enhance the activity of nanoparticles even in those cases where the precious coating did not have significant antibacterial activity. The Fe^{3+}DTPA-coated control particles, containing only one cargo, also displayed greater antibacterial activity that those coated with the free DTPA as summarized in (Table 3.S1)

Furthermore, and more interestingly, we were able to estimate the concentration of released **Van**, based on *in vitro* experiments. Estimated concentration of **Van** for **Fe^{3+}DTPA@SiO_2⊃Ru-Van** were between 5.0 and 0.6 μg/mL (± 12 % SD), showing a significant reduction of required **Van** compared with DTPA-coated nanoparticles.

Table 3.1. Minimal inhibitory concentration (MIC, mg/mL) of Vancomycin HCl (**Van**) and nanoparticles with different surface functionalizations for *S. aureus* (ATCC23851), *E. coli* (MG1655), *A. baumannii* (AYE), *K. pneumoniae* (ATCC43816R), *K. oxytoca* (080-KPC CHD), *C. feundii* (NCTC9750), *S. enterica* (SL1344), *P. aeruginosa* (PA14) and *B. cenocepacia* (K57-2, CF isolate) upon shaking at 150 rpm at 37 ^{O}C in LB media. Depicted results are based on 3 biological replicas. * Estimated *in vitro* **Van** release in μg/mL (± 16 % for **DTPA@SiO_2⊃Ru-Van** and ± 12 % for **Fe^{3+}DTPA@SiO_2⊃Ru-Van**).

	E. coli	***A. baumannii***	***K. pneumoniae***	***K. oxytoca***	***C. freundii***	***S. enterica***	***P. aeruginosa***	***B. cenocepacia***	***S. aureus***
Vancomycin HCl (**Van**)	> 0.25	> 0.25	> 0.25	> 0.25	> 0.25	> 0.25	> 0.25	> 0.25	0.001
SiO_2	> 10	> 10	> 10	> 10	> 10	> 10	> 10	> 10	> 10
DTPA@SiO_2	> 10	> 10	> 10	> 10	> 10	> 10	> 10	> 10	2.50
Fe^{3+}DTPA@SiO_2	5.00	5.00	5.00	5.00	5.00	5.00	5.00	5.00	1.25
SiO_2⊃Ru-Van	5.00	2.50	2.50	5.00	5.00	2.50	5.00	5.00	1.25
DTPA@SiO_2⊃Ru-Van	1.25 (4.1)*	0.75 (2.4)*	0.75 (2.4)*	2.50 (8.2)*	2.50 (8.2)*	0.75 (2.4)*	5.00 (16.4)*	5.00 (16.4)*	0.37 (1.2)*
Fe^{3+}DTPA@SiO_2⊃Ru-Van	0.40 (1.3)*	0.40 (1.3)*	0.40 (1.3)*	0.80 (2.5)*	0.40 (1.3)*	0.20 (0.6)*	1.60 (5.0)*	0.40 (2.5)*	0.20 (0.6)*

Furthermore, synergy between the water soluble **DTPA-Si$_2$** analogue (**DTPA-Bua$_2$**) and **Van** and between **Fe^{3+}DTPA-Bua$_2$** and **Van** was explored using checkerboard MIC assays (Figure 3.S20) for *S. aureus*, *E. coli* and *P. aeruginosa*. Synergy was only observed between **DTPA-Bua$_2$** and **Van** for *S. aureus* and *E. coli*, as previous reported between aminocarboxylates and antibiotics for these species.[48,49] We were not able to determine a MIC value of **DTPA-Bua$_2$** and **Fe^{3+}DTPA-Bua$_2$** for *P. aeruginosa* before reaching their limit of solubility (20 mg/mL). Therefore, we could not investigate their synergy through MIC checkerboard MIC assays.

3.3.1.2. Effect of medium Fe(III) concentration in nanoparticles antibacterial activity

In order to explore the mechanism of action of novel Fe^{3+}DTPA-coated nanoparticles, and the potential interactions with membrane siderophore receptors, we decided to follow strategies previously employed with molecular SACs.[27,27,31] These strategies rely on the antibacterial activity of SAC's upon siderophore receptor overexpression, achieved by decreasing Fe(III) availability.[50] In reduced Fe(III) media, bacterial cells overexpress siderophore uptake systems in order to maximize Fe(III) uptake.[2] If these receptors are involved in the mechanism of action of the SAC, or nanoparticles in this case, overexpression of membrane receptor would result in higher conjugate-receptor interaction, and hence, higher antibacterial activity.

We selected *S. aureus* as a Gram-positive representative and *E. coli* and *P. aeruginosa* as Gram-negative representatives, as *P. aeruginosa* displays lipid-A aminoarabinosylation while *E. coli* does not. We first explored the viability of selected species under reduced Fe(III) conditions using MOPS minimal media with different

Fe(III) concentrations (10 μM – 20 nM). An initial concentration of 10 μM (standard Fe(III) concentration in MOPS media) was first employed to ensure growth of cells. Then, Fe(III) concentration was decreased and bacterial growth monitored by measuring the optical density at a wavelength of 600 nm. For *S. aureus*, as Fe(III) concentration was reduced to 1.8 μM, a significant growth decrease was observed (Figure 3.13). In concentrations lower than 1.8 μM, *S. aureus* growth was not observed; highlighting its Fe(III) dependency. However, at 1.8 μM no significant change in growth was observed for *E. coli* and only a small decrease for *P. aeruginosa.* The ability of these species to overcome nutrients limitation is well described and this is mediated by siderophore uptake system overexpression.[51,52]

Thereby, Fe(III) concentration was decreased to 20 nM which is, a clinically relevant Fe(III) concentration, as it is the Fe(III) concentration found in infection areas in human bodies, as a result of the human immune system scavenging essential nutrients from bacteria.[53] It was, interestingly, at this concentration when a significant reduction in bacterial growth was observed (Figure 3.13).

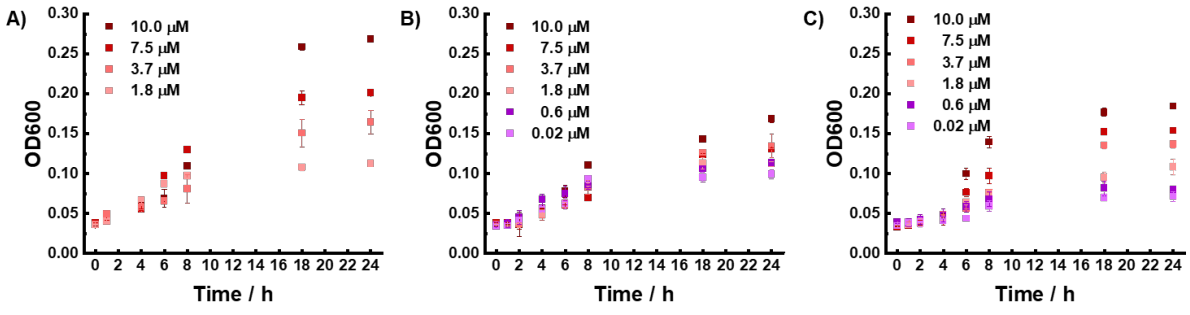

Figure 3.13. Fe(III) growth dependency of (A) *S. aureus* (ATCC23851), (B) *E. coli* (MG1655) and (C) *P. aeruginosa* (PA14). Overnight inocula in MOPS with [Fe(III)] = 10 μM were centrifuged, washed with PBS buffer (0.1 M, pH 7.4) and 1:100 dilutions in reduced Fe(III) media growth was monitored by OD600 measurements. Depicted values represent the average ± SD based on 3 biological replicates.

Based on these results, the activity of **DTPA@SiO_2⊃Ru-Van** and **Fe^{3+}DTPA@SiO_2⊃Ru-Van** nanoparticles was investigated in the different Fe(III) concentration MOPS media. As bacterial growth is dependent on the media Fe(III) concentration, instead of MIC determination, time-killing assays were employed.

For the experiment, bacterial cultures were incubated at 37 ^oC overnight in 10 μM Fe(III) MOPS media to ensure maximum growth. Cultures were then centrifuged, the pellet washed twice with PBS buffer (0.1 M, pH 7.4), to ensure removal of any Fe(III) trace, and diluted in MOPS media with different Fe(III) concentrations with a final OD600 of 0.01. These cultures were incubated for 2 h at 37 ^oC to ensure overexpression of siderophore receptors. Then, cultures were centrifuged, washed with PBS and, finally, redispersed in clean PBS buffer with MIC nanoparticle concentrations. During the experiments the suspensions were incubated at 37 ^oC with shaking (150 rpm) and an aliquot was taken at different time points, diluted, plated onto LB agar to enumerate, and incubated overnight at 37 ^oC for CFU/mL determination.

Time killing assays with bacterial cells in presence of **DTPA@SiO_2⊃Ru-Van** (Figure 3.14) showed no significant change in the antibacterial activity of the nanoparticles in reduced Fe(III) conditions, suggesting that Fe(III) acquisition systems are not involved in their mechanism of action. However, a clear dependency between the antibacterial activity of **Fe^{3+}DTPA@SiO_2⊃Ru-Van** nanoparticles and the media Fe(III) concentration was observed. Upon reduction of Fe(III) in media, an increase in the activity of nanoparticles was observed (Figure 3.14).

Furthermore, we estimated the time required to half the initial bacterial viability (CFU/mL) in presence of nanoparticles (Figure 3.14D-14F). No change was observed

for DTPA-coated nanoparticles, while the time required to half the initial CFU/mL in presence of Fe^{3+}DTPA-coated nanoparticles decreased upon siderophore receptor overexpression.

These results suggest that the Fe(III) acquisition systems play an important role in the mechanism of action of **Fe^{3+}DTPA@SiO_2⊃Ru-Van** nanoparticles.

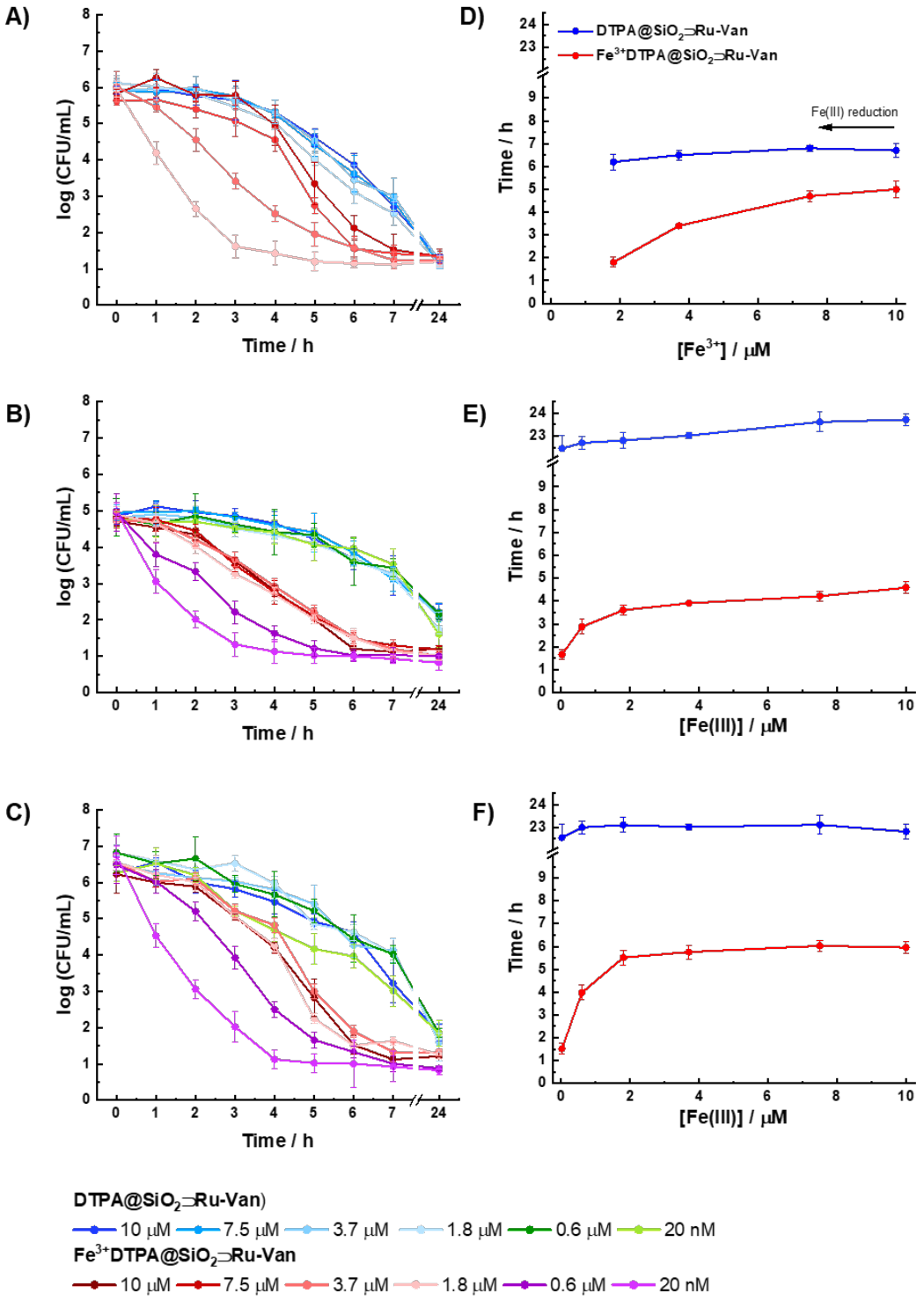

Figure 3.14. Effect of media Fe(III) concentrations in the antibacterial activity of DTPA- and Fe^{3+}DTPA- coated hybrid nanoparticles. (A-C) Time-killing assay and (D-F) required time to reduce the initial bacteria CFU to half in presence of coated nanoparticles in PBS buffer (0.1 M, pH 7.4). Cells were incubated in different Fe(III) concentration MOPS media for (A, D) *S. aureus* (ATCC23581), (B, E) *E. coli* (MG1655) and (C, F) *P. aeruginosa* (PA14). n = 3.

3.3.2. Identification of siderophore uptake systems involved in the uptake of Fe^{3+}DTPA@SiO_2⊃Ru-Van

Previous experiments demonstrated the implication of siderophore uptake systems in the activity of **Fe^{3+}DTPA@SiO_2⊃Ru-Van** nanoparticles. Bacterial cells do not only express one iron uptake system, but a plethora of different systems. Receptors are substrate specific, and hence, the uptake of each siderophores is regulated by specific receptors.[50] To identify which of the different uptake systems was involved in the nanoparticle's activity we measured nanoparticle activity against bacterial mutants with a single outer membrane siderophore receptor inactivated at a time. The mutants used in this study are summarised in Table 3.2.

Table 3.2. List of bacteria mutants in this study and siderophore and siderophore type that knocked out membrane receptors recognised. *S. aureus* mutants were kindly given by Dr. Andrew Edwards (Imperial College London), *E. coli* mutants by Prof. Mark Webber (Quadram Institute) and *P. aeruginosa* by Dr. Enea Sancho-Vaello and Prof. Marc Torrent Burgas (Autonomous University of Barcelona).

S. aureus

Strain	Genotype	Siderophore type	Siderophore
ATCC23851	WT		
SAUSA300_0117[54]	*ΔsirA*[55]	Carboxylate	Staphyloferrin A
SAUSA300_0718[56]	*ΔfecA*[56]	Carboxylate	Citrate
SAUSA300_0720[57]	*ΔfhuA*[58]	Hydroxamate	Ferrichrome B

E. coli

Strain[59]	Genotype	Siderophore type	Siderophore
MG1655	*WT*		
ECK4281	*ΔfecA*[60]	Carboxylate	Citrate
ECK0576	*ΔfepA*[61]	Catecholate	Enterobactin
ECK0149	*ΔfhuA*[62]	Hydroxamate	Ferrichrome B

P. aeruginosa

Strain[63]	Genotype	Siderophore type	Siderophore
PA01	*WT*		
PA4221	*ΔfptA*[64]	Mixed	Pyocheline
PA2398	*ΔfpvA*[65]	Mixed	Pyoverdine
PA4168	*ΔfpvB*[66]	Mixed	Pyoverdine
PA2466	*ΔfoxA*[67]	Hydroxamate	Ferrioxamine B
PA0470	*ΔfiuA*[30]	Hydroxamate	Ferrichrome
PA3901	*ΔfecA*[68]	Carboxylate	Citrate
PA2688	*ΔfepA*[69]	Catecholate	Enterobactin
PA0931	*ΔpirA*[70]	Catecholate	Enterobactin

Bacterial strains were incubated in PBS (0.1 M, pH 7.4) with DTPA- or Fe^{3+}DTPA-coated hybrid nanoparticles (MIC concentration of WT strains) for 2 h and the viability checked by enumerating CFU/mL. Moreover, the strains were incubated at standard (10 μM) or reduced (1.8 μM or 20 nM) Fe(III) concentration MOPS before the

experiment to overexpress the siderophore uptake systems. If a receptor is involved in the mechanism of action of the nanoparticles, inactivation or deletion of the receptor would decrease the activity of the nanoparticle, and this would be more prominet under low Fe(III) concentrations.[12]

For *S. aureus*, we explored three siderophore uptake systems: citrate (carboxylate), staphyloferrin A (carboxylate) and ferrichrome (hydroxamate) siderophore receptors (Figure 3.15).[56] Upon inactivation or deletion of individual receptors, we observed no change in DTPA-coated nanoparticles activity. An increase in nanoparticle's activity was observed upon Fe^{3+}DTPA-coating; which further decreased upon receptor overexpression. Nevertheless, in case of studied mutants (*ΔsirA*, *ΔfecA* and *ΔfhuA*), this effect was not observed. Fe^{3+}DTPA-coating did not have a significant effect in the viability of *ΔsirA* and *ΔfhuA* strains. *ΔfecA* showed a decreased in viability upon incubation with Fe^{3+}DTPA-coated nanoparticles compared with DTPA-coated ones, but not further decrease upon iron limitation (receptor overexpression). These results suggest that *SirABC* and *FhuABC* uptake systems are involved in the mechanism of action of **Fe^{3+}DTPA@SiO_2⊃Ru-Van**.

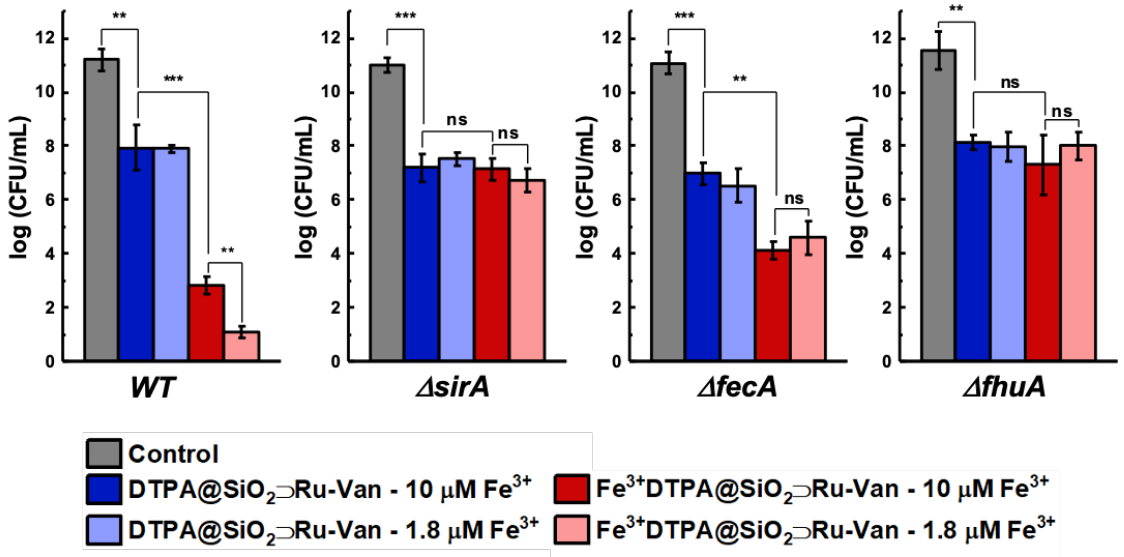

Figure 3.15. CFU counting of *S. aureus* wild type and mutants after incubation with particles at MIC concentration for 2 h in PBS after been incubated in MOPS media with different Fe(III) concentrations for 2 h. Depicted values represent the average ± SD based on 3 biological replicates. Statistical analysis performed by t-test; ns = $p > 0.05$, * = $p < 0.05$, ** = $p < 0.01$, *** = $p < 0.001$.

For *E. coli*, three uptake systems were explored: those specific for citrate (*ΔfecA*[60]), enterobactin (Ent, *ΔfepA*[61]) and ferrochrome (*ΔfhuA*[62]) siderophores as representatives of all types of siderophore structures. DTPA-coated nanoparticles did not affect significant activity (Figure 3.16). However, **Fe^{3+}DTPA@SiO_2⊃Ru-Van** showed a increase in activity against the WT strain, which further increased upon incubation in reduced Fe(III) media prior the experiment, was observed. Inactivation of *fepA* receptor did not impact the activity of the Fe^{3+}DTPA-coated particles. FepA is the outer membrane receptor for $[Fe^{3+}Ent]^{3-}$ siderophore complex.[71] The native siderophore is a negatively charged specie, while Fe^{3+}DTPA is a neutral complex, which could explain why FepA might not recognize the nanoparticle coating. Furthermore, Ent is a catecholate-based siderophore whose geometry and size differ significantly from the Fe^{3+}DTPA complex.

Nevertheless, *ΔfecA* and *ΔfhuiA* strains showed no significant viability decrease upon incubation with **Fe^{3+}DTPA@SiO_2⊃Ru-Van**. This suggest that the siderophore-uptake pathways that contains the membrane receptors FecA and FhuA are involved in the mechanism of actions of the nanoparticles, as in *E. coli*.

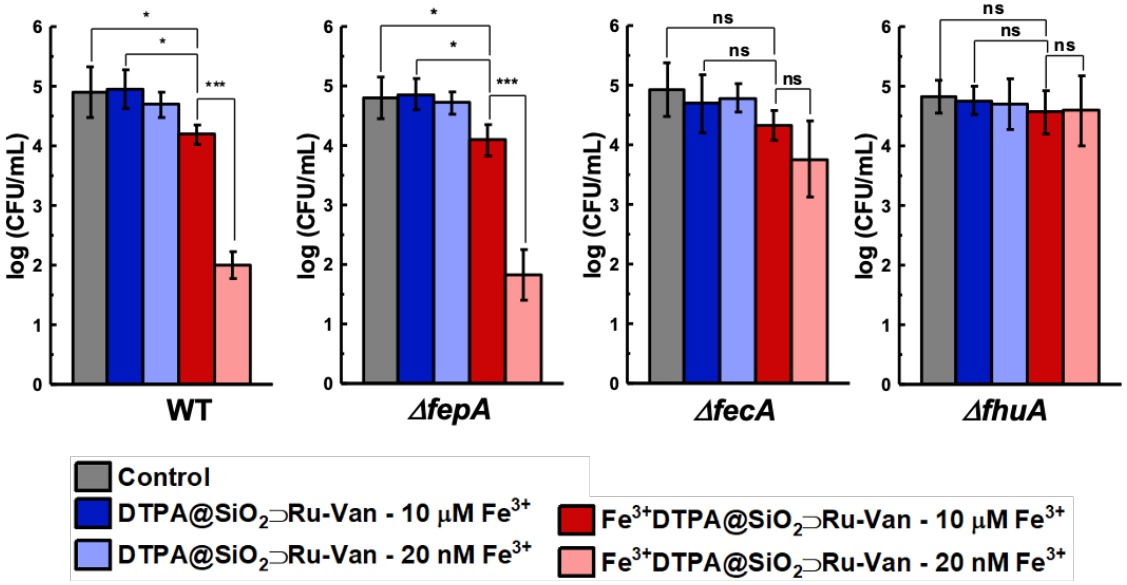

Figure 3.16. CFU counting of *E. coli* wild-type and mutants after incubation with particles at MIC concentration for 2 h in PBS after been incubated in MOPS media with different Fe(III) concentrations for 2 h. Depicted values represent the average ± SD based on 3 biological replicates. Statistical analysis performed by t-test; ns = $p > 0.05$, * = $p < 0.05$, ** = $p < 0.01$, *** = $p < 0.001$.

Finally, the siderophore-uptake systems of *P. aeruginosa* were investigated. *P. aeruginosa* displays lipid A aminoarabinosylation, protecting the divalent cations present in the outer membrane against the chelating abilities of DTPA-coated nanoparticles. Nevertheless, the Fe^{3+}DTPA-coated nanoparticles showed an increased activity compared with **SiO_2⊃Ru-Van** nanoparticles, suggesting that this new Fe^{3+}DTPA-coating was able to overcome the resistance showcased against **DTPA@SiO_2⊃Ru-Van**. Thereby, we decided to expand the siderophore-uptake

system library studied in order to elucidate the mechanism of actions of **Fe^{3+}DTPA@SiO_2⊃Ru-Van** nanoparticles. Eight different mutants were investigated (Table 3.17). The selected mutants present inactivation of surface receptor proteins of pyochelin (mixed siderophore, FptA), pyoverdine (mixed siderophore, FpvA[65] and FpvB[66]), ferrioxamine and ferrochrome (two hydroxamate-based siderophore, FoxA[67] and FiuA[30]), citrate-based complex (FecA[68]) and Ent (FepA[69] and PirA[70]). Selected mutants displayed inactivation of the majority of *P. aeruginosa* siderophore uptake systems.[27]

After 2 h incubation no change in DTPA-coated nanoparticles was observed in any of the Fe(III) conditions tested. Nevertheless Fe^{3+}DTPA-coated hybrid nanoparticles displayed higher antibacterial activity against the WT strain at 10 μM Fe(III) which further increased when cells were incubated in 20 nM Fe(III) before the experiment. In case of *P. aeruginosa* knockouts, no change in the activity of DTPA-coated was observed, suggesting that the resistance mechanism is also present in those strains.

For **Fe^{3+}DTPA@SiO_2⊃Ru-Van** nanoparticles two different behaviours were observed. nanoparticles displayed increased antibacterial activity againt *ΔfptA, ΔfpvA, ΔfpvB, ΔfepA and ΔpirA* strains at 10 μM Fe(III) which a further increased in Fe(III) limitation conditions. These results suggested that those uptake systems are not involved in the mechanism of action n of the nanoparticles, as their inactivation did not have any consequence to the activity of the nanoparticles. Receptors that recognize catecholate-based and mixed siderophores in *P. aeruginosa* are not able to interact with surface Fe^{3+}DTPA complex.[72,73]

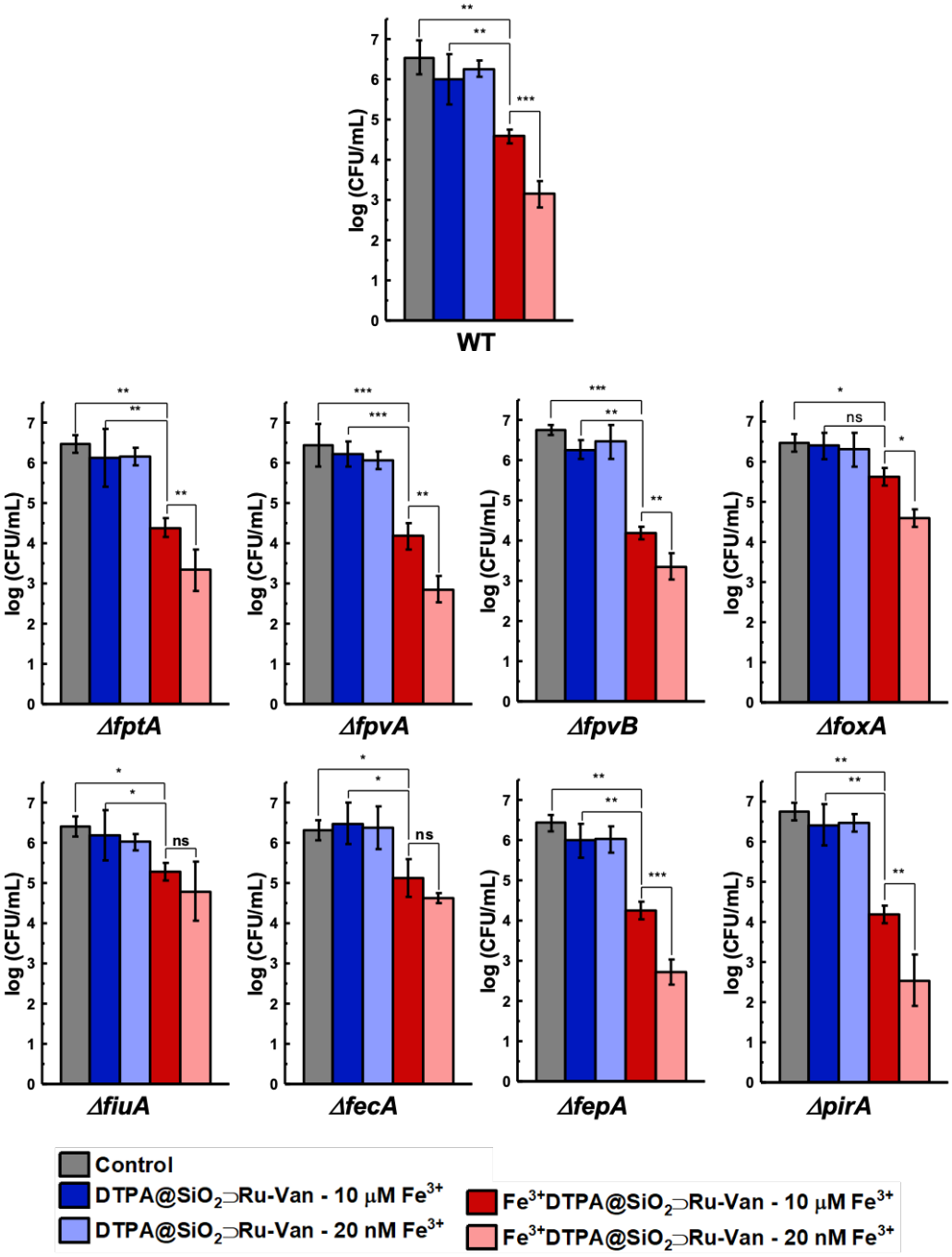

Figure 3.17. CFU counting of *P. aeruginosa* wild-type and mutants after incubation with particles at MIC concentration for 2 h in PBS after been incubated in MOPS media with different Fe(III) concentrations for 2 h Depicted values represent the average ± SD based on 3 biological replicates. Statistical analysis performed by t-test; ns = $p > 0.05$, * = $p < 0.05$, ** = $p < 0.01$, *** = $p < 0.001$.

However, a decrease on the antibacterial activity of **Fe^{3+}DTPA@SiO_2⊃Ru-Van** nanoparticles was observed in case of *ΔfoxA, ΔfiuA and ΔfecA* strains, with carboxylate or hydroxamate-based membrane receptors' expression inactivated. Similarly, even if cells were incubated with 20 nM Fe(III), very low (in case of *ΔfoxA*) or no statistical significant difference (*ΔfiuA and ΔfecA*) was observed compared with standard Fe(III) concentrations (10 μM), suggesting that these are involved in nanoparticles activity.

In conclusion, and after examining a library of bacteria mutants we observed that the antimicrobial activity of **Fe^{3+}DTPA@SiO_2⊃Ru-Van** nanoparticles is directly linked with carboxylate and hydroxamate-based siderophore receptors, as upon gene inactivation, the antibacterial activity of nanoparticles was significantly reduced. Moreover, uptake systems specific for catecholates or mixed siderophores appeared not to be involved in the activity of particles, as their inactivation did not have any effect on their activity.

Nevertheless, we need to further explore whether the increase in activity of **Fe^{3+}DTPA@SiO_2⊃Ru-Van** nanoparticles is due to increased internalization through identified siderophore uptake systems.

3.3.3. Internalization of Fe^{3+}DTPA@SiO_2⊃Ru-Van nanoparticles

In order to elucidate if the antibacterial effect of these nanoparticles is due to their enhanced internalization, Structured Illumination Microscopy (SIM) was employed. Taking advantage of the highly luminescent **Ru** complex within the nanoparticles, their internalization was studied in Hoechst-stained live bacterial cells. The studies also examined the effect of medium Fe(III) concentration and the inactivation of surface

siderophore-receptor expression on nanoparticle internalization was explored using the same approach

Bacterial cells ere incubated with desired nanoparticles with a final concentration of 2.5 mg/mL in PBS buffer (0.1 M, pH 7.4) for 1 h for *S. aureus* and 2 h for Gram-negative species. In order to overexpress the siderophore uptake systems, bacterial cells well were incubated 2 h in reduced Fe(III) MOPS media prior to the experiments. Finally, cells were stained with Hoechst and live imaged using SIM microscopy (ZEIS ELYRA microscope). Nanoparticle internalization was then calculated using z-stack images by two different methodologies: we first calculated the Manders' overlapping coefficient between the cell's signal (Hoechts) and the nanoparticles (**Ru**)[74] and, secondly, we determine the number of cells containing nanoparticles using an image processing technique previously developed within the groups and reported in Dosumu *et al*.[75]

After 1 h incubation of WT *S. aureus* with uncoated particles, very low particle internalization percentage was estimated, as seen in Figure 3.18, regardless of whether cells were previously incubated in standard or reduced Fe(III) conditions. Upon DTPA-coating, nanoparticle internalization increased but no difference between Fe(III) conditions was observed, in good agreement with the antibacterial activity study (section 3.4.1). Upon Fe^{3+}DTPA-coating, nanoparticles internalization increased significantly comparing with **DTPA@SiO_2⊃Ru-Van** nanoparticles, after 1 h incubation, with Mander's overlapping coefficient of 0.52 ± 0.09 and 51 ± 3 % of cells containing **Fe^{3+}DTPA@SiO_2⊃Ru-Van** nanoparticles. Furthermore, in iron limitation conditions (causing receptor overexpression), internalization of nanoparticles increased even further with 83 ± 9 % of cells displaying internalised nanoparticles. Internalisation results support the antibacterial activity observed in previous experiments. We also

explored 2 h incubation time for *S. aureus*; however, due to the permeability of cells to nanoparticles, after 2 h no difference between coated nanoparticle and Fe(III) conditions could be observed (Figure S.21).

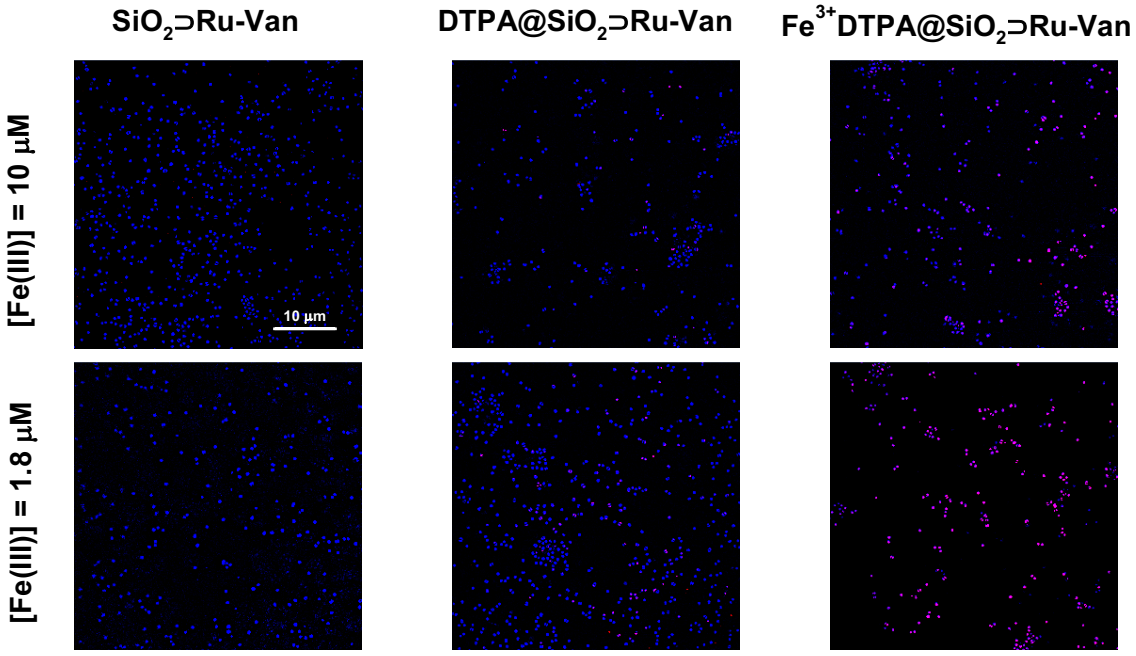

Figure 3.18. Representative structural illumination microscopy images (n = 5 for 3 biological replicates) of WT *S. aureus* cells incubated with **SiO_2⊃Ru-Van**, **DTPA@SiO_2⊃Ru-Van** and **Fe^{3+}DTPA@SiO_2⊃Ru-Van** nanoparticles ([NPs] = 2.5 mg/mL) for 1 h in PBS buffer (1 mM, pH 7.4) at 37 ºC under mild shaking (150 rpm) after 1 h incubation in standard (10 μM) and reduced (1.8 μM) Fe(III) MOPS media. Images show overlay of channels depicting the bacterial cell outline (blue) and particle luminescence (red). Blue channel, Hoechst H33342 (λ_{exc} = 405 nm, λ_{em} = 410 – 455 nm) and red channel, **Ru** emission (λ_{exc} = 455 nm, λ_{em} = 580 – 620 nm).

These results can also be further reinforced by TEM imaging of the same samples (Figure 3.19) showing a higher degree of particle internalization upon coating and a higher number of nanoparticle-cell interactions of **Fe^{3+}DTPA@SiO_2⊃Ru-Van** nanoparticles upon siderophore uptake system overexpression. *S. aureus* cells

incubated with **SiO_2⊃Ru-Van** nanoparticles only shows nanoparticles attached to the cell surface with nor significant change in cell morphology. Upon DTPA-coating, the cell morphology changed observing deflated cells due to the activity of the coating, as also observed in control experiments. Nevertheless, no difference between iron conditions was observed (Figure 3.S22). Finally, cells, incubated with **Fe^{3+}DTPA@SiO_2⊃Ru-Van** displayed higher number of internalised nanoparticle (indicated with red arrows) which increased even further in iron limitation conditions.

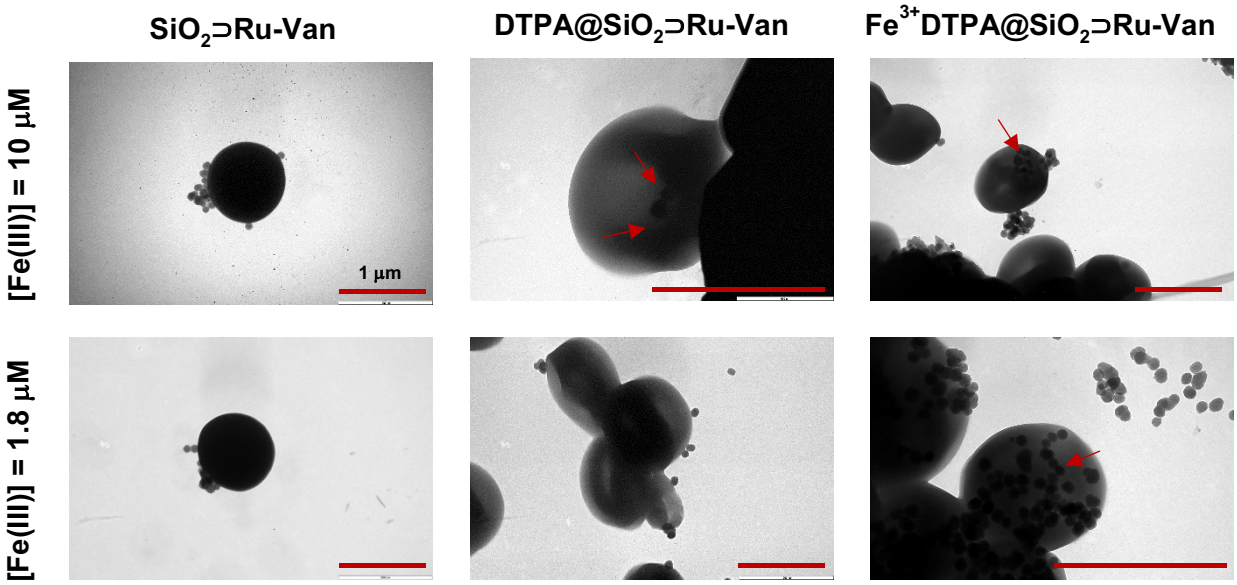

Figure 3.19. Representative Transmission Electron Microscopy (TEM) images (n = 5 per condition) of wild-type *S. aureus* cells incubated with **SiO_2⊃Ru-Van**, **DTPA@SiO_2⊃Ru-Van** and **Fe^{3+}DTPA@SiO_2⊃Ru-Van** nanoparticles (2.5 mg/mL) for 1 h in PBS buffer (1 mM, pH 7.4) at 37 ºC under mild shaking (150 rpm) after 2 h incubation in standard (10 μM) and reduced (1.8 μM) Fe(III) MOPS media. Red arrows highlight internalised nanoparticles.

Next, we explored nanoparticle uptake in *S. aureus* mutants where **Fe^{3+}DTPA@SiO_2⊃Ru-Van** nanoparticles showed lower antibacterial activity compared with the WT strain. *ΔsirA*, *ΔfecA* and *ΔfhuA* strains showed similar particle internalization after incubation with **SiO_2⊃Ru-Van** and **DTPA@SiO_2⊃Ru-Van**

nanoparticles, compared with the WT strain. However, upon incubation with **Fe^{3+}DTPA@SiO_2⊃Ru-Van** nanoparticles, internalization values decreased, plus, no significant difference between Fe(III) conditions was observed. For instance, after 1 h incubation with **DTPA@SiO_2⊃Ru-Van** nanoparticles, 27 ± 5 % of *ΔsirA* strain cells presented internalised nanoparticles, these values decreased to 13 ± 3 % when **Fe^{3+}DTPA@SiO_2⊃Ru-Van** nanoparticles were tested. In case of *ΔfecA*, moreover, 28 ± 7 % of cells displayed internalised DTPA-coated nanoparticles, but Fe^{3+}DTPA-coated nanoparticles were only present in 17 ± 3 % of cells. Finally, a similar trend was observed in case of *ΔfhuA* where no significant difference was observed between the percentage of cells with internalised **DTPA@SiO_2⊃Ru-Van** (28 ± 6 %) and **Fe^{3+}DTPA@SiO_2⊃Ru-Van** (30 ± 3 %) nanoparticles (Figure 3.21).

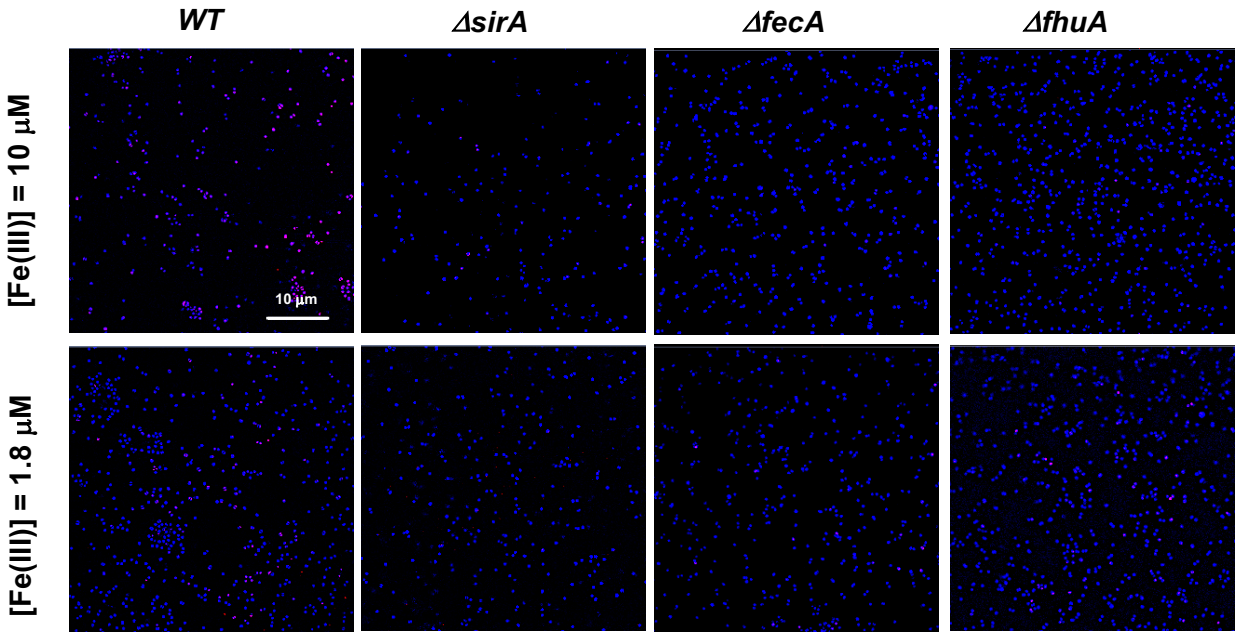

Figure 3.20. Representative structural illumination microscopy images (n = 5 for 3 biological replicates) of wild-type *S. aureus* and mutants cells incubated with **Fe^{3+}DTPA@SiO_2⊃Ru-Van** nanoparticles (2.5 mg/mL) for 1 h in PBS buffer (1 mM, pH 7.4) at 37 °C under mild shaking (150 rpm) after 2 h incubation in standard (10 μM) and reduced (1.8 μM) Fe(III) MOPS media. Images show overlay of channels depicting the bacterial cell outline (blue) and particle luminescence (red). Blue channel, Hoechst

H33342 (λ_{exc} = 405 nm, λ_{em} = 410 – 455 nm) and red channel, Ru emission (λ_{exc} = 455 nm, λ_{em} = 580 – 620 nm).

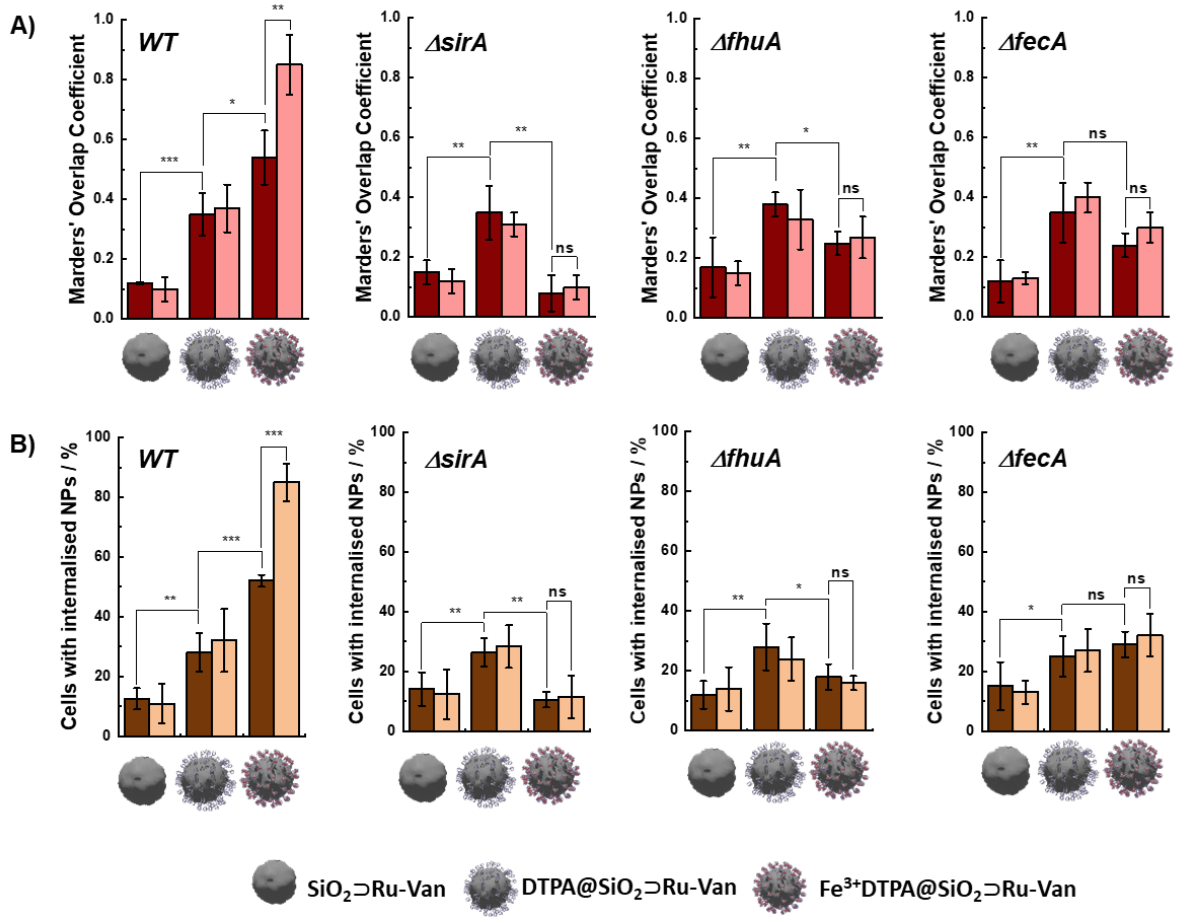

Figure 3.21. Quantification of particle internalization in *S. aureus* strains after 1h incubation in PBS buffer (0.1 M, pH 7.4) at 37 °C and mild shaking (150 rpm) by (A) Manders' overlapping coefficient and (B) determination of bacterial cells with internalized nanoparticles based on SIM images under standard (dark red and brown) and reduced (light red and brown) Fe(III) conditions. (Average ± SD, n = 5 for 3 biological replicates). Statistical analysis performed by t-test; ns = $p > 0.05$, * = $p < 0.05$, ** = $p < 0.01$, *** = $p < 0.001$.

Uncoated nanoparticles were not internalised into WT *E. coli* cells, and DTPA-coating only increased this slightly, with only 18 ± 4 % of cells having internalised nanoparticles (Figure 3.22). Moreover, no significant difference between Fe(III) conditions was observed. However, upon incubation with **Fe^{3+}DTPA@SiO_2⊃Ru-Van** nanoparticles, internalization of particles increased to 31 ± 3 % of cells, which increased to 62 ± 11

% if siderophore-uptake systems are overexpressed under Fe(III) restrictive conditions. The estimated increased in nanoparticle internalization supports the mechanism of action of nanoparticles involving siderophore uptake system.

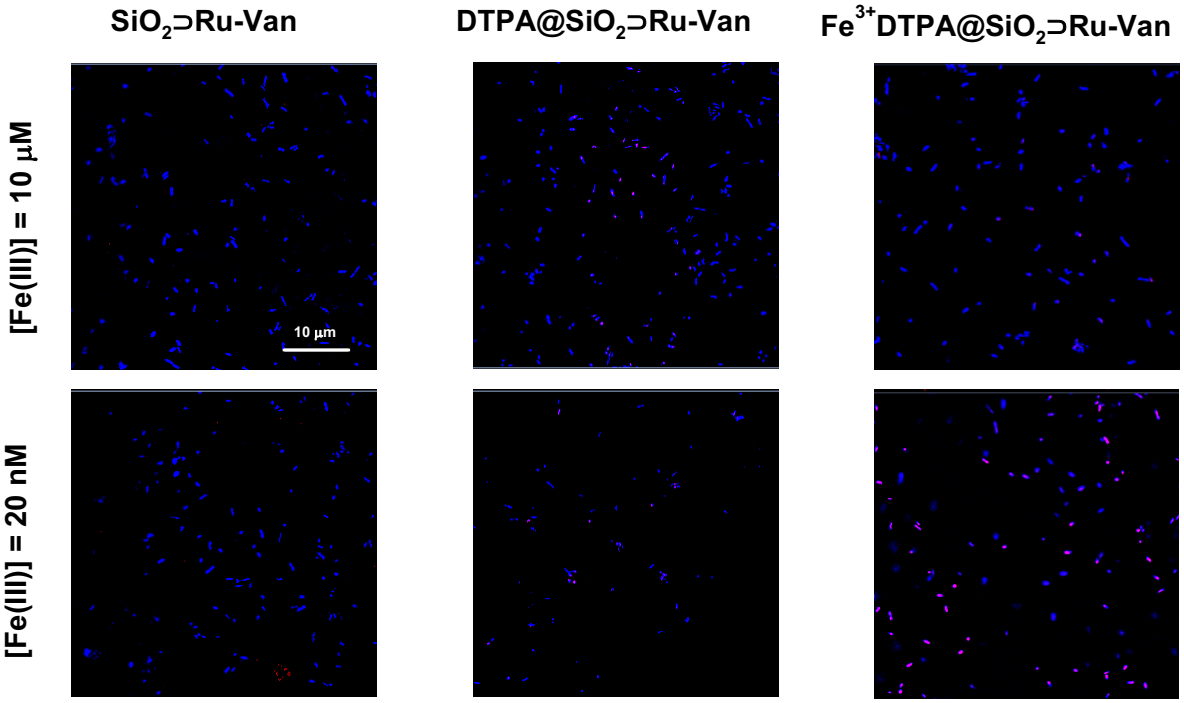

Figure 3.22. Representative structural illumination microscopy images (n = 3) of WT *E. coli* cells incubated with **SiO_2⊃Ru-Van**, **DTPA@SiO_2⊃Ru-Van** and **Fe^{3+}DTPA@SiO_2⊃Ru-Van** nanoparticles ([NPs] = 2.5 mg/mL) for 1 h in PBS buffer (1 mM, pH 7.4) at 27 ºC under mild shaking (150 rpm) after 2 h incubation in standard (10 μM) and reduced (20 nM) Fe(III) MOPS media. Images show overlay of channels depicting the bacterial cell outline (blue) and particle luminescence (red). Blue channel, Hoechst H33342 (λ_{exc} = 405 nm, λ_{em} = 410 – 455 nm) and red channel, Ru emission (λ_{exc} = 455 nm, λ_{em} = 580 – 620 nm).

Minimal interactions between **SiO_2⊃Ru-Van** particles and WT *E. coli* cells were observed in TEM micrographs (Figure 3.23), In case of **DTPA@SiO_2⊃Ru-Van** nanoparticles, even if no difference between Fe(III) concentrations is observed, more interactions were observed, with higher number of nanoparticles interaction with

bacteria surface, plus some internalised nanoparticles. Finally, upon incubation with **Fe^{3+}DTPA@SiO_2⊃Ru-Van** nanoparticles an enhancement on cell-nanoparticle interactions was observed in standard Fe(III) concentrations, where cells were surrounded by a large number of nanoparticles and a change in cell morphology could be seen. Under reduced Fe(III) concentration conditions, the interactions of Fe^{3+}DTPA-coated nanoparticles with bacterial cells increased, observing cell disruption is certain cases. Alongside the SIM images, TEM micrographs supported the antibacterial activity of developed **Fe^{3+}DTPA@SiO_2⊃Ru-Van** nanoparticles.

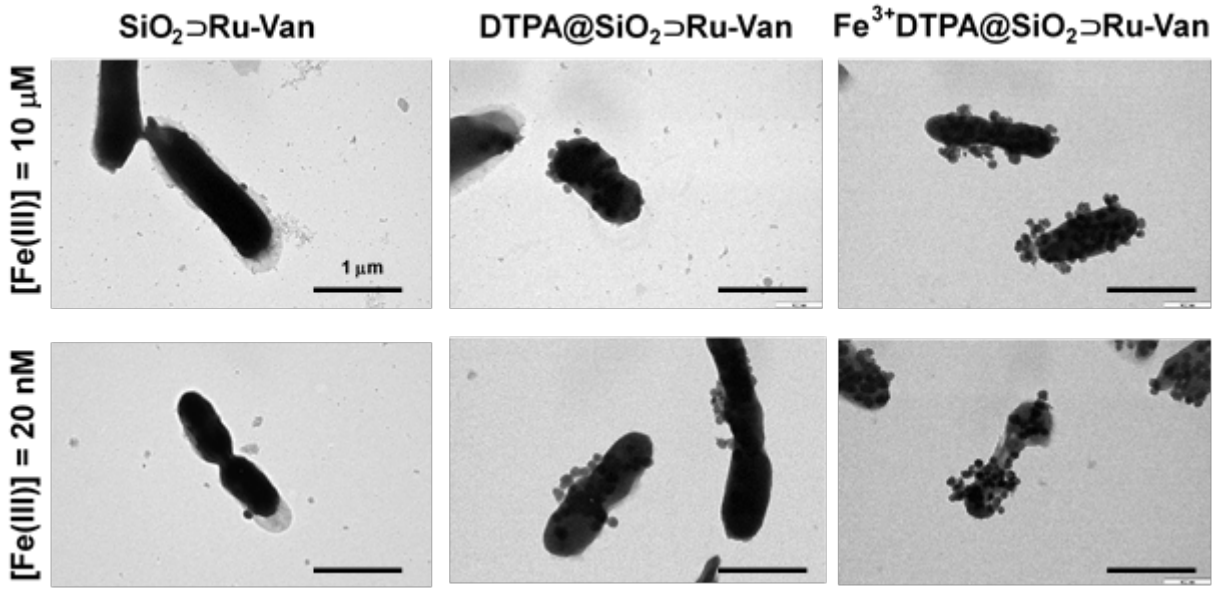

Figure 3.23. Representative Transmission Electron Microscopy (TEM) images (n = 5 per condition) of wild-type *E. coli* cells incubated with incubated with **SiO_2⊃Ru-Van**, **DTPA@SiO_2⊃Ru-Van** and **Fe^{3+}DTPA@SiO_2⊃Ru-Van** nanoparticles (2.5 mg/mL) for 2 h in PBS buffer (1 mM, pH 7.4) at 37 ºC under mild shaking (150 rpm) after 2 h incubation in standard (10 μM) and reduced (20 nM) Fe(III) MOPS media

ΔfecA and *ΔfhuA E. coli* strains, however, displayed reduced Fe^{3+}DTPA-coated nanoparticles internalization, with no significant difference with DTPA-coated nanoparticles or between Fe(III) conditions (Figure 3.S25). Whereas 19 ± 3 % of *ΔfhuA*

E. coli cells presented DTPA-coated nanoparticle internalization, only 17 ± 6 % of cells did show internalised nanoparticles after incubation with **Fe^{3+}DTPA@SiO_2⊃Ru-Van** nanoparticles after siderophore-uptake overexpression. Similarly, *ΔfecA* strain showed similar number of cells with internalised nanoparticle for **DTPA@SiO_2⊃Ru-Van** (18 ± 3 %) and **Fe^{3+}DTPA@SiO_2⊃Ru-Van** (24 ± 5 %) after incubation in reduced Fe(III) conditions. These internalization results support the mechanism of action suggested from previous experiments; suggesting that nanoparticle internalization, and hence, activity, relies of siderophore-uptake systems.

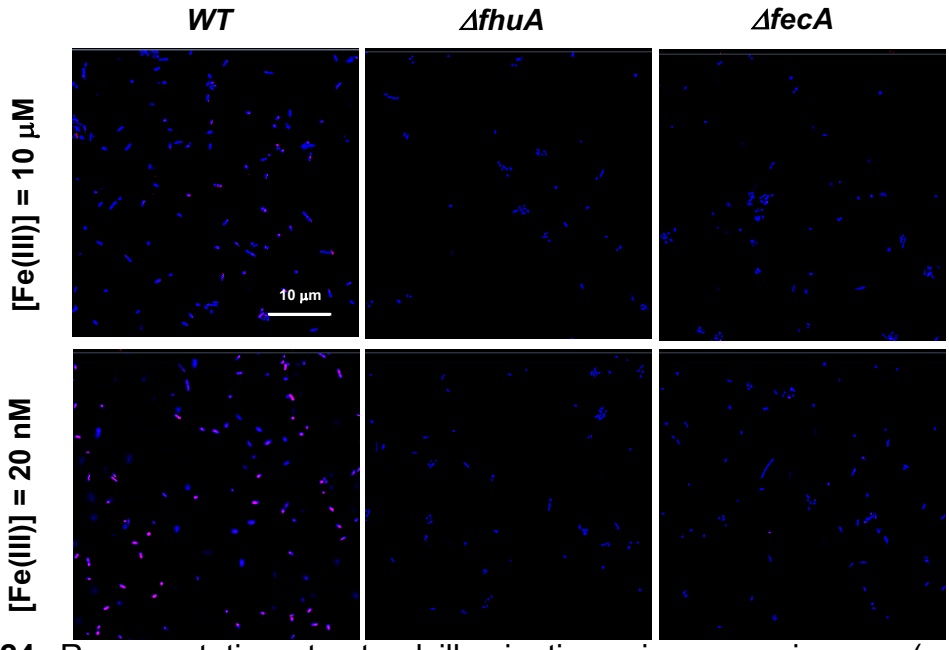

Figure 3.24. Representative structural illumination microscopy images (n=5 for 3 biological replicas) of WT *E. coli* and mutants strains incubated with **Fe^{3+}DTPA@SiO_2⊃Ru-Van** nanoparticles ([NPs] = 2.5 mg/mL) for 1 h in PBS buffer (1 mM, pH 7.4) at 27 ºC under mild shaking (150 rpm) after 2 h incubation in standard (10 μM) and reduced (20 nM) Fe(III) MOPS media. Images show overlay of channels depicting the bacterial cell outline (blue) and particle luminescence (red). Blue channel, Hoechst H33342 (λ_{exc} = 405 nm, λ_{em} = 410 – 455 nm) and red channel, Ru emission (λ_{exc} = 455 nm, λ_{em} = 580 – 620 nm).

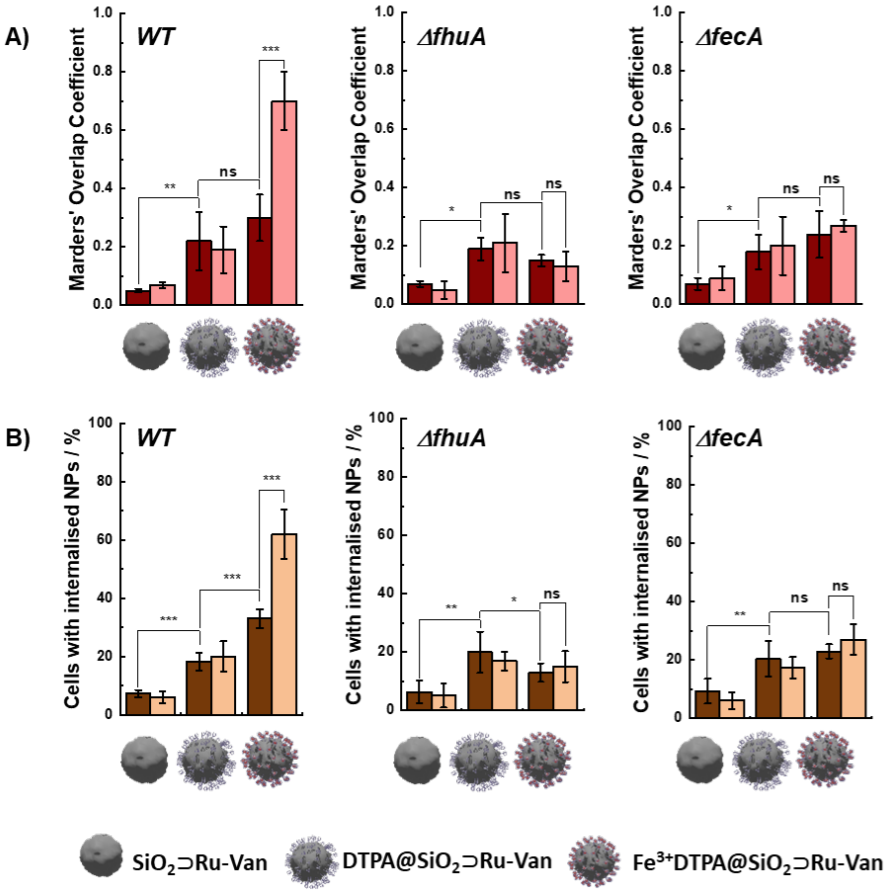

Figure 3.25. Quantification of particle internalization in *E. coli* strains after 2 h incubation in PBS buffer (0.1 M, pH 7.4) at 37 ºC and mild shaking (150 rpm) by (A) Manders' overlapping coefficient and (B) determination of bacterial cells with internalized nanoparticles based on SIM images under standard (dark red and brown) and reduced (light red and brown) Fe(III) conditions. (Average ± SD, n=5 for 3 biological replicas). Statistical analysis performed by t-test; ns $p>0.05$, * $p<0.05$, ** $p<0.01$, *** $p<0.001$.

We finally explored nanoparticle internalization in *P. aeruginosa* strains. As mentioned, due to the resistance mechanism against chelators, DTPA-coated nanoparticles were not able to penetrate the bacterial cells. This could also be observed in SIM images where no luminescent signal of **Ru** was detected in bacterial cells (Figure 3.26). Furthermore, overexpression of siderophore-uptake system did not have any effect on particle internalization. Nevertheless, upon incubation with **Fe^{3+}DTPA@SiO_2⊃Ru-Van**

nanoparticles at Fe(III) = 10 μM, internalization of nanoparticles slightly increased with 25 ± 5 % of *P. aeruginosa* cells containing nanoparticles. These results constitute the first evidence of the enhanced internalization abilities of the nanoparticles in *P. aeruginosa*. Moreover, upon incubation with Fe(III) = 20 nM and receptor overexpression, nanoparticles were internalised in 46 ± 3 % of cells; confirming the proposed uptake mechanism through siderophore-uptake systems.

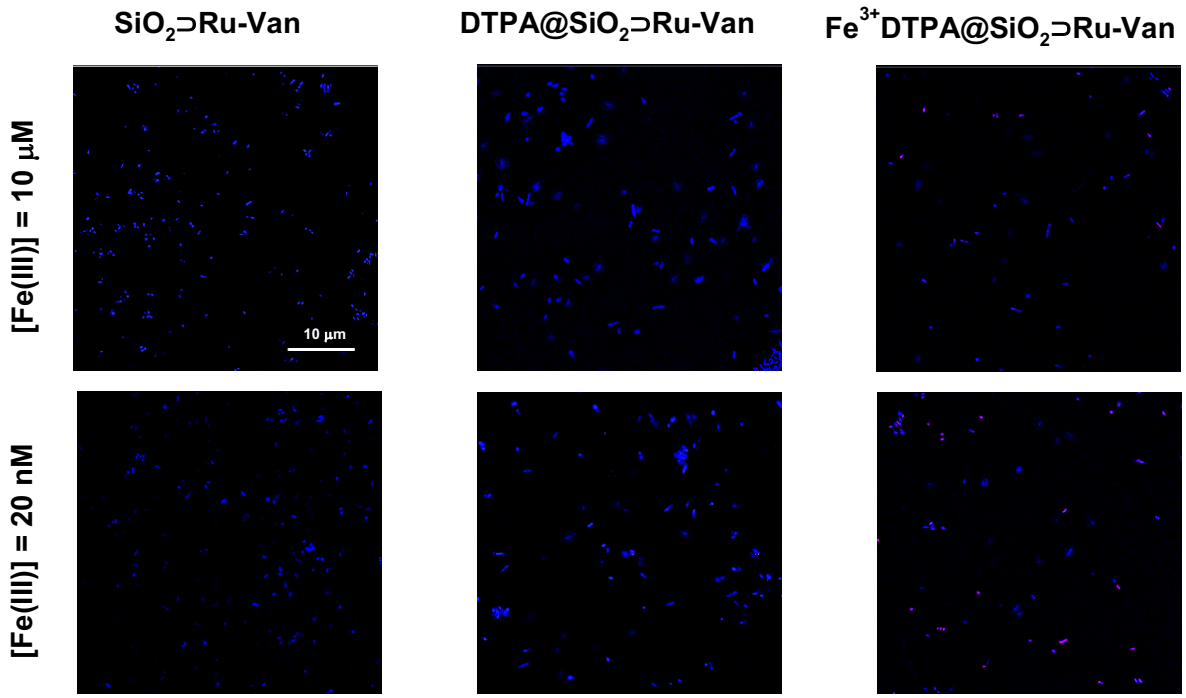

Figure 3.26. Representative structural illumination microscopy images (n=5 for 3 biological replicas) of WT *P. aeruginosa* cells incubated with **SiO_2⊃Ru-Van**, **DTPA@SiO_2⊃Ru-Van** and **Fe^{3+}DTPA@SiO_2⊃Ru-Van** nanoparticles ([NPs] = 2.5 mg/mL) for 1 h in PBS buffer (1 mM, pH 7.4) at 27 ºC under mild shaking (150 rpm) after 2 h incubation in standard (10 μM) and reduced (20 nM) Fe(III) MOPS media. Images show overlay of channels depicting the bacterial cell outline (blue) and particle luminescence (red). Blue channel, Hoechst H33342 (λ_{exc} = 405 nm, λ_{em} = 410 – 455 nm) and red channel, Ru emission (λ_{exc} = 455 nm, λ_{em} = 580 – 620 nm).

TEM images of WT *P. aeruginosa* incubated with the nanoparticle library (Figure 3.27) also confirmed the lack on interactions between uncoated and DTPA-coated nanoparticles, while Fe^{3+}DTPA-coated nanoparticles were found to have more interactions with bacterial cells. Moreover, overexpression of siderophore-receptors upon incubation at 20 nM Fe(III) resulted in an increased of interactions, observing cells fully covered by nanoparticles.

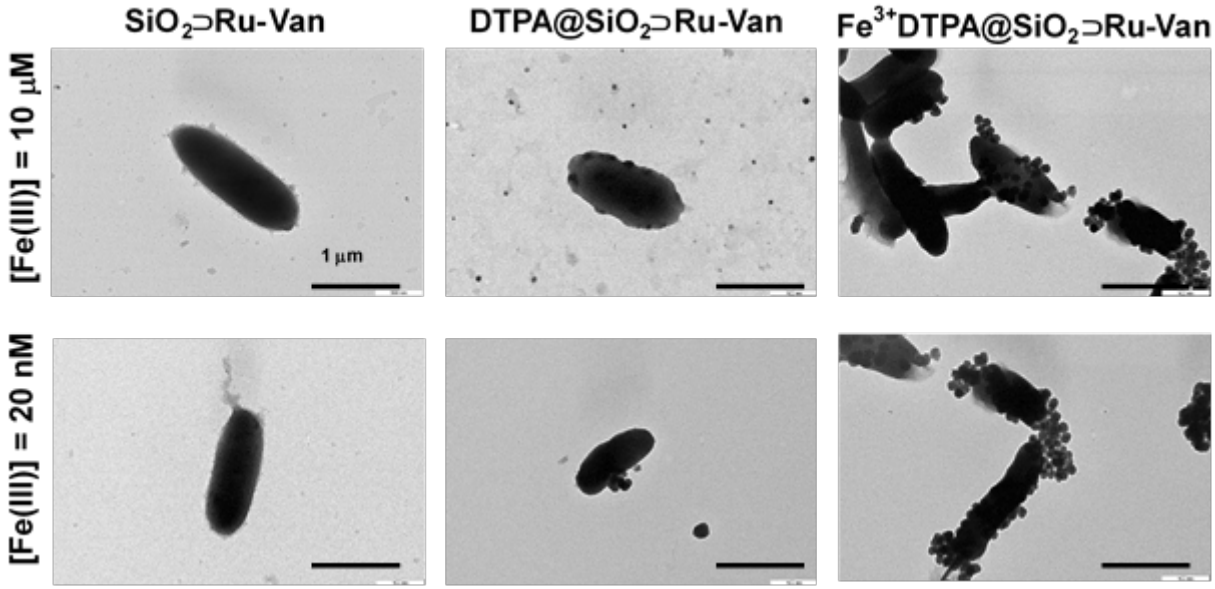

Figure 3.27. Representative Transmission Electron Microscopy (TEM) images (n = 5 per condition) of wild-type *P. aeruginosa* cells incubated with incubated with **SiO_2⊃Ru-Van**, **DTPA@SiO_2⊃Ru-Van** and **Fe^{3+}DTPA@SiO_2⊃Ru-Van** nanoparticles (2.5 mg/mL) for 2 h in PBS buffer (1 mM, pH 7.4) at 37 ºC under mild shaking (150 rpm) after 2 h incubation in standard (10 μM) and reduced (20 nM) Fe(III) MOPS media.

We further investigated nanoparticle uptake in *P. aeruginosa* mutants where **Fe^{3+}DTPA@SiO_2⊃Ru-Van** nanoparticles displayed lower antibacterial activity (*ΔfecA*, *ΔfiuA* and *ΔfoxA*). Uncoated and DTPA-coated nanoparticle did not displayed significant internalization in cells (Figure 3.S25, Figure 3.28), as in WT *P. aeruginosa*. In case of Fe^{3+}DTPA-coated nanoparticle, opposite to the WT strain, very low particle internalization was observed at 10 μM Fe(III), estimating that 11 ± 3 %, 8 ± 3 % and

6 ±4 % of cells were carrying internalised nanoparticles, respectively. Upon siderophore-uptake system overexpression the internalisation of nanoparticle slightly increased but still estimating lower values compared with the WT strain.

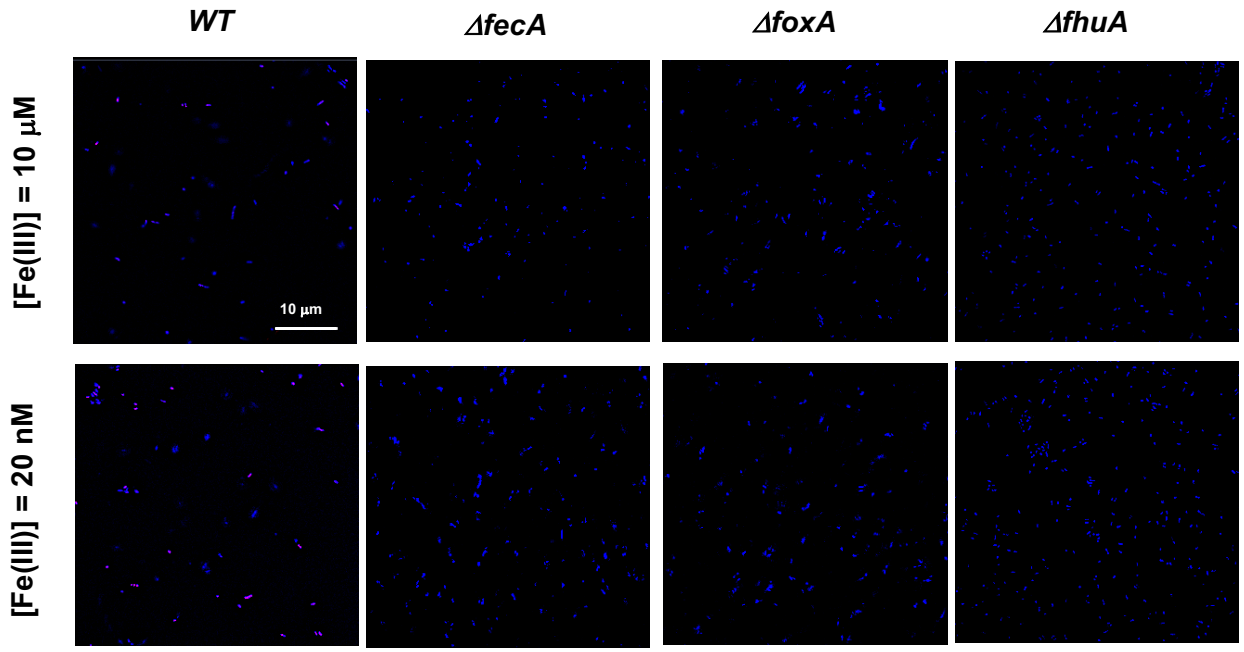

Figure 3.28. Representative structural illumination microscopy images (n=5 for 3 biological replicas) of WT *P. aeruginosa* and mutants strains incubated with **Fe^{3+}DTPA@SiO_2⊃Ru-Van** nanoparticles ([NPs] = 2.5 mg/mL) for 1 h in PBS buffer (1 mM, pH 7.4) at 27 ºC under mild shaking (150 rpm) after 2 h incubation in standard (10 μM) and reduced (20 nM) Fe(III) MOPS media. Images show overlay of channels depicting the bacterial cell outline (blue) and particle luminescence (red). Blue channel, Hoechst H33342 (λ_{exc} = 405 nm, λ_{em} = 410 – 455 nm) and red channel, Ru emission (λ_{exc} = 455 nm, λ_{em} = 580 – 620 nm).

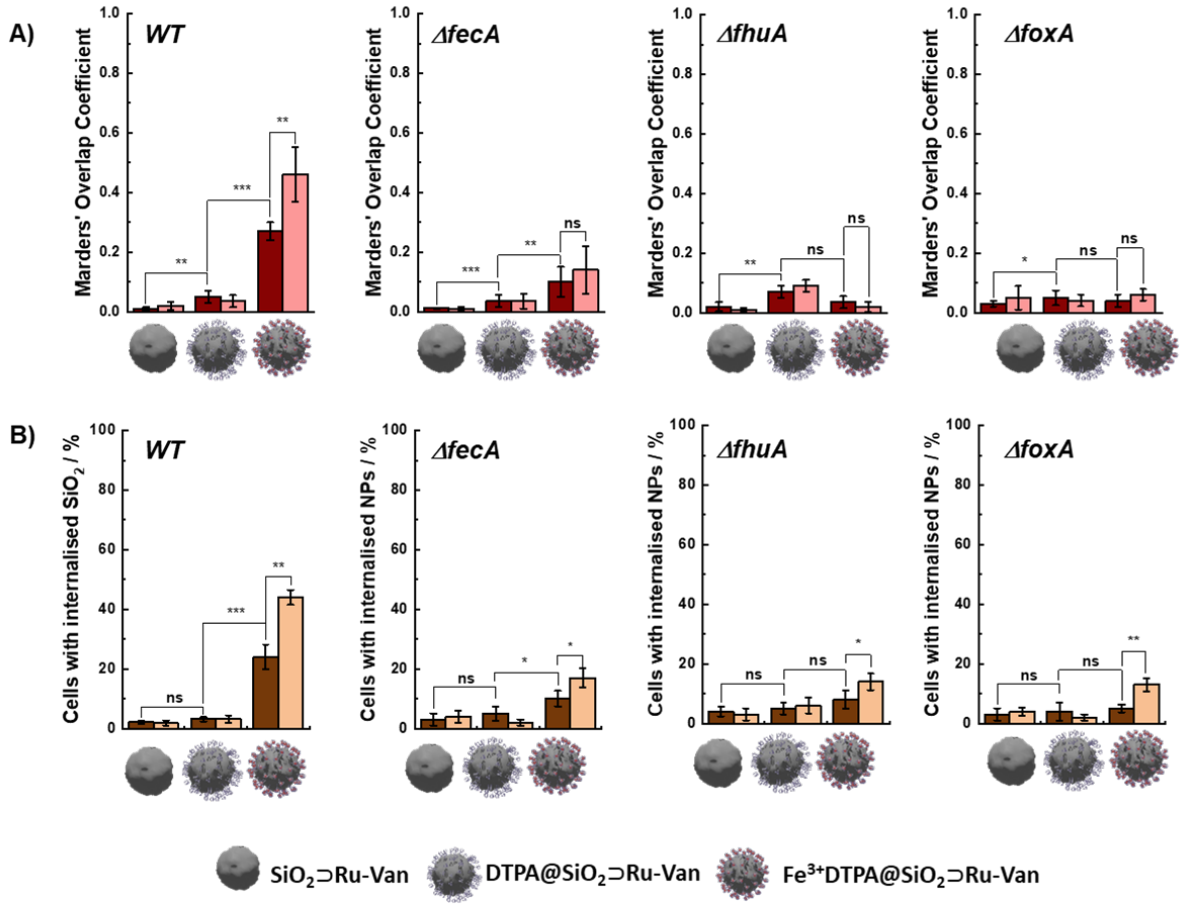

Figure 3.29. Quantification of particle internalization in *E. coli* strains after 2 h incubation in PBS buffer (0.1 M, pH 7.4) at 37 ºC and mild shaking (150 rpm) by (A) Manders' overlapping coefficient and (B) determination of bacterial cells with internalized nanoparticles based on SIM images under standard (dark red and brown) and reduced (light red and brown) Fe(III) conditions. (Average ± SD, n=5 for 3 biological replicas). Statistical analysis performed by t-test; ns $p>0.05$, * $p<0.05$, ** $p<0.01$, *** $p<0.001$.

3.3.3.1. Internalization of control nanoparticles

We also explored the internalization abilities of three control nanoparticles: **Fe^{3+}DTPA@SiO_2⊃Ru**, **[Fe^{3+}DTPA-Bua_2]@SiO_2⊃Ru-Van** and **[Fe^{3+}Ent]$^{3-}$@SiO_2⊃Ru-Van** (Full characterization in Figure 3.S17-S18).

Fe^{3+}DTPA@SiO_2⊃Ru represents a control particle without antibiotic. **Van** inhibits the cell wall synthesis, leading to membrane permeabilization. Thereby, we wanted to explore if the presence of **Van** influenced the uptake of nanoparticles, or if the internalization was predominantly driven by the coating. Internalization quantification by SIM microscopy and image processing techniques revealed no difference in particle internalization for Gram-negative species, while a decrease in particle internalization was observed for *S. aureus* (Figure 3.S28 and Figure 3.S29). We attribute this difference to the antibacterial effect of released **Van** before particle internalization, permeabilizing the membrane allowing higher particle internalization. For the Gram-negative bacteria, due to membrane impermeability to **Van**, this effect was not observed.

The second control, **[Fe^{3+}DTPA-Bua_2]@SiO_2⊃Ru-Van**, was proposed in order to study whether the covalent attachment of the metal complex to the nanoparticle surface was essential for the nanoparticle's activity. Thereby, we designed a hybrid particle with **Fe^{3+}DTPA-Bua_2** complex adsorbed onto the surface of the nanoparticles (**[Fe^{3+}DTPA-Bua_2]@SiO_2⊃Ru-Van**). Internalization studies concluded no significant nanoparticle internalization in Gram-negative bacterial cells, and particle internalization comparable to uncoated particles in the case of *S. aureus* (Figure 3.S29 and Figure 3.S26).

[Fe^{3+}Ent]$^{3-}$@SiO_2⊃Ru-Van was designed as similar system to **[Fe^{3+}DTPA-Bua_2]@SiO_2⊃Ru-Va** but with a coating composed by a natural Fe^{3+}-siderophore complex, the catecholate-based siderophore enterobactin (Ent) (Full characterization in Figure 3.S17). With this control nanoparticle we wanted to explore if the present of a natural siderophore would lead to particle internalization even though it was not covalently attached. **[Fe^{3+}Ent]$^{3-}$** complex is recognised by the SstD receptor in *S.*

aureus and the FepA and PirA receptors in *E. coli* and *P. aeruginosa*, among others.[5] Internalization quantification, by SIM, revealed no significant particle internalization in any of the bacterial species studied upon incubation with **$[Fe^{3+}Ent]^{3-}$@SiO_2⊃Ru-Van** nanoparticles, even after siderophore-receptor overexpression (Figure 3.S28 and Figure 3.S29). These results evidenced the importance of the covalent attachment of the coating to the particle surface.

3.3.4. Molecular analogue of Fe^{3+}DTPA@SiO_2⊃Ru-Van: Fe^{3+}DTPA-$Amox_2$

Siderophore and siderophore-like antibiotic conjugates have been widely explored in the literature and standardized methodologies have been reported for their study.[9] Thereby, a Amoxicillin (**Amox**) DTPA-conjugate (**DTPA-$Amox_2$**) and its Fe(III) complex (**Fe^{3+}DTPA-$Amox_2$**) were developed as molecular analogues to the preciously explored nanoparticles, and their antibacterial activity and mechanism of action investigated.

3.3.4.1. Synthesis and characterization of DTPA-$Amox_2$ and Fe^{3+}DTPA-$Amox_2$

The antibiotic conjugate **DTPA-$Amox_2$** (Figure 3.30) was previously reported in the literature by S. Akter *et al*.[76] Nevertheless, reported synthesis procedure was based on nucleophilic opening of DTPA bis-anhydride by **Amox** in aqueous carbonate buffer. Due to synthesis conditions beside the desired **DTPA-$Amox_2$**, also single-conjugate DTPA-Amox and unconjugated DTPA were produced. Purification of **DTPA-$Amox_2$** by HPLC was required. Furthermore, purity of desired conjugated was only investigated by mass-spectrometry techniques.

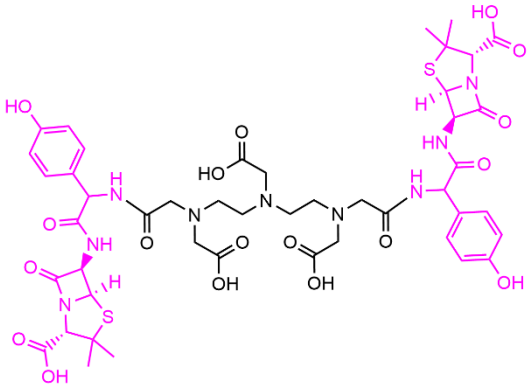

Figure 3.30. Chemical structure of **DTPA-Amox$_2$** with conjugate **Amox** molecules highlighted in pink.

Thereby, an improved methodology for the synthesis of **DTPA-Amox$_2$** was developed. Briefly, DTPA bis-anhydride and **Amox** (1:2 molar ratio) were reacted in anhydrous pyridine under N_2 flow at room temperature for 24 h (Figure 3.31). The absence of water would prevent the formation of side-products. **DTPA-Amox$_2$** was isolated as a white power.

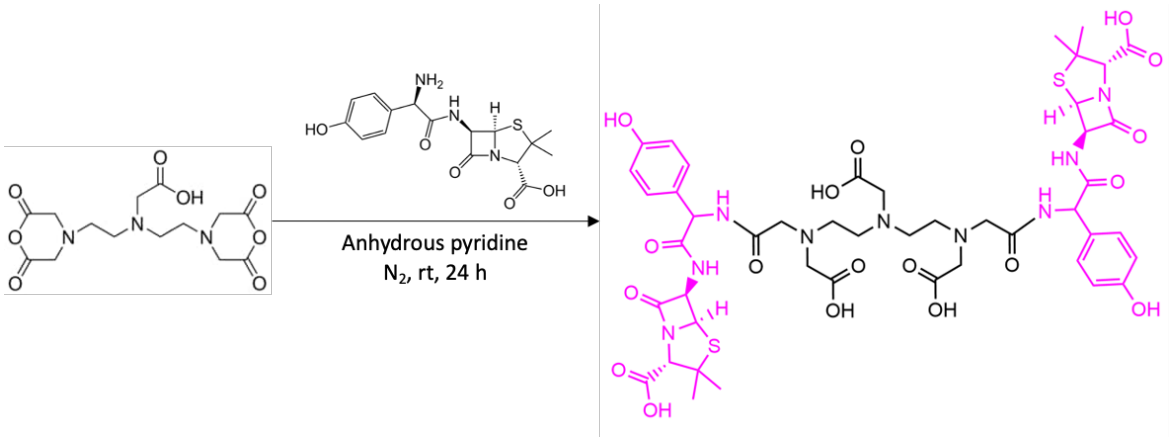

Figure 3.31. Synthesis scheme of **DTPA-Amox$_2$**.

Formation of **DTPA-Amox$_2$** was investigated by NMR (Figure 3.32-S33 and Figure 3.S30-33) and mass spectrometry studies (negative mode) (Figure 3.S.34). ^{1}H-NMR of **DTPA-Amox$_2$** in D_2O showed 11 different proton environments, 10 of them from the symmetrical molecule. H_F and H_G are equivalent protons arising in a single doublet. Similarly, H_D and H_E overlapped resulting in a multiplet. The successful conjugation of **Amox** to DTPA was firstly confirmed by the downfield shift of H_C to 5.37 ppm from 5.18 ppm due to proton deshielding upon amide formation (Figure 3.S30).

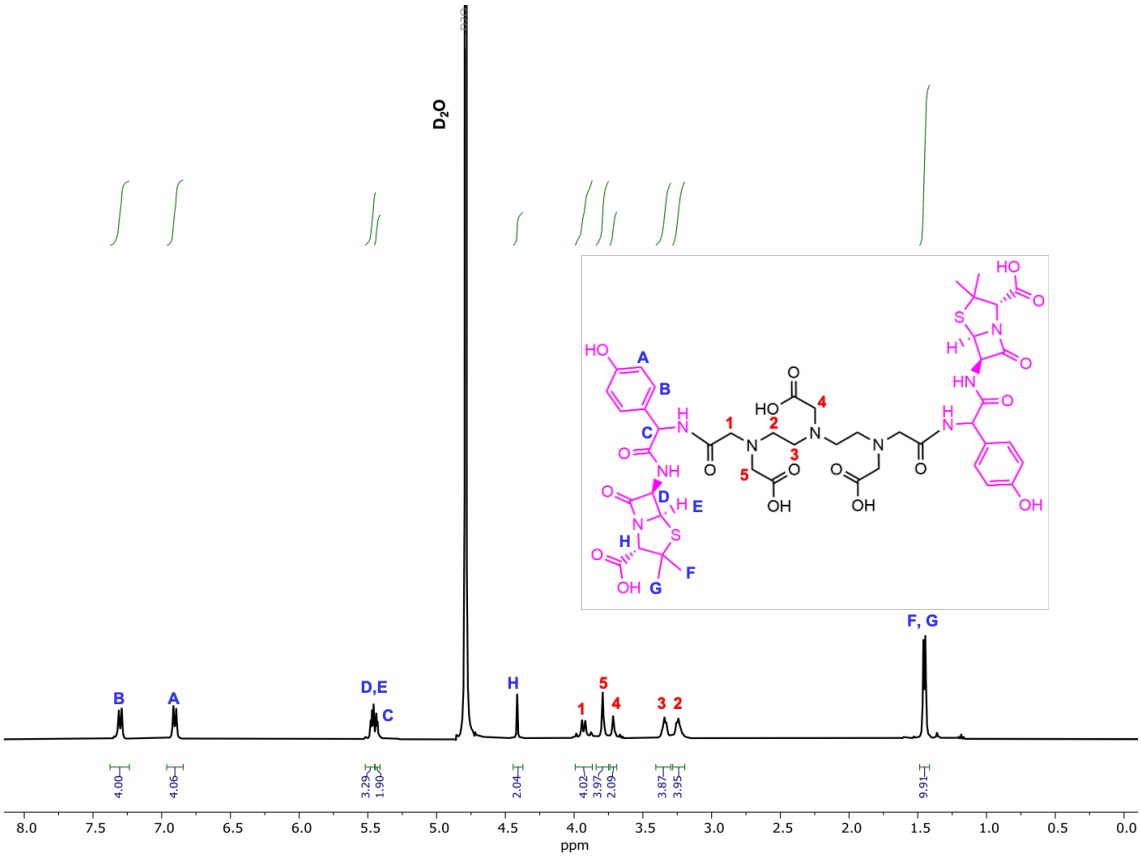

Figure 3.32. ^{1}H-NMR (400 MHz, D_2O) of **DTPA-Amox$_2$**.

DEPT ^{13}C-NMR spectrum showed 22 different signals, 20 assigned to the symmetric unit of the molecule, 14 of those assigned to CH_2 and carbonyl carbons and the other

8 assigned to CH_3 or CH carbons (Figure 3.33). Furthermore, Heteronuclear Single Quantum Coherence (HSQC) spectroscopy experiments (Figure 3.S32) further confirmed amide bond formation as cross peaks between H_C and H_B (56.9 ppm) were observed. Heteronuclear Multiple Bond Correlation (HMBC, Figure 3.S33) spectroscopy also confirmed amide bond formation as seen by cross peaks between H_C and C_{15} (174.3) and C_{16} (57.1). ESI-MS (positive mode) detected the $[M+H]^+$ specie with m/z = 1088.3363 (caldc. m/z = 1088.3341).

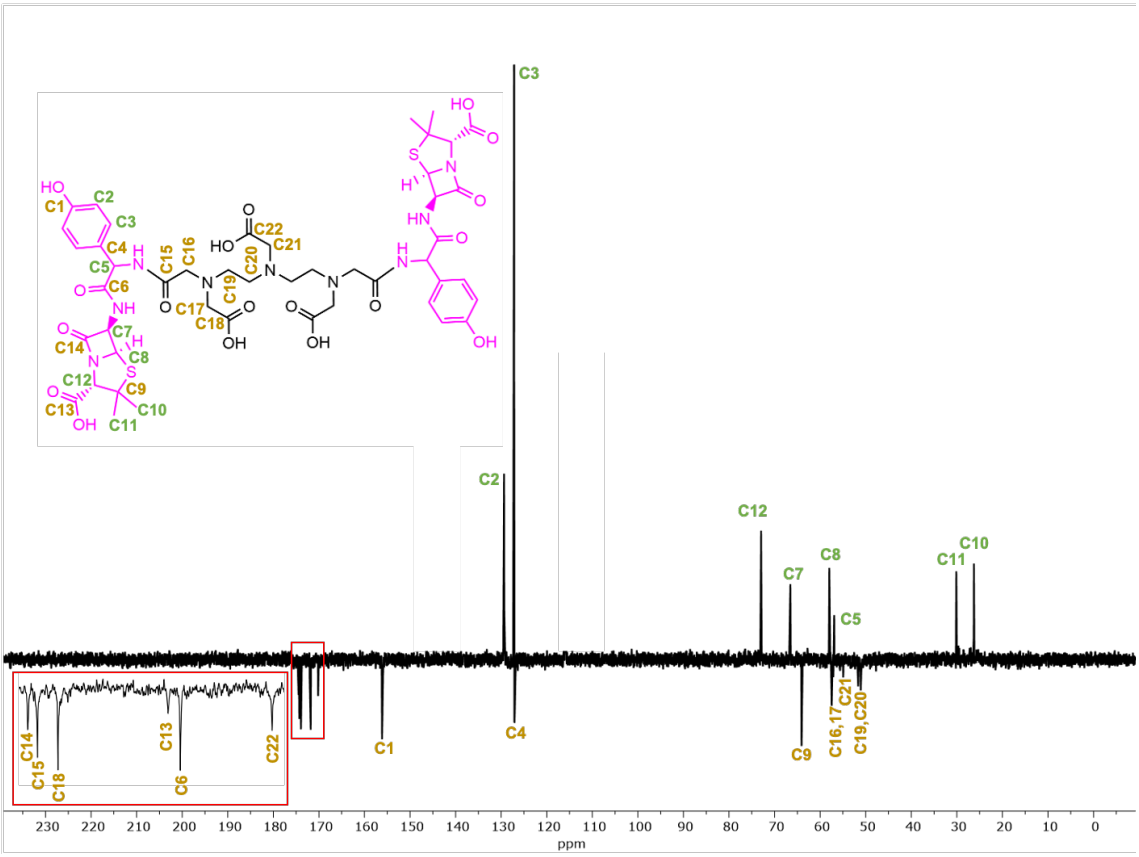

Figure 3.33. DEPT ^{13}C-NMR (101 MHz, D_2O) of **DTPA-Amox$_2$**

After synthesis of **DTPA-Amox$_2$**, its Fe(III) complex, **Fe^{3+}DTPA-Amox$_2$** (Figure 3.34), analogue was synthetized. Complexation was performed in aqueous solution of Fe(III) in presence of tetrabutylammonium hydroxide. Successful synthesis of **Fe^{3+}DTPA-**

Amox$_2$ was confirmed by ESI-MS were $[M+H]^+$ was detected with a m/z of 1141.2465 (theoretical m/z = 1141.2457).

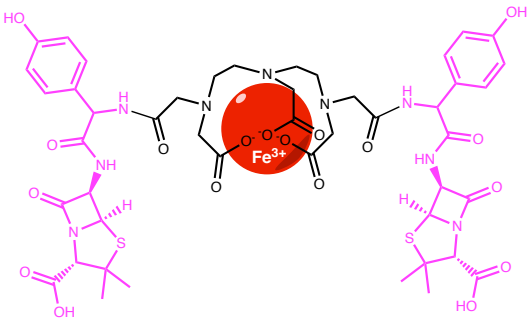

Figure 3.34. Chemical structure of **Fe^{3+}DTPA-Amox$_2$**.

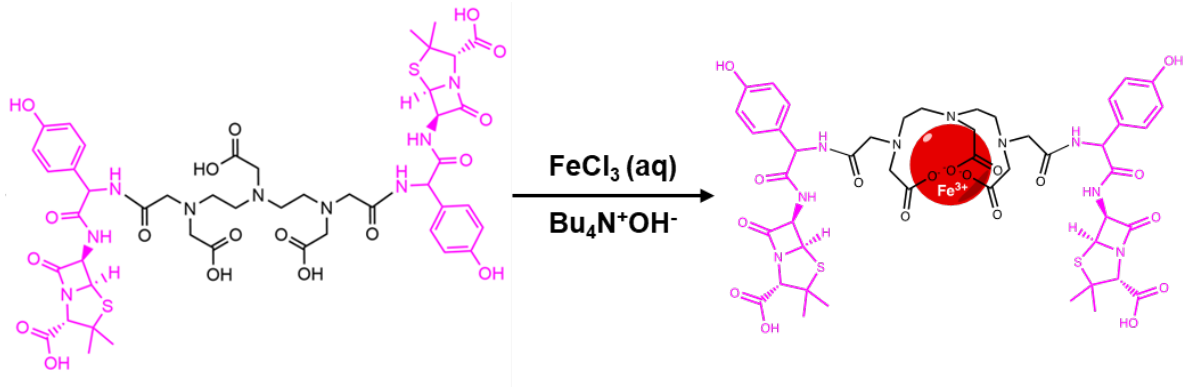

Figure 3.35. Synthesis scheme of **Fe^{3+}DTPA-Amox$_2$**.

3.3.4.2. Antimicrobial activity of DTPA-Amox$_2$ and Fe^{3+}DTPA-Amox$_2$

Firstly, we investigated the antibacterial activity of developed aminocarboxylate-antibiotic conjugates by MIC determination for wild type *S. aureus*, *E. coli* and *P. aeruginosa*. Similarly, we determined the MIC of **DTPA-Bua$_2$** plus Amoxicillin and **Fe^{3+}DTPA-Bua$_2$** plus amoxicillin (in 1:2 molar ratio as in **DTPA-Amox$_2$** and **Fe^{3+}DTPA-Amox$_2$**) to investigate if the antibacterial activity is associated with the

antibiotic moiety, amino carboxylate moiety or the conjugate. Table 3.3 contains the MIC values respect to the concentration of **Amox**. The MIC values respect to the concentration of the conjugate can be found in Table 3.S6.

Table 3.3. Minimal inhibitory concentration (MIC, mg/mL of **Amox**) of **Amox**, **DTPA-Amox$_2$**, **Fe^{3+}DTPA-Amox$_2$** and control mixtures (based on **Amox** concentration) for *S. aureus* (ATCC23851), *E. coli* (MG1655) and *P. aeruginosa* (PA14) upon shaking at 150 rpm at 37 °C in LB media. Depicted results are based on 3 biological replicas.

	S. aureus	***E. coli***	***P. aeruginosa***
Amox	0.2	4	8
DTPA-Amox$_2$	1.6	32	64
DTPA-Bua$_2$ + Amox	0.05	2	8
Fe^{3+}DTPA-Amox$_2$	0.4	4	4
Fe^{3+}DTPA-Bua$_2$ + Amox	0.2	4	8

Explored bacterial species present different MIC values for plain **Amox**. While **Amox** MIC for *S. aureus* is 0.2 μg/mL and for *E. coli* 4 μg/mL; for *P. aeruginosa* the MIC value is 8 μg/mL.

The **Amox**-relative MIC values for developed **DTPA-Amox$_2$** conjugate, however, increased in all cases respect to free **Amox**. This decrease in antibacterial activity was associated with the mechanism of action of the conjugated antibiotic. **Amox** inhibits cell wall synthesis by binding to the PBP in a one-to-one antibiotic – binding site mode.[77] Even if the developed conjugate bears two antibiotic molecules, we believe, upon further study, that only one of the antibiotic moieties was able to interact with the PBP, making the second conjugated **Amox** not able to reach another PBP binding site. Moreover, MIC values of the **DTPA-Bua$_2$**+**Amox** mixture, containing 1:2 ratio **DTPA-Bua$_2$**:**Amox**, presented a decrease in **Amox**-relative MIC value for *S. aureus* and *E. coli,* while no difference was observed for *P. aeruginosa*. The additive

effect of DTPA and antibiotics was previously described for antibiotics and widely reported in the literature, as it increases the cell-wall permeability.[78,79] Nevertheless, *P. aeruginosa* presents a resistance mechanism against the chelator, as previously explained.

Antibacterial study of **Fe^{3+}DTPA-Amox$_2$** resulted in higher activity compared with **DTPA-Amox$_2$**, with **Amox**-related MIC values of 0.05 μg/mL for *S. aureus*, 4 μg/mL for *E. coli* and 8 μg/mL for *P. aeruginosa*. Similar to the DTPA-coated particles, chelating Fe(III) enhanced the activity of the system. In case of *S. aureus*, **Fe^{3+}DTPA-Amox$_2$** showed higher activity than free **Amox**, based on **Amox** concentration, which is mentioning. In case of Gram-negative species, the same MIC values were observed, but, as only one of conjugated **Amox** would be able to interact with the penicillin-binding protein (PBP), we could conclude that, in Gram-negative species, Fe(III) chelation also increases the activity of the conjugate.

3.3.4.3. Effect of Fe(III) availability on antibacterial activity of conjugates

As previously explored with nanoparticles, we investigated the antibacterial activity of **DTPA-Amox$_2$** of **Fe^{3+}DTPA-Amox$_2$** upon overexpression of siderophore-receptors. Equally, incubation of bacteria inoculate in reduced Fe(III) MOPS media was employed for siderophore-receptor overexpression. CFU/mL was calculated after 2 h incubation with desired compounds, at MIC concentrations, in PBS buffer (0.1 M, pH 7.4) (Figure 3.36).

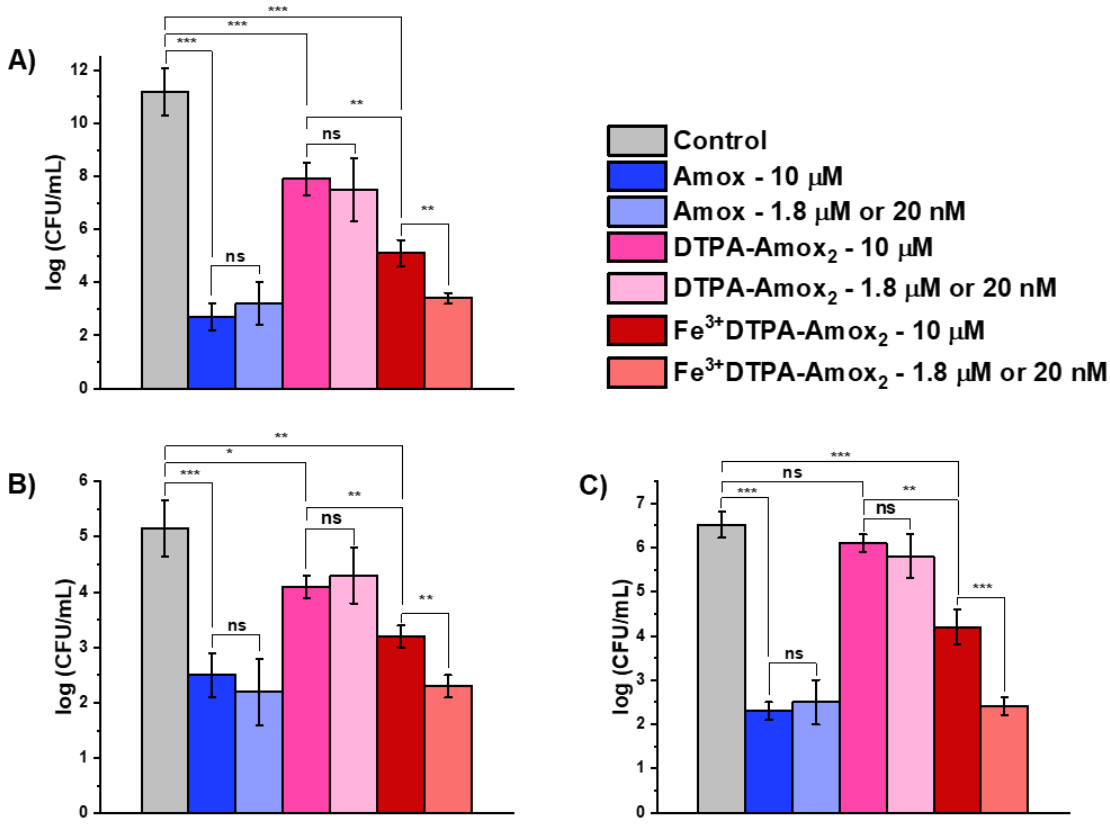

Figure 3.36. Viability of (A) *S. aureus* (ATCC23851), (B) *E. coli* (MG1655) and (C) *P. aeruginosa* (PA14) after 2 h incubation with desired compounds in PBS buffer (0.1 M, pH 7.4) at MIC concentrations. Bacterial cells were incubated in standard Fe(III) concentration (10 μM) or reduced (1.6 μM for *S. aureus* and 20 nM for *E. coli* and *P. aeruginosa*) MOPS media prior the experiments. Control samples was untreated and incubated in PBS buffer (0.1 M, pH 7.4). Depicted values are average ± SD, n= 3 biological replicas. Statistical analysis performed by t-test; ns = $p > 0.05$, * = $p < 0.05$, ** = $p < 0.01$, *** = $p < 0.001$.

In all bacterial species investigated there was no difference between Fe(III) concentrations observed for free **Amox** and **DTPA-Amox$_2$** , while a significant increase in activity was detected for **Fe^{3+}DTPA-Amox$_2$** upon siderophore-receptor overexpression. These results are in good agreement with explored nanoparticles, where a significant increase in activity upon siderophore-receptor overexpression was only observed in case of Fe^{3+}DTPA-coated nanoparticles, indicating that the developed molecular analogue displayed a similar mechanism of action to

nanoparticles and confirming the role of siderophore-uptake systems in the mechanism of action of the complex.

3.3.4.4. Identification of involved siderophore-uptake system in Fe^{3+}DTPA-Amox$_2$ activity.

Finally, we decided to identity the siderophore receptors involved in the activity of developed molecular conjugate to determine whether the conjugate behaves in the same way that the Fe^{3+}DTPA-coated nanoparticles. With that aim, the bacterial mutants previously employed with nanoparticles were explored (Table 3.X). Bacterial cells were incubated in low Fe(III) concentration MOPS for 2 h prior incubation with **Fe^{3+}DTPA-Amox$_2$** (MIC concentration of the wild type strain) for 2 h and viability was assessed by CFU counting (Figure 3.37).

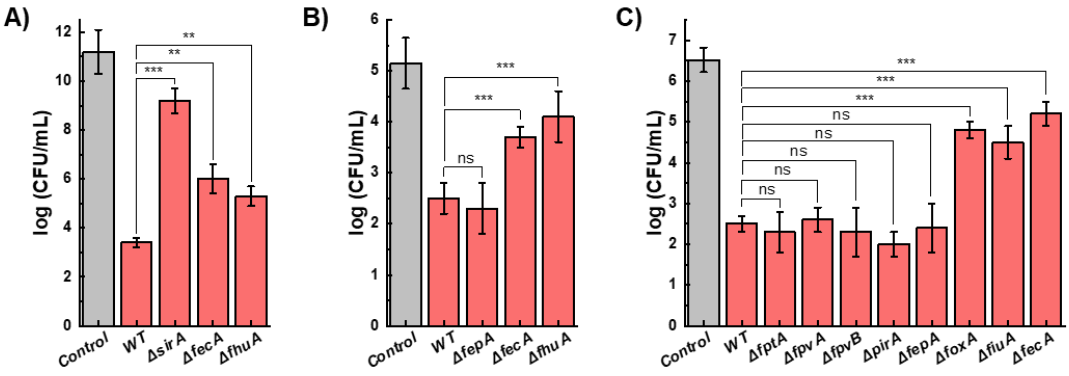

Figure 3.37. Viability of (A) *S. aureus*, (B) *E. coli* and (C) *P. aeruginosa* strains upon incubation with **Fe^{3+}DTPA-Amox$_2$** for 2 h in PBS buffer (0.1 M, pH 7.4). *S. aureus* were incubated in 1.8 μM Fe(III) MOPS media and *E. coli* and *P. aeruginosa* in 20 nM Fe(III) MOPS media 2 h at 37 ºC prior to the experiment in order to trigger siderophore-receptor overexpression. Control samples was untreated and incubated in PBS buffer (0.1 M, pH 7.4). Depicted values are average ± SD, n=3 biological replicas. Statistical analysis performed by t-test; ns = $p > 0.05$, * = $p < 0.05$, ** = $p < 0.01$, *** = $p < 0.001$.

Comparison between untreated (control) and wild type strains of all species showed a significant viability decrease upon incubation with **Fe^{3+}DTPA-Amox$_2$**. Nevertheless, for mutant strains different viabilities were observed. In the case of *S. aureus*, the biggest increase in viability compared to WT was observed for *ΔsirA* strains, which has inactivation of the carboxylate-based siderophore membrane receptor. In case of *ΔfecA* and *ΔfhuA* strains, with inactivated receptors for citrate-based and hydroxamate-based receptors, also an increase in viability compared to WT was observed, but not as prominent as in the case of *ΔsirA*. The increase in viability in strains lacking the SirA, FecA and FhuA receptors cases suggests that, as in case of the nanoparticles, those receptors are involved in the conjugate's internalization.

In case of *E. coli*, a similar viability decrease, compared with control experiments, was observed for the WT and *ΔfepA* strains treated with **Fe^{3+}DTPA-Amox$_2$**. *fepA* encodes the outer-membrane receptor for the catecholate-based siderophore Ent.[68] We previously observed no change in nanoparticles activity upon *fepA* inhibition and it was associated with the disparity between **Fe^{3+}DTPA** and **$[Fe^{3+}Ent]^{3-}$** shape, size, and charge. Nevertheless, inactivation of citrate-based (*ΔfecA*) and hydroxamate-based (*ΔfhuA*) receptors led to an increase in cell viability compared with WT, indicating the involvement of theses receptors in the uptake of the **Fe^{3+}DTPA-Amox$_2$** conjugate as previously described for **Fe^{3+}DTPA@SiO_2⊃Ru-Van** nanoparticles.

Finally, investigation of the antibacterial activity of **Fe^{3+}DTPA-Amox$_2$** in *P. aeruginosa* strains upon receptor overexpression revealed a decrease in activity the conjugate in the case of *ΔfoxA*, *ΔfiuA* and *ΔfecA* strains with inactivation of hydroxamate-based and citrate-based siderophore receptors, following the same trend in *E. coli*. However,

inactivation of catecholate-based (*ΔfepA* and *ΔpirA*) or mixed *(ΔfptA*, *ΔfpvA* and *ΔfpvB*) siderophore receptors did not impact the activity of the conjugate. Like in the case of *E. coli*, differences between the native siderophores recognised by those receptors could hinder conjugate interaction, and hence, internalization.

In conclusion, we identified that the siderophore-receptors that are involved in the mechanism of action of **Fe^{3+}DTPA-Amox$_2$** are those that selectively recognise citrate-based, carboxylate-based, and hydroxamate-based siderophores in all bacterial species studied. Furthermore, interestingly, the receptors involved are the same that mediate the internalization of **Fe^{3+}DTPA@SiO_2⊃Ru-Van** nanoparticles. All these findings confirmed that the molecular conjugate analogue of nanoparticles possess the same mechanism of action that nanoparticles which supposes a step forward for the design of nanoparticle-based DDS inspired by bacteria-recognisable molecules.

3.4. Conclusion

In this study, a new strategy for **SiO_2** nanoparticles has been developed. A Fe^{3+}DTPA-coating was achieved by in situ formation of the Fe(III)-aminocarboxylate complex. The affinity constant between Fe(III) and the bisamide aminocarboxylate was found to be similar to carboxylate-based siderophores. The presence of the Fe^{3+} in hybrid nanoparticles (**Fe^{3+}DTPA@SiO_2⊃Ru-Van**) was confirmed by a plethora of surface characterization techniques. **Fe^{3+}DTPA@SiO_2⊃Ru-Van** nanoparticles displayed cumulative **Van** release alongside a stable red luminescence from the encapsulated **Ru**. Finally, particles showed good biocompatibility properties based on MTT assays.

Novel nanoparticles displayed enhanced antibacterial properties compared with the DTPA-coated nanoparticles, even in those species were DTPA-coated nanoparticles

did not have a significant activity (*P. aeruginosa* and *B. cenocepacia*). The mechanism of action of nanoparticles was explored, focusing on the interactions between nanoparticles and bacterial siderophore uptake systems. Firstly, nanoparticles presented enhanced activity in Fe(III) reduced conditions, where siderophores uptake systems are overexpressed. Subsequently, the receptors involved in the activity of nanoparticles were identified using membrane siderophore receptor knock outs of representative bacterial species. Receptors specific for carboxylate- and hydroxamate-based siderophores were found to be involved as their suppression decreased nanoparticles activity.

Nanoparticle-cell interactions and internalization of **Fe^{3+}DTPA@SiO_2⊃Ru-Van** nanoparticles was explored using SIM and TEM microscopy. Novel nanoparticles displayed higher internalization degree in bacterial cells compared with uncoated and DTPA-coated nanoparticles, even in case of *P. aeruginosa*, where no particle internalization was observed for previous **DTPA@SiO_2⊃Ru-Van** nanoparticles. Furthermore, upon suppression of involved receptors lower internalization was observed, highlighting their role as nanoparticles uptake systems.

Finally, a molecular analogue of the designed nanoparticles, **Fe^{3+}DTPA-$Amox_2$**, was designed and explored. The analogue also displayed enhanced antibacterial activity upon siderophore-receptor overexpression. The same receptors involved in the activity of nanoparticles were found to be linked with activity of **Fe^{3+}DTPA-$Amox_2$**, as upon their suppression the analogues; activity decreased.

Hereby, **Fe^{3+}DTPA@SiO_2⊃Ru-Van** represents the first example of a nanoparticle system whose internalization is mediated by siderophore-uptake systems. Furthermore, thedeveloped coating is also able to overcome the resistance

mechanism of aminoarabinosylosis expressing bacterial species and allowing the delivery of Van into *P. aeruginosa* and *B cenocepacia* cells.

3.5. Experimental section

3.5.1. Synthetic procedures

All chemicals and consumables were purchased from Sigma-Aldrich and they were of the higher quality available.

Fe^{3+}DTPA-Si_2. Diethylenetriaminepentaacetic acid dianhydride (100 mg, 0.28 mmol), diisoporpylamine (DIPA, 125 μL, 0.97 mmol, 3.5 eqv) and 4-dimethylamonopyridine (DMAP, catalytic amount) were dissolved in anhydrous pyridine (2 mL) under nitrogen. Then, 3-(aminopropyl)triethoxysilane (APTES, 37 μL, 0.6 mmol, 2.1 eqv) was added dropwise and final solution stirred at room temperature under N_2 overnight. Then anhydrous $FeCl_3$ (45.5 mg, 0.28 mL, 1 eqv) was added and the resulted yellow solution was stirred at room temperature for 2 h. The formed complex was isolated by precipitation in hexane. Resulting yellow precipitate was further washed with hexane and dried under vacuum (202.6 mg, 85 %). ESI-MS (m/z) = 851.3115 ($[M-H]^-$, calcd. 851.3104). FTIR (cm^{-1}) = 3215 (w, N-H), 2965 (m, C-H_2), 2920 (m, C-H_2), 2875 (m, N-H), 1653 (s, C=O), 1355 (m, C-OCH_2CH_3), and 1073 (s, C-O).

Fe^{3+}DTPA@SiO_2. **Fe^{3+}DTPA-Si_2** and desired uncoated **SiO_2** nanoparticles were added to anhydrous pyridine with a final **SiO_2**:**Fe^{3+}DTPA-Si_2** mass ratio of 1:3. Formed suspension was stirred at room temperature overnight. Coated nanoparticles, **Fe^{3+}DTPA@SiO_2**, were centrifuged and washed with water to remove unreacted

Fe^{3+}DTPA-Si_2. Finally, coated nanoparticles were dried under vacuum. FTIR (cm^{-1}) = 3215 (w, N-H), 2965 (m, C-H2), 2920 (m, CH2), 2875 (m, N-H), 1653 (s, C=O), and 1073 (s, C-O); (+)MALDI-ToF (m/z) = 717.291 $[C_{20}H_{24}O_{13}N_5Si_2Fe+Na]^+$ (calcd. = 717.290).

DTPA-Bua_2, butyl-derivative bisamide diethyelenetriaminepentaacetic acid. Synthesis was reproduced from L. L. Ruston e*t al.*[80] Diethylenetriaminepentaacetic acid dianhydride (0.10 g, 0.28 mmol) added in small portions to ice-cold 1-butylamine (1.4 mL, 14 mmol) under vigorous stirring. Water (1 mL) was added, and the solution was stirred at room temperature for 24 h. Then the volumen was reduced under vacuum and obtained yellow oil dissolved in water (5 mL). The solution was acidified with concentrated HCl to pH 2 and a white precipitate was formed. The solid was further washed with water (10 mL), acetone (10 mL) and diethyl ether (10 mL) and then dried under vacuum. (0.11 g, 80 %). ^{1}H NMR (400 MHz, DMSO-d_6): δ=8.02 (quintet, 2 H; N*H*$CH_2CH_2CH_2CH_3$), 3.42 (s, 2 H; NC*H*$_2CO_2H$ central), 3.36 (s, 4 H; NC*H*$_2CO_2H$ terminal), 3.32 (s, 4 H; NC*H*$_2CO$), 3.01 (quartet, 4 H, NC*H*$_2CH_2N$), 2.92 (quartet, 4 H, NCH_2CH_2N), 2.79 (sextet, 4 H; NC*H*$_2CH_2CH_2CH_3$), 1.39 (m, 4 H; $NCH_2CH_2CH_2CH_3$), 1.30 (m, 4 H; $NCH_2CH_2CH_2CH_3$), 0.87 (t, 6 H; $NCH_2CH_2CH_2CH_3$) ppm; ^{13}C NMR (100 MHz, DMSO-d_6): δ=174.6 (CO_2H terminal), 168.4 (CO_2H central), 171.2 (CONH), 56.9, (NCH_2CONH), 58.0 (NCH_2CO_2H terminal), 55.4 (NCH_2CO_2H central), 52.6, 51.1 (NCH_2CH_2N), 38.7 ($NCH_2CH_2CH_2CH_3$), 31.2 ($NCH_2CH_2CH_2CH_3$), 21.5 ($NCH_2CH_2CH_2CH_3$), 13.4 ppm ($NCH_2CH_2CH_2CH_3$); (+)ESI-MS (m/z) = 504.3039 ($[M+H^+]^+$, calcd. 504.3033). FT-IR (cm^{-1}) = 3227 (w, N-H), 2947 (m, C-H_2), 2866 (m, C-H_2), 1616 (s, C=O_{amide}), 1555 (s, C=O_{acid}), 1375 (m, C-H), 1305 (m, N-$CH_2CH_2CH_2CH_3$).

Fe^{3+}DTPA-Bua_2. **DTPA-Bua_2** (50 mg, 0.1 mmol) was added to an aqueous solution of $FeCl_3$ (2 mL, 0.2 M, 0.1 mmol Fe^{3+}, 1 eqv). The solution was diluted to 10 mL and stirred until all solid was dissolved. Tetrabutylammonium hydroxide (40 % w/w H_2O) was added until pH~5 and the solution stirred at room temperature for 1 h. Then, the volume was reduced and the complex isolated by precipitated after acetonitrile addition. The yellow solid, **Fe^{3+}DTPA-Bua_2**, was washed with diethyl ether (2 x 10 mL) and dried under vacuum (53.4 mg, 96 %). ESI-MS (m/z) = 557.2153 ($[M+H]^+$, calcd. 557.2148).

DTPA-$Amox_2$, **amoxicillin-derivative bisamide diethyelenetriaminepentaacetic acid**. Diethylenetriaminepentaacetic acid dianhydride (0.5 g, 1.4 mmol) was dissolved in anhydrous pyridine (20 mL) under nitrogen. To the stirred solution, amoxicillin (Amox, 1.2 g, 3.1 mmol, 2.2 eqv) was added and the resulting solution stirred at room temperature for 24 h. Then the volume was reduced and the formed oil was dissolved in water (5 mL) and acidified with concentrated HCl to pH~2 leading to a white precipitate. The solid was then washed with diethyl ether (2 x 20 mL) and dried under vacuum (1.35 g, 92 %). ^{1}H-NMR (400 MHz, D_2O) = 7.30 (d, 4H, *J = 7.1 Hz*, H_B), 6.9 (d, 4H, *J = 7.1 Hz*, H_C), 5.47 (m, 4H, $H_D + H_E$), 5.43 (d, *J = 3.20 Hz*, H_C), 4.41 (s, 2H, H_H), 3.93, (quartet, 4H, 16.2 Hz, H_1), 3.79 (s, 2H, H_4), 3.72 (s, 2H, H_5), 3.34 (quartet, *J = 5.4 Hz*, 4H, H_3), 3.25 (quartet, *J = 5.4 Hz*, 4H, H_3), 1.45 (d 12 H, *J = 6.0 Hz*, $H_F + H_G$) ppm; ^{13}C-NMR (100 MHz, D_2O) = 174.5 (C_{14}), 174.3 (C_{15}), 173.9 (C_{18}), 172.0 (C_{13}), 171.8 (C_6), 170.2 (C_{22}), 156.2 (C_1), 129.3 (C_2), 127.1 (C_3), 127.0 (C_4), 72.9 (C_{12}), 66.5 (C_7), 57.9 (C_8), 57.5 (C_9, C_{17}), 57.1 (C_{16}), 56.9 (C_5), 54.9 (C_{21}), 51.1 (C_{19}), 30.1 (C_{11}),

26.8 (C_{10}) ppm. ESI-MS (m/z) = 1088.3363 ([M+H]+, caldc. 1088.3341). FT-IR (cm^{-1}) = 3450 (s, N-H), 3541 (s, N-H), 3031 (m, C-H_{Ar}), 2967 (m, C-H_2), 1779 (s, C=$O_{\beta\text{-lactam}}$), 1682 (s, C=O), 1247 (m, N-C), 736 (m, S-C).

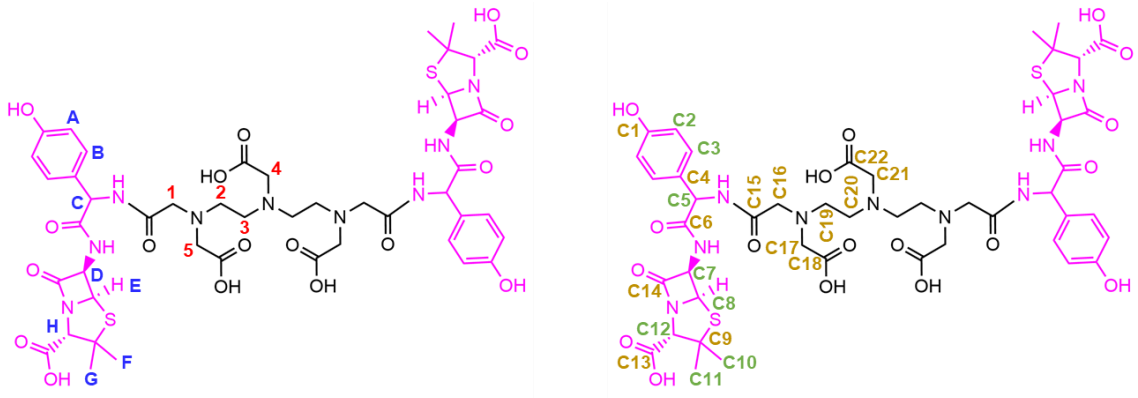

Synthesis of Fe^{3+}DTPA-Amox$_2$. **DTPA-Amox$_2$** (50 mg, 0.05 mmol) was added to an aqueous solution of $FeCl_3$ (2 mL, 0.1 M, 0.05 mmol Fe^{3+}, 1 eqv). The solution was diluted to 10 mL and stirred until all solid was dissolved. Tetrabutylammonium hydroxide (40 % w/w H_2O) was added until pH~5 and the solution stirred at room temperature for 1 h. Then, the volume was reduced and the complex isolated by precipitated after acetonitrile addition. The yellow solid, **Fe^{3+}DTPA-Amox$_2$**, was washed with diethyl ether (2 x 10 mL) and dried under vacuum (53.4 mg, 96 %). ESI-MS (m/z) = 1141.2465 ($[M+H]^+$, calcd. 1141.2457).

3.5.2. Methodology

Isothermal Titration Calorimetry (ITC). Binding constant of Fe^{3+} with **DTPA-Bua$_2$** was determined by ITC in PBS (0.1 M, pH 7.4) at 25 °C titrating a solution of $FeCl_3$ (30

mM) into a **DTPA-Bua$_2$** solution (2.5 mM). Recorded data was fitted using the Malvern MicroCal PEAQ-ITC V1.41 software.

Antibiotic release studies. Full methodology can be found in chapter 2, section 4.

MTT (3-(4,5-dimethylthiazol-2-yl)-2,5-diphenyltetrazolium bromide) cell viability assays. Full methodology can be found in chapter 2, section 4.

Minimal Inhibitory Concentration (MIC) **determination**. Full methodology can be found in chapter 2, section 4. Nanoparticles MIC was investigated between 10 mg/mL and 0.1 mg/mL and molecular conjugates' between 100 μg/mL and 0.01 μg/mL.

Fe(III) dependency in bacterial growth. With the aim of studying the effect of media Fe(III) content in the growth of bacterial cells, single colonies of bacteria inculated into MOPs minimal medium with different Fe(III) concentration (10 μM, 7.5 μM, 3.7 μM, 1.8 μM, 0.6 μM and 20 nM) at 37 ^{o}C shacking at 150 rpm. At different time points aliquots were taken, diluted and plated in LB agar plates to enumerate CFU/mL. Plates were incubated at 37 ^{o}C overnight and CFU/mL calculated. Determined viability is based on 3 biological replicates.

Bacteria killing kinetics. Bacterial single colonies were incubated in 5 mL of 10 μM Fe(III) MOPs overnight at 37ºC and 150 rpm. Overnight cultures were centrifuged and washed twice with PBS buffer (0.1 M, pH 7.4). Then, 1:100 dilution was done in MOPs medium with standard (10 μM) or limited Fe(III) concentrations (1.8 μM for *S. aureus* and 20 nM for *E. coli* and *P. aeruginosa*). Diluted cell suspensions were incubated for 2 h at 37ºC and 150 rpm to promote siderophore receptor overexpression. Then, cells were centrifuged, washed twice with PBS buffer (0.1 M, pH 7.4) and resuspended in PBS suspension of desired nanoparticles or compounds concentration at MIC. Suspensions were incubated at 37ºC and 150 rpm for 24 h and aliquots were taken at different time points. Finally, aliquots were diluted, plated in LB agar, incubated overnight at 37 ºC and resulting CFU/mL calculated. Determined viability is based on 3 biological replicates.

Structured illumination microscopy (SIM) imaging. Full methodology can be found in chapter 2, section 4.

Transmission electron microscopy (TEM) imaging of bacterial cells. . In order to study the cell-uptake of nanoparticles, overnight cultures in 10 mM Fe(III) MOPs wre centrifuged, washed twice with PBS buffer (0.1 M, pH 7.4), resuspended in standard (10 μM) or limited (1.8 mM for *S. aureus* strains or 20 nM for *E. coli* and *P. aeruginosa* strains) Fe(III) MOPs medium and incubated 2 h at 37 ºC and 150 rpm. Then, cells were centrifuged and redisposed in PBS buffer (0.1 M, pH 7.4) containing 2.5 mg/mL of desired nanoparticles and incubated at 37 ºC and 150 rpm for 1 h or 2 h. 1 mL of incubated cells was centrifuged, washed with PBS (0.1 M, pH 7.4), redispersed in PBS

containing 4 % glutaraldehyde and incubated 1 h at room temperature. Then, fixed cells were centrifuged, washed with PBS (0.1 M, pH 7.4) and dehydrated by subsequent washing with PBS solutions of increasing ethanol concentration (5%, 15 %, 25%, 50%, 75%, 90% and 100%). Finally, fixed and dried cells were placed onto TEM grids for imaging (Agar Scientific 400 mesh Cu/C coated grids, JEOL 1400 TEM instrument).

3.6. Appendix

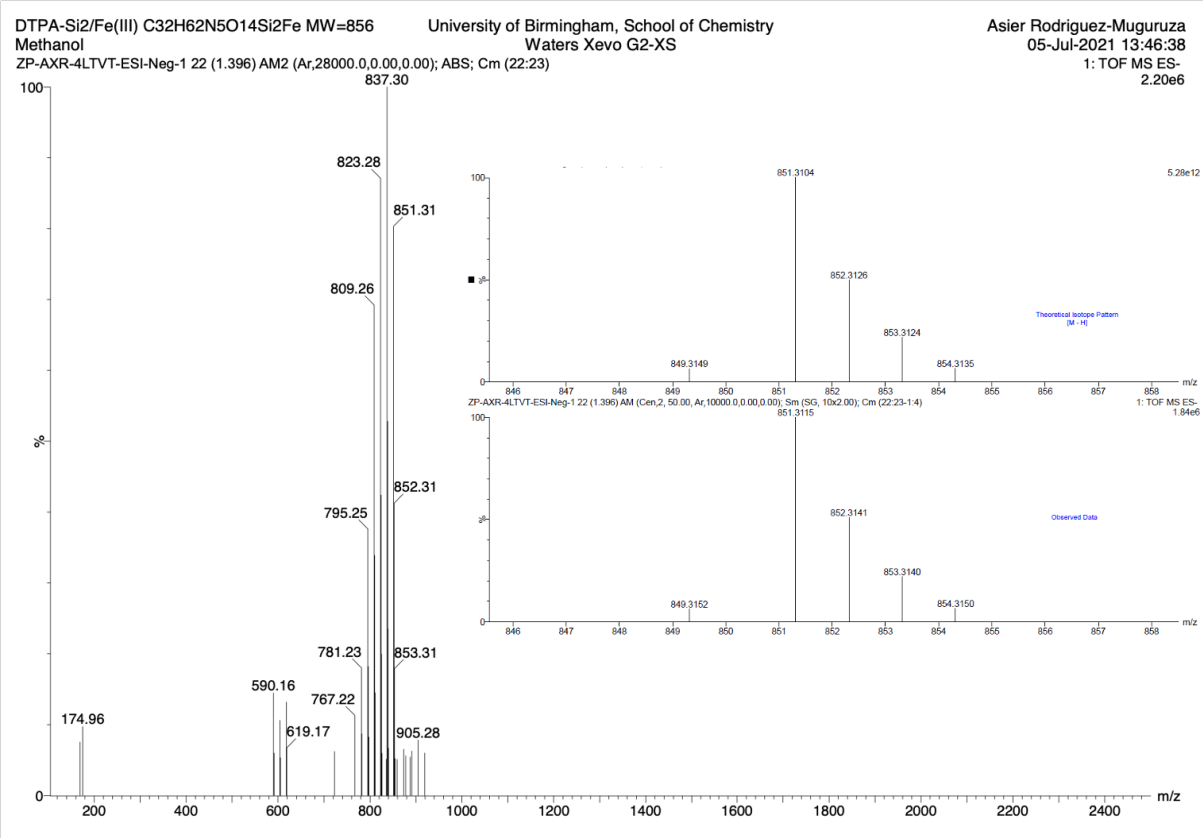

Figure 3.S1. (-)ESI-MS of **Fe^{3+}DTPA-Si_2**.

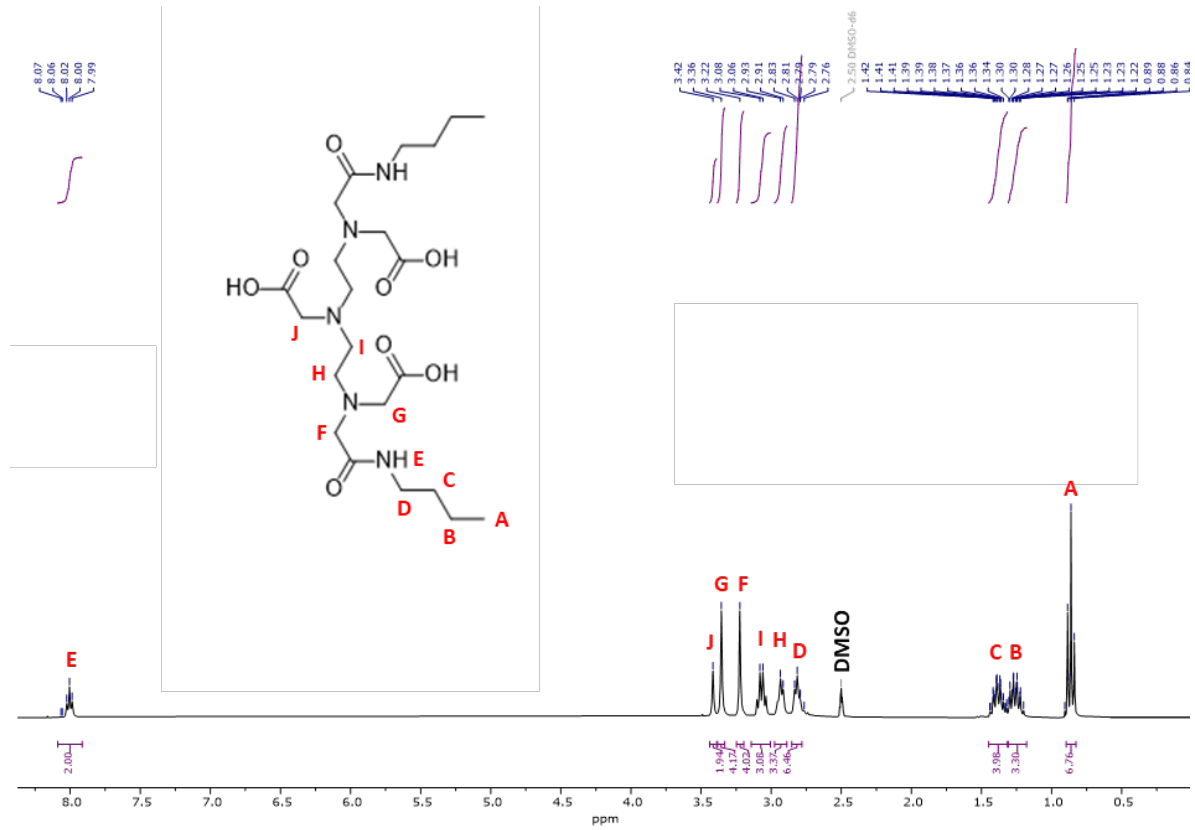

Figure 3.S2. ^{1}H-NMR (400 MHz, *d*$_6$-DMSO) of **DTPA-Bua$_2$**

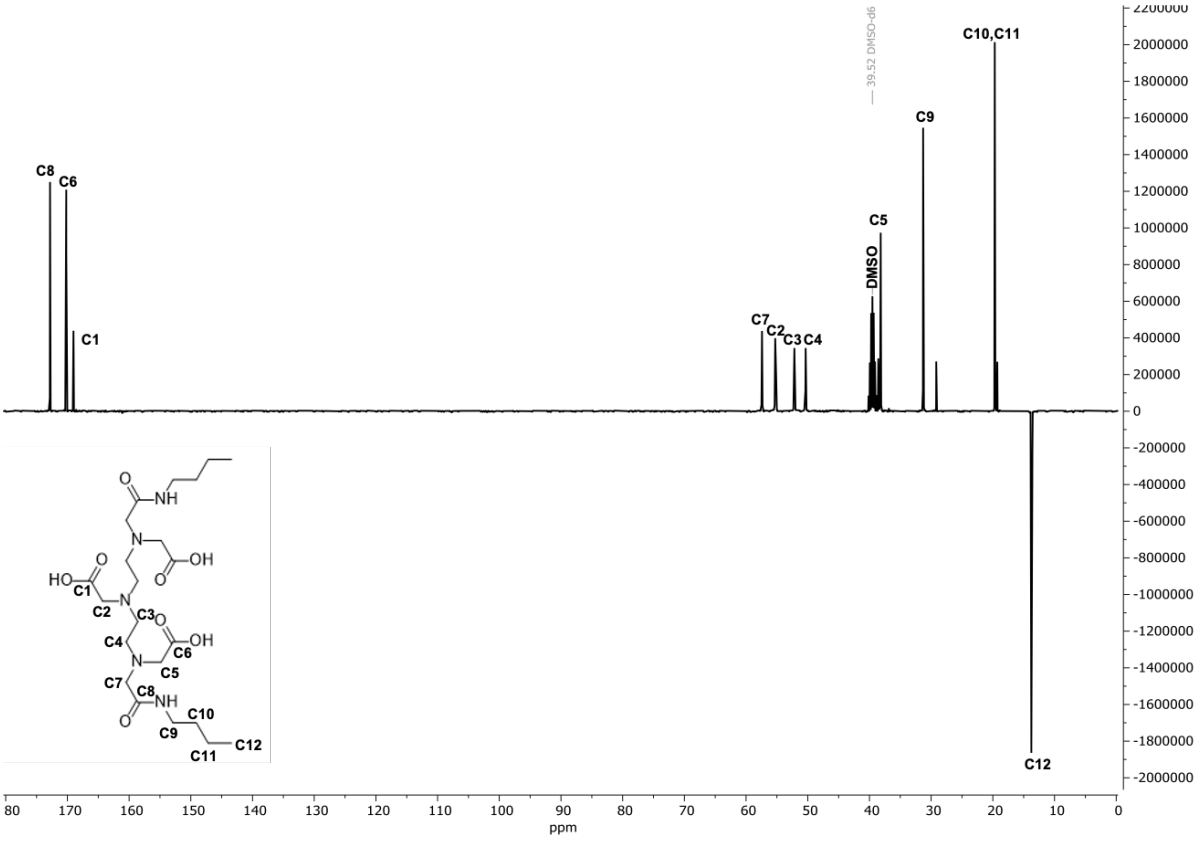

Figure 3.S3. ^{13}C-NMR (101 MHz, *d*$_6$-DMSO) of **DTPA-Bua$_2$**

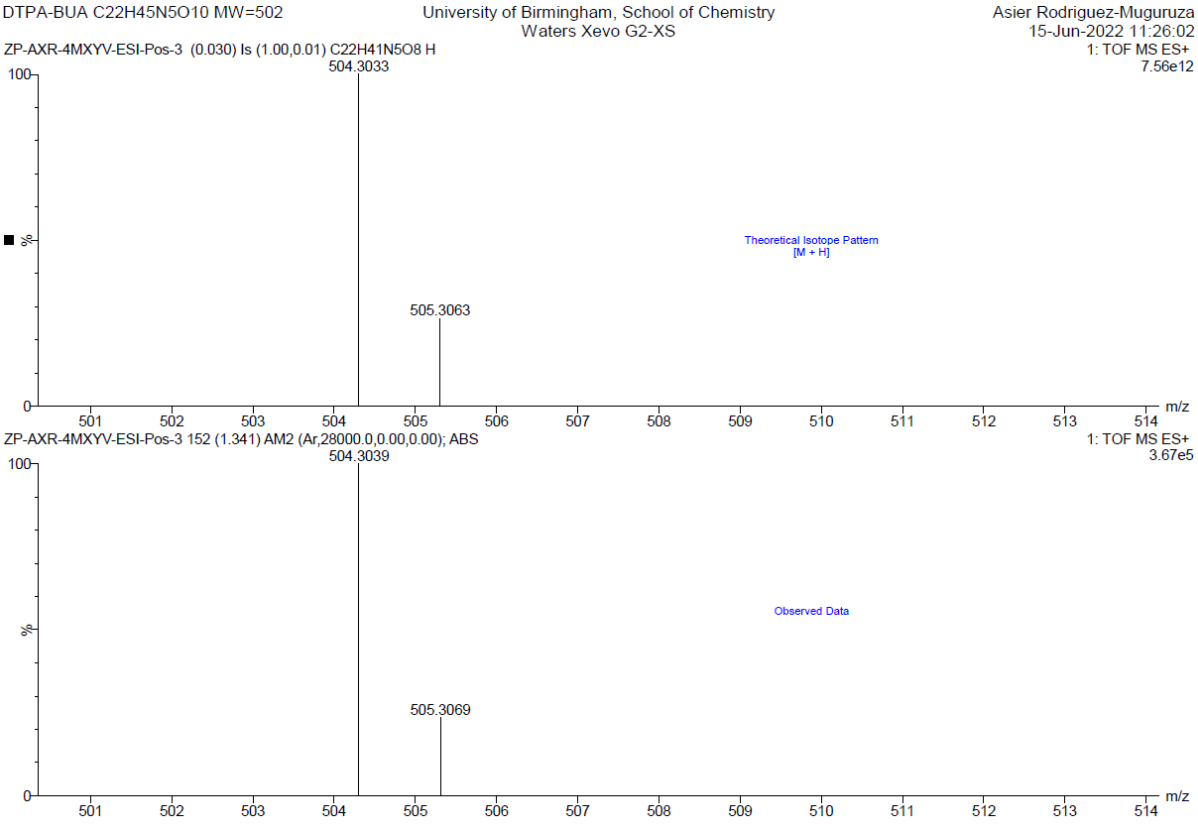

Figure 3.S4. (+)ESI-MS of **DTPA-Bua$_2$**.

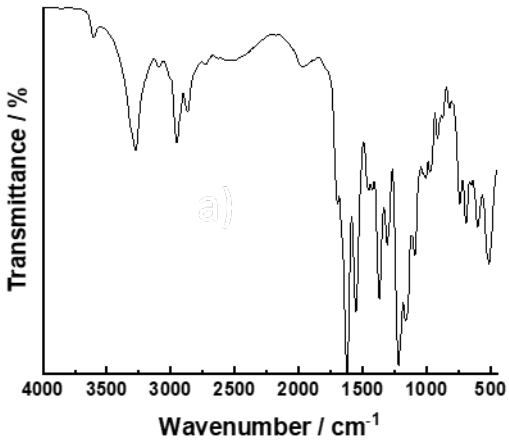

Figure 3.S5. FT-IR spectrum of **DTPA-Bua$_2$**.

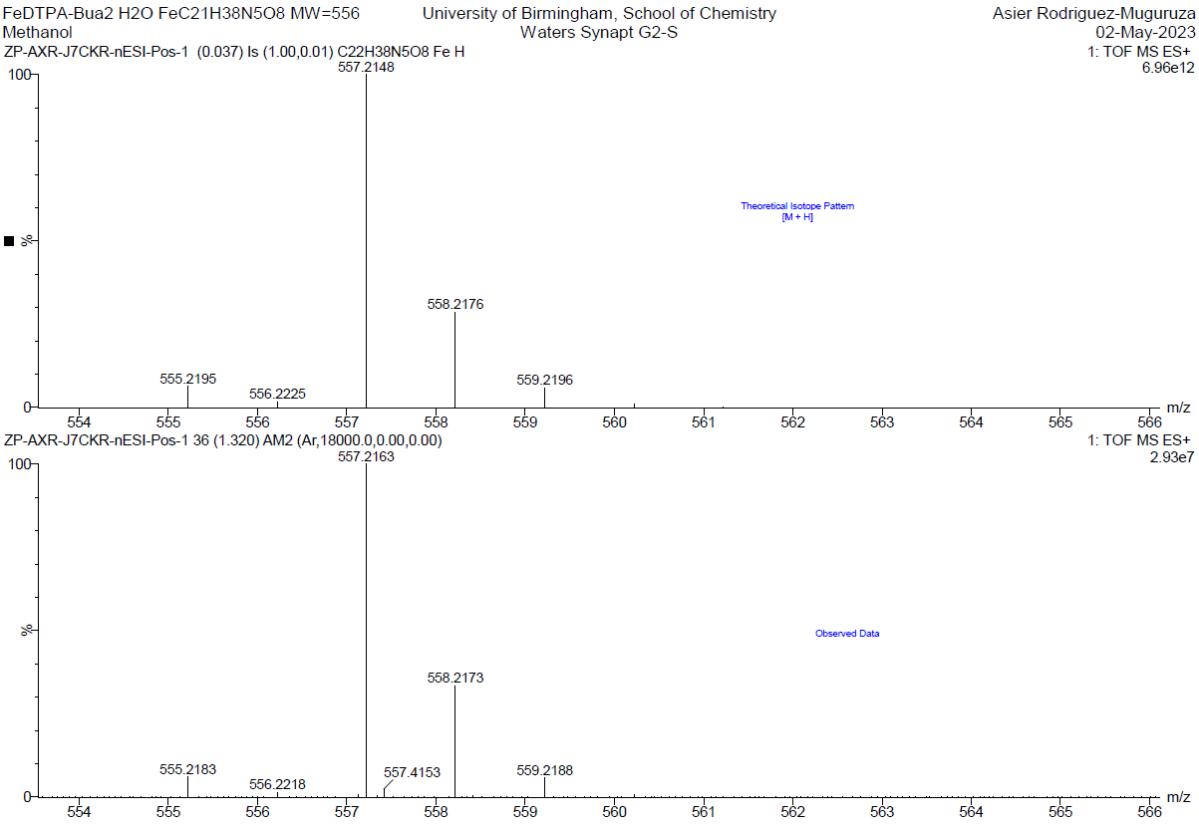

Figure 3.S6. (+)ESI-MS of **Fe^{3+}DTPA-Bua_2**.

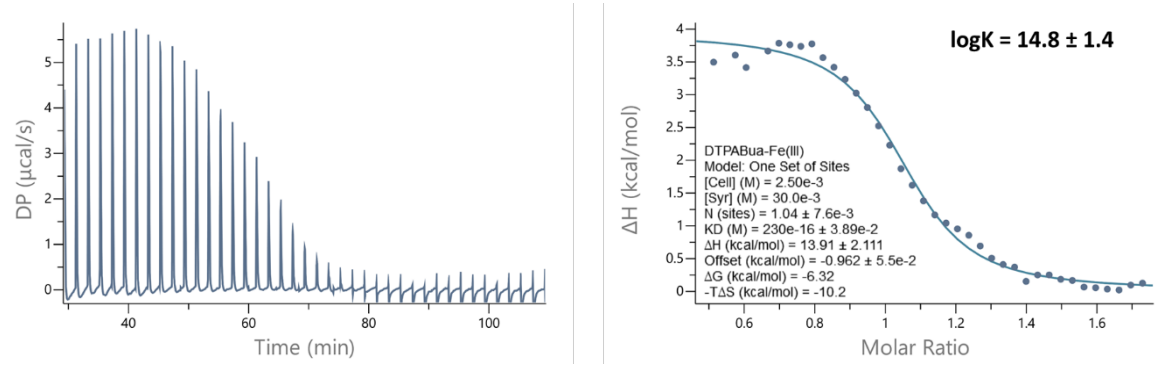

Figure 3.S7. Isothermal Titration Calorimetry (ITC) and fitted data of **Fe^{3+}DTPA-Bua_2** in PBS buffer (0.1 M, pH 7.4).

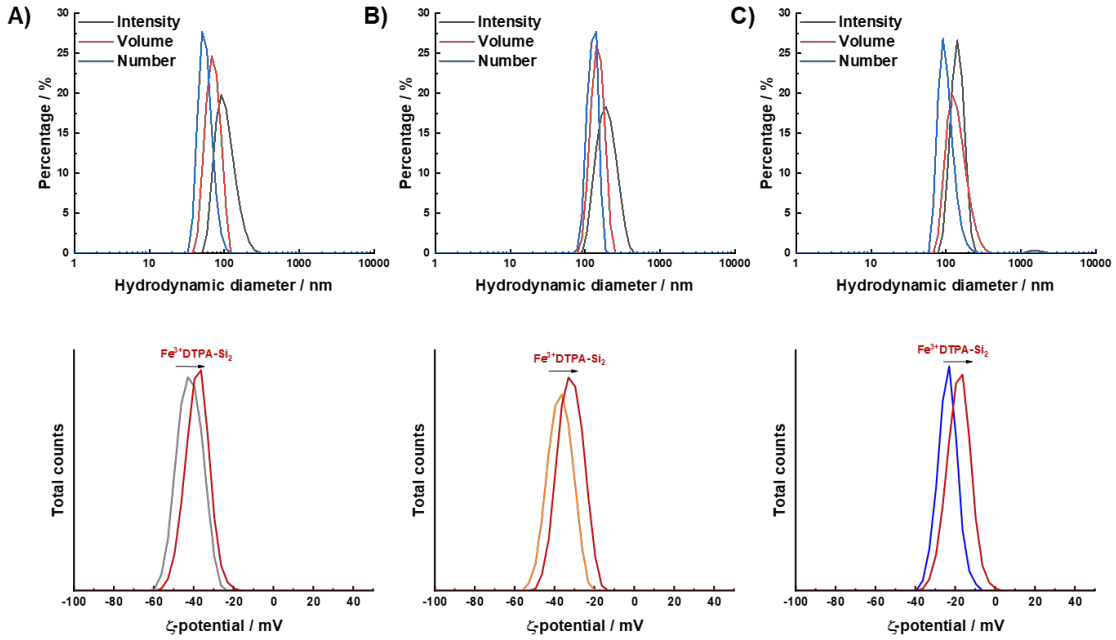

Figure 3.S8. Dynamic light scattering and ζ-potential of coated (A) **Fe^{3+}DTPA@SiO_2**, (B) **Fe^{3+}DTPA@SiO_2⊃Ru** and (C) **Fe^{3+}DTPA@SiO_2⊃Van** in PBS buffer (0.1 M, pH 7.4).

Table 3.S1. Dynamic light scattering (n = 5) and ζ-potential (n = 3) of Fe^{3+}DTPA-coated nanoparticles in PBS buffer (0.1 M, pH 7.4).

	Hydrodynamic diameter (D_h) / nm				ζ-potential / mV
	Intensity	Volume	Number	PDI	
Fe^{3+}DTPA@SiO_2	97 ± 14	90 ± 7	84 ± 4	0.14	-40 ± 4
Fe^{3+}DTPA@SiO_2⊃Ru	98 ± 10	85 ± 6	78 ± 4	0.16	-34 ± 5
Fe^{3+}DTPA@SiO_2⊃Van	124 ± 24	114 ± 18	101 ± 12	0.24	-20 ± 5
Fe^{3+}DTPA@SiO_2⊃Ru-Van	102 ± 21	98 ± 12	95 ± 9	0.21	-14 ± 7

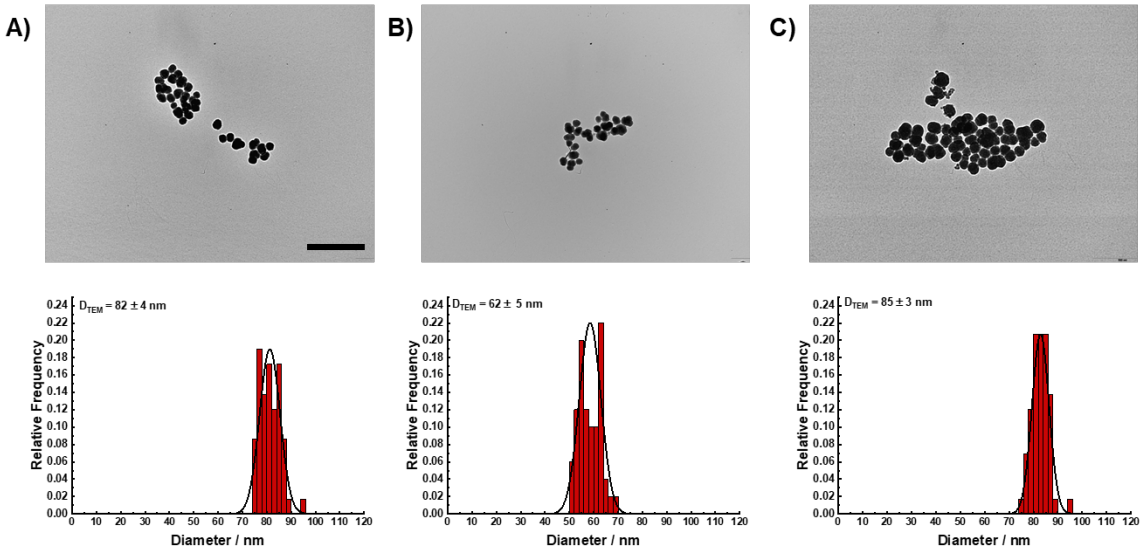

Figure 3.S9. Transmission Electron Microscopy (TEM) images of particle size distribution (n = 50) of (A) **Fe^{3+}DTPA@SiO_2**, (B) **Fe^{3+}DTPA@SiO_2⊃Ru** and (C) **Fe^{3+}DTPA@SiO_2⊃Van.** Scale bar = 500 nm.

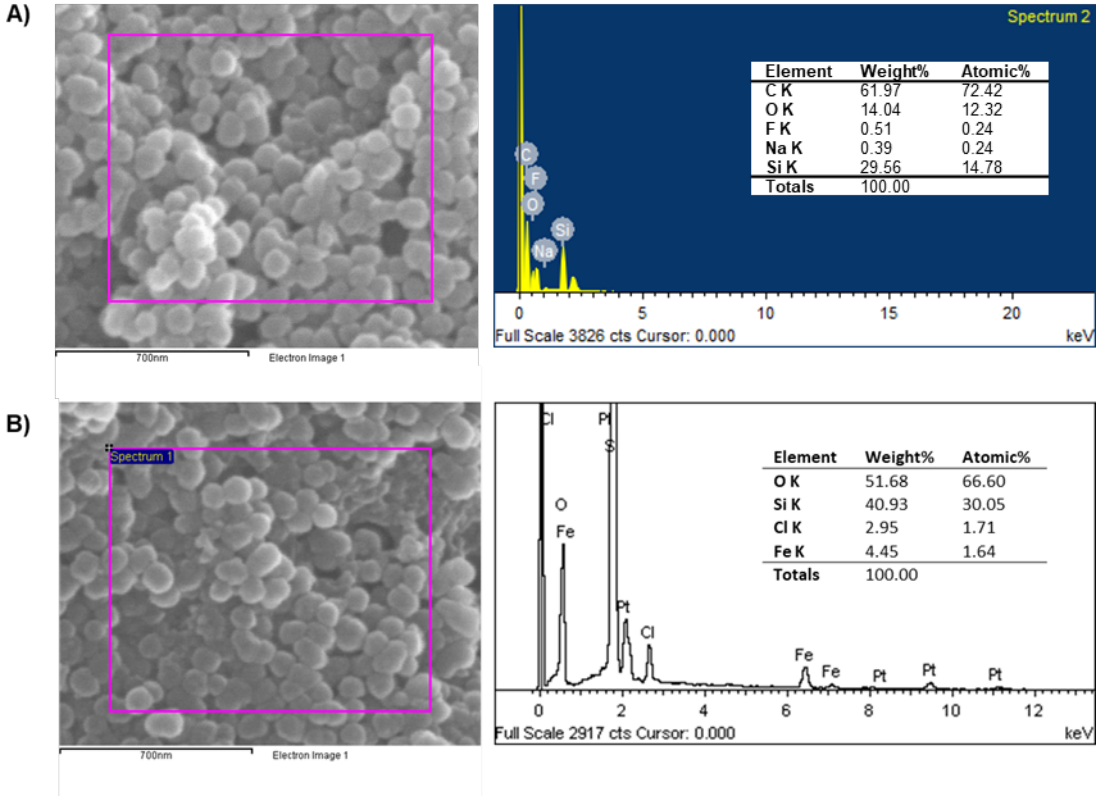

Figure 3.S10. Representative Scanning electron Microscopy (SEM) and Energy Disperse X-Ray Scattering (EDS) and elemental quantification of Pt-coated (A) **SiO_2⊃Ru-Van** and (B) **Fe^{3+}DTPA@SiO_2⊃Ru-Van**

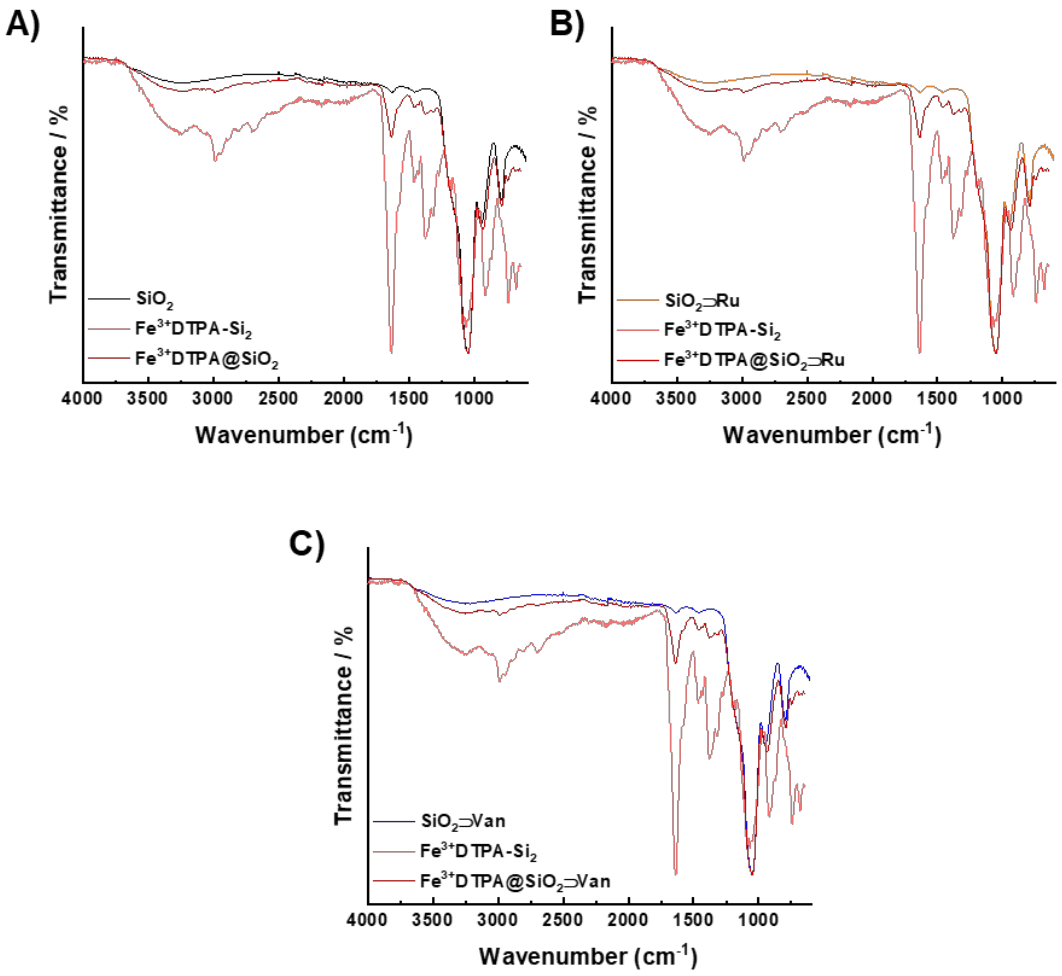

Figure 3.S11. FT-IR spectra of (A) **Fe^{3+}DTPA@SiO_2**, (B) **Fe^{3+}DTPA@SiO_2⊃Ru** and (C) **Fe^{3+}DTPA@SiO_2⊃Van.**

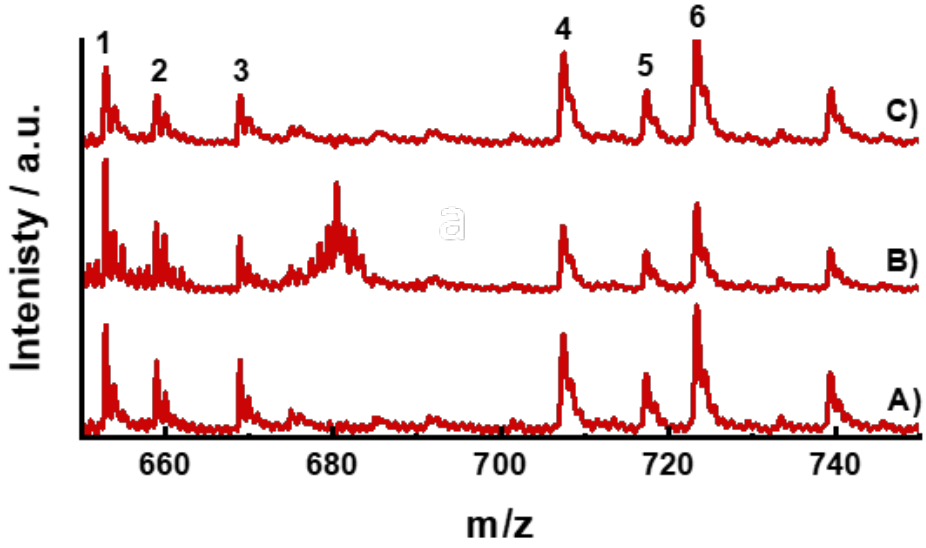

Figure 3.S12. MALDI-ToF (positive mode) spectra of (A) **DTPA@SiO_2**, (B) **DTPA@SiO_2⊃Ru** and (C) **DTPA@SiO_2⊃Van** before and after Fe^{3+}DTPA-coating. α-Cyano-4-hydroxycinnamic acid (CHCA) was employed as MADI-ToF matrix.

Table 3.S2. Summary of observed and calculated masses from MADI-ToF spectra from Figure 3.S12 confirming the attachment of **Fe^{3+}DTPA-Si_2** complexes.

Peak	Formula	Observed mass	Calculated mass
1	$[C_{20}H_{24}O_9N_5Si_2Fe+EtOH+H]^+$	652.889	652.875
2	$[C_{20}H_{24}O_{10}N_5Si_2Fe+MeOH+H]^+$	658.836	658.835
3	$[C_{20}H_{24}O_{10}N_5Si_2Fe+EtOH+H]^+$	669.111	669.124
4	$[C_{20}H_{24}O_{12}N_5Si_2Fe+MeOH+H]^+$	707.505	707.508
5	$[C_{20}H_{24}O_{13}N_5Si_2Fe+Na]^+$	717.291	717.290
6	$[C_{20}H_{24}O_{14}N_5Si_2Fe+MeOH+H]^+$	723.480	723.477

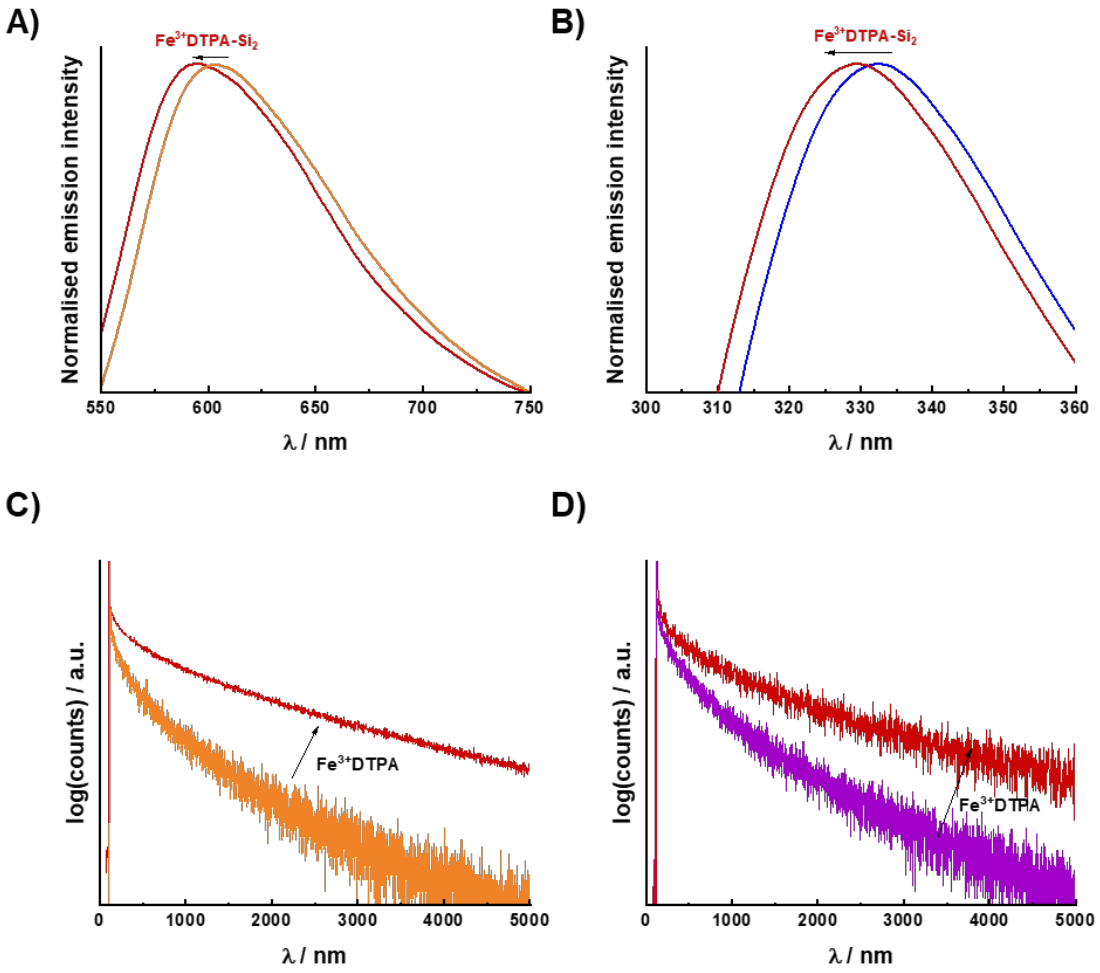

Figure 3.S13. Solid-state luminescent spectroscopy of (A) **Fe^{3+}DTPA@SiO_2⊃Ru** (λ_{exc} = 450 nm) and (B) **Fe^{3+}DTPA@SiO_2⊃Van** (λ_{exc} = 270 nm) and Ru's luminescence decay of (C) **Fe^{3+}DTPA@SiO_2⊃Ru** and (D) **Fe^{3+}DTPA@SiO_2⊃Ru** (λ_{exc} = 455 nm, λ_{em} = 600 nm) before and after Fe^{3+}DTPA-coating.

Table 3.S3. Solid-state photophysical parameters of **Ru**-containing **Fe^{3+}DTPA**-coated nanoparticles (for λ_{max} λ_{exc} = 450 nm and for lifetime measurements λ_{exc} = 455 nm, λ_{em} = 600 nm).

	λ_{max} / nm	τ_1 / μs (%)	τ_2 / μs (%)	χ^2
Fe^{3+}DTPA@SiO_2⊃Ru	593	3.12 (86)	0.85 (14)	1.068
Fe^{3+}DTPA@SiO_2⊃Ru-Van	595	2.62 (85)	0.27 (15)	1.124

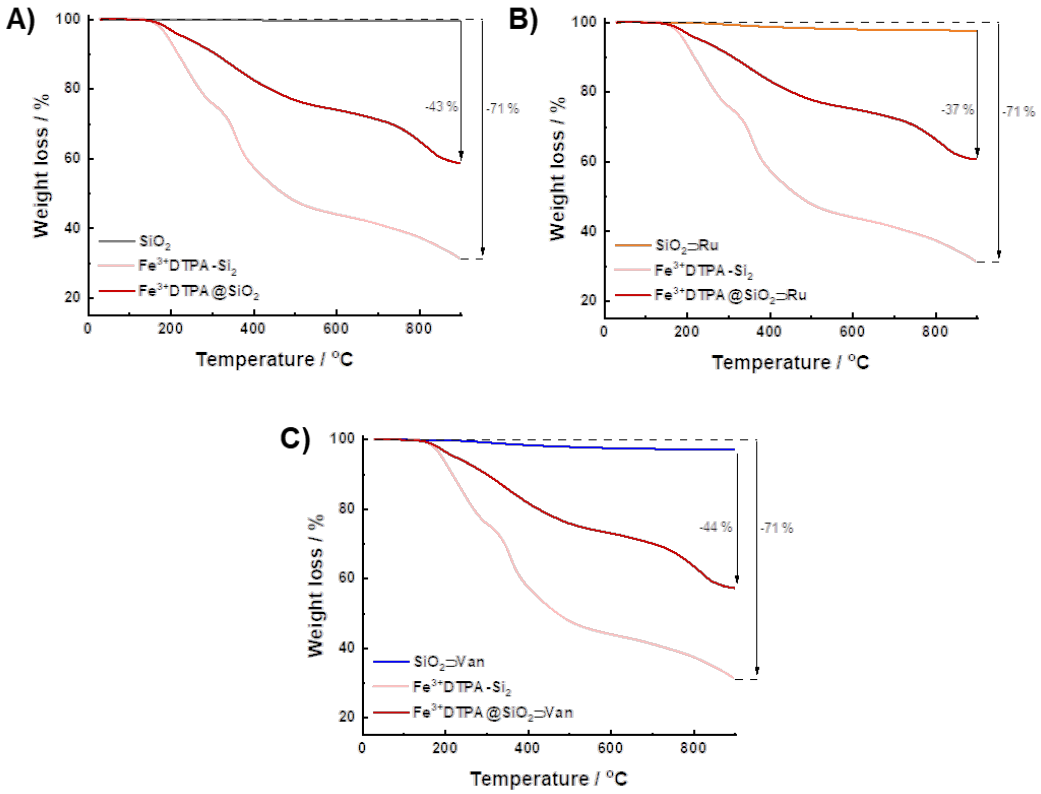

Figure 3.S15. Thermogravimetric analysis (TGA) of (A) **Fe^{3+}DTPA@SiO_2**, (B) **Fe^{3+}DTPA@SiO_2⊃Ru** and (C) **Fe^{3+}DTPA@SiO_2⊃Van**. Samples were dried at 120 C for 1 h before the analysis. Samples were heated at 5 °C/min from 30 °C to 900 °C under nitrogen atmosphere.

Table 3.S4. Estimation of coating in Fe^{3+}DTPA-coated nanoparticles based on TGA profiles.

	$mg_{Complex}/g_{NPs}$	**$mmol_{Complex}/g_{NPs}$**
Fe^{3+}DTPA@SiO_2	57	0.12
Fe^{3+}DTPA@SiO_2⊃Ru	58	0.12
Fe^{3+}DTPA@SiO_2⊃Van	52	0.10
Fe^{3+}DTPA@SiO_2⊃Ru-Van	59	0.13

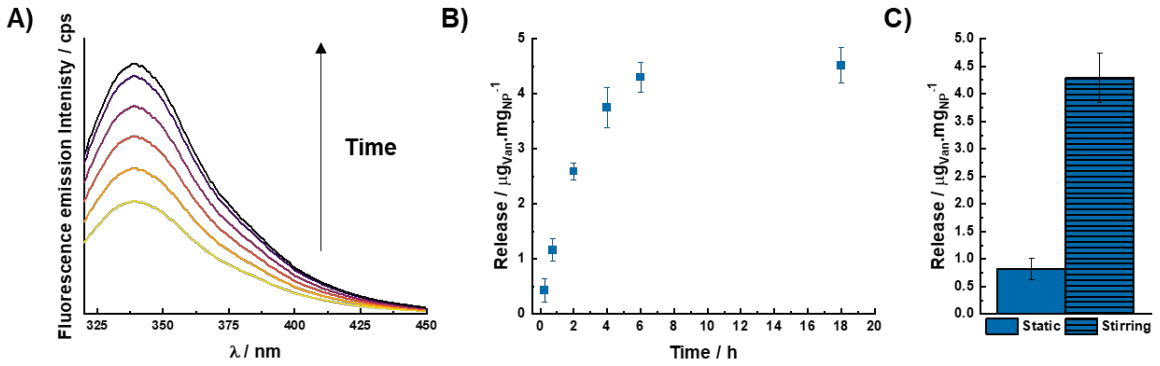

Figure 3.15. Van release studied from **Fe^{3+}DTPA@SiO_2⊃Van**. (A) Representative fluorescence monitoring release of **Van** (λ_{exc} = 270 nm, λ_{em} = 330 nm) at 37 ºC and 150 rpm and (B) cumulative **Van** release graph (n = 3). (C) Comparative Van release after 18 h at 37 ºC upon static conditions or stirring at 150 rpm (n = 3).

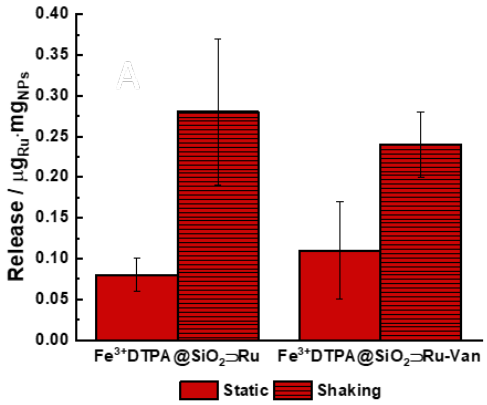

Figure 3.S16. **Ru** leakage from **Ru**-containing nanoparticles under static and stirring (150 rpm) conditions at 37 ºC. **Ru** was quantified by luminescent spectroscopy (λ_{exc} = 450 nm, λ_{em} = 600 nm). (n = 3)

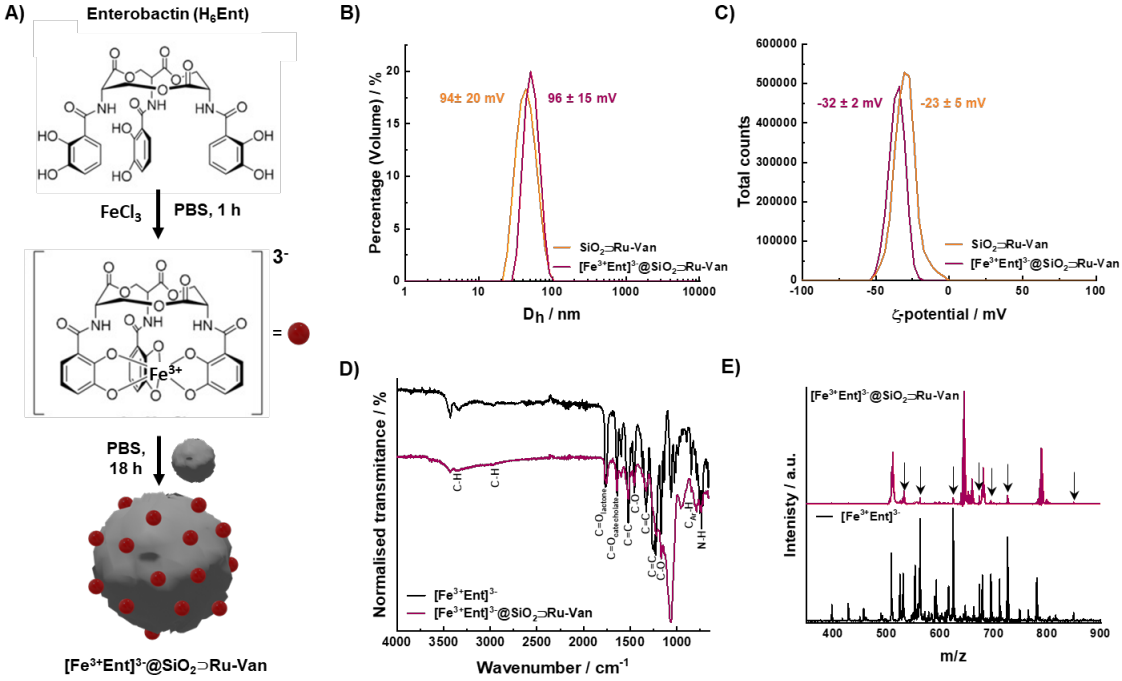

Figure 3.S17. (A) Synthesis and (B-E) characterization and **$[Fe^{3+}Ent]^{3-}$@SiO_2⊃Ru-Van**. **$[Fe^{3+}Ent]^{3-}$** adsorption onto nanoparticles surface was confirmed by (B) DLS in PBS buffer (0.1 M, pH 7.4) and (C) ζ-potential measuring, where a slight increase in the hydrodynamic size (D_h) of the nanoparticle is observed alongside a change in the ζ-potential to more negative values. Furthermore, (D) FT-IR spectroscopy further evidenced the presence of **$[Fe^{3+}Ent]^{3-}$** as stretching associated with the N-H (3434 cm^{-1} and 3348 cm^{-1}), C=O (1758 cm^{-1} and 1636 cm^{-1}), C=C (1524 cm^{-1}, 1224 cm^{-1} and 1330 cm^{-1}), C-H_{ar} (790 cm^{-1}) and N-H (736 cm^{-1}) were observed for **$[Fe^{3+}Ent]^{3-}$@SiO_2⊃Ru-Van**. (E) MALDI-ToF mass spectrometry of coated particles also revealed **$[Fe^{3+}Ent]^{3-}$** species on the nanoparticles (indicated with arrows). α-cyano-4-hydroxy-cinnamic acid (CHCA) was employed as MALDI-ToF matrix.

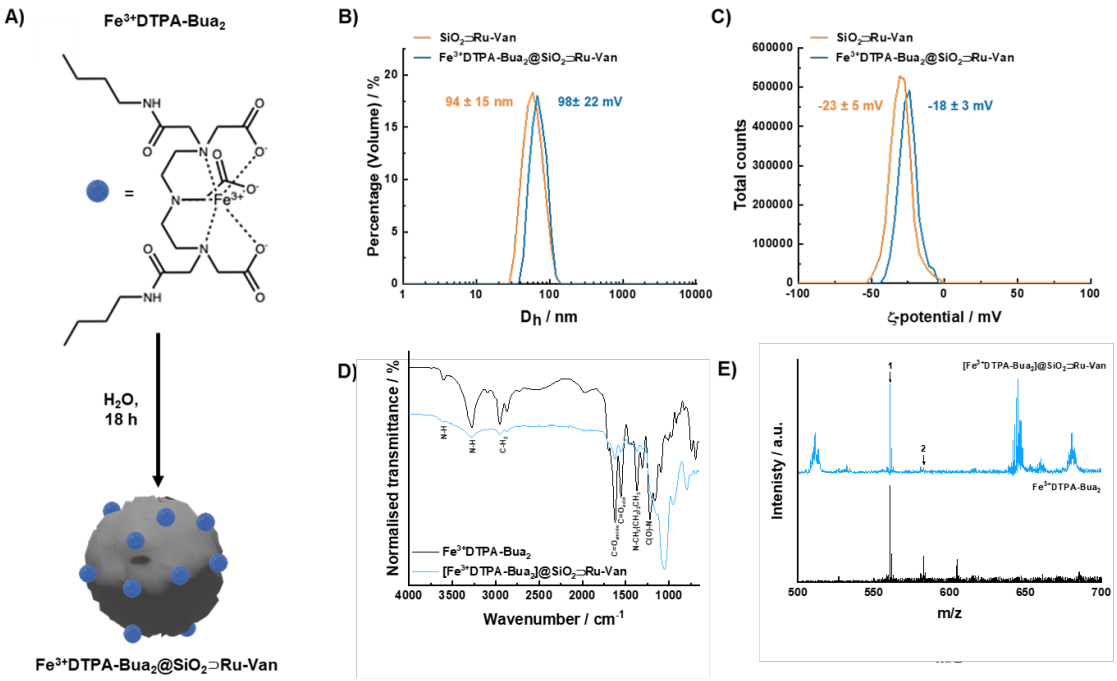

Figure 3.S18. (A) Synthesis and (B-E) characterization and **[Fe^{3+}DTPA-Bua_2]@SiO_2⊃Ru-Van**. **Fe^{3+}DTPA-Bua_2** adsorption onto nanoparticles surface was confirmed by (B) DLS in PBS buffer (0.1 M, pH 7.4) and (C) ζ-potential measuring, where a slight increase in the hydrodynamic size (D_h) of the nanoparticle is observed alongside a change in the ζ-potential to more positive values. Furthermore, (D) FT-IR spectroscopy further evidenced the presence of **Fe^{3+}DTPA-Bua_2** as stretching associated with the N-H (3600 cm^{-1} and 3271 cm^{-1}) C-H (2956 cm^{-1} and 2866 cm^{-1}), C=O (1619 cm^{-1} and 1551 cm^{-1}) and C(O)-N (1222 cm^{-1}) were observed for **[Fe^{3+}DTPA-Bua_2]@SiO_2⊃Ru-Van**. (E) MALDI-ToF mass spectrometry of coated particles also revealed **Fe^{3+}DTPA-Bua_2** species on the nanoparticles finding signals associated with, $[M+H]^+$ (1, observed m/z 559.707, calculated m/z 559.602) and $[M+Na]^+$ (2, observed 582.9187, calculated 582.8956). α-cyano-4-hydroxy-cinnamic acid (CHCA) was employed as MALDI-ToF matrix.

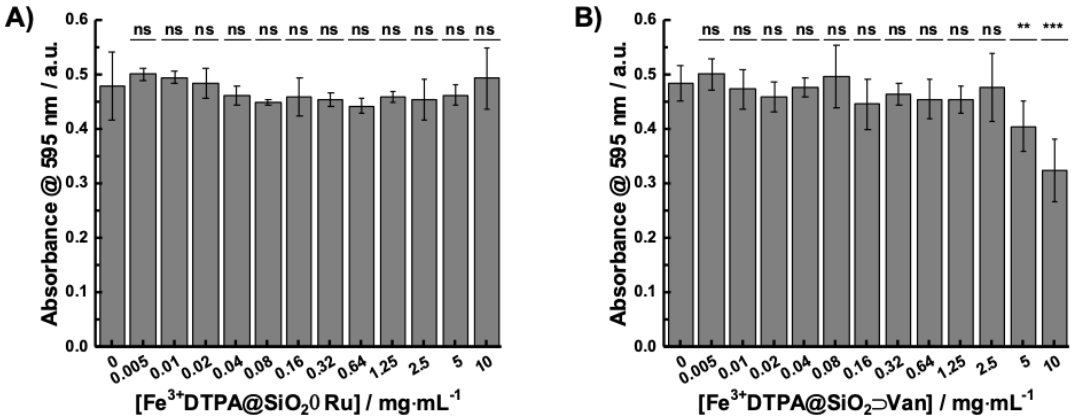

Figure 3.19. MTT cell viability assays of A549 cell line incubated with (A) **Fe^{3+}DTPA@SiO_2⊃Ru** and (B) **Fe^{3+}DTPA@SiO_2⊃Van** nanoparticles for 18 h. Significance was calculated based on 1-way ANOVA followed by Dunnett's t-test corrected for multiple comparisons, ns = no significance * = $p<0.05$, ** $p<0.01$ and *** $p<0.001$, n = 3.

Table 3.S5. Minimal inhibitory concentration (MIC, mg/mL) of **DTPA-Bua$_2$**, **Fe^{3+}DTPA-Bua$_2$** and control nanoparticles for *S. aureus* (ATCC23851), *E. coli* (MG1655), *A. baumannii* (AYE), *K. pneumoniae* (ATCC43816R), *K. oxytoca* (080-KPC CHD), *C. feundii* (NCTC9750), *S. enterica* (SL1344), *P. aeruginosa* (PA14) and *B. cenocepacia* (K57-2, CF isolate) upon shaking at 150 rpm at 37 ^{O}C in LB media. Depicted results are based on 3 biological replicas.

	E. coli	***A. baumannii***	***K. pneumoniae***	***K. oxytoca***	***C. freundii***	***S. enterica***	***P. aeruginosa***	***B. cenocepacia***	***S. aureus***
DTPA-Bua$_2$	5.00	10	5.00	5.00	5.00	10	> 20	> 20	0.32
Fe^{3+}DTPA-Bua$_2$	> 20	> 20	> 20	> 20	> 20	> 20	> 20	> 20	1.25
DTPA@SiO$_2$⊃Ru	5.00	5.00	5.00	5.00	10	5.00	10	10	1.25
DTPA@SiO$_2$⊃Van	5.00	5.00	5.00	5.00	5.00	10	10	10	0.37
Fe^{3+}DTPA@SiO$_2$⊃R	1.25	1.25	2.50	1.25	2.50	1.25	2.50	2.50	0.75
Fe^{3+}DTPA@SiO$_2$⊃V	0.80	0.40	0.40	0.80	0.40	0.20	1.60	0.40	0.20

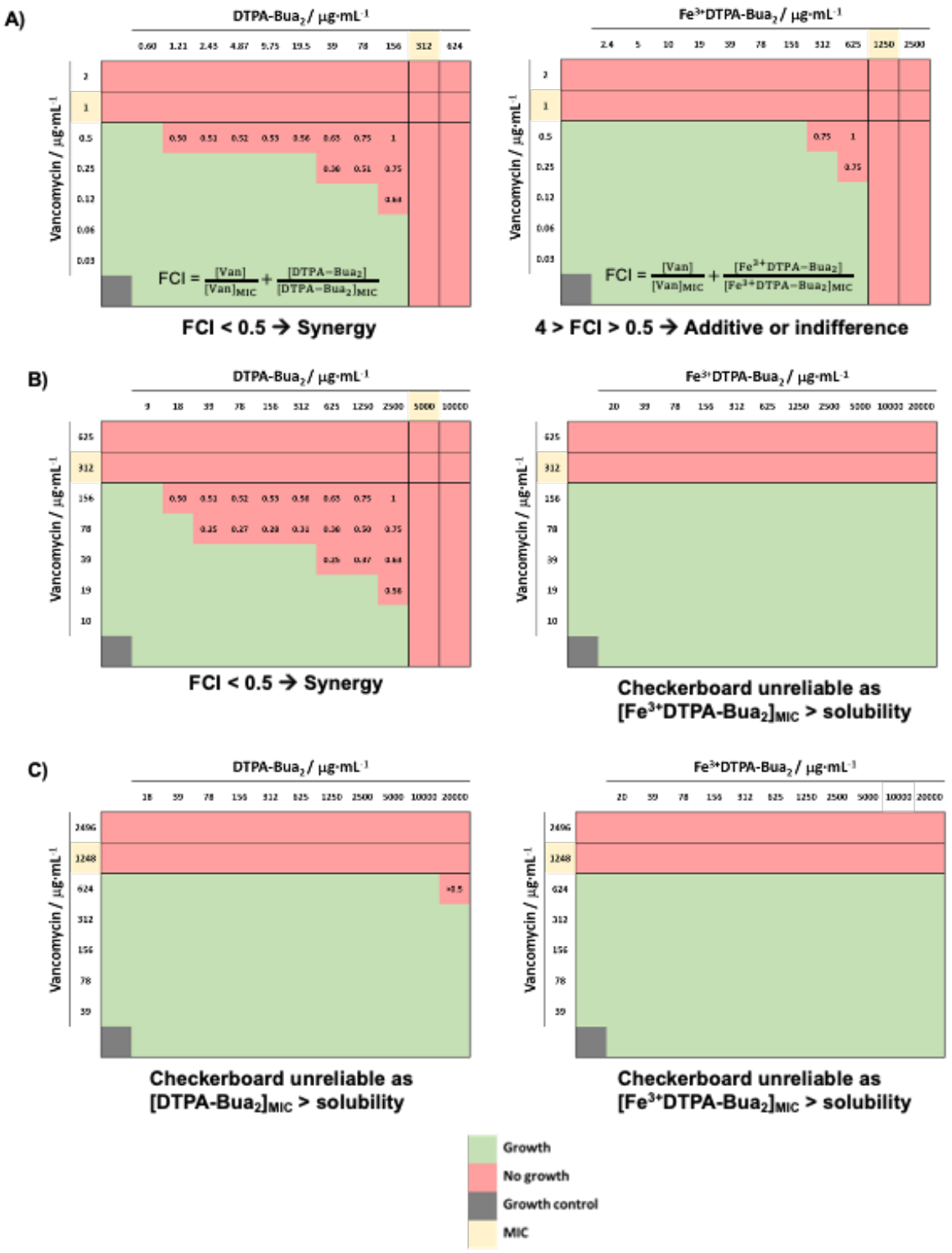

Figure 3.S20. Checkerboard assays between **DTPA-Bua$_2$** and **Van** and **Fe^{3+}DTPA-Bua$_2$** and **Van** for (A) *S. aureus* (ATCC23851), (B) *E. coli* (MG1655) and *P. aeruginosa* (PA14) in LB media. Depicted results are based on 2 biological replicas.

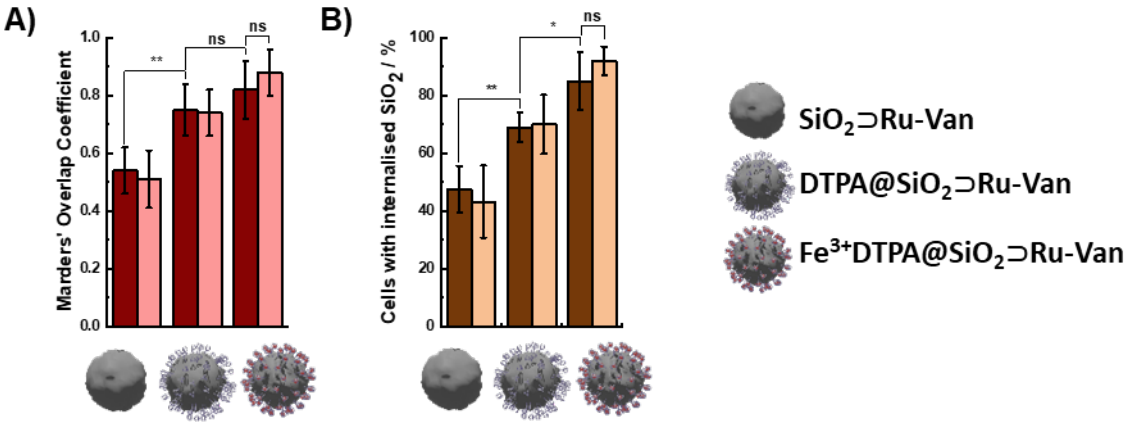

Figure 3.21. Quantification of particle internalization in wild-type *S. aureus* strain after 2 h incubation in PBS buffer (0.1 M, pH 7.4) at 37 ºC and mild shaking (150 rpm) by (A) Manders' overlapping coefficient and (B) determination of bacterial cells with internalized nanoparticles based on SIM images under standard (dark red and brown) and reduced (light red and brown) Fe(III) conditions. (n=5 for 3 biological replicas). Statistical analysis performed by t-test; ns $p>0.05$, * $p<0.05$, ** $p<0.01$, *** $p<0.001$.

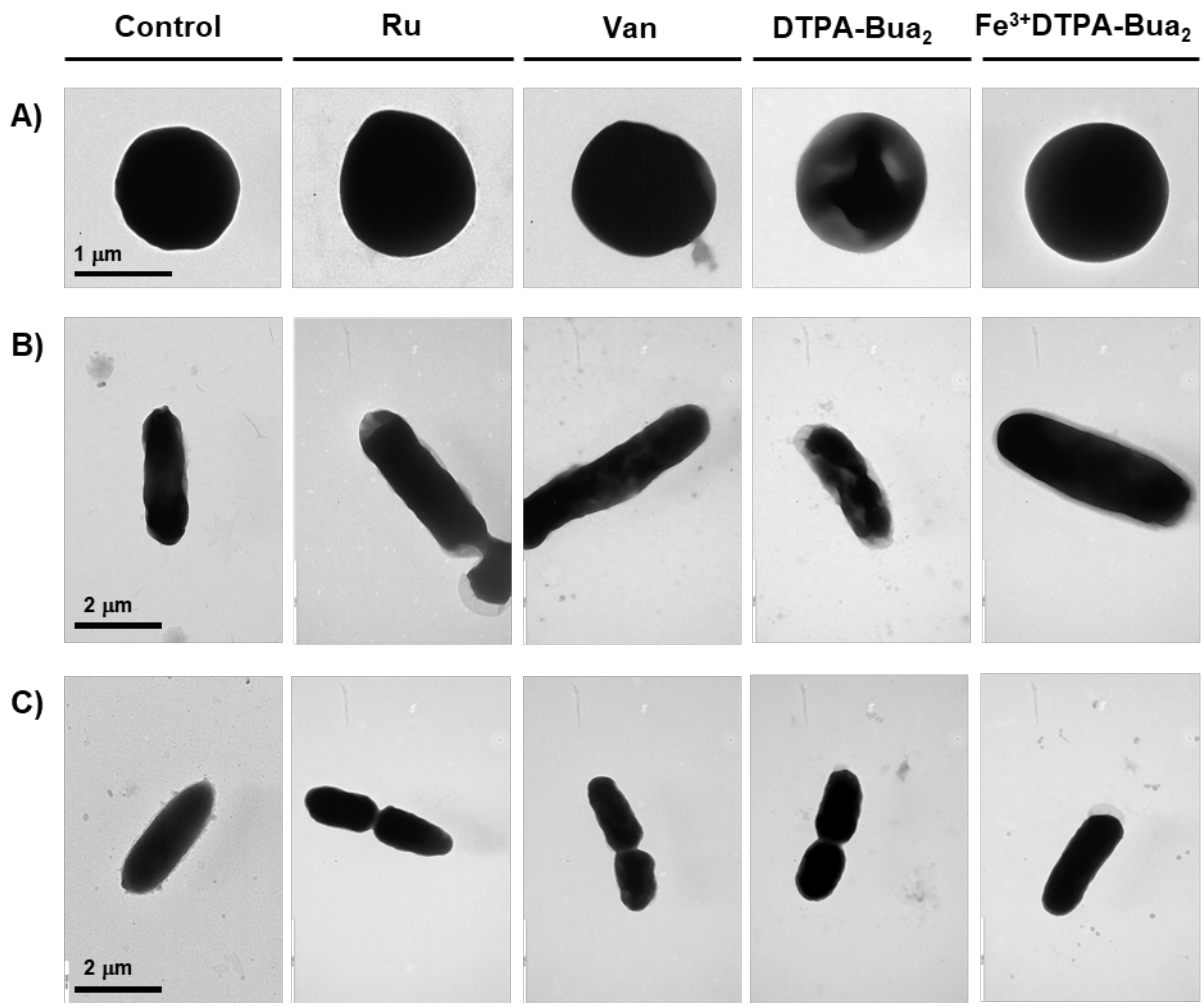

Figure 3.S22. Transmission Electron Microscopy (TEM) imaging of (A) *S. aureus*, (B) *E. coli* and (C) *P. aeruginosa* cells incubated with different compounds for 2 h in PBS buffer (0.1 M, pH 7.4). Compounds concentration was estimated from the concentration of each component in 2.5 mg/mL of DTPA- or Fe^{3+}DTPA-coated nanoparticles.

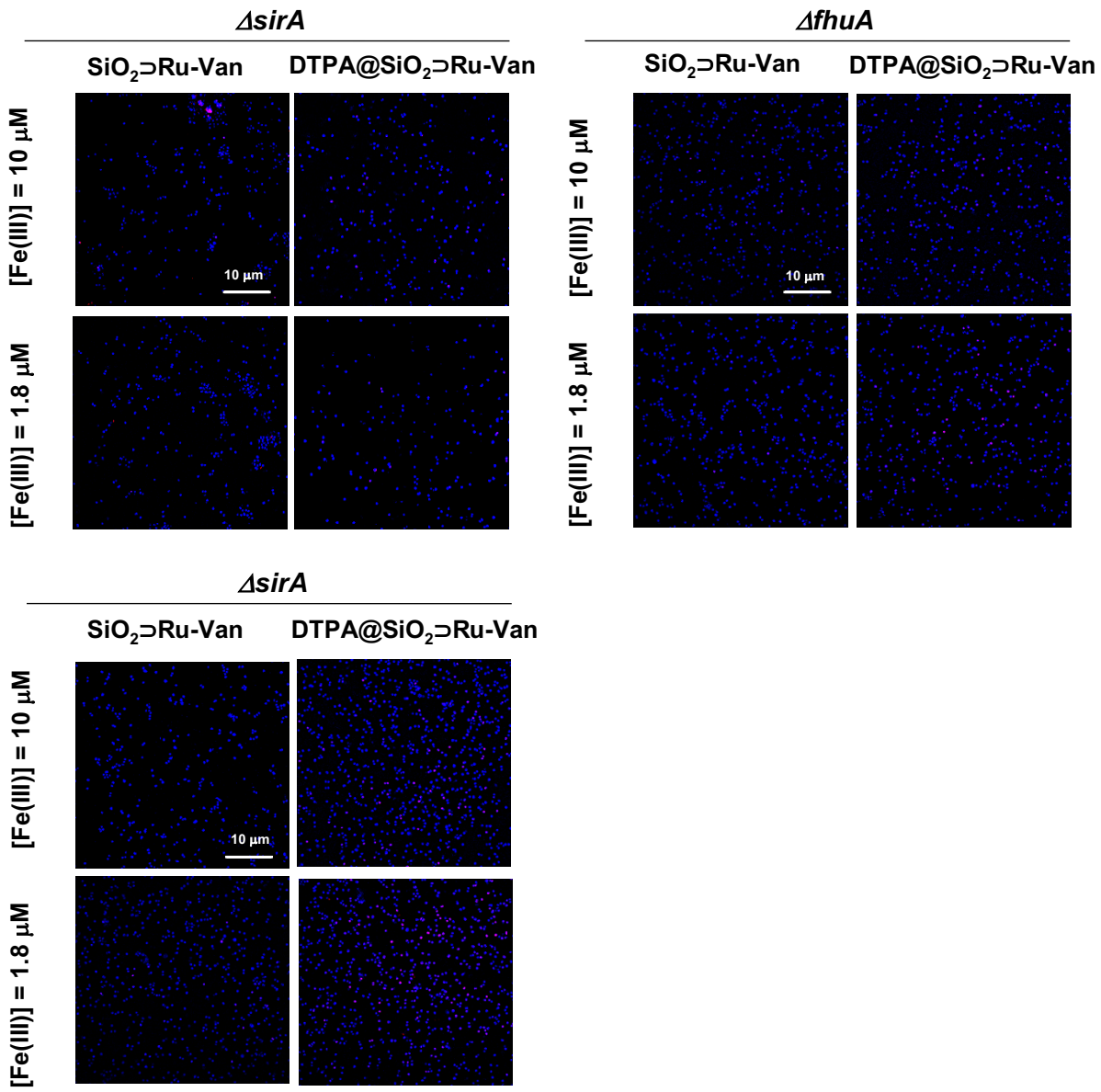

Figure 3.S23. Representative structural illumination microscopy images (n = 3) of *S. aureus* mutant cells incubated with **SiO₂⊃Ru-Van** and **DTPA@SiO₂⊃Ru-Van** nanoparticles ([NPs] = 2.5 mg/mL) for 1 h in PBS buffer (1 mM, pH 7.4) at 37 °C under mild shaking (150 rpm) after 2 h incubation in standard (10 μM) and reduced (1.8 μM) Fe(III) MOPS media. Images show overlay of channels depicting the bacterial cell outline (blue) and particle luminescence (red). Blue channel, Hoechst H33342 (λ_{exc} = 405 nm, λ_{em} = 410 – 455 nm) and red channel, Ru emission (λ_{exc} = 455 nm, λ_{em} = 580 – 620 nm).

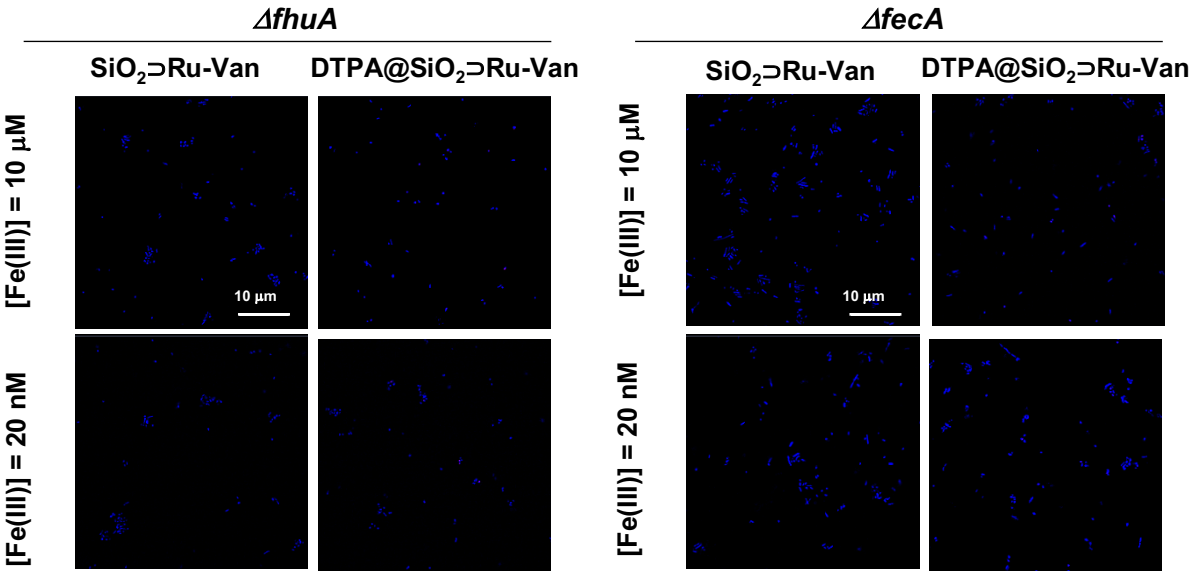

Figure 3.S24. Representative structural illumination microscopy images (n = 3) of *E. coli* mutant cells incubated with **SiO_2⊃Ru-Van** and **DTPA@SiO_2⊃Ru-Van** nanoparticles ([NPs] = 2.5 mg/mL) for 2 h in PBS buffer (1 mM, pH 7.4) at 37 °C under mild shaking (150 rpm) after 2 h incubation in standard (10 μM) and reduced (20 nM) Fe(III) MOPS media. Images show overlay of channels depicting the bacterial cell outline (blue) and particle luminescence (red). Blue channel, Hoechst H33342 (λ_{exc} = 405 nm, λ_{em} = 410 – 455 nm) and red channel, Ru emission (λ_{exc} = 455 nm, λ_{em} = 580 – 620 nm).

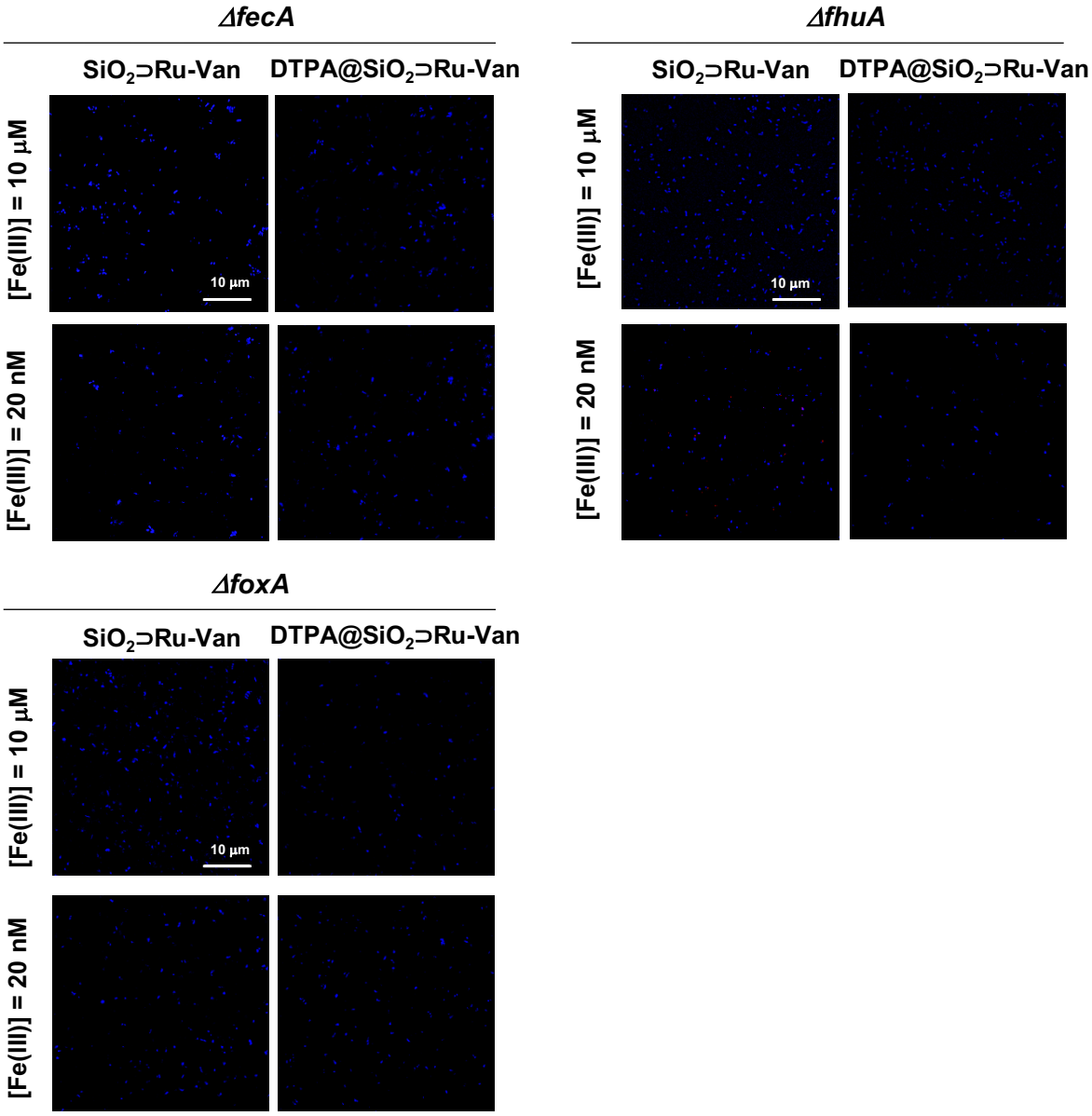

Figure 3.S25. Representative structural illumination microscopy images (n = 3) of *P. aeruginosa* mutant cells incubated with **Fe^{3+}DTPA@SiO_2⊃Ru** nanoparticles ([NPs] = 2.5 mg/mL) for 2 h in PBS buffer (1 mM, pH 7.4) at 37 ºC under mild shaking (150 rpm) after 2 h incubation in standard (10 μM) and reduced (20 nM) Fe(III) MOPS media. Images show overlay of channels depicting the bacterial cell outline (blue) and particle luminescence (red). Blue channel, Hoechst H33342 (λ_{exc} = 405 nm, λ_{em} = 410 – 455 nm) and red channel, Ru emission (λ_{exc} = 455 nm, λ_{em} = 580 – 620 nm).

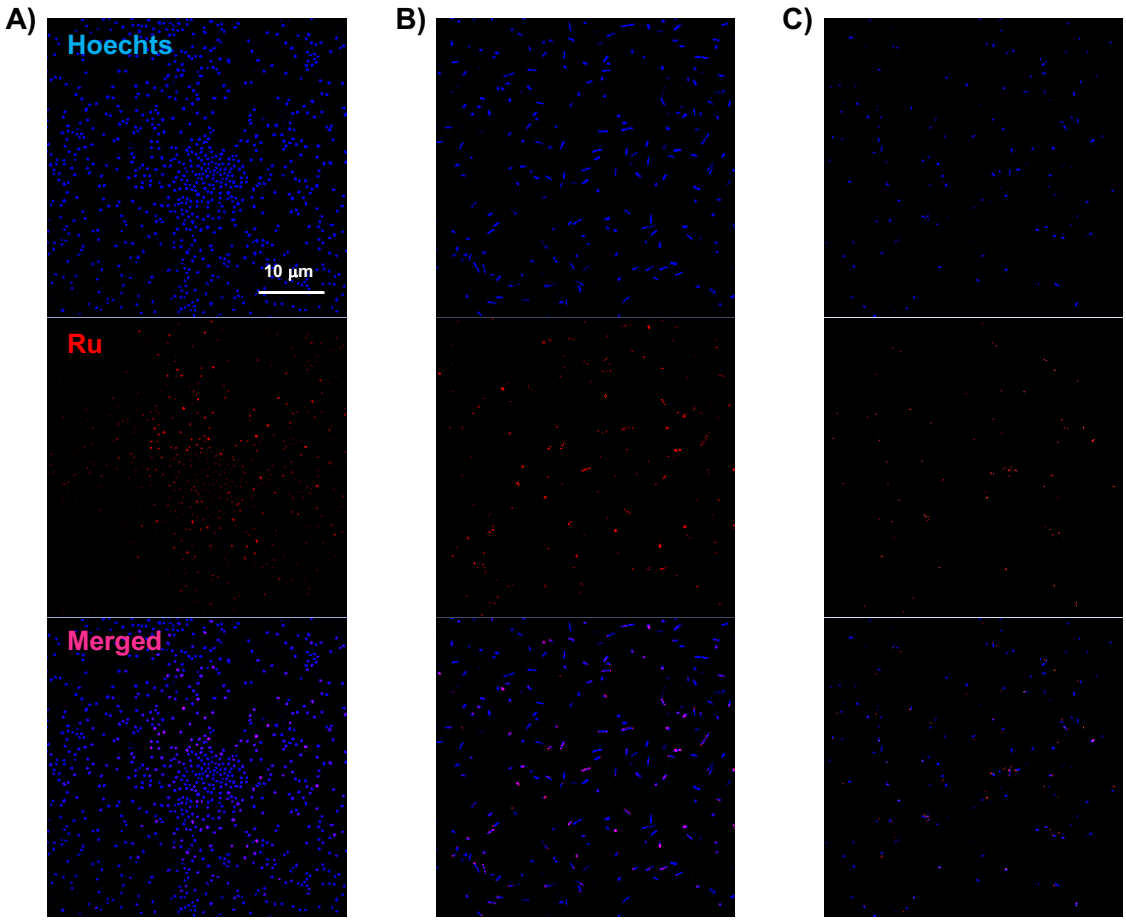

Figure 3.S26. Representative structural illumination microscopy images (n = 3) of wild-type (A) *S. aureus,* (B) *E. coli* and (C) *P. aeruginosa* cells incubated with **Fe^{3+}DTPA@SiO_2⊃Ru** nanoparticles ([NPs] = 2.5 mg/mL) for 1 h for *S. aureus* and 2 h for *E. coli* and *P. aeruginosa* in PBS buffer (1 mM, pH 7.4) at 37 °C under mild shaking (150 rpm) after 2 h incubation in standard (10 μM) and reduced (1.8 μM or 20 nM) Fe(III) MOPS media. Images show overlay of channels depicting the bacterial cell outline (blue) and particle luminescence (red). Blue channel, Hoechst H33342 (λ_{exc} = 405 nm, λ_{em} = 410 – 455 nm) and red channel, Ru emission (λ_{exc} = 455 nm, λ_{em} = 580 – 620 nm).

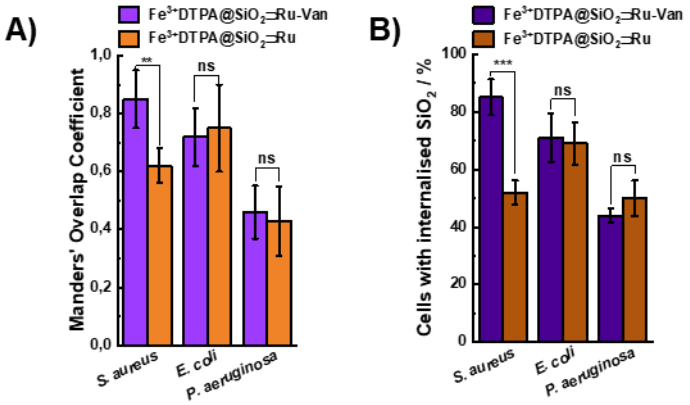

Figure 3.27. Quantification of **Fe^{3+}DTPA@SiO_2⊃Ru** nanoparticles internalization in wild type *S. aureus*, *E. coli* and *P. eruginosa* strains after 2 h incubation in PBS buffer (0.1 M, pH 7.4) at 37 ºC and mild shaking (150 rpm) by (A) Manders' overlapping coefficient and (B) determination of bacterial cells with internalized nanoparticles based on SIM images under standard (dark red and brown) and reduced (light red and brown) Fe(III) conditions. (n=5 for 3 biological replicas). Statistical analysis performed by t-test; ns $p>0.05$, * $p<0.05$, ** $p<0.01$, *** $p<0.001$.

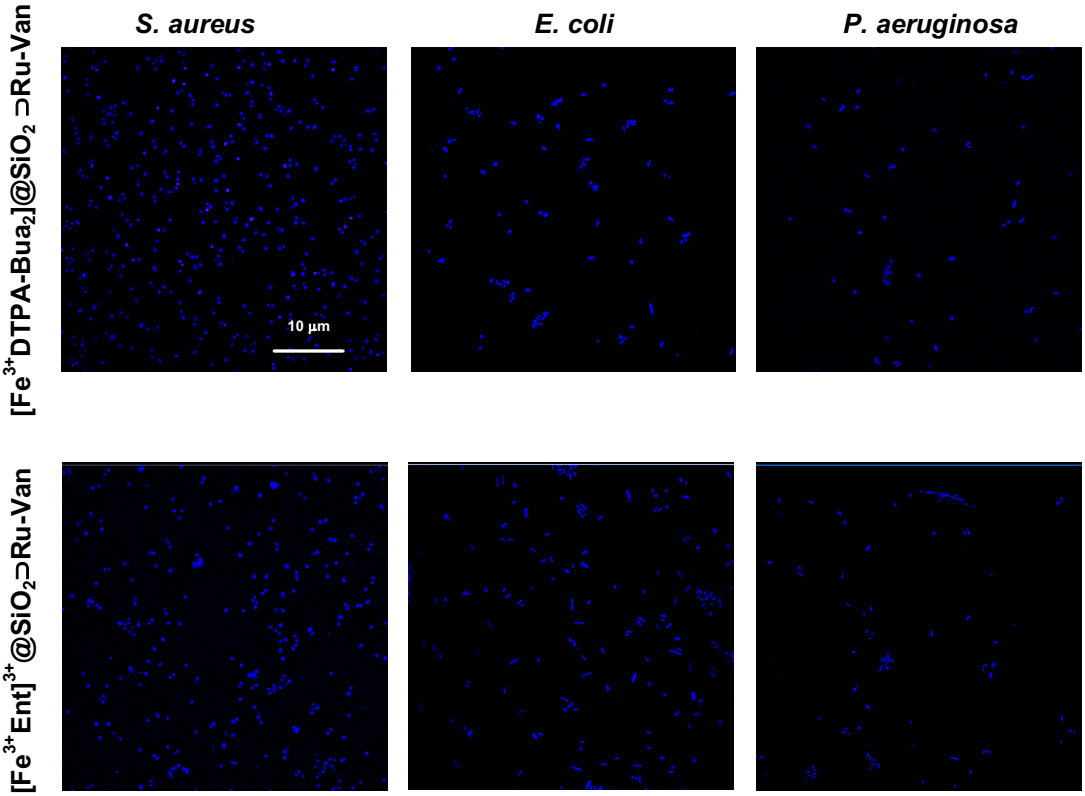

Figure 3.S28. Representative structural illumination microscopy images (n = 3) of wild-type (A) *S. aureus,* (B) *E. coli* and (C) *P. aeruginosa* cells incubated with **[Fe^{3+}DTPA-Bua$_2$]@SiO$_2$⊃Ru-Van** and **[Fe^{3+}Ent]$^{3-}$@SiO$_2$⊃Ru-Van** nanoparticles ([NPs] = 2.5 mg/mL) for 1 h for *S. aureus* and 2 h for *E. coli* and *P. aeruginosa* in PBS buffer (1 mM, pH 7.4) at 37 ºC under mild shaking (150 rpm) after 2 h incubation in standard (10 μM) and reduced (1.8 μM or 20 nM) Fe(III) MOPS media. Images show overlay of channels depicting the bacterial cell outline (blue) and particle luminescence (red). Blue channel, Hoechst H33342 (λ_{exc} = 405 nm, λ_{em} = 410 – 455 nm) and red channel, **Ru** emission (λ_{exc} = 455 nm, λ_{em} = 580 – 620 nm).

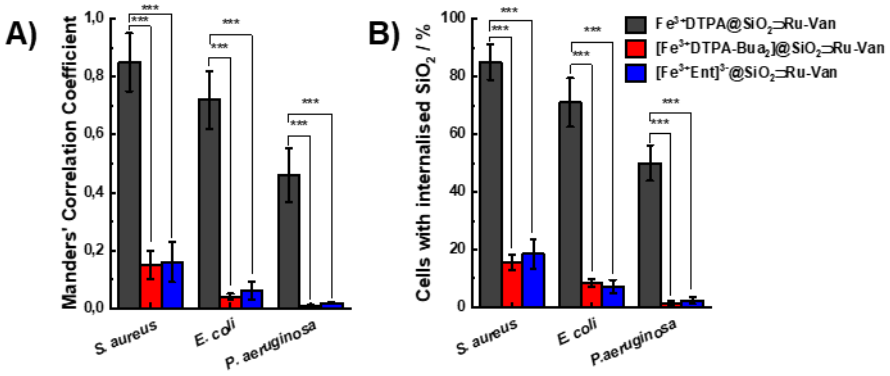

Figure 3.S29. Quantification of particle internalization in wild type *S. aureus*, *E. coli* and *P. eruginosa* strains after 2 h incubation in PBS buffer (0.1 M, pH 7.4) at 37 ºC and mild shaking (150 rpm) by (A) Manders' overlapping coefficient and (B) determination of bacterial cells with internalized nanoparticles based on SIM images under standard (dark red and brown) and reduced (light red and brown) Fe(III) conditions. (n=5 for 3 biological replicas). Statistical analysis performed by t-test; ns p>0.05, * p <0.05, ** p<0.01, *** p<0.001.

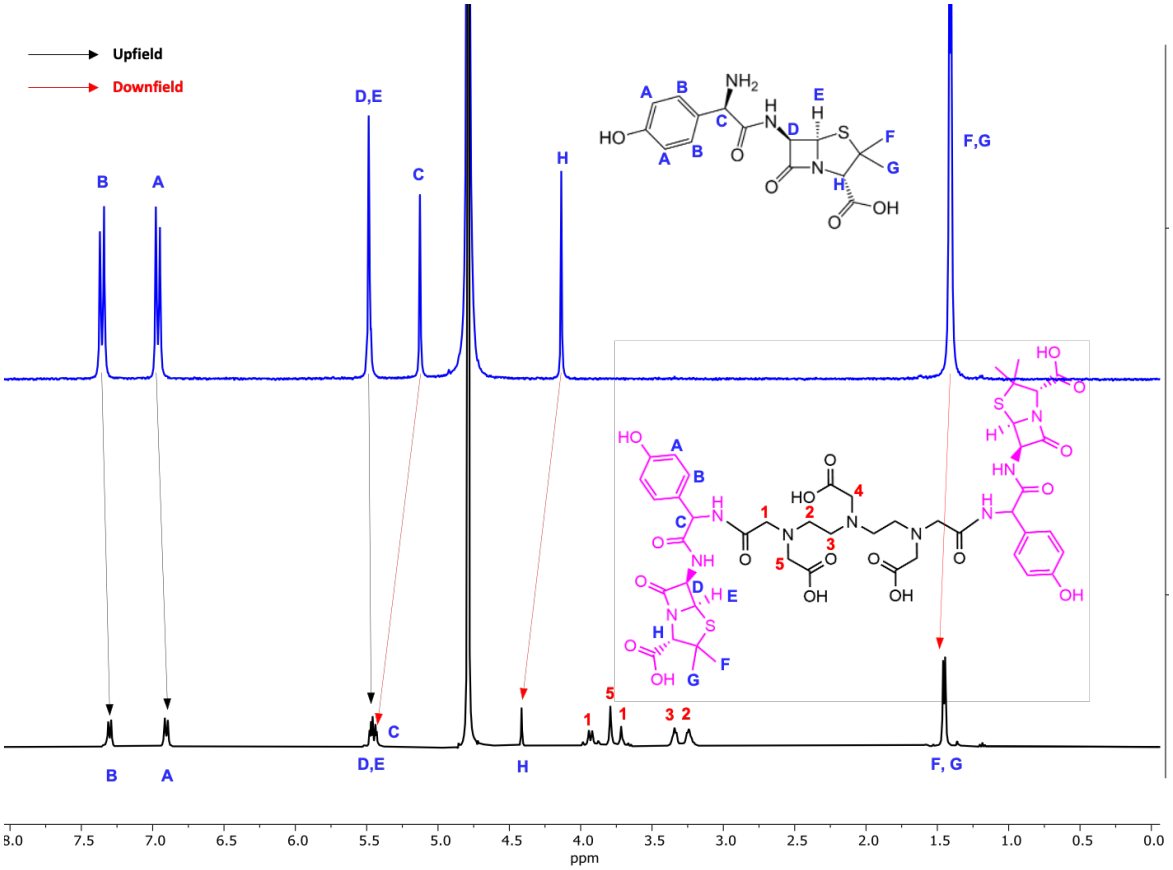

Figure 3.S30. ^{1}HNMR (400 MHz, D_2O) of **Amox** (blue) and **DTPA-Amox$_2$** (black).

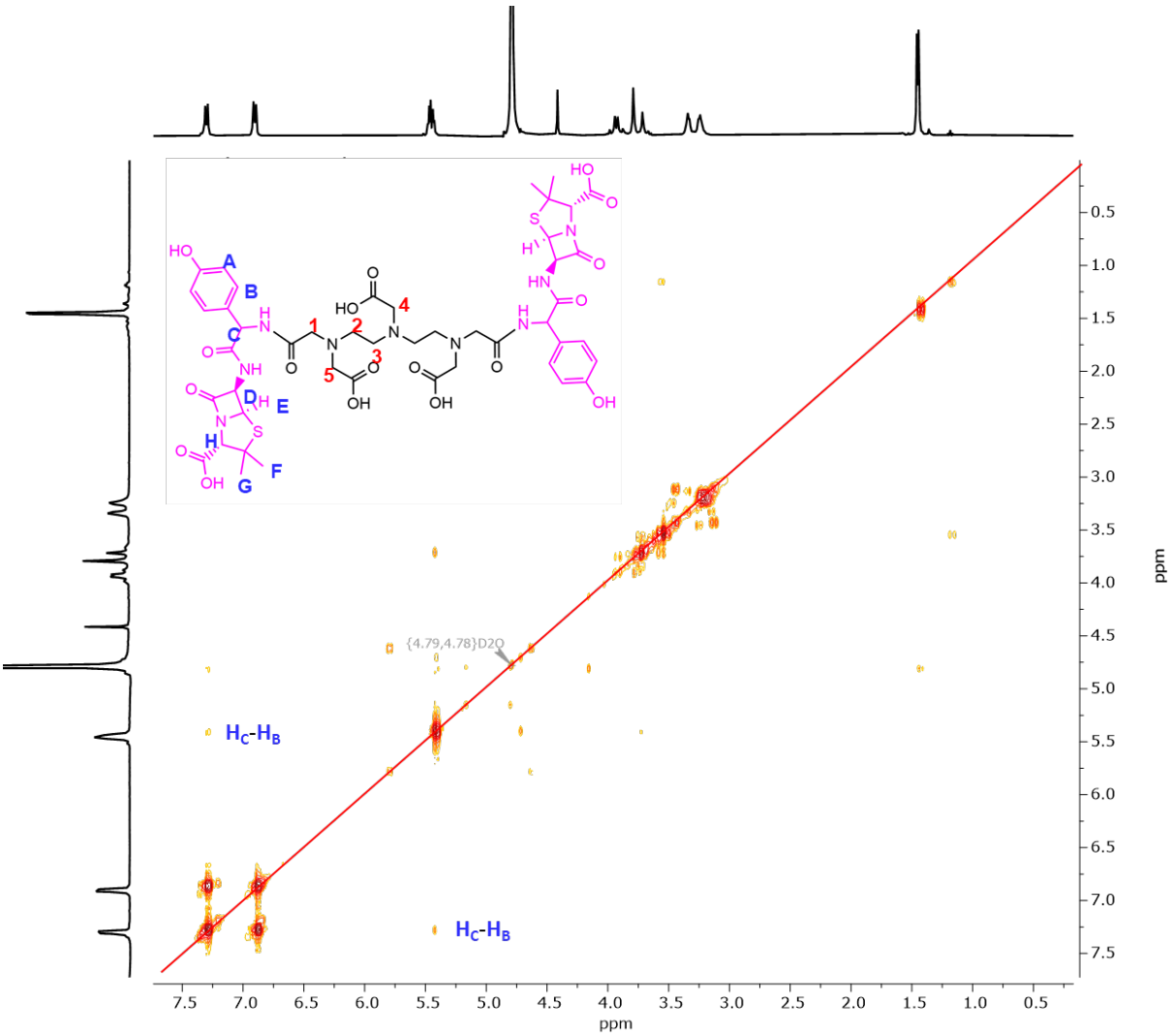

Figure 3.S31. COSY ^{1}H-NMR (400 MHz, D_2O) of **DTPA-Amox$_2$**.

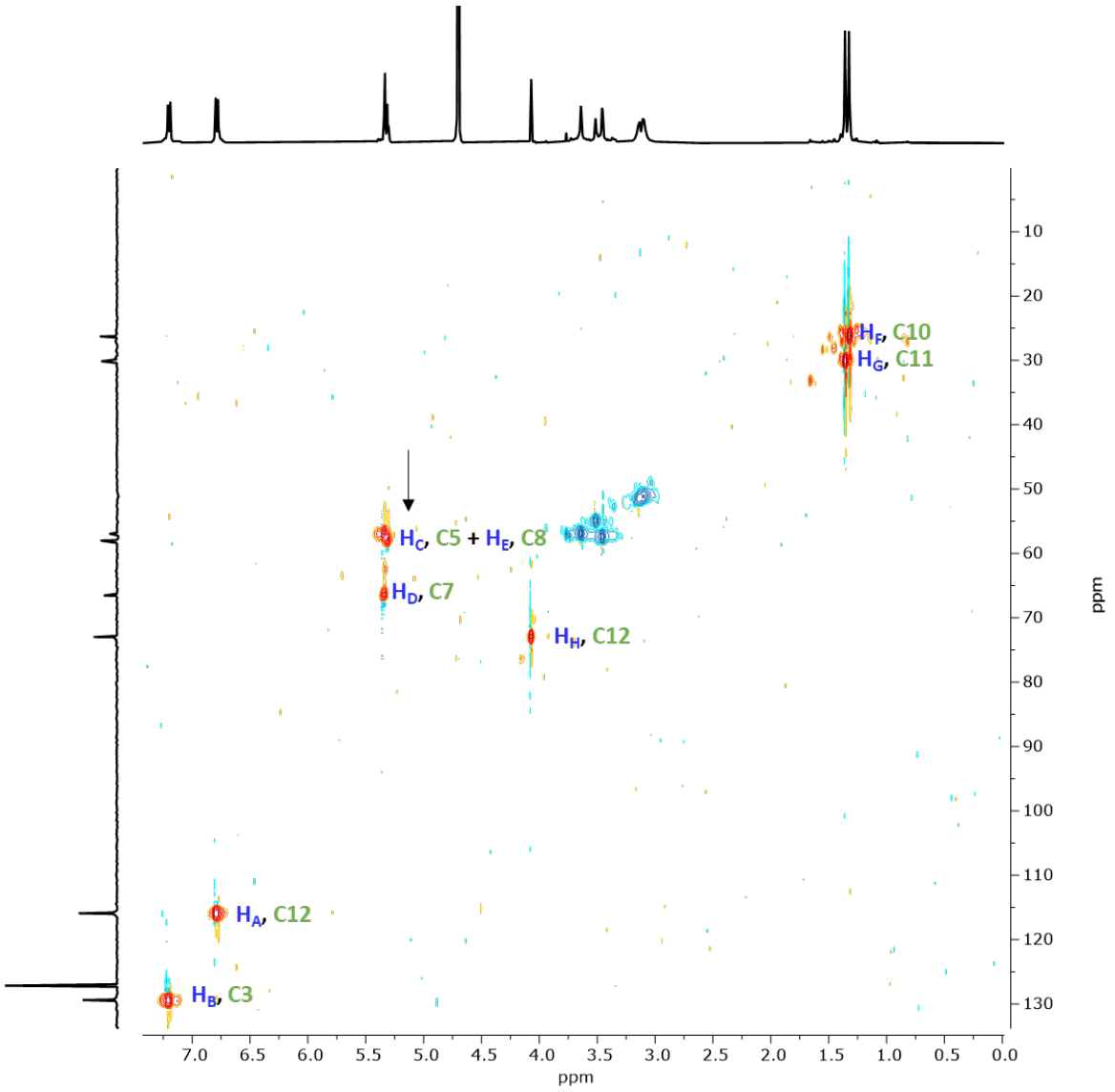

Figure 3.S32. HSQC (400 MHz, D_2O) spectrum of **DTPA-Amox$_2$**.

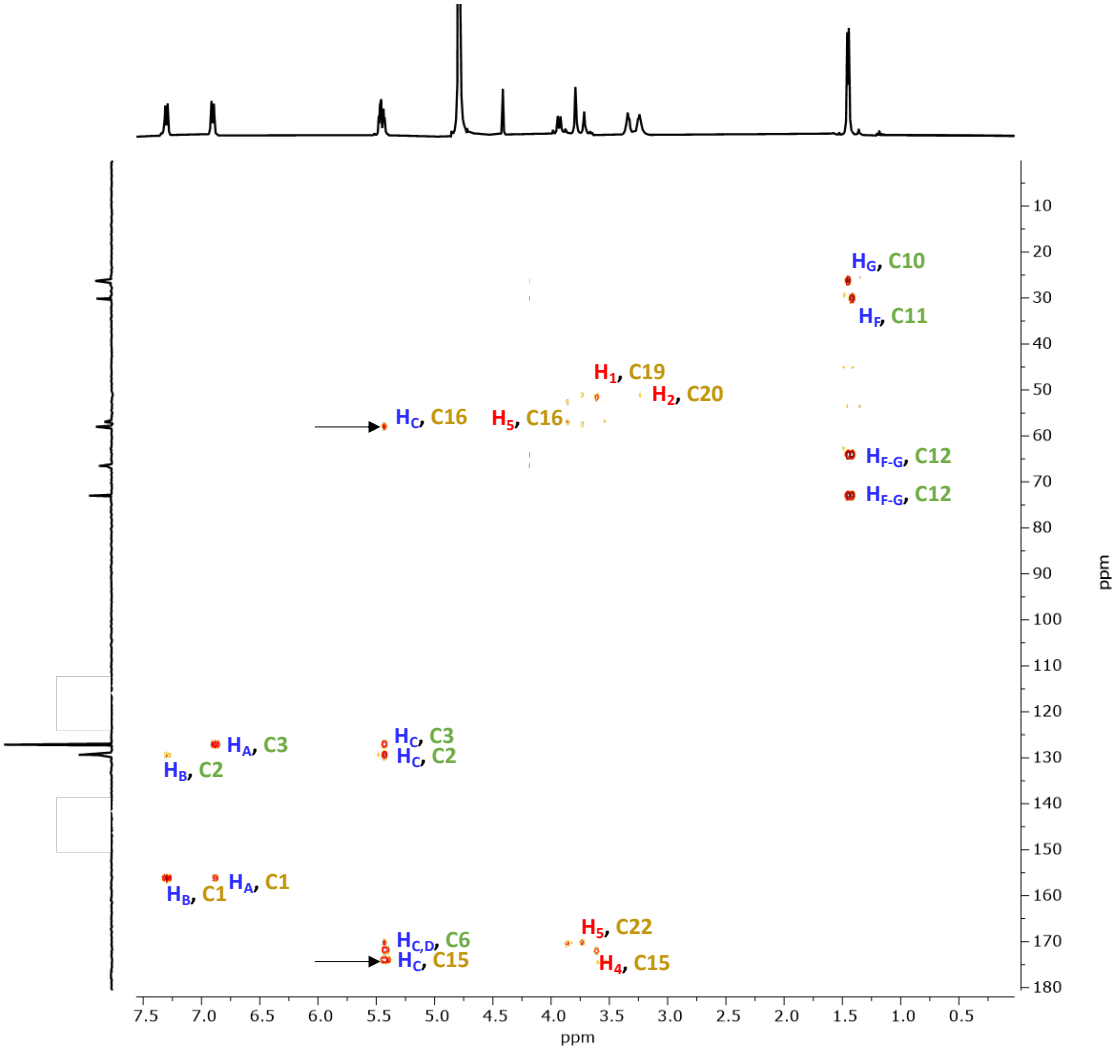

Figure 3.S33. HMBC (400 MHz, D_2O) spectrum of **DTPA-Amox$_2$**.

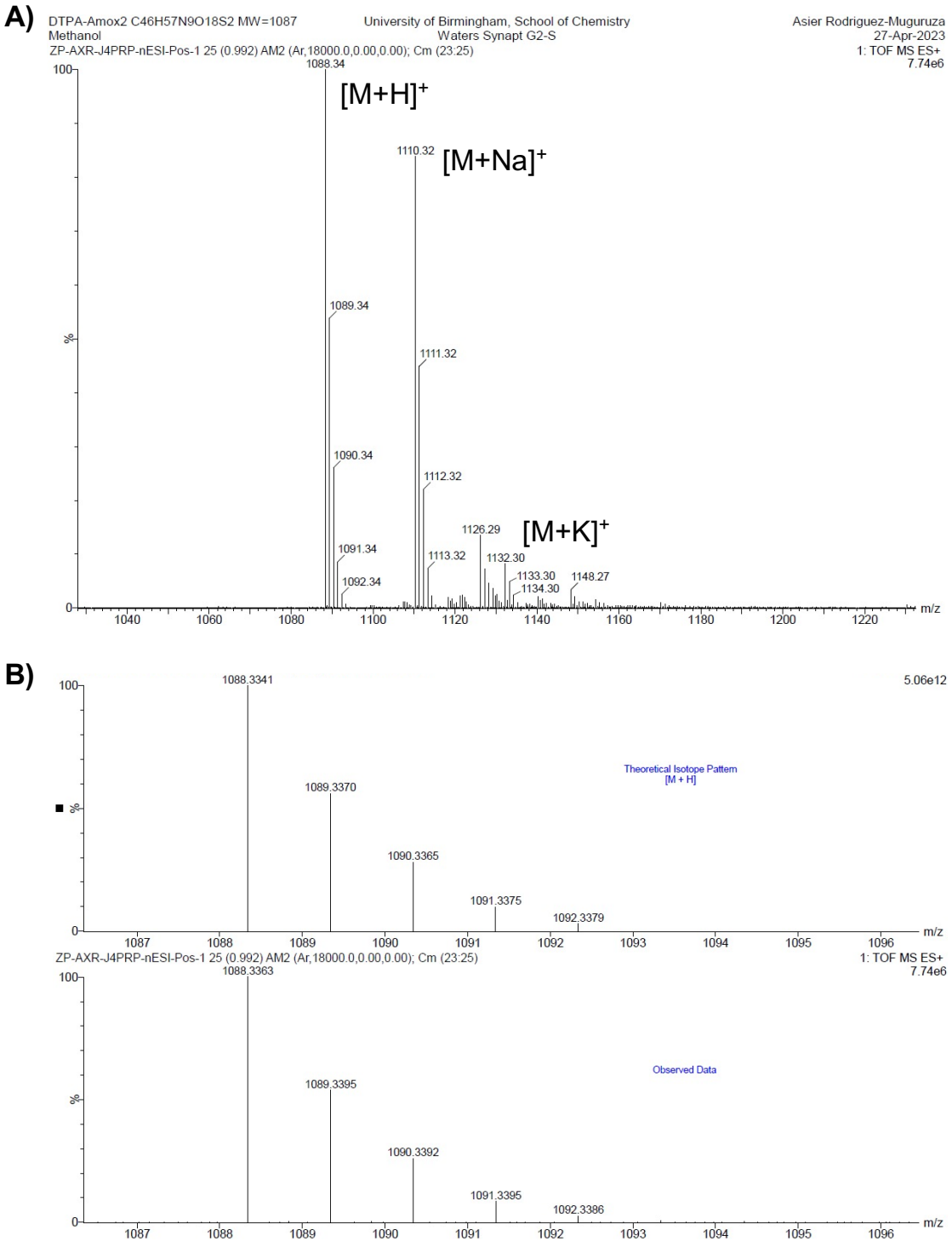

Figure 3.S34. (+)ESI-MS of **DTPA-Amox$_2$**. (B) comparison between observed and theoretical isotope pattern.

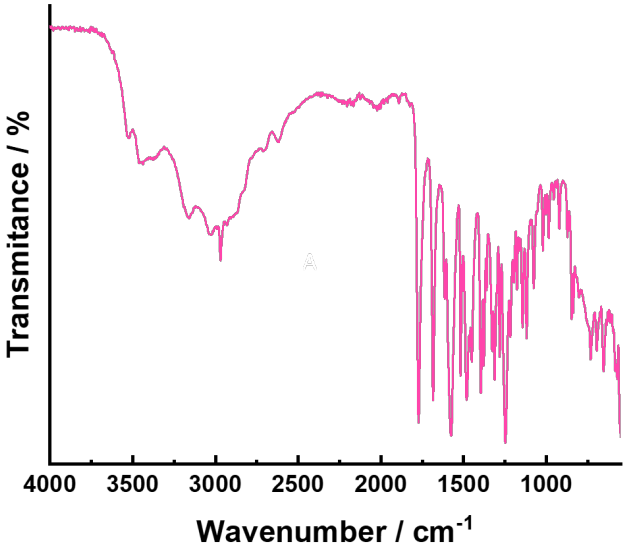

Figure 3.S35. FT-IR spectra of **DTPA-Amox$_2$**.

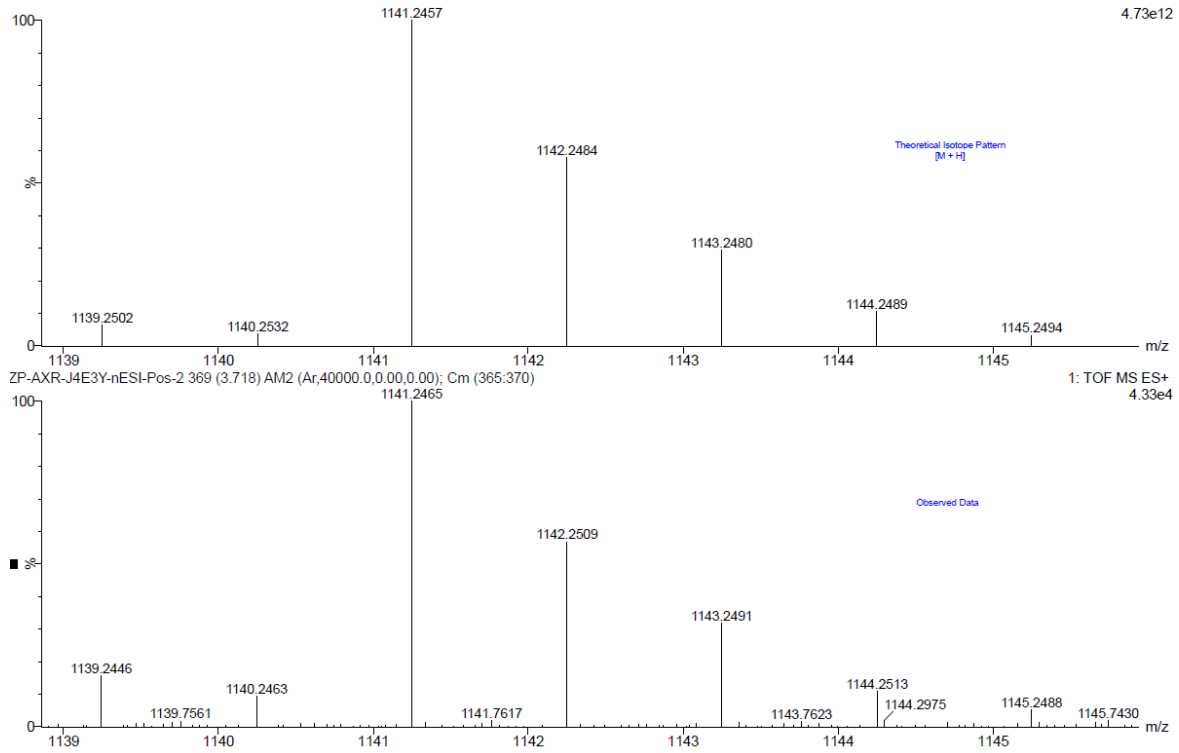

Figure 3.S36. ESI-MS (+) of **Fe^{3+}DTPA-Amox$_2$**.

Table 3.S6. Minimal inhibitory concentration (MIC, mg/mL) of **DTPA-Amox$_2$**, **Fe^{3+}DTPA-Amox$_2$** for *S. aureus* (ATCC23851), *E. coli* (MG1655) and *P. aeruginosa* (PA14) upon shaking at 150 rpm at 37 °C in LB media. Depicted results are based on 3 biological replicas.

	S. aureus	***E. coli***	***P. aeruginosa***
DTPA-Amox$_2$	2.4	47.6	95.3
Fe^{3+}DTPA-Amox$_2$	0.6	6.2	6.2

3.7. References

1 R. Saha, N. Saha, R. S. Donofrio and L. L. Bestervelt, *J. Basic Microbiol.*, 2013, **53**, 303–317.

2 M. Saha, S. Sarkar, B. Sarkar, B. K. Sharma, S. Bhattacharjee and P. Tribedi, *Environ. Sci. Pollut. Res.*, 2016, **23**, 3984–3999.

3 A. Khan, P. Singh and A. Srivastava, *Microbiol. Res.*, 2018, **212**–**213**, 103–111.

4 J. Kramer, Ö. Özkaya and R. Kümmerli, *Nat. Rev. Microbiol.*, 2020, **18**, 152–163.

5 K. N. Raymond, E. A. Dertz and S. S. Kim, *Proc. Natl. Acad. Sci. U. S. A.*, 2003, **100**, 3584–3588.

6 D. Al Shaer, O. Al Musaimi, B. G. de la Torre and F. Albericio, *Eur. J. Med. Chem.*, 2020, **208**, 112791.

7 J. L. H. Madsen, T. C. Johnstone and E. M. Nolan, *J. Am. Chem. Soc.*, 2015, **137**, 9117–9127.

8 T. B. Field, J. L. McCourt and W. A. E. McBryde, *Can. J. Chem.*, 1974, **52**, 3119–3124.

9 D. Rodríguez and C. González-Bello, *Bioorganic Med. Chem. Lett.*, 2023, 87, 129282.

10 R. M. Pollet, L. M. Martin and N. M. Koropatkin, *Mol. Microbiol.*, 2021, **115**, 490–501.

11 J. S. Brown and D. W. Holden, *Microbes Infect.*, 2002, **4**, 1149–1156.

12 G. L. A. Mislin and I. J. Schalk, *Metallomics*, 2014, **6**, 408–420.

13 G. Ganne, K. Brillet, B. Basta, B. Roche, F. Hoegy, V. Gasser and I. J. Schalk, *ACS Chem. Biol.*, 2017, **12**, 1056–1065.

14 S. C. Andrews, A. K. Robinson and F. Rodríguez-Quiñones, *FEMS Microbiol. Rev.*, 2003, **27**, 215–237.

15 Y. Seyoum, K. Baye and C. Humblot, *Gut Microbes*, 2021, **13**, e1874855.

16 T. E. Clarke, S. Y. Ku, D. R. Dougan, H. J. Vogel and L. W. Tari, *Nat. Struct. Biol.*, 2000, **7**, 287–291.

17 T. E. Clarke, V. Braun, G. Winkelmann, L. W. Tari and H. J. Vogel, *J. Biol. Chem.*, 2002, **277**, 13966–13972.

18 B. Rayner, A. D. Verderosa, V. Ferro and M. A. T. Blaskovich, *RSC Med. Chem.*, 2023, **14**, 800–822.

19 D. Rodríguez and C. González-Bello, *Bioorganic Med. Chem. Lett.*, 2023, **87**,

129282.

20 W. Neumann, M. Sassone-Corsi, M. Raffatellu and E. M. Nolan, *J. Am. Chem. Soc.*, 2018, **140**, 5193–5201.

21 C. Ji and M. J. Miller, *Bioorganic Med. Chem.*, 2012, **20**, 3828–3836.

22 L. Pinkert, Y. H. Lai, C. Peukert, S. K. Hotop, B. Karge, L. M. Schulze, J. Grunenberg and M. Brönstrup, *J. Med. Chem.*, 2021, **64**, 15440–15460.

23 T. Katsube, R. Echols and T. Wajima, *Clin. Infect. Dis.*, 2019, **69**, S552–S558.

24 S. Yoganathan and S. J. Miller, *J. Med. Chem.*, 2015, **58**, 2367–2377.

25 I. S. Shchelik and K. Gademann, *ACS Med. Chem. Lett.*, 2021, **12**, 1898–1904.

26 C. Peukert, A. C. Vetter, H. L. S. Fuchs, K. Harmrolfs, B. Karge, M. Stadler and M. Brönstrup, *Chem. Sci.*, 2023, **14**, 5490–5502.

27 C. Peukert, V. Gasser, T. Orth, S. Fritsch, V. Normant, O. Cunrath, I. J. Schalk and M. Brönstrup, *J. Med. Chem.*, 2023, **66**, 553–576.

28 A. Pandey, C. Savino, S. H. Ahn, Z. Yang, S. G. Van Lanen and E. Boros, *J. Med. Chem.*, 2019, **62**, 9947–9960.

29 B. Yang, F. Hoegy, G. L. A. Mislin, P. J. Mesini and I. J. Schalk, *J. Inorg. Biochem.*, 2011, **105**, 1293–1298.

30 M. Hannauer, Y. Barda, G. L. A. Mislin, A. Shanzer and I. J. Schalk, *J. Bacteriol.*, 2010, **192**, 1212–1220.

31 C. Guo and E. M. Nolan, *J. Am. Chem. Soc.*, 2022, **144**, 12756–12768.

32 D. Martínez-Matamoros, S. Castro-García, M. Balado, A. Matamoros-Veloza, M. A. Camargo-Valero, O. Cespedes, J. Rodríguez, M. L. Lemos and C. Jiménez, *RSC Adv.*, 2019, **9**, 13533–13542.

33 R. Biesuz, G. Emma, C. Milanese, G. Dacarro, A. Taglietti, V. M. Nurchi and G. Alberti, *Analyst*, 2014, **139**, 3932–3939.

34 M. Pawlaczyk and G. Schroeder, *ACS Omega*, 2021, **6**, 15168–15181.

35 G. Alberti, G. Emma, R. Colleoni, M. Pesavento, V. M. Nurchi and R. Biesuz, *Analyst*, 2014, **139**, 3940–3948.

36 P. Duenas-Ramirez, C. Bertagnolli, R. Müller, K. Sartori, A. Boos, M. Elhabiri, S. Bégin-Colin and D. Mertz, *J. Colloid Interface Sci.*, 2020, **579**, 140–151.

37 A. Rasheed, A. A. C. Carvalho, G. G. A. de Carvalho, T. Ghous, C. S. Nomura and B. P. Esposito, *Environ. Sci. Pollut. Res.*, 2020, **27**, 15635–15644.

38 M. Raju, S. Srivastava, R. R. Nair, I. H. Raval, S. Haldar and P. B. Chatterjee, *Biosens. Bioelectron.*, 2017, **97**, 338–344.

39 D. J. Phillips, G. L. Davies and M. I. Gibson, *J. Mater. Chem. B*, 2015, **3**, 270–275.

40 R. M. Smith and A. E. Martell, *Critical Stability Constants*, 1976, vol. 6.

41 A. R. Muguruza, A. di Maio, N. J. Hodges, J. M. A. Blair and Z. Pikramenou, *Nanoscale Adv.*, 2023, **5**, 2453–2461.

42 F. Ahangaran and A. H. Navarchian, *Adv. Colloid Interface Sci.*, 2020, **286**, 102298.

43 K. Braun, A. Pochert, M. Lindén, M. Davoudi, A. Schmidtchen, R. Nordström and M. Malmsten, *J. Colloid Interface Sci.*, 2016, **475**, 161–170.

44 Y. Jiang, W. Zheng, K. Tran, E. Kamilar, J. Bariwal, H. Ma and H. Liang, *Nat. Commun.*, 2022, **13**, 197–204.

45 A. Lo Sciuto and F. Imperi, *Antimicrob. Agents Chemother.*, 2018, **62**, e01820-17.

46 A. Lo Sciuto, M. Cervoni, R. Stefanelli, C. Mancone and F. Imperi, *Int. J. Antimicrob. Agents*, 2020, **55**, 105957.

47 J. Ghimire, S. Guha, B. J. Nelson, L. A. Morici and W. C. Wimley, *J. Membr. Biol.*, 2022, **255**, 503–511.

48 V. Prachayasittikul, C. Isarankura-Na-Ayudhya, T. Tantimongcolwat, C. Nantasenamat and H. J. Galla, *Acta Biochim. Biophys. Sin. (Shanghai).*, 2007, **39**, 901–913.

49 M. Vaara, *Microbiol. Rev.*, 1992, **56**, 395–411.

50 K. D. Krewulak and H. J. Vogel, *Biochim. Biophys. Acta - Biomembr.*, 2008, **1778**, 1781–1804.

51 I. L. Lamont, P. A. Beare, U. Ochsner, A. I. Vasil and M. L. Vasil, *Proc. Natl. Acad. Sci. U. S. A.*, 2002, **99**, 7072–7077.

52 A. Luscher, L. Moynié, S. Auguste, D. Bumann and L. Mazza, *Antimicrob. Agents Chemother.*, 2018, **62**, e00097-18.

53 J. E. Cassat and E. P. Skaar, *Cell Host Microbe*, 2013, **13**, 509–519.

54 B. A. Diep, Q. Phung, S. Date, D. Arnott, C. Bakalarski, M. Xu, G. Nakamura, D. L. Swem, M. K. Alexander, H. N. Le, T. T. Mai, M. W. Tan, E. J. Brown and M. Nishiyama, *J. Infect. Dis.*, 2014, **209**, 1533–1541.

55 J. C. Grigg, J. Cheung, D. E. Heinrichs and M. E. P. Murphy, *J. Biol. Chem.*, 2010, **285**, 34579–34588.

56 J. A. Morrissey, A. Cockayne, P. J. Hill and P. Williams, *Infect. Immun.*, 2000, **68**, 6281–6288.

57 A. Cherkasov, M. Hsing, R. Zoraghi, L. J. Foster, R. H. See, N. Stoynov, J. Jiang, S. Kaur, T. Lian, L. Jackson, H. Gong, R. Swayze, E. Amandoron, F. Hormozdiari, P. Dao, C. Sahinalp, O. Santos-Filho, P. Axerio-Cilies, K. Byler, W. R. McMaster, R. C. Brunham, B. B. Finlay and N. E. Reiner, *J. Proteome Res.*,

2011, **10**, 1139–1150.

58 G. Cabrera, A. Xiong, M. Uebel, V. K. Singh and R. K. Jayaswal, *Appl. Environ. Microbiol.*, 2001, **67**, 1001–1003.

59 M. Riley, T. Abe, M. B. Arnaud, M. K. B. Berlyn, F. R. Blattner, R. R. Chaudhuri, J. D. Glasner, T. Horiuchi, I. M. Keseler, T. Kosuge, H. Mori, N. T. Perna, G. Plunkett, K. E. Rudd, M. H. Serres, G. H. Thomas, N. R. Thomson, D. Wishart and B. L. Wanner, *Nucleic Acids Res.*, 2006, **34**, 1–9.

60 C. Härle, I. S. Kim, A. Angerer and V. Braun, *EMBO J.*, 1995, **14**, 1430–1438.

61 B. A. Ozenberger, M. Schrodt Nahlik and M. A. McIntosh, *J. Bacteriol.*, 1987, **169**, 3638–3646.

62 A. Mademidis and W. Köster, *Mol. Gen. Genet.*, 1998, **258**, 156–165.

63 G. L. Winsor, E. J. Griffiths, R. Lo, B. K. Dhillon, J. A. Shay and F. S. L. Brinkman, *Nucleic Acids Res.*, 2016, **44**, D646–D653.

64 K. Poole, S. Neshat and D. Heinrichs, *FEMS Microbiol. Lett.*, 1991, **78**, 3680–3684.

65 K. Poole, S. Neshat, K. Krebes and D. E. Heinrichs, *J. Bacteriol.*, 1993, **175**, 4597–4604.

66 B. Ghysels, B. T. M. Dieu, S. A. Beatson, J. P. Pirnay, U. A. Ochsner, M. L. Vasil and P. Cornelis, *Microbiology*, 2004, **150**, 1671–1680.

67 M. A. Llamas, M. Sparrius, R. Kloet, C. R. Jiménez, C. Vandenbroucke-Grauls and W. Bitter, *J. Bacteriol.*, 2006, **188**, 1882–1891.

68 E. Banin, M. L. Vasil and E. P. Greenberg, *Proc. Natl. Acad. Sci. U. S. A.*, 2005, **102**, 11076–11081.

69 C. R. Dean and K. Poole, *Mol. Microbiol.*, 1993, **8**, 1095–1103.

70 B. Ghysels, U. Ochsner, U. Möllman, L. Heinisch, M. Vasil, P. Cornelis and S. Matthijs, *FEMS Microbiol. Lett.*, 2005, **246**, 167–174.

71 T. C. Johnstone and E. M. Nolan, *J. Am. Chem. Soc.*, 2017, **139**, 15245–15250.

72 A. R. Kaplan, D. G. Musaev and W. M. Wuest, *ACS Infect. Dis.*, 2021, **7**, 544–551.

73 I. J. Schalk and L. Guillon, *Environ. Microbiol.*, 2013, **15**, 1661–1673.

74 S. Bolte and F. P. Cordelieres, *J. Microsc.*, 2006, **224**, 213–232.

75 A. N. Dosumu, S. Claire, L. S. Watson, P. M. Girio, S. A. M. Osborne, Z. Pikramenou and N. J. Hodges, *JACS Au*, 2021, **1**, 174–186.

76 S. Akter, Y. Migiyama, H. Tsutsuki, K. Ono, C. Hamasaki, T. Zhang, K. Miyao, T. Toyomoto, K. Yamamoto, W. Islam, T. Sakagami, H. Matsui, Y. Yamaguchi and T. Sawa, *Microbiol. Immunol.*, 2021, **65**, 449–461.

77 L. M. Lima, B. N. M. da Silva, G. Barbosa and E. J. Barreiro, *Eur. J. Med. Chem.*, 2020, **208**, 112829.

78 C. M. J. Wesseling and N. I. Martin, *ACS Infect. Dis.*, 2022, **8**, 1731–1757.

79 R. J. W. Lambert, G. W. Hanlon and S. P. Denyer, *J. Appl. Microbiol.*, 2004, **96**, 244–253.

80 L. L. Ruston, G. M. Robertson and Z. Pikramenou, *Chem. - An Asian J.*, 2010, **5**, 571–580.

4. SPIROPYRAN-CONTAINING PHOTORESPONSIVE ORGANOSILICA NANOPARTICLES FOR ANTIBIOTICS DELIVERY IN URINARY TRACT INFECTIONS

4.1. Introduction

4.1.1. Catheter Associated Urinary Tract Infections

Catheters are silicone or latex based medical devices used to treat numerous conditions where the drainage of internal fluids is required. Most catheters are used in order to treat conditions related to bladder dysfunction and manage of urine output.[1] Moreover, urinary catheters are the source of most of bacterial infections produced due to catheters use. Apart from bacterial infections, the use of catheters may also produce nonbacterial urethral inflammation, urethral strictures, mechanical trauma, and mobility impairment.[2,3]

Infections arising from the use of indwelling biomedical devices cause an indisputable increase in morbidity and mortality, including patient discomfort and high medical cost.[2] Bacteria may migrate from adjacent tissues, leading to biofilms formation. In fact, according to UK's National Health systems' (NHS) data, an average of £10,000 per patient are used to treat catheter-associated urinary tract infections (CAUTIs).[4] However, bacteria colonization of the urinal tract may not manifest any symptoms, but

can couse asymptomatic bacteriuria.[5] Risk of CAUTI increases with the time of use of catheters; thereby, long-term users (c.a. more than 2 week), mostly patients with severe conditions or in community or nurse care home settings, will be more likely to suffer from these infections; being also one of the most vulnerable patient groups.[1]

The most common bacterial species isolated from CAUTI patients are those naturally present in the patient's natural bacterial flora or from the hand of healthcare personal; these organisms include *Escherichia coli, Proteus mirabilis* and *Pseudomonas, Klebsiella, Enterobacter* genus bacteria or *Candida* fungus. Furthermore, isolated Gram-negative bacteria usually present multidrug resistance.[6]

4.1.2. Nanotechnology against catheter-associated UTIs

CAUTI treatment is mainly focused for short-term treatments, as long-term infections associated with catheterisations are almost impossible to fully treat.[7] In fact, most trials related to the use of antimicrobial agents conclude the same: antimicrobial compounds are effective for short-term treatments, but in case on long-terms treatments, bacteriuria and UTI can be suppressed temporarily, but resistant flora eventually appear.[3,8] Resistant bacteria are able to overcome the antibiotic action and due to the constant nutrient flow, bacteria with antibacterial resistance may grow.[9] Moreover, some of most common commercialised antimicrobial compounds are not indicated for long-term use.[10]

Prevention of CAUTI using nanotechnology has mainly focused on the modification of the catheter surface for prevention of biofilm formation and/or *in-situ* antibiotic delivery (Figure 4.1).[11–13]

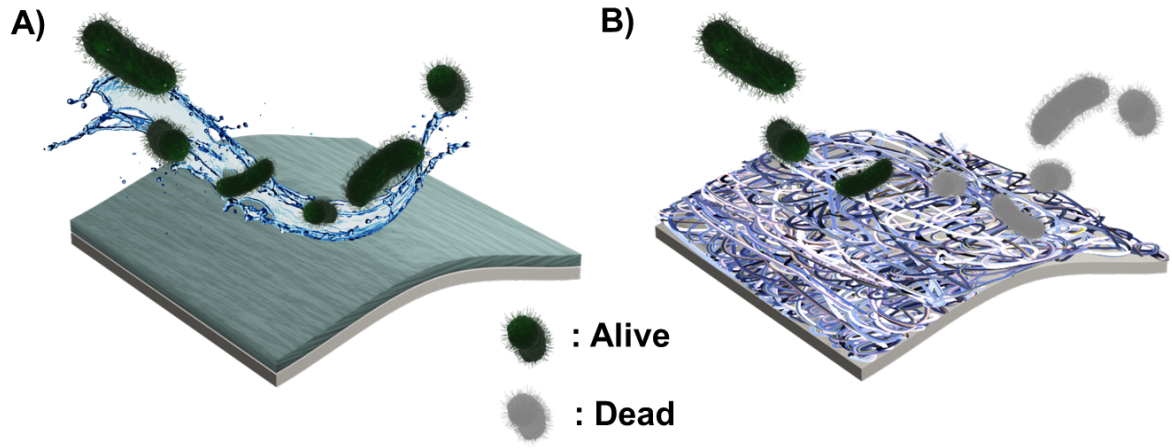

Figure 4.1. Scheme of CAUTI prevention by (A) catheter antifouling surface modification and (B) *in-situ* drug delivery from catheter's surface.

Prevention of biofilm formation has been achieved in catheter surfaces by modification with polymer brushes (polymer chains tethered to a surface) to increase surfaces' hydrophobicity.[7] For instance, polydopamine coating was applied over silicone-based catheters, for further conjugation of lysine and α-aminoisobutyric acid with polydopamine resulted in coatings with increased antifouling properties.[14] Furthermore, hydrophobicity of polydopamine was further increased by conjugation with the hydrophobic perfluorodecanethiol.[15] Results proved the antifouling ability of the coating using *E. coli* and *B. subtilis* as model organisms.[14,15] Similarly, anionic and cationic polymer brushes conjugated with dopamine were synthetized and then conjugated to the surface, preventing *S. aureus* addeshion.[16]

Most catheter coatings for drug delivery are based on functionalization of polymer brushed where the antibiotic of interest is entrapped. The presence of polymer brushes also enhances the antifouling properties of the surface. Nevertheless, this strategy leads to burst and uncontrolled release of antibiotics, not been adequate for long-term catheterizations.[17] Hydrogels have also been deposited onto hydrophobic surfaces in catheter devices. Release of antibacterials such as vancomycin and antimicrobial peptides has been achieved through this approach.[18] Nevertheless, the bacterial

species that mainly colonize catheters are Gram-negative bacteria, and vancomycin is not active against them.[19] Deposition of **AgNPs** also resulted in catheters with antibacterial properties due to the leakage of Ag^+ ions.[15,20–22]

Catheters have also been coated with nanoparticles containing antibiotics. Catheter coated with polymer nanoparticles containing chlorhexidine displayed antibacterial activity against *E. coli* and *S. aureus* species over 10 days since catheterization.[23] Similarly, other molecules with antibacterial properties such as resveratrol and quercetin have been release from polymer nanoparticle-coated catheter surfaces under dynamic flow conditions.[24] Wu *et al*. reported the surface functionalisation of a silicone-based cardiovascular catheter with agarose and heparin loaded mesoporous silica nanoparticles (**MSNs**). Nanoparticles were covalently anchored onto the surface. *E. coli* and *S. aureus* attachment inhibition was confirmed due to heparin release.[25]

4.1.3. Photoresponsive silica nanoparticles for drug delivery

Due to the chemical versatility of **SiO_2**, triggered drug delivery systems have been widely studied in order to develop DDS to deliver the desired cargo on demand. One of the main triggers studied has been light. Three different approaches have been followed in the literature for the design of photoresponsive silica-based DDS: conjugation of photoresponsive pore valves or nanoimpillers in case of **MSNs** and development of non-porous **SiO_2** with photocleavable bonds for their photodegradation (Figure 4.2). [26,27]

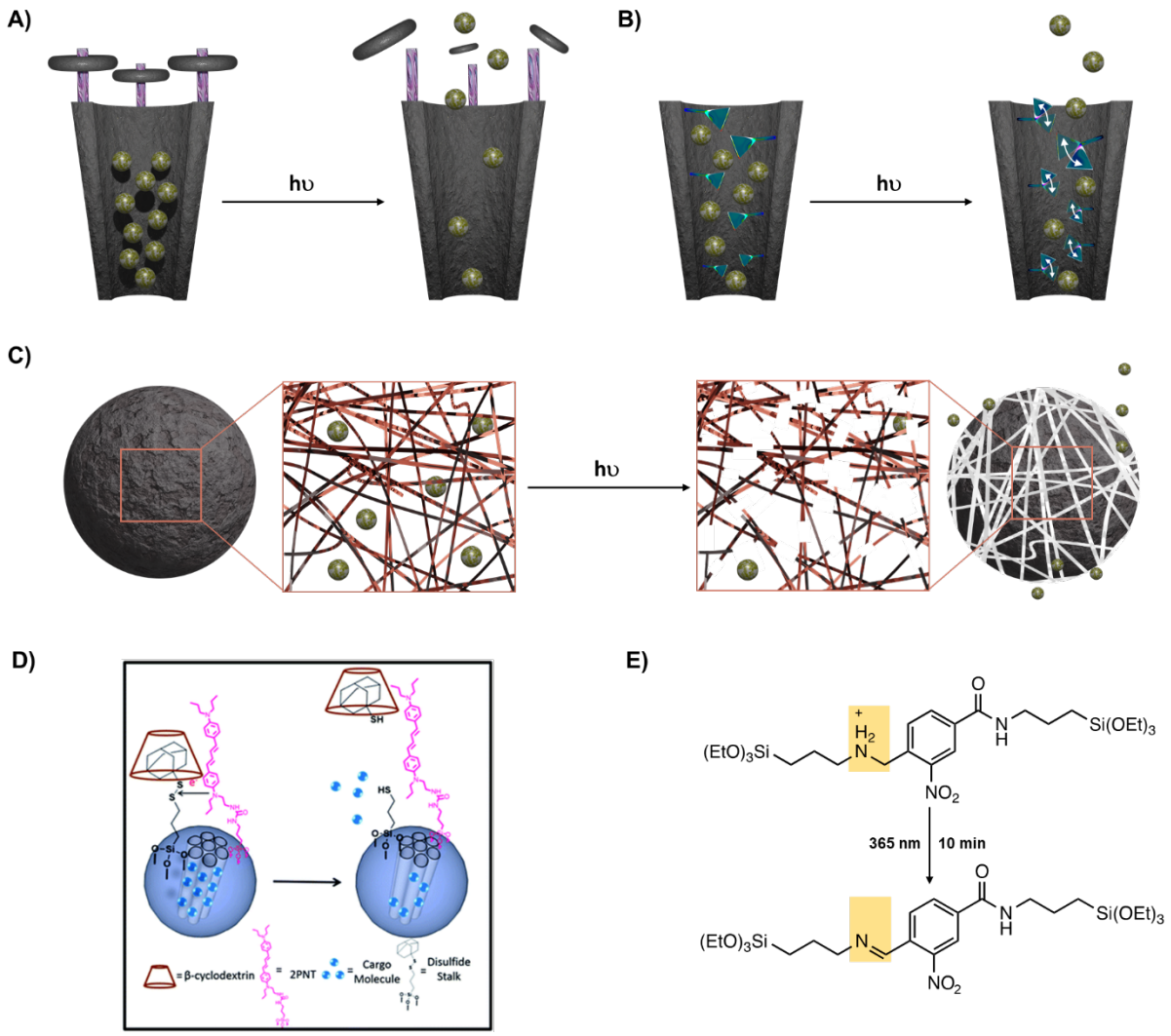

Figure 4.2. (A-C) Scheme for different strategies for the development of photoresponsive silica nanoparticles for drug delivery. (D) Scheme of cyclodextrin-capped dye loaded MSNs adapted from Zink and co-workers.[28] (E) Chemical structure of photoresposive silica precursors where the photoconversion of the ammonium group to imine upon blue light irradiation adapted from Y. Fatieiev *et al*.[29]

MSNs' pores have been blocked with photoresponsive gates to control the burst release of cargos (Figure 4.2A). [30–32] Cyclodextrins has been widely employed as pore gates due to their host-guest properties and large size of their inner cavity. **MSNs**' surface has been modified with azobenzene-containing brushes where the cyclodextrin can complex, being the azo-compounds the guest structure within the cyclodextrin cavity. The large volume of the resulting complex prevents the release of

loaded cargos. However, upon light irradiation (green light), *trans*-to-*cis* isomerization of the azo compounds leads to cyclodextrin decomplexation and release of the cargo.[30–32] Similarly, cyclodextrins have be conjugated onto **MSNs** surface *via* disulphide bonds, cleavable by two-photon induced energy transfer (Figure 4.2D).[28] Furthermore, photocleaving of guest surface stack has been also widely reported as strategy for gate opening.[33] Finally, cyclodextrin-decorated **AuNPs** have been added on to **MSNs**' surface. Upon irradiation, isomerization of the guest structure within the cyclodextrin cavity lead to **AuNPs** dissociation and cargo release.[34] Most of the reported studies were performed using dyes as cargo. Release of drugs such as anticancer[35–37] or anti-inflammatory[38,39] have also been explored from photoresponsive silica nanoparticles. However, none of the reported systems has been applied for the delivery of antibiotics.

Another reported approach is the design of silica nanoparticles with photoresponsive building units. Silyl-derivatives of azobenzene have been anchored within the **MSNs**' pores. The azobenzene moieties worked as nanoimpillers upon irradiation, leading to enhanced cargo release (Figure 4.2B).[40–42] Nevertheless, the introduction of photoresponsive building units within the framework of **SiO_2** is very limited in the literature and mainly focused on the structural properties of the resulting nanomaterials (Figure 4.2C). Fatieiev *et al*. reported a hollow **SiO_2** nanoparticle composed by *o*-nitrophenylene–ammonium bridges. The presence of these bridges resulted in an overall positive surface charged nanoparticle (+46 mV) where negatively charge DNA could be loaded within the surface *via* electrostatic interactions. Upon irradiation (365 nm) the ammonium moiety photoconverted into a neutral imine, changing the overall particle surface charge to -39 mV releasing the surface-interacting DNA (Figure 4.2D).[29] Beside this system, other organosilica nanoparticles containing *o*-nitrobenzyl

groups have been developed and their degradation confirmed upon irradiation (320 nm).[43]

4.1.4. Spiropyran-containing silica nanoparticles

Photoswitches are molecules that are able to change their conformation upon irradiation, in a reversible way. Spiropyrans are unique photoswitches that have attracted the interest of the scientific community due to their unique photophysical properties, versatility and biocompatibility.[44,45] In contrast with other well-known photoswitches, such as, azobenzenes or stilbenes, spiropyrans displayed unique isomers with vastly different properties (Figure 4.3). Furthermore, spiropyran isomerization can be driven by a large number of stimuli, including, light, temperature, solvents, metal cations or redox potential, among others.[44]

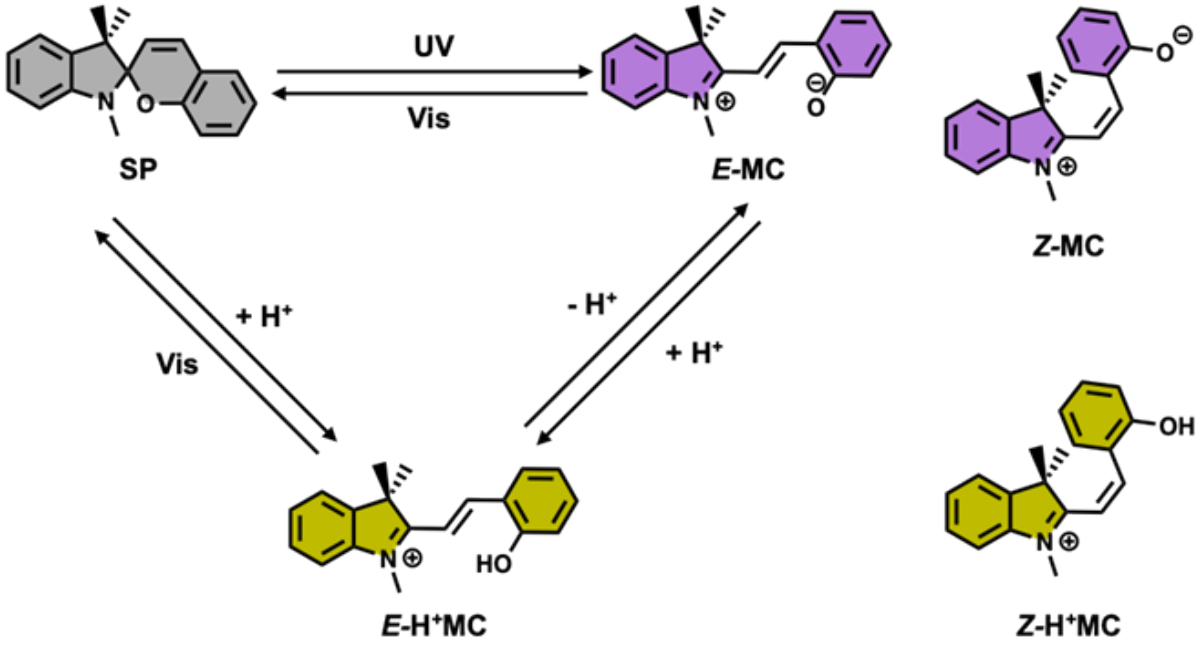

Figure 4.3. General chemical formula of spiropyrans and the different isomers.

The closed form of spiropyran will be donated as **SP**, while the open isomer (merocyanine) will be abbreviated as **MC**. Furthermore, the **MC** isomer can be protonated, leading to the **H^+MC** form (Figure 4.3). Similarly, due to the C=C double bond in the **MC** isomer, ***E*-MC** and ***Z*-MC** isomers can be defined, as well as the ***E*-H^+MC** and ***Z*- H^+MC** isomers. ***SP*-*to*-*MC*** isomerization takes place upon UV irradiation and its reverse isomerization upon visible light (> 360 nm).[44] Due to the chemical versatility of spiropyrans, functionalization of the aromatic moieties can be employed to tune wavelength requited for isomerization.[46]

Spiropyrans have been included in a multitude types of materials, as previously reviewed.[47,48] In case of silica-base materials, the majority of reported systems are based on the direct encapsulation of the spiropyran molecule within the **SiO_2** framework during the nanoparticle formation.[49–51] Such systems have been explored as nanothermometers due to the thermoresponsive behaviours of the photoswitch.[52] Furthermore, a very interesting feature of such materials is the negative photochromism.[50,51,53] While usually, the primary form of the spiropyran is the **SP**, which isomerized in the **MC** upon UV irradiation; when it is embedded in the **SiO_2** framework, the **MC** form is stabilized through H-bonding between the molecule and the hydroxyl groups of the framework. The resulting stabilised **MC** form is able to isomerized to the **SP** form upon visible light irradiation, returning then to the **MC** form spontaneously.

Furthermore, silyl-functionalised spiropyran molecules (Figure 4.4) have been anchored to the silica framework of nanoparticles and xerogels.[54–58] Euchler *et al*. reported a xerogel containing the silyl-modified spiropyran where they managed to prevent the negative photochromism by employing dimethyldiethoxysilane (DMDES)

as framework precursor instead of the pure silica precursor triethoxysilane (TEOS); which yielded to a hydrophobic framework with lower density of hydroxyl groups.[54]

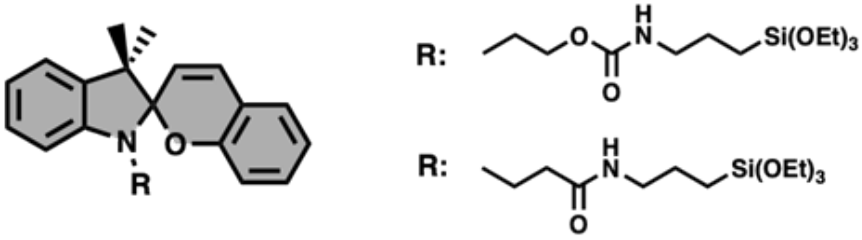

Figure 4.4. Chemical structure of previously reported silyl-modified spiropyran, adapted from Euchler *et al*.[54] and Allouche *et al*.[55]

Nevertheless, the use of spiropyran-containing **SiO_2** for drug delivery is very limited in the literature. Chen *et al*. reported the functionalization of **MSNs** containing fluorescein with APTES-modified spiropyran. The final system displayed a hydrophobic surface that prevented cargo release. Upon UV irradiation the surface **SP** isomerized to the hydrophilic **MC** form, allowing the cargo to be released.[59] The same principle was followed by He *et al*. for the delivery of the anticancer drug doxorubicin but using pH as triggering stimuli.[60] To our knowledge photoresponsive spiropyran-based antibiotic delivery systems have not been reported in the literature.

4.1.5. Chapter outline

In the current chapter the development of spyropiran-containing nanoparticles for the photoresponsive delivery of the first line UTI antibiotic trimethoprim (**TMP**) is explored (Figure 4.5). Optimization of the nanoparticle framework is investigated in order to obtain nanoparticles with high photoswitch content. Furthermore, the effect of hydrophobicity of the framework was studied. The antibacterial properties of nanoparticles were evaluated against a range of *E. coli* UTI clinical isolates. Hereby,

we present the first photoresponsive non-porous silica nanoparticle for antibiotic delivery, supposing a step forward for light responsive coating of clinical long-term catheters.

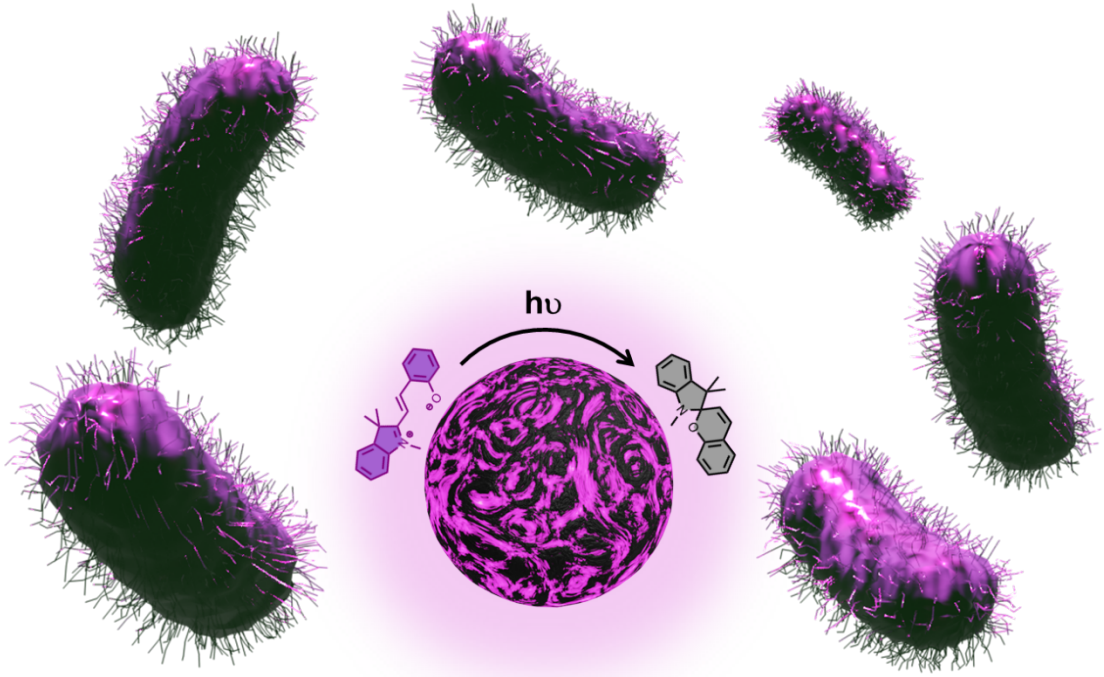

Figure 4.5. Schematic representation of developed photoresponsive nanoparticles a light-triggered antibiotic release.

4.2. Results and discussion

4.2.1. Synthesis of the photoresponsive silica precursor

The photoresponsive bridged-silyl derivative (**Si-SP-Si**, Figure 4.6) was designed to contain two silyl-moieties that could lead to a **SiO_2** framework with organic bridges between Si atoms. The synthesis of **Si-SP-Si** was developed by Daniel Cerasale, PhD student in Dr. Timothy Easun group. The full synthetic scheme and characterization of the **Si-SP-Si** precursor can be found in Figure 4.S1-S5.

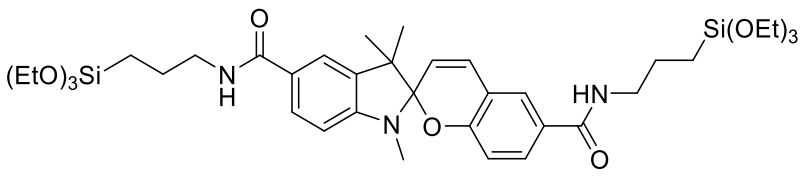

Figure 4.6. Structure of the photoresponsive **Si-SP-Si** precursor.

4.2.2. Optimization of SP-content in phoresponsive nanoparticles

We first wanted to find the how much **SP** can be in the nanoparticles without affecting their polydispersity and colloidal stability, and its effect in particle size and morphology. **Si-SP-Si** has never been explored in the literature, but spiropyran with a single APTES functionalization in the nitrogen atom of the indoline ring has been previously grafted within the **SiO_2** framework.[54,55,61] Previous work reported the initial content of the **SP** between 0.2 % and 2 % molar ratio respect to the silica precursor TEOS.[54,62] Nevertheless, if the content of the SP can be increase, and what effect could it have in the nanoparticles was investigated. Thereby, the synthesis of **SiO_2** nanoparticles with initial **SP** content of 0.2 %, 2 % and 5 % (molar ratio respect to TEOS) was explored. Above concentration of 5 %, the **Si-SP-Si** precursor was not soluble in the synthesis conditions. **SP-SiO_2** particles were synthetised based on a one-pot strategy previously described (Figure 4.7).[63] Particles only synthetised with TEOS were employed as control (**SiO_2**).

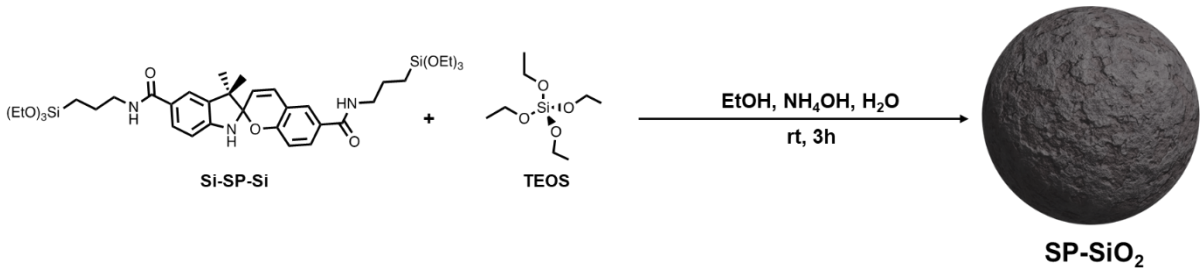

Figure 4.7. Synthesis scheme of **SP-SiO_2**.

SP-SiO$_2$ particles were first studied by DLS (Table 4.1 and Figure 4.S6) and TEM microscopy (Figure 4.8) to investigate their resulting size, morphology, and polydispersity.

DLS analysis revealed that the presence of **Si-SP-Si** reduced particle size, with a reduction in the hydrodynamic size of the particles when the initial content of **Si-SP-Si** was increased up to 2 %. While pure TEOS particles showed a hydrodynamic size (by volume) on 99 ± 30 nm, the use 0. 2 % **Si-SP-Si** did not significantly change the size of nanoparticles. Nevertheless, hydrodynamic size of nanoparticles decreased to 55 ± 18 nm with 2 % **Si-SP-Si**. Similarly, nanoparticle synthetized with initial 5 % **Si-SP-Si** display similar hydrodynamic diameter to those synthetized with 2 % **Si-SP-Si**. All nanoparticles display similar ζ-potential values around -30 mV, indicating that the presence of **SP** does not influence their colloidal stability.

Table 4.1. Dynamic light scattering (n = 5) and ζ-potential (n = 3) results of **SP-SiO$_2$** nanoparticles in PBS buffer (0.1 M, pH 7.4).

	Hydrodynamic diameter (D_H) / nm				**ζ-potential**
SP / %	**Intensity**	**Volume**	**Number**	**PDI**	**/ mV**
0	115 ± 24	99 ± 30	84 ± 10	0.03	- 32 ± 11
0.2	108 ± 31	93 ± 20	75 ± 10	0.08	-31 ± 7
2	69 ± 20	55 ± 18	41 ± 11	0.14	-28 ± 8
5	70 ± 27	53 ± 21	38 ± 12	0.15	-28 ± 9

TEM micrographs of particles (Figure 4.8) revealed spherical morphology nanoparticles. **SP-SiO$_2$** nanoparticle's size also decreased upon addition of **Si-SP-Si** precursor. Nevertheless, all particles displayed good monodispersity.

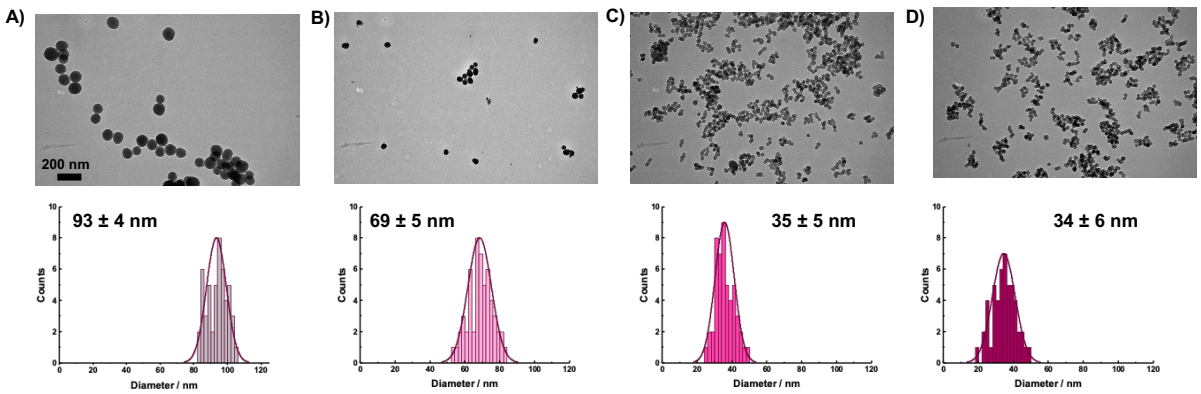

Figure 4.8. Transmission Electron Microscopy (TEM) images of **SP-SiO$_2$** nanoparticles synthetised with initial (A), 0 % (B) 0.2 %, (C) 2 % and (D) 5 % of **Si-SP-Si**, and nanoparticle size distribution (n = 50) based on TEM images.

Then, the composition of nanoparticles was explored by FT-IR (Figure 4.S8) and solid-state UV/Vis spectroscopy (Figure 4.9A). FT-IR confirmed the presence of the photoswitch moieties based on the C-H bendings and stretching observed at 2971 cm^{-1}, 2925 cm^{-1} and 2879 cm^{-1} alongside the carbonyl stretching of the amide at 1629 cm^{-1} (Figure 4.S8). Nevertheless, FT-IR spectra were dominated by the Si-O-Si and Si-OH stretches. Furthermore, based on solid-state UV/Vis spectroscopy, **SP**-containing nanoparticles displayed four absorption bands cantered at 235 nm, 295 nm, 430 nm and 525 nm. The high energy bands at 235 nm and 295 nm were assigned to the closed form of the photoswitch (**SP**), as compared with the UV/Vis spectra of **Si-SP-Si** in solid-state (Figure 4.S14) and the simulated UV/Vis profile of **SP** and **MC** (Figure 4.S15), while the bands at 430 nm and 530 nm were assigned to the open **H$^+$MC** and **MC** forms, as previously reported in the literature.[49,64] The bands assigned to the open forms of the **SP** were not present in the **Si-SP-Si** precursor. H-bonding and π–π stacking between spiropyran molecule in solid-state prevent their isomerization into the **MC** and **H$^+$MC** forms.[44] Nevertheless, it has been previously reported the spontaneous isomerization of the **SP** form into the **MC** form in **SiO$_2$** matrices due to

the H-bonding between the framework and the photoswitch, stabilizing it and locking the photoswitch in the **MC** form.[51,55] The **H⁺MC** form is the result of the **MC** protonation by the **SiO_2** framework, which is slightly acidic.[50,65]

The **SP-SiO_2** nanoparticle with initial 5 % **Si-SP-Si** was chosen for further studies as is displayed the highest content of the photoswitch (based on UV/Vis) alongside good polydispersity and colloidal stability.

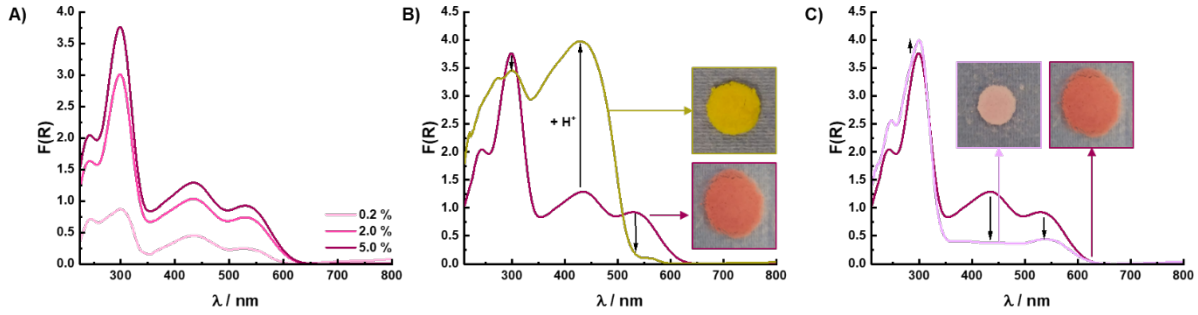

Figure 4.9. Solid-state UV/Vis spectra of (A) **SP-SiO_2** nanoparticles synthetised with different initial concentrations of **Si-SP-Si** and solid-state UV/Vis of selected **SP-SiO_2** after (B) acidic treatment and (C) solvent exchange with hexane. Inserts are photographs of the particles before UV/Vis measurements.

We further explored the UV/Vis profile of the selected **SP-SiO_2** nanoparticles to confirm that the 430 nm band was associated with the **H⁺MC** form and that the formation of the open **MC** and **H⁺MC** forms is driven by H-bonding with the framework. **SP-SiO_2** nanoparticles were subjected to acidic treatment by dispersion in aqueous concentrated HCl solution (6 M). Pink particles quickly turned bright yellow (Figure 4.9B insert) and after centrifugation and drying, solid-state UV/Vis spectroscopy releveled an increase in the 430 nm band (212 %) and the disappearance of the 530 nm band associated with the unprotonated **MC** form (Figure 4.9B); confirming that the 430 nm band correspond to the **H⁺MC** form. Furthermore, **SP-SiO_2** nanoparticles

were subjected to solvent exchanged, first with acetone to removed remaining water from the purification procedure, and then centrifuged and resuspended in hexane. Particles lost most colour, turning into pale pink (Figure 4.9C insert). Solid-state UV/Vis profile of the nanoparticles also revealed a significant decrease of the 430 nm (71 %) and 530 nm (49 %) bands and a small increase of the 235 nm and 295 nm bands; suggesting that a fraction of the open forms was converted into the close **SP** form due to the reduction of potential H-bonds.

4.2.3. Effect of hydrophobicity in SP

We further explored the effect of the nanoparticle framework in the isomerization of the included photoswitch by increasing the hydrophobicity of the framework (**SP-HSiO$_2$**). Encapsulation and anchoring of spiropyran molecules into **SiO$_2$** framework with increase hydrophobicity has shown stabilization of the **SP** form over the open **MC** and **H$^+$MC** forms.[49,54] For this, dimethydiethoxysolane (DMDES) was employed alongside TEOS and **Si-SP-Si** in the synthesis of the nanoparticles (Figure 4.10). The content of DMDES was increased from 5 % to 90 % respect to TEOS, always keeping the molar ratio between **Si-SP-Si** and the other precursors (TEOS and DMDES) to 5%. An acidic hydrolysis of DMDES before the addition into the reaction was required, due to its slower base-catalysed hydrolysis, as previously reported.[66]

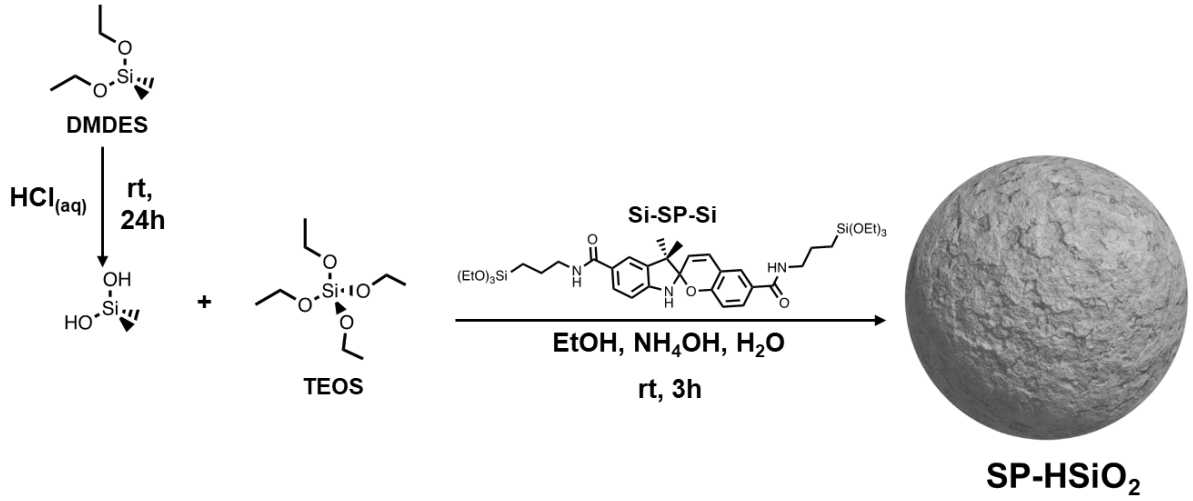

Figure 4.10. Synthetic scheme of **SP-HSiO$_2$**

Resulting nanoparticles were analysed by DLS (Figure 4.S9) and their surface ζ-potential (Figure 4.S9) determined (Table 4.2). Based on DLS results, upon addition of DMDES resulting nanoparticles hydrodynamic diameter increase, compared with **SP-SiO$_2$** nanoparticle, was observed alongside a decrease in their ζ-potential. Regarding the ζ-potential measurements, **SP-HSiO$_2$** with 50 % and 90 % of initial DMDES displayed low colloidal stability in PBS buffer (0.1 M, pH 7.4) with ζ-potential values of -8 ± 5 mV and -3 ± 4 mV; attributed to the presence of methyl groups within the **SiO$_2$** framework. Nevertheless, **SP-HSiO$_2$** particles with initial 5 % and 25 % DMDES still presented colloidal stability with ζ-potential values of - 25 ± 7 mV and -19 ± 5 mV, respectively. Furthermore, colloidally stable **SP-HSiO$_2$** nanoparticles (5 % and 25 % DMDES) displayed a hydrodynamic diameter (by volume) of 71 ± 22 nm and 122 ± 22 nm, bigger than **SP-SiO$_2$** nanoparticles (53 ± 21 nm). TEM analysis (Figure 4.S10) of colloidally stable particles revealed spherical particles with average diameter (n = 50) of 79 ± 4 nm and 87 ± 7 nm for 5% and 25 % DMDES, respectively.

Table 4.2. Dynamic Light Scattering (n = 5) and ζ-potential (n = 3) measurements of **SP-HSiO$_2$** in PBS buffer (0.1 M, pH 7.4).

	Hydrodynamic diameter (D_H) / nm				ζ-potential
DMDES / %	**Intensity**	**Volume**	**Number**	**PDI**	**/ mV**
5	81 ± 25	71 ± 22	62 ± 18	0.13	-25 ± 7
25	132 ± 25	122 ± 22	91 ± 18	0.15	-19 ± 5
50	151 ± 30	140 ± 26	110 ± 25	0.50	-8 ± 5
90	155 ± 49	155 ± 39	130 ± 32	0.48	-2 ± 4

Further characterization was performed in order to confirm the presence of DMDES and the structure of the photoswitch. Due to the presence of C-H stretches from the **Si-SP-Si**, FTI-IR analysis (Figure 4.S11) was not able to confirm the presence of DMDES moieties.

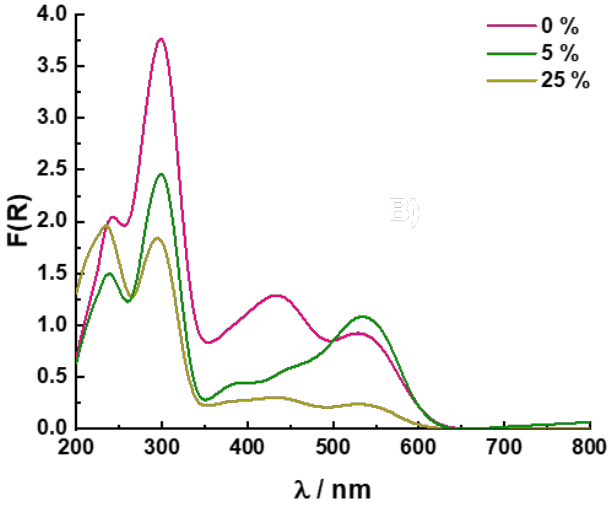

Figure 4.11. Solid state UV/Vis spectra of **SP-HSiO$_2$** nanoparticles with different initial content of DMDES.

Solid-state UV/Vis of resulting nanoparticles (Figure 4.11) showed a significant difference with **SP-SiO$_2$** nanoparticles. 5% **SP-HSiO$_2$**'s spectra showed 5 bands centred at 235 nm, 295 nm, 380 nm, 430 nm and 530 nm. However, the band at

430 nm, assigned to **H⁺MC**, decreased in intensity compared to **SP-SiO₂**, while the **MC** band (530 nm) increased (F(R)@430nm/F(R)@530nm = 0.48 compared with 1.39 for 0 % DMDES). This change was associated with the increase in the hydrophobicity of the framework, that could prevent the protonation of the **MC** form but not the ***SP-to-MC*** isomerization. Nevertheless, upon increase of DMDES percentage a decrease in all bands associated with the open forms was observed (F(R)@430nm/F(R)@530nm = 1.27) . The change in the UV/Vis profile was attributed with the hydrophobicity of the framework that prevented the protonation of the **MC** form and the stabilization of the **MC** form within the framework. Furthermore, a decrease in the **SP** bands was observed, which indicated lower content of photoswitch in the particles.

Based on these results, initial 25 % DMDES was chosen as optimal conditions as produced nanoparticles were colloidally stable while displaying the biggest decrease in the **MC** and **H⁺MC** forms.

4.2.4. Synthesis and characterization of TMP-containing nanoparticles

TMP inclusion in selected nanoparticles was achieved by addition of **TMP** during the nanoparticle formation, as previously reported,[67,68] leading to **SP-SiO₂⊃TMP** and **SP-HSiO₂⊃TMP** nanoparticles. Similarly, control particles without **Si-SP-Si**, **SiO₂⊃TMP** and **HSiO₂⊃TMP** were synthesised following the same methodology.

4.2.4.1. Size and morphology

First, nanoparticles were investigated by DLS (Table 4.3, Figure 4.S12 and Table S.1) and TEM microscopy (Figure 4.12 and Figure 4.S13). DLS analysis of particle revealed nanoparticle's hydrodynamic diameter (by volume) to be 84 ± 32 nm (PDI =

0.09) for **SP-SiO$_2$⊃TMP** and 99 ± 34 nm (PDI = 0.15) for **SP-HSiO$_2$⊃TMP** with good monodispersity. Moreover, nanoparticles displayed a ζ-potential of -34 ± 7 mV for **SP-SiO$_2$⊃TMP** and -35 ± 10 mV for **SP-HSiO$_2$⊃TMP**, highlighting their high colloidal stability. The decrease in the ζ-potential value upon inclusion of **TMP** was associated with the presence of **TMP** molecules close to the surface.

TEM images of particles (Figure 4.12) revealed spherical-shape nanoparticles with average size of 78 ± 9 nm for **SP-SiO$_2$⊃TMP** (n = 50) and 83 ± 9 nm for **SP-HSiO$_2$⊃TMP** (n = 50). Similarly, estimated diameters are bigger than **SP-SiO$_2$** (36 ± 5 nm) and **SP-SiO$_2$** (50 ± 6 nm) and was associated with the presence of **TMP** during the particle formation. Control nanoparticles also exhibited sub-100 nm diameter with high monodisperisty and spherical shape (Figure 4.S13 and Table 4.S1).

Table 4.3. Dynamic Light Scattering (n = 5) and ζ-potential (n = 3) measurements of **TMP**-containing photoresposive nanoparticles in PBS buffer (0.1 M, pH 7.4).

	Hydrodynamic diameter (D_H) / nm				**ζ-potential**
	Intensity	**Volume**	**Number**	**PDI**	**/ mV**
SP-SiO$_2$⊃TMP	108 ± 40	84 ± 32	62 ± 18	0.09	-34 ± 7
SP-HSiO$_2$⊃TMP	168 ± 95	99 ± 34	78 ± 32	0.15	-35 ± 10

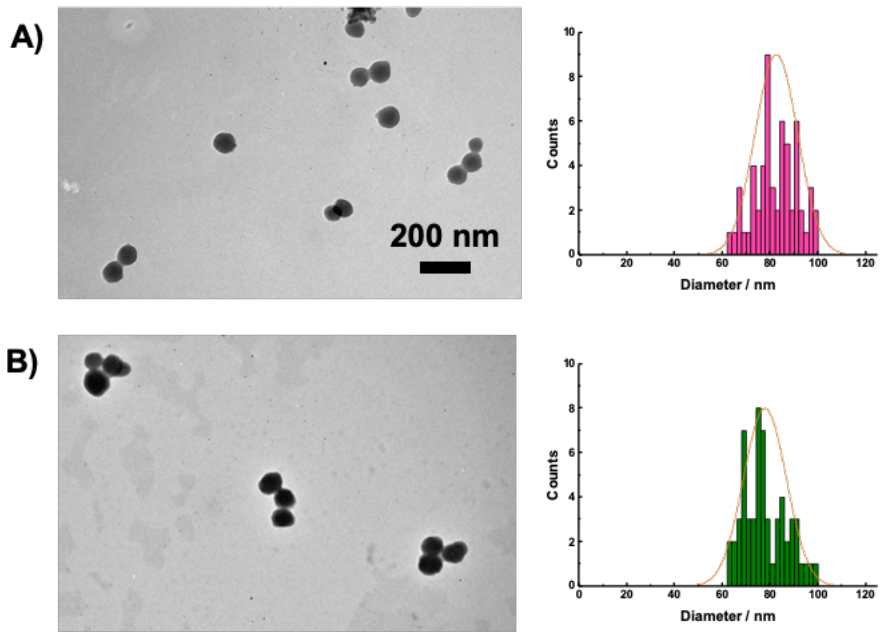

Figure 4.12. Transmission Electron Microscopy (TEM) images and particle size distribution (n = 50) of (A) **SP-SiO$_2$⊃TMP** and (B) **SP-HSiO$_2$⊃TMP**.

4.2.4.2. Composition of TMP-containing nanoparticles

Furthermore, the composition and presence of **TMP** was analysed by solid-state UV/Vis spectroscopy (Figure 4.13). The UV/Vis spectra of **SP-SiO$_2$⊃TMP** revealed four absorption bands with maximum at 235 nm, 295 nm, 380 nm and 537 nm. While the 235 nm and 295 nm bands were assigned to the close **SP** form of the photoswitch, the bands at 380 nm and 537 nm to different forms of the open **MC** isomer. Interestingly, the band at 430 nm previously observed in **SP-SiO$_2$**, corresponding to the **H$^+$MC** form was not observed. This difference was associated with the **TMP** H-bonding with the photoswitch and preventing its protonation. In fact, it is very well known the ability of **TMP** to stablish H-bonds as it is its mode of interactions with the active site of the target dihydrofolate reductase.[69]

However, the absorption band of **TMP** (283 nm) could not be observed, due to the overlapping with the **SP** band at 295 nm. Similarly, **SP-HSiO$_2$⊃TMP** showed the same

bands alongside the band at 430 nm from the **H⁺MC** form. All bands displayed a lower intensity which was associated with the lower content of photoswitch. The absorption band of **TMP** could not be identified, for the same reason that in case of **SP-SiO₂⊃TMP**. Furthermore, the ratio between the **SP** (285 nm) and **MC** (535 nm) bands in **SP-SiO₂⊃TMP** (2.1) is lower than in case of **SP-HSiO₂⊃TMP** (8.0), as previously observed for photoresponsive particle with no **TMP**. The higher hydrophobicity of the framework would allow the **SP** form to remain closed as the H-bonds between the framework and the photoswitch.

Control **SiO₂⊃TMP** and **SiO₂⊃TMP** nanoparticles displayed the characteristic **TMP** absorption band at 283 nm in solid-state (Figure 4.S16).

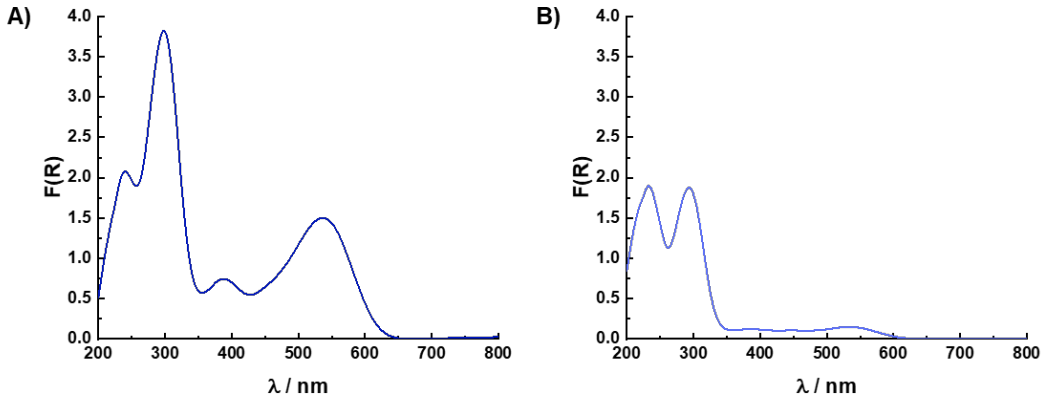

Figure 4.13. Solid-state UV/Vis spectra of (A) **SP-SiO₂⊃TMP** and (B) **SP-HSiO₂⊃TMP**.

Furthermore, other materials characterization techniques such as fluorescence spectroscopy (Figure 4.14) and MALDI-ToF mass spectrometry (Figure 4.S19) were employed to further evidence the presence of **TMP**. FT-IR spectroscopy confirmed presence of **TMP** based on the amine N-H stretching at 3460 cm^{-1} (Figure 4.S17). However, MALDI-ToF mass spectrometry of nanoparticles (Figure 4.S19) confirmed

the presence of **TMP** as signal associated with the [**TMP**+H]$^+$ and [**TMP**-OMe+2Na$^+$]$^+$ species were detected.

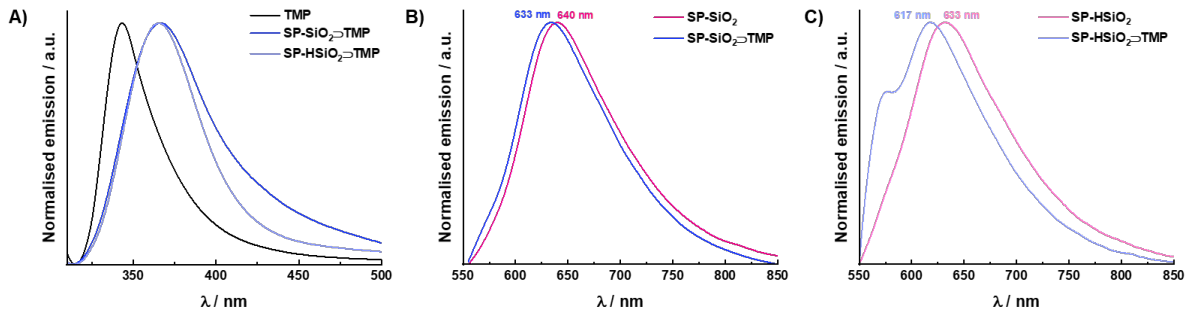

Figure 4.14. Solid-state fluorescence emission of (A) **TMP** (λ_{exc} = 280 nm) and **MC** (λexc = 530 nm) from (B) **SP-SiO$_2$** and **SP-SiO$_2$⊃TMP** and (C) **SP-HSiO$_2$** and **SP-HSiO$_2$⊃TMP**.

We took advantage of the fluorescence properties of **TMP** and **MC** to explore the influence of the presence of **TMP** within the framework. Powder **TMP** displayed an emission with λ_{max} = 343 nm upon excitation at 280 nm, while powder **Si-SP-Si** did not display any emission in that λ range. Control **SiO$_2$⊃TMP** and **HSiO$_2$⊃TMP** nanoparticles displayed an emission band at 329 nm upon excitation at 280 nm (Figure 4.S20). The blue shifts observed could be attributed to the inclusion of the antibiotic within the framework as previously described with another fluorescence antibiotics.[67,68] **SP-SiO$_2$⊃TMP** and **SP-HSiO$_2$⊃TMP** displayed **TMP** emission bands at 367 nm and 365 nm, upon excitation at 280 nm (Figure 4.14A). Interestingly, a red shift respect to solid-state **TMP** was observed, which could be due to different types on interactions between **TMP** and the framework. Previous emission studies of compounds containing 1,3,5-triazine moieties revealed a bathochromic shift on their emission as a result of H-bonding with other molecules in solution,[70] as further confirmed by V. Rotello and co-workers.[71] Based on the ability of the **MC** form and

TMP to H-bonds, the observed bathochromic shift support the interactions between the **TMP** and the anchored **MC**, previously proposed based on the solid-state UV/Vis analysis of the nanoparticles.

The emissive properties of the **MC** form of spiropyran have been previously explored and applied for sensing and imaging.[47,72] The **MC** emission of powder **Si-SP-Si** molecule could not be studied as it does not present a **MC** UV/Vis band (Figure 4.S14). Nonetheless, we decided to explore the **MC** emission in photoresponsive particles and the effect of **TMP** on it (Figure 4.14B and 14C)**. SP-SiO_2** displayed an emission band with λ_{max} = 640 nm (λ_{exc} = 530 nm). Nevertheless, **SP-SiO_2⊃TMP**'s emission (λ_{exc} = 530 nm) was blue shifted 7 nm with λ_{max} = 633 nm. Similarly, **MC** emission in **SP-$HSiO_2$⊃TMP** (λ_{exc} = 530 nm, λ_{em} = 617 nm) was 16 nm blue shifted compared to **SP-$HSiO_2$**'s (λ_{exc} = 530 nm, λ_{em} = 633 nm). The observed shift in presence of **TMP** could be associated with the change in the **MC** environment due to the presence of the antibiotic.

4.2.4.3. Porous structure of TMP-containing nanoparticles

The use of silyl-derivatives bridged by organic moieties has been previously reported to increase the porosity of the nanoparticles.[73] **Si-SP-Si** is a large molecule that would have an effect in the porous structure of the particles. Hence, porosimetry studies were conducted (Figure 4.15 and Figure 4.S2)

SiO_2 and **$HSiO_2$** nanoparticles displayed a type I isotherm with low BET surface area and a non-porous structure (Figure 4.S21 and Table 4.S2), as previously described.[74] Nevertheless, the BET surface area of **$HSiO_2$** (57.1 ± 0.7 m^2g^{-1}) was larger than **SiO_2** (35.6 ± 0.3 m^2g^{-1}), which was associated with the presence of the methyl groups within

the framework forming voids, as previously reported for other **SiO_2** nanoparticles containing organic pendant groups.[75–77] Furthermore, their surface area decreased when **TMP** was included within the framework, which also confirmed the presence of the antibiotic within the framework.

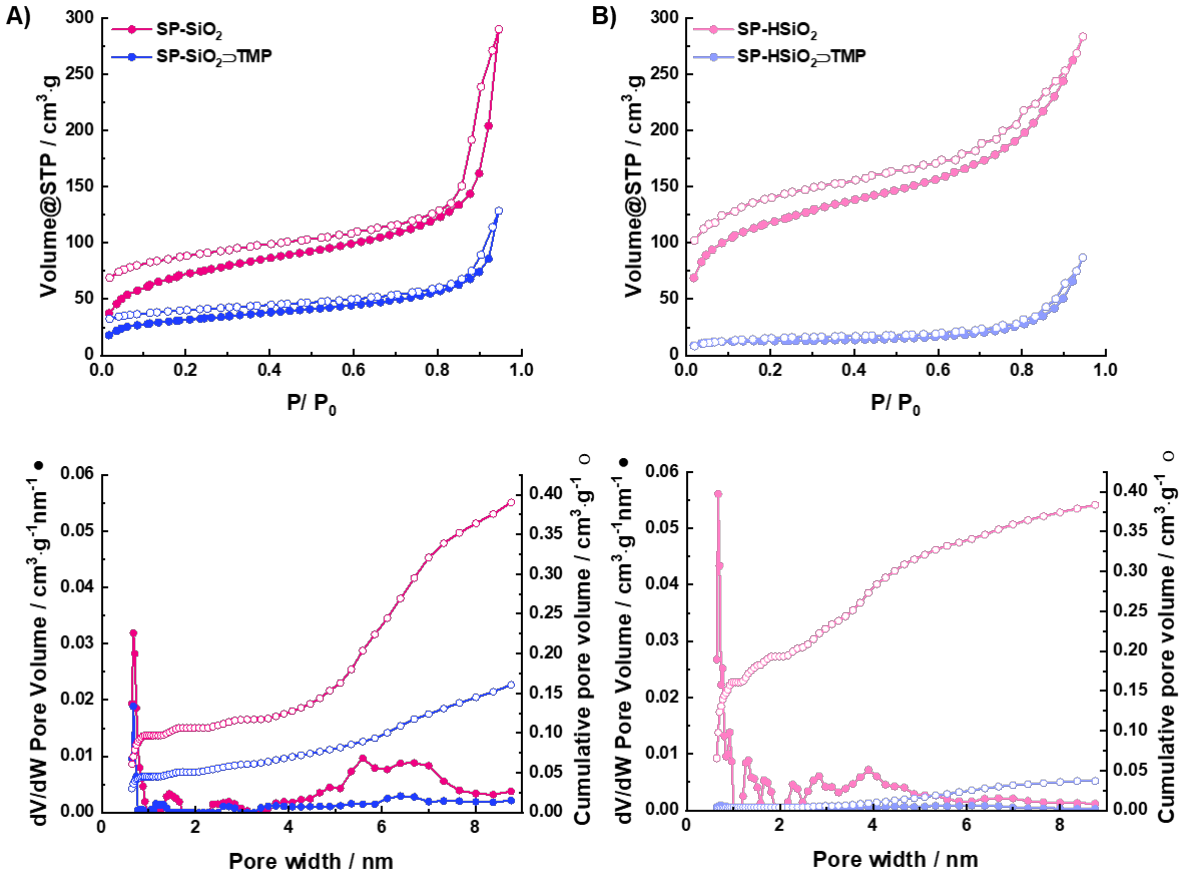

Figure 4.15. Nitrogen adsorption-desorption isotherms at 77 K and DFT pore distribution calculation of (A) **SP-SiO_2** and **SP-SiO_2⊃TMP** and (B) **SP-$HSiO_2$** and **SP-$HSiO_2$⊃TMP**. Samples were activated under vacuum at 120 ºC prior the measurement.

Spiropyran-containing nanoparticles, while still exhibiting a type I isotherm (Figure 4.15), they displayed a higher BET surface area of 250.7 ± 7.8 m^2g^{-1} in case of **SP-SiO_2** and 400.8 ± 2.5 m^2g^{-1} for **SP-$HSiO_2$**. The inclusion of the organic spacer within the nanoparticle framework was associated with the increase in the porosity of the

particle. Equally, the presence of methyl groups within the framework further increased the surface area of **SP-HSiO$_2$**. Interestingly, absorption and desorption isotherms did not close in either of the particles, leaving the adsorption-desorption isotherm open. This result is unusual and can be due to the presence of supermicroporosity (pore size < 2 nm) or due to instrumental artefacts if defined equilibration time between desroption points was too short.[78–80] In order to elucidate if the open isotherm was real or an artefact of short equilibration time, the equilibration time was increased from 2 min to 30 min. Recorded N_2 adsorption-desorption isotherms did not change shape (Figure 4.S22), supporting the presence of supermicroporosity. Furthermore, pore size distribution was further estimated by DFT calculation (Figure 4.15, Table 4.S2) confirmed the presence of supermicroporosity, revealing pore sizes below 2 nm.

Upon addition of **TMP**, the nanoparticles still displayed a type I isotherm with lower BET surface area (Table 4.S2) as a results of pore filling with the antibiotic. **SP-SiO$_2$⊃TMP** displayed a BET surface area of 107.7 ± 1.2 m^2g^{-1} while **SP-HSiO$_2$⊃TMP** surface area was estimated to be 56.1 ± 0.9 m^2g^{-1}. Similarly, **SP-SiO$_2$⊃TMP** still exhibited and open isotherm due to the presence of 1.5 nm pores, according to the DFT calculations. On the contrary, **SP-HSiO$_2$⊃TMP**'s isotherm closed and no micropores was observe in the DFT calculations.

4.2.4.4. Quantification of TMP in SP-SiO$_2$⊃TMP and SP-HSiO$_2$⊃TMP

Quantification of included photoswitch and **TMP** was estimated by two different methodologies: determination of free species after nanoparticle synthesis by UV/Vis spectroscopy and by thermogravimetric analysis (TGA) of formed nanoparticles (Figure 4.S23-S24).

Interestingly, after synthesis, **Si-SP-Si** could not be observed in the supernatant and in the washings by UV/Vis spectroscopy in any of the explored nanoparticles; suggesting full condensation of the precursor within the nanoparticle framework (Table 4.4). Furthermore, based UV/Vis spectroscopy, a **TMP** loading of 15.2 $\mu g_{TMP}/mg_{NPs}$ and 20.4 $\mu g_{TMP}/mg_{NPs}$ was estimated for **SP-SiO$_2$⊃TMP** and **SP-HSiO$_2$⊃TMP**, respectively. Similarly, a loading of 12.5 $\mu g_{TMP}/mg_{NPs}$ and 16.2 $\mu g_{TMP}/mg_{NPs}$ was estimated for **SiO$_2$⊃TMP** and **HSiO$_2$⊃TMP**. Higher loading in case of photoresponsive nanoparticles could be attributed to the attractive H-bonding interactions between **TMP** and the anchored **MC**. Similarly, a higher loading was estimated in case of those nanoparticles with increased hydrophobicity, maybe due **TMP** preferring hydrophobic environments. Table 4.4 summarises the estimated **Si-SP-Si** and **TMP** content of nanoparticles.

Table 4.4. Estimated **Si-SP-Si** and **TMP** content of nanoparticles based on UV/Vis spectroscopy of the supernatant and washings.

	Si-SP-Si / $\mu g_{Si\text{-}SP\text{-}Si}mg_{NPs}^{-1}$	**TMP / $\mu g_{TMP}mg_{NPs}^{-1}$**
SiO$_2$⊃TMP	-	12.5
HSiO$_2$⊃TMP	-	16.2
SP-SiO$_2$	54.2	-
SP-SiO$_2$⊃TMP	48.2	15.2
SP-HSiO$_2$	26.6	-
SP-HSiO$_2$⊃TMP	30.1	20.4

TGA analysis of the nanoparticles displayed higher weight loss when nanoparticles contained more organic components (Figure 4.S23-S24). For instance, **SiO$_2$** displayed a weight loss of 2.3 % after heating to 800 ^{o}C, associated with the degradation of remaining ethoxy and hydroxyl groups within the framework. TGA degradation profile of **SP-SiO$_2$** displayed a further 4.2 % weight loss compared with **SiO$_2$**, associated with

the thermal degradation of the photoswitch. Finally, **SP-SiO_2⊃TMP** displayed an extra 2.4 % of weight loss compared with **SP-SiO_2**, associated with the presence of TMP. Nevertheless, due to the small change in weight loss and the absence of thermal degradation steps that can be associated with a single species, quantification of individual cargo could not be estimated by TGA in case of photo responsive nanoparticles. In case of control nanoparticles, and due to the presence of a single organic component beside he framework, the **TMP** content of 14.5 $\mu g_{TMP}/mg_{NPs}$ and 16.0 $\mu g_{TMP}/mg_{NPs}$ was estimated for **SiO_2⊃TMP** and **HSiO_2⊃TMP**, in good agreement with UV/Vis analysis.

4.2.5. Responsive properties of nanoparticles

4.2.5.1. Solid-state photoswitching properties of nanoparticles

SP-containing nanoparticles presented a predominant **MC** and **H^+MC** bands at 530 nm and 430 nm due to the H-bonding driven **SP** isomerization. Negative photochromism has been previously reported in the literature and conversion of the **MC** and **H^+MC** forms has been achieved previously with visible light irradiation (> 360 nm).[50] Hence, we wanted, first, to explore the photoswitching properties of nanoparticles in absence of **TMP** using white light irradiation. White light was chosen over green light due to easier access of instrumentation.

Samples were irradiated for 10 min and the solid-state absorbance of powder samples measured after each minute (Figure 4.16A and 16D). Both particles displayed a fast decrease of the **MC** and **H^+MC** bands after 1 min irradiation which does not further decreases during the consecutive 10 min of irradiation (Figure 4.16C and 16F). Similarly, a small increase in the **SP** band (295 nm) was observed.

After 10 min of white light irradiation, samples were kept in the dark and their UV/Vis spectra recorded every 2 min for 120 min (Figure 4.16B and 16E). An initial fast recovery of both bands was observed, followed by a slower but sustained step (Figure 4.16C and 16F). After 120 min, full recovery of **MC** and **H$^+$MC** bands was not observed (Figure 4.S26). Nevertheless, after 24 h in the dark the initial **MC** and **H$^+$MC** bands were recovered.

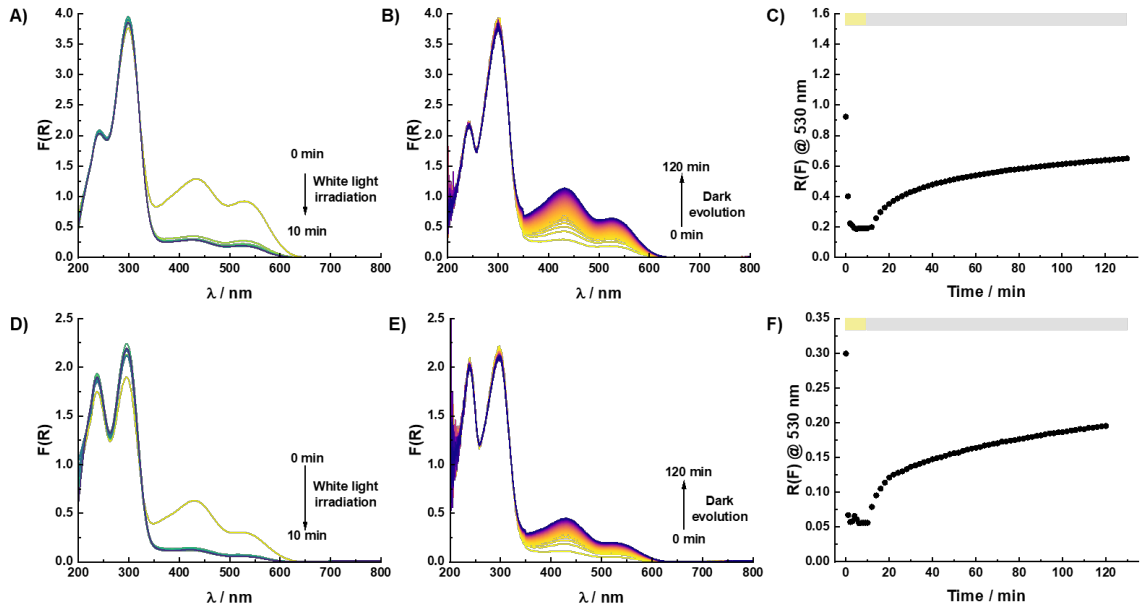

Figure 4.16. Solid-state photoswitching properties of (A-C) **SP-SiO$_2$** and (D-F) **SP-HSiO$_2$**. Samples were (A and D) irradiated for 10 min (22 W, λ > 393 nm) and then (B and E) kept in the dark for 120 min. (C and F) **MC** isomerization was monitored based on the 530 nm UV/Vis band.

Then, the photoswitching properties of **TMP** containing nanoparticles were examined following the same methodology (Figure 4.17). In this case, upon white light irradiation, a slower **MC**-to-**SP** conversion was observed in both cases. In case of **SP-SiO$_2$⊃TMP**, the **MC** band decreased during the first 8 min of irradiation (Figure 4.17A and 17C), while further decrease after the first minute was not observed for **SP-HSiO$_2$⊃TMP** (Figure 4.17D, 17F and Figure 4.S25). The slower **MC**-to-**SP** conversion was

associated to the presence of **TMP** in the framework, which stabilized the **MC** form through H-bonding.

Dark evolution of the **MC** band was then explored after 10 min white light irradiation (Figure 4.17B and 17E) upon monitoring of the 537 nm band (Figure 4.17C and 17F). Like previous nanoparticles, a fast first recovery was observed followed by a slower step, in both cases. In this case after 120 min in the dark, full **MC** back conversion was not observed. 24 h later, however, full recovery of **MC** and **H$^+$MC** bands was observed.

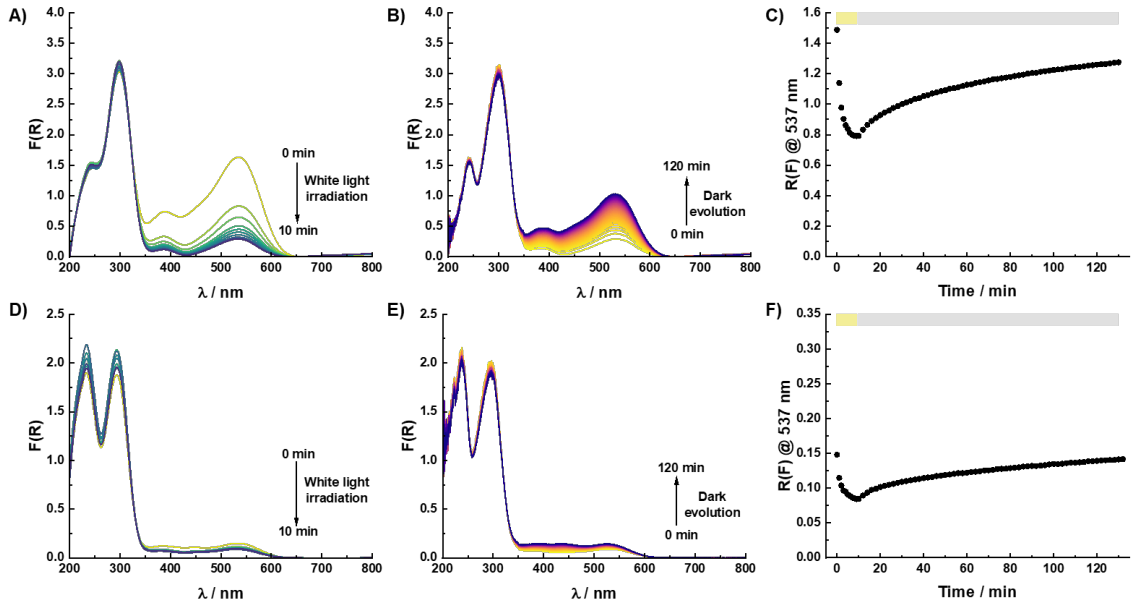

Figure 4.17. Solid-state photoswitching properties of (A-C) **SP-SiO$_2$⊃TMP** and (D-F) **SP-HSiO$_2$⊃TMP**. Samples were (A and D) irradiated for 10 min (22 W, λ > 393 nm) and then (B and E) kept in the dark for 120 min. (C and F) **MC** back conversion was monitored based on the 537 nm UV/Vis band.

In order to quantitatively analyse if the presence of **TMP** did have any effect in the photosetting properties of nanoparticles, the dark evolution of the **MC** band after 10 min of white light irradiation was fitted with a biexponential function (Eq. 4.S1, Figure 4.S27 and Table 4.S3). Nevertheless, further investigation is required to fully

understand the photoconversion mechanism occurring in the nanoparticles in solid state.

Analysis of the estimated kinetic rates (Table 4.S3) revealed a faster conversion rate for those nanoparticles containing **TMP**, which was associated with the higher probability of interaction with the **SP** form, thermodynamically favouring the **MC** form. Moreover, **MC** dark recovery takes place in s faster rate in hydrophilic $\mathbf{SiO_2}$ framework rather compared to the more hydrophobic $\mathbf{HSiO_2}$, also associated with the **MC** stabilization through H-bonding, more predominant in the $\mathbf{SiO_2}$ framework.

4.2.5.2. Solid-state reversible photoswitching

Based on the application of developed nanoparticles in long-term catheter coating, fast photoswitching is a crucial feature for their prolonged used. In previous experiment we observed that after 10 min of white irradiation **TMP**-containing nanoparticles required up to 24 h to fully recover their initial state. Thereby, we wanted to explore the dark recovery upon different white light irradiation times to decide to best time frame for the release and *in-vitro* experiments.

Hence, **TMP**-containing nanoparticles were irradiated for 10 s, 30 s, 1 min and 10 min, and the dark recovery of the **MC** band (530 nm) monitored by solid-state UV/Vis spectroscopy (Figure 4.18 and Figure 4.S28 and S29).

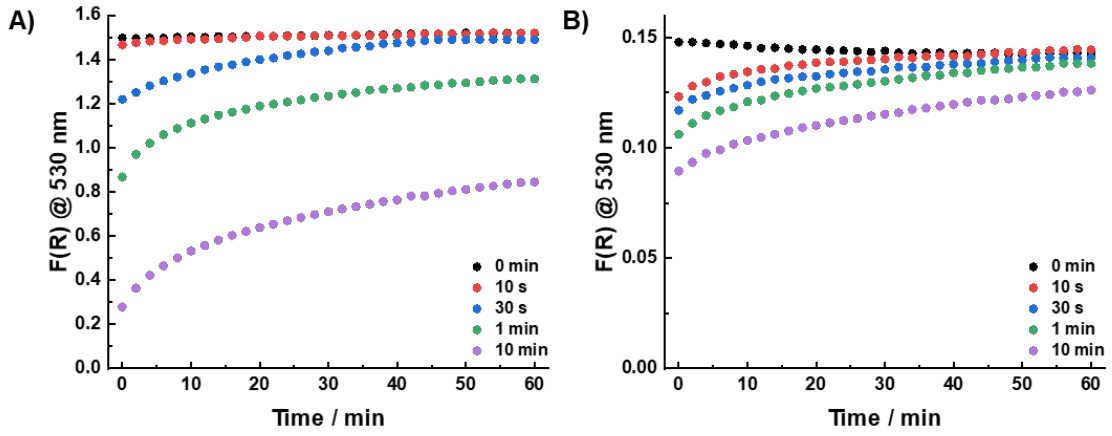

Figure 4.18. Solid-state dark evolution of the **MC** band (530 nm) of (A) **SP-SiO$_2$⊃TMP** and (B) **SP-HSiO$_2$⊃TMP** after different irradiation times.

SP-SiO$_2$⊃TMP displayed no significant change in the **MC** band 10 s of irradiation, which has been associated with a fast back conversion, that could not be measured. After 30 s of irradiation, full conversion to the initial state was observed after 45 min and after 1 min irradiation, no full conversion was observed up to 60 min. **SP-HSiO$_2$⊃TMP** showed a slower recovery after 10 s of irradiation, which full back conversion after 35 min, which increased to 45 min after 30 s irradiation, and over 60 min for 1 min irradiation. Based on these results, 30 s irradiation was chosen as irradiation time for the release and in-vitro experiments.

4.2.5.3. Stability of solid-state reversible photoswitching

The stability of reversible photoswitching abilities of **SP-SiO$_2$⊃TMP** and **SP-SiO$_2$⊃HTMP** was investigated. Solid-state samples were irradiated for 30 s and then kept in the dark 45 min to achieve full recovery of the **MC** band (530 nm). Samples were subjected to five consecutives light-dark cycles (Figure 4.19). After five cycles

no change in the UV/V profiles was observed and full recovery of the **MC** band was achieved, highlighting the stability of the nanoparticles.

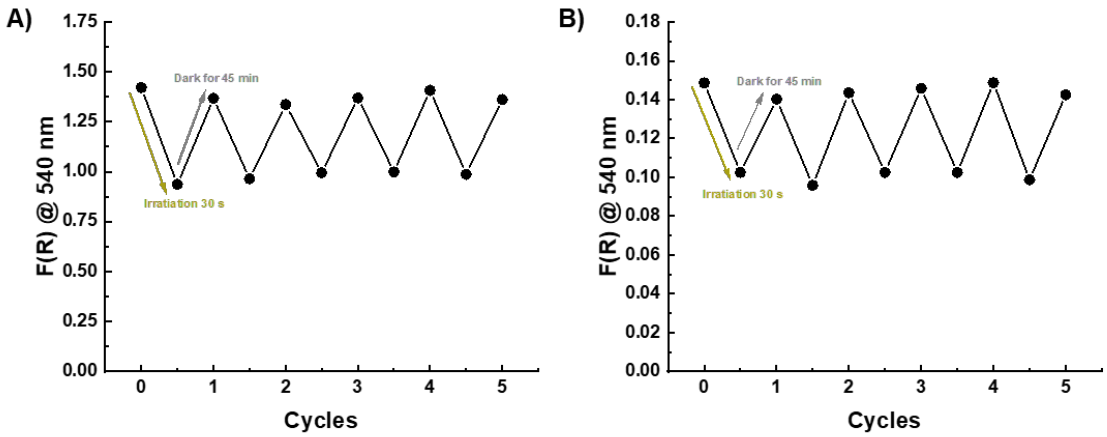

Figure 4.19. Reversible solid-state photoswitching properties of (A) **SP-SiO$_2$⊃TMP** and (B) **SP-HSiO$_2$⊃TMP**. The **MC** band (530 nm) was monitored after 30 s white light irradiation followed by 45 min in the dark.

4.2.6. Release studies

4.2.6.1. Light triggered antibiotic release

We first studied the **TMP** release from nanoparticles in the dark and upon white light irradiation to investigate the photoresponsive behaviour of developed **SP**-containing nanoparticles in PBS buffer (0.1 M, pH 7.4) under continuous stirring (150 rpm) (Figure 4.20). As control, release studies were also performed with control **TMP**-containing nanoparticles. Released **TMP** was quantified by UV/Vis spectroscopy (Figure 4.S30).

In the dark, 0.40 ± 0.12 $\mu g_{TMP}/mg_{NPs}$ release was estimated from **SiO$_2$⊃TMP** after 10 min, while 0.42 ± 0.24 $\mu g_{TMP}/mg_{NPs}$ was estimated for **HSiO$_2$⊃TMP**. Nevertheless, upon continuous irradiation, no significant difference on **TMP** release was observed after 10 min, estimating 0.39 ± 0.18 $\mu g_{TMP}/mg_{NPs}$ for **SiO$_2$⊃TMP** and 0.45 ± 0.11 $\mu g_{TMP}/mg_{NPs}$ for **HSiO$_2$⊃TMP**.

An estimated 0.45 ± 0.12 $\mu g_{TMP}/mg_{NPs}$ for **SP-SiO$_2$⊃TMP** and 0.65 ± 0.24 $\mu g_{TMP}/mg_{NPs}$ for **SP-HSiO$_2$⊃TMP** was released in the dark, after 10 min. Nevertheless, upon 10 min of continuous while light irradiation (22 W, λ > 393 nm) the **TMP** release increased to 1.43 ± 0.19 $\mu g_{TMP}/mg_{NPs}$ and 1.17 ± 0.14 $\mu g_{TMP}/mg_{NPs}$, respectively. Interestingly, **TMP** release from **SP-SiO$_2$⊃TMP** was significantly higher (t test, $p < 0.05$) after only 30 s irradiation, which kept increasing over time. In case of **SP-HSiO$_2$⊃TMP** it was not until 6 min of continuous irradiation when a significant difference between **TMP** release in the dark was observed. This difference was associated with the lower ***SP-to-MC*** conversion degree in case of **SP-HSiO$_2$⊃TMP**.

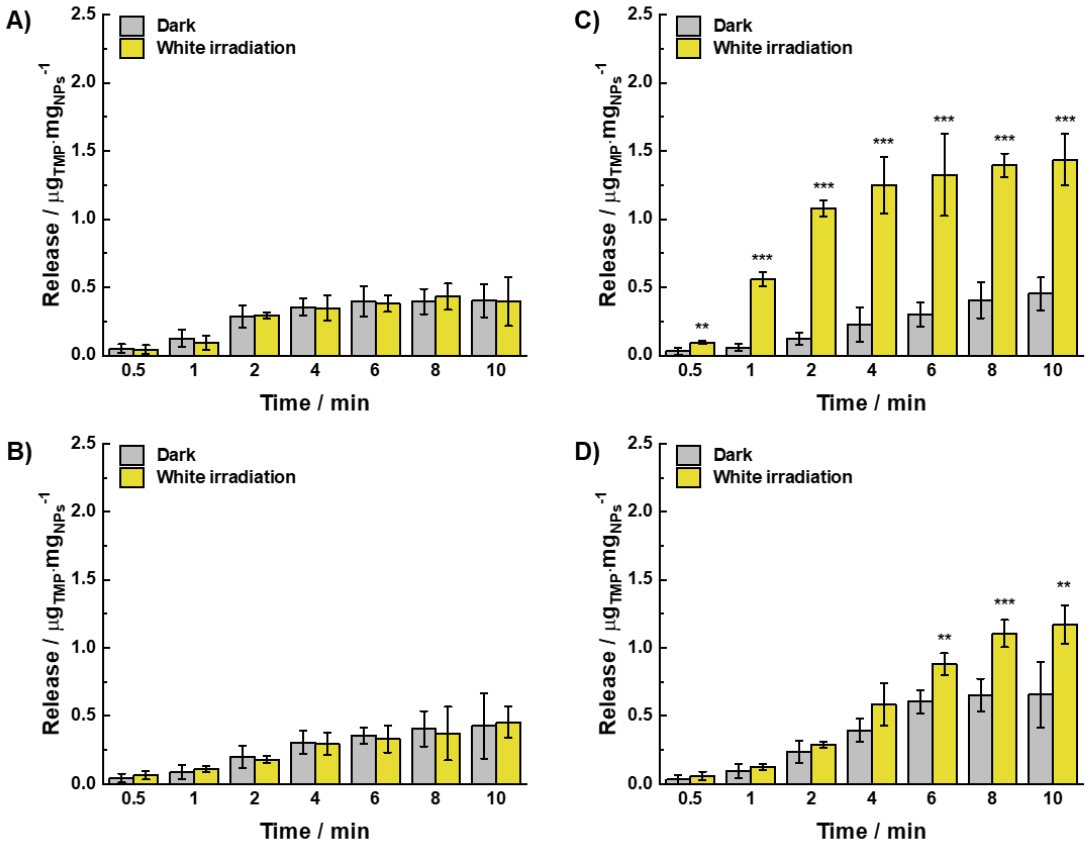

Figure 4.20. **TMP** release from (A) **SiO$_2$⊃TMP**, (B) **HSiO$_2$⊃TMP**, (C) **SP-SiO$_2$⊃TMP** and (D) **SP-HSiO$_2$⊃TMP** in PBS buffer (0.1 M, pH 7.4) under mild stirring (150 rpm) in the dark or upon white light irradiation (n = 3). Released **TMP** was quantified by UV/Vis spectroscopy. Statistical significance was assessed by t-test; * = $p < 0.5$, ** = $p < 0.01$ and *** = $p < 0.001$.

The difference in the **TMP** release upon irradiation was associated with the different composition and photoswitching properties of the nanoparticles. **SP-SiO_2⊃TMP** present a higher **MC** content and a fast response to irradiation. **SP-SiO_2⊃TMP**, on the contrary, presented lower **MC** content and, upon irradiation the overall change in the structure was less evidence.

Liqui Chromatography – Mass Spectrometry (LC-MS) was employed to confirmed that **SP** was not released from the nanoparticles (Figure 4.S31-S32). Furthermore, longer irradiation times were not explored as heating of nanoparticles suspension was observed (Figure 4.S.37), which would also influence the release of the antibiotic from the nanoparticles.

4.2.6.2. On-off TMP release from SP-containing nanoparticles

After confirming the light triggered release of **TMP** from **SP**-containing nanoparticles and the photoswitchable properties of the nanoparticles (Figure 4.21), we decided to explore if the **TMP** release would be controlled in an *on-off* mode. A 30 s irradiation time was chosen as particle showed full conversion back to the initial **MC** form after 45 min. Release experiments were performed in PBS buffer (0.1 M, pH 7.4), samples were irradiated for 30 s and release **TMP** estimated immediately. Then, the sample was kept int the dark for 45 min to allow fully back conversion and the release TMP estimates by UV/Vis spectroscopy. This process was repeated 5 times, which correspond to 225 min (Figure 4.21). Samples was continuously stirred at 150 rpm.

After the total duration of the experiments, when particles were kept in the dark, **SP-SiO_2⊃TMP** released 0.40 ± 0.21 $\mu g_{TMP}/mg_{NPs}$ while **SP-$HSiO_2$⊃TMP** released 0.56 ±

0.15 $\mu g_{TMP}/mg_{NPs}$. Both nanoparticles displayed a cumulative release profiled up to 80 min when TMP releases of both nanoparticles plateaued. However, under light-dark cycles, **SP-SiO$_2$⊃TMP** displayed an *on-off* **TMP** release with burst **TMP** release after 30 irradiation with no significant **TMP** leakage after 45 min in the dark. After 5 cycles, a cumulative total release of 1.75 ± 0.20 $\mu g_{TMP}/mg_{NPs}$ was estimated. Moreover, after 5 cycles the **TMP** release did not reach a plateau. Nevertheless, **SP-HSiO$_2$⊃TMP** did not show significant different on **TMP** release in the first 3 dark-cycles, with an overall lower release after 5 cycles (0.93 ± 0.11 $\mu g_{TMP}/mg_{NPs}$). Based on estimated release, after 4 cycles **TMP** release plateaued.

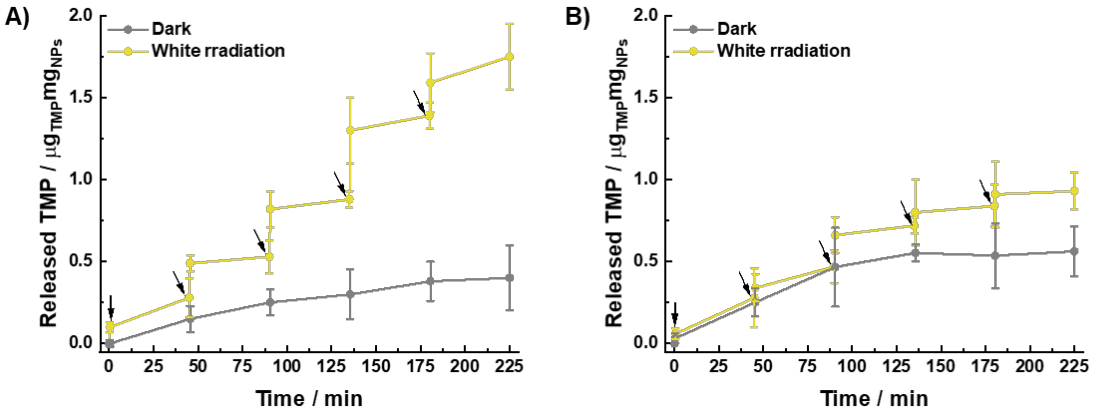

Figure 4.21. Time-dependant **TMP** release from (A) **SP-SiO$_2$⊃TMP** and (B) **SP-HSiO$_2$⊃TMP** in PBS buffer (0.1 M, pH 7.4). Samples were irradiated for 30 s (indicated with black arrows) and kept in the ark afterward for 45 min. Released TMP was estimated by UV/Vis spectroscopy (n = 3).

These results confirmed the on-off release behaviour of nanoparticles which could be advantageous for their long-term use, being able to release included **TMP** when required while still bearing **TMP** that could be released in the future.

4.2.7. Antibacterial activity

The antibacterial properties of designed photoresponsive nanoparticles were tested against 3 *E. coli* UTI clinical isolates (UTI-12, UTI-36 and UTI-42) and the reference *E. coli* strain MG1655. The *E. coli* UTI clinal isolates were kindly provided by Prof Alan McNally (Institute of Microbiology and Infection, University of Birmingham).

4.2.7.1. Minimal inhibitory concentration (MIC) determination

First, the MIC values for the antibiotic **TMP** was determined in LB agar (Table 4.5). A MIC value of 1 μg/mL was observed for refence strain. The MIC values for the clinical isolates were found to be 4 μg/mL for UTI-42, 16 μg/mL for UTI-12 and 128 μg/mL for UTI-36. The lower sensitivity of UTI clinical isolates to antibiotics has been previously reported.[81] Resistance mechanisms against **TMP** have been identified due to mutations in the target enzyme dihydrofolate reductase (dfr), encoded by the *drf*-genes.[82] Nevertheless, we have not further information about the genotype of the clinical isolates.

Table 4.5. Minimal Inhibitory concentration (MIC, mg/mL) values of **TMP** and developed nanoparticle library in LB media in the dark at 37 ºC and 250 rpm. Depicted values are based on 3 biological replicas.

	MG1665	**UTI-12**	**UTI-36**	**UTI-42**
TMP	0.001	0.004	0.128	0.016
SiO_2⊃TMP	0.75	2.50	>10	10
$HSiO_2$⊃TMP	0.75	2.50	>10	10
SP-SiO_2⊃TMP	0.75	2.50	>10	10
SP-$HSiO_2$⊃TMP	0.37	2.50	>10	5.00

Then, the MIC values for photoresponsive and control (unloaded and **SiO_2⊃TMP** and

$HSiO_2$⊃TMP) nanoparticles was determined in the dark (Table 4.5). Particles not bearing any antibacterial agent (**SiO_2**, **$HSiO_2$**, **SP-SiO_2** and **SP-$HSiO_2$**) did not display any antibacterial activity even up to 10 mg/mL (Table 4.S4). For the reference strain, MIC values of 0.75 mg/mL were found for control particle, same as for **SP-SiO_2⊃TMP**. **SP-$HSiO_2$⊃TMP** displayed an MIC value of 0.37 mg/mL. For the UTI-12 strain, all particles had a MIC value of 2.50 mg/mL. **SiO_2⊃TMP**, **$HSiO_2$⊃TMP** and **SP-SiO_2⊃TMP** displayed an MIC of 10 mg/mL for UTI-42, and 5.00 in case of **SP-$HSiO_2$⊃TMP**. In case of UTI-36, all particles did not show any activity even up to 10 mg/mL. The low susceptibility of UTI-36 to **TMP** is also translated to loaded nanoparticles.

4.2.7.2. Effect of light irradiation in nanoparticle activity

Subsequently, the activity of nanoparticles was explored upon irradiation by enumerating cell viability (CFU/mL). Firstly, time-killing assays of **TMP** against *E. coli* strains were determined, in order to define a time frame where the released **TMP** would have the highest effect in cell viability (Figure 4.S33). After incubation of bacterial cell with **TMP** (MIC concentration) in PBS buffer (0.1 M, pH 7.4), a viability decrease was observed up to 24 h, from where no further viability change was observed.

The effect of different white light irradiation (W) times in the antibacterial activity of nanoparticles was studied. Irradiation times of 30 s, 1 min and 5 min were studied, and MIC nanoparticle concentration was employed. The experiment was performed in PBS buffer (0.1 M, pH 7.4) and cell viability was analysed after 24 h incubation after irradiation. Due to the low susceptibility of UTI-36 to the **TMP**-loaded nanoparticles,

an MIC value for nanoparticles could not be determined. Thereby, UTI-36 was not further investigated.

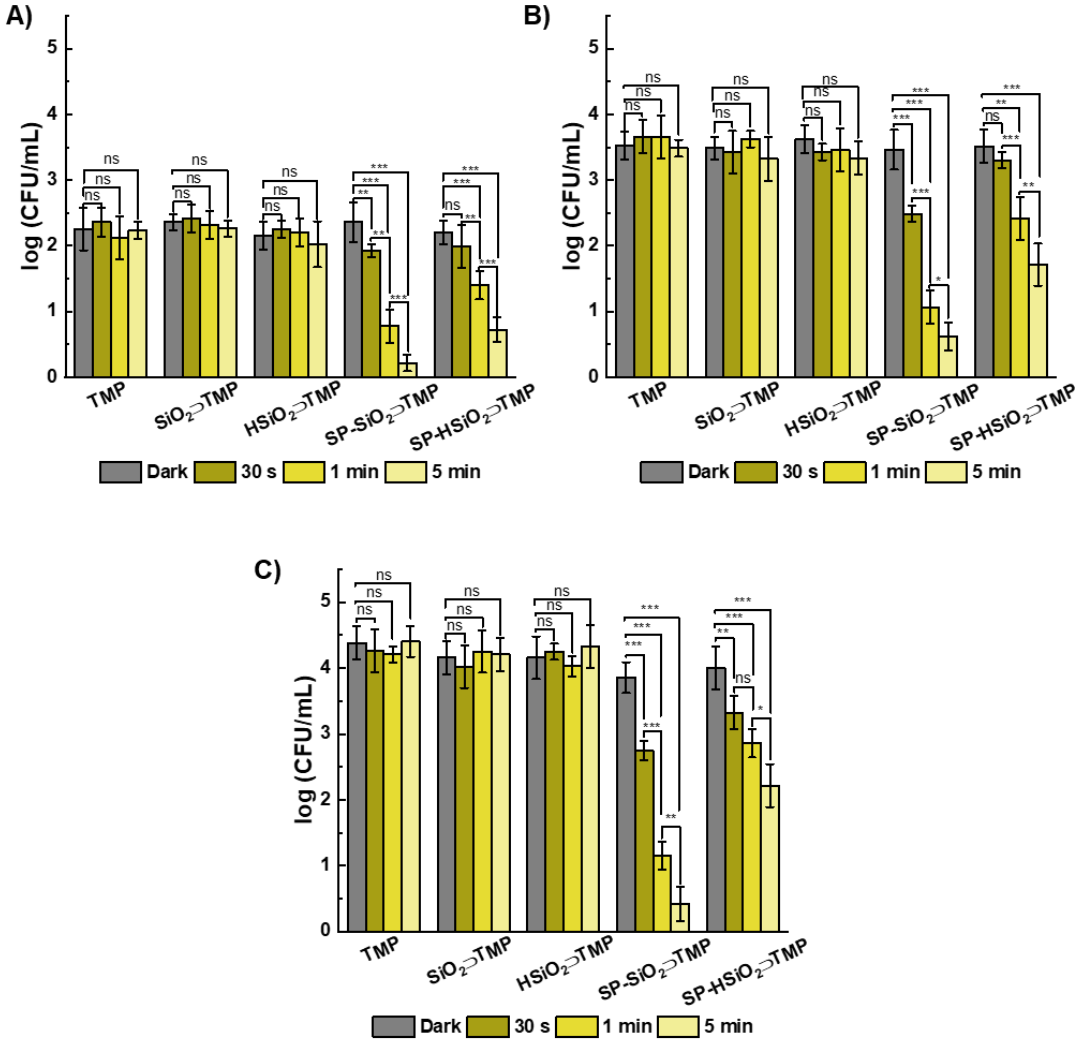

Figure 4.22. Cell viability of (A) MG1655, (B) UTI-12 and (C) UTI-42 *E. coli* strains incubated with **TMP** and nanoparticles and after different white light irradiation times (22 W, λ > 393 nm). Diluted inoculate (~10^7 CFU/mL) were incubated MIC concentration of **TMP** and nanoparticles and irradiated during different times. Then, cells were incubated for 24 h in the dark at 37 ºC and 150 rpm, and viability checked. Depicted values are based on 3 biological replicas. Statistical significance was determined by t-test, ns = p > 0.5, * = p < 0.5, ** = p < 0.01 and *** = p < 0.001.

No change in the antibacterial activity of **TMP**, **SiO_2⊃TMP** and **$HSiO_2$⊃TMP** was observed after any irradiation time (Figure 4.22). However, upon irradiation, the activity of **SP**-containing nanoparticles increased. In case of MG1655 a increased activity of

nanoparticles was observed upon longer irradiation times. **SP-SiO$_2$⊃TMP** nanoparticles displayed higher irradiation dependant activity and overall effect in cell viability compared with **SP-HSiO$_2$⊃TMP**. In fact, these results are in good agreement with the *in vitro* release studies where the different between released **TMP** in the dark and upon irradiation was more significant in case of **SP-SiO$_2$⊃TMP**. In case of the UTI-12 strain, similar tendency was observed upon irradiation. Irradiation dependant increased in the activity of photoresponsive nanoparticles was observed. Similar results were also observed in case of the UTI-42 strain.

These results confirm the light-triggered activity of **SP**-containing nanoparticles for UTI *E. coli* clinical isolates.

4.2.7.3. Effect of on-off release in bacterial cell viability

The *on-off* release abilities of **SP**-containing nanoparticles was previously confirmed in *in-vitro* release studies. Thereby, we wanted, to study it in presence of bacterial cells. Catheter associated UTI infections are characterized by a continuous formation of bacterial biofilm on the outer surface of the catheter, due to the continuous flow of planktonic bacterial cells.[1] Hence, the *on-off* antibiotic release is a crucial ability to avoid biofilm growth while the catheter is used.

Overnight culture re-suspended in PBS buffer (0.1 M, pH 7.4, ~10^7 CFU/mL) was incubated with MIC concentration of **TMP** and **SP**-containing nanoparticles for 5 days. Control samples were kept in the dark and cell viability evaluated every day. The investigated samples were irradiated for 30 s each day and cell viability evaluated the next day before another 30 s irradiation treatment. This process was repeated for 5

consecutive days. After light irradiation cells were incubated in the dark at 37 ºC and 150 rpm shaking.

Cells incubated in the dark with **TMP** and nanoparticles only displayed antibacterial activity after the first day, associated with the passive release of **TMP** from particles. After the first day no further activity was observed. White light irradiation did not impact the activity of **TMP** (Figure 4.S.34), as also observed in previously experiments (Figure 4.22).

After the first day irradiation a significant activity of the **SP**-containing nanoparticles was observed in all strains, associated with the leakage of **TMP**. However, nanoparticles still displayed antibacterial activity the following days upon irradiation, achieving full eradiation after 4 days for MG1655 and 5 days for UTI clinical isolates treated with **SP-SiO$_2$⊃TMP**. Cells incubated with **SP-HSiO$_2$⊃TMP** did not achieved full eradication after 5 days of treatment, which was associated with the lower **TMP** release upon irradiation as observed in *in-vitro* studies.

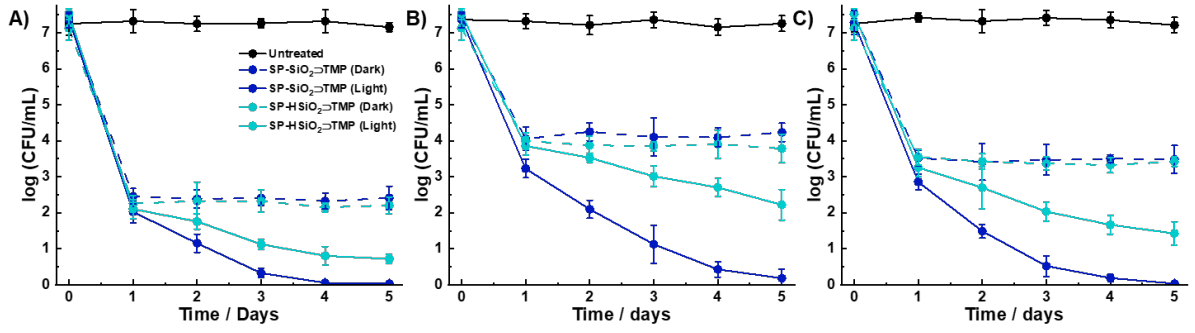

Figure 4.23. Cell viability of (A) MG1655, (B) UTI-12 and (C) UTI-42 *E. coli* strains incubated with **SP**-containing nanoparticle (MIC concentrations) upon daily white light irradiation (22 W, λ > 393 nm) or in the dark. Overnight diluted inoculate in PBS buffer (0.1 M, pH 7.4, ~10^7 CFU/mL) were incubated with **SP**-containing nanoparticle

Finally, we wanted to further confirm the *on-off* release abilities of the **SP**-containing nanoparticles, using the UTI-12 *E. coli* clinical isolate as model organism. **SP-SiO$_2$⊃TMP** nanoparticle was employed in this experiment as full cell eradication was observed. During the previous experiment (Figure 4.23B), after each day irradiation, an aliquot was separated, kept in the dark, and its viability checked every day up to the end of the irradiation experiment (Figure 4.24). As it can be seen in Figure 4.24., cell viability only experienced a decrease upon irradiation. Those aliquots kept in the dark did not exhibited further decrease in viability, confirming that the **TMP** release only takes place upon irradiation in an *on-off* fashion.

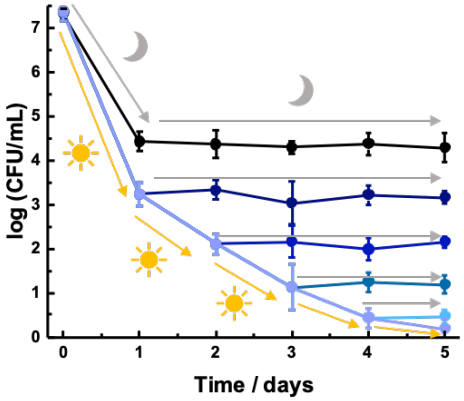

Figure 4.24. Effect of on-off **TMP** release from in UTI-12 cell viability **SP-SiO$_2$⊃TMP**. Bacterial cells were incubated in PBS buffer (0.1 M, pH 7.4, ~10^7 CFU/mL) with MIC concentration of **SP-SiO$_2$⊃TMP** nanoparticles. Each day an aliquote was separated and kept in the dark. The rest of cells were irradiated with white light (22 W, λ > 393 nm) for 30 s and incubated at 37 ºC and 150 rpm in the dark for 24 h. Next day the cell viability was evaluated. This process was repeated during five consecutive days. Sun represent irradiation and moon keeping the samples in the dark. Depicted values are based on 3 independent biological replicas.

4.3. Conclusion

In this study, a novel photoswitchable antibiotic delivery system, **SP-SiO$_2$⊃TMP**, has been developed by co-condensation of a silyl-derivative spiropyran photoswitch within

the SiO_2 framework. This platform was employed for the delivery of the UTI fist line antibiotic **TMP**. Furthermore, the effect of hydrophobicity of the framework in the photoresponsive behaviours of nanoparticles was explored by addition of dimethyldiethoxysilane as **SiO_2** precursor. Developed nanoparticles displayed negative photochromism where the spiropyran **MC** form was locked with the silica framework due to H-bonding with the framework. Upon white light irradiation the **MC** converts into the close **SP** form, which recovered in the dark. Increasing framework hydrophobicity decreased the **MC** form within the nanoparticles and slowed the **MC** recovery after irradiation. Inclusion of **TMP** prevented the formation of the **H^+MC** form which was associated with H-bonding interactions between the **MC** form and **TMP**. Furthermore, an irradiation dependent increase in **TMP** release was observed as well as a light triggered on-off release. Thereby, the system in this chapter represents the first non-porous **SiO_2** photoswitchable nanoparticles for drug delivery, which is a step forward for the development of on demand drug delivery systems.

4.4. Experimental section

4.4.1. Synthesis procedures

Trimethoprim (**TMP**), tetraethoxysilane (TEOS) and dimethyldiethoxysilane (DMDES) were purchase from Sigma-Aldrich. Rest of chemicals and consumables were purchased from Sigma-Aldrich and were of the highest quality available.

Synthesis of Si-SP-Si. The full procedure for the synthesis of the silyl-functionalised spiropyran (Si-SP-Si) was fully performed by Daniel Cerasale (Dr Timothy Easun group) and synthetic details and characterization can be found in the appendix.

Optimization of SP-SiO_2. Optimization of spiropyran content in **SP-SiO_2** nanoparticles was achieved by varying the initial concentration of the **Si-SP-Si** precursor, always keeping the molar concentration of combined silica precursors (**Si-SP-Si** + TEOS) constant based on the synthesis procedure reported by D. J. Lewis *et al*.[63] The exact quantities of each precursor can be found in Table 4.6.

Briefly, a solution containing 1.6 mL EtOH, 100 μL 28 % NH_4OH and 20 μL H_2O was stirred at room temperature. To this solution **Si-SP-Si** (see Table 4.6) was added and the solution stirred at room temperature until all solid was dissolved. Then, an EtOH solution (0.3 mL) containing TEOS (see Table 4.6) was added dropwise and the resulting solution was stirred for 2 h at room temperature, followed by 15 min of sonication treatment (200 W, 50 Hz) before another hour of stirring. Finally, obtained pink suspension was centrifuged (7450 rpm, 15 min) and the supernatant removed. **SP-SiO_2** were washed with water (3 x 20 mL) and dried overnight under vacuum.

Table 4.6. Mass and mols of **Si-SP-Si** and TEOS employed in the optimization of **SP-SiO_2** nanoparticles.

	Si-SP-Si		**TEOS**	
	Mass / mg	**mmol**	**Volume / μL**	**mmol**
0 %	-	-	130	0.58
0.2 %	0.9	0.01	128.1	0.57
2 %	9.2	0.02	125.8	0.56
5 %	15.3	0.03	121.9	0.55

Optimization of SP-$HSiO_2$. Optimization framework hydrophobicity in **SP-$HSiO_2$** nanoparticles was achieved by varying the initial concentration of DMDES precursor, always keeping the molar concentration of combined silica precursors (DMDES +

TEOS) constant based on the synthesis procedures reported by D. J. Lewis *et al.*[63] and S. Diré *et al*.[66] The exact quantities of each precursor can be found in Table 4.7.

Acidic hydrolysis of DMDES was performed by addition of DMDES (0.23 mL, 1.34 mmol) and 100 mL conc. HCl into 1 mL EtOH. The solution, denoted as H^+DMDES, was stirred at room temperature for 24 h.

Briefly, a solution containing 1.6 mL EtOH, 100 μL 28 % NH_4OH and 20 μL H_2O was stirred at room temperature. To this solution **Si-SP-Si** (15.3 mg, 0.03 mmol) was added and the solution stirred at room temperature until all solid was dissolved. Then, a 0.3 mL EtOH solution containing TEOS (see Table 4.7) and H^+DMDES (see table 4.7) was added dropwise and the resulting solution was stirred for 2 h at room temperature, followed by 15 min of sonication treatment (200 W, 50 Hz) before another hour of stirring. Finally, obtained pale pink suspension was centrifuged (7450 rpm, 15 min) and the supernatant removed. **SP-HSiO$_2$** were washed with water (3 x 20 mL) and dried overnight under vacuum.

Table 4.7. Composition of the solution added containing hydrolysed DMDES and TEOS.

	H^+DMDES		**TEOS**	
	Volume / μL	**mmol$_{DMDES}$**	**Volume / μL**	**mmol**
5 %	0.02	0.03	115.8	0.52
25 %	0.11	0.14	91.4	0.41
50 %	0.22	0.27	60.1	0.27
90 %	0.40	0.49	12.2	0.06

Synthesis of SP-SiO$_2$⊃TMP. A solution containing 1.6 mL EtOH, 100 μL 28 % NH_4OH and 20 μL H_2O was stirred at room temperature. To this solution **Si-SP-Si** (15.3 mg, 0.03 mmol) and **TMP** (1 mg, 3 μmol) were added and the solution stirred at room

temperature until all solid was dissolved. Then, an EtOH solution (0.3 mL) containing TEOS (121.9 μL, 0.55 mmol) was added dropwise and the resulting solution was stirred for 2 h at room temperature, followed by 15 min of sonication treatment (200 W, 50 Hz) before another hour of stirring. Finally, obtained pink suspension was centrifuged (7450 rpm, 15 min) and the supernatant removed. **SP-SiO_2⊃TMP** were washed with water (3 x 20 mL) and dried overnight under vacuum.

Synthesis of SP-$HSiO_2$⊃TMP. Acidic hydrolysis of DMDES was performed by addition of DMDES (0.23 mL, 1.34 mmol) and 100 mL conc. HCl into 1 mL EtOH. The solution, denoted as H^+DMDES, was stirred at room temperature for 24 h.

Briefly, a solution containing 1.6 mL EtOH, 100 μL 28 % NH_4OH and 20 μL H_2O was stirred at room temperature. To this solution **Si-SP-Si** (15.3 mg, 0.03 mmol) and **TMP** (1 mg, 3 μmol) were added and the solution stirred at room temperature until all solid was dissolved. Then, a 0.3 mL EtOH solution containing TEOS (91.4 μL, 0.41 mmol) and H^+DMDES (0.11 μL, 0.14 mmol DMDES) was added dropwise and the resulting solution was stirred for 2 h at room temperature, followed by 15 min of sonication treatment (200 W, 50 Hz) before another hour of stirring. Finally, obtained pale pink suspension was centrifuged (7450 rpm, 15 min) and the supernatant removed. **SP-$HSiO_2$⊃TMP** were washed with water (3 x 20 mL) and dried overnight under vacuum.

4.4.2. Methodology

Antibiotic release studies. Release studies were performed in PBS buffer (0.1 M, pH 7.4) under mild stirring (150 rpm) with nanoparticles concentration of 2 mg/mL.

Irradiation of samples was done with a 2000 Lumen Moweeto© flashlight positioned at c.a. 1 cm from the nanoparticle suspension. Released **TMP** was quantified by UV/Vis spectroscopy based on the absorption λ_{max} at 278 nm. n= 3 in all experiments. Statistical significance was evaluated by t-test where ns = $p > 0.5$, * = $p < 0.1$, ** = $p < 0.01$ and *** = $p < 0.001$.

Minimal Inhibitory Concentration (MIC) determination. MIC values of studied nanoparticles and **TMP** were determined for reference *E. coli* (MG1655) and the clinical UTI *E. coli* isolates (UTI-12, UTI-42 and UTI-36) following the methodology described in Chapter 2 Section 4. Nanoparticles were tested between 20 mg/mL and 0.08 mg/mL and TMP between 250 μg/mL and 0.25 μg/mL.

Bacterial viability upon different irradiation times. Bacterial inoculum of 10^7 - 10^9 colony forming units per mL (CFU/mL) were incubated with MIC concentration of **TMP** or nanoparticles. Suspensions were irradiated with a 2000 Lumen Moweeto© flashlight at c.a. 1 cm from the samples. Then, the suspensions were placed in the dark at 37 °C under mild shaking (150 rpm) for 24 h before viability evaluation by CFU/mL determination in LB agar plates. Statistical significance was evaluated by t-test where ns = $p > 0.5$, * = $p < 0.1$, ** = $p < 0.01$ and *** = $p < 0.001$.

Bacterial viability across different days. Bacterial inoculum of 10^7 - 10^9 colony forming units per mL (CFU/mL) were incubated with MIC concentration of **TMP** or spiropyran-containing nanoparticles. Suspensions were then irradiated for 30 s with A

2000 Lumen Moweeto© flashlight at c.a. 1 cm from the samples under continuous stirring at 150 rpm. Then, the suspensions were incubated in the dark at 37 °C under mild shaking (150 rpm) for 24 h. An aliquot was then taken, and its viability evaluated by CFU/mL determination in LB agar. The rest of the suspensions were subjected to the light-dark cycle for other four consecutive days and the viability after each cycle evaluated by CFU/mL determination in LB agar. Control experiments were not subjected to irradiation. Statistical significance was evaluated by t-test where ns = $p > 0.5$, * = $p < 0.1$, ** = $p < 0.01$ and *** = $p < 0.001$.

4.5. Appendix

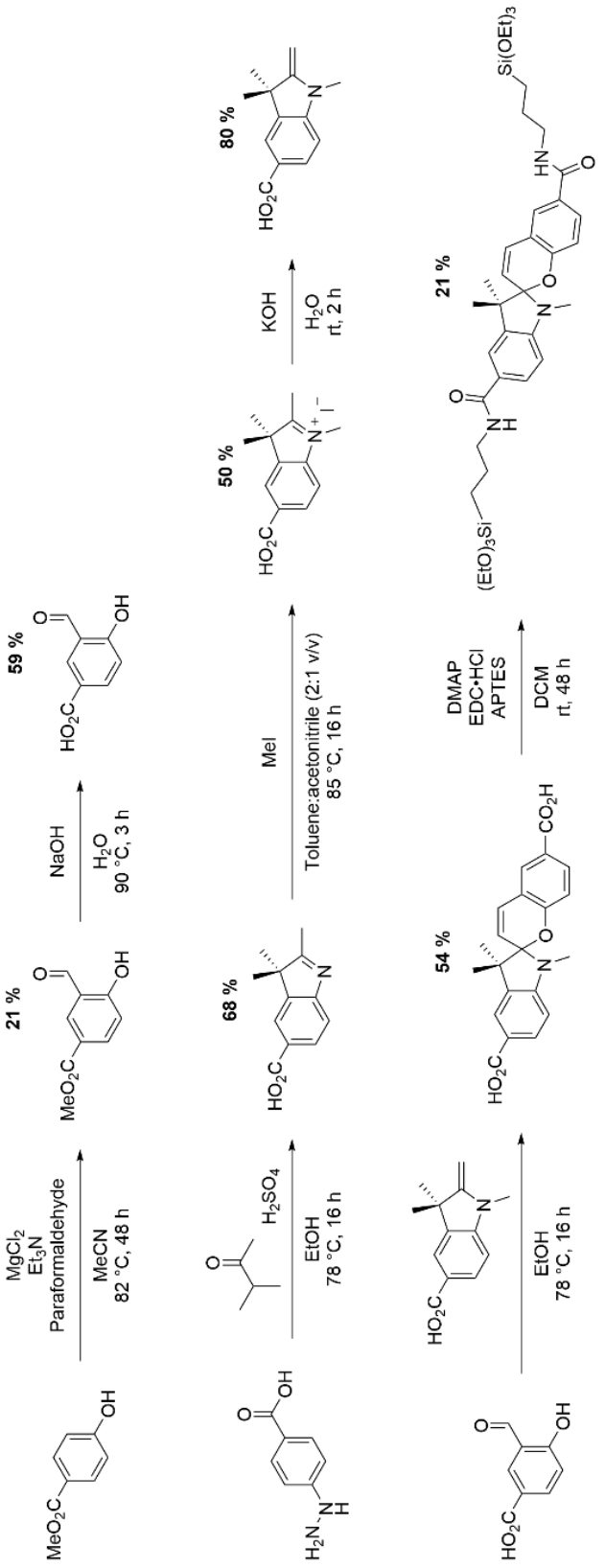

Figure 4.S1. Synthesis scheme of **Si-SP-Si** developed by Daniel Cerasale (Dr. Timothy Easun group).

2,3,3-Trimethyl-3*H*-indole-5-carboxylic acid. To a peach-coloured suspension of 4-hydrazinobenzoic acid (5.00 g, 33.0 mmol) in EtOH (120 mL), 3-methyl-2-butanone (3.90 mL, 36.0 mmol) and H_2SO_4 (18 M, 1 mL) were added with stirring. The reaction was heated to reflux for 12 h giving a red-brown solution with yellow precipitate. After cooling to room temperature, the mixture was filtered, saturated $NaHCO_3$ solution (50 mL) was added, and the solution was extracted with DCM (3 x 20 mL). The aqueous phase was adjusted to pH 4 with HCl (1.0 M) and extracted with DCM (3 x 20 mL). The organic phases were combined, dried over anhydrous $MgSO_4$ and evaporated under reduced pressure to give 2,3,3-trimethyl-3*H*-indole-5-carboxylic acid as a brown solid (4.56 g, 68 %). **^{1}H NMR** (300 MHz, DMSO-d_6): δ 12.86 (s, 1H), 8.00 (d, *J = 1.6 Hz*, 1H), 7.92 (dd, *J = 8.0 Hz*, 1.7 Hz, 1H), 7.51 (d, *J = 8.0 Hz*, 1H), 2.26 (s, 3H), 1.28 (s, 6H). **MS** (ESI +): *m/z* 204.1024 ($[M+H]^+$), theoretical *m/z* 204.1029 ($[M+H]^+$).

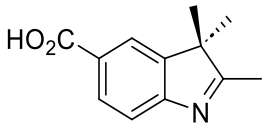

5-Carboxy-1,2,3,3-tetramethyl-3*H*-indol-1-ium iodide. To a solution of 2,3,3-trimethyl-3*H*-indole-5-carboxylic acid (2.00 g, 10.0 mmol) in toluene/MeCN (2:1 v/v, 60 mL), iodomethane (0.61 mL, 10.0 mmol) was added. The red solution was heated to 80 °C under an atmosphere of N_2 for 72 h. The resulting red mixture was cooled to 0 °C, filtered and the precipitate washed with EtOH (10 mL) and hexane (80 mL) to afford 5-carboxy-1,2,3,3-tetramethyl-3*H*-indol-1-ium iodide as an orange-brown solid (1.68 g, 50%). **^{1}H NMR** (300 MHz, DMSO-d6): δ 8.38 (s, 1H), 8.23 – 8.14 (m, 1H), 8.02 (d,

J = 8.4 Hz, 1H), 3.99 (s, 3H), 2.81 (s, 3H), 1.56 (s, 6H). **MS** (ESI-pos): *m/z* 218.19 ($[M+H]^+$).

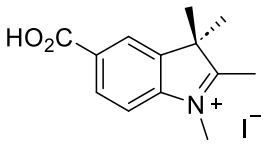

1,3,3-Trimethyl-2-methyleneindoline-5-carboxylic acid. A solution of 5-carboxy-1,2,3,3-tetramethyl-3*H*-indol-1-ium iodide (1.45 g, 4.20 mmol) in aqueous KOH solution (0.42 M, 20.0 mL) was stirred for 2 h at room temperature. The solution was adjusted to pH 7 using HCl (1.0 M) and extracted with isopropanol/DCM (1:1 v/v, 6 x 15 mL). The organic extracts were combined and dried over anhydrous $MgSO_4$, filtered and solvent was removed *in vacuo* to yield 1,3,3-trimethyl-2-methyleneindoline-5-carboxylic acid as an orange-brown solid (0.73 mg, 80%). **^{1}H NMR** (400 MHz, DMSO-d_6): δ 12.27 (s, 1H), 7.76 (dd, *J = 8.3 Hz*, 1.8 Hz, 1H), 7.67 (d, *J = 1.7 Hz*, 1H), 6.73 (d, *J = 8.3 Hz*, 1H), 4.05 – 3.98 (m, 2H), 3.07 (s, 3H), 1.29 (s, 6H). **MS** (ESI-pos): *m/z* 218.1185 ($[M+H]^+$), theoretical *m/z* 218.1181 ($[M+H]^+$).

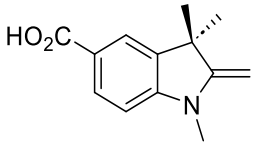

Methyl 3-formyl-4-hydroxybenzoate. Methyl 4-hydroxybenzoate (10.0 g, 65.7 mmol) and anhydrous $MgCl_2$ (10.0 g, 105 mmol) were dissolved in dry MeCN (600 mL) followed by addition of dry triethylamine (33.0 mL, 237 mmol) with stirring. Paraformaldehyde (40.0 g, 1.33 mol as monomer) was added, and the mixture was refluxed for 48 h. The reaction mixture was allowed to cool to room temperature and

the solvent was removed *in vacuo*. H_2O (100 mL) was added, and the solution was acidified to pH 3 with HCl (1.0 M). The aqueous solution was extracted with EtOAc (3 x 50 mL), and the organic extracts combined. The organic phase was dried over anhydrous $MgSO_4$ and evaporated under reduced pressure to obtain a yellow oil. Recrystallisation from hot EtOH yielded methyl 3-formyl-4-hydroxybenzoate as a white powder (2.50 g, 21%). **^{1}H NMR** (300 MHz, Chloroform-d): δ 11.38 (s, 1H), 9.94 (d, *J = 0.6 Hz*, 1H), 8.31 (dd, *J = 2.2, 0.4 Hz*, 1H), 8.17 (dd, J = 8.8, 2.2 Hz, 1H), 7.02 (dt, *J = 8.8, 0.6 Hz*, 1H), 3.91 (s, 3H). **MS** (GCMS - CI): *m/z* 180.0425 ($[M]^-$), theoretical *m/z* 180.0428 ($[M]^-$).

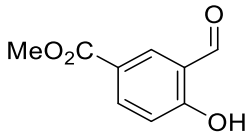

3-Formyl-4-hydroxybenzoic acid. To a stirred solution of 2 M NaOH in H_2O (35 mL, 70.0 mmol) was added methyl 3-formyl-4-hydroxybenzoate (500 mg, 2.78 mmol). The resulting mixture was refluxed for 3 hours and allowed to cool to room temperature. The solution as to pH 7 with 10% HCl aqueous solution to induce precipitation of the product. The solid was extracted with EtOAc, (3 x 50 mL), extracts were combined, dried with anhydrous $MgSO_4$ evaporated under reduced pressure to give 3-formyl-4-hydroxybenzoic acid as a white powder (270 mg, 59%). **^{1}H NMR** (300 MHz, Chloroform-d): δ 11.49 (s, 2H), 9.98 (d, *J = 0.6 Hz*, 2H), 8.40 (d, *J = 2.1 Hz*, 2H), 8.26 (dd, *J = 8.8, 2.1 Hz*, 2H), 7.08 (d, *J = 8.8 Hz*, 2H). **MS** (GCMS - CI): *m/z* 166.0270 ($[M]^-$), theoretical *m/z* 166.0272 ($[M]^-$).

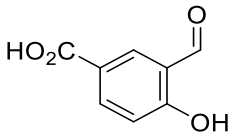

1',3',3'-Trimethylspiro[chromene-2,2'-indoline]-5',6-dicarboxylic acid (HO2C-SP-CO2H). 3-Formyl-4-hydroxybenzoic (270 mg, 1.63 mmol) was dissolved in EtOH (50 mL) and 1,3,3-trimethyl-2-methyleneindoline-5-carboxylic acid (353 mg, 1.63 mmol) was added. The reaction mixture was heated to reflux for 16 hours before being reduced *in vacuo* and cooled to 0 °C to aid precipitation. The solid was filtered, washed with cold EtOH (2 x 100 mL) and dried to yield 1',3',3'-trimethylspiro[chromene-2,2'-indoline]-5',6-dicarboxylic acid (HO_2C-SP-CO2H) as a white powder (320 mg, 54%). **^{1}H NMR** (400 MHz, DMSO-d6): δ 12.51 (s, 2H), 7.87 – 7.78 (m, 2H), 7.71 (dd, *J = 8.5, 2.1 Hz*, 1H), 7.67 (d, *J = 1.7 Hz*, 1H), 7.21 – 7.14 (m, 1H), 6.82 – 6.75 (m, 1H), 6.67 (d, *J = 8.3 Hz*, 1H), 5.88 (d, *J = 10.2 Hz*, 1H), 2.76 (s, 3H), 1.25 (s, 3H), 1.13 (s, 3H). **^{13}C NMR** (101 MHz, DMSO): δ 167.89, 167.22, 157.70, 151.87, 136.57, 131.93, 131.24, 129.73, 129.14, 123.53, 123.36, 121.77, 119.83, 118.75, 115.08, 106.58, 105.33, 51.73, 28.85, 25.98, 20.09. **MS** (ESI-neg): *m/z* 364.1189 ($[M-H]^-$), theoretical *m/z* 364.1185 ($[M-H]^-$).

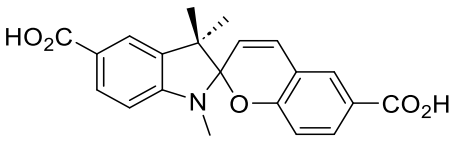

1',3',3'-Trimethyl-N5',N6-bis(2-(triethoxysilyl)ethyl)spiro[chromene-2,2'-indoline]-5',6-dicarboxamide (Si-SP-Si). 1',3',3'-Trimethylspiro[chromene-2,2'-indoline]-5',6-dicarboxylic acid (680 mg, 1.86 mmol), 4-Dimethylaminopyridine (477

mg, 3.90 mmol) and (3-Dimethylamino-propyl)-ethyl-carbodiimide hydrochloride (821 mg, 4.28 mmol) were dissolved in dry DCM (120 mL) under an atmosphere of nitrogen. (3-aminopropyl)triethoxysilane (0.96 mL, 4.10 mmol) was added and the mixture was stirred at room temperature for 48 h until the starting material was no longer visible by TLC. Solvent was removed *in vacuo* and the crude product was purified by column chromatography (silica gel: 80 % EtOAc in hexane to 100% EtOAc) to yield 1',3',3'-trimethyl-N5',N6-bis(2-(triethoxysilyl)ethyl)spiro[chromene-2,2'-indoline]-5',6-dicarboxamide (**Si-SP-Si**) as a pinkish white powder (300 mg, 21%). **^{1}H NMR** (400 MHz, Chloroform-d): δ 7.63 – 7.54 (m, 3H), 7.49 (dd, J = 8.5, 2.3 Hz, 1H), 6.91 (dd, *J = 10.4, 0.7 Hz*, 1H), 6.69 (d, *J = 8.4 Hz*, 1H), 6.49 (d, J = 8.1 Hz, 1H), 6.34 (dt, *J = 19.7, 5.8 Hz*, 2H), 5.72 (d, *J = 10.2 Hz*, 1H), 3.83 (qd, *J = 7.0, 4.6 Hz*, 12H), 3.49 – 3.41 (m, 4H), 2.76 (s, 3H), 1.79 – 1.70 (m, 4H), 1.31 (s, 3H), 1.22 (td, *J = 7.05.2 Hz*, 18H), 1.17 (s, 3H), 0.74 – 0.67 (m, 4H). **^{13}C NMR** (101 MHz, CDCl3): δ 167.60, 166.77, 156.70, 150.66, 136.79, 129.39, 128.33, 127.24, 127.07, 126.32, 125.90, 121.03, 119.59, 118.48, 114.80, 105.92, 105.00, 58.51, 51.77, 42.19, 28.81, 25.71, 23.12, 22.94, 19.97, 18.32, 18.29, 7.84. **MS** (ESI-pos): *m/z* 772.4030 ($[M+H]^+$), theoretical *m/z* 772.4025 ($[M+H]^+$). **IR**: σ(ATR)/cm^{-1} 3296 (v(N-H)), 2972-2884 (v(C-H)), 1692 (v(C=O)), 1547 (v(C=C aromatic)), 1320 (v(C-N)), 1261 (v(C-O)), 1073 (v(Si-O)).

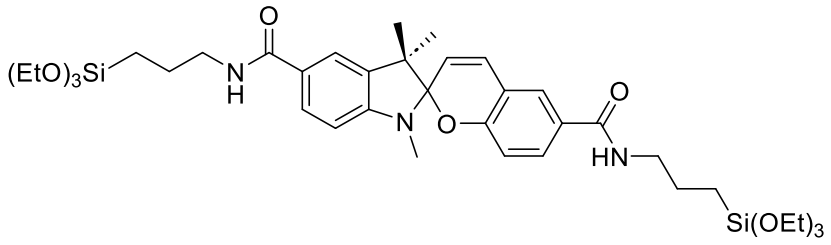

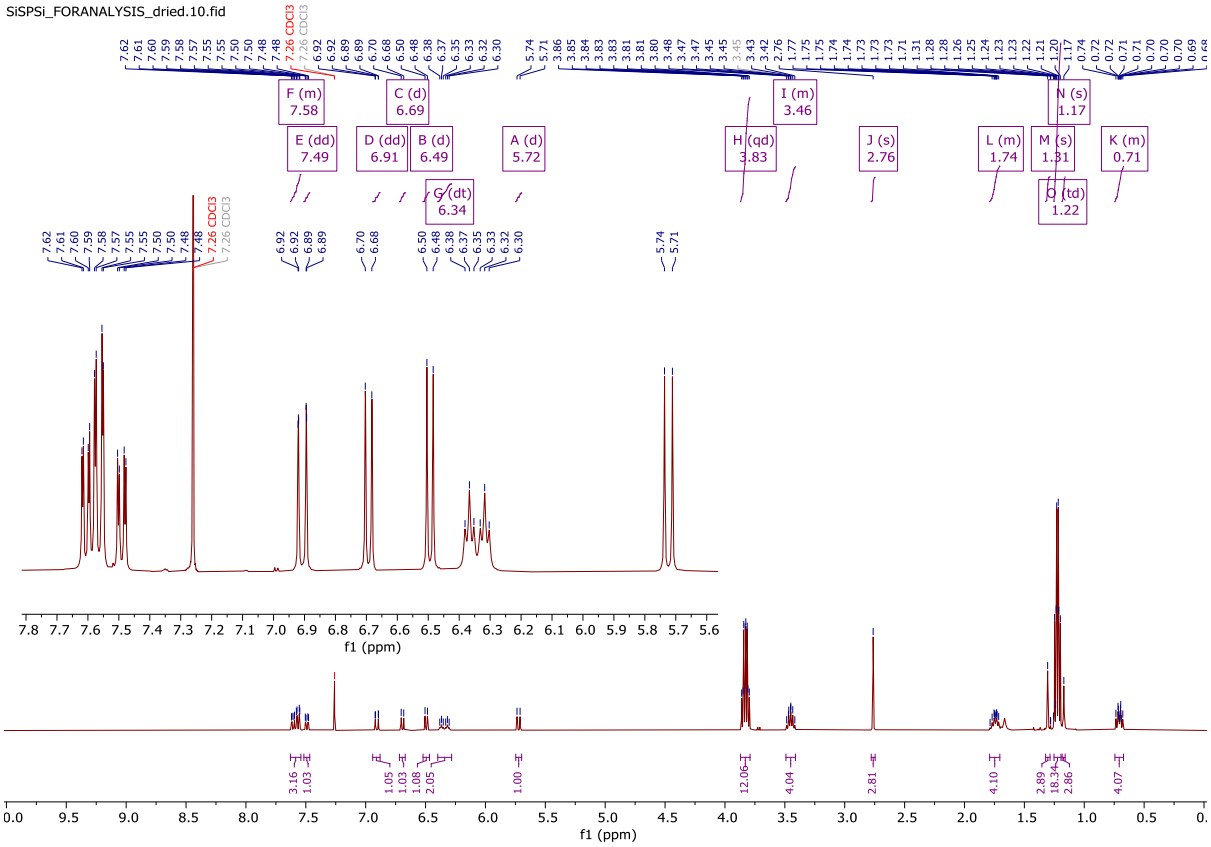

Figure 4.S2. ^{1}HNMR (400 MHz, $CDCl_3$) of **Si-SP-Si**.

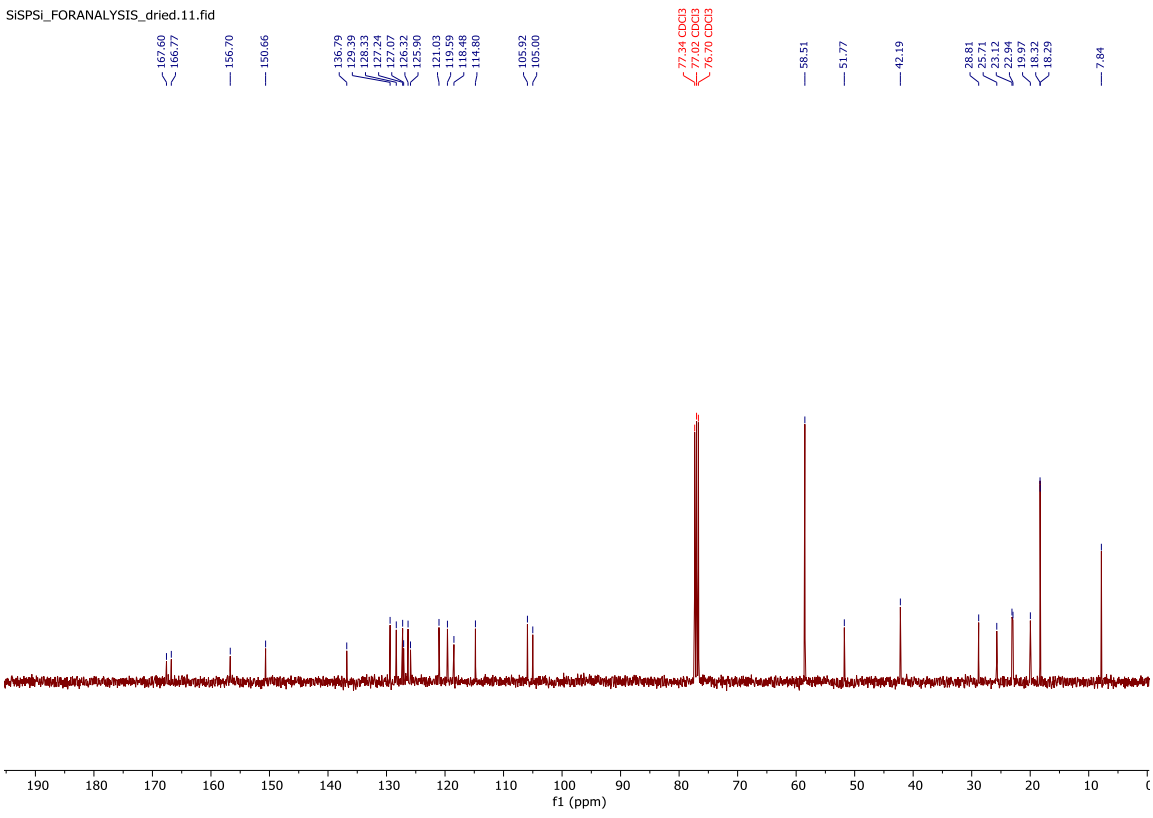

Figure 4.S3. ^{13}CNMR (101 MHz, $CDCl_3$) of **Si-SP-Si**.

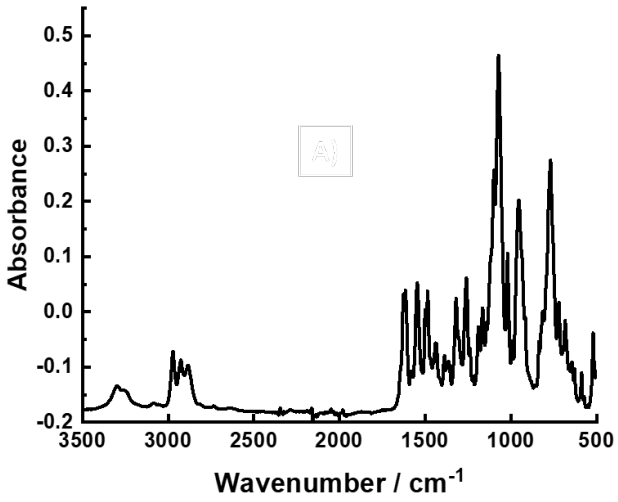

Figure 4.S4.IR spectra of **Si-SP-Si**.

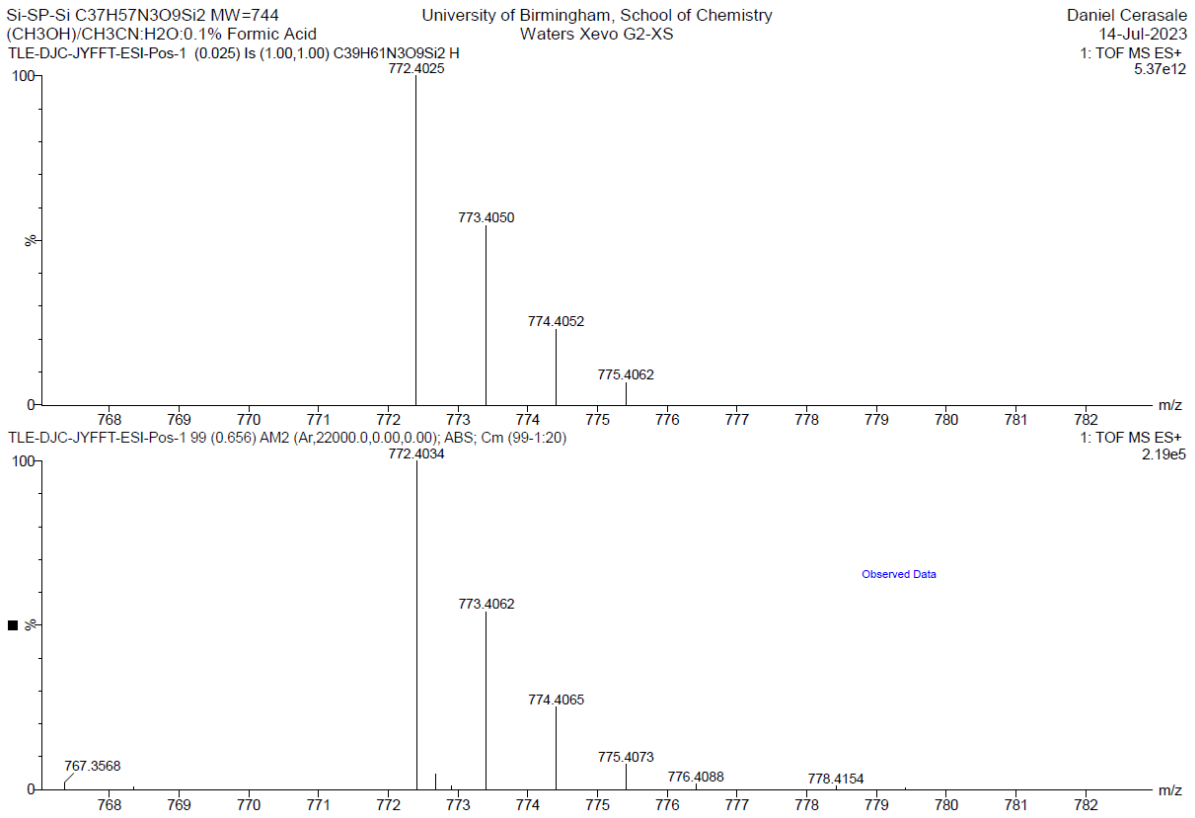

Figure 4.S5. ESI-MS (Positive mode) of **Si-SP-Si**. Calculated $[M+H]^+$ is displayed on top.

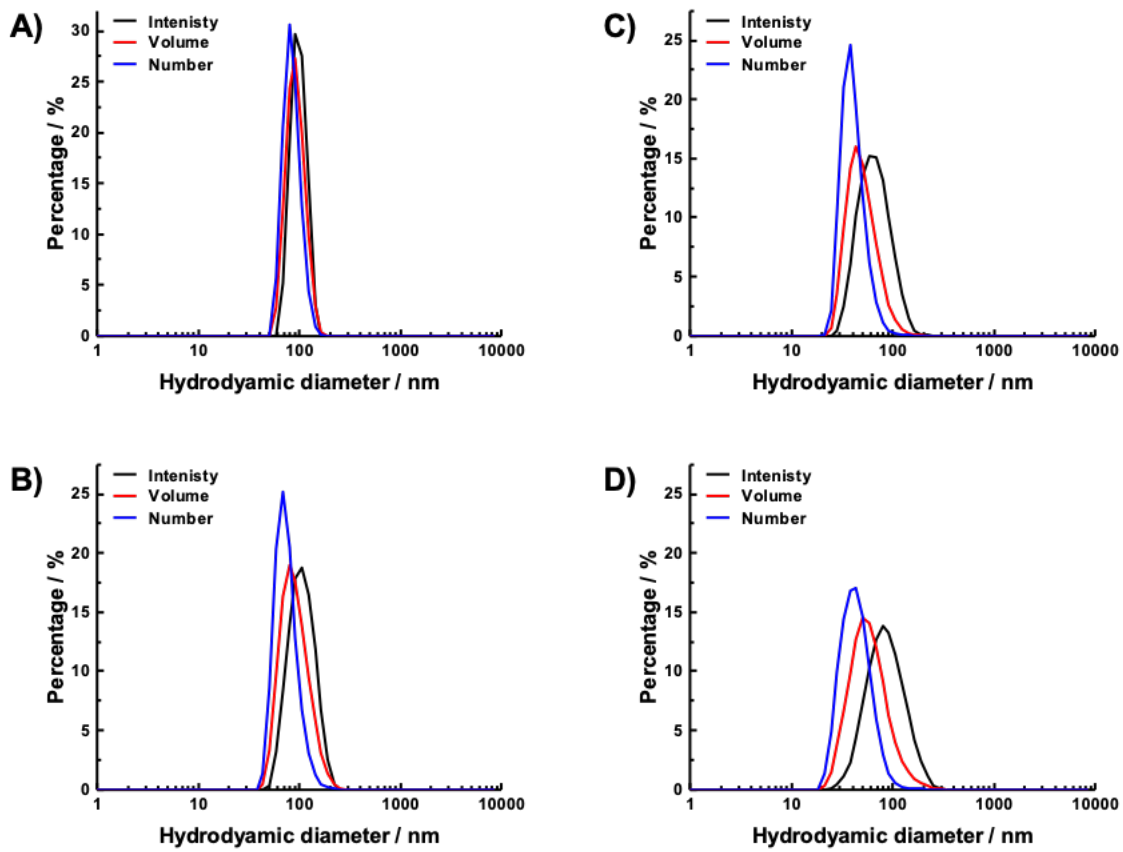

Figure 4.S6. Dynamic light scattering distribution analysis of **SP-SiO$_2$** nanoparticles with initial (A) 0 %, (B) 0.2 %, (C) 2 % and (D) 5 % **Si-SP-Si** molar ratio respect to TEOS in PBS buffer (0.1M, pH 7.4).

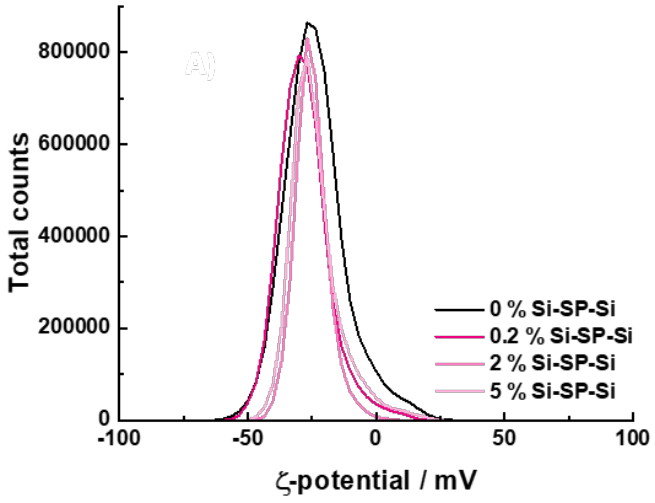

Figure 4.S7. Surface ζ-potential distribution in of **SP-SiO$_2$** nanoparticles with initial (A) 0 %, (B) 0.2 %, (C) 2 % and (D) 5 % **Si-SP-Si** molar ratio respect to TEOS in PBS buffer (0.1M, pH 7.4).

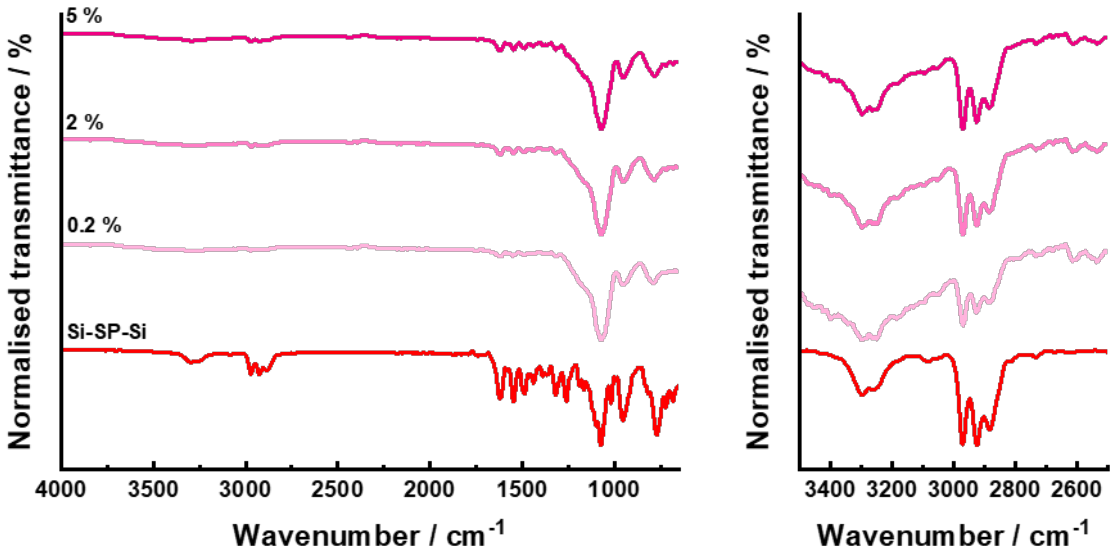

Figure 4.S8. FT-IR spectra of **SP-SiO$_2$** nanoparticles synthetized with different ratios of **Si-SP-Si**. Right graph displaces the 3500-2500 cm^{-1} region where the starched associated with the N-H and C-H and C-H$_{Ar}$ bonds are shown.

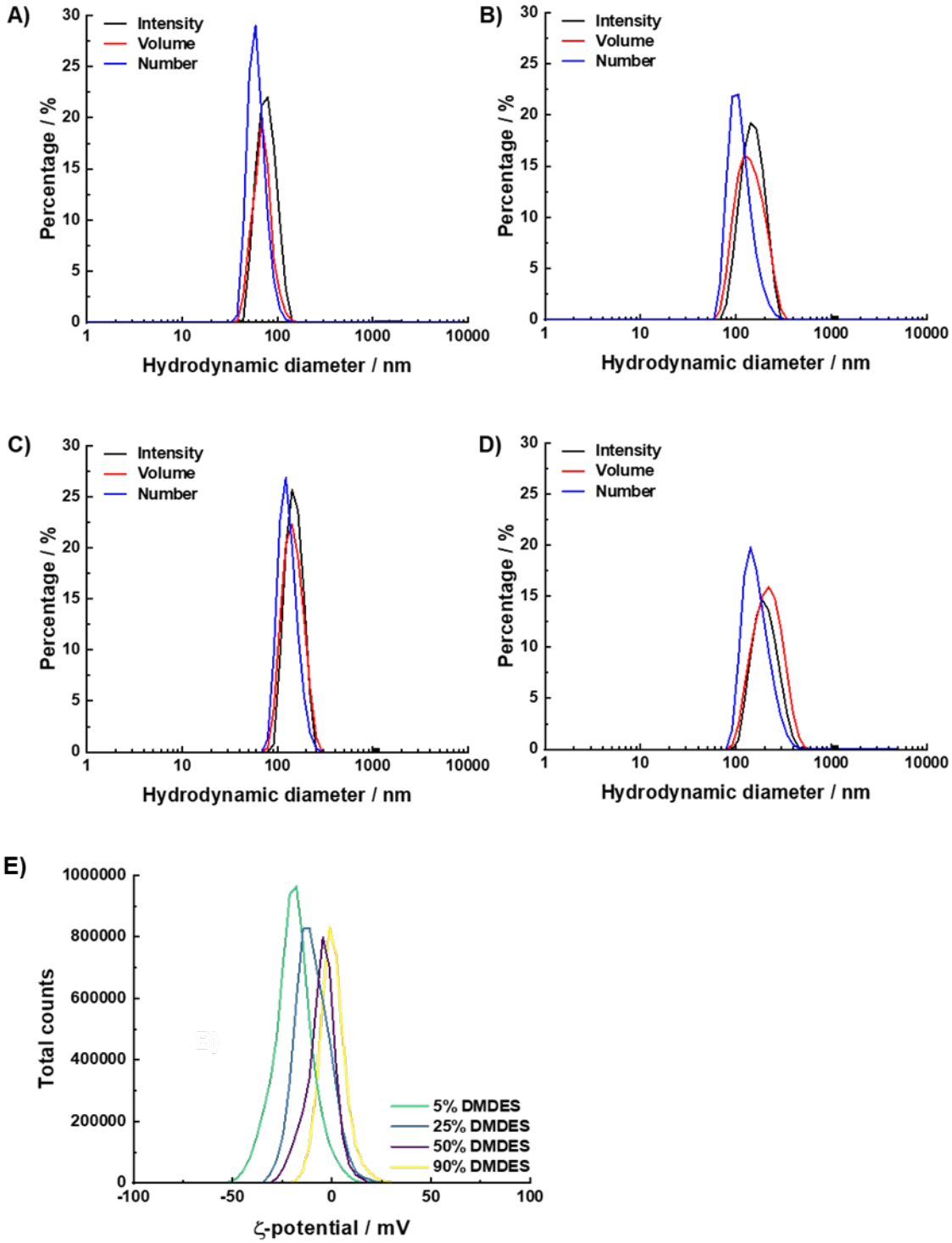

Figure 4.S9. (A-D) Dynamic light scattering and (E) ζ-potential distribution of **SP-$HSiO_2$** nanoparticles synthetized with initial (A) 5%, (B) 25 %, (C) 50 % and (D) 90 % DMDES respect to TEOS in PBS buffer (0.1 M, pH 7.4),

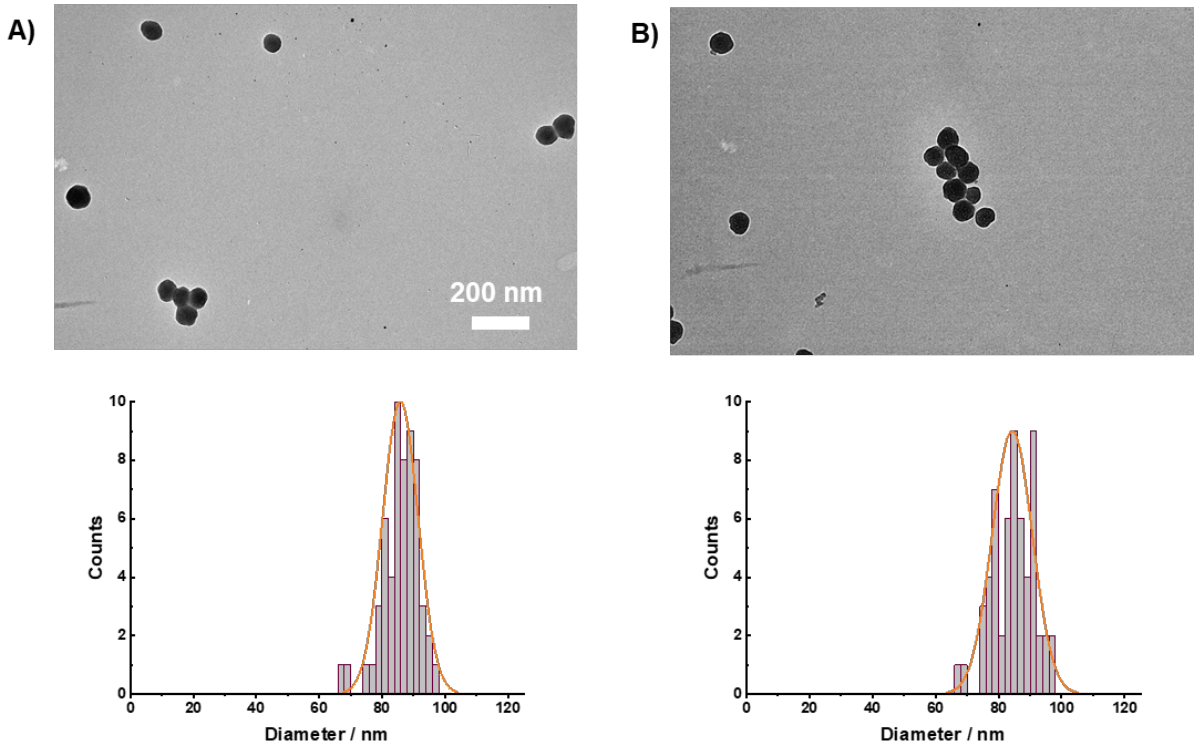

Figure 4.S10. Transmission Electron Microscopy and nanoparticle size distribution (n = 50) of **SP-HSiO$_2$** nanoparticles synthetized with (A) 5 % and (B) 25 % DMDES respect to TEOS.

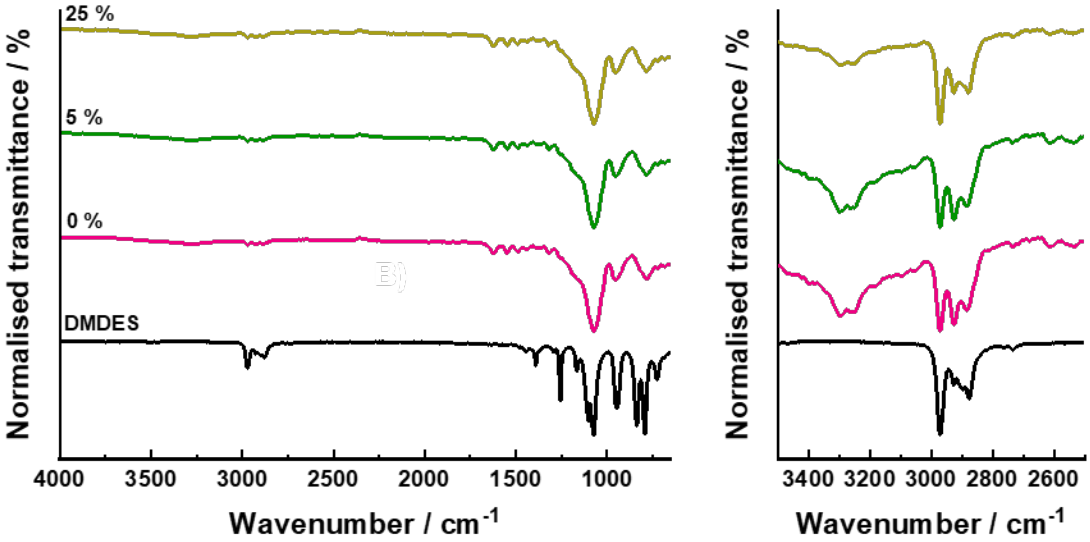

Figure 4.S11. FT-IR spectra of **SP-HSiO$_2$** nanoparticles synthetized with different ratios of DMDES. Right graph displaces the 3500-2500 cm^{-1} region.

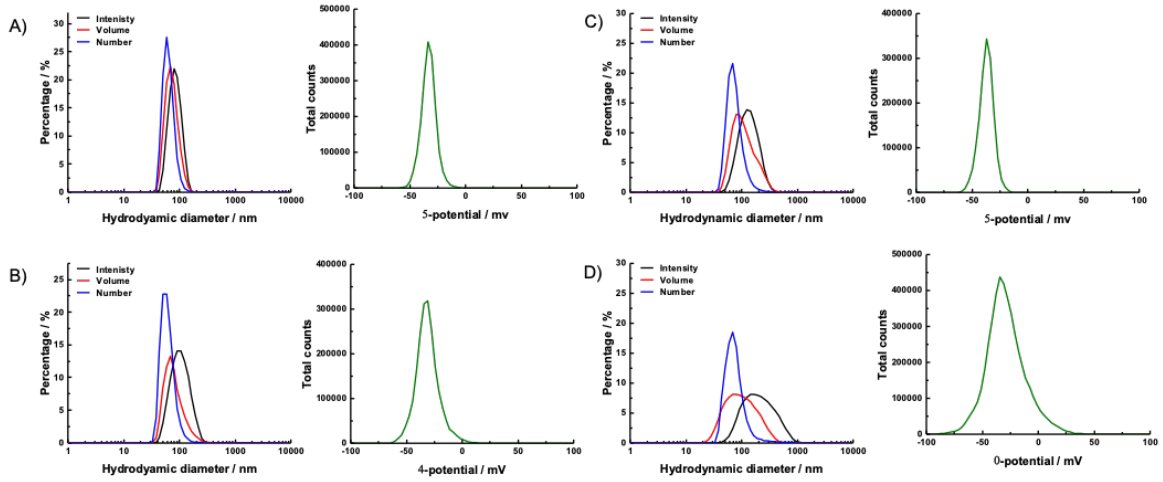

Figure 4.S12. Dynamic light scattering and ζ-potential distribution in PBS buffer (0.1 M, pH 7.4) of (A) **SiO_2⊃TMP**, (B) **$HSiO_2$⊃TMP**, (C) **SP-SiO_2⊃TMP** and (D) **SP-$HSiO_2$⊃TMP**.

Table 4.S1. Dynamic Light Scattering (n = 5) and ζ-potential (n = 3) measurements of **TMP**-containing control nanoparticles in PBS buffer (0.1 M, pH 7.4).

	Hydrodynamic diameter (D_H) / nm				ζ-potential
	Intensity	Volume	Number	PDI	/ mV
SiO_2⊃TMP	85 ± 21	74 ± 20	64 ± 15	0.03	-33 ± 6
$HSiO_2$⊃TMP	130 ± 56	108 ± 40	66 ± 27	0.12	-33 ± 7

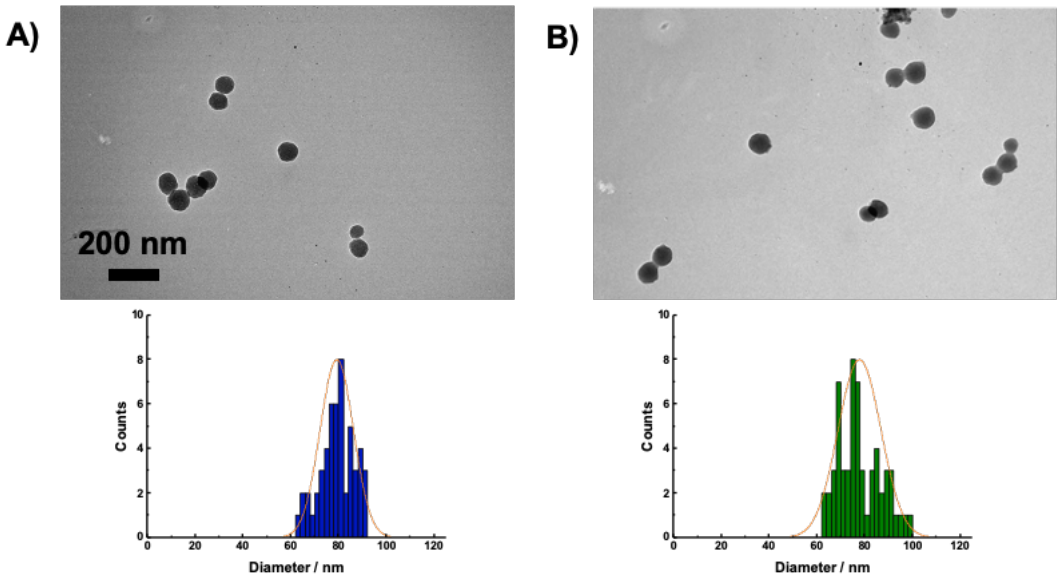

Figure 4.S13. Transmission Electron Microscopy (TEM) images and nanoparticle size distribution (n = 50) of (A) **SiO_2⊃TMP** and (B) **$HSiO_2$⊃TMP**.

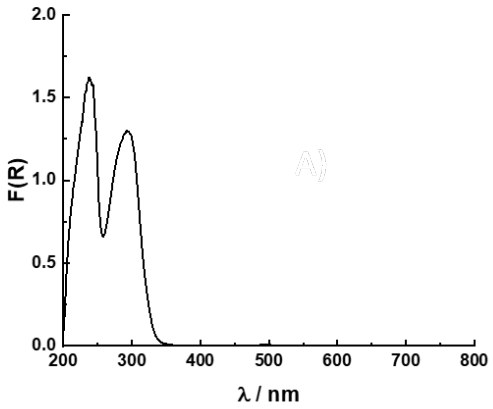

Figure 4.S14. Solid-state UV/Vis spectra of **Si-SP-Si.**

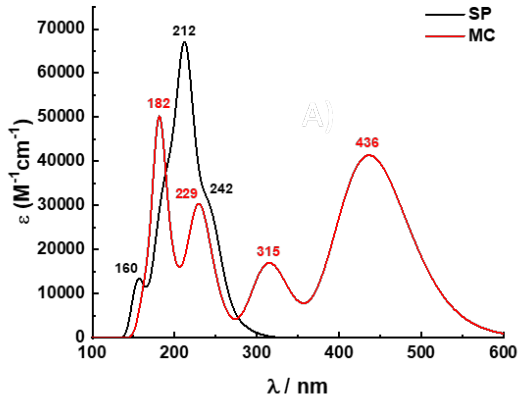

Figure 4.S15. Simulation of **SP** and **MC** UV/Vis spectra *in vacuo* by Daniel Cerasale (Dr. Timothy Easun). Calculations were run on Gaussian09. For both geometry optimisation and TDDFT calculations, the functional used was ωB97XD and the basis set used was 6-31G(d). For TDDFT calculations, 50 states were solved.

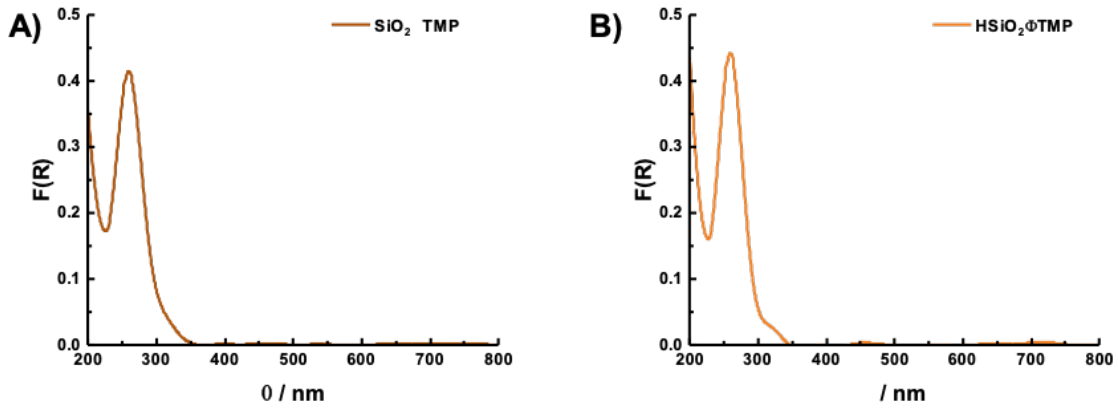

Figure 4.S16. Solid-state UV/Vis spectra of (A) **SiO_2⊃TMP** and (B) **$HSiO_2$⊃TMP**.

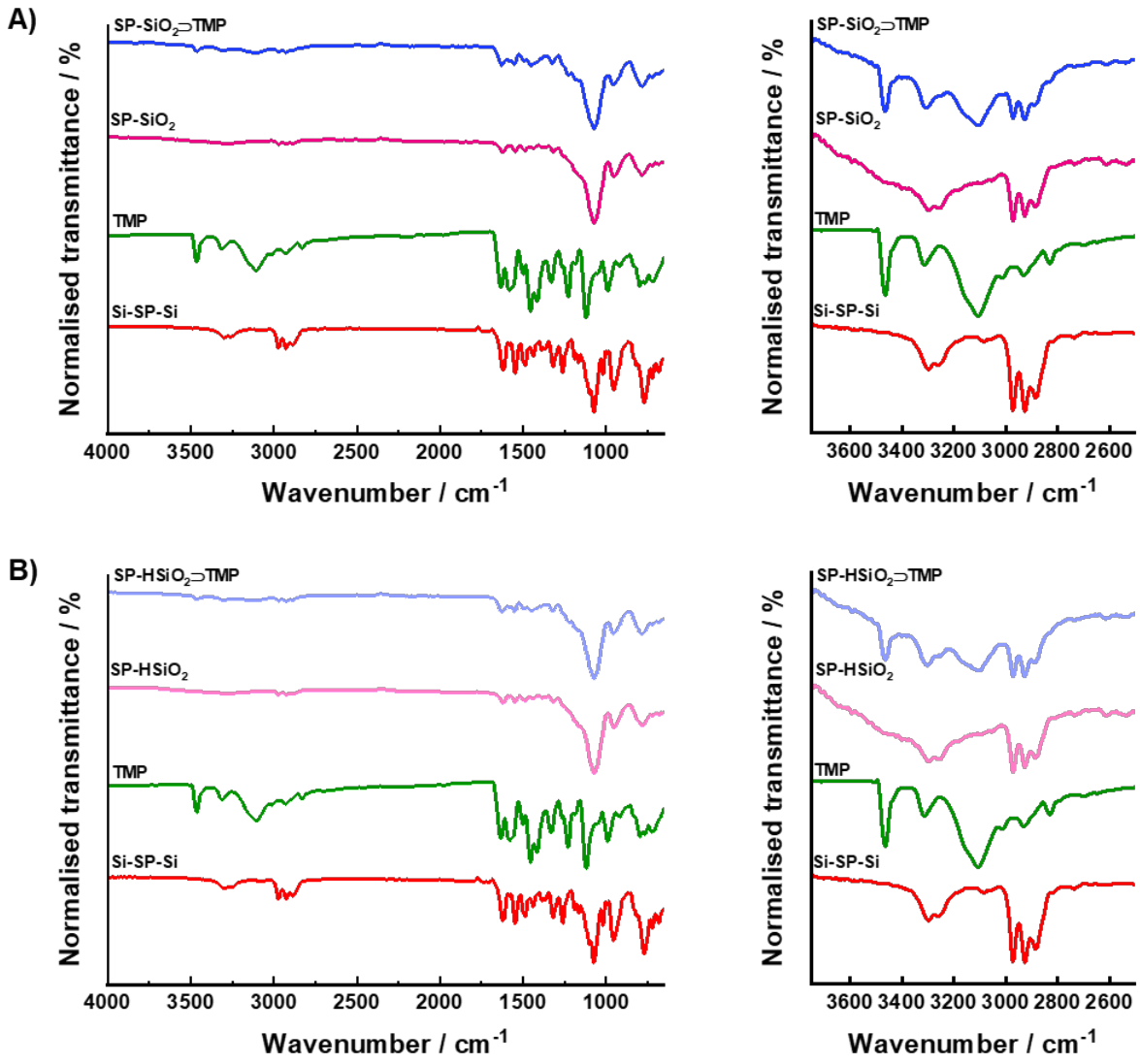

Figure 4.S17. FT-IR spectra of (A) **SP-SiO$_2$⊃TMP** and (B) **SP-HSiO$_2$⊃TMP**

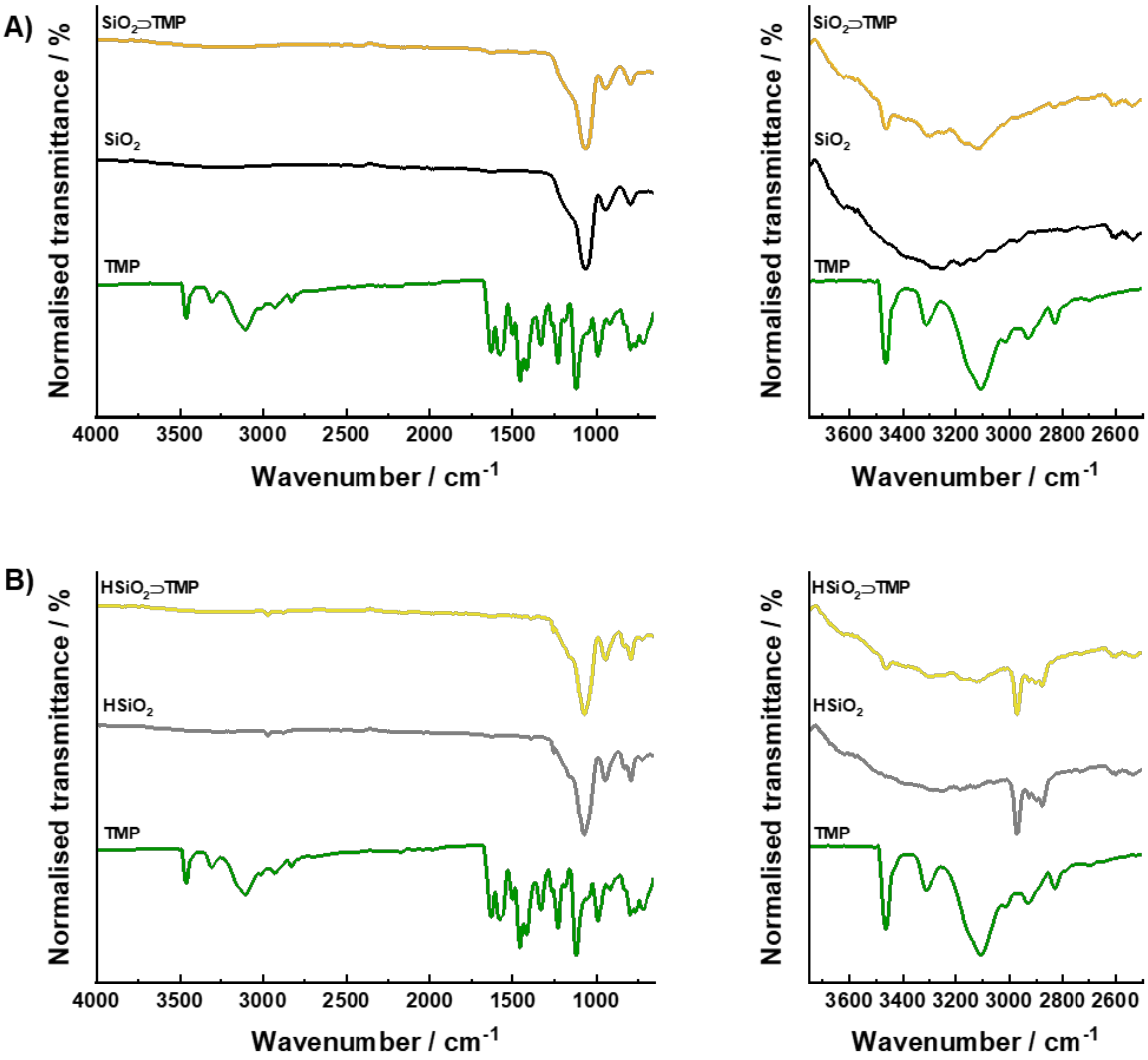

Figure 4.S18. FT-IR spectra of (A) **SiO_2⊃TMP** and (B) **$HSiO_2$⊃TMP**

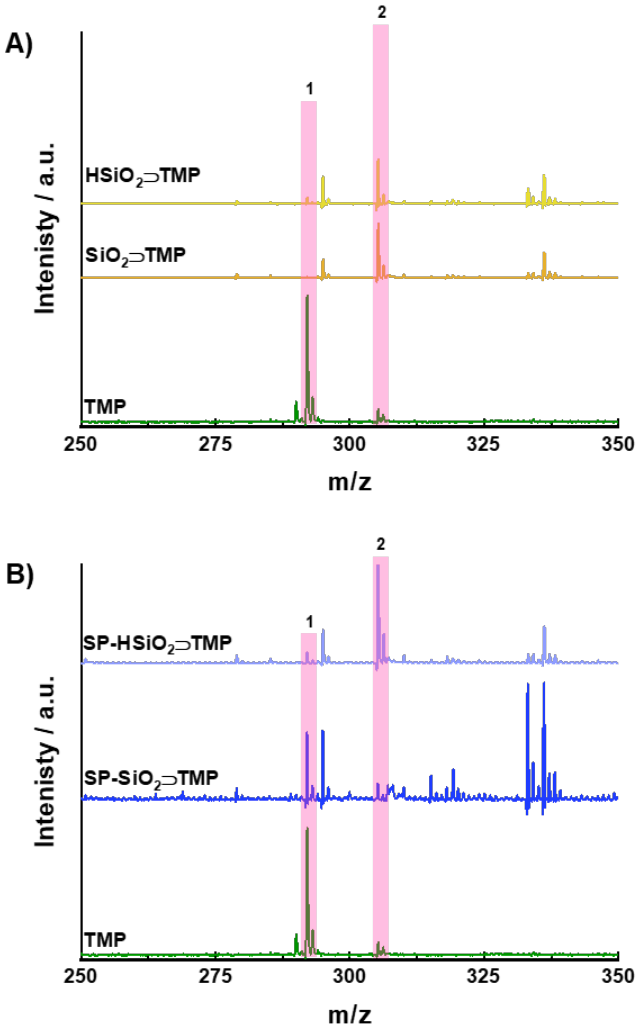

Figure 4.S19. MALDI-ToF mass spectrometry (positive mode) of (A) control and (B) photoresponsive **TMP**-containing nanoparticles confirming the presence of the antibiotic. Signal associated with [**TMP**+H]$^+$ (m/z = 291.162, caldc. m/z = 291.146) and [**TMP**-OMe+2Na$^+$]$^+$ (m/z = 305.203, caldc. m/z = 305.199) were detected. α-cyano-4-hydroxycinnamic acid (CHCA) was employed as matrix.

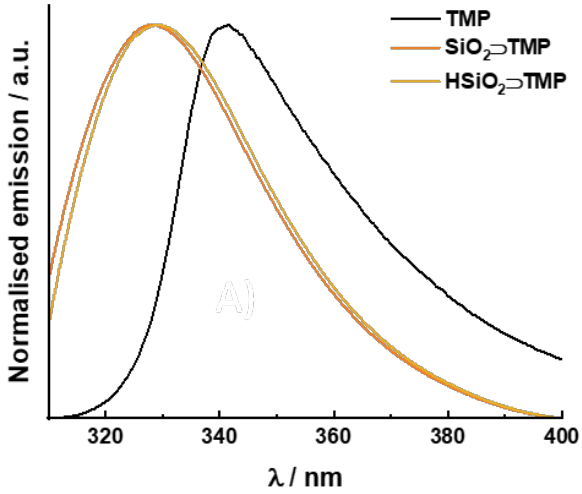

Figure 4.S20. Solid-state fluorescence emission of **TMP** (λ_{exc} = 270 nm) from (A) **SiO_2⊃TMP** and (B) **$HSiO_2$⊃TMP.**

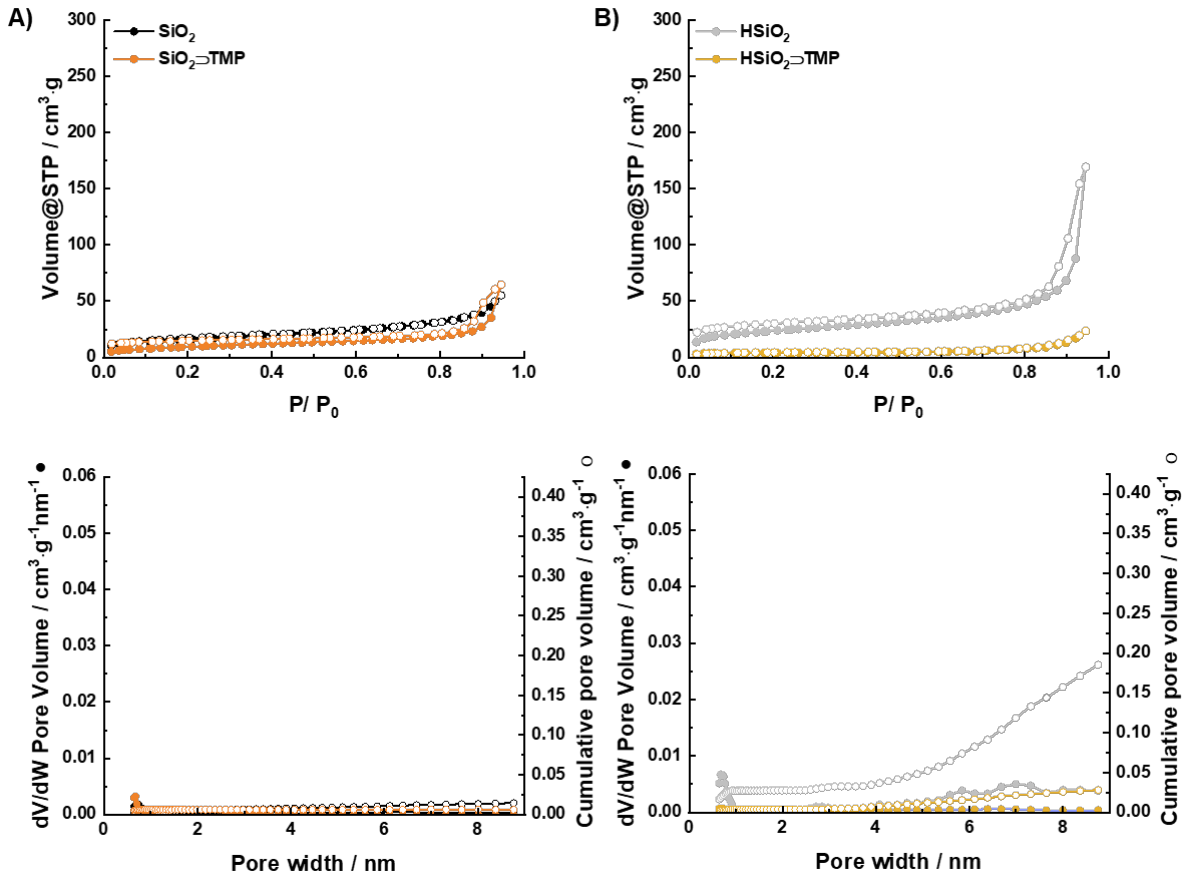

Figure 4.S21. Nitrogen adsorption-desorption isotherms at 77 K and DFT pore distribution calculation of (A) **SiO_2** and **SiO_2⊃TMP** (B) **$HSiO_2$** and **$HSiO_2$⊃TMP**

Table 4.S2. BET surface area, total pore volume and pore dimeter of control nanoparticles based on nitrogen adsorption-desorption isotherms.

	BET surface area / m^2g^{-1}	Total pore volume / cm^3g^{-1}	Pore diameter / nm
SiO_2	35.6 ± 0.3	0.020	-
SiO_2⊃TMP	10.5 ± 0.3	0.005	-
$HSiO_2$	57.1 ± 0.7	0.210	0.7, 1.6, 2.8
$HSiO_2$⊃TMP	8.4 ± 0.2	0.043	-
SP-SiO_2	250.7 ± 7.8	0.375	0.7, 1.5, 2.7
SP-SiO_2⊃TMP	107.7 ± 1.2	0.172	0.7, 1.5, 2.5
SP-$HSiO_2$	400.8 ± 2.5	0.405	0.8, 1.3, 1.7, 2.3, 3.8
SP-$HSiO_2$⊃TMP	56.1 ± 0.9	0.053	0.8

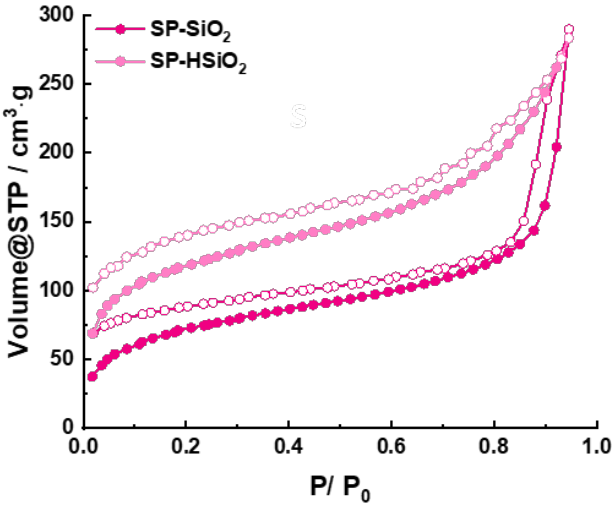

Figure 4.S22. Nitrogen adsorption-desorption isotherms at 77 K of **SP-SiO_2** and **SP-$HSiO_2$⊃TMP** with equilibration time of 30 min.

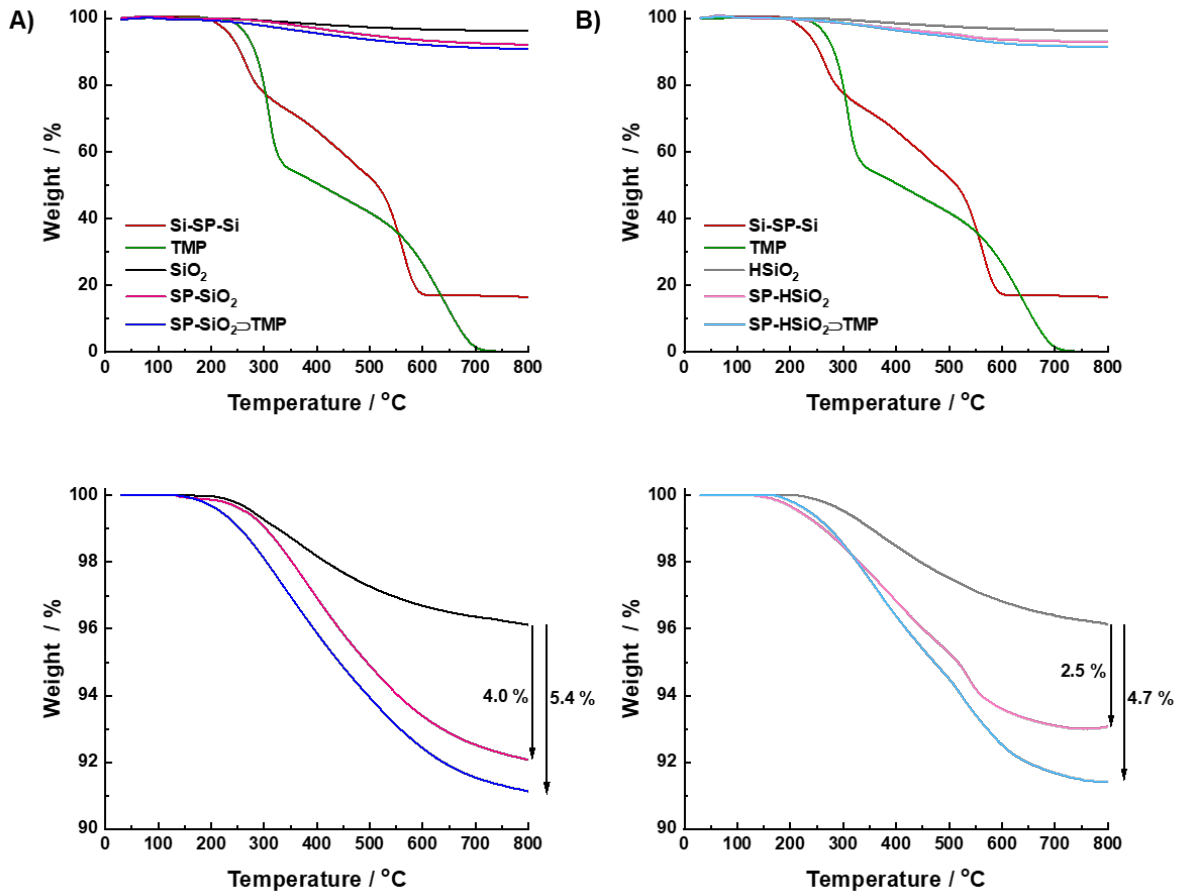

Figure 4.S23. Thermogravimetric analysis (TGA) of (A) **SP-SiO_2⊃TMP** and (B) **SP-$HSiO_2$⊃TMP**. Samples were dried at 120 ºC for 1 h before the experiments. Samples were heated at 5 ºC/min from 30 ºC until 800 ºC under air.

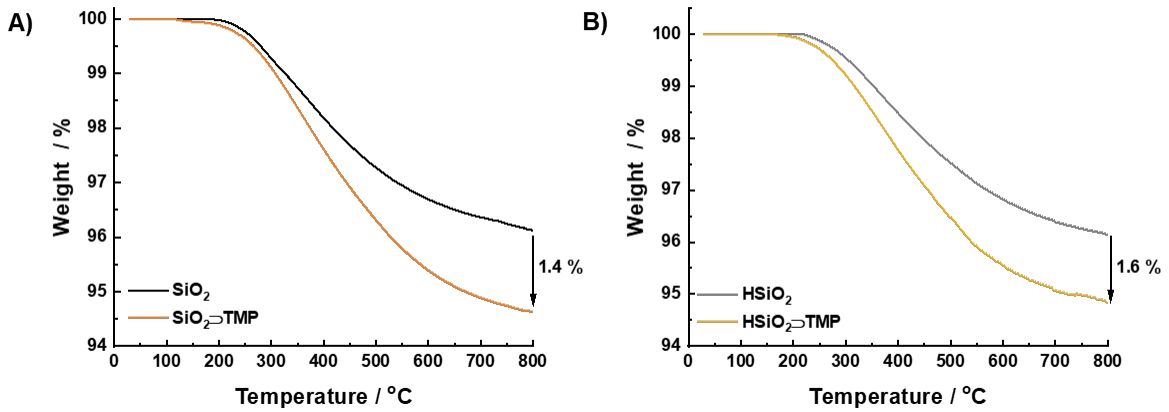

Figure 4.S24. Thermogravimetric analysis (TGA) of (A) **SiO_2⊃TMP** and (B) **$HSiO_2$⊃TMP**. Samples were dried at 120 ºC for 1 h before the experiments. Samples were heated at 5 ºC/min from 30 ºC until 800 ºC under air.

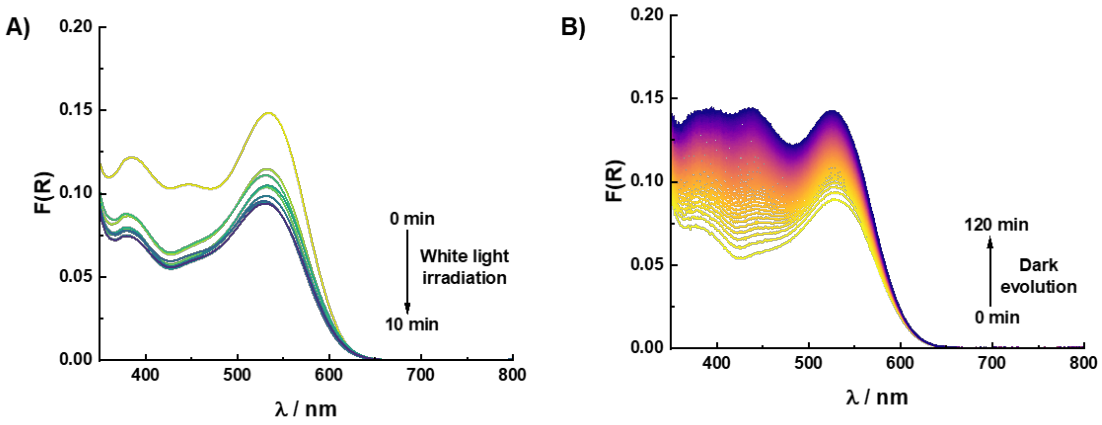

Figure 4.S25. Enlarged UV/Vis spectra of **SP-HSiO$_2$⊃TMP**, Figure 4.17, (A) upon white light irradiation and (B) in the dark.

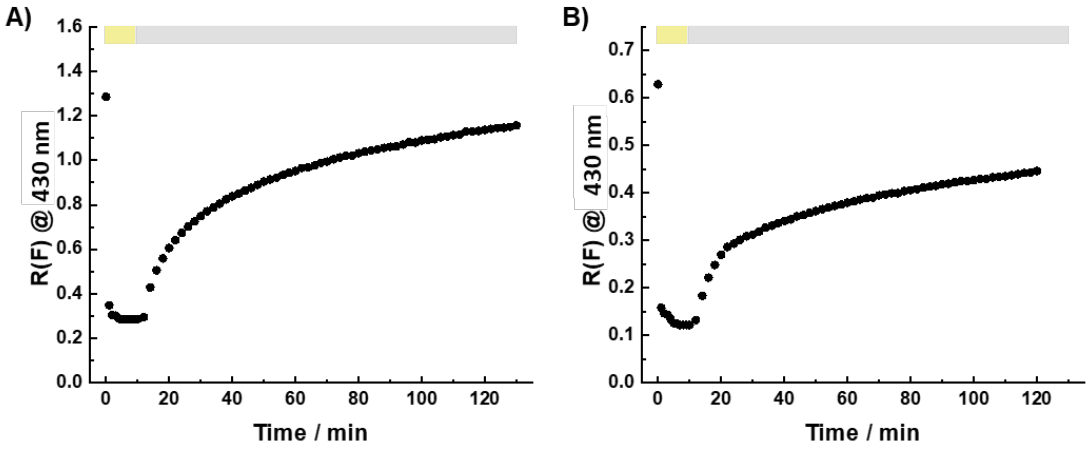

Figure 4.S26. Monitorization of solid-state UV/Vis dark conversion of the **H$^+$MC** band at 430 nm of (A) **SP-SiO$_2$** and (B) **SP-HSiO$_2$** after 10 min of continuous white light irradiation.

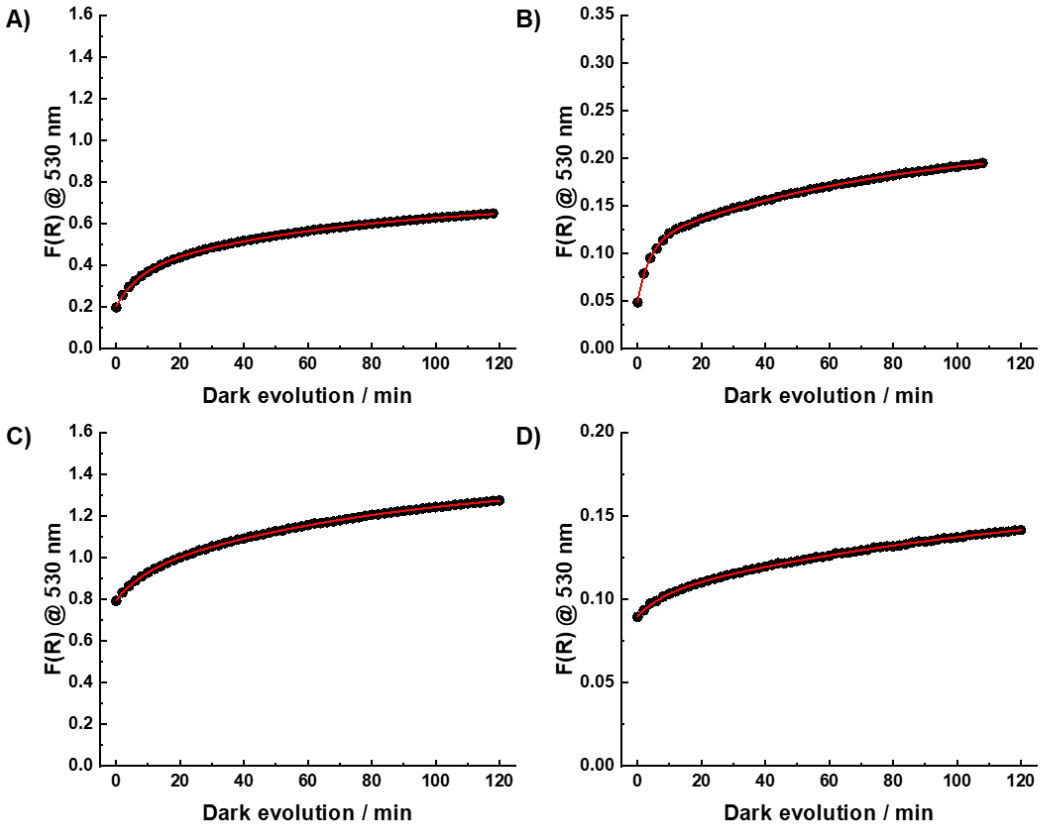

Figure 4.S27. Exponential fitting of solid-state dark evolution of the **MC** band (530 nm) after 10 min of continuous white light irradiation of (A) **SP-SiO$_2$**, (B) **SP-HSiO$_2$,** (C) **SP-SiO$_2$⊃TMP** and (D) **SP-HSiO$_2$⊃TMP.**

$$y = A_1 e^{-x/t_1} + A_2 e^{-x/t_2} + y_0 \qquad \text{Eq. 4.S1}$$

Table 4.S3. Exponential fitting parameters (Figure 4.S27) of dark evolution of the **MC** band (530 nm) after 10 min of continuous white light irradiation.

	y_0 / F(R)	A_1 / F(R)	t_1^{-1} / min^{-1}	A_2 / F(R)	t_2^{-1} / min^{-1}	R^2
SP-SiO$_2$	0.70 ± 0.01	-0.16 ± 0.01	3.87 ± 0.10	-0.34 ± 0.02	78.52 ± 2.44	0.99964
SP-SiO$_2$⊃TMP	1.38 ± 0.01	-0.11 ± 0.01	7.02 ± 0.27	-0.47 ± 0.02	67.88 ± 2.34	0.99967
SP-HSiO$_2$	0.22 ± 0.01	-0.06 ± 0.01	8.27 ± 0.62	-0.11 ± 0.01	127.31 ± 8.66	0.99949
SP-HSiO$_2$⊃TMP	0.16 ± 0.02	-0.010 ± 0.002	8.31 ± 0.43	-0.06 ± 0.01	83.60 ± 2.76	0.99981

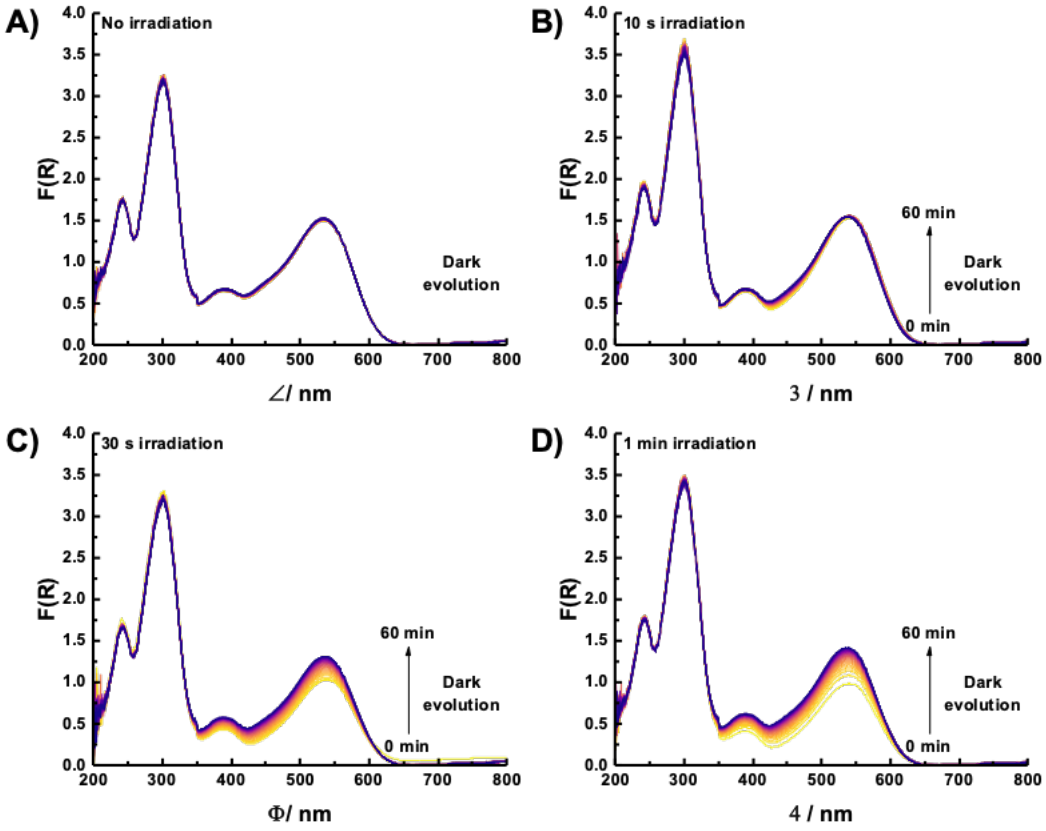

Figure 4.S28. Solid-state UV/Vis dark evolution of **SP-SiO$_2$⊃TMP** after (A) 0 min, (B) 10 s, (C) 30 s and (D) 1 min of white light irradiation.

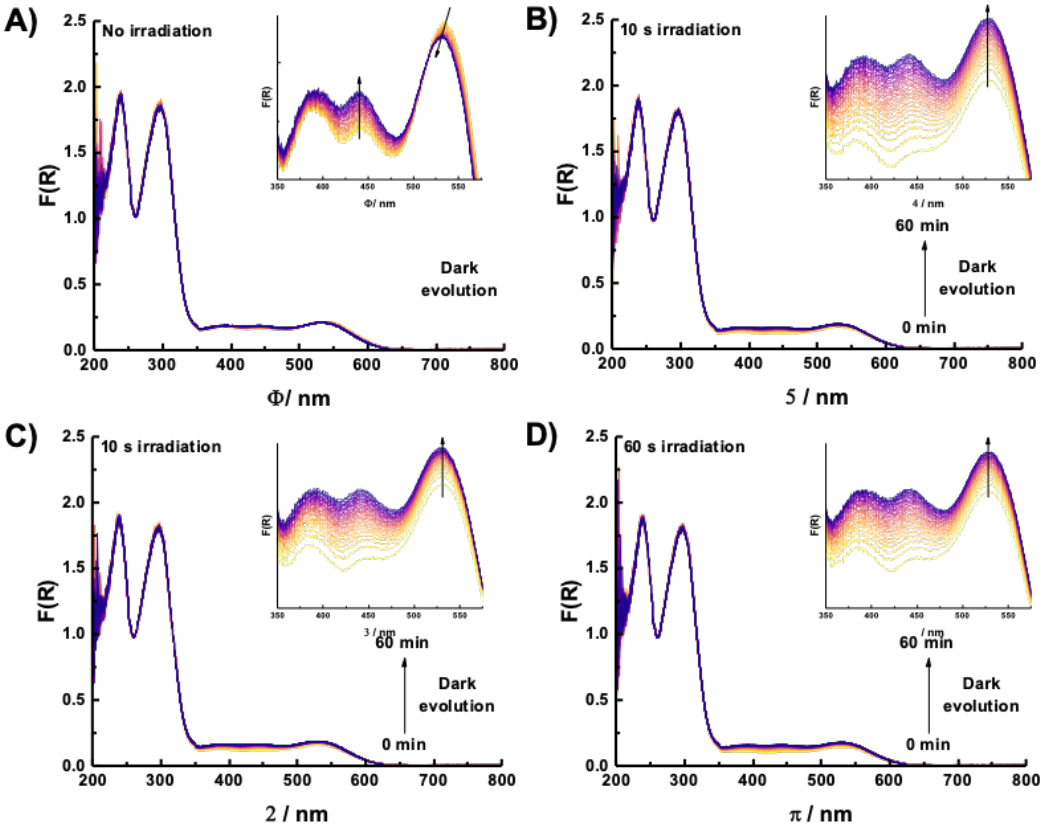

Figure 4.S29. Solid-state UV/Vis dark evolution of **SP-HSiO$_2$⊃TMP** after (A) 0 min, (B) 10 s, (C) 30 s and (D) 1 min of white light irradiation. Insert displays an enlarged view of the 350 nm – 600 nm region where the **MC** and **H$^+$MC** bands are.

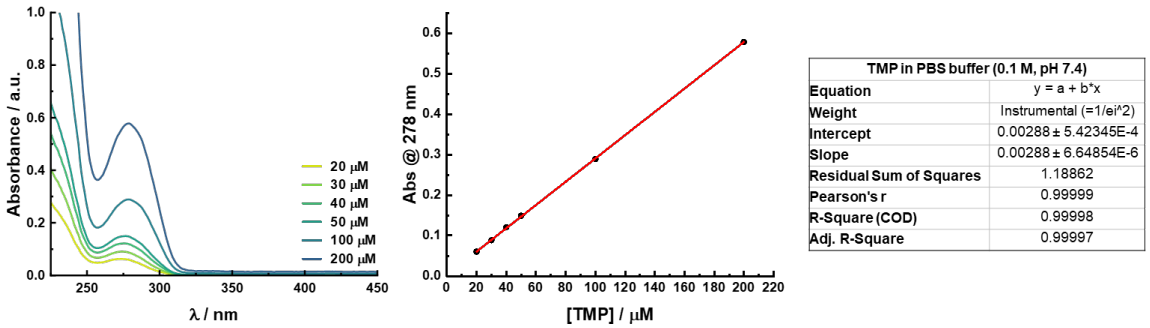

TMP in PBS buffer (0.1 M, pH 7.4)	
Equation	y = a + b*x
Weight	Instrumental (=1/ei^2)
Intercept	0.00288 ± 5.42345E-4
Slope	0.00288 ± 6.64854E-6
Residual Sum of Squares	1.18862
Pearson's r	0.99999
R-Square (COD)	0.99998
Adj. R-Square	0.99997

Figure 4.S30. UV/Vis calibration of **TMP** in PBS buffer (0.1 M, pH 7.4).

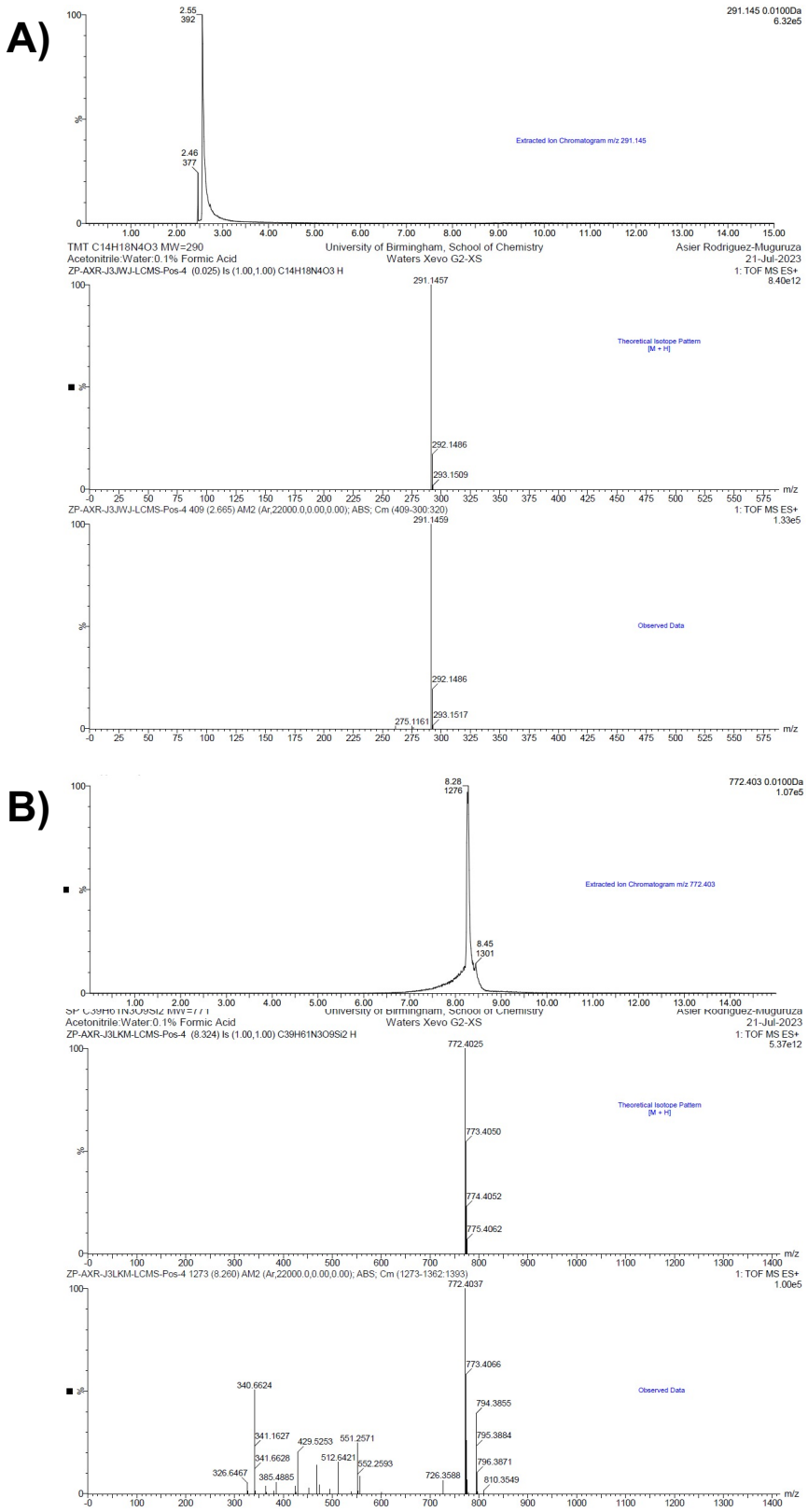

Figure 4.S31. Liquid Chromatography-Mass Spectrometry (LC-MS) of (A) **TMP** and (B) **Si-SP-Si**. Mobile phase was composed by v/v 50:50 acetonitrile:H_2O (0.1 % Formic acid), flow rate 1 mL/min. **TMP** was eluted at 2.55 min (observed $[M+H]^+$ 291.1459 m/z, calc. 291.1457 m/z) and **Si-SP-Si** was eluted at 8.28 min (observed $[M+H]^+$ 772.4025 m/z, calc. 772.4066 m/z).

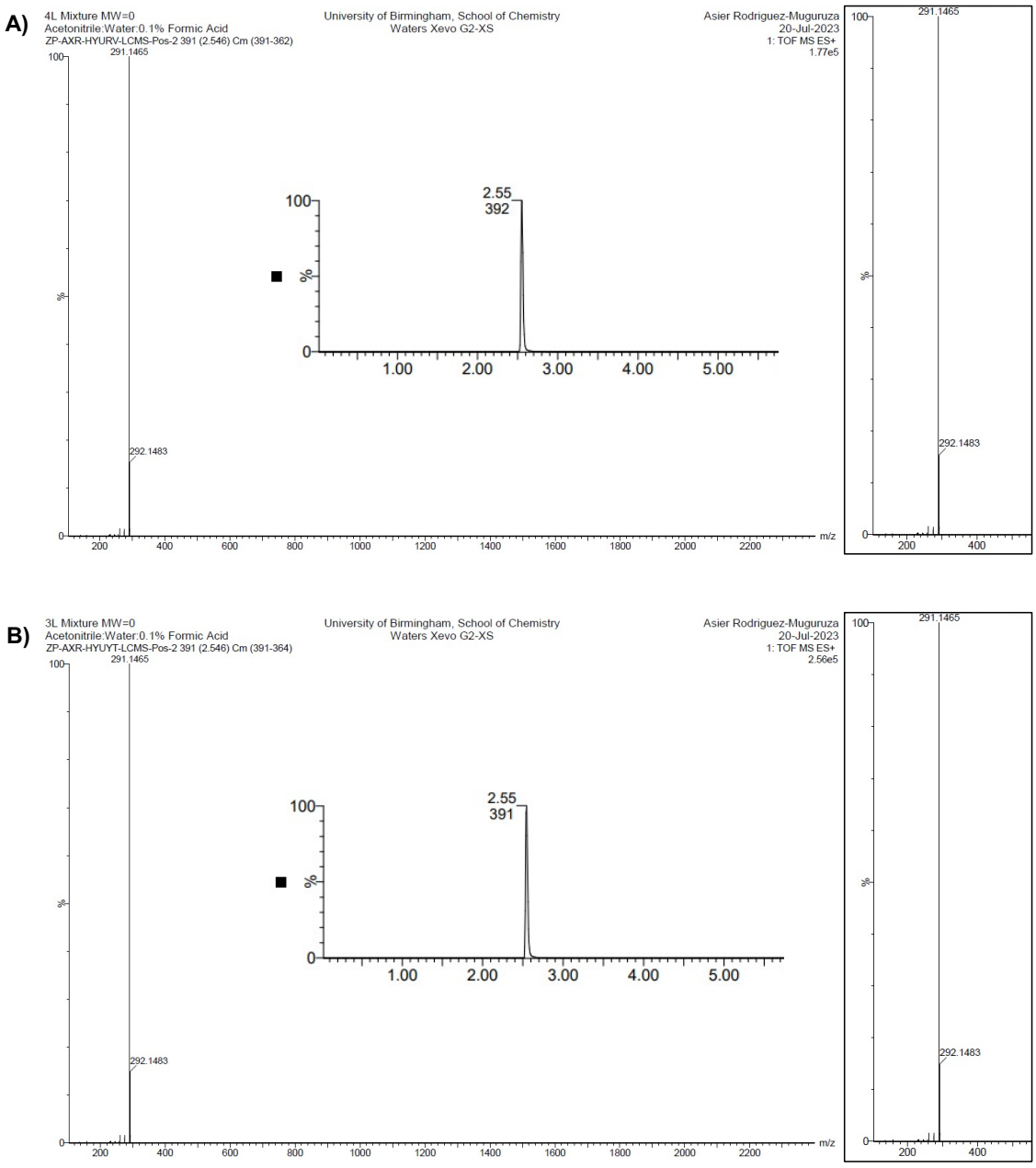

Figure 4.S32. Liquid Chromatography-Mass Spectrometry (LCMS) of release from (A) **SP-SiO$_2$⊃TMP** and (B) **SP-HSiO$_2$⊃TMP** after 10 min with continuous irradiation. Mobile phase was composed by v/v 50:50 acetonitrile: H_2O (0.1 % Formic acid), flow rate 1 mL/min. Only one peak was observed in the chromatographs with elution time of 2.55 min and observed both of 291.1465 m/z in both cases; corresponding to **TMP**.

Table 4.S4. Minimal Inhibitory concentration (MIC, mg/mL) values of unloaded nanoparticles in LB media in the dark. Depicted values are based on 3 biological replicas.

	MG1665	UTI-12	UTI-36	UTI-42
SiO_2	>10	>10	>10	>10
$HSiO_2$	>10	>10	>10	>10
SP-SiO_2	>10	>10	>10	>10
SP-$HSiO_2$	>10	>10	>10	>10

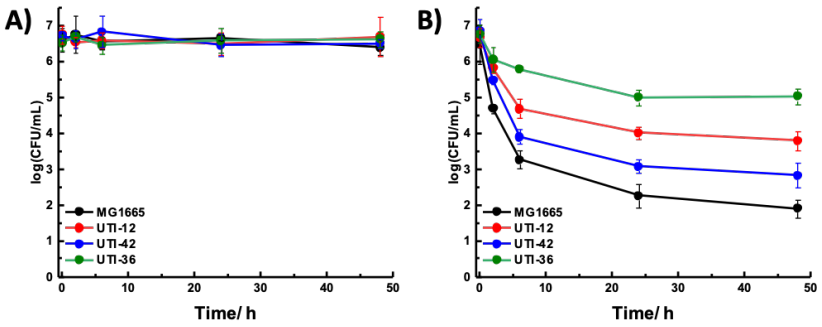

Figure 4.S33. Cell viability of reference and UTI clinical isolates E. coli strains in PBS (0.1 M, pH 7.4) (A) without and (B) with **TMP** at MIC concentrations. Cells were incubated at 37 ºC and 150 rpm and aliquots were taken at different time points.

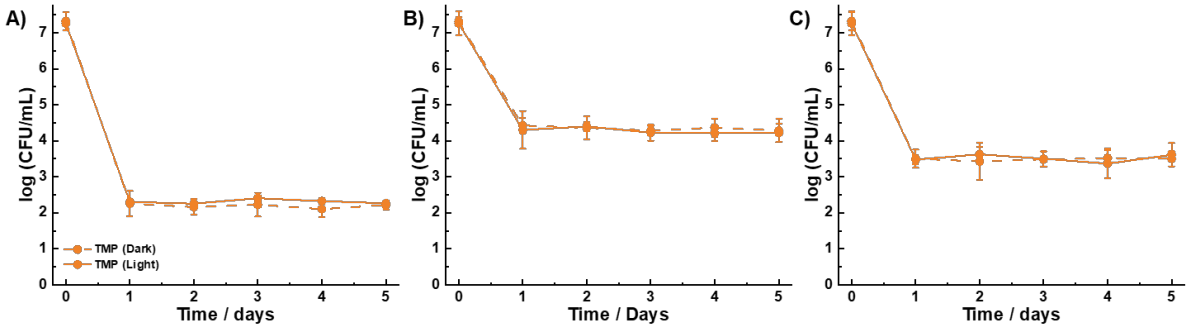

Figure 4.S34. Cell viability of (A) MG1655, (B) UTI-12 and (C) UTI-42 *E. coli* strains incubated with **TMP** (MIC concentration) upon daily irradiation or in the dark. Overnight diluted inoculate in PBS buffer (0.1 M, pH 7.4, ~10^7 CFU/mL) were incubated with **SP**-containing nanoparticles.

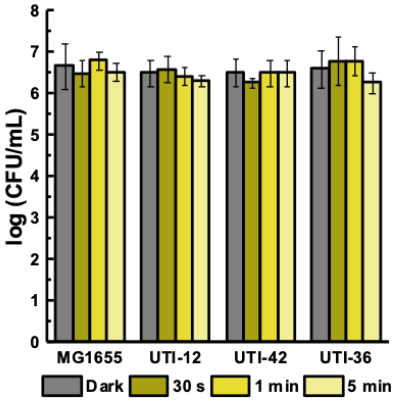

Figure 4.S35. Cell viability of reference (MG1655) and UTI clinical isolate *E. coli* strains after different irradiation times in PBS buffer (0.1 M, pH 7.4). Overnight inoculate dilutions in PBS buffer (0.1 M, pH 7.4, ~10^7 CFU/mL) were subjected to different irradiation time of white light and then incubated at 37 ^{o}C and 150 rpm for 24 h before viability evaluation.

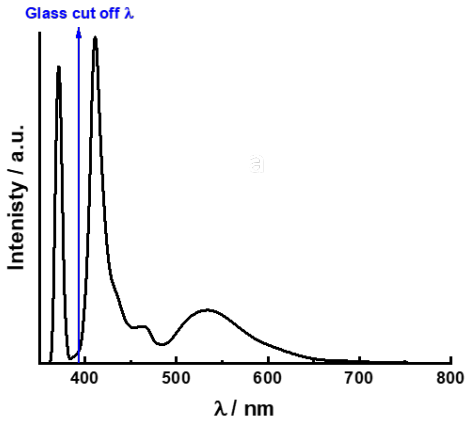

Figure 4.S36. Emission spectrum of the 2000 Lumen Moweeto© flashlight indicating the glass cut of wavelength (λ) at 393 nm.

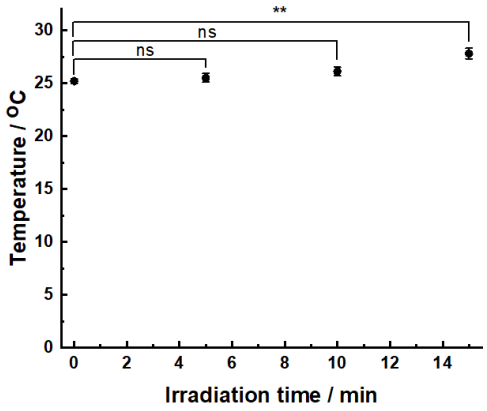

Figure 4.S37. Effect of white light irradiation (22 W, λ > 393 nm) time in nanoparticle suspension with [SiO_2] = 2.5 mg/mL. Statistical significance was determined by t-test analysis. ns = p > 0.5, * = p < 0.5, ** = p > 0.01 and *** = p< 0.0001.

4.6. References

1 H. Pelling, J. Nzakizwanayo, S. Milo, E. L. Denham, W. M. MacFarlane, L. J. Bock, J. M. Sutton and B. V. Jones, *Lett. Appl. Microbiol.*, 2019, **68**, 277–293.

2 J. M. Hollingsworth, M. M. A. Rogers, S. L. Krein, A. Hickner, L. Kuhn, A. Cheng, R. Chnag and S. Saint, *Ann. Intern. Med.*, 2013, **159**, 401–410.

3 L. E. Nicolle, *Antimicrob. Resist. Infect. Control*, 2014, **3**, 23–30.

4 Royal College of Physicians, *National Audit of Continence Care Combined Organisational and Clinical Report*, 2010.

5 T. M. Hooton, S. F. Bradley, D. D. Cardenas, R. Colgan, S. E. Geerlings, J. C. Rise, S. Saint, A. J. Schaeffer, P. A. Tambayh, P. Tenke and L. E. Nicolle, *Clin. Infect. Dis.*, 2010, **10**, 321–324.

6 D. G. Maki and P. A. Tambyah, *Emerg. Infect. Dis.*, 2001, **7**, 342–347.

7 C. M. C. Faustino, S. M. C. Lemos, N. Monge and I. A. C. Ribeiro, *Adv. Colloid Interface Sci.*, 2020, **284**, 102230.

8 J. Meddings, M. A. M. Rogers, S. L. Krein, M. G. Fakih, R. N. Olmsted and S. Saint, *BMJ Qual. Saf.*, 2014, **23**, 277–289.

9 W. C Reygaert, *AIMS Microbiol.*, 2018, **4**, 482–501.

10 S. B. Meropol, K. A. Chan, Z. Chen, J. A. Finkelstein, S. Hennesy, S. D. Schech, D. Shatin and J. P. Metlay, *Pharmacoepidemiol. Drug Saf.*, 2008, **17**, 523–532.

11 L. Atkins, A. Sallis, T. Chadborn, K. Shaw, A. Schneider, S. Hopkins, A. Bunten, S. Michie and F. Lorencatto, *Implement. Sci.*, 2020, **15**, 44–65.

12 K. G. Neoh, M. Li, E. T. Kang, E. Chiong and P. A. Tambyah, *J. Mater. Chem. B*, 2017, **5**, 2045–2067.

13 R. Teixeira-Santos, L. C. Gomes and F. J. M. Mergulhão, *Curr. Opin. Biomed. Eng.*, 2022, **22**, 100394.

14 K. Patel, P. Kushwaha, S. Kumar and R. Kumar, *ACS Appl. Bio Mater.*, 2019, **2**, 5799–5809.

15 S. Zhang, X. Liang, G. M. Gadd and Q. Zhao, *ACS Appl. Bio Mater.*, 2020, **3**, 282–291.

16 Y. He, X. Wan, K. Xiao, W. Lin, J. Li, Z. Li, F. Luo, H. Tan, J. Li and Q. Fu, *Biomater. Sci.*, 2019, **7**, 5369–5382.

17 T. Richey, H. Iwata, H. Oowaki, E. Uchida, S. Matsuda and Y. Ikada, *Biomaterials*, 2000, **21**, 1057–1065.

18 A. Stepulane, A. K. Rajasekharan and M. Andersson, *ACS Appl. Bio Mater.*, 2022, **5**, 5289–5301.

19 J. M. Pagès, C. E. James and M. Winterhalter, *Nat. Rev. Microbiol.*, 2008, **6**, 893–903.

20 D. Roe, B. Karandikar, N. Bonn-Savage, B. Gibbins and J. baptiste Roullet, *J. Antimicrob. Chemother.*, 2008, **61**, 869–876.

21 Y. Shalom, I. Perelshtein, N. Perkas, A. Gedanken and E. Banin, *Nano Res.*, 2017, **10**, 520–533.

22 J. Lellouche, A. Friedman, R. Lahmi, A. Gedanken and E. Banin, *Int. J. Nanomedicine*, 2012, **7**, 1175–1188.

23 S. Srisang, N. Wongsuwan, A. Boongird, M. Ungsurungsie, P. Wanasawas and N. Nasongkla, *Int. J. Polym. Mater. Polym. Biomater.*, 2019, 1–9.

24 T. R. Dugas, G. Brewer, M. Longwell, T. Fradella, J. Braun, C. E. Astete, M. H. Jennings and C. M. Sabliov, *J. Biomed. Mater. Res. - Part B Appl. Biomater.*, 2019, **107**, 646–651.

25 F. Wu, T. Xu, G. Zhao, S. Meng, M. Wan, B. Chi, C. Mao and J. Shen, *Langmuir*, 2017, **33**, 5245–5252.

26 P. Yang, S. Gai and J. Lin, *Chem. Soc. Rev.*, 2012, **41**, 3679–3698.

27 S. Angelos, E. Choi, F. Vögtle, L. De Cola and J. I. Zink, *J. Phys. Chem. C*, 2007, **111**, 6589–6592.

28 T. M. Guardado-Alvarez, L. S. Devi, J. M. Vabre, T. A. Pecorelli, B. J. Schwartz, J. O. Durand, O. Mongin, M. Blanchard-Desce and J. I. Zink, *Nanoscale*, 2014, **6**, 4652–4658.

29 Y. Fatieiev, J. G. Croissant, S. Alsaiari, B. A. Moosa, D. H. Anjum and N. M. Khashab, *ACS Appl. Mater. Interfaces*, 2015, **7**, 24993–24997.

30 J. Croissant, A. Chaix, O. Mongin, M. Wang, S. Clément, L. Raehm, J. O. Durand, V. Hugues, M. Blanchard-Desce, M. Maynadier, A. Gallud, M. Gary-Bobo, M. Garcia, J. Lu, F. Tamanoi, D. P. Ferris, D. Tarn and J. I. Zink, *Small*, 2014, **10**, 1752–1755.

31 D. P. Ferris, Y. L. Zhao, N. M. Khashab, H. A. Khatib, J. F. Stoddart and J. I. Zink, *J. Am. Chem. Soc.*, 2009, **131**, 1686–1688.

32 D. Tarn, D. P. Ferris, J. C. Barnes, M. W. Ambrogio, J. F. Stoddart and J. I. Zink, *Nanoscale*, 2014, **6**, 3335–3343.

33 T. M. Guardado-Alvarez, L. Sudha Devi, M. M. Russell, B. J. Schwartz and J. I. Zink, *J. Am. Chem. Soc.*, 2013, **135**, 14000–14003.

34 R. Zhang, L. Li, J. Feng, L. Tong, Q. Wang and B. Tang, *ACS Appl. Mater. Interfaces*, 2014, **6**, 9932–9936.

35 N. Ž. Knežević, B. G. Trewyn and V. S. Y. Lin, *Chem. - A Eur. J.*, 2011, **17**, 3338–3342.

36 M. Wu, X. Lin, X. Tan, J. Li, Z. Wei, D. Zhang, Y. Zheng, A. X. Zheng, B. Zhao, Y. Zeng, X. Liu and J. Liu, *ACS Appl. Mater. Interfaces*, 2018, **10**, 19416–19427.

37 Y. Yang, B. Velmurugan, X. Liu and B. Xing, *Small*, 2013, **9**, 2937–2944.

38 W. Zhao, H. Wang, H. Wang, Y. Han, Z. Zheng, X. Liu, B. Feng and H. Zhang, *Nanoscale*, 2021, **13**, 6394–6399.

39 M. F. Chung, W. T. Chia, W. L. Wan, Y. J. Lin and H. W. Sung, *J. Am. Chem. Soc.*, 2015, **137**, 12462–12465.

40 J. Croissant, M. Maynadier, A. Gallud, H. Peindy N'Dongo, J. L. Nyalosaso, G. Derrien, C. Charnay, J. O. Durand, L. Raehm, F. Serein-Spirau, N. Cheminet, T. Jarrosson, O. Mongin, M. Blanchard-Desce, M. Gary-Bobo, M. Garcia, J. Lu, F. Tamanoi, D. Tarn, T. M. Guardado-Alvarez and J. I. Zink, *Angew. Chemie - Int. Ed.*, 2013, **52**, 13813–13817.

41 A. Noureddine, M. Gary-Bobo, L. Lichon, M. Garcia, J. I. Zink, M. Wong Chi Man and X. Cattoën, *Chem. - A Eur. J.*, 2016, **22**, 9624–9630.

42 K. Wang, Q. Wu, X. Wang, G. Liang, A. Yang and J. Li, *Nanoscale*, 2020, **12**, 10106–10116.

43 P. Picchetti, B. N. Dimarco, L. Travaglini, Y. Zhang, M. C. Ortega-Liebana and L. De Cola, *Chem. Mater.*, 2020, **32**, 392–399.

44 L. Kortekaas and W. R. Browne, *Chem. Soc. Rev.*, 2019, **48**, 3406–3424.

45 A. B. Grommet, L. M. Lee and R. Klajn, *Acc. Chem. Res.*, 2020, **53**, 2600–2610.

46 Y. Shiraishi, S. Takagi, K. Yomo and T. Hirai, *ACS Omega*, 2021, **6**, 35619–35628.

47 M. Mandal, D. Banik, A. Karak, S. K. Manna and A. K. Mahapatra, *ACS Omega*, 2022, **7**, 36988–37007.

48 R. Klajn, *Chem. Soc. Rev.*, 2014, **43**, 148–184.

49 T. Yamaguchi, A. Maity, V. Polshettiwar and M. Ogawa, *Inorg. Chem.*, 2018, **57**, 3671–3674.

50 K. Kinashi, S. Nakamura, M. Imamura, K. Ishida and Y. Ueda, *J. Phys. Org. Chem.*, 2012, **25**, 462–466.

51 T. Yamaguchi, K. J. Imwiset and M. Ogawa, *Langmuir*, 2021, **37**, 3702–3708.

52 A. Iqbal, G. Iqbal, M. N. Umar, H. Rashid and S. W. Khan, *R. Soc. Open Sci.*, , DOI:10.1098/rsos.211385.

53 M. J. Feeney and S. W. Thomas, *Macromolecules*, 2018, **51**, 8027–8037.

54 D. Euchler, C. R. Ehgartner, N. Hüsing and A. Feinle, *ACS Appl. Mater. Interfaces*, 2020, **12**, 47754–47762.

55 J. Allouche, A. Le Beulze, J. C. Dupin, J. B. Ledeuil, S. Blanc and D. Gonbeau, *J. Mater. Chem.*, 2010, **20**, 9370–9378.

56 L. R. Lee, V. K. Karapala, Y. L. Lin, H. C. He and J. T. Chen, *J. Phys. Chem. C*, 2020, **124**, 11870–11876.

57 S. Gorelik, S. Hongyan, M. J. Lear and J. Hobley, *Photochem. Photobiol. Sci.*, 2010, **9**, 141–151.

58 J. Opel, L. C. Rosenbaum, J. Brunner, A. Staiger, R. Zimmermanns, M. Kellermeier, T. Gaich, H. Cölfen and J. M. García-Ruiz, *J. Mater. Chem. B*, 2020, **8**, 4831–4835.

59 L. Chen, W. Wang, B. Su, Y. Wen, C. Li, Y. Zhou, M. Li, X. Shi, H. Du, Y. Song and L. Jiang, *ACS Nano*, 2014, **8**, 744–751.

60 Y. He, L. Shao, I. Usman, Y. Hu, A. Pan, S. Liang and H. Xu, *Biomater. Sci.*, 2020, **8**, 3418–3429.

61 F. May, M. Peter, A. Hütten, L. Prodi and J. Mattay, *Chem. - A Eur. J.*, 2012, **18**, 814–821.

62 A. Yamano and H. Kozuka, *Thin Solid Films*, 2011, **519**, 1772–1779.

63 D. J. Lewis, V. Dore, N. J. Rogers, T. K. Mole, G. B. Nash, P. Angeli and Z. Pikramenou, *Langmuir*, 2013, **29**, 14701–14708.

64 T. Yamaguchi, A. Maity, V. Polshettiwar and M. Ogawa, *J. Phys. Chem. A*, 2017, **121**, 8080–8085.

65 K. Kinashi, S. Nakamura, Y. Ono, K. Ishida and Y. Ueda, *J. Photochem. Photobiol. A Chem.*, 2010, **213**, 136–140.

66 S. Dirè, V. Tagliazucca, E. Callone and A. Quaranta, *Mater. Chem. Phys.*, 2011, **126**, 909–917.

67 A. R. Muguruza, A. di Maio, N. J. Hodges, J. M. A. Blair and Z. Pikramenou, *Nanoscale Adv.*, 2023, **5**, 2453–2461.

68 A. R. Muguruza, M. L. Odyniec, M. Manhota, Z. Habib, K. Rurack, J. M. A. Blair, S. A. Kuehne, A. D. Walmsley and Z. Pikramenou, *Microporous Mesoporous Mater.*, 2024, **363**, 112841.

69 M. S. Manna, Y. T. Tamer, I. Gaszek, N. Poulides, A. Ahmed, X. Wang, F. C. R. Toprak, D. N. R. Woodard, A. Y. Koh, N. S. Williams, D. Borek, A. R. Atilgan, J. D. Hulleman, C. Atilgan, U. Tambar and E. Toprak, *Nat. Commun.*, 2021, **12**, 2949.

70 R. F. Landis, M. Yazdani, B. Creran, X. Yu, V. Nandwana, G. Cooke and V. M. Rotello, *Chem. Commun.*, 2014, **50**, 4579–4581.

71 B. J. Jordan, M. A. Pollier, Y. Ofir, S. Joubanian, J. G. Mehtala, C. Sinkel, S. T. Caldwell, A. Kennedy, G. Rabani, G. Cooke and V. M. Rotello, *Chem. Commun.*, 2008, 1653–1655.

72 J. Chen, P. Zhang, G. Fang, P. Yi, X. Yu, X. Li, F. Zeng and S. Wu, *J. Phys. Chem. B*, 2011, **115**, 3354–3362.

73 K. Okamoto, Y. Goto and S. Inagaki, *J. Mater. Chem.*, 2005, **15**, 4136–4140.

74 M. Thommes, K. Kaneko, A. V. Neimark, J. P. Olivier, F. Rodriguez-Reinoso, J. Rouquerol and K. S. W. Sing, *Pure Appl. Chem.*, 2015, **87**, 1051–1069.

75 M. Guo, M. Kanezashi, H. Nagasawa, L. Yu, K. Yamamoto, T. Gunji, J. Ohshita and T. Tsuru, *J. Memb. Sci.*, 2019, **584**, 56–65.

76 M. Guo, J. Qian, R. Xu, X. Ren, J. Zhong and M. Kanezashi, *J. Memb. Sci.*, 2022, **643**, 120018.

77 H. Zhang, D. He, S. Niu and H. Qi, *Int. J. Hydrogen Energy*, 2021, **46**, 17221–17230.

78 L. S. Blankenship, J. Jagiello and R. Mokaya, *Mater. Adv.*, 2022, 3961–3971.

79 A. M. Silvestre-Albero, J. Manuel and J. Silvestre-albero, *J. Phys. Chem. C*, 2012, **116**, 16652–16655.

80 K. Sing, *Colloids Surfaces A Physicochem. Eng. Asp.*, 2001, **187**, 3–9.

81 A. Vellinga, S. Tansey, B. Hanahoe, K. Bennett, A. W. Murphy and M. Cormican, *J. Antimicrob. Chemother.*, 2012, **67**, 2523–2530.

82 A. Brolund, M. Sundqvist, G. Kahlmeter and M. Grape, *PLoS One*, 2010, **5**, e9233.

5. NEW APPROACHES FOR CIPROFLOXACIN DELIVERY FROM SILICA NANOPARTICLES

5.1. Introduction

5.1.1. Delivery of hydrophobic molecules from silica nanoparticles

The delivery of many therapeutic small molecules from certain nanoparticles is limited by their poor water solubility.[1] Due to the thermal and chemical stability and versatility of silica nanoparticles, they represent an ideal scaffold for the design of nanocarriers for hydrophylic molecules delivery.[2] Unfortunately, silica nanoparticles have an overall surface negatively charge due to the hydroxyl groups on the framework and surface, making them hydrophilic. Even if this feature results in a high colloidal stability, the hydrophilic nature of the nanoparticle hinders the inclusion or even the loading of hydrophobic molecules.

In order to overcome this problem, post-synthetic surface functionalization[3–5] or capping strategies[6,7] have been developed to increase particle-molecule interactions or to ease inclusion of the hydrophobic molecule inside the pores of silica nanoparticles (Figure 5.1). Increase of hydrophobic nature of nanoparticles cavities by functionalization of surface hydroxyl groups has been one of the most followed strategies reported in the literature. Polyethylene glycol (PEG)[3] and/or *N*-isopropylacrylamide (NIPAM) derivative polymers[4] have been employed, among others, with this aim. However, uncontrollable functionalization led to decrease in the

colloidal stability of loaded particles and a case-by-case study is required in order to assess the best polymer-cargo pairing to achieve the highest loading.

The inclusion of hydrophobic molecules in silica nanoparticles pores can be achieved by incubating unloaded particles in organic solutions with high concentration of desired cargo. Due to difference in concentration between outside and inside pores, a small fraction of hydrophobic molecules will be adsorbed within the cavities. This approach results in a very low loading efficiency and a rapid release of adsorbed cargos. Because of this, capping strategies, can be modulated to prevent the hydrophobic molecule from rapidly leakaging out from the hydrophobic framework. Capping strategies have been profoundly reported and usually require a multi-step synthesis process, being a very time consuming process.[8]

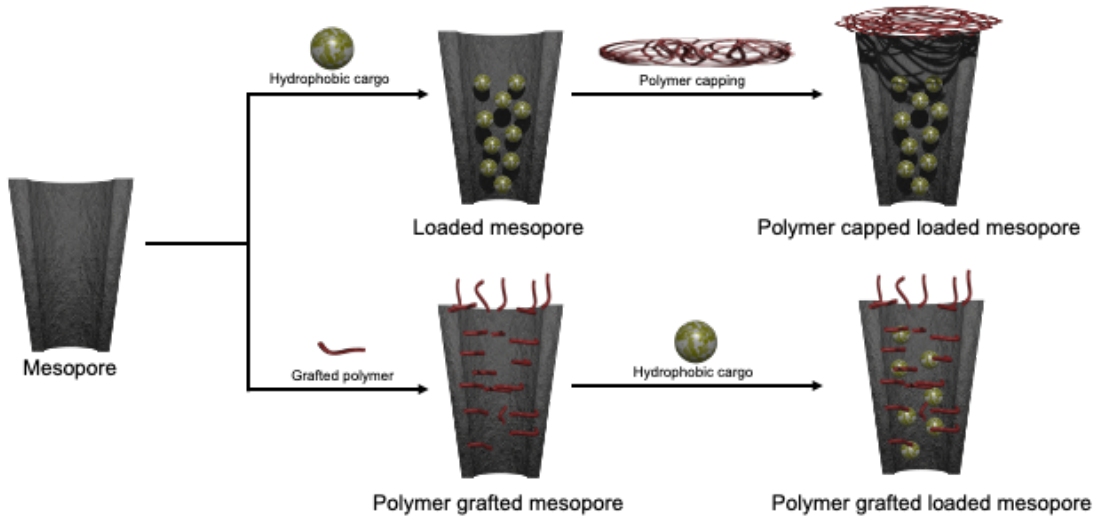

Figure 5.1. Scheme of reported strategies to enhance the delivery of hydrophobic molecules from porous silica nanoparticles.

Beside silica nanoparticles, delivery of hydrophobic molecules has been enhanced by inclusion in amphiphile structures such us micelles or polymer particles.[9–11] Resulting loaded nanocarriers displayed a hydrophobic core where the molecule of interests in entrapped and a hydrophilic surface, which provides colloidal stability to the carrier.

Nevertheless, micelle-based drug delivery systems lack thermal stability and their proper storage in solution is crucial for their final application, reducing their usage.[12] Polymer nanocarriers, on the other hand, cannot be extrapolated to all hydrophobic molecules as the interactions between the hydrophobic core and the hydrophobic molecule has to be tailored case by case.[11]

The use of therapeutic micelles, such us, amphibolic antibiotic, have, however, not be widely explored for the solubilization of therapeutic hydrophobic molecules. The only reported cases described the encapsulation of non-therapeutic molecules such us dyes in these kind of antibacterial micelles.[13–15]

5.1.2. Antibiotic templated silica nanoparticles

As previously explained in the introduction section, porous silica nanoparticles are synthetized using a liquid-phase template. In a standard porous silica nanoparticle synthesis, a liquid-phase template is formed initially by addition of a surfactant or amphibolic polymer to the synthesis media. Then, the silica precursor is added and the silica framework formation takes place around the already formed template. Finally, and in order to make the formed porosity accessible for inclusion of molecules, the template must be fully removed (Figure 5.2).[16,17] In addition, remaining template, beside reducing the porosity of the particle for future applications, also increases cytotoxicity of the final nanoparticle, due to the toxicity of the template. A clear example is CTAB, a widely employed quaternity ammonium surfactant for MSNs (MCM-41) synthesis, highly toxic (IC_{50} = 30 μM)[18] and challenging to be fully removed from the framework.[2,19] Hence, thorough removal of the template is a crucial step in the development of porous silica nanoparticles for biomedical applications.

Considering this disadvantage, porous silica nanoparticles where the template agents are also the therapeutic agents have been developed (Figure 5.2). In these cases, the removal of the template is not required as it if formed by the therapeutic agent that is meant to be released later. Moreover, if the right therapeutic agents are chosen, resulting nanoparticle also displays a porous structure, which allows high drug loading. Unfortunately, this approach is limited to those therapeutic agents able to form a template in the silica particle synthesis conditions. Nevertheless, the presence of open pores to the outside, such us in case of MCM-41, SBA-15 or SBA-16 topologies, can result in uncontrollable release of the therapeutic template.[2]

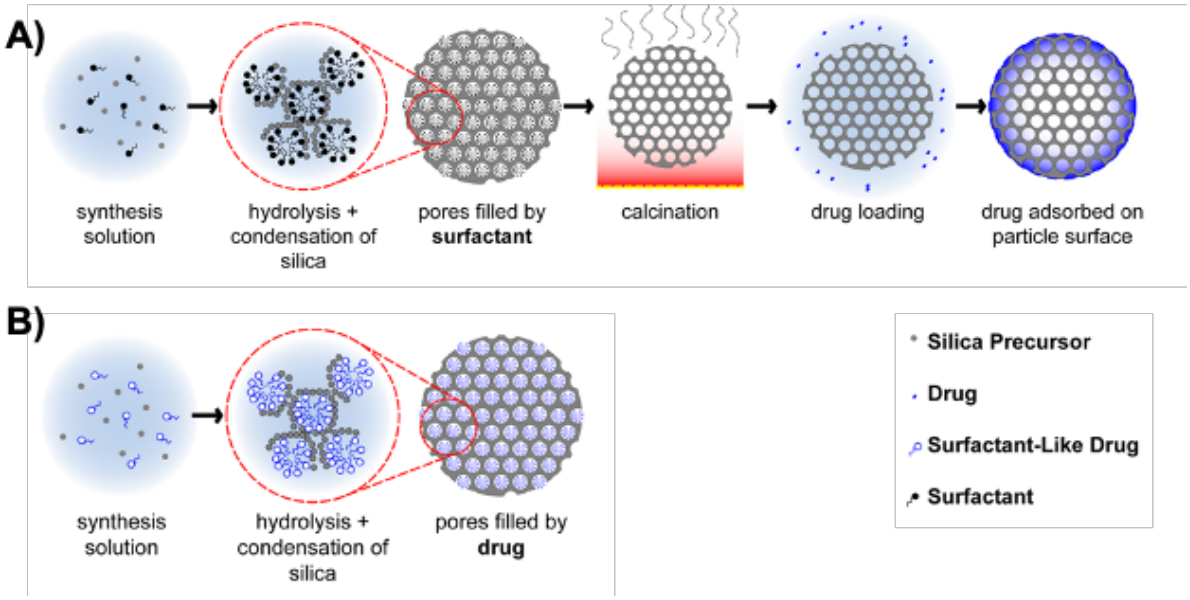

Figure 5.2. Scheme of the synthesis of porous silica nanoparticles using (A) a traditional non-therapeutic templating agent and (B) a therapeutic templating agent. Reproduced from C. A. Stewart *et al*.[20]

In case of silica particles for antibiotic delivery, the reported antibiotic templated porous silica nanoparticles with antibacterial purposes are not very common. Until 2018 examples of antibiotic-templated porous silica nanoparticles were limited to the structural study of resulting porous particles with no further experimentation about their antibacterial properties.[20–22] It was not until 2018 when porous silica nanoparticles

templated with antibacterial compounds such us octanedione hydrochloride[23–25], benzalkonium chloride[26,27], chlorohexidine[28] or miramistin[29,30] were developed, displaying a MCM-41 porous structure, and their antibacterial activity was explored (Figure 5.3). Activity of octadentidine-templates nanoparticles was confirmed against oral *S. mutans*[23,25] and *E. faecalis*[24] biofilms, while benzalkonium-template particles showed antibacterial activity against planktonic *S. aureus*, *S. enterica* and *E. coli*[26,27], and chlorohexidine-templated particles were active against planktonic *S. aureus* and *E. coli*.[28]

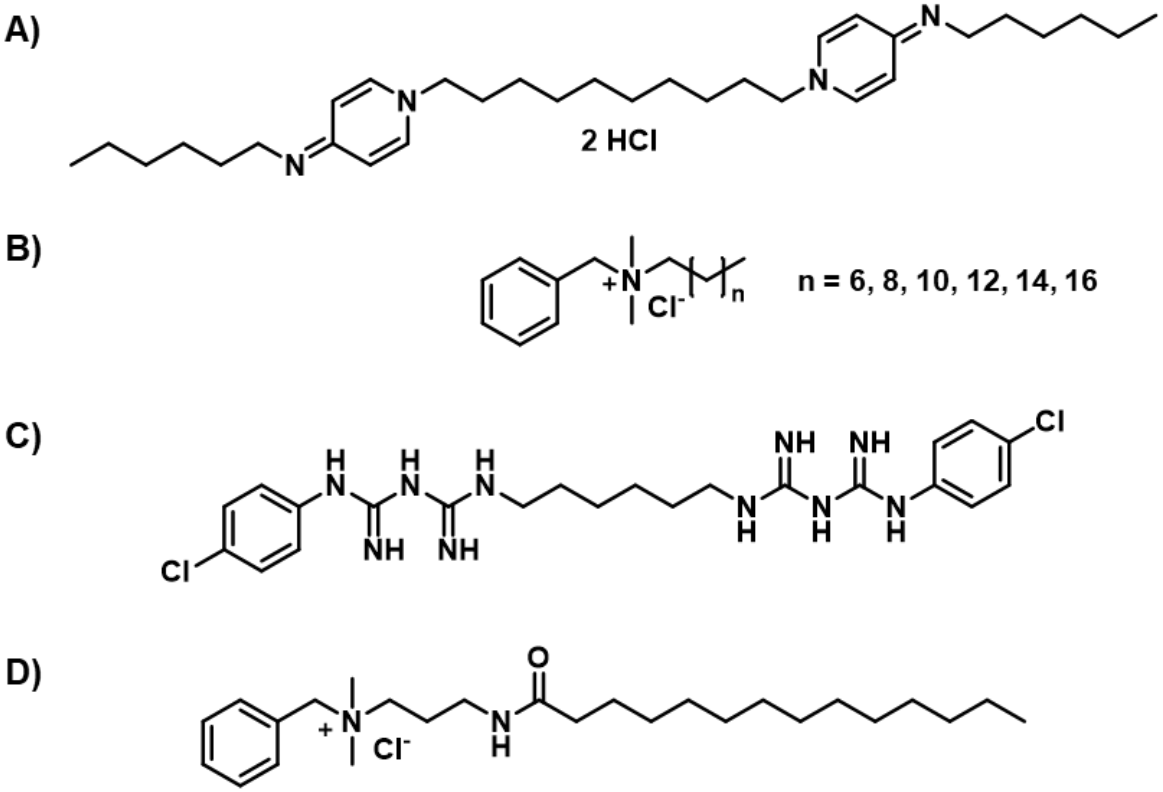

Figure 5.3. Chemical structure of antibacterial templating agents (A) octenidine hydrochloride (B) benzalkonium chloride, (C) chlorhexidine and (D) miramistin.

Similar to previously mentioned surfactants, cetylpyridinium chloride (CPC) (Figure 5.4) is another surfactant-like antibacterial agent able to act as liquid-phase template for the synthesis of porous silica nanoparticles, as firstly reported by D. Khushalani *et*

al.[21], further explored by F. Testa *et al.*[22], and then applied against *E. faecalis* and *S. mutans* biofilms by A. Brezhnev *et al.*[31] Reported porous particles presented a MCM-41 porous structure with unidimensional periodic pores, leading to uncontrollable release of the therapeutic template as previously demonstrated by diffusion assays.

In fact, CPC is an antiseptic compound widely employed in dental hygiene products, such as mouthwashes. It possesses a cationic quaternary ammonium head group and a hexadecyl aliphatic tail which allows micelle formation above the critical micelle concentration (CMC). CPC mechanism of action varies depending on CPC's concentration.[32] At low concentration, bellow the CMC, CPC is able to interfere with the osmoregulation and homeostasis of the bacterial cell.[33] At higher concentrations, above the CMC, disintegration of cell membrane with subsequent leakage of cytoplasmatic content has been described by F. Cieplik *et al*.[34] The ability of cationic surfactants to interact with the negatively charged bacterial membrane has been previously reported, leading to displacement of divalent cations and increase in membrane permeability.[35]

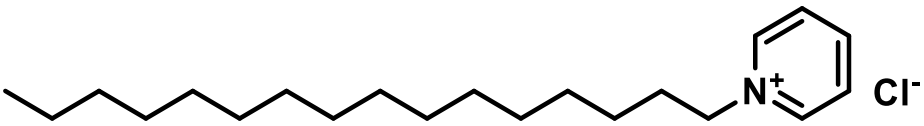

Figure 5.4. Chemical structure of cetylpyridinium chloride (**CPC)**.

Above its CMC (1 mM in H_2O at 25 ^oC and pH 7.4), CPC is able to form spherical shape micelles with a diameter of 2.7 ± 0.1 nm according to differential function theory and quasi-elastic dynamic light scattering simulations.[36–38] Nevertheless, CPC-micelle structures vary depending on the solvent system they are formed.[36,39,40]

Furthermore, CPC-micelles have been extensively employed to investigate the interactions between small molecules and micellar structures through nuclear and optical spectroscopic techniques. These studied have elucidated that the chemical nature of the guest molecule will direct its position in the hydrophilic surface, in the palisade (region localised between the hydrophobic core and the hydrophilic outer region of the micelle) or in the hydrophobic core. Nevertheless, explored small molecules were primarily organic dyes and macrocycles.[13–15,39] Ibuprofen, is the only therapeutic agent whose interactions with CPC-micelles, to this date, have been explored for delivery application from the micelles.[41] As expected, higher solubilization of ibuprofen was observed upon combination with CPC-micelles.

5.1.3. Silica nanoparticles with organic bridges

As previously mentioned, tailoring the interactions between the nanoparticle framework and the desired cargo is a crucial strategy for its efficient inclusion. While earlier described systems are based on the functionalization of the nanoparticle or/and pore surface to increase its hydrophobicity, a more straightforward approach can also be explored based on the use of silyl precursors bridged by organic moieties. Silyl-precursors with one of more organic pendant groups has been also explored, and widely reviewed.[42,43] Following this strategy, the chemical nature of the framework can be modified, which also alters the porosity of the framework. Inclusion of bulkier spacers within the framework expands the porous network of the nanoparticle, leading to nanoparticles with higher porosity. Guo *et al.* demonstrated how the length and rigidity of the organic bridge can affect the porosity of the resulting amorphous materials.[44–46] They first studied the formation of bridged organosilica xerogel membranes containing ethane (R-C-C-R), ethene (R-C=C-R) or ethyne (R-C≡C-R)

bridges. As the rigidity of the C-C bong increased so did the porosity of the resulting material, obtaining BET surface area of 475 m^2g^{-1} for ethane containing xerogels, which increased to 597 m^2g^{-1} for ethyne-bridged materials.[45] Similarly, they investigated the effect of extending the phenyl linker to biphenyl. Resulting materials displayed higher porosity and gas permeability in case of the biphenyl-based memebrane.[46] Even though this features has been while explored for gas separation purposed, the expansion of amorphous silica framework for drug delivery has not been examined yet. Nevertheless, PMO nanoparticles has been previously reported for this purpose, but doe to their high open porosity the face the same limitations than MSNs regarding fast and burst cargo release.[47,48]

Moreover, inclusion of organic moieties in the framework, as also shown in the previous chapter, can result in interesting interactions with the included cargo. In this context and continuing with the aim of enhancing the inclusion and release of hydrophobic antibiotic in silica nanoparticles we decided to explore the behaviour of 1,4-bis(triethoxysilyl)benzene (BTEB, Figure 5.5A) based polysilesquioxane (PSQ) nanoparticles. BTEB-containing nanoparticles has previously shown, for instance, selective gas permeability for hydrophobic gases such us CO_2.[46] The affinity of phenyl moieties for hydrophobic cargos could be employed for the enhancement of hydrophobic drug inclusion within PSQ framework. Finally, as reported by Okamoto *et al.*[49], BTEB-based PSQ nanoparticles displayed a high intrinsic porosity (Figure 5.5B) which would be beneficial to facilitate the diffusion and, thereby, release of the included antibiotics.

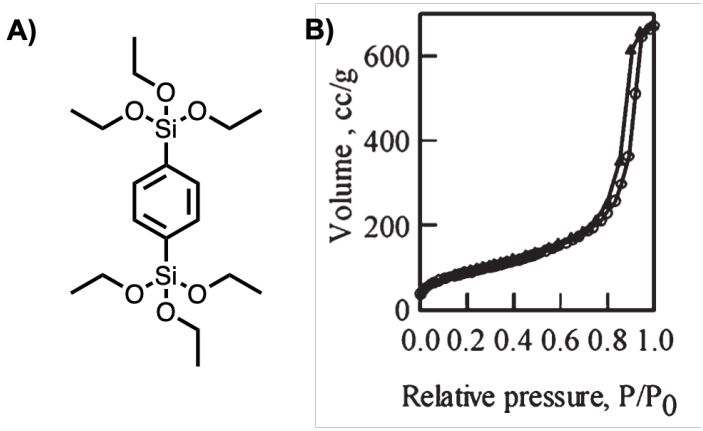

Figure 5.5. (A) Chemical structure of 1,4-bis(triethoxysilyl)benzene (BTEB) and (B) N_2 adsorption-desorption isotherm of BTEB-based PSQ as reported by Okamoto *et al*.[49]

There are no examples of BTEB-based PSQ nanoparticles for drug delivery in the literature. Reported silica-based DDS containing phenyl bridges are limited to nanoparticles formed *via* condensation of BTEB with (mesoporous organosilica nanoparticles) or without (periodic mesoporous organosilica) TEOS in presence of a liquid-phase template. Nevertheless, reported systems have shown higher encapsulation efficiency of hydrophobic cargos, such us dyes or drugs, due to hydrophobic interactions with the framework;[50–53] highlighting the potential of PSQ nanoparticles to act as efficiently DDS for hydrophobic antibiotics.

5.1.4. Chapter outline

We report two different approaches for the enhanced encapsulation and release of hydrophobic antibiotics (Figure 5.6). Inclusion of model antibiotic ciprofloxacin (**CPX**), a hydrophobic antibiotic widely used in antibacterial therapies, was chosen. We firstly explored its entrapment in **CPC** micelles and subsequent inclusion of the **CPC-CPX** assemblies in silica nanoparticles resulting in a significant improvement in **CPX**'s loading. Moreover, the use of the **CPC** micelles acts as a template in the particle formation, achieving a non-periodic porous structure that also contributes to the

efficient delivery of included cargos. Secondly, we took advantage of the use of BTEB-based **PSQ** nanoparticles for encapsulation and release of **CPX**. The interactions between the organic bridged and the antibiotic molecules, along with the intrinsic porosity of resulting nanoparticles display an ideal scenario for efficient antibiotic delivery.

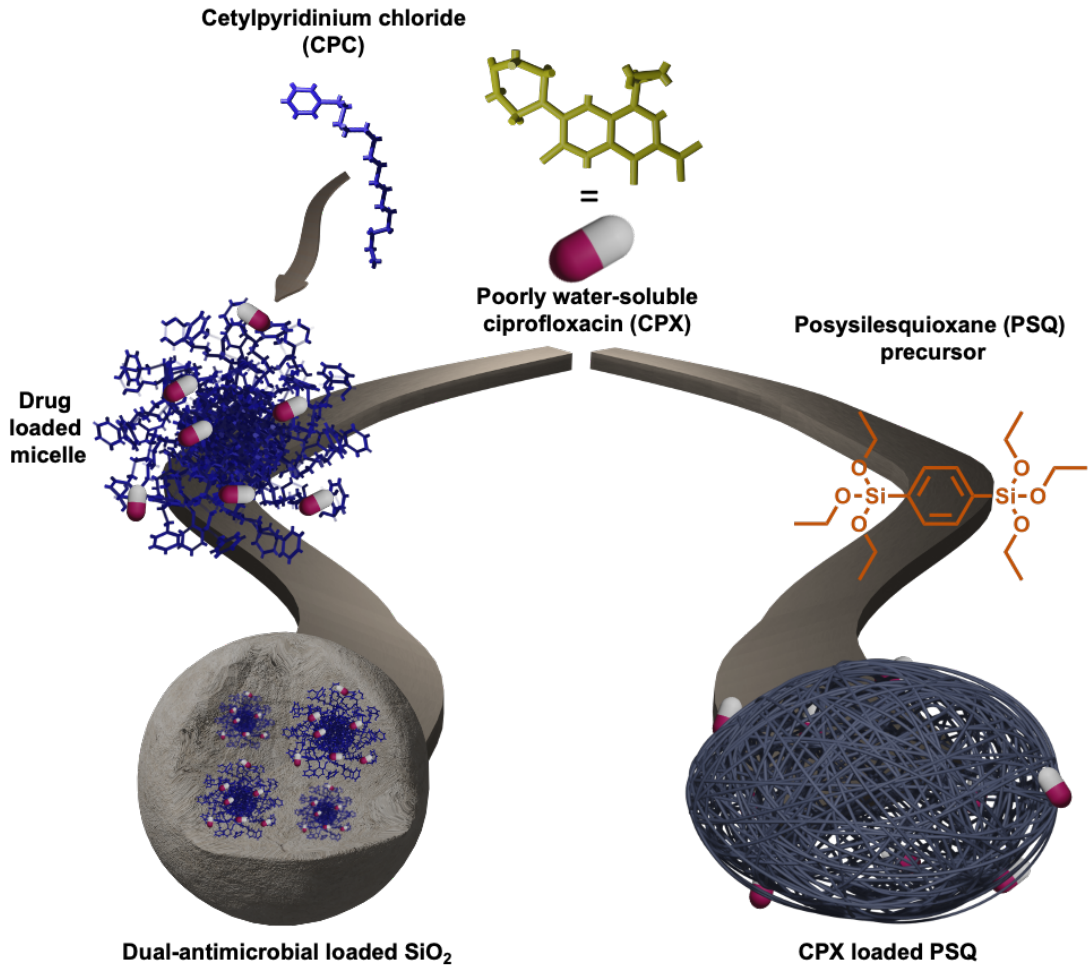

Figure 5.6. Schematic representation of developed strategy of hydrophobic antibiotic encapsulation in silica nanoparticles via entrapment in antiseptic micelles.

The first part of the work presented in this chapter resulted in the following publication:

A. R. Muguruza, M. L. Odyniec, M. Manhota, Z. Habib, K. Rurack, J. M. A. Blair, S. Kuehne, A. D. Walmsley, Z. Pikramenou, *Microporous Mesoporous Mater.*, 2024, **363**, 112841.

5.2. Results and discussion

5.2.1. Interactions between CPX and CPC micelles

The antibiotic **CPX** (Figure 5.7) was chosen as a model molecule as it represents a widely employed clinical antibiotic and it possess characteristics optical properties that will allows us to better understand the interactions between **CPX** and the **CPC** micelles. Interactions between **CPX** and **CPC** micelles were studied by a plethora of techniques, from Dynamic Light Scattering (DLS) to optical (UV/Vis and fluorescence spectroscopy), Nuclear Magnetic Resonance (NMR) spectroscopy and Isothermal Titration Calorimetry (ITC). All analysis were performed in carbonate buffer (HCO_3^- /CO_3^{2-}, 0.1 M, pH 10.6) in order to mimic the synthesis conditions of the silica particles.[54] **CPX** is a poorly-water soluble antibiotic.[55,56] At this pH, **CPX** presents a monoanionic form as the carboxylate group is deprotonated (pKa = 5.90). The piperazine group, at pH 10.6 remains neutral (pKa = 8.89).[57]

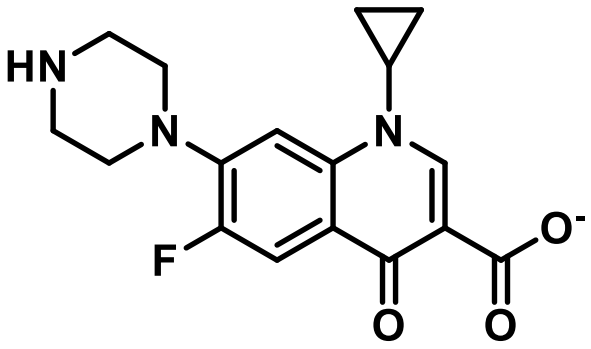

Figure 5.7. Chemical structure of model antibiotic **CPX** at pH 10.6.

5.2.1.1. Dynamic Light Scattering

Firstly, interactions between **CPX** and **CPC** micelles were explored by DLS. **CPC** micelles were formed in carbonate buffer at 2 mM, above its CMC (1 mM). The formation of micelles in carbonate buffer was monitored by DLS to ensure micelle formation at 2 mM (Figure 5.S.1). Under these conditions, formed **CPC** micelles

displayed a hydrodynamic diameter (by volume) of 4.9 ± 1.2 nm (Figure 5.8 and Figure 5.S.1). Upon addition of **CPX** up to 6 mM, the **CPC** micelle size increased until 6.8 ± 1.2 nm (Figure 5.8). Similarly, the hydrodynamic sized by intensity and number also increased upon addition of **CPX** (Table 5.S1). The increase in the hydrodynamic size of micelle upon entrapment of molecules has been previously reported.[13,58,59] Moreover, surface ζ-potential of **CPC** micelles before addition of **CPX** was measured to be +23 ± 2 mV, due to the positive charged pyridinium heads, that in oil-in-water systems, will be on the micelle outer surface.[60] Upon addition of **CPX** (6 mM), ζ-potential of resulted micelles decreased to +15 ± 1 mV, associated with the changes in the electron density of the pyridinium head of the **CPC**.[14,61] This supposes the first evidence of interactions between **CPX** and **CPC** micelles. Nevertheless, DLS analysis is not enough to elucidate the precise interaction between **CPX** and **CPC**-micelles, neither the location of the antibiotic within the micelle. Therefore, NMR spectroscopy was employed in order to clarify these interactions.

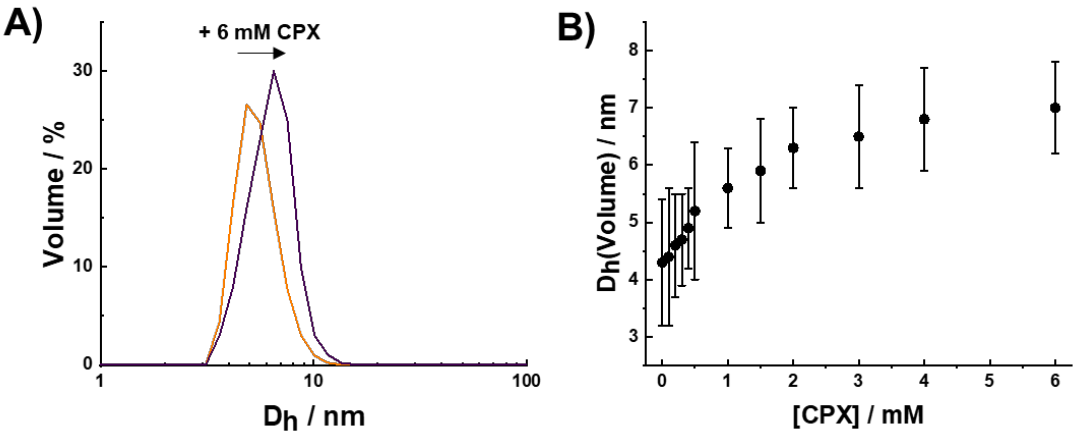

Figure 5.8. Monitoring of **CPC** micelle's (2mM) hydrodynamic diameter (by volume) and upon addition of **CPX** in carbonate buffer (HCO_3^-/CO_3^{2-}, 0.1 M, pH 10.6) (n = 5).

5.2.1.2. Nuclear Magnetic Resonance

Based on the results from DLS analysis of micelles in presence and absence of **CPX**, Proton Nuclear Magnetic Resonance (^{1}H-NMR) spectroscopy was employed to further elucidate the interactions between **CPX** and **CPC** micelles. ^{1}H NMR spectroscopy is able to detect changes in the local electronic environment of protons provoked by binding events. These changes, translated in shifts in protons NMR resonances allows us to elucidate the precise interactions between molecules.

^{1}H NMR analyses of **CPC** in carbonate buffer (D_2O, HCO_3^-/CO_3^{2-}, 0.1 M, pD 10.6) bellow (0.5 mM) and above (2 mM) its CMC, confirmed the presence of CPC micelles at 2 mM based on the characteristic shifts in proton resonances when the concentration increases from 0.5 mM to 2 mM (Figure 5.9 and Table 5.S2). The pyridinium protons $H_{1,5}$ (δ=8.89 ppm) and alkyl protons H_7 (δ=1.94 ppm) and H_8 (δ=4.63 ppm) experienced upfield shifts (Δδ= +0.01–0.03 ppm), while the remaining proton resonances of the aliphatic tail $H_{9–22}$ (δ=1.08–1.26 ppm) showed downfield resonance shifts. These results indicate a change in **CPC** environment due to micelle formation and it is supported by previous studied undertaken in D_2O.[39,62]

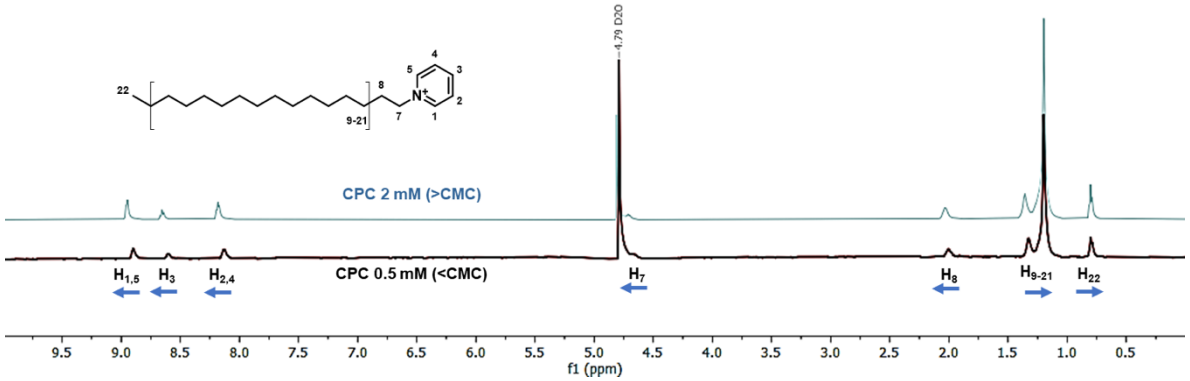

Figure 5.9. ^{1}H NMR (500 MHz, HCO_3^-/CO_3^{2-} D_2O buffer, 0.1 M, pD 10.6) of **CPC** bellow (0.5 mM) and above (2 mM) the CMC, showing proton shift due to micelle formation.

Furthermore, ^{1}H two-dimensional Nuclear Overhauser effect spectroscopy (NOESY) revealed intermolecular interactions between **CPC** molecules above its CMC (2 mM) (Figure 5.10). The observed interactions by NOESY were between pyridinium protons $H_{2,4}$ (δ=8.08 ppm) and $H_{1,5}$ (δ=8.89 ppm) with aliphatic protons $H_{9–21}$ (δ=1.08–1.26 ppm) and between H_8 (δ=4.63 ppm) with $H_{9–21}$ (δ=1.08–1.26 ppm) and H_8 (δ=4.63 ppm) with pyridinium protons $H_{1,5}$ (δ=8.89 ppm). Intramolecular interactions of **CPC** molecules were identified from the NOESY spectra based on ^{1}H-NMR Correlated Spectroscopy (COSY) experiments (Figure 5.S3). Elucidated intermolecular interactions between **CPC** molecules above its CMC supports the close proximity of monomer in the micellar structure.

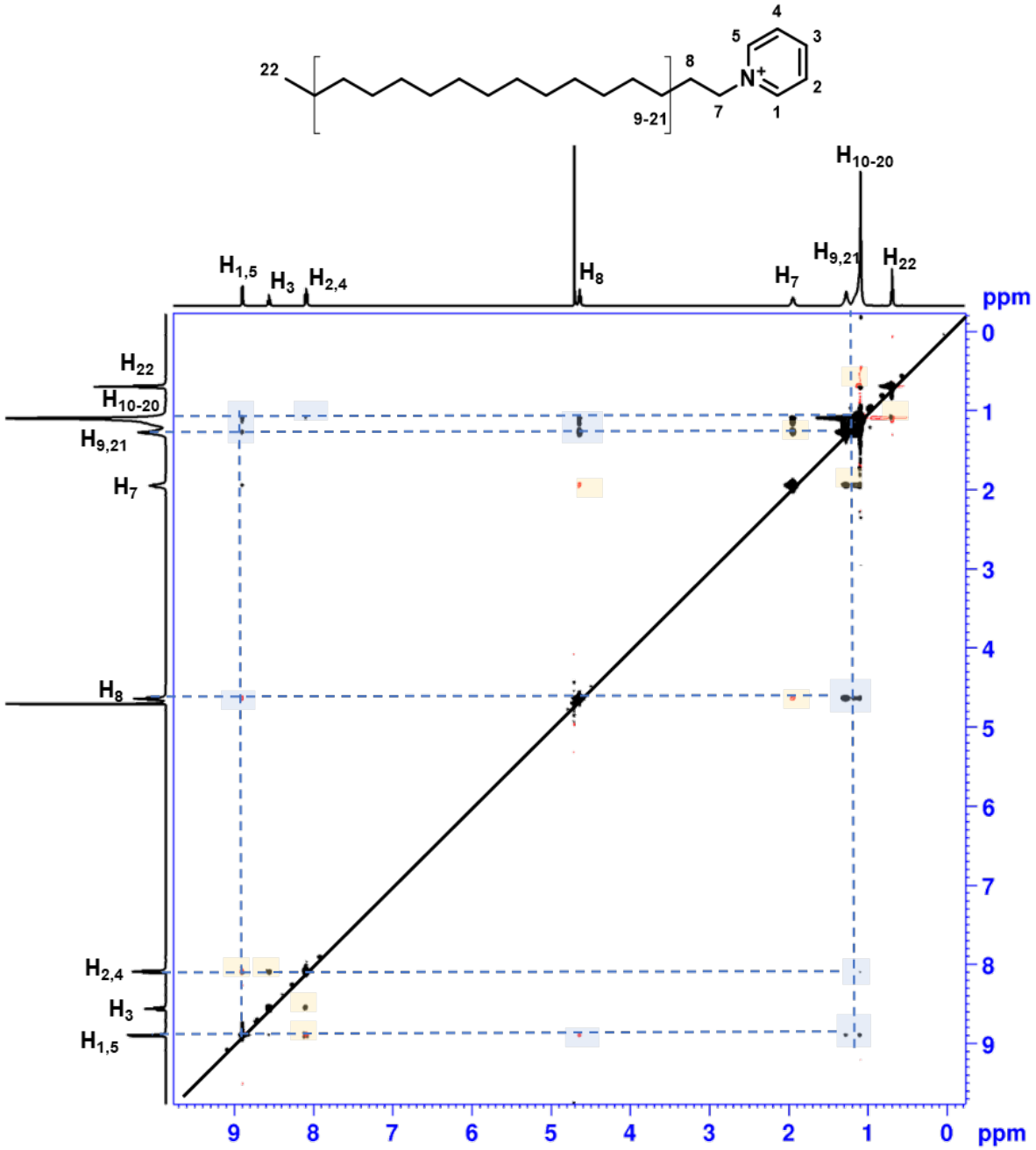

Figure 5.10. NOESY (500 MHz, HCO_3^-/CO_3^{2-} D_2O buffer, 0.1 M, pD 10.6) of **CPC** (2mM) above the CMC. NOESY interactions (intermolecular) are labelled in blue boxes and COSY interactions (intramolecular) in yellow boxes.

With the aim of exploring the interactions between **CPX** and **CPC** micelles, a carbonate buffer (HCO_3^-/CO_3^{2-}, 0.1 M, pD 10.6) solution of both antibiotics with molar ratio of 1:12 of **CPX** (4 mM) to **CPC** (43 mM) was employed. The 1:12 **CPX**:**CPC** ratio

was chosen to ensure that the majority of **CPX** molecules would be interacting with the **CPC** micelles. An excess of **CPX** would result in **CPX** molecules not interacting with the **CPC** micelles, being translated into different NMR resonances, being challenging to interpret. Furthermore, in the synthesis of silica nanoparticles the 1:12 ratio of **CPX**:**CPC** would be employed.

Firstly, we investigated the resonance shifts of **CPC** protons upon addition of **CPX** (Figure 5.11 and Table. 5.S3). The ^{1}H-NMR spectra of **CPC** micelles showed a small upfield resonance shifts in all protons beside the terminal methyl protons (H_{22}, δ=0.77 ppm), which did not suffer any shift. Observed shifts indicated that in the presence of **CPX** the environment of the **CPC** monomers changed. In fact, this result has been previously reported as consequence of interactions between cationic micelles and aromatic molecules.[62,63] The lack of change in the proton NMR resonance of the terminal group suggests that the **CPX** could be located at the micelle-water interface, far from the terminal H_{22} located in the inner hydrophobic core of the micelle. These interactions have been previously described for polar molecules on addition to anionic and cationic micelles.[62–64]

With respect to the proton NMR spectra of **CPX** in presence of **CPC** micelles, all resonances of **CPX** displayed an upfield shift except for the resonances assigned to the cyclopropane protons (H^{x}_{11}). Beside the changes in resonance shifts, splitting of **CPX** proton signals is also affected by the presence of **CPC** micelles. Piperazine protons $H^{x}_{20,24}$ and cyclopropane protons H^{x}_{11} and $H^{x}_{19,18}$ appear broadened and the aromatic protons H^{x}_{6}, $H^{x}_{3,}$ H^{x}_{8} appear with two sets of resonances. These patterns may indicate the molecules are in different environments affected either by the viscosity of solution,[63] local environments[65] or changes in molecular tumbling.[66] The significant changes observed in ^{1}H NMR spectra of **CPX** in the aromatic region may be attributed

to interactions of the negatively charged π system of **CPX** with the positively charged pyridinium group of **CPC** through cation-π interactions.[66–68]

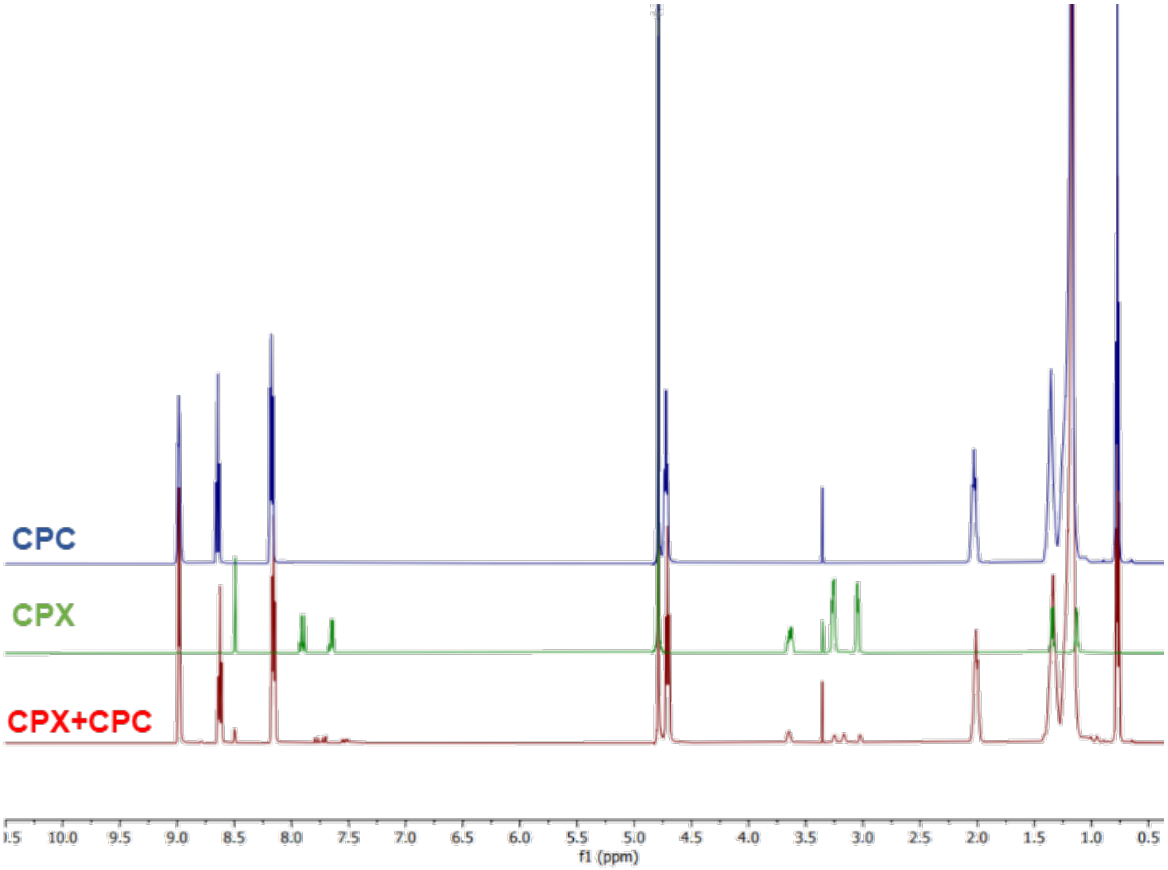

Figure 5.11. ^{1}H-NMR (500 MHz, HCO_3^-/CO_3^{2-} D_2O buffer, 0.1 M pD 10.6) of **CPX** (4 mM), **CPC** (43 mM) and a **CPX** (4 mM) **CPC** (43 mM) mixture.

Interaction between **CPX** and **CPC** micelles were further investigated by NOESY experiments (Figure 5.12). Two distinctive Nuclear Overhauser Effects (NOEs) were observed between **CPX** and **CPC**, labelled in purple in Figure 5.12. One of the signals correspond to the interactions between the protons of the cyclopropane ring at δ=3.5 ppm and the aliphatic chain protons of **CPC** ($H_{9–21}$) at δ=1.30 ppm. The other NOE corresponds to the H^x_{11} proton on the cyclopropane ring at δ=3.5 ppm and the aliphatic chain protons of **CPC** ($H_{9–21}$) at δ=1.30 ppm. Furthermore, NOEs between **CPC**

micelles identified in Figure 5.12 did not suffer any change upon addition of **CPX**, which indicates that the **CPC** micellar structure remains stable in presence of **CPX**. Interestingly, a new NOE between CPC monomers was observed in presence of CPX. The new interaction was observed between **CPC** pyridinium protons $H_{1,5}$ (δ=8.89 ppm) and neighbouring **CPC** protons H_7 (δ=1.94 ppm), suggesting a closer packing of these protons within the **CPC** micelles through-space than without **CPX**.

Thereby, the shifts in ^{1}H NMR spectra and presence of NOEs indicate that the cyclopropane ring of **CPX** is interacting with the aliphatic tails of **CPC** micelles in the palisade layer of the micelle, namely between the hydrophilic groups and first few carbon atoms of hydrophobic groups as there is no change in resonance of the terminal protons of H_{22} (δ=0.77 ppm).[68] In addition, cation-π interactions between pyridinium headgroups of **CPC** micelles and **CPX** aromatic protons (H^x_6, H^x_8, H^x_3) at δ=7.74 ppm, δ=7.53 ppm and δ=8.49 ppm, illustrate the **CPX** molecule is sitting at the micelle-water interface, with the piperazine group ($H^x_{20\text{-}24}$ at δ=3.24-2.28 ppm) pointing outwards as there is an absence of NOEs and the piperazine group is able to hydrogen bond with solvent molecules. Based on this study we propose the interactions fashion depicted in Figure 5.13. Moreover, an Isothermal Titration Calorimetry (ITC) experiment confirmed the interaction, calculating a K_D of 6.30 ± 0.7 mM (Figure 5.S5).

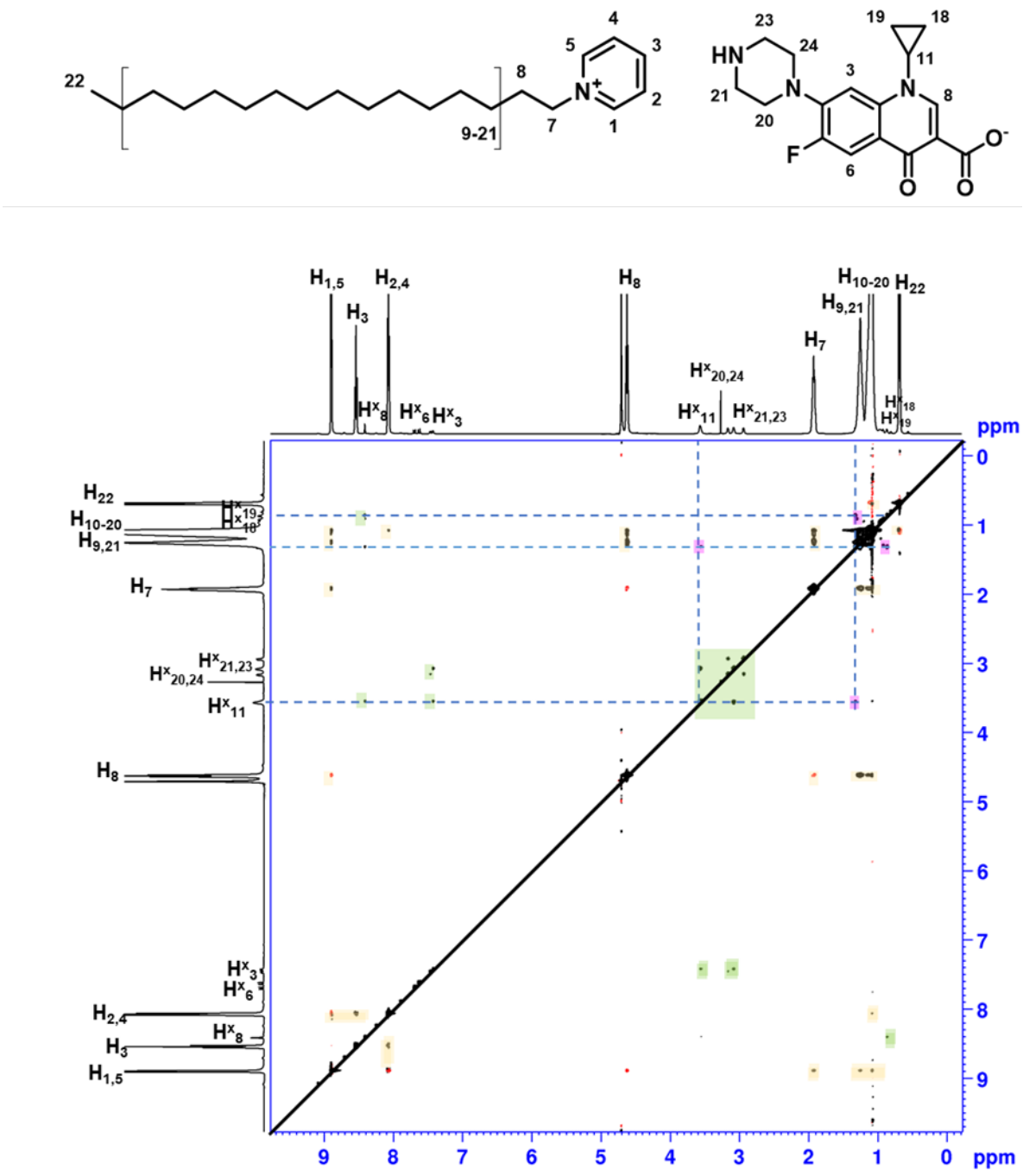

Figure 5.12. NOESY (500 MHz, HCO_3^-/CO_3^{2-} D_2O buffer, 0.1 M, pD 10.6) of **CPX** (4 mM) and **CPC** micelles (43 mM). NOESY interactions (intermolecular) are labelled in purple boxes and COSY interactions (intramolecular) in yellow (for **CPX**) and green (for CPC**)** boxes.

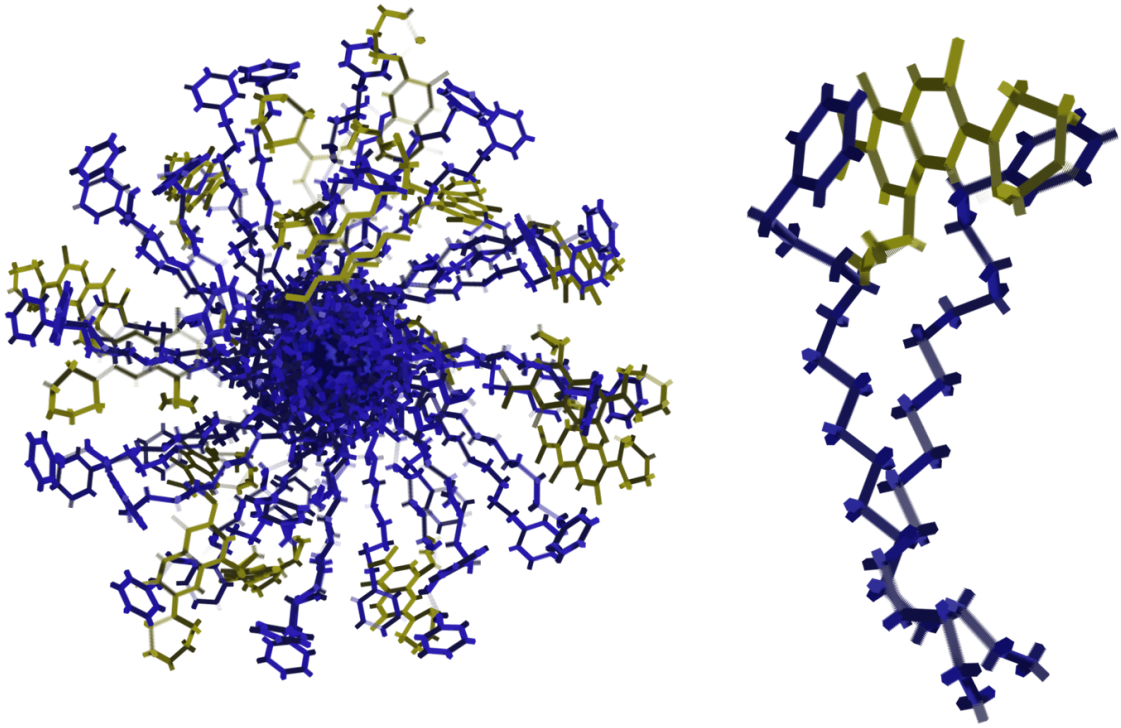

Figure 5.13. Illustration of proposed interactions between **CPX** molecules (yellow) and **CPC** micelles (blue). For clarity interactions between one **CPX** molecule and two **CPC** monomers are also depicted.

5.2.1.3. Optical spectroscopy

Additionally, optical spectroscopy was employed to further explore the interactions between the antibiotics and **CPC**. The absorption properties of **CPX** were investigated in a **CPC** micellar medium at pH 10.6. The UV-Vis spectra of **CPC** show a single absorption band with maximum at 259 nm (ε = 4190 $M^{-1}cm^{-1}$). In carbonate buffer **CPX** has two absorption bands at 270 nm (ε = 39000 $M^{-1}cm^{-1}$) and 325 nm (ε = 17000 $M^{-1}cm^{-1}$) (Figure 5.S6). Due to the overlapping between the higher energy absorption band of **CPX** with **CPC**, changes in this band cannot be monitored. Therefore, interactions between molecules will be investigated by monitoring the **CPX** lower energy absorption band at 325 nm. Upon addition of **CPC** to a **CPX** solution (10 μM) in carbonate buffer (HCO_3^-/CO_3^{2-}, 0.1 M, pH 10.6), a bathochromic shift of the 325 nm band was observed. The shift continued until the **CPC** concentration reached its CMC

(1 mM). In the highest CPC concentration explored (6 mM, >CMC), there was a bathochromic shift to 334 nm ($\Delta\lambda$ = +9 nm) (Figure 5.14). These data indicate that in the presence of **CPC** micelles there is a change in environment for the antibiotics, supporting the interactions described by NOESY.

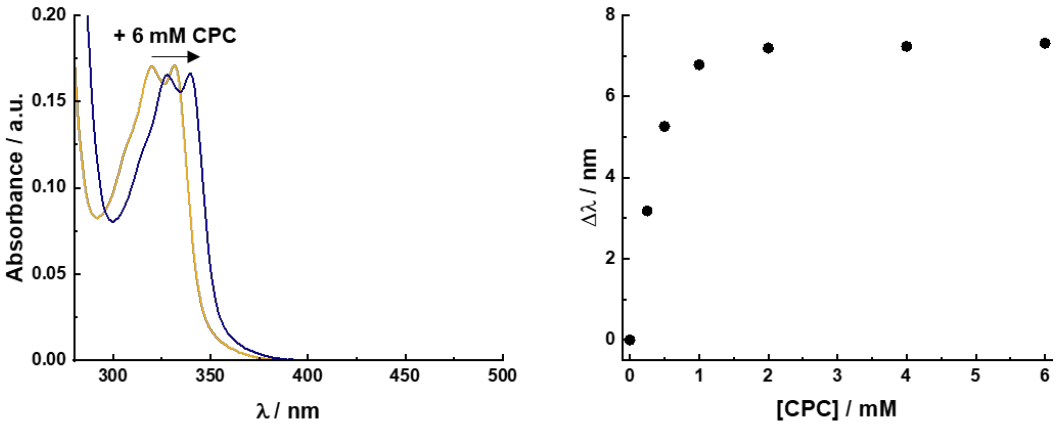

Figure 5.14. UV/Vis spectroscopy study of **CPX** (10 μM) upon addition of **CPC** up to 6 mM in carbonate buffer (HCO_3^-/CO_3^{2-}, 0.1 M, pH 10.6).

Furthermore, the change of the environment upon micelle formation was also investigated by steady-state and time resolved fluorescence spectroscopy (Figure 5.15). **CPX** (10 μM) displays a maximum emission wavelength at 425 nm upon excitation at 340 nm at pH 10.6. However, after addition of **CPC** (2 mM > CMC), **CPX** emission suffered a significant decrease in intensity. Accordingly, time-revolved fluorescence studies showed a decrease in luminescence lifetime decay (λ_{exc} = 375 nm, λ_{em} = 425 nm) upon **CPC** addition from 7.3 ns to 3.3 ns (Table 5.S4). The spectroscopic observations indicate that there is a change of the environment of **CPX** which quenches the luminescence. There may be aggregation-induced quenching which has been previously described for other fluoroquinolines, caused by the close proximity of **CPX** molecules within the **CPC** micelle, or quenching from **CPC** as observed for other anionic aromatic fluorescent dyes.[69,70]

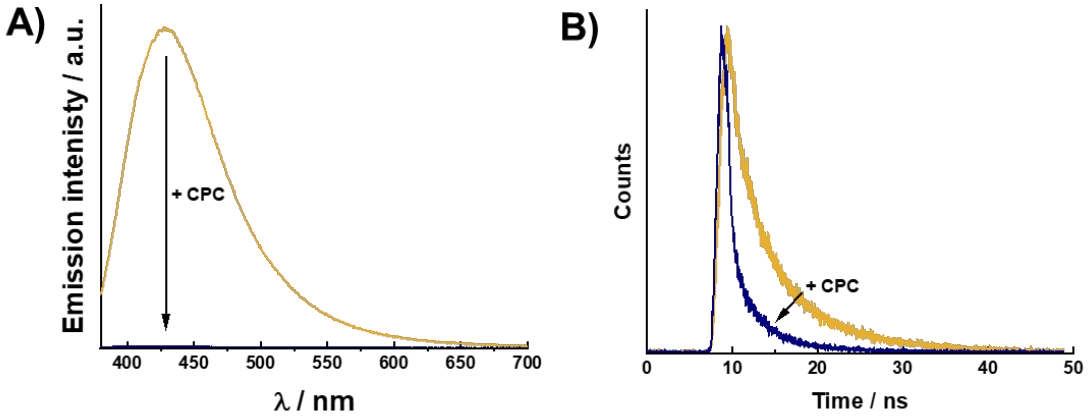

Figure 5.15. Optical spectroscopy of antibiotics in presence of **CPC.** (A) Steady state (λ_{exc} = 340 nm) and (B) time-resolved exponential fluorescence decay (λ_{exc} = 375 nm, λ_{em} = 425 nm) of a **CPX** solution (10 μM) before and after addition of **CPC** (2 mM) in carbonate buffer (HCO_3^-/CO_3^{2-}, 0.1 M, pH 10.6).

These results from optical spectroscopy further confirms the interactions between **CPX** and **CPC** micelles, also sustaining the location of **CPX** molecules close to the hydrophilic surface of the micelle.

5.2.2. Synthesis of SiO_2⊃CPC-CPX

After thoroughly investigating the interactions between **CPX** and **CPC** molecules, we decided to include them in silica particles for the development of dual antimicrobial loaded nanoparticle with enhanced delivery of **CPX**. For that, we decided to follow a previously reported synthesis of silica nanoparticles.[54] Briefly, the silica synthesis is started by combining the silica precursor (TEOS), ethanol, water and ammonium hydroxide for 3 h and then a solution containing **CPX** and **CPC** in 1:12 ratio is added. Finally, the silica particle formation is continued for another 6 h (Figure 5.16). This synthesis strategy yields silica particles (**SiO_2⊃CPC-CPX**) with a solid silica core

(formed in the first 3 h of the reaction) and a silica shell containing the desired cargo or cargos which is formed in the subsequent 6 h.

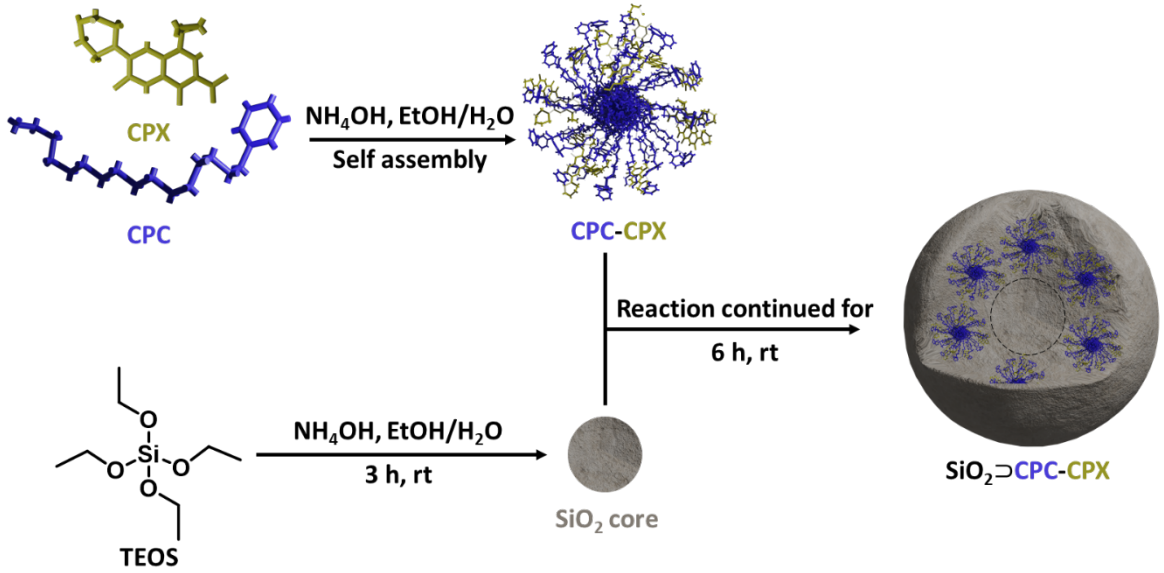

Figure 5.16. Scheme of the synthesis of **SiO_2⊃CPC-CPX.**

As control particles, and in order to study the enhanced delivery of **CPX** from **SiO_2⊃CPC-CPX**, particles containing only **CPC** micelles (**SiO_2⊃CPC**) or **CPX** (**SiO_2⊃CPX**) were synthetized following the same methodology.

5.2.3. Characterization of SiO_2⊃CPC-CPX

5.2.3.1. Size and morphology of CPC-CPX micelles and SiO_2⊃CPC-CPX

Initially, the size and morphology of the **CPC-CPX** micelles before their inclusion in the silica nanoparticles was explored by TEM. Premixed solution of **CPX** and **CPC** in 1:12 ratio was deposited in carbon-coated copper grids and they were imaged by TEM

(Figure 5.17). Recorded images showed spherical micelles with two different size populations of 3 ± 2 nm (n = 50) and 7 ± 2 nm (n = 50). The two population of **CPC-CPX** can be attributed to the drying process of the sample before imaging. Similarly, **CPC** micelles in the absence of **CPX** resulted predominant population of 3 ± 1 nm (n = 50) (Figure 5.S7).

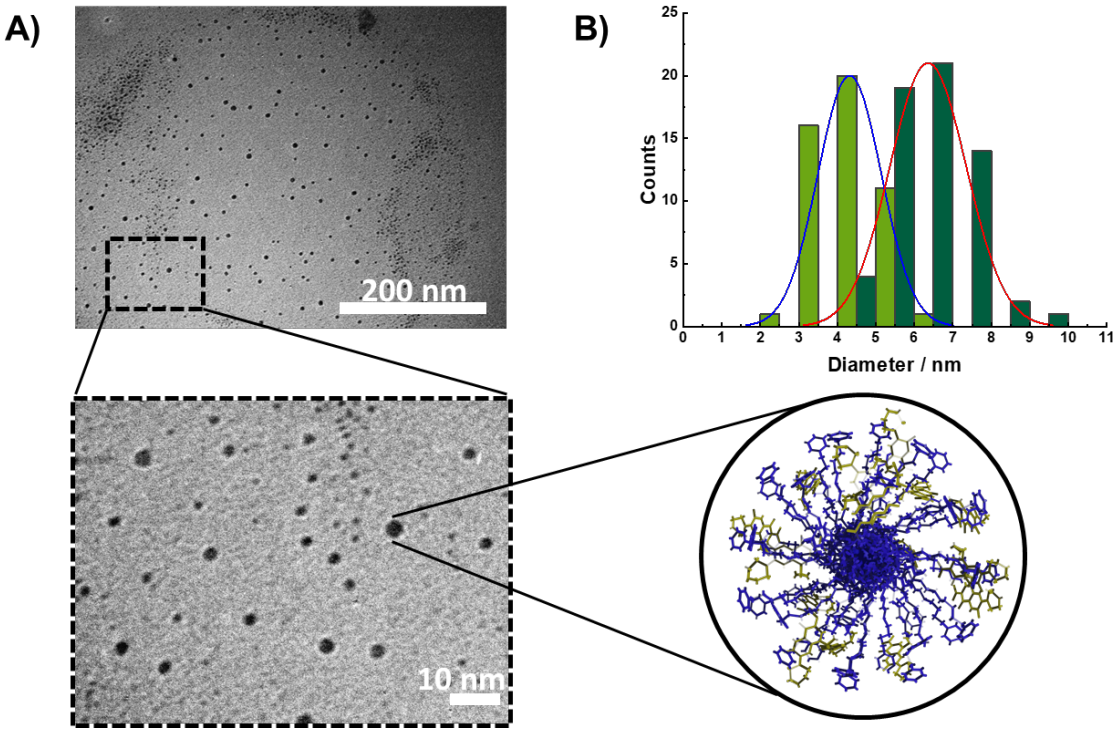

Figure 5.17. (A) Representative Transmission Electron Microscopy (TEM) image of **CPC-CPX** micelles formed by addition of **CPX** (4 mM) to a **CPC** micelle solution (43 mM) and (B) normal size distribution of micelles (n =50).

Afterward, size and morphology of **SiO_2⊃CPC-CPX** was explored. DLS analysis of particles is summarised in Table 5.1, Table 5.S5 and Figure 5.S8. **SiO_2⊃CPC-CPX** particles displayed a hydrodynamic diameter by volume of 237 ± 42 nm and 215 ± 30 by number. Moreover, nanoparticles had a positive ζ-potential of + 35 ± 8 mV which was assigned to the present of the positively charged **CPC** in the nanoparticles surface. **SiO_2⊃CPC** and **SiO_2⊃CPX** particles displayed a hydrodynamic diameter (D_h),

by volume, of 263 ± 47 nm and 187 ± 22 nm, respective. **SiO_2⊃CPC** also displayed a positive ζ-potential of + 35 ± 17 mV while **SiO_2⊃CPX** had a negative ζ-potential of -15 ± 5 mV. The negative ζ-potential of **SiO_2⊃CPX** is a result of the absence of CPC in the synthesis, and hence, in the particle surface. Electron microscopy analysis of **SiO_2⊃CPC-CPX** particles (Figure 5.18) revealed spherical particle with uniform size with a size distribution by SEM of 230 ± 25 nm (n = 50). **SiO_2⊃CPC** and **SiO_2⊃CPX**, meanwhile, resulted in a size distribution by SEM of 210 ± 55 nm and 251 ± 44 nm.

Presence of **CPC** and **CPX** within the nanoparticles was confirmed by solid-state UV//Vis absorption spectroscopy (Figure 5. 18D). Spectrum of the nanoparticles powder showed two adsorption bands, a clear adsorption bad of **CPX** centred at 325 nm and a broad band at lower wavelength with λ_{max} at 260 nm which was attributed to the combination of the absorption band of **CPC** at 259 nm and the higher energy adsorption band of **CPX** at 270 nm. Equally, solid-state UV/Vis spectroscopy confirmed the presence of **CPC** in **SiO_2⊃CPC** and of **CPX** in **SiO_2⊃CPX**.

Table 5.1. DLS and ζ-potential measurements of **SiO_2⊃CPC-CPX** particles

Hydrodynamic diameter (D_h) / nm				**ζ-potential**
Intensity	**Volume**	**Number**	**PDI**	**/ mV**
250 ± 50	237 ± 42	215 ± 30	0.33	+35 ± 8

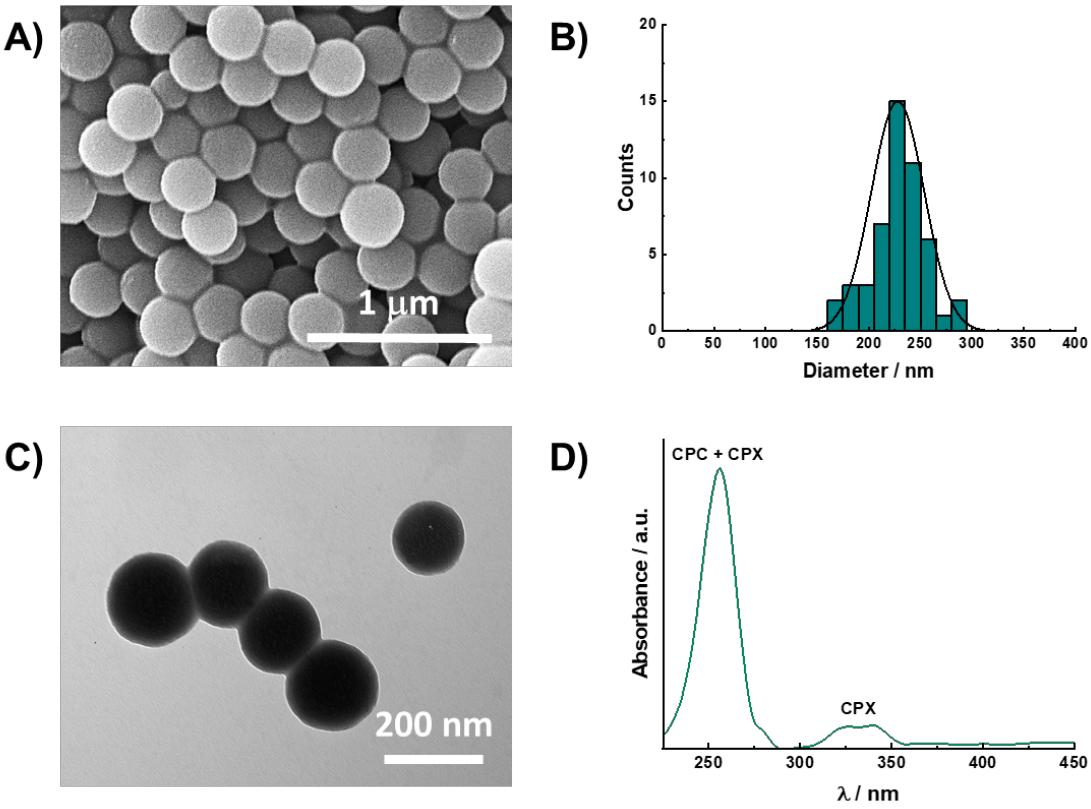

Figure S.18. Characterization of **SiO_2⊃CPC-CPX.** (A) SEM and (C) TEM images of nanoparticles and (C) nanoparticle size distribution based on SEM images (n = 50). Presence of CPC and CPX was confirmed by (D) solid-state UV/Vis absorption.

5.2.3.2. Quantification of SiO_2⊃CPC-CPX loading

Quantification of included **CPC** and **CPX** in **SiO_2⊃CPC-CPX** nanoparticles was calculated through two different methodologies. Firstly, estimation of included cargos was done by calculating the remaining **CPC** and **CPX** in the synthesis solution after particle synthesis by UV/Vis spectroscopy. For the UV/Vis analysis the absorption band at 340 nm was employed to calculate the **CPX** loading and the combined band at lower wavelength was deconvoluted in order to quantify the absorption of **CPC** at 270 nm. Secondly, Thermogravimetric Analysis (TGA) was employed to estimate the organic content in the particle.

UV/Vis spectroscopy analysis of the synthesis supernatant resulted in an estimated loading of **CPX** of 7.2 $\mu g_{CPX}/mg_{NPs}$ and 120 $\mu g_{CPC}/mg_{NPs}$ for **CPC**. The estimated loading represents a loading efficiency 84 % for **CPX**. Meanwhile, in the absence of **CPC**, the loading efficiency of **CPX** dropped to 35 % (30 $\mu g_{CPX}/mg_{NPs}$). This difference highlights the importance of **CPC** micelles as carries for **CPX** for its inclusion in silica nanoparticles. In fact, **CPX**, in synthesis conditions (pH 11) has a negatively charge arisen from the deprotonation of the carboxylic groups. The silica framework is, also, negatively charged due to the abundance of hydroxyl groups that at pH 11 are mostly deprotonated (pka = 7.5-9.5).[71–73] The repulsive interactions between the antibiotic and the framework would lead to the estimated low loading efficiency in case of **SiO_2⊃CPX.** The loading of **CPC** in **SiO_2⊃CPC** does not significantly differ from **SiO_2⊃CPC-CPX** with a loading of 10.0 $\mu g_{CPC}/mg_{NPs}$.

Thermogravimetric analysis (TGA) was also utilised in order to quantify antibiotics loading. However, due to the broad thermal degradation pattern of antibiotic inside the silica framework, the quantification of each antibiotic individually was not possible in case of **SiO_2⊃CPC-CPX**, estimating an overall organic content from the TGA curve (Figure 5.19). The thermal degradation curve of **SiO_2⊃CPC-CPX** showed initial weigh loss step between 30 and 120 ^oC was associated with the loss of absorbed water molecules, the second step between 120 ^oC and 225 ^oC with the uncondensed ethoxy groups of the silica precursor and the rest of the degradation was associated to the presence of the antibiotics. Upon direct comparison with unloaded silica nanoparticles, synthetized by the same methodology with no antibiotic addition, a total organic content of 185 $\mu g/mg_{NPs}$ was estimated for **SiO_2⊃CPC-CPX**, which is in good agreement with the calculated loading by UV/Vis spectroscopy (191 $\mu g/mg_{NPs}$) considering the limitations and error of each technique. TGA curve of **SiO_2⊃CPC**

showed a weight loss of 98 μg/mg$_{NPs}$ assigned to **CPC** and **SiO$_2$⊃CPC** an organic content of 27 μg/mg$_{NPs}$ associated with included **CPX** (Figure 5.S13).

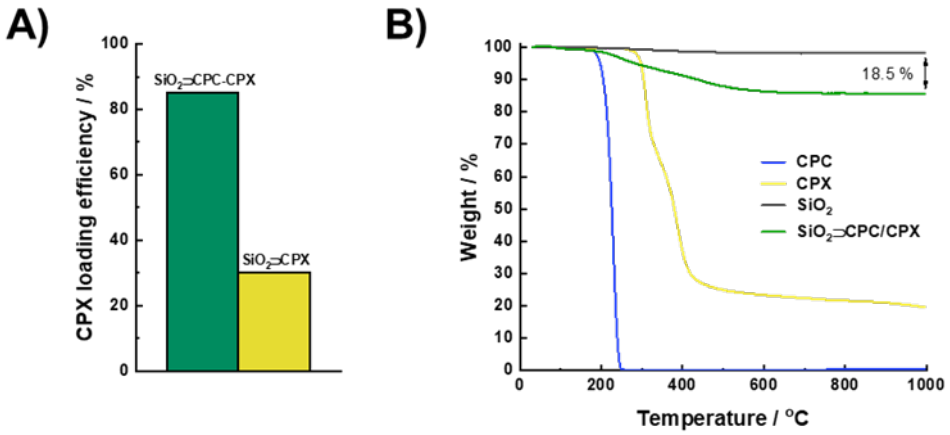

Figure 5.19. Quantification of loaded antibiotics. (A) Loading efficiency of **CPX** estimated by UV/Vis of synthesis supernatant in presence and absence of **CPC** micelles and (B) thermogravimetric curve of **SiO$_2$⊃CPC-CPX.** Nanoparticles were dried at 120 ºC for 2 h prior the measurements. Thermal degradation curve of unloaded nanoparticles (**SiO$_2$**) and antibiotics in added as reference. TGA profile was recorded in a 5 ºC min^{-1} heating ramp from 30 to 1000 ºC under air flow.

5.2.3.3. Porous structure of SiO$_2$⊃CPC-CPX

As previously reported in the literature, the inclusion of micellar structures formed by antimicrobials amphiphilic lead to porous silica nanoparticles. Thereby, we studied the porosity of nanoparticles resulted after the inclusion of CPC micelles**.** For it, we employed N_2 porosimetry. N_2 porosimetry is a standardised technique for porous materials that measure the adsorption and desorption amount of N_2 at 77 K at different pressures (Figure 5.21).[74] From this data, the surface area of the materials can be calculated based on the Braunauer-Emmett-Teller (BET) theory and the pore size distribution.[75,76] All samples were dried at 120 ºC prior to the experiment to ensure the evacuation of solvent molecules and gases trapped within the framework.

In order to reveal the porosity formed by the micelles, nanoparticles were subjected to a calcination process at 600 ºC for 18 h to ensure fully removal of the antibiotics. 600 ºC was chosen as calcination temperature based on thermal degradation profiles (Figure 5.19) that showed weight loss in nanoparticles until 600 ºC. N_2 adsorption-desorption isotherm of calcinated **SiO_2⊃CPC** resulted on a type II isotherm with a calculated BET surface area of 153 ± 3 m^2g^{-1}. Upon calcination, **SiO_2⊃CPC-CPX** also displayed a type II isotherm with a BET surface area of 215 ± 4 m^2g^{-1}. Before calcination, however, a type I isotherm, associated to non-porous materials, was recorded in both nanoparticles with BET surface area of 17 ± 1 m^2g^{-1} and 5 ± 1 m^2g^{-1} for **SiO_2⊃CPC-CPX** and **SiO_2⊃CPC**, respectively. The reduced BET surface area before calcination is due to the presence of the antibiotic micelles within the framework, which, during the calcination process are removed and the empty pores revealed. This process is a common methodology in MCM-41 and other porous materials preparation in order to empty the pores before drug inclusion.

Furthermore, calculate average pore size for **SiO_2⊃CPC** was 2.5 nm and for **SiO_2⊃CPC-CPX** was 2.7 nm. The calculated pore sizes, however, may not reflect the size difference calculate by TEM imagine of micelles (Figure 5.17 and Figure 5.S7) given the changes on the silica framework during calcination.

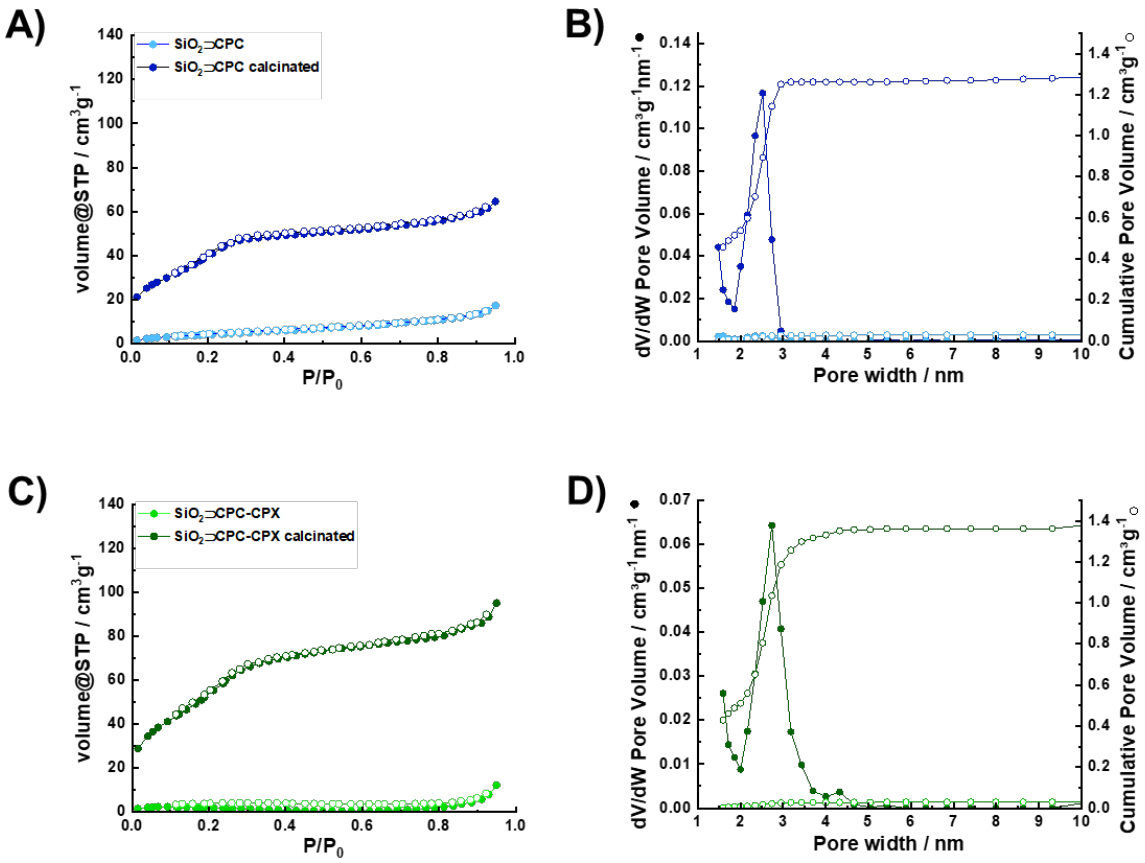

Figure 5.20. N_2 adsorption-desorption isotherms at 77 K of (A) **SiO_2⊃CPC** and (B) **SiO_2⊃CPC-CPX** and calculated pore size distribution for (C) **SiO_2⊃CPC** and (D) **SiO_2⊃CPC-CPX** before and after calcination at 600 ºC for 18 h.

N_2 adsorption-desorption analysis of **SiO_2⊃CPX** (Figure 5.S14) was also performed to ensure that the increase of porosity observed in **CPC**-containing nanoparticles was due to the inclusion of the micelles, acting as template. Isotherm of calcinated **SiO_2⊃CPX** resulted in a type I isotherm, characteristic of non-porous materials, with a calculated BET surface area of 11 ± 2 m^2g^{-1}, showing no significance difference with the analysis of the particle before calcination (BET = 7 ± 1 m^2g^{-1}). These results confirmed that the described porosity is related with the inclusion of the **CPC** micelles within the silica framework.

Previously reported antibacterial templated silica nanoparticles resulted in BET surface areas between 798 m^2g^{-1} and 1579 m^2g^{-1}.[26,31,77] Specially, reported CPC-templated silica nanoparticles displayed BET surface area between 856 m^2g^{-1} and 1050 m^2g^{-1}.[20,22,31] The lower BET surface area of **SiO_2⊃CPC** and **SiO_2⊃CPC-CPX** can be attributed to the template assembly. While previously reported CPC-templated nanoparticles showed an MCM-41 or SBA-15 structure with unidimensional pores due to the hexagonal packing of the CPC cylindrical micelles in synthesis conditions (Figure 5.21A). In the reported synthesis conditions, **CPC** and **CPC-CPX** micelles showed a spherical shape by TEM (Figure 5.17 and Figure 5.S7). In fact, morphology of CPC micelles is very dependent on the dispersant composition, and preciously reported.[40] Furthermore, previously reported CPC-templated MSNs displayed a Type IV N_2 isotherm, while **SiO_2⊃CPC** and **SiO_2⊃CPC-CPX** displayed a Type II. Alongside estimated pore size and template confirmation we propose the "closed-pore" porous structure, as previously reported for other materials.[78] This porous structure is composed by spherical shaped nanometre-sized pores connected or not between them (Figure 5.21B).

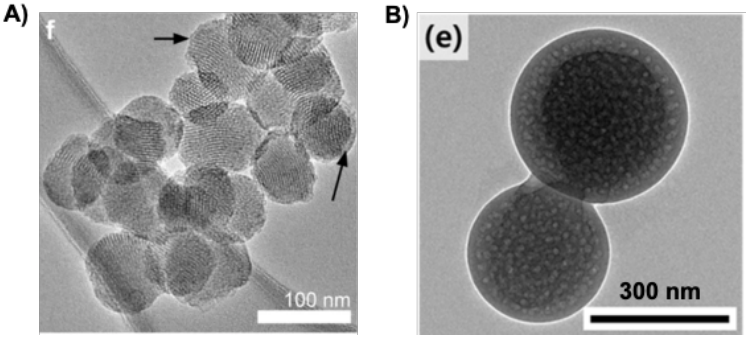

Figure S21. Difference between porous structure of (A) previously reported CPC-templated silica nanoparticles[20,31] and (B) proposed porous structure of nanoparticles reported in this work, reproduced from K. Hee Ku *et al*. [78]

5.2.4. Release studies of SiO_2⊃CPC-CPX

Release studies were conducted to demonstrate the ability of produced nanoparticles to act as drug delivery systems. For it, nanoparticles were dispersed in water and, upon stirring, the released antibiotic was quantified by UV/Vis spectroscopy of the supernatant after particle removal by centrifugation. Release experiments were conducted for 48 h to explore the capacity of the particles to release the included antibiotic over time.

Release studies of **SiO_2⊃CPC-CPX** (2 mg/mL) in water (Figure 5.22) showed a cumulative **CPC** release up to 23 ± 2 μg_{CPC}/mL after 48 h where it looks that the **CPC** release has not reached the maximum yet, as the release curve did not plateau. In addition, **CPX** release of 0.9 ± 0.2 μg_{CPX}/mL is observed after 48 h, exhibiting release of both antimicrobials from **SiO_2⊃CPC-CPX**. **SiO_2⊃CPC** nanoparticles released up to 35 ± 7 μg_{CPC}/mL after 48 h (Figure 5.S15A). However, **SiO_2⊃CPX** released a maximum of 0.7 ± 0.2 μg_{CPX}/mL (Figure 5.S15B). Moreover, it must be highlighted that **SiO_2⊃CPX** nanoparticles did not showed any detectable release up to 24 h of release studies. The concentration of antibiotics released from **SiO_2⊃CPC-CPX** are above the Minimal Inhibitory Concentration (MIC) values for susceptible bacterial strains, demonstrating their potential of the developed nanoparticles for drug delivery.[79]

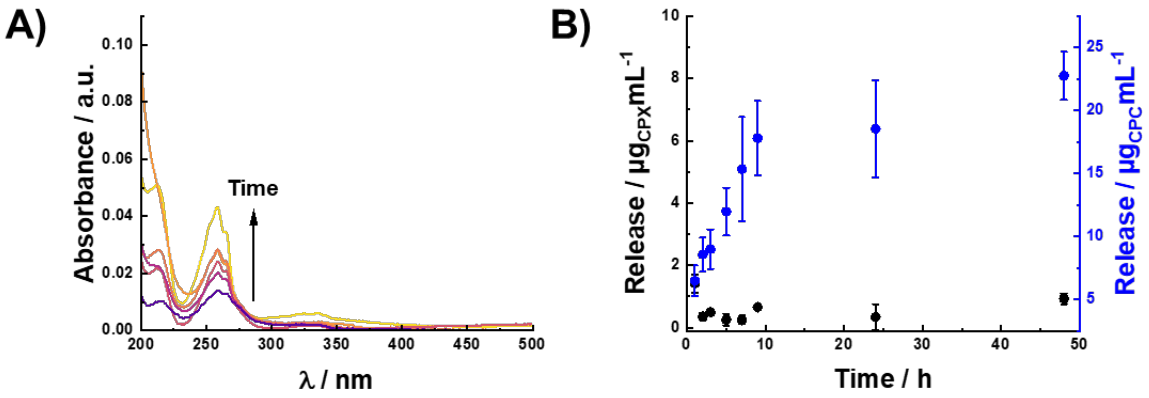

Figure 5.22. Release studies of **SiO_2⊃CPC-CPX** under stirring at 25 ºC. (A) representative UV/Vis spectra of released antibiotic in water and (B) cumulative release of **CPC** and **CPX** over 48 h.

We further explored the release abilities of designed nanoparticles by physical disruption of included micelles by chemical trapping. This procedure allowed us to explore the maximum release of antibiotics from nanoparticles. Chemical trapping has been previously reported as a phenomenon taking place when short length alcohol concentration is increased in an aqueous micelle solution, which lead to micelle size reduction, and eventually, micelle disruption.[80] Upon increasing alcohol concentration micelle destabilisation takes place, ending in micelle breakdown and subsequent release of entrapped cargo.

Upon stirring of nanoparticles in methanol (2 mg/mL) for 24 h, a release of 6.4 ± 0.7 μg_{CPX}/mL of **CPX** and 140 ± 14 μg_{CPC}/mL of **CPC** was calculated for **SiO_2⊃CPC-CPX**; similar to the released 165 ± 20 μg_{CPC}/mL from **SiO_2⊃CPC**.

5.2.5. Validation of encapsulation strategy with rifampicin

Beside **CPX**, another hydrophobic antibiotic, rifampicin (**RIF**), was chosen to explore the ability of **CPC** micelles to enhance the encapsulation and delivery of hydrophobic antibiotics from silica nanoparticles. This work was fully performed by Dr. Maria L. Odyniec, and it is part of the scientific publication resulted from this work. Thereby, a brief overview of the results will be presented in this section in order to demonstrate that the designed encapsulation strategy can be translated to other hydrophobic antibiotics. All data related to the encapsulate of **RIF** via entrapment in **CPC** micelles can be found in the article associated with this chapter.[81]

5.2.6. Synthesis and characterization of PSQ⊃CPX

PSQ nanoparticles containing **CPX** antibiotic (**PSQ⊃CPX**) were synthetized based on previously reported methodology by K. Okamoto *et al*.[49] Briefly, **PSQ⊃CPX** were synthetized in aqueous basic conditions in presence of **CPX**. Due to the low solubility of the BTEB precursor, the aqueous mixture of BTEB was sonicated in order to achieve a homogenous emulsion. Then, the emulsion was stirred at room temperature for 20 h followed by 72 h in reflux, yielding a white precipitate. **PSQ** particle with no antibiotic were synthetized through the same methodology in absence of **CPX**.

5.2.6.1. Size and morphology of PSQ and PSQ⊃CPX

Electron microscopy imaging of **PSQ⊃CPX** particles (Figure 5.23A and 23C) revealed leaf-like nanoparticles with uniform dimensions with size distributions by TEM of 72 ± 8 nm and 38 ± 8 nm, for both, longitudinal and axial dimensions (n = 50). Observed morphology was previously reported by K. Okamoto *et al*.[49] PSQ nanoparticles also

displayed described morphology, with again, very similar dimensions compared with **CPX** containing **PSQ⊃CPX** (Figure 5.S17).

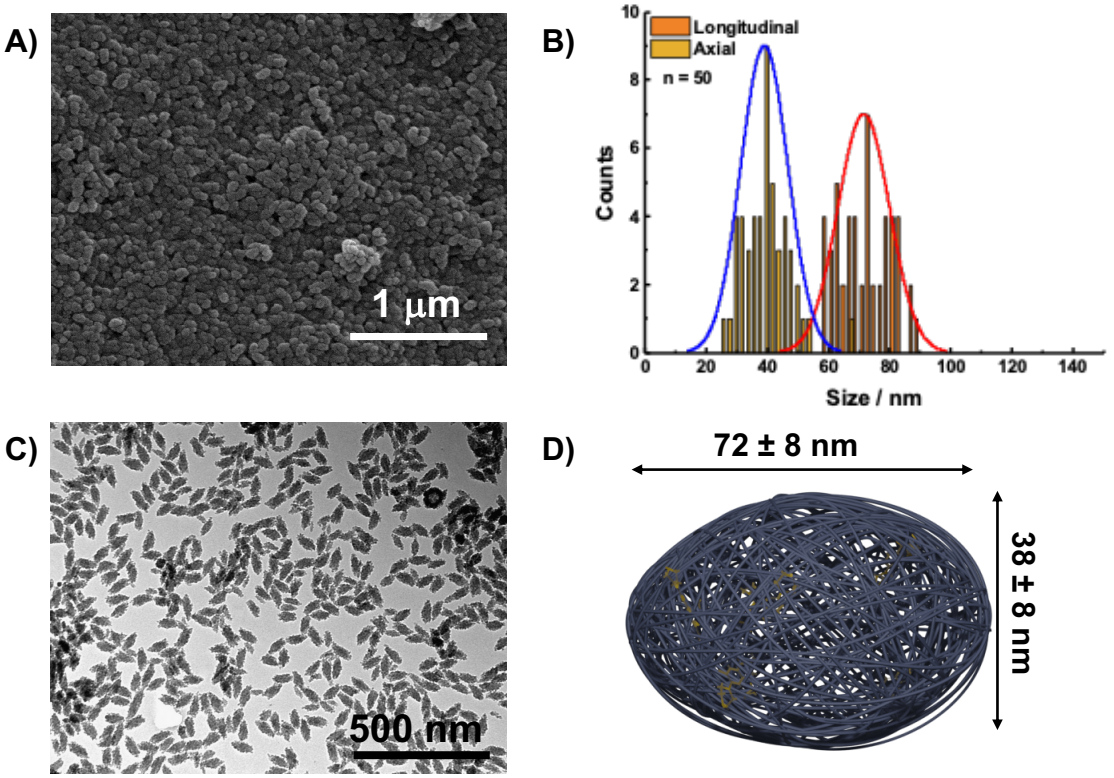

Figure 5.23. Morphological study of **PSQ⊃CPX**. (A) SEM and (C) TEM images of **PSQ⊃CPX** and (B) nanoparticle size distribution based on TEM images (n = 50). (D) graphical representation of a single **PSQ⊃CPX** nanoparticle with estimated dimensions based on TEM images.

Resulted **PSQ⊃CPX** displayed a hydrodynamic size of 94 ± 44 nm by volume and 66 ± 32 by number; with a PDI of 0.14 indicating that the nanoparticles had good monodispersion (Figure 5.S16, Table 5.6). Nevertheless, due to the non-spherical morphology of nanoparticle, DLS measurements are not fully representative, as DLS assume the morphology of particles to be spherical.[82] Moreover, a ζ-potential of – 48 ± 9 mV was measured. Yielded nanoparticles would present a high concentration of benzene moieties within the framework, which would increase the hydrophobicity of the it; however, the high concentration of hydroxyl groups from the silyl moieties of the

precursor also contributed to the final surface ζ-potential, resulting in negative values. Unloaded particles, **PSQ**, displayed very similar ζ-potential, summarised in Table 5.S6 and Figure 5.S16.

Presence of **CPX** in **PSQ⊃CPX** was confirmed by spectroscopic techniques (Figure 5.24). Solid-state absorption UV/Vis spectrum of **PSQ⊃CPX** (Figure 5.24A) showed two broad absorption bands, one centred at 270 nm and the other one centred at 333 nm. The band at 270 nm is the results of overlapping of **CPX** high energy absorption band (270 nm), which has undergone a small red shift (5 nm) and the absorption band arising from the benzene groups of the frameworks (264 nm), as it was also observed in case of **PSQ** nanoparticles. The band centred at 333 nm was assigned to the broad band of **CPX** in solid-state centred at 325 nm. Observed bathochromic shift in both absorption bands was associated with potential π–π interactions between the antibiotic and the benzene groups of the framework. In fact, same bathochromic shift was observed previously in case of **CPC-CPX** micelles, were π–π interactions were confirmed by NMR studies (Figure 5.10) and previously described in the literature.[83] Moreover, solid-state emission of **PSQ⊃CPX** (Figure 5.24B) upon excitation at 340 nm, showed a emission profile with λ_{max} = 440 nm, which is 7 nm red shifted compared with **CPX**'s emission (λ_{em} = 340 nm, λ_{max} = 433 nm), which also confirmed **CPX** successful encapsulation in the **PSQ** framework (Figure 5.24B). Fluorescence lifetime measurement of **CPX** in **PSQ⊃CPX** (λ_{exc} = 372 nm, λ_{em} = 440 nm) (Figure 5.24C, Table 5.3) showed no significance difference respect to **CPX**. Usually, when fluorescence molecules are included in **SiO_2** frameworks, their lifetimes are lengthened as they are protected from oxygen quenching.[84] The absence of change in this case was associated to a quenching, also due to the π–π interactions with the

framework. These consequences resemble to the lifetime shortening of **CPX** upon **CPC** micelle entrapment (Figure 5.15). The emission quenching due to interactions with the framework was also confirmed after measuring **CPX** lifetime in **SiO_2⊃CPX** (Figure 5.24C). In this case, a lifetime lengthening was observed (Table 5.3) alongside a blue shift in **CPX**'s emission (λ_{max} = 426 nm, Figure 5.24B). Finally, FT-IR analysis (Figure 5.S18) of nanoparticles confirmed the presence benzene groups in the nanoparticle framework as C-H_{Ar} vibrations were observed at 3050 cm^{-1} and 2990 cm^{-1}, along with Si-C vibrations at 730 cm^{-1}. IR vibrations associated with **CPX** were also observed at 1710 cm^{-1} (C=O carbonyl) and at 1620 cm^{-1} (N-H bending).

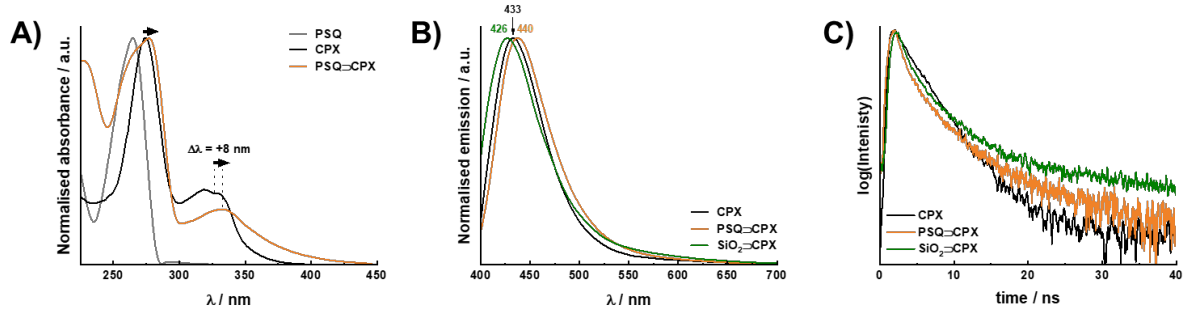

Figure 5.24. Spectroscopic analysis of powder **PSQ⊃CPX, SiO_2⊃CPX** and **CPX**. Solid-state (A) UV/Vis, (B) fluorescence emission (λ_{exc} = 340 nm) and (C) lifetime decay (λ_{exc} = 372 nm, λ_{em} = 440 nm) of **PSQ⊃CPX**.

Table 5.3. Exponential decay fitting of solid-state **CPX** in **PSQ⊃CPX** and **SiO_2⊃CPX** solid state fluorescence (λ_{exc} = 372 nm, λ_{em} = 440 nm)

	τ_1 / ns (%)	τ_1 / ns (%)	χ^2
CPX	2.4 (59 %)	3.8 (41 %)	1.099
PSQ⊃CPX	0.9 (30 %)	3.6 (41 %)	1.093
SiO_2⊃CPX	1.1 (32 %)	4.5 (68 %)	1.105

5.2.6.2. Quantification of PSQ⊃CPX loading

Quantification of included **CPX** within **PSQ⊃CPX** was estimated, as previously described, by UV/Vis spectroscopic estimation of remaining **CPX** in the synthesis

solution and washings, and by TGA (Figure 5.S23). UV/Vis analysis of synthesis supernatant and washings lead to an estimated loading of 14 $\mu g_{CPX}/mg_{NPs}$, with a loading efficiency of 65 %. The thermal degradation curve of **PSQ⊃CPX** (Figure 5.S23B) showed initial weigh loss step between 30 ^oC and 120 ^oC that was associated with the loss of absorbed water molecules. The later degradation step from 200 ^oC to 775 ^oC was dominated by the thermal degradation of the framework, being **CPX**'s degradation pattern not very visible. Nevertheless, in case of **PSQ⊃CPX** a small degradation step between 250 ^oC and 400 ^oC which was also present in **CPX**'s thermal degradation, confirming its presence. Upon direct comparison with unloaded silica nanoparticles, **PSQ**, a total antibiotic content of 16 $\mu g_{CPX}/mg_{NPs}$ was estimated for **PSQ⊃CPX**, which is in good agreement with the calculated loading by UV/Vis spectroscopy.

5.2.6.3. Porous structure of PSQ and PSQ⊃CPX

Finally, the porous structure of resulted **PSQ** nanoparticles was explored by nitrogen porosimetry. Initially, the N_2 isotherm of unloaded **PSQ** was investigated (Figure 5.25A). Recorded isotherm displayed an estimated BET surface area of 332 ± 2 m^2g^{-1} with a type 3 hysteresis associated with the presence of groove pores according to the IUPAC guidelines.[85] Observed porous structure was already described by K. Okamoato *et al*.[49] A estimated pore size of 5.6 nm and 8.8 nm was calculated from the isotherm. Pore with above 10 nm was associated with interparticle gaps. The observed porous structure, in fact, would ease the diffusion of molecules through the framework. Furthermore, absorption-desorption isotherm of loaded **PSQ**, **PSQ⊃CPX** (Figure 5.25B), did, however, result in a decrease of BET surface area to 26.1 ± 0.2 m^2/g, which was associated with the presence of the antibiotic within the framework.

Similarly, a decrease in all pore size was observed, associated with the presence of **CPX**.

In order to further confirm if the reduction in BET surface area of **PSQ⊃CPX** was due to the presence of **CPX**; **PSQ⊃CPX** nanoparticles were stirred in water for 48 h, in order to achieve maximum antibiotic release. Then, particles were isolated, washed and dried. Porosimetry investigation of particles after release (Figure 5.25B) showed an increase in BET surface area, from 21.6 ± 0.2 m^2/g to 38.9 ± 0.3 m^2/g, with no significant alteration in isotherm shape or hysteresis.

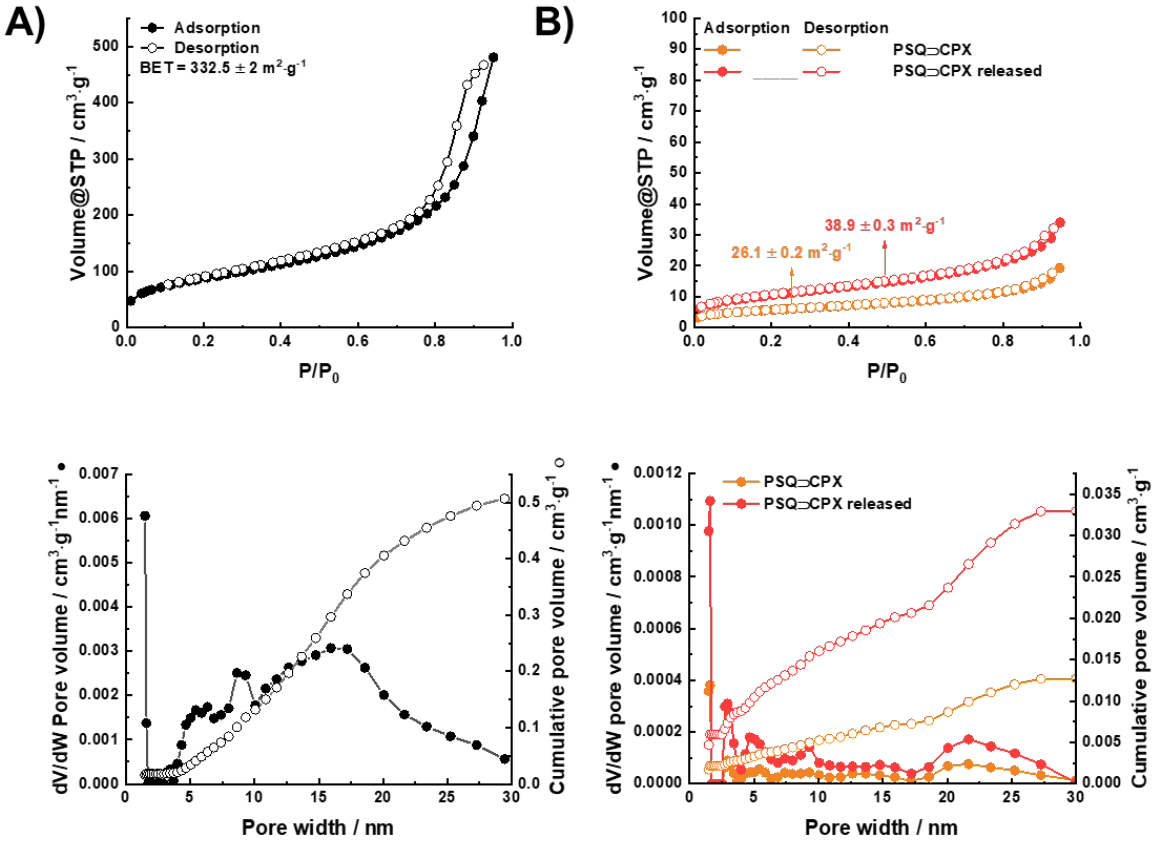

Figure 5.25. N_2 adsorption-desorption isotherms at 77 K and calculated pore size distribution of (A) **PSQ**, (B) **PSQ⊃CPX** before and after 48 h of stirring release.

5.2.7. Release studies of PSQ⊃CPX

The ability of developed **PSQ⊃CPX** to release included antibiotic was studied. For it, as with previous nanoparticles, **PSQ⊃CPX** suspension of 2 mg/mL were stirred in water at 25 ºC, and released **CPX** was quantified by UV/Vis spectroscopy at different time points (Figure 5.26). Release profile of **CPX** shows a cumulative release up to 120 min, where it seemed the maximum release of the antibiotic was not reached yet. At 120 min a cumulative release of 1.4 ± 0.1 $\mu g_{CPX}/mg_{NPs}$ was estimated, which was estimated to be 14.1 ± 1.1 % of included **CPX**. Furthermore, **CPX** release from **PSQ⊃CPX** under static conditions after 120 min was also analysed, resulting in a release of 0.70 ± 0.04 $\mu g_{CPX}/mg_{NPs}$ (6.7 ± 0.4 %).

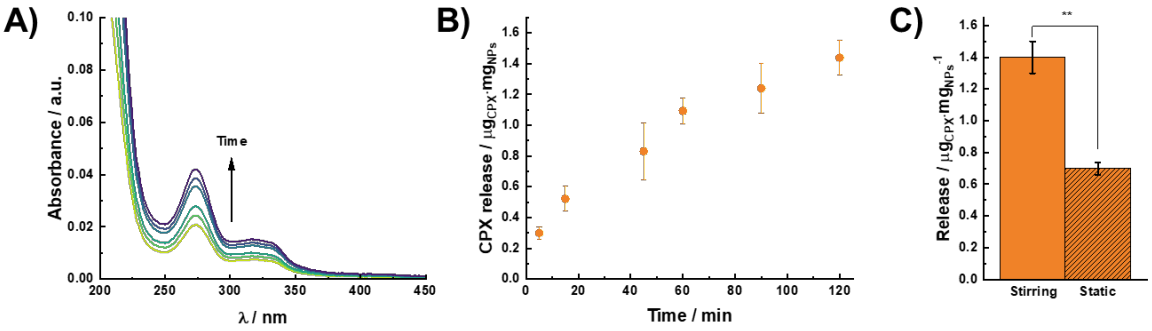

Figure 5.26. Release studies of **PSQ⊃CPX**. (A) representative UV/Vis spectra of released antibiotic in water and (B) cumulative release of **CPX** over 120 min under stirring at 25 ºC. (C) Comparative release of **CPX** from **PSQ⊃CPX** under static and stirring conditions at 25 ºC after 120 min. Statistical significance calculated by t-test, ns = not significant, * p < 0.05, ** p < 0.01 and *** p < 0.001, n = 3 for all studies.

5.2.8. Comparative study of CPX release from novel nanoparticles

As the main objective of these studies is to explore the design of novel nanoparticles for more efficient **CPX** release, a comparative release study between nanoparticles containing **CPX** was performed. For it, silica nanoparticles with included **CPX** (**SiO_2⊃CPX**), novel silica nanoparticles with included **CPX** via **CPC** micelle entrapment

(**SiO_2⊃CPC-CPX**) and **PSQ** nanoparticles with included **CPX** (**PSQ⊃CPX**) were compared. Moreover, as the most explored silica-base drug delivery system are MCM-41 MSN nanoparticles, MSN nanoparticles with adsorbed **CPX** (**MSN@CPX,** estimated loading of 115 $\mu g_{CPX}/mg_{NPs}$) were also included in these studies (Full characterization in Figure 5.S19). **MSN@CPX** were synthetized and characterized by Grace Ball, and kindly given for these studies.

For comparison purposes, cumulative release studies over 120 min under stirring at 25 ºC were analysed (Figure 5.27A). Release profile of **MSN@CPX** showed a burst initial released before reaching the plateau within the first 30 min with a cumulative maximum release of 73.4 ± 5.3 % after 120 min. **MSN@CPX**, was, in fact, the nanoparticles design with the higher **CPX** cumulative release after 120 min of stirring. After it, **PSQ⊃CPX** showed the highest cumulative release. Nevertheless, **PSQ⊃CPX** showed a cumulative **CPX** release, and, after 120 min, the plateau was not reached. Both, **SiO_2⊃CPX** and **SiO_2⊃CPC-CPX** showed lower cumulative **CPX** release of 2.4 ± 0.2 % and 1.4 ± 0.3 %, respectively. However, **SiO_2⊃CPC-CPX** did show cumulative release over time, while **SiO_2⊃CPX** resulted in a fast-initial release with no cumulative release after it.

The release behaviour of **MSN@CPX** can be explain based on the nanoparticle's structure. **CPX** is adsorbed within the pores of the MSN, open to the outside. This architecture leads to fast and uncontrollable release of cargo within the pores, as previously described.[2] **SiO_2⊃CPX**, in the contrary, presents a non-porous structure where the diffusion of included **CPX** is hindered by the lack of porosity. Observed burst initial release was associated with **CPX** molecules in or close to the surface, while those **CPX** molecules further into the nanoparticle core could not be released. The

inclusion of **CPX** *via* entrapment of **CPC** micelles, as previously shown, lead to a nanoparticle architecture with higher porosity, which would facilitate **CPX** diffusion, and hence, achieving a more prolonged antibiotic release for **SiO_2⊃CPC-CPX.** Nevertheless, formed porosity is not interconnected, also hindering the release of those antibiotic molecules further into the nanoparticle core. This would explain that **CPX** release from **SiO_2⊃CPC-CPX** reached its plateau within 60 min. Finally, **PSQ⊃CPX** nanoparticles present a higher intrinsic porous structure, and surface area, through which **CPX**'s diffusion could took take place, leading to cumulative release over time.

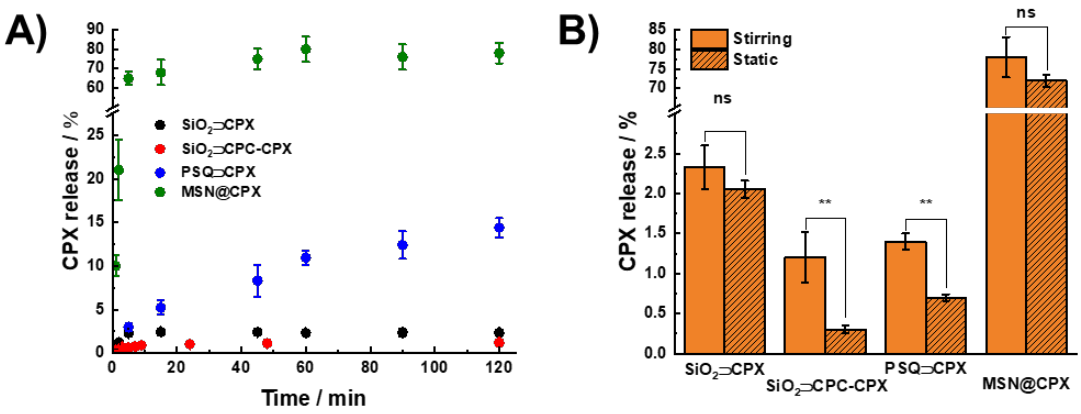

Figure 5.27. Comparative release studied among selected **CPX**-loaded nanoparticles. (A) Time dependant release of **CPX** from nanoparticles in water upon stirring at 25 ºC and (B) Comparative release of **CPX** from nanoparticles under static and stirring conditions at 25 ºC after 120 min. Statistical significance calculated by t-test, ns = not significant, * $p < 0.05$, ** $p < 0.01$ and *** $p < 0.001$, n = 3 for all studies.

In addition, comparative release studies of developed nanoparticle library under static and stirring for 120 min (Figure 5.27B) revealed that only developed **SiO_2⊃CPC-CPX** and **PSQ⊃CPX** nanoparticles have a trigger dependant release, with low **CPX** leakage under static conditions. **SiO_2⊃CPX** and **MSN@CPX** did not show any difference between both conditions. The presence of unidimensional open pores in case of

MSN@CPX and the release of only **CPX** molecules in or close to the surface of **SiO_2⊃CPX** were the reasons associated with observed results.

Lastly, experimental release profiles were fitted according to two different release kinetic models for quantitatively study (Equations 1 and 2, Table 5.4 and Figure 5.S20). The Higuchi and Korsmeyer-Peppas model (Eq. 4.1) were chosen as they represent the most employed kinetic-release models in the literature. The Higuchi model (Eq, 4.2), developed in 1963, represents the first mathematical drug release model and its main assumption is that the drug is released from a flat surface (ointment bases).[86] Its application for drug release modelling from nanoparticles is supported by the fact that at microscopic level, the nanoparticle surface can be considered a flat surface. The Korsmeyer-Peppas model, firstly proposed in 1983 for polymeric matrixes, does not assume the geometry of the drug delivery system.[87]

Korsmeyer-Peppas equation:

$$\frac{M_t}{M_\infty} = K_{kp} t^n \qquad \text{Eq. 4.1}$$

Higuchi equation:

$$\frac{M_t}{M_\infty} = K_{kp} t^{1/2} \qquad \text{Eq. 4.2}$$

From both fitting a constant related with the antibiotic release rate (K_h for Higuchi model and K_{kp} for Korsmeyer-Peppas model). In both cases, the same tendency is observed. **MSN@CPX** is the nanoparticle design that displayed the faster release rate, followed by **SiO_2⊃CPX**. **SiO_2⊃CPC-CPX** leads to a release rate 3 to 5 time slower than **SiO_2⊃CPX**, as it could be expected based on the experimental drug release

profile. Finally, **PSQ⊃CPX** had the slower release rate, which was estimated to be between 2 and 3 times slowed than **SiO_2⊃CPC-CPX**.

Table 5.4. Kinetic parameter of **CPX** release from studies nanoparticles by Higuchi and Korsmeyer-Pepas models. (M_t/M_∞ = relative **CPX** release respect to the total loading).

	Higuchi model $M_t/M_\infty = K_h t^{1/2}$		**Krosmeyer-Peppas model** $M_t/M_\infty = K_{kp} t^n$		
	K_h / $min^{-1/2}$	**R^2**	**K_{kp} / min^{-1}**	**n**	**R^2**
SiO_2⊃CPX	0.0154 ± 0.0016	0.988	0.0153 ± 0.0021	0.56 ± 0.05	0.993
SiO_2⊃CPC-CPX	0.0035 ± 0.0003	0.983	0.0063 ± 0.0012	0.46 ± 0.03	0.964
PSQ⊃CPX	0.0012 ± 0.0001	0.995	0.0028 ± 0.0004	0.50 ± 0.02	0.993
MSN@CPX	0.4335 ± 0.0550	0.978	0.0974 ± 0.0037	1.17 ± 0.03	0.998

5.2.9. Biocompatibility of novel CPX delivery nanoparticles

To conclude, biocompatibility of developed novel **CPX** delivery systems was assessed by MTT experiments using A549 lung cancer cell line as reference cell line. Obtained results for **SiO_2⊃CPC-CPX** showed no significance cytotoxicity up to 5.00 mg/mL, similar to **SiO_2⊃CPC** (Figure 5.28). In fact, it is well-known the cytotoxicity of **CPC** in concentrations above 8 μg/mL (Figure 5.S22), as previously reported.[88]

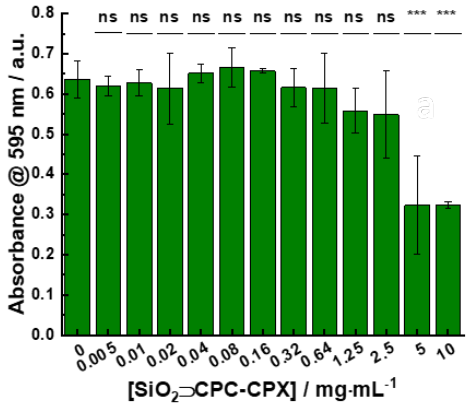

Figure 5280. MTT cell viability assays of A549 cell line incubated with **SiO_2⊃CPC-CPX** nanoparticles for 18 h. Significance was calculated based on 1-way ANOVA followed by Dunnett's t-test corrected for multiple comparisons, ns = no significance * = $p<0.05$, ** $p<0.01$ and *** $p<0.001$, n = 3.

In case of **PSQ** nanoparticles (Figure 5.29), the biocompatibility of unloaded particles was firstly assessed as it has never been explored in the literature before. MTT assays of **PSQ** nanoparticles showed no cytotoxicity of nanoparticle up to 5 mg/mL. The increased toxicity with respect to **SiO_2** nanoparticles was associated with the benzene groups o the framework, which has been known to increase the toxicity of nanoparticles if they are present in their surface.[89] Moreover, nanoparticle shape has been also reported as a factor that influence their biocompatibility, being elongated shaped nanoparticles more toxic.[90] Loaded **PSQ⊃CPX** nanoparticles, similarly, only showed significance toxicity in concentrations over 5 mg/mL. Regarding the MIC of CPX for non-resistant Gram-negative bacterial species (0.25 – 1 μg/mL)[79] a **PSQ⊃CPX** concentration between 0.17 and 0.7 mg/mL would be required, which lays below cytotoxic concentrations.

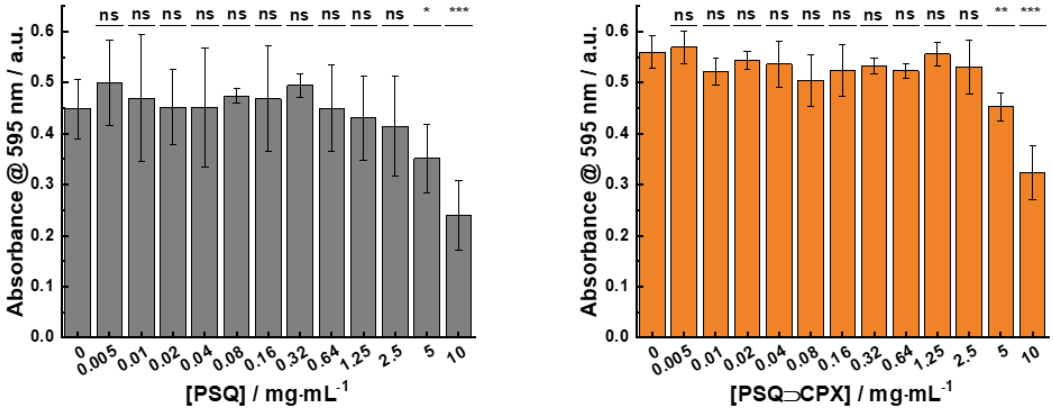

Figure 5.29. MTT cell viability assays of A549 cell line incubated with **PSQ** and **PSQ⊃CPX** nanoparticles for 18 h. Significance was calculated based on 1-way ANOVA followed by Dunnett's t-test corrected for multiple comparisons, ns = no significance * = $p<0.05$, ** $p<0.01$ and *** $p<0.001$, n = 3.

5.3. Conclusion

We developed a new encapsulation method for hydrophobic antibiotics in silica nanoparticles by entrapment of these in antiseptic micelles, leading to high loaded dual antibiotic containing silica nanoparticles. The interactions of model hydrophobic antibiotic **CPX** with **CPC** micelles were explored by DLS, NMR and optical spectroscopy elucidating the interactions and placement of **CPX** antibiotic within the **CPC** micelles, locating it in the palisade region of the micelles. Inclusion of **CPX** via pre-entrapment in **CPC** micelles resulted in a higher loading efficiency of **CPX** comparing with the encapsulation of **CPX** on its own. These results support the efficiency of the entreaty for the encapsulation oh hydrophobic antibiotics. Furthermore, resulting nanoparticles, **SiO_2⊃CPC-CPX,** displayed a porous structure as result of the incorporation of the micelles within the siliceous framework and they were able to release both antibiotics simultaneously. Finally, same study conducted with **RIF** further validated the versatility of developed encapsulation approach.

Antibacterial activity study of designed dual-loaded antibiotic nanoparticles, alongside checkboard assay to explore the synergistic activity of antibiotics, would finalise the study of these nanoparticles and stablish them as a potential antibiotic delivery system.

5.4. Experimental section

5.4.1. Synthesis procedures

SiO_2⊃CPC The Stöber method with modifications was used to synthesise the non-porous silica nanoparticles.[54] First a solution containing EtOH (25 mL), NH_4OH (1.9 mL, 0.93 M), H_2O (1.6 mL, 2.9 M) and TEOS (2.4 mL, 12.4 mmol, 1 equiv, 0.41 M) were added together. The reaction was left to stir (750 rpm) for 3 h at rt. After 3 h a solution of CPC (0.465 g, 1.36 mmol, 0.1 equiv) in H_2O (3 mL) was added and stirred at RT for 6 h. The silica nanoparticles were isolated by centrifugation (15 min, 7830 rpm) and washed with H_2O (3 x 20 mL). After three cycles of the centrifugation-washing procedures, the silica nanoparticles were dried *in-vacuo* to yield a white solid (0.54 g).

SiO_2⊃CPC. The Stöber method with modifications was used to synthesise the non-porous silica nanoparticles. [54] First a solution containing EtOH (25 mL), NH_4OH (1.9 mL, 0.93 M), H_2O (1.6 mL, 2.9 M) and TEOS (2.4 mL, 12.4 mmol, 1 equiv, 0.41 M) were added together. The reaction was left to stir (750 rpm) for 3 h at rt. After 3 h a solution of CPX (0.016 g, 0.048 mmol, 0.004 equiv) in H_2O (3 mL) was added and stirred at RT for 6 h. After three cycles of the centrifugation-washing procedures, the silica nanoparticles were dried *in-vacuo* to yield a white solid (0.32 g).

SiO_2⊃CPC-CPX. The Stöber method with modifications was used to synthesise the non-porous silica nanoparticles.[54] First a solution containing EtOH (25 mL), NH_4OH

(1.9 mL, 0.93 M), H_2O (1.6 mL, 2.9 M) and TEOS (2.4 mL, 12.4 mmol, 1 equiv, 0.41 M) were added together. The reaction was left to stir (750 rpm) for 3 h at rt. After 3 h a premixed solution of CPX (0.016 g, 0.048 mmol, 0.004 equiv) and CPC (0.465 g, 1.36 mmol, 0.1 equiv) in H_2O (3 mL) was added and stirred at RT for 6 h. After three cycles of the centrifugation-washing procedures, the silica nanoparticles were dried *in-vacuo* to yield a white solid (0.34 g).

PSQ. Previously reported methodology reported by K. Okamoto *et al*.[49] was followed. To an aqueous NaOH solution (0.5 N, 13.5 mL) BTEB (0.5 mL, 1.25 mmol) were added. The formed biphasic mixture was sonicated at room temperature for 20 min leading to a white emulsion. Then, the emulsion was stirred at room temperature for 24 h, followed by 72 h in reflux. After three cycles of the centrifugation-washing procedures, the silica nanoparticles were dried *in-vacuo* to yield a white solid (0.25 g).

PSQ⊃CPX. Previously reported methodology reported by K. Okamoto *et al*.[49] was followed. To an aqueous NaOH solution (0.5 N, 13.5 mL) CPX (0.008 g, 0.024 mmol) and BTEB (0.5 mL, 1.25 mmol) were added. The formed biphasic mixture was sonicated at room temperature for 20 min leading to a white emulsion. Then, the emulsion was stirred at room temperature for 24 h, followed by 72 h in reflux. After three cycles of the centrifugation-washing procedures, the silica nanoparticles were dried *in-vacuo* to yield a white solid (0.31 g).

5.4.2. Methodologies

Release studies. Release studies were performed using loaded nanoparticles suspensions (2 mg/mL) in water or in methanol at 25 ^oC under stirring (750 rpm) or

static conditions. Aliquots were then centrifuged (5 min at 14000 rpm) to remove nanoparticles and released **CPC** and **CPX** using a Cary 60 UV/Vis spectrometer.

MTT assays. Cytotoxicity of studied in A549 cell line were performed following the methodology described in Chapter 1 Section 2.4.2.

5.5. Appendix

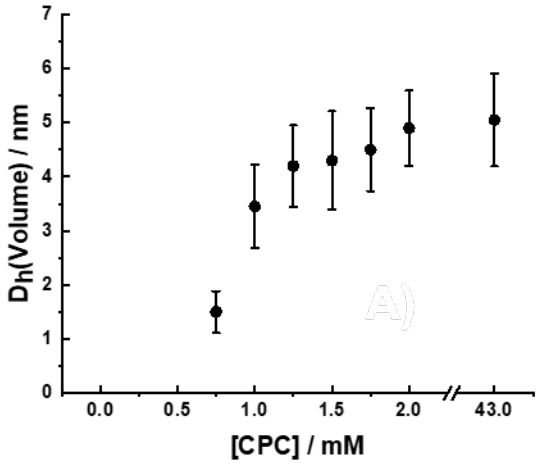

Figure 5.S1. Dynamic light scattering monitoring of the **CPC** micelle formation upon increased **CPC** concentration in carbonate buffer (HCO_3^-/CO_3^{2-}, 0.1 M, pH 10.6). (n=5)

Table 5.S1. Hydrodynamic diameter and ζ-potential measurements of CPC micelles (2 mM) before and after CPX addition (6 mM) in carbonate buffer (HCO_3^-/CO_3^{2-}, 0.1 M, pH 10.6). (n = 5 for hydrodynamic diameter and n = 3 for ζ-potential)

	Hydrodynamic diameter / nm				
	Intensity	**Volume**	**Number**	**PDI**	**ζ-potential / mV**
CPC micelles	5.6 ± 1.4	4.9 ± 1.2	4.2 ± 0.8	0.28	+23 ± 2
CPC micelles + CPX	7.1 ± 1.2	6.8 ± 1.2	6.5 ± 0.9	0.25	+15 ± 1

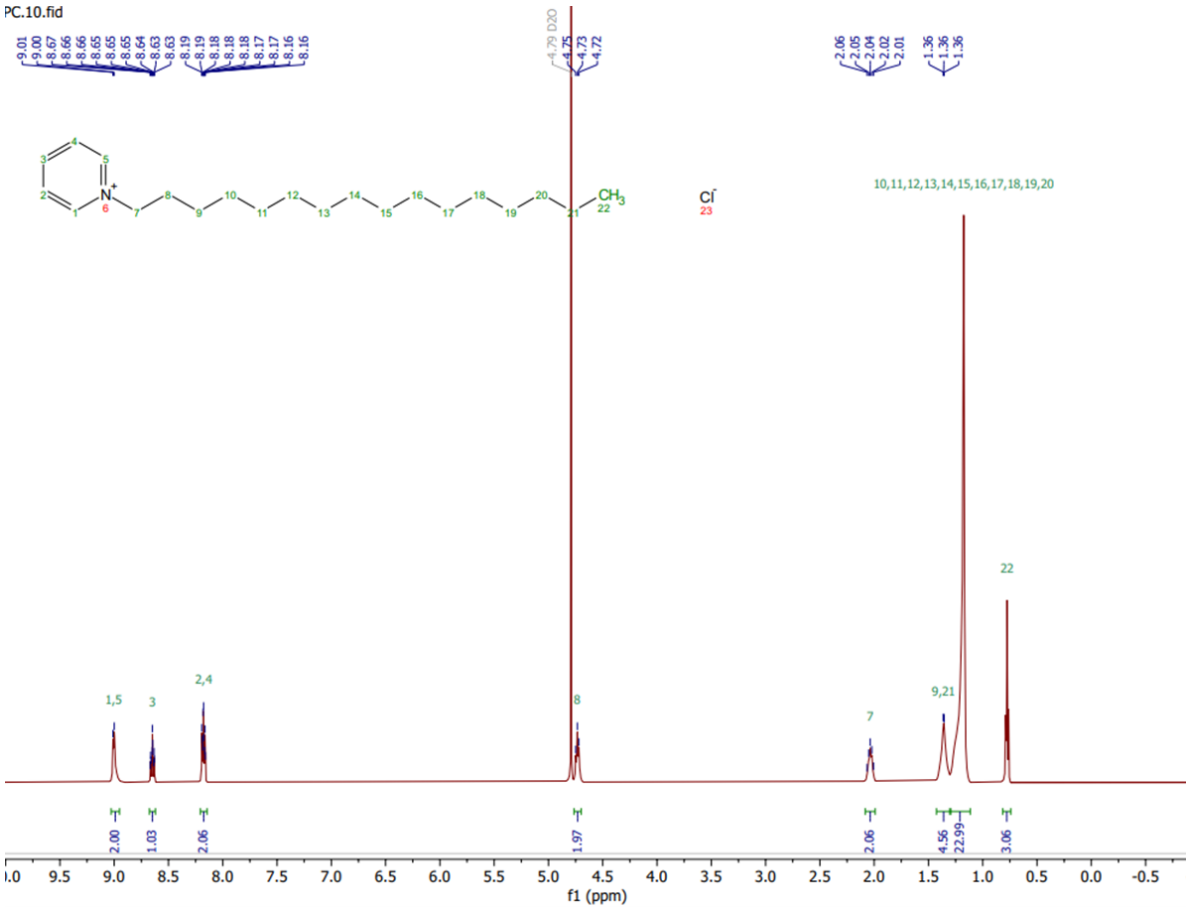

Figure 5.S2. ^{1}H-NMR (500 MHz, HCO_3^-/CO_3^{2-} D_2O buffer, 0.1 M pD 10.6) of **CPC** (0.5 mM).

Table 5.S2. ^{1}H-NMR (500 MHz, HCO_3^-/CO_3^{2-} D_2O buffer, 0.1 M pD 10.6) chemical shifts between **CPC** bellow (0.5 mM) and above (2 mM) the CMC.

Proton	**1 & 5**	**3**	**2 & 4**	**8**	**7**	**9,21**	**10-20**	**22**
Δδ ppm	+0.031	+0.023	+0.031	+0.014	+0.03	−0.006	−0.026	−0.024

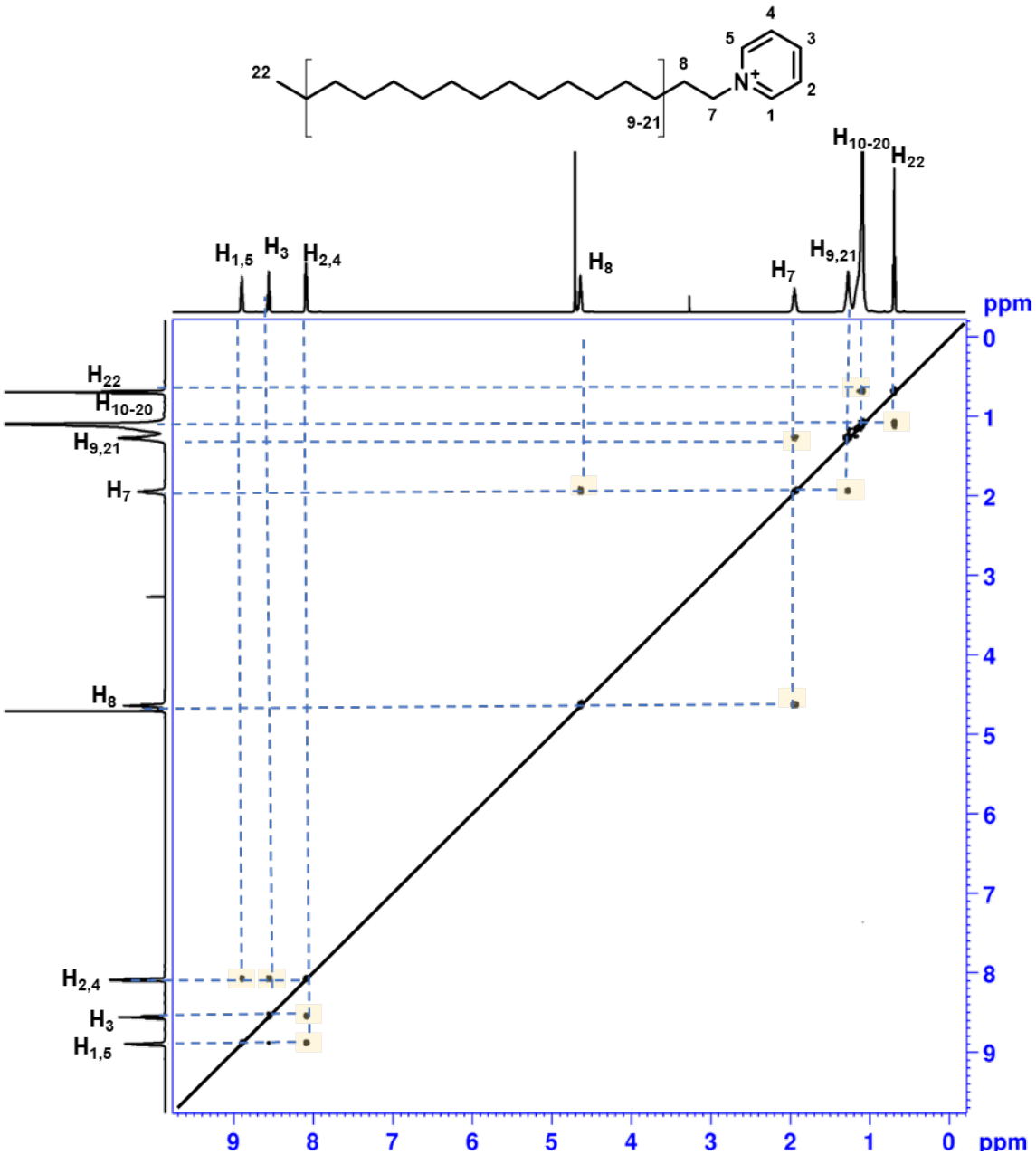

Figure 5.S3. COSY (500 MHz, HCO_3^-/CO_3^{2-} D_2O buffer, 0.1 M, pD 10.6) of **CPC** (2 mM) above the CMC.

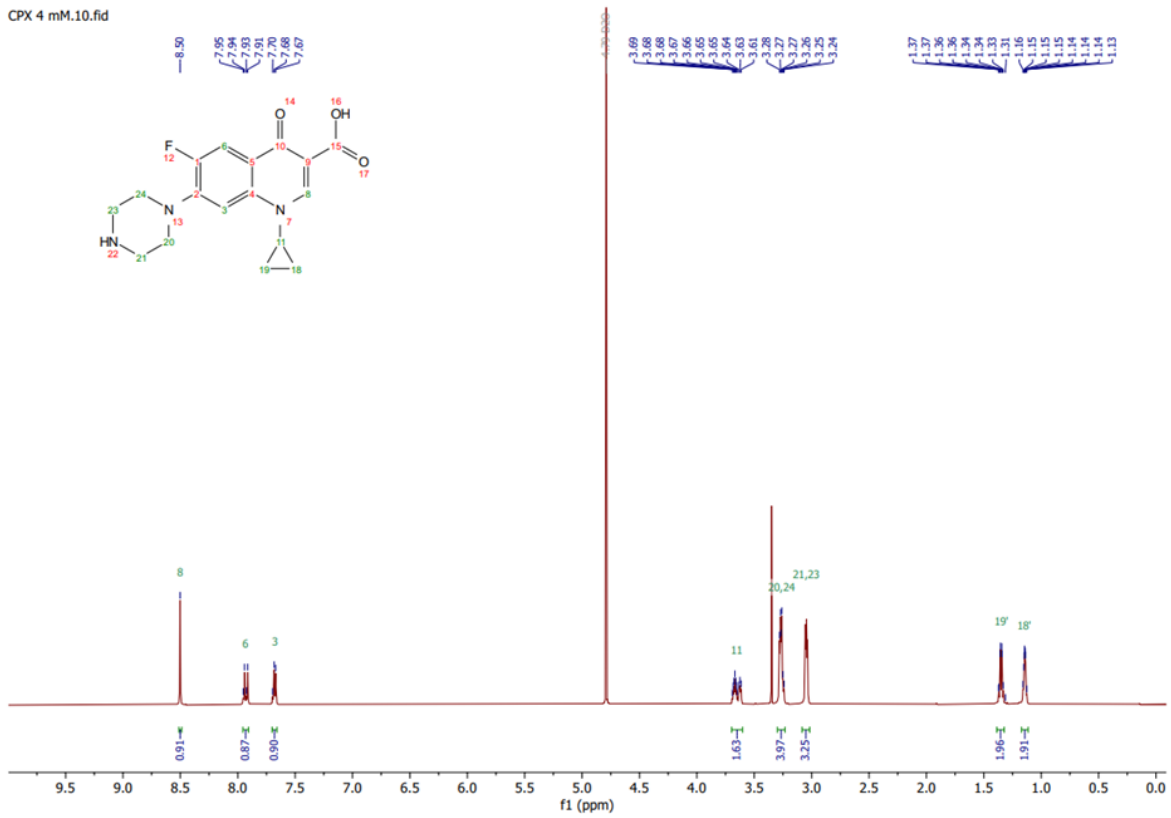

Figure 5.S4. ^{1}H-NMR (500 MHz, HCO_3^-/CO_3^{2-} D_2O buffer, 0.1 M pD 10.6) of **CPX** (4 mM).

Table 5.S3. ^{1}H-NMR (500 MHz, HCO_3^-/CO_3^{2-} D_2O buffer, 0.1 M pD 10.6) chemical shifts of (top) **CPX** (4 mM) and (bottom) **CPC** (43 mM) mixture respect **CPX** (4 mM) and **CPC** (43 mM) on their own.

Proton	**8**	**6**	**3**	**11**	**20&24**	**21&23**	**19**	**18**
Δδ ppm	−0.014	−0.183	−0.139	0	−0.033	−0.032	−0.331	−0.197

Proton	**1&5**	**3**	**2&4**	**8**	**7**	**9,21**	**10-20**	**22**
Δδ ppm	−0.032	−0.060	−0.054	−0.055	−0.062	−0.062	−0.020	0

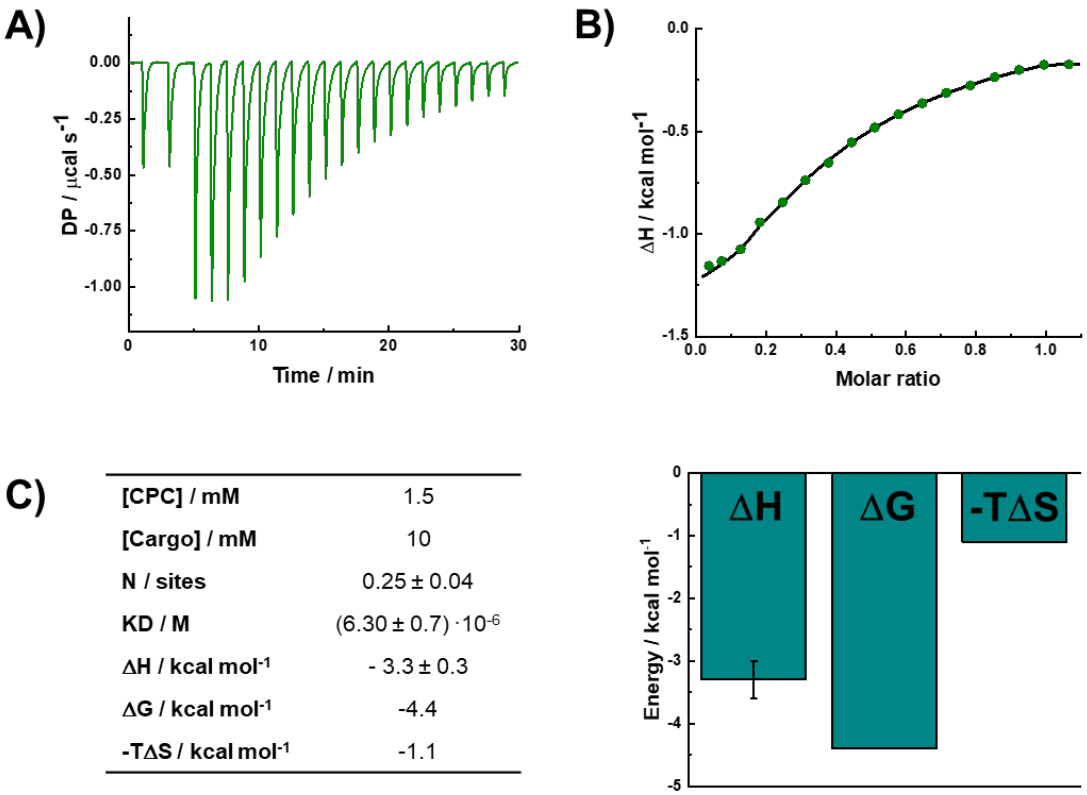

Figure 5.S5. Isothermal Titration Calorimetry (ITC) profiles showing **CPX** interaction with **CPC** micelles. **CPX** titration on **CPC** (2 mM) in carbonate buffer (HCO_3^-/CO_3^{2-}, 0.1 M, pH 10.6). (A, B) Fitted ITC binding curve and (C) thermodynamic parameters estimated from measured binding curve.

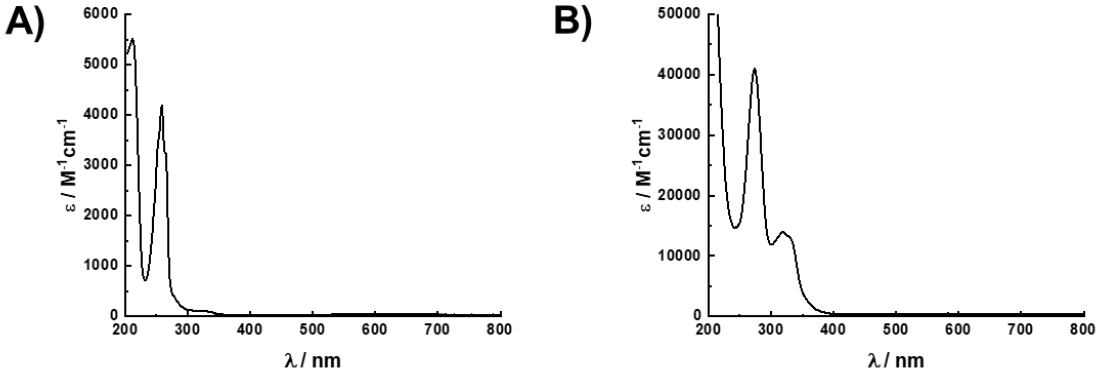

Figure 5.S6. UV/Vis absorption spectrum of (A) **CPC** and (B) **CPX**.

Table 5.S4. Exponential fitting of time-resolved fluorescence studied of **CPX** (10 μM) in absence and presence of **CPC** micelles (2 mM) in carbonate buffer. (λ_{exc} = 375 nm, λ_{em} = 425 nm)

[CPC] / mM	τ_1 / ns (%)	τ_2 / ns (%)	χ^2
0	7.3 (79)	0.8 (21)	1.052
2	3.3 (89)	0.7 (11)	1.147

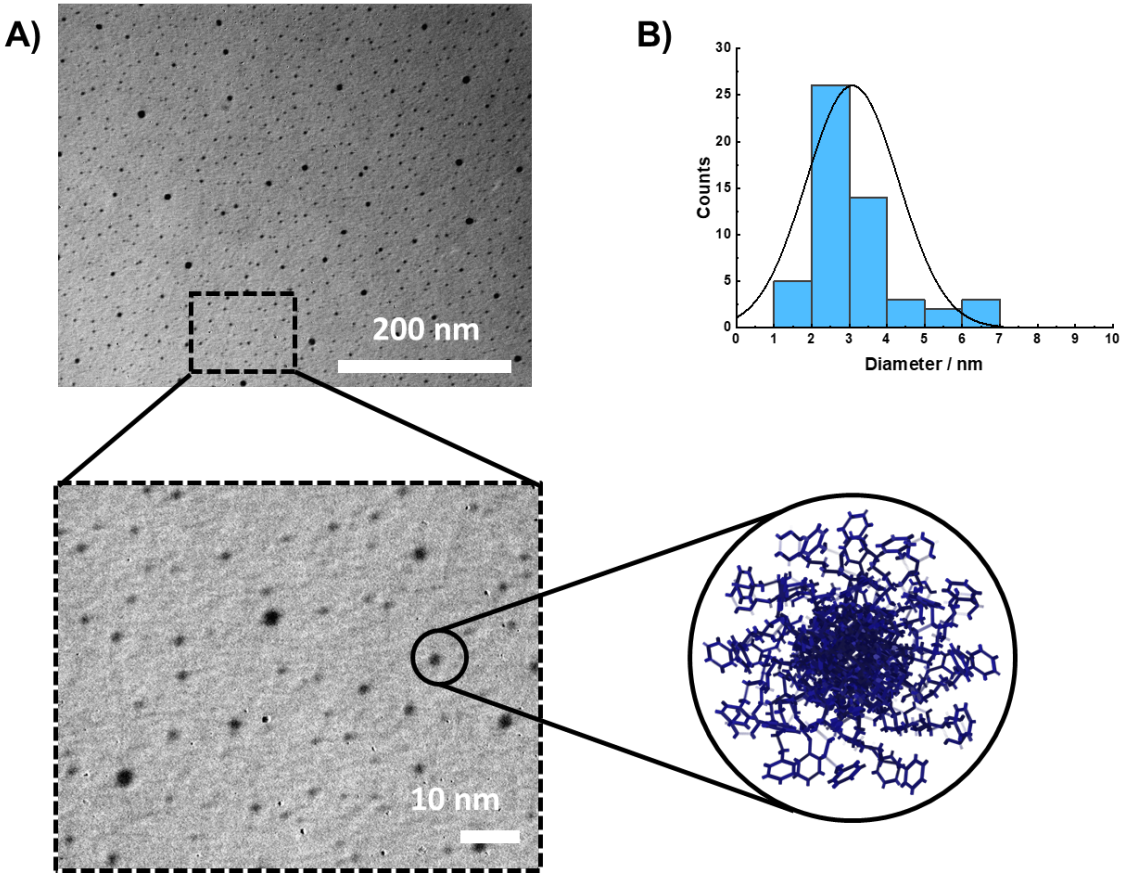

Figure 5.S7. Transmission electron microscopy (TEM) images of **CPC micelles** (43 mM) and normal size distribution of micelles (n = 50).

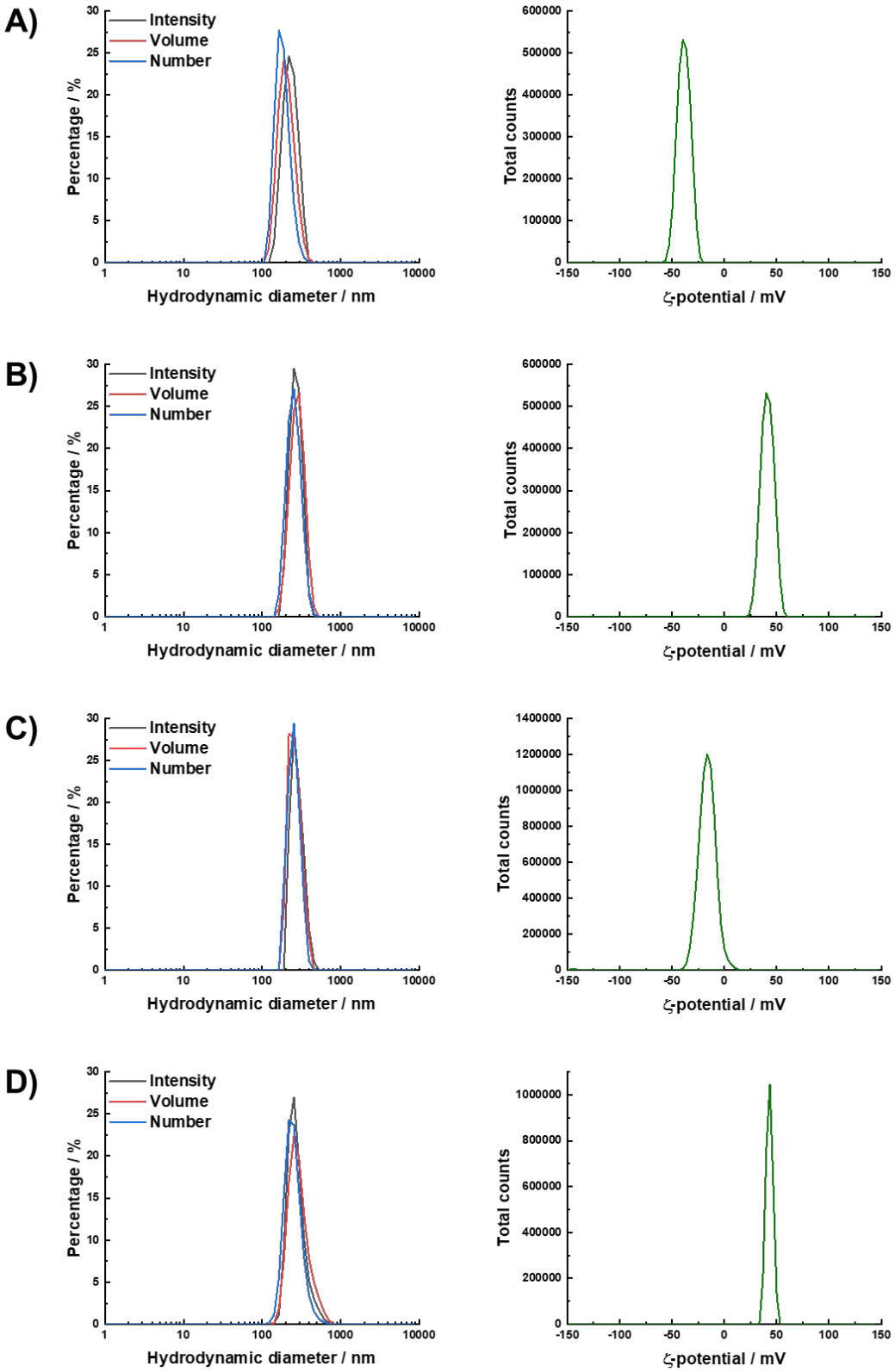

Figure 5.S8. Dynamic Light Scattering and ζ-potential distribution of (A) **SiO_2**, (B) **SiO_2⊃CPC-CPX**, (C) **SiO_2⊃CPC** and (D) **SiO_2⊃CPX**.

Table 5.S5. Dynamic Light Scattering (n = 5) and ζ-potential (n = 3) measurements of **SiO_2**, **SiO_2⊃CPC** and **SiO_2⊃CPC** in water.

	Hydrodynamic diameter / nm				ζ-potential / mV
	Intensity	**Volume**	**Number**	**PDI**	
SiO_2	350 ± 88	405 ± 105	375 ± 90	0.27	−45 ± 7
SiO_2⊃CPC	257 ± 37	263 ± 47	253 ± 45	0.03	+35 ± 17
SiO_2⊃CPX	195 ± 28	187 ± 22	175 ± 14	0.31	−15 ± 5
SiO_2⊃CPC/CPX	250 ± 50	237 ± 42	215 ± 30	0.33	+35 ± 8

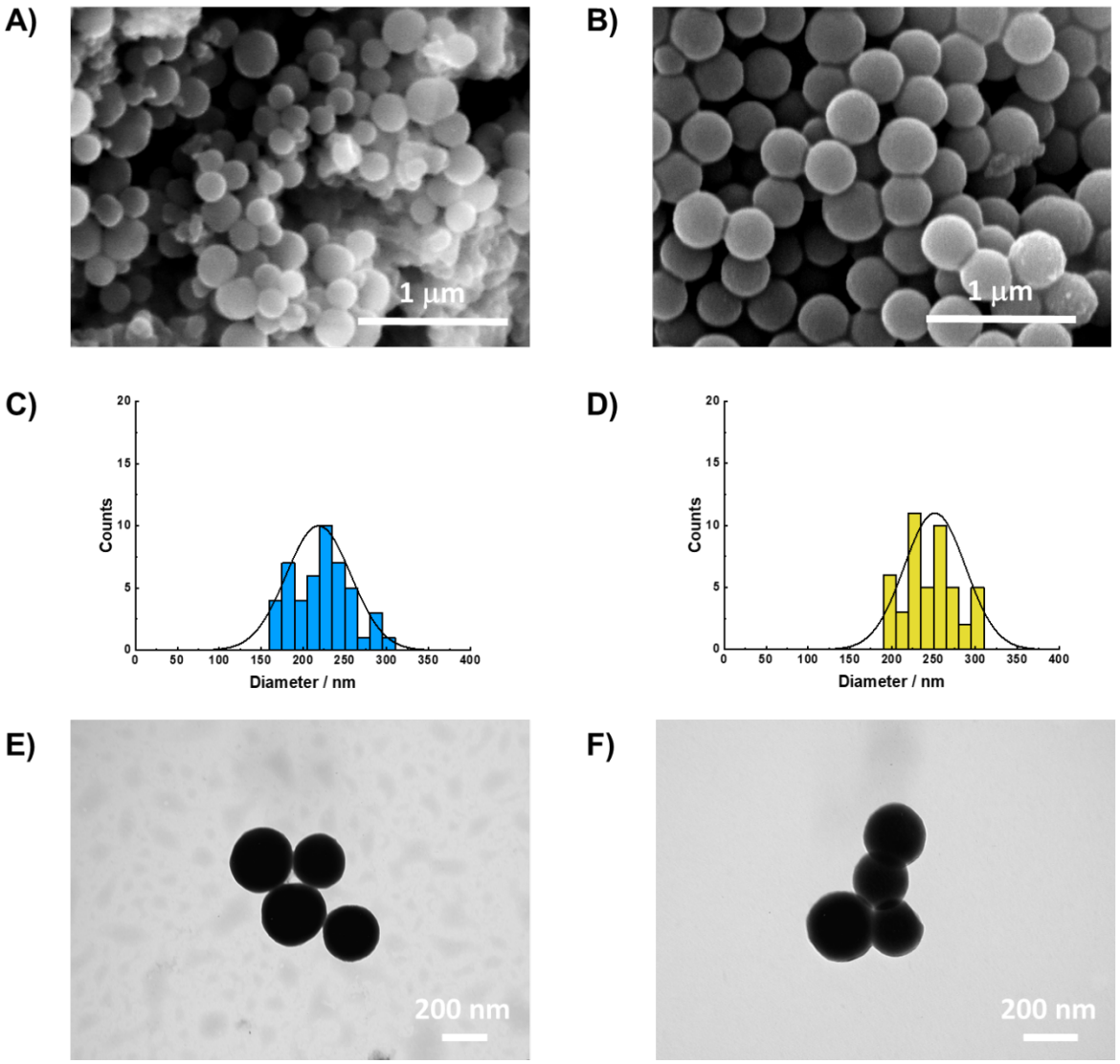

Figure 5.S9. Scanning and Transmission Electron Microscopy of (A and E) **SiO_2⊃CPC** and (B and F) of **SiO_2⊃CPX**. Corresponding size distribution by SEM for (C) **SiO_2⊃CPC** and (D) **SiO_2⊃CPX**.

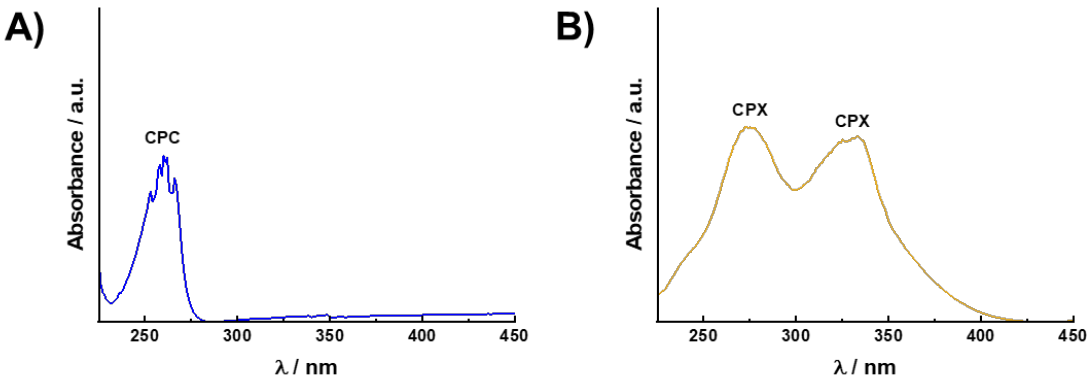

Figure 5.S10. Solid-state UV/Vis spectra of (A) **SiO_2⊃CPC** and (B) **SiO_2⊃CPX.**

A)

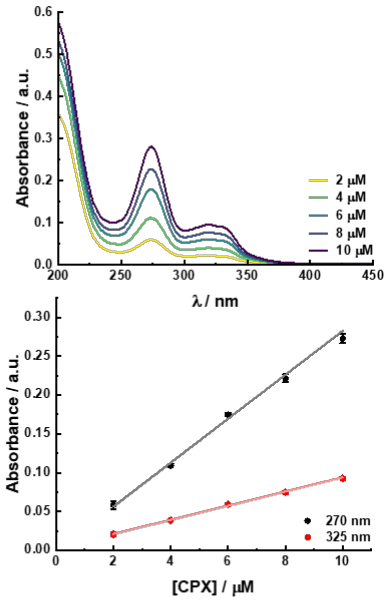

λ = 270 nm	
Equation	y = a + b*x
Weight	Instrumental (=1/ei^2)
Intercept	-2.28826E-4 ± 0.00853
Slope	0.02827 ± 0.00155
Residual Sum of Squares	13.51418
Pearson's r	0.99554
R-Square (COD)	0.9911
Adj. R-Square	0.98813

λ = 325 nm	
Equation	y = a + b*x
Weight	Instrumental (=1/ei^2)
Intercept	0.00292 ± 0.00191
Slope	0.00912 ± 3.26166E-4
Residual Sum of Squares	3.88786
Pearson's r	0.99809
R-Square (COD)	0.99618
Adj. R-Square	0.9949

B)

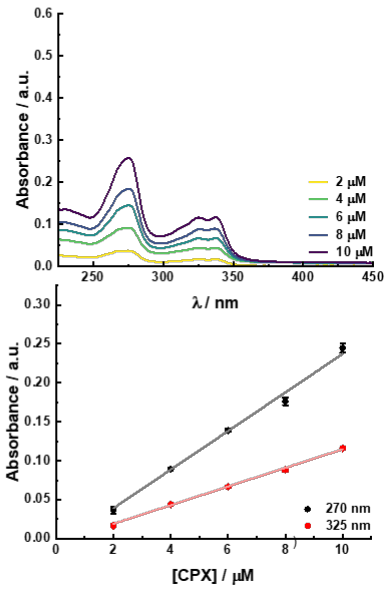

λ = 270 nm	
Equation	y = a + b*x
Weight	Instrumental (=1/ei^2)
Intercept	-0.01044 ± 0.00626
Slope	0.02477 ± 0.00114
Residual Sum of Squares	7.27947
Pearson's r	0.99686
R-Square (COD)	0.99374
Adj. R-Square	0.99165

λ = 325 nm	
Equation	y = a + b*x
Weight	Instrumental (=1/ei^2)
Intercept	-0.00492 ± 0.00211
Slope	0.01197 ± 3.61425E-4
Residual Sum of Squares	4.77386
Pearson's r	0.99863
R-Square (COD)	0.99727
Adj. R-Square	0.99636

Figure 5.S11. UV/Vis calibration of **CPX** in (A) water and (B) EtOH/NH_4OH. (n = 3)

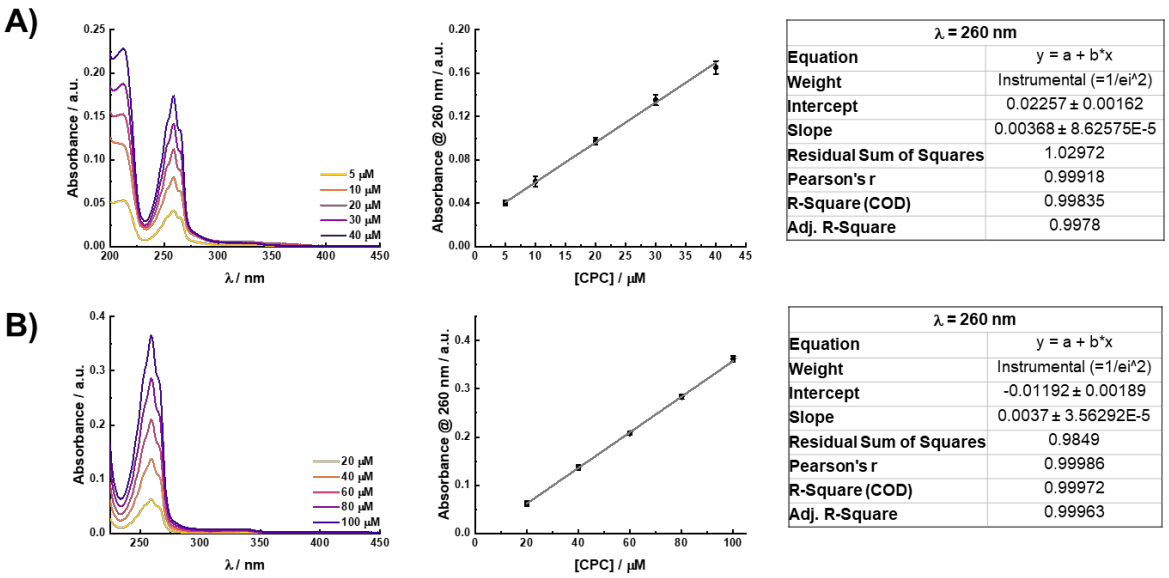

λ = 260 nm	
Equation	y = a + b*x
Weight	Instrumental (=1/ei^2)
Intercept	0.02257 ± 0.00162
Slope	0.00368 ± 8.62575E-5
Residual Sum of Squares	1.02972
Pearson's r	0.99918
R-Square (COD)	0.99835
Adj. R-Square	0.9978

λ = 260 nm	
Equation	y = a + b*x
Weight	Instrumental (=1/ei^2)
Intercept	-0.01192 ± 0.00189
Slope	0.0037 ± 3.56292E-5
Residual Sum of Squares	0.9849
Pearson's r	0.99986
R-Square (COD)	0.99972
Adj. R-Square	0.99963

Figure 5.S12. UV/Vis calibration of **CPC** in (A) water and (B) EtOH/NH_4OH. (n = 3)

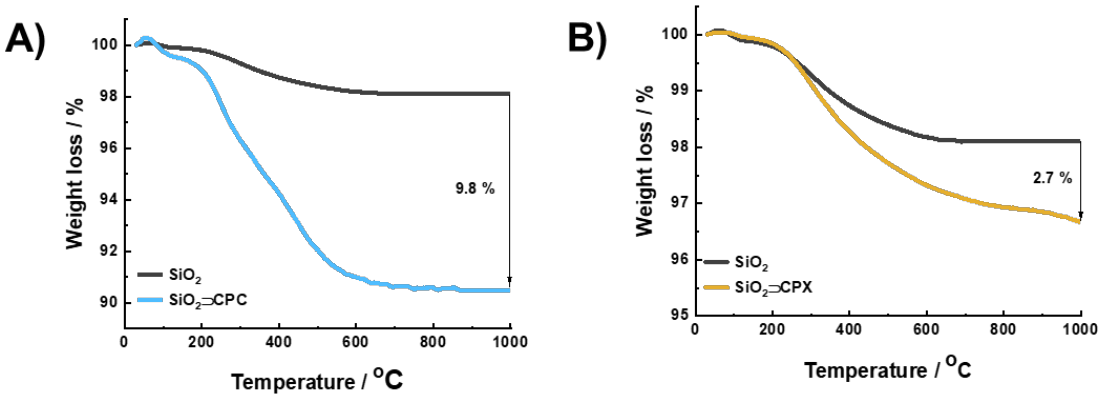

Figure 5.S13. Thermogravimetric analysis (TGA) of (A) **SiO_2⊃CPC** and (B) **SiO_2⊃CPX**. Samples were dried at 120 °C for 2 h prior the analysis. Then samples were heated from 30 °C to 1000 °C at 2 °C min^{-1} under air flow.

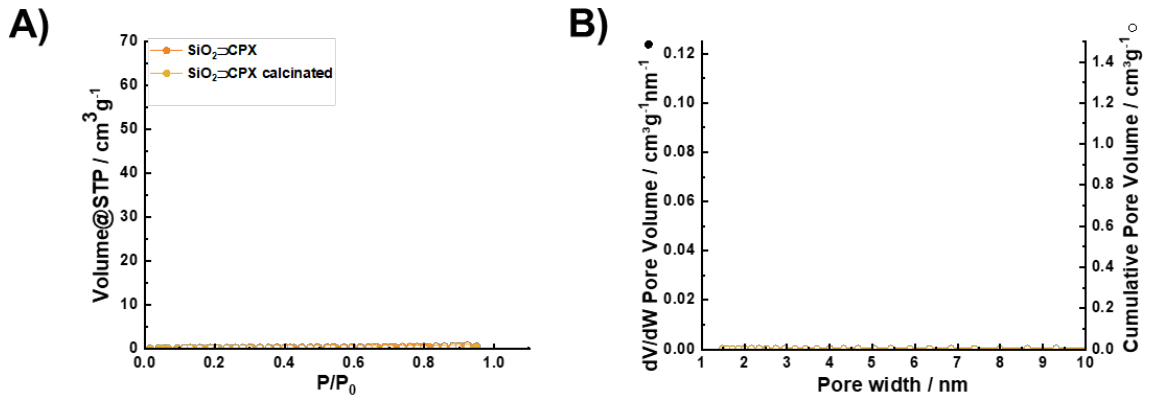

Figure 5.S14. N_2 absorption-desorption isotherms at 77 K and DFT pore distribution of **SiO_2⊃CPX** before and after calcination at 600 ºC for 18 h.

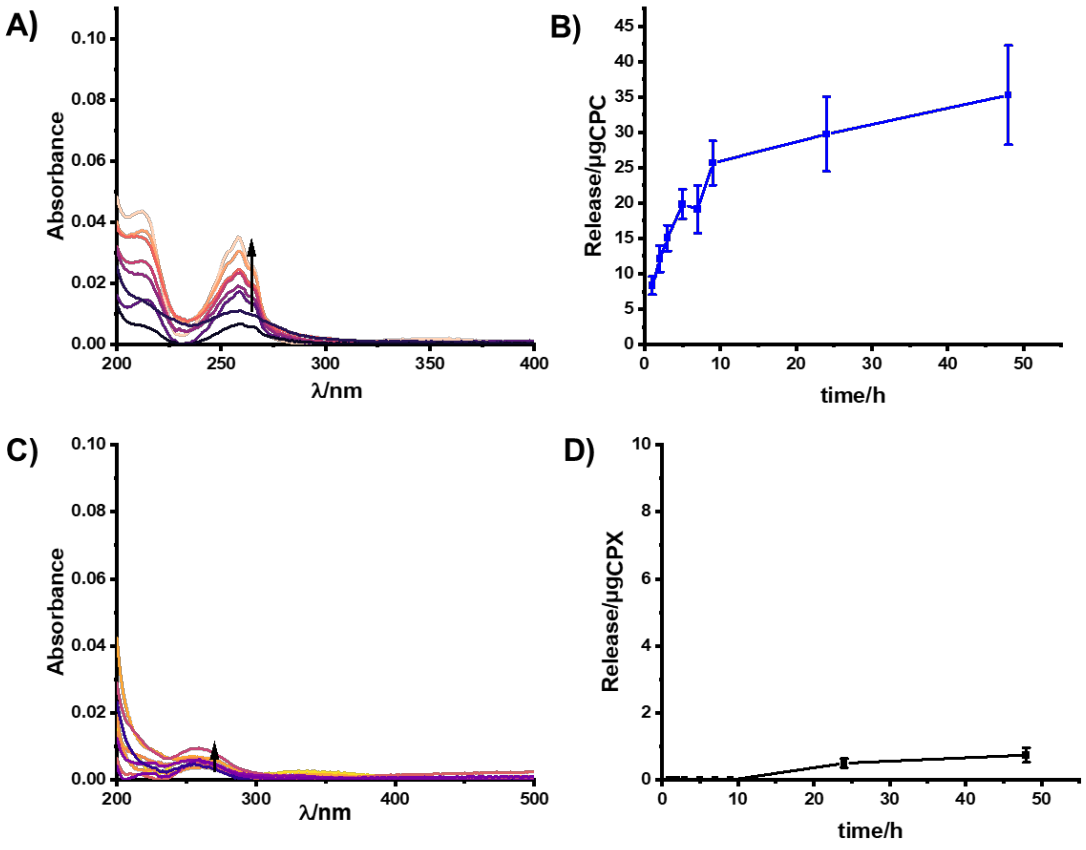

Figure 5.S15. (A, C) Representative absorption spectra of release studies of (A) **CPC** from **SiO_2⊃CPC** and (C) **CPX** from **SiO_2⊃CPX** in H_2O at 25 °C. (B, D) Cumulative release of (B) **CPC** from **SiO_2⊃CPC** and (D) **CPX** from **SiO_2⊃CPX** in H_2O at 25 °C.

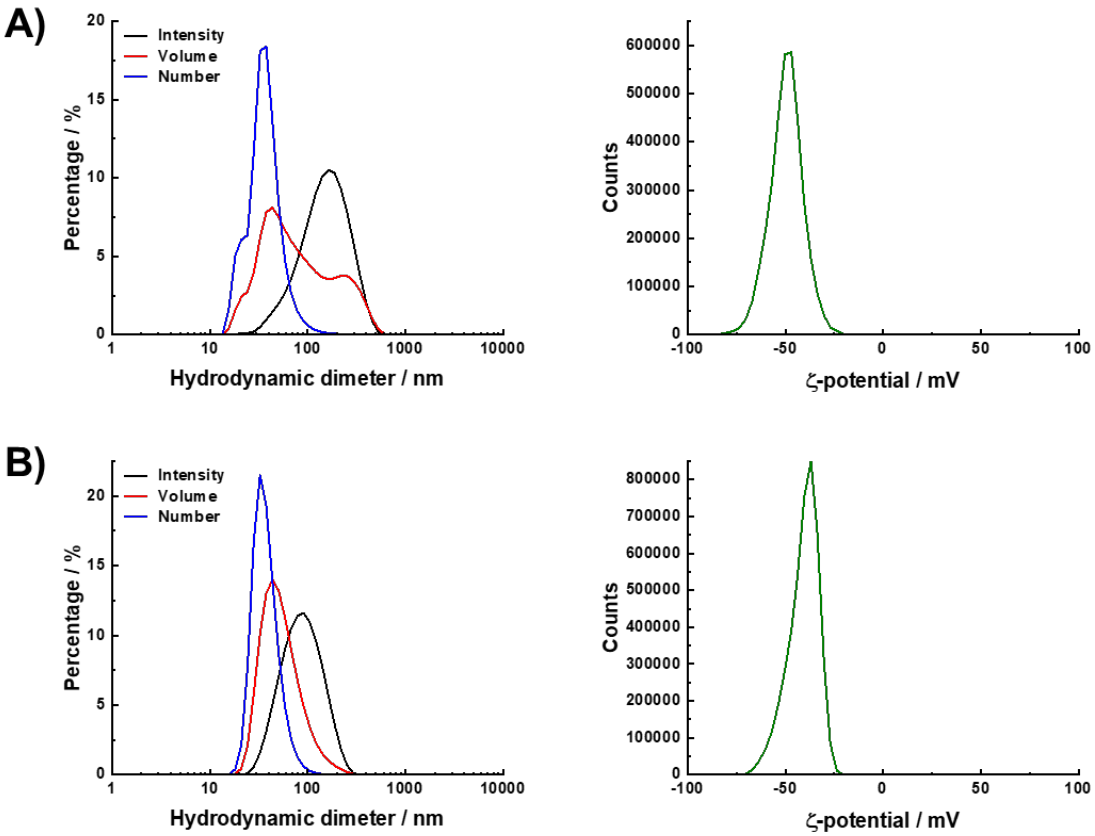

Figure 5.S16. Dynamic Light Scattering and ζ-potential distribution of (A) **PSQ** and (B) **PSQ⊃CPX**.

Table 5.6. DLS (n = 5) and ζ-potential (n = 3) measurements of **PSQ** and **PSQ⊃CPX** particles in PBS buffer (0.1 M, pH 7.4).

	Hydrodynamic diameter (D_h) / nm				**ζ-potential**
	Intensity	**Volume**	**Number**	**PDI**	**/ mV**
PSQ⊃CPX	119 ± 46	94 ± 44	66 ± 22	0.14	-48 ± 9
PSQ	150 ± 89	66 ± 39	59 ± 18	0.24	-50 ± 10

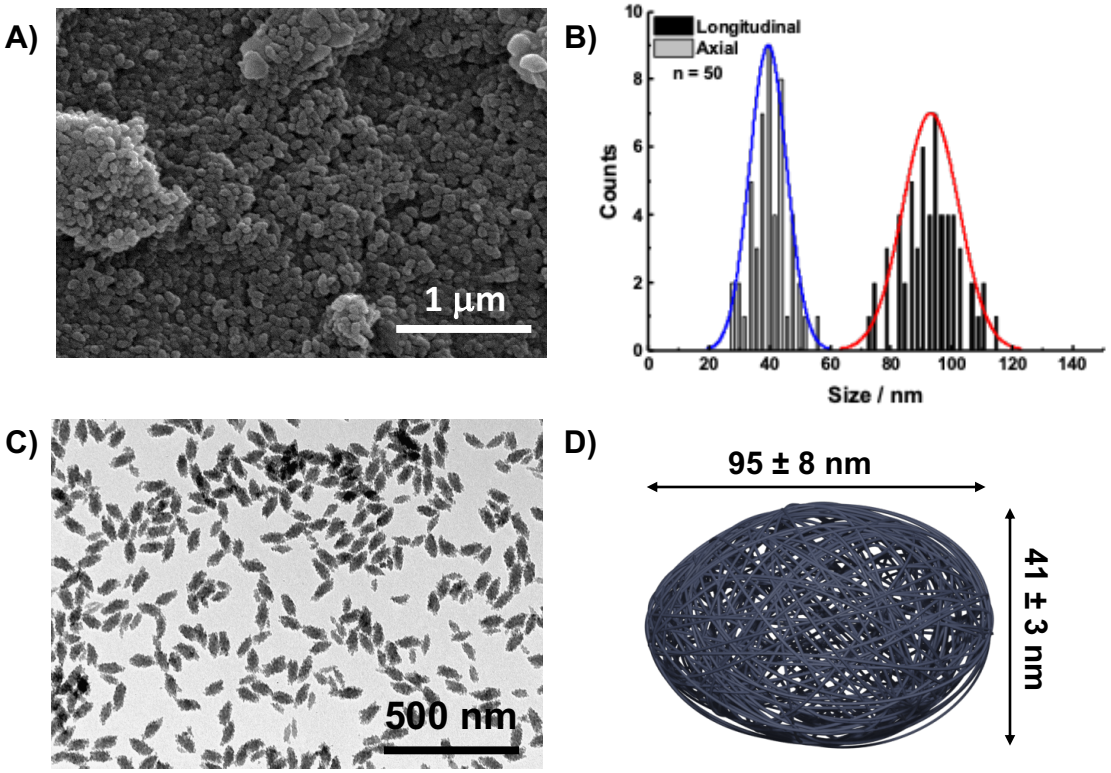

Figure 5.S17. Morphological study of **PSQ**. (A) SEM and (C) TEM images of **PSQ** and (B,D) nanoparticle size distribution based on TEM images (n = 50).

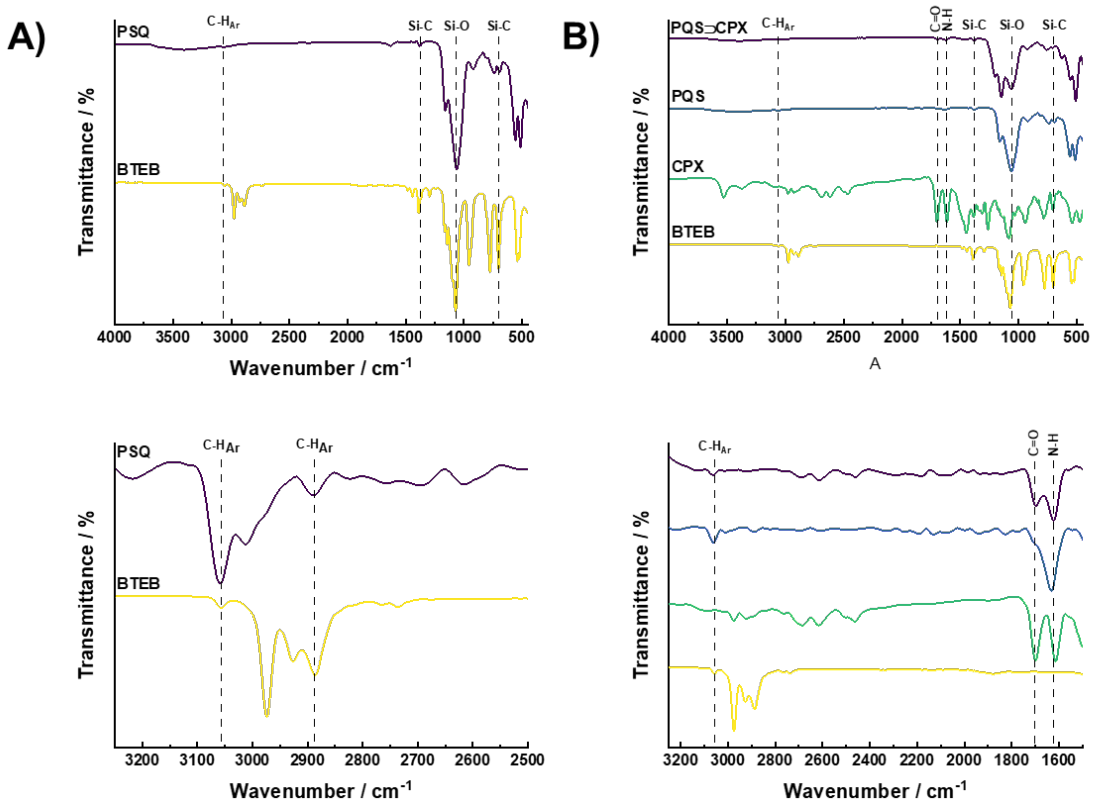

Figure 5.S18. FT-IR spectra of (A) **PSQ** and (B) **PSQ⊃CPX**.

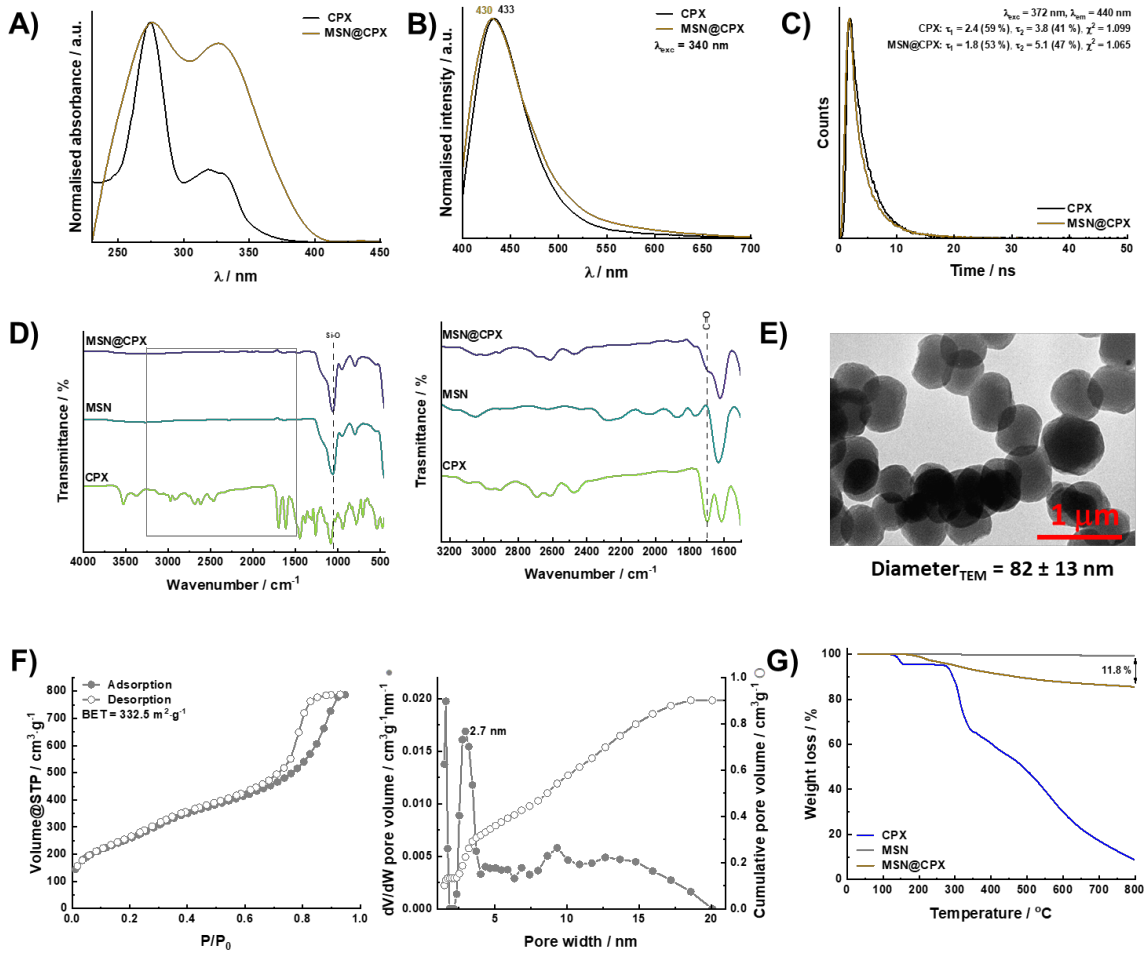

Figure 5.S19. Characterization of **MSN@CPX**. Solid-state (A) UV/Vis, (B) fluorescence emission (λ_{exc} = 350 nm) and (C) emission lifetime decays with fitted parameters. (D) FT-IR spectroscopy of **CPX**, MSNs and **MSN@CPX** nanoparticles confirming CPX inclusion . (E) Transmission Electron Microscopy (TEM) image of nanoparticles and calculated average particle size based on 50 individual particles. (F) N_2 adsorption-desorption isotherm at 77 K displaying the characteristic Type IV isotherm of MSNs and estimate pore size distribution based on DFT calculations. (G) Quantification of adsorbed **CPX** in **MSN@CPX** by thermogravimetric Analysis (TGA). Samples were dried at 120 ºC for 2 h prior the analysis. Then samples were heated from 30 ºC to 1000 ºC at 2 ºC min^{-1} under air flow. Included **CPX** was estimated by direct comparison between unloaded and loaded particles.

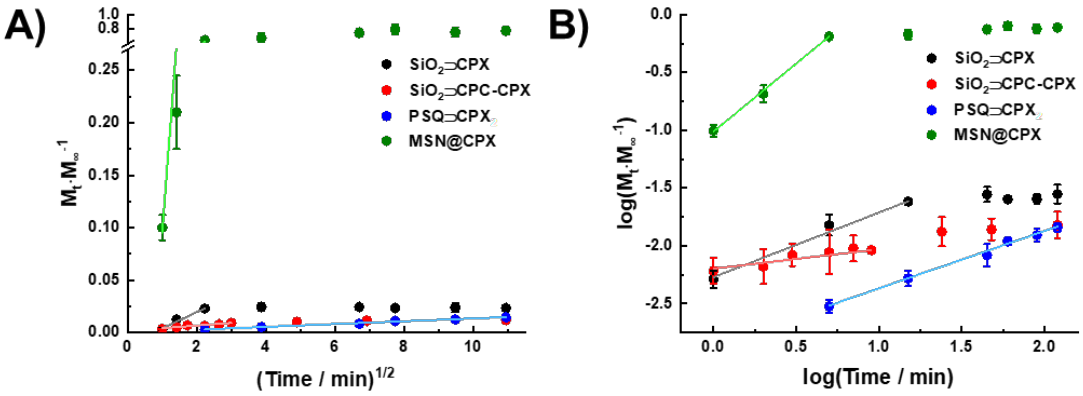

Figure 5.S20. Fitting of **CPX** release data from nanoparticle library. (A) Higuchi and (B) Krosmeyer-Peppas moles were employed for fitting.

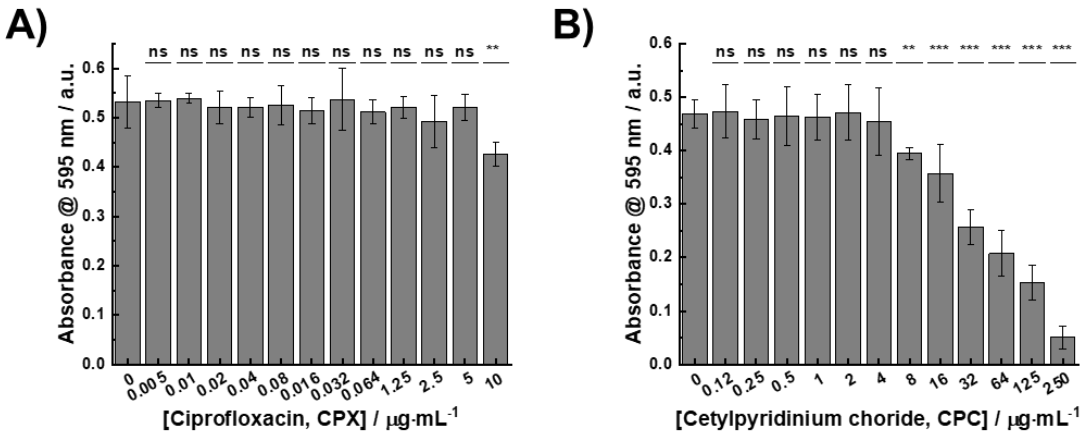

Figure 5.21. MTT cell viability assays of A549 cell line incubated with **CPX** and **CPC** nanoparticles for 18 h. Significance was calculated based on 1-way ANOVA followed by Dunnett's t-test corrected for multiple comparisons, ns = no significance * = $p<0.05$, ** $p<0.01$ and *** $p<0.001$, n = 3.

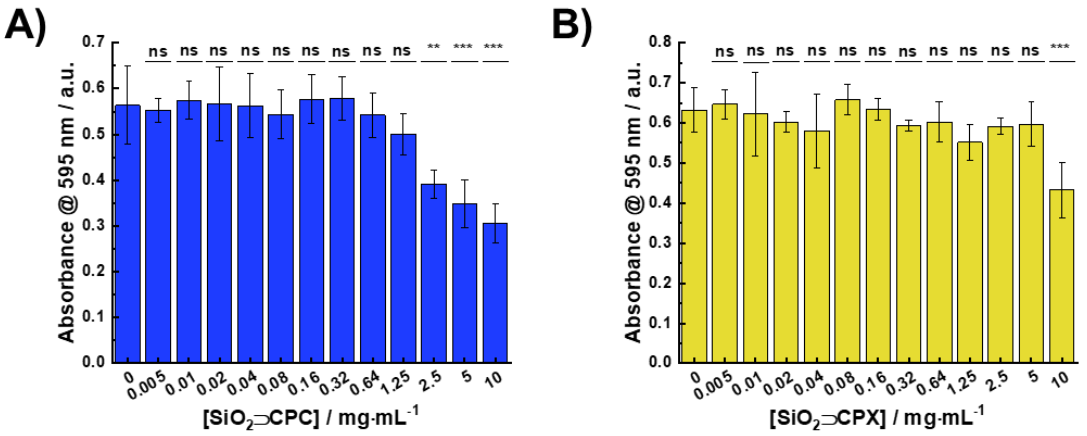

Figure 5.22. MTT cell viability assays of A549 cell line incubated with (A) **SiO_2⊃CPX** and (B) **SiO_2⊃CPX** nanoparticles for 18 h. Significance was calculated based on 1-way ANOVA followed by Dunnett's t-test corrected for multiple comparisons, ns = no significance * = $p<0.05$, ** $p<0.01$ and *** $p<0.001$, n = 3.

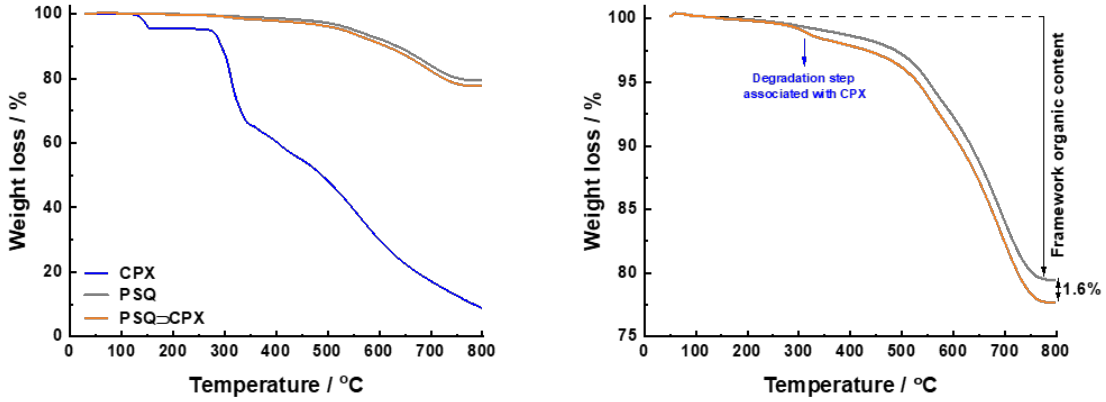

Figure 5.S23. Thermogravimetric Analysis of **PSQ⊃CPX.** Nanoparticles were dried at 120 °C for 1 h prior the measurements. Thermal degradation curve of unloaded nanoparticles (**PSQ**) and antibiotics in added as reference. TGA profile was recorded in a 5 °C min^{-1} heating ramp from 30 to 800 °C under air flow.

Microporous and Mesoporous Materials 363 (2024) 112841

Contents lists available at ScienceDirect

Microporous and Mesoporous Materials

journal homepage: www.elsevier.com/locate/micromeso

Antibiotic entrapment in antibacterial micelles as a novel strategy for the delivery of challenging antibiotics from silica nanoparticles

Asier R. Muguruza [a,1], Maria L. Odyniec [a,1], Menisha Manhota [a,b], Zaina Habib [a], Knut Rurack [c], Jessica M.A. Blair [d], Sarah A. Kuehne [e], A. Damien Walmsley [e], Zoe Pikramenou [a,*]

[a] School of Chemistry, College of Engineering and Physical Sciences, University of Birmingham, Edgbaston, Birmingham, B15 2TT, United Kingdom
[b] Doctoral Training Centre in Physical Sciences for Health, University of Birmingham, Edgbaston, Birmingham, B15 2TT, United Kingdom
[c] Chemical and Optical Sensing Division, Bundesanstalt für Materialforschung und -prüfung (BAM), Richard-Willstätter-Str. 11, 12489, Berlin, Germany
[d] Institute of Microbiology and Infection, College of Medical and Dental Sciences, University of Birmingham, Edgbaston, Birmingham, B15 2TT, United Kingdom
[e] School of Dentistry, College of Medical and Dental Sciences, University of Birmingham, Birmingham, B5 7EG, United Kingdom

ARTICLE INFO

Keywords:
Cetylpyridinium chloride
Micelles
Nuclear magnetic resonance
Antibiotics
Porous silica nanoparticles
Drug delivery

ABSTRACT

Silica materials are popular in biomedical applications as composites and drug delivery platforms due to their low toxicity and biocompatibility. Mesoporous silica nanoparticles are attractive drug delivery systems based on their porous silica framework with high surface area. In the preparation of mesoporous silica frameworks, most commonly, MCM-41, the efficient removal of the template responsible for introducing porous networks, cetyltrimethyl ammonium bromide (CTAB), is a critical step due to the template's high toxicity in the environment and human health. In this work, we present a new one-pot approach of introducing challenging antibiotics within a silica framework without the need of toxic templates, but instead using micelle formation by an antibacterial agent. We demonstrate that micelles formed by cetylpyridinium chloride (CPC), a known antibacterial agent, entrap antibiotics such as rifampicin and ciprofloxacin. Extensive NMR studies elucidate the precise localisation of the antibiotic within the CPC micelle. Ciprofloxacin is placed between the outer and palisade region while rifampicin is located further into the hydrophobic CPC micelle core. In both cases, the formation of the silica framework can be built around the CPC-antibiotic loaded micelles. The resulting silica nanoparticles show loading of both CPC and antibiotic agents, porosity and dual antibacterial release upon disruption of the micelle within the silica framework. The design not only provides a strategy of a therapeutic design to form porous frameworks but also highlights the potential of precise antibiotic dose and release in nanoparticle systems.

1. Introduction

Designs of efficient delivery systems for antibiotics is a key step in controlling antibiotic dose and ultimately plays a role in combatting antibiotic resistance. Silica nanoparticles (SiO_2) are popular drug delivery systems due to their biocompatibility, facile synthesis and tuneable size, from nanometre to micrometres, shape and surface chemistry for functionalisation. [1] Entrapment of drugs in the silica framework is limited by the drugs' solubility and compatibility with the polarity of the silica network. [2,3] This property is particularly pertinent for hydrophobic antibiotics with challenging inclusion in polar frameworks. One of the common approaches for entrapment of antibiotics is the formation of porous networks within the siliceous framework in order to achieve high surface area for drug loading. [1,4] MCM-41 and SBA-15 are among the most popular mesoporous silica nanoparticle topologies, which are well established for agent inclusion in their porous networks. [1] Their formation is based on surfactant based liquid templates which lead to a periodic mesoporous network after its removal. [5–7] The templates used for porosity formation in MCM-41 and SBA-15 are cetyltrimethylammonium bromide (CTAB) and Pluronic P123, respectively. However, CTAB and Pluronic P123 are highly toxic to aquatic life and potential carcinogens (IC_{50} – 30 μM for CTAB and 12–30 μM for P123) [8,9] and complete removal can be challenging. Additionally, the drug uptake of the mesoporous particles relies on the adsorption of the drug within the pores of the particle which results in uncontrolled dose loading and "burst" release upon dispersion of the particles in a liquid medium. Blocking the pores of the particle with chemical functionalisation has been introduced to control of the drug release which requires additional synthesis steps and a reactive stimulus to enable full control over release. [10,11].

An alternative approach to introducing porosity in silica particles uses antibacterial amphiphiles such as octenidine dihydrochloride, [12] cetylpyridinium chloride (CPC), [13,14] and benzalkonium chloride [15] which all adopted MCM-41 topology. We have been interested in alternative methods for inclusion of agents of interest within the silica framework, accompanied by surface modification for imaging [16–18] and drug delivery. [19].

In this work, we introduce a strategy to deliver challenging antibiotics from silica nanoparticles through entrapping into micelles. We employed CPC, an antibacterial amphiphile with a positively charged quaternary ammonium headgroup and a hexadecyl aliphatic tail, widely used in dental products such as mouthwashes [20] which forms micelles. We have examined the inclusion of rifampicin (RIF) and ciprofloxacin (CPX), as examples of poorly water-soluble antibiotics. RIF has previously been shown to only be included in mesoporous silica by its adsorption in the pores, [21] but direct inclusion within silica framework remains a challenge due to its hydrophobicity. Similarly, CPX loading in silica particles is limited to those mesoporous particles with surface functionalisation to assist adsorption. [22,23] Herein we study the entrapment of the antibiotic in micelles and growth of silica nanoparticles in a one-pot approach in order to incorporate antibiotic within the silica framework and examine their release (Fig. 1).

2. Materials and methods

2.1. Materials

Rifampicin (RIF), cetylpyridinium chloride (CPC) and tetraethoxysilane (TEOS) were purchased from Merck and ciprofloxacin (CPX) was purchased from Fluorophen. Rest of chemicals and consumables were purchased from Merck and were of the highest quality available.

2.2. Synthesis of SiO_2

Synthesis of SiO_2 – general procedure 1. The Stöber method with modifications was used to synthesise the non-porous silica nanoparticles. [24] First a solution containing EtOH (25 mL), NH_4OH (1.9 mL, 0.93 M), H_2O (1.6 mL, 2.9 M) and TEOS (2.4 mL, 12.4 mmol, 1 equiv, 0.41 M) were added together. The reaction was left to stir (750 rpm) for 3 h at rt. After 3 h, a solution of antimicrobials was added and stirred at RT for 6 h. The silica nanoparticles were isolated by centrifugation (15 min, 7830 rpm) and washed with H_2O (3 x 20 mL). After three cycles of the centrifugation-washing procedures, the silica nanoparticles were dried *in-vacuo* to yield a powder.

SiO_2 ⊃ CPC. Following general procedure 1, after 3 h a solution of CPC (0.465 g, 1.36 mmol, 0.1 equiv) in H_2O (3 mL) was added. Nanoparticles were isolated as a white powder (0.54 g).

SiO_2 ⊃ CPX. Following general procedure 1, after 3 h a solution of CPX (0.016 g, 0.048 mmol, 0.004 equiv) in H_2O (3 mL) was added. Nanoparticles were isolated as a white powder (0.17 g).

SiO_2 ⊃ RIF. Following general procedure 1, after 3 h a solution of RIF (0.040 g, 0.048 mmol, 0.004 equiv) in EtOH (3 mL) was added. Nanoparticles were isolated as a white powder (0.28 g).

SiO_2 ⊃ CPC-CPX. Following general procedure 1, after 3 h a premixed solution of CPX (0.016 g, 0.048 mmol, 0.004 equiv) and CPC (0.465 g, 1.36 mmol, 0.1 equiv) in H_2O (3 mL) was added. Nanoparticles were isolated as a white powder (0.19 g).

SiO_2 ⊃ CPC-RIF. Following general procedure 1, after 3 h a premixed solution of RIF (0.040 g, 0.048 mmol, 0.004 equiv) and CPC (0.465 g, 1.36 mmol, 0.1 equiv) in EtOH/H_2O (1/3 mL) was added. Nanoparticles were isolated as an orange powder (0.41 g).

2.3. Quantification of antibiotics loaded by UV/Vis

UV/Vis absorption measurements were carried out to determine the amount of antibiotics loaded into the materials using the lowest-energy absorption maximum (Abs_{max}). The concentration of each antibiotic in synthesis conditions were measured before adding to synthesis mixture. Then after synthesis, all supernatants and washings were collected to measure the remaining antibiotic in solution by absorption and analysis via the *Beer-Lambert* law.

Encapsulation efficiency (*EE* in %) is calculated as the percentage of drug that is successfully entrapped into the nanoparticle eq (1):

$$EE = \left(\frac{total\ drug\ added - free\ non\ entrapped\ drug}{total\ drug\ added}\right) \times 100 \qquad \text{eq (1)}$$

The encapsulation efficiency is converted into weight percent (wt%) eq (2):

$$wt = \frac{(EE) \times total\ drug\ added}{mass\ of\ nanoparticles\ synthesised} \qquad \text{eq (2)}$$

2.4. Release studies

Release studies were performed using loaded SiO_2 suspensions (2 mg/mL) in water or in methanol at 25 °C under stirring (750 rpm) for up to 48 h. Aliquots (0.5 mL) were taken at set time points, then centrifuged (5 min at 14000 rpm) to remove nanoparticles and released CPC, CPX and RIF quantified by measuring the remaining supernatant, using a Cary 60 UV/Vis spectrometer by absorption and analysis via the *Beer-Lambert* law. The release experiments were repeated three times.

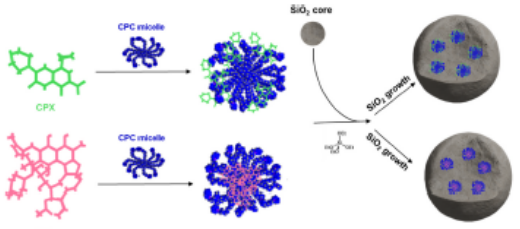

Fig. 1. Scheme of the antibiotic entrapment in CPC micelles and their inclusion in SiO_2 nanoparticles.

* Corresponding author.
E-mail address: z.pikramenou@bham.ac.uk (Z. Pikramenou).
[1] These authors contributed equally to this work.

https://doi.org/10.1016/j.micromeso.2023.112841
Received 28 June 2023; Received in revised form 20 September 2023; Accepted 1 October 2023
Available online 5 October 2023
1387-1811/© 2023 Published by Elsevier Inc.

3. Results and discussion

3.1. Characterisation of CPC micelle-antibiotic interactions

CPC micelle formation has been previously investigated and the critical micelle concentration (CMC) is widely agreed to be 1 x 10^{-3} M in pH neutral aqueous systems at 25 °C. [25–27] In addition, computational DFT simulations have been able to elucidate the most energetically favourable conformation in different solvents, showing that the aliphatic chains are non-linear. [27] In this study, we first investigated the CPC micelles by Dynamic Light Scattering (DLS). We used a CPC concentration of 2 mM which is above the CMC and carbonate buffer (0.1 M, pH 10.6) as dispersing medium to mimic the SiO_2 nanoparticles synthesis conditions (pH 10.5). [28] Under these conditions, CPC micelles are formed with a hydrodynamic diameter of 4.9 ± 1.2 nm (Fig. S1, Table S1).

Titrations of antibiotics, CPX or RIF, into a solution of CPC micelles (2 mM) shows an increase in hydrodynamic diameter with increase in antibiotic concentration up to 6 mM (Fig. 2): from 4.9 ± 1.2 nm to 6.8 ± 1.2 nm for addition of CPX and 7.5 ± 1.2 nm for addition of RIF. An increase in micelle size is previously reported, for other drugs incorporated or associated within micelles. [29–31] The ζ-potentials of unloaded CPC micelles display a positive value of +23 ± 2 mV, due to positively charged pyridinium heads on micelle-water interface. [27] The ζ-potential decreases to +15 ± 1 mV and +19 ± 1 mV upon addition of CPX or RIF, respectively. This decrease is attributed to changes in electron density at the pyridinium head of CPC at pH 10.6. [32,33].

In order to further evidence the interactions between CPC micelles and antibiotics we used Nuclear Magnetic Resonance (NMR) techniques. CPC micelle formation is confirmed by ^{1}H NMR. As the concentration of CPC increases from 0.5 mM (<CMC) to 2 mM (>CMC), characteristic shifts in proton resonances are observed (Fig. S2, Table S2). The pyridinium protons $H_{1,5}$ (δ = 8.89 ppm) and alkyl protons H_7 (δ = 1.94 ppm) and H_8 (δ = 4.63 ppm) show upfield shifts ($\Delta\delta$ = +0.01–0.03 ppm), while the remaining proton resonances of the aliphatic tail $H_{9\text{-}22}$ (δ = 1.08–1.26 ppm) show downfield shifts. These data indicate a change in the environment of CPC upon micelle formation and is supported by previous studies undertaken in D_2O. [34,35] Above the CMC (45 mM), CPC micelles show intermolecular interactions in the NOESY which are not present in the COSY (Fig. S3). The CPC micelles show additional interactions between pyridinium protons $H_{2,4}$ (δ = 8.08 ppm) and $H_{1,5}$ (δ = 8.89 ppm) with aliphatic protons $H_{9\text{-}21}$ (δ = 1.08–1.26 ppm). There are also intermolecular interactions between H_8 (δ = 4.63 ppm) with $H_{9\text{-}21}$ (δ = 1.08–1.26 ppm) and H_8 (δ = 4.63 ppm) with pyridinium protons $H_{1,5}$ (δ = 8.89 ppm), supporting close proximity of CPC molecules.

Firstly, we investigated the proton shifts upon addition of CPX (^{1}H NMR before addition, Fig. S4) to CPC micelles (1:12). CPX is a poorly water-soluble molecule. [36,37] The pKa values for CPX are 5.90 and 8.89 and are associated to the carboxylic acid group and the amine in the piperazine group, respectively. [38] At pD 10.6, it is likely that the carboxylate will interact with the positively charged pyridinium group. In the presence of CPX, the ^{1}H NMR spectra of CPC micelles show small upfield shifts except for the terminal methyl protons (H_{22}, δ = 0.77 ppm) which show no shifts (Fig. S5, Table S3). This phenomenon indicates that the presence of CPX changes the molecular environment of CPC protons. The upfield trend in ^{1}H proton resonance shifts has been reported as evidence between cationic micelles and aromatic molecules. [35,39] As the terminal methyl groups in CPC micelles were not affected by CPX, this suggests the location of CPX is at the micelle-water interface, as previously described for polar molecules on addition to both anionic and cationic surfactant micelles. [35,39,40] Additionally, there are changes in the ^{1}H NMR resonances of CPX in the presence of CPC micelles. Similar to CPC micelles the CPX proton resonances show upfield shifts except for the cyclopropane proton H^a_{11}. However, the fine structures of the splitting patterns change with those of the piperazine protons $H^a_{20,24}$ and cyclopropane protons H^a_{11} and $H^a_{9,18}$ appear broadened and the aromatic protons H^a_6, H^a_3, H^a_8 appear with two sets of resonances. These patterns may indicate the molecules are in different environments affected either by the viscosity of solution, [39] local environments [41] or changes in molecular tumbling. [42] The significant changes observed in ^{1}H NMR spectra of CPX in the aromatic region may be attributed to interactions of the negatively charged π system of CPX with the positively charged pyridinium group of CPC through cation-π interactions. [43–45].

The interactions between CPC micelles and CPX are further investigated by NOESY studies. Two significant NOEs are observed between CPC and CPX (Fig. 3). One NOE corresponds to the interaction between the protons of the cyclopropane ring (H^a_{18}, H^b_{18}) at δ = 0.85 ppm of CPX and the aliphatic chain protons of CPC ($H_{9\text{-}21}$) at δ = 1.30 ppm. The other NOE corresponds to the H^a_{11} proton on the cyclopropane ring at δ = 3.5 ppm and the aliphatic chain protons of CPC ($H_{9\text{-}21}$) at δ = 1.30 ppm. The NOEs for CPC micelle interactions do not change in the presence of CPX which indicates that the micelle has not broken apart, this is also supported by DLS studies. For the CPC micelles a new NOE is observed between CPC pyridinium protons $H_{1,5}$ (δ = 8.89 ppm) and neighbouring CPC protons H_7 (δ = 1.94 ppm), suggesting a closer interaction of these protons within the CPC micelles through-space than without CPX. The shifts in ^{1}H NMR spectra and presence of NOEs indicate that the cyclopropane ring of CPX is interacting with the aliphatic tails of CPC micelles in the palisade layer of the micelle, namely between the hydrophilic groups and first few carbon atoms of hydrophobic groups [45] as there is no change in resonance of the terminal protons of H_{22} (δ = 0.77 ppm). In addition, cation-π interactions between pyridinium headgroups of CPC micelles and CPX aromatic protons (H^a_6, H^a_8, H^a_3) at δ = 7.74 ppm, δ = 7.53 ppm and δ = 8.49 ppm, illustrate the CPX molecule is sitting at the micelle-water interface, with the piperazine group ($H^a_{20\text{-}24}$ at δ = 3.24–2.28 ppm) pointing outwards as there is an absence of NOEs and the piperazine group is able to hydrogen bond with solvent molecules.

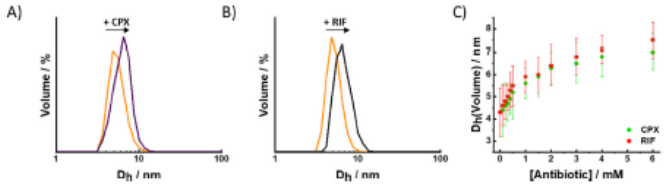

Fig. 2. Dynamic light scattering for monitor the hydrodynamic diameter (volume distribution) of CPC micelles (2 mM) upon addition of antibiotics (A) CPX and (B) RIF in carbonate buffer (HCO_3^-/CO_3^{2-}, 0.1 M, pH 10.6).

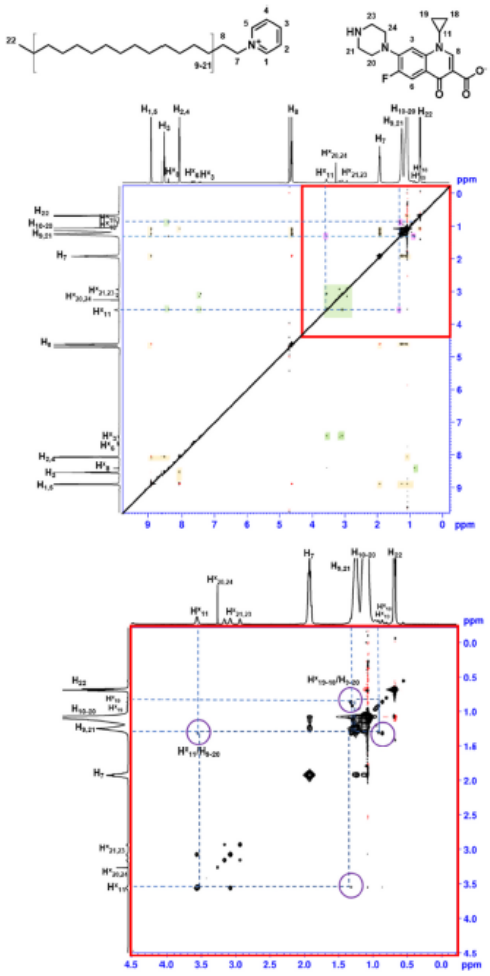

Fig. 3. 500 MHz NOESY spectra of CPX and CPC (1:12) in carbonate buffer (HCO_3^-/CO_3^{2-}, 0.1 M, pH 10.6). CPX cross peaks are labelled in green, CPC cross peaks are labelled in yellow. CPC-CPX cross peaks are labelled as purple boxes.

We also studied the proton shifts to determine interactions between RIF and CPC micelles. In the presence of RIF, the ^{1}H NMR spectra of CPC micelle show shifts in proton resonances. The proton resonances show small upfield shifts except for the terminal methyl protons of CPC, H_{22} ($\delta = 0.81$ ppm) and bulk aliphatic protons $H_{19\text{-}20}$ ($\delta = 1.20$ ppm) which show downfield shifts (Fig. S6, Table S4); indicating that RIF is situated further into the core of the micelle. The pKa values of RIF are 1.7 and 7.9, relating to the 4-hydroxy and 3-piperazine nitrogen respectively. Thereby, under basic conditions (pD = 10.6), RIF is neutral and converted to RIF quinone. [46] The ^{1}H NMR spectrum of RIF in carbonate buffer shows the presence of two species; one major and one minor, indicated by additional peaks in the spectra (Fig. S7). It is reported in mildly basic conditions RIF can slowly undergo deacetylation to form 22-desacetylrifampin and hydrolysis to formyl-rifampicin can also occur. [46] In the presence of CPC, the ^{1}H NMR shows a single set of RIF resonances, the fine structure of the resonance peaks of RIF merge together changing from sharp and narrow to smooth and wide in the presence of CPC micelles. The protons of RIF show upfield shifts ($\Delta\delta \sim 0.03$–0.15 ppm) except for the resonance of H^{R}_{25} and H^{R}_{31} which have small ($\Delta\delta < 0.05$ ppm) downfield shifts.

There are a significant number of NOEs between RIF and CPC (Fig. 4). In general, most of the NOEs are between the aliphatic chain of CPC and RIF than with the pyridinium head of CPC. NOEs are observed between RIF piperazine protons $H^{R}_{54\text{-}57}$ ($\delta = 3.05$ ppm, $\delta = 2.49$ ppm), RIF piperazine *N*-methyl H^{R}_{58} ($\delta = 2.22$ ppm) and CPC pyridinium head protons $H_{2,4}$ ($\delta = 8.14$ ppm). The RIF methyl group H^{R}_{31} ($\delta = 0.61$ ppm) also shows a cross peak with proton $H_{2,4}$ ($\delta = 8.14$ ppm) of CPC. An additional cross peak between the pyridinium head of CPC and RIF is observed between CPC $H_{1,5}$ ($\delta = 8.93$ ppm) and RIF *O*-methoxy protons H_{59} ($\delta = 2.96$ ppm). RIF alkene protons H^{R}_{4} ($\delta = 6.51$ ppm), H^{R}_{8} ($\delta = 6.29$ ppm), H^{R}_{28} ($\delta = 6.13$ ppm), H^{R}_{1} ($\delta = 5.99$ ppm), H^{R}_{25} ($\delta = 5.16$ ppm), show NOEs exclusively with CPC's aliphatic protons H_{22} ($\delta = 0.82$ ppm), $H_{9\text{-}21}$ ($\delta = 1.27$ ppm) and H_8 ($\delta = 1.97$ ppm). However, the RIF alkene proton H^{R}_{22} ($\delta = 5.02$ ppm) shows NOEs only with CPC $H_{9\text{-}21}$ ($\delta = 1.27$ ppm) and H_8 ($\delta = 1.97$ ppm), which illustrates that alkene H^{R}_{22} ($\delta = 5.02$ ppm) is oriented away from terminal CPC micelle protons H_{22} ($\delta = 0.82$ ppm).

The NOEs for CPC micelle interactions do not change in the presence of RIF which indicates that the micelle has not broken apart and this is also supported by DLS studies. Multiple additional NOEs are observed for CPC micelles only. There is a new NOE interaction within the CPC micelles between H_7 ($\delta = 1.94$ ppm) and pyridinium protons $H_{1,5}$ ($\delta = 8.89$ ppm) as well as new CPC micelle NOEs of H_7 ($\delta = 1.94$ ppm) with pyridinium protons $H_{2,4}$ ($\delta = 8.08$ ppm), aliphatic protons $H_{9\text{-}21}$ ($\delta = 1.08$–1.26 ppm) and terminal alkyl protons H_{22} ($\delta = 0.68$ ppm). In addition, aliphatic proton H_8 ($\delta = 4.63$ ppm) has two additional NOEs with pyridinium protons $H_{2,4}$ ($\delta = 8.08$ ppm) and H_3 ($\delta = 8.55$ ppm). H_3 ($\delta = 8.55$ ppm) has an extra interaction with alkyl protons $H_{9\text{-}21}$ ($\delta = 1.08$–1.26 ppm). Finally, terminal alkyl protons H_{22} ($\delta = 0.68$ ppm) have two additional NOEs with pyridinium protons $H_{2,4}$ ($\delta = 8.08$ ppm) and $H_{1,5}$ ($\delta = 8.89$ ppm).

Overall, the significant number of NOEs described between the aliphatic chain of CPC micelles and RIF indicate the presence of RIF on the inside of the CPC micelle within the hydrophobic core. Specifically, the NOEs between CPC terminal alkyl protons (H_{22}) and rifampicin protons, H^{R}_{4}, H^{R}_{8}, H^{R}_{28}, H^{R}_{1}, and H^{R}_{25}. This is supported by an increased number of NOEs for the CPC micelle itself, which indicates a new arrangement of aliphatic tails inside the micelle in the presence of RIF. NOEs between the piperazine protons $H^{R}_{54\text{-}57}$ at $\delta = 3.05$ ppm and $\delta = 2.49$ ppm and piperazine *N*-methyl H^{R}_{58} at $\delta = 2.22$ ppm of RIF and pyridinium protons of CPC at $H_{2,4}$ ($\delta = 8.14$ ppm) support orientation of piperazine group of RIF towards the pyridinium headgroup of CPC micelles within the palisade layer. In addition, the single set of proton resonances observed in ^{1}H NMR for RIF in the presence of CPC indicates that this interaction may protect RIF from hydrolysis and degradation, which is important for maintaining bioavailability of RIF. [46,47].

The interaction of the CPX and RIF with CPC micelles were further explored by Isothermal Titration Calorimetry (ITC). Upon titration of the antibiotics into a 2 mM CPC micellar solution in carbonate buffer, K_D value of 6.30 ± 0.7 μM for CPX and 1.96 ± 0.05 μM for RIF with CPC micelles (Fig. 5) were calculated.

Additionally, optical spectroscopy was employed to further explore the interactions between the antibiotics and CPC. The absorption properties of CPX and RIF were investigated in a CPC micellar medium at pH 10.6. The UV–Vis spectra of CPC show a single absorption band with maximum at 259 nm ($\varepsilon = 4190\ M^{-1}cm^{-1}$) (Fig. S8). In carbonate buffer CPX has two absorption bands at 270 nm ($\varepsilon = 39000\ M^{-1}cm^{-1}$) and 325 nm ($\varepsilon = 17000\ M^{-1}cm^{-1}$). Due to the overlapping between the higher energy absorption band of CPX with CPC, changes in this band cannot be monitored. However, at 325 nm, in the presence of CPC (6 mM, >CMC), there is a bathochromic shift to 334 nm ($\Delta\lambda = +9$ nm) (Fig. 6A). Similarly, RIF has two absorption bands at 334 nm ($\varepsilon = 13000\ M^{-1}cm^{-1}$) and 479 nm ($\varepsilon = 8000\ M^{-1}cm^{-1}$) corresponding to $\pi \rightarrow \pi^*$ transitions. In the presence of CPC (6 mM, >CMC), there is a bathochromic shift in both absorption bands of RIF to 339 nm ($\Delta\lambda = +5$ nm) and 490 nm ($\Delta\lambda = +11$ nm) with a change in shape of the lower energy absorption band (Fig. 6B). These data indicate that in the presence of CPC micelles there is a change in environment for the antibiotics, supporting the interactions described by NOESY.

Furthermore, the change of the environment upon micelle formation was also investigated by steady-state and time resolved fluorescence spectroscopy (Fig. 6C and D). CPX displays a maximum emission wavelength at 425 nm upon excitation at 340 nm at pH 10.6. However, after addition of CPC (2 mM), CPX emission suffers a significant decrease in intensity of 93%. Accordingly, time-revolved fluorescence studies showed a decrease in luminescence lifetime decay ($\lambda_{exc} = 375$ nm, $\lambda_{em} = 425$ nm) upon CPC addition from 7.3 ns to 3.3 ns. The spectroscopic observations indicate that there is a change of the environment of CPX which quenches the luminescence. There may be aggregation-induced quenching which has been previously described for other fluoroquinolines, [48,49] caused by the close proximity of CPX molecules within the CPC micelle, or quenching from CPC as observed for other anionic aromatic fluorescent dyes. [49].

3.2. Development of silica nanoparticles with CPC micelle loaded antibiotics

Taking advantage of the CPC-**antibiotic** interactions, we used the micelle incorporation to form SiO_2 nanoparticles for delivery of dual antimicrobials. Briefly, a silica core is firstly formed for 3 h, then a solution containing CPC micelles with or without antibiotic of choice is added and silica growth continued for 6 h (Fig. S9). The size of micelles in the synthesis was studied by Transmission Electron Microscopy (TEM) (Fig. 7). TEM of CPC-CPX micelles reveals two populations with average sizes of 3 ± 2 nm (n = 50) and 7 ± 2 nm (n = 50), while CPC-RIF micelles show a single population of 5 ± 1 nm (n = 50) (Fig. S15). The two populations of CPC-CPX micelles in TEM can be attributed to the drying process before imaging. Subsequently, the sizes of synthesised silica nanoparticles were explored by Scanning Electron Microscopy (SEM). The average nanoparticle sizes are 230 ± 25 nm for $SiO_2 \supset$ CPC-CPX and 300 ± 20 nm for $SiO_2 \supset$ CPC-RIF (n = 50). Confirmation of the presence of antibiotics was obtained by solid-state absorption spectroscopy (Fig. 7) of powders of the silica particles, $SiO_2 \supset$ CPC-CPX and $SiO_2 \supset$ CPC-RIF which show absorption bands at 340 nm and 330 nm and 480 nm, respectively, characteristic of the presence of CPX and RIF antibiotics.

Loading of incorporated antibiotics in nanoparticles was calculated by UV/Vis spectroscopy based on remaining antibiotic in the synthesis media and washings. An encapsulation efficiency of 84%, corresponding to 7.2 wt% (72 $\mu g_{CPX}/mg_{NP}$) of CPX $SiO_2 \supset$ CPC-CPX was calculated. In the absence of CPC, the encapsulation efficiency of CPX decreases to 35%, corresponding to 3.0 wt% (30 $\mu g_{CPX}/mg_{NP}$). An encapsulation

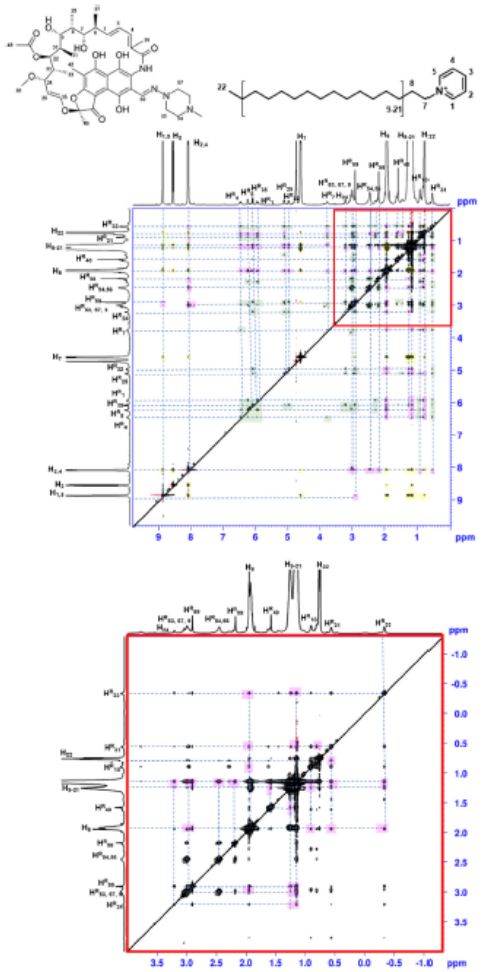

Fig. 4. 500 MHz NOESY 1H NMR spectra of **RIF** and **CPC** (1:12) in carbonate buffer ($^{(HCO_3^-/CO_3^{2-}}$, 0.1 M, pH 10.6). RIF cross peaks are labelled in green; CPC cross peaks are labelled in yellow. CPC-RIF cross peaks are labelled as purple boxes.

391
Asier Rodriguez Muguruza – December 2023

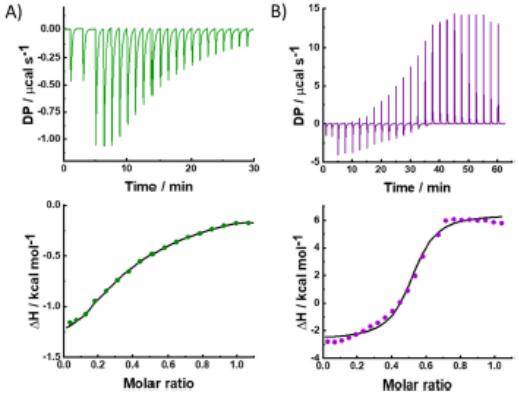

Fig. 5. Isothermal Titration Calorimetry (ITC) profiles showing antibiotic interaction with CPC micelles. (A) **CPX** and (B) **RIF** titration on CPC (2 mM) in carbonate buffer (HCO_3^-/CO_3^{2-}, 0.1 M, pH 10.6).

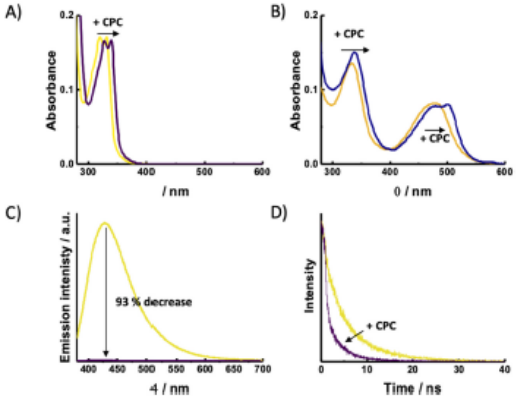

Fig. 6. Optical spectroscopy of antibiotics in presence of **CPC**. UV/Vis absorption spectra of (A) **CPX** (10 µM) and (B) **RIF** (10 µM) upon addition of **CPC** up to 6 mM in carbonate buffer (HCO_3^-/CO_3^{2-}, 0.1 M, pH 10.6), **CPC** absorption band is omitted for clarity. (C) Steady state (λ_{exc} = 340 nm) and (D) time-resolved exponential fluorescence decay (λ_{exc} = 375 nm, λ_{em} = 425 nm) of a **CPX** solution (10 µM) before and after addition of CPC (2 mM) in carbonate buffer (HCO_3^-/CO_3^{2-}, 0.1 M, pH 10.6).

efficiency of 20%, corresponding to 2.5 wt% (25 $\mu g_{RIF}/mg_{NP}$) for **RIF** in SiO_2 ⊃ **CPC-RIF** was determined, whereas no loading was achieved in absence of CPC. Loading of CPC, however, is similar in all nanoparticles, calculated to be between 8% (125 $\mu g_{CPC}/mg_{NP}$) and 11% (195 $\mu g_{CPC}/mg_{NP}$). Thermogravimetric analysis (TGA) is used for the determination of loading of drugs in silica nanoparticles based on continuous monitoring of sample weight loss upon heating at a defined rate under a controlled atmosphere. The amount of organic composition (µg/mg) was calculated from the TGA weight loss from 150 to 900 °C. TGA analysis of CPC shows a single weight loss step at 180–250 °C and 100%

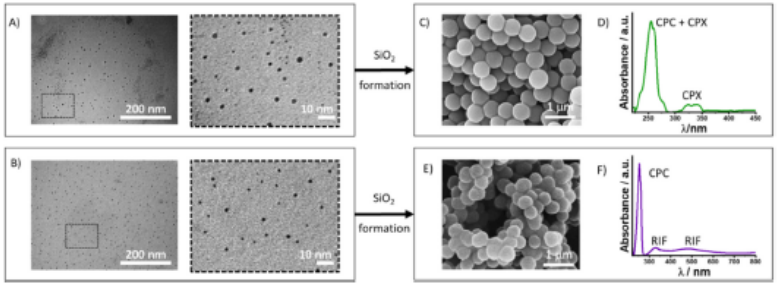

Fig. 7. Characterisation of CPC-antibiotic micelles and corresponding silica nanoparticles. TEM images of (A) **CPC-CPX** and (B) **CPC-RIF** micelles in carbonate buffer (HCO_3^-/CO_3^{2-}, 0.1 M, pH 10.6) to mimic conditions in synthesis. SEM images of (C) **SiO_2⊃CPC-CPX** and (E) **SiO_2⊃CPC-RIF** Solid state absorption spectra of (D) **SiO_2⊃CPC-CPX** and (F) **SiO_2⊃CPC-RIF**.

degradation. TGA analysis of **SiO_2⊃CPC** shows a weight loss of 9.8% compared to unloaded SiO_2, corresponding to encapsulation of CPC and loading of 98 $\mu g_{CPC}/mg_{SiO2}$. In comparison the **SiO_2⊃CPC-CPX** and **SiO_2⊃CPC-RIF** particles showed a loss of weight of 18.0% and 18.5% weight loss compared to unloaded SiO_2, corresponding to total organic content. These data are consistent with calculation of loading by UV/Vis spectroscopy where total organic content is calculated as 15.2% and 13.5% for **SiO_2⊃CPC-CPX** and **SiO_2⊃CPC-RIF** particles respectively.

Nitrogen adsorption-desorption isotherm studies at 77 K were employed to study the porous structure of nanoparticles (Fig. 8). Nanoparticles were subjected to a calcination process in order to fully remove the antibiotic template. After calcination, it was calculated a BET surface area of 153 ± 3 m^2g^{-1} for **SiO_2 ⊃ CPC**. Similarly, analysis of **SiO_2 ⊃ CPC-CPX** and **SiO_2 ⊃ CPC-RIF** after calcination, resulted in a calculated BET surface area of 215 ± 4 m^2g^{-1} and 334 ± 5 m^2g^{-1}, respectively. Before calcination, and due to the presence of CPC-antibiotic micelles within the porous structure, BET surface areas of 17 ± 1 m^2g^{-1}, 5 ± 1 m^2g^{-1} and 5 ± 1 m^2g^{-1} were calculated for **SiO_2 ⊃ CPC**, **SiO_2 ⊃ CPC-CPX** and **SiO_2 ⊃ CPC-RIF**. Before calcination, N_2 adsorption-desorption isotherm of nanoparticles exhibit a Type I(a) isotherm, according to IUPAC classification, characteristic of microporous materials with relatively low surface area. The increase on adsorbed gas at high P/P_0 is associated with intraparticle spaces. After calcination process, nanoparticles display a Type II isotherm characteristic of microporous material with wider pore size range from micropores (<1 nm) to narrow mesopores (≤2.5 nm). The absence of type IV isotherm and type H1 hysteresis loop suggests the absence of unidimensional pores within nanoparticles.

Recorded isotherms, proves the ability of CPC to act as template during the silica formation. Furthermore, calculated average pore size for **SiO_2 ⊃ CPC** was 2.5 nm, which is in good agreement with micelle size simulations [27] and proves the ability of the CPC micelles to form a porous structure within the silica framework. In case of **SiO_2 ⊃ CPC-CPX** and **SiO_2 ⊃ CPC-RIF** average pore size of 2.7 nm and 2.8 nm were estimated, respectively with a cumulative pore volume of 1.37 cm^3/g and 1.33 cm^3/g. However, estimated pore sizes may not be reflected accurately given the changes in silica structure upon calcination (Fig. 8). [50] These data illustrate that the presence of the antibiotic does not

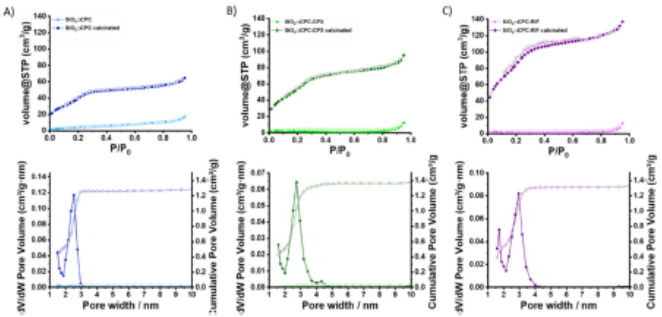

Fig. 8. Nitrogen adsorption-desorption isotherm at 77 K and calculated pore size distribution of (A) **SiO_2⊃CPC**, (B) **SiO_2⊃CPC-CPX** and (C) **SiO_2⊃CPC-RIF** as synthetized and after calcination treatment at 600 °C for 18 h.

alter the templating-abilities of CPC micelles. Furthermore, $SiO_2 \supset$ CPX particles display a nonporous structure based on the adsorption isotherm, before and after calcination (Fig. S11), confirming that the described porosity is achieved only when CPC micelles are included in the silica nanoparticle.

Release studies were conducted to demonstrate the potential use of developed nanoparticles as drug delivery system. Nanoparticles were suspended in water and examined for antibiotic release overtime upon stirring. The presence of antibiotics was detected by absorption spectroscopy of the supernatant solutions following centrifugation to remove particles (Fig. 9). Dual loaded antimicrobial particles, $SiO_2 \supset$ CPC-CPX (2 mg/mL) in water shows a time dependent cumulative release of CPC up to 12.9 ± 0.7 μg_{CPC}/mL after 48 h. In addition, CPX release 0.3 ± 0.1 μg_{CPX}/mL is observed after 48 h, illustrating release of both antimicrobials from $SiO_2 \supset$ CPC-CPX. Instead, in $SiO_2 \supset$ CPX (2 mg/mL), a maximum release at 48 h of 0.08 ± 0.03 μg_{CPX}/mL is observed (Fig. S12). Release from $SiO_2 \supset$ CPC-RIF (2 mg/mL) in PBS buffer (pH 7.4), also shows a time dependent cumulative release of CPC up to 15.2 ± 0.6 μg_{CPC}/mL. The release of RIF is below the limit of detection for UV–Vis and therefore not quantified in this experiment, this is due to the low water solubility of RIF in addition to a low molar extinction coefficient. The presence of RIF in the supernatant is confirmed by mass spectrometry (Fig. S13). Finally, $SiO_2 \supset$ CPC (2 mg/mL) particles in PBS buffer (pH 7.4) show a similar time dependent cumulative release up to 14.9 ± 1.0 μg_{CPC}/mL. Furthermore, methanol was chosen for the efficient disruption of the micelles as previously reported. [51] Release of the antibiotics from a suspension of nanoparticles was estimated: for $SiO_2 \supset$ CPC-CPX (2 mg/mL) in methanol after 24 h as 6.4 ± 0.7 μg_{CPX}/mL and 140 ± 14 μg_{CPC}/mL. Similarly, for $SiO_2 \supset$ CPC-RIF: in methanol 3.8 ± 1.5 μg_{RIF}/mL and 57 ± 5 μg_{CPC}/mL release was determined (Fig. S14). The quantity of antimicrobials released are within the Minimum Inhibitory Concentration values for susceptible bacteria strains, demonstrating the potential of the silica platform for their delivery. [52]

4. Conclusions

CPC micelles have shown to incorporate antibiotics in their structure which makes them promising vehicles for the loading of CPX and RIF antibiotics into silica nanoparticles. The antibiotic-CPC interactions were elucidated by ^{1}H NMR and NOESY experiments. The CPC-CPX interactions indicate that CPX is placed between the outer and palisade region of the CPC micelle. The NMR studies show that RIF is located further into the hydrophobic micelle core. The micelle incorporation of the antibiotics is also shown by a suite of analytical techniques. Introducing CPC micelles into SiO_2 nanoparticles led to a porous structure within the SiO_2 framework as shown by porosimetry studies, providing CPC as an ideal antimicrobial drug template, replacing toxic surfactants or polymers. The incorporated antibiotics can be released from silica particles due to disruption of the micelles alongside release of CPC molecules, providing a system of dual antimicrobial delivery. Our results represent a novel strategy for the development of porous SiO_2 using a therapeutic template which can find applications in enhancing loading and release of poorly-water soluble antibiotics.

CRediT authorship contribution statement

Asier R. Muguruza: Writing – original draft, Investigation, Formal analysis, Conceptualization. **Maria L. Odyniec:** Writing – original draft, Methodology, Formal analysis, Conceptualization. **Menisha Manhota:** Writing – review & editing, Methodology, Investigation, Formal analysis, Conceptualization. **Zaina Habib:** Investigation. **Knut Rurack:** Writing – review & editing. **Jessica M.A. Blair:** Supervision. **Sarah Kuehne:** Writing – review & editing, Supervision. **A. Damien Walmsley:** Writing – review & editing, Supervision. **Zoe Pikramenou:** Writing – review & editing, Writing – original draft, Supervision, Conceptualization.

Declaration of competing interest

The authors declare that they have no known competing financial interests or personal relationships that could have appeared to influence the work reported in this paper.

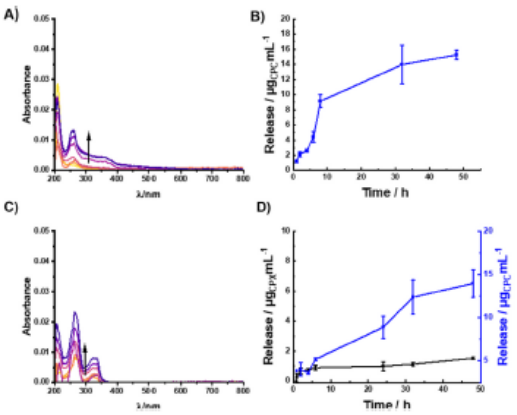

Fig. 9. (A, C) Representative absorption spectra of release studies of (A) CPC from $SiO_2 \supset$CPC-RIF and (C) CPX and CPC from $SiO_2 \supset$CPC-CPX in PBS buffer (pH 7.4) at 25 °C. (B, D) Cumulative release of (B) CPC from $SiO_2 \supset$CPC-RIF and (D) CPX and CPC from $SiO_2 \supset$CPC-CPX in PBS buffer (pH 7.4) at 25 °C.

Data availability

Data will be made available on request.

Acknowledgements

The authors wish to acknowledge the funding agencies for support: Biotechnology and Biological Sciences Research Council (BBRSC) BB/M01116X/1 MIBTP (A.R.M.), and Engineering and Physical Sciences Research Council (EPSRC) EP/V028553/1, *SONATA* project (M.L.O., Z. P.) and EP/L016346/1 *Sci-Phy-4-Health* (M.M.). The authors would like to acknowledge Dr. Cécile Le Duff for her assistance with the NMR experiments.

Appendix A. Supplementary data

Supplementary data to this article can be found online at https://doi.org/10.1016/j.micromeso.2023.112841.

References

[1] A.B. Nik, H. Zare, S. Razavi, H. Mohammadi, P.T. Ahmadi, N. Yazdani, M. Bayandori, N. Rahbar, J.J. Mobarakeh, Smart drug delivery: capping strategies for mesoporous silica nanoparticles, Microporous Mesoporous Mater. 229 (2020), 110115, https://doi.org/10.1016/j.micromeso.2020.110115.

[2] J. Allouche, A. Le Beulze, J.C. Dupin, J.B. Ledeuil, S. Blanc, D. Gonbeau, Hybrid spiropyran-silica nanoparticles with a core-shell structure: sol-gel synthesis and photochromic properties, J. Mater. Chem. 20 (2010) 9370–9378, https://doi.org/10.1039/C0JM01780A.

[3] X. Li, D. Li, Z. Liu, Superiority of biomimetric micelle-entrapped nanoporous silica xerogel to deliver poorly water-soluble itraconazole, RSC Adv. 12 (2022) 28422–28432, https://doi.org/10.1039/D2RA04698A.

[4] J.M.V. Makabenta, A. Nabawy, C.H. Li, S. Schmidt-Malan, R. Patel, V.M. Rotello, Nanomaterial-based therapeutics for antibiotic-resistant bacterial infections, Nat. Rev. Microbiol. 19 (2021) 23–36, https://doi.org/10.1038/s41579-020-0420-1.

[5] M. Vallet-Regí, F. Schüth, D. Lozano, M. Colilla, M. Manzano, Engineering mesoporous silica nanoparticles for drug delivery: where are we after two decades? Chem. Soc. Rev. 51 (2022) 5365–5451, https://doi.org/10.1039/D1CS00658B.

[6] T. Asefa, Z. Tao, Chem., Biocompatibility of mesoporous silica nanoparticles, Res. Toxicol. 25 (2012) 2265–2284, https://doi.org/10.1021/tx300166a.

[7] G.C. Carvalho, G.D. Marena, J.C.F. Karnopp, J. Jorge, R.M. Sábio, M.A.U. Martines, T.M. Banabi, M. Chorilli, Cetyltrimethylammonium bromide in the synthesis of mesoporous silica nanoparticles: general aspects and in vitro toxicity, Adv. Colloid Interface Sci. 307 (2022), 102746, https://doi.org/10.1016/j.cis.2022.102746.

[8] E. Ito, K.W. Yip, D. Katz, S.B. Fonseca, D.W. Hedley, S. Chow, G.W. Xu, T.E. Wood, C. Bastianutto, A.D. Schimmer, S.O. Kelley, F.F. Liu, Potential use of cetrimonium bromide as an apoptosis-promoting anticancer agent for head and neck cancer, Mol. Pharmacol. 76 (2009) 969–983, https://doi.org/10.1124/mol.109.055277.

[9] Z. Lui, D. Lui, L. Wang, J. Zhang, N. Zhang, Docetaxel-loaded Pluronic P123 polymeric micelles: in vitro and in vivo evaluation, Int. J. Mol. Sci. 12 (3) (2011) 1684–1696, https://doi.org/10.3390/ijms12031684.

[10] N.K. Mal, M. Fujiwara, Y. Tanaka, Photocontrolled reversible release of guest molecules from coumarin-modified mesoporous silica, Nature 421 (2003) 350–353, https://doi.org/10.1038/nature01362.

[11] C.-A. Cheng, T. Deng, F.-C. Lin, Y. Cai, J.I. Zink, Supramolecular nanomachines as stimuli-responsive gatekeepers on mesoporous silica nanoparticles for antibiotic and cancer drug delivery, Theranostics 9 (2019) 3341–3364, https://doi.org/10.7150/thno.34576.

[12] C.A. Stewart, Y. Finer, B.D. Hatton, Drug self-assembly for synthesis of highly-loaded antimicrobial drug-silica particles, Sci. Rep. 8 (2018) 895–906, https://doi.org/10.1038/s41598-018-19166-8.

[13] A. Brezhnev, F.-K. Tang, C.-S. Kwan, M.S. Basabrain, J.K.H. Tsoi, J.P. Matinlinna, P. Neshkeatan, K.C.-P. Leung, One-pot preparation of cetylpyridinium chloride-containing nanoparticles for biofilm eradication, ACS Appl. Bio Mater. 6 (2023) 1221–1230, https://doi.org/10.1021/acsabm.2c01080.

[14] D. Khushalani, A. Kuperman, N. Coombs, G.A. Ozin, Mixed surfactant assemblies in the synthesis of mesoporous silicas, Chem. Mater. 8 (8) (1996) 2188–2193, https://doi.org/10.1021/cm960094S.

[15] V. Dubovoy, A. Gunti, T. Zhang, H. Al-Tameemi, J.D. Cerezo, J.M. Boyd, T. Asefa, One-pot hydrothermal synthesis of benzalkonium-templated nanostructured silica antibacterial agents, J. Am. Chem. Soc. 140 (2018) 13534–13537, https://doi.org/10.1021/jacs.8b04843.

[16] D.J. Lewis, V. Dore, M.J. Goodwin, A.C. Savage, G.B. Nash, P. Angeli, Z. Pikramenou, Luminescent ruthenium(II) tris-bipyridyl complex caged in nanoscale silica for particle velocimetry studies in microchannels, Meas. Sci. Technol. 23 (2012), 084004, https://doi.org/10.1088/0957-0233/23/8/084004.

[17] A.N. Dosumu, S. Claire, L.S. Watson, P.M. Girio, S.A.M. Osborne, Z. Pikramenou, N. J. Hodges, Quantification by luminescence tracking of red emissive gold nanoparticles in cells, JACS Au 1 (2021) 174–186, https://doi.org/10.1021/jacsau.0c00033.

[18] D.J. Lewis, V. Dore, N.J. Rogers, T.K. Mole, G.B. Nash, P. Angeli, Z. Pikramenou, Silica nanoparticles for micro-particle imaging velocimetry: fluorosurfactant improves nanoparticle stability and brightness of immobilised iridium(iii) complexes, Langmuir 29 (2013) 14701–14708, https://doi.org/10.1021/la403172m.

[19] A.R. Muguruza, A. di Maio, N.J. Hodges, J.M.A. Blair, Z. Pikramenou, Chelating silica nanoparticles for efficient antibiotic delivery and particle imaging in Gram-negative bacteria, Nanoscale Adv. 5 (2023) 2453, https://doi.org/10.1039/D2NA00884J.

[20] X. Mao, D.L. Auer, W. Buchalla, K.A. Hiller, T. Maisch, E. Hellwig, A. Al-Ahmad, F. Cieplik, Cetylpyridinium chloride: mechanism of action, antimicrobial efficacy in biofilms, and potential risk of resistance, Antimicrob. Agents Chemother. 64 (2020), e00576, https://doi.org/10.1128/AAC.00576-20, 20.

[21] S. Wu, Y. Huang, J. Yan, Y. Li, J. Wang, Y.Y. Yang, P. Yuan, X. Ding, Bacterial outer membrane-coated mesoporous silica nanoparticles for targeted delivery of antibiotic rifampicin against gram-negative bacterial infection in vivo, Adv. Funct. Mater. 31 (2021), 2103442, https://doi.org/10.1002/adfm.202103442.

[22] Q. Liu, Y. Zhang, J. Huang, Z. Xu, X. Li, J. Yang, H. Huang, S. Tang, Y. Chai, J. Lin, C. Yang, J. Liu, S. Lin, Mesoporous silica-coated silver nanoparticles as ciprofloxacin/siRNA carriers for accelerated infected wound healing, J. Nanotechnol. 20 (2022) 386, https://doi.org/10.1186/s12951-022-01600-9.

[23] B. de Juan Mora, L. Filipe, A. Forte, M.M. Santos, C. Alves, F. Teodoro, R. Pedrosa, M.R. Carrott, L.C. Branco, S. Gago, Boosting antimicrobial activity of ciprofloxacin by functionalization of mesoporous silica nanoparticles, Pharmaceuticals 13 (2021) 218, https://doi.org/10.3390/pharmaceutics13020218.

[24] D. Zhang, Z. Wu, J. Xu, J. Liang, J. Li, W. Yang, Tuning the emission properties of $Ru(dpp_3)^{2+}$ doped silica nanoparticles by changing the addition time of the dye during the stöber process, Langmuir 26 (2010) 6657–6662, https://doi.org/10.1021/la903995r.

[25] I. Molinero, M.L. Sierra, M. Valiente, E. Rodenas, Physical properties of cetylpyridinium chloride micelles and their behaviours as reaction media, J. Chem. Soc., Faraday Trans. 92 (1996) 59–63, https://doi.org/10.1039/FT9969200059.

[26] D. Varade, T. Joshi, V.K. Aswal, P.S. Goyal, P.A. Hassan, P. Bahadur, Effect of salt on the micelles of cetyl pyridinium chloride, Colloids Surfaces A Physicochem. Eng. Asp. 259 (2005) 95–101, https://doi.org/10.1016/j.colsurfa.2005.02.018.

[27] R. Verma, A. Mishra, K.R. Mitchell-Koch, Molecular modelling of cetylpyridinium bromide, a cationic surfactant, in solution and micelle, J. Chem. Theor. Comput. 11 (2015) 5415–5425, https://doi.org/10.1021/acs.jctc.5b00475.

[28] J. Mirtič, A. Pandel, P. Laggner, S. Hudoklin, M.E. Kreft, J. Kristl, Polyelectrolyte-surfactant-complex nanoparticles as a delivery platform for poorly soluble drugs: a case study of ibuprofen loaded cetylpyridinium-alginate system, Int. J. Pharm. 580 (2020), 119199, https://doi.org/10.1016/j.ijpharm.2020.119199.

[29] A. Srivastava, K. Ismail, Binding of phenol red to cetylpyridinium chloride at air-solution and micelle-solution interfaces in aqueous ethylene glycol media, Colloids Surfaces A Physicochem. Eng. Asp. 462 (2014) 115–123, https://doi.org/10.1016/j.colsurfa.2014.08.021.

[30] T. Mondal, P. Rajdev, A. Makhal, S.K. Pal, Interaction of an antituberculosis drug with a nanoscopic macromolecular assembly: temperature-dependent forster resonance energy transfer studies on rifampicin in an anionic sodium dodecyl sulfate micelle, J. Phys. Chem. B 115 (2011) 2924–2930, https://doi.org/10.1021/jp108115h.

[31] A. Barve, A. Jain, H. Liu, Z. Zhao, K. Cheng, Enzyme-responsive polymeric micelles of cavazitaxel for prostate cancer targeted therapy, Acta Biomater. 113 (2020) 501–511, https://doi.org/10.1016/j.actbio.2020.06.019.

[32] Y. Wang, X. Ke, Z.X. Voo, S.S.L. Yap, C. Yang, S. Gao, S. Liu, S. Venkataraman, S.A. O. Obuobi, J.S. Khara, Y.Y. Yang, P.L.R. Ee, Biodegradable functional polycarbonate micelles for controlled release of amphotericin B, Acta Biomater. 46 (2016) 211–220, https://doi.org/10.1016/j.actbio.2016.09.036.

[33] S.D. Chaudhury, N. Barooah, V.K. Aswal, H. Pal, A.C. Bhasikuttan, J. Mohanty, Stimuli-responsive supramolecular micellar assemblies of cetylpyridinium chloride with curcubit[5/7]uril, Soft Matter 10 (2014) 3485–3493, https://doi.org/10.1039/C3SM52048.

[34] K. Xu, H.-Q. Ren, G.-M. Zeng, L.-L. Ding, J.-H. Huang, Investigation of interaction between phenol and cetylpyridinium micelle in absence and presence of electrolyte by ^{1}H NMR spectroscopy, Colloids Surfaces A Physicochem. Eng. Asp. 356 (2010) 150–155, https://doi.org/10.1016/j.colsurfa.2010.01.011.

[35] J.P. Mata, V.K. Aswal, P.A. Hassan, P. Bahadur, A phenol-induced structural transition in aqueous cetyltrimethylammonium bromide solution, J. Colloid Interface Sci. 299 (2006) 910–915, https://doi.org/10.1016/j.jcis.2006.02.032.

[36] U. Tehler, J.H. Fagerberg, R. Svensson, M. Larhed, P. Artursson, C.A.S. Bergström, Optimising solubility and permeability of a biopharmaceutics classification system (bcs) class 4 antibiotic drug using lipophilic fragments disturbing the crystal lattice, J. Med. Chem. 56 (2013) 2690–2694, https://doi.org/10.1021/jm301721e.

[37] A. Czyrski, J. Szmura, The application of Box-Behnken-Design in the optimization of HPLC separation of fluoroquinolones, Sci. Rep. 9 (2019) 1–10, https://doi.org/10.1038/s41598-019-55761-z.

[38] D.L. Ross, C.M. Riley, Aqueous stability of some variously substituted quinolone antimicrobials, Int. J. Pharm. 63 (1990) 237–250, https://doi.org/10.1016/0378-5173(90)90130-Y.

[39] B.J. Kim, S.S. Im, S.G. Oh, Investigation on the solubilization locus of aniline-HCl salt in SDS micelles with ^{1}H NMR spectroscopy, Langmuir 17 (2001) 565–566, https://doi.org/10.1021/la0012889.

Asier Rodriguez Muguruza – December 2023

[40] N. Maurer, K.F. Wong, M.J. Hope, P.R. Cullis, Anomalous solubility behaviour of the antibiotic ciprofloxacin encapsulated in liposomes: a ^{1}H-NMR study, Biochim. Biophys. Acta - Biomembr. 1374 (1998) 9–20, https://doi.org/10.1016/s0005-2736(98)00125-4.

[41] C.M. Franzin, X.M. Gong, K. Thai, J. Yu, F.M. Marassi, NMR of membrane proteins in micelles and bilayers: the FXYD family proteins, Methods 41 (2007) 398–408, https://doi.org/10.1016/j.ymeth.2006.08.011.

[42] W. Chen, S.A. Elfeky, Y. Nonne, L. Male, K. Ahmed, C. Amiable, P. Axe, S. Yamada, T.D. James, S.D. Bull, J.S. Fossey, A pyridinium cation-π interaction sensor for the fluorescent detection of alkyl halides, Chem. Commun. 47 (2011) 253–255, https://doi.org/10.1039/CDCC01420F.

[43] Y.J. Huang, Y.B. Jiang, S.D. Bull, J.S. Fossey, T.D. James, Diols and anions can control the formation of an exciplex between pyridinium boronic acid with an aryl group connected via a propylene linker, Chem. Commun. 46 (2010) 8180–8182, https://doi.org/10.1039/CDCC03099F.

[44] E.V. Pletneva, A.T. Laederach, D.B. Fulton, N.M. Kostić, The role of cation-π interactions in biomolecular association. the design of peptides favouring interactions between cationic and aromatic amino acid side chains, J. Am. Chem. Soc. 123 (2001) 6232–6245, https://doi.org/10.1021/ja010401u.

[45] Q. Zhao, S. Zhang, X. Zhang, L. Lei, W. Ma, C. Ma, L. Song, J. Chen, B. Pan, B. Xing, Cation-Pi interaction: a key force for sorption of fluoroquinolone antibiotics on pyrogenic carbonaceous materials, Environ. Sci. Technol. 51 (2017) 13659–13667, https://doi.org/10.1021/acs.est.7b02317.

[46] H.Ç. Arca, I.I. Mosquera-Giraldo, J.M. Pereira, N. Strangusathan, L.S. Taylor, K. J. Edgar, Rifampicin stability and solution concentration enhancement through amorphous solid dispersion in cellulose ω-carboxyalkanoate matrices, J. Pharmaceut. Sci. 107 (2018) 127–138, https://doi.org/10.1016/j.xphs.2017.05.036.

[47] M. Motiei, L. Pleno de Gouveia, T. Sopík, R. Vícha, D. Škoda, J. Císt, R. Khalili, E. Dominková Bergerová, L. Münster, H. Fei, V. Sedlařík, P. Saha, Nanoparticle-based rifampicin delivery system development, Molecules 26 (2021) 1–19, https://doi.org/10.3390/molecules26072067.

[48] G. De Guidi, G. Bracchitta, A. Catalfo, Photosensitization reactions of fluoroquinolones and their biological consequences, Photochem. Photobiol. 87 (2011) 1214–1229, https://doi.org/10.1111/j.1751-1097.2011.00978.x.

[49] A.R. Soenz, J.E. Pemberton, Combined quenching mechanism of anthracene fluorescence by cetylpyridinium chloride in sodium dodecyl sulfate micelles, J. Fluoresc. 24 (2014) 295–299, https://doi.org/10.1007/s10895-013-1319-2.

[50] J.W.M. Osterrieth, J. Rampersad, D. Madden, N. Rampal, L. Skoric, B. Connolly, M. D. Allendorf, V. Stavila, J.L. Snider, R. Ameloot, J. Marreiros, C. Ania, D. Azevedo, E. Vilaseca-Garcia, B.F. Santos, X.H. Bu, Z. Chang, H. Bunzen, N.R. Champness, S. L. Griffin, B. Chen, R.B. Lin, B. Coasne, S. Cohen, J.C. Moreton, Y.J. Colón, L. Chen, R. Clowes, F.X. Coudert, Y. Cui, B. Hou, D.M. D'Alessandro, P.W. Doheny, M. Dincă, C. Sun, C. Doonan, M.T. Huxley, J.D. Evans, P. Falcaro, R. Ricco, O. Farha, K.B. Idrees, T. Islamoglu, P. Feng, H. Yang, R.S. Forgan, D. Bara, S. Furukawa, E. Sanchez, J. Gascon, S. Telalović, S.K. Ghosh, S. Mukherjee, M. R. Hill, M.M. Sadiq, P. Horcajada, P. Salcedo-Abraira, K. Kaneko, R. Kukobat, J. Kenvin, S. Keskin, S. Kitagawa, K. ichi Otake, R.P. Lively, S.J.A. DeWitt, P. Llewellyn, B.V. Lotsch, S.T. Emmerling, A.M. Pütz, C. Martí-Gastaldo, N. M. Padial, J. García-Martínez, N. Linares, D. Maspoch, J.A. Suárez del Pino, P. Moghadam, R. Oktavian, R.E. Morris, P.S. Wheatley, J. Navarro, C. Petit, D. Danaci, M.J. Rosseinsky, A.P. Katsoulidis, M. Schröder, X. Han, S. Yang, C. Serre, G. Mouchaham, D.S. Sholl, R. Thyagarajan, D. Siderius, R.Q. Snurr, R. B. Goncalves, S. Telfer, S.J. Lee, V.P. Ting, J.L. Rowlandson, T. Uemura, T. Iiyuka, M.A. van der Veen, D. Rega, V. Van Speybroeck, S.M.J. Rogge, A. Lamaire, K. S. Walton, L.W. Bingel, S. Wuttke, J. Andreo, O. Yaghi, B. Zhang, C.T. Yavuz, T. S. Nguyen, F. Zamora, C. Montoro, H. Zhou, A. Kirchon, D. Fairen-Jimenez, How reproducible are surface areas calculated from the bet equation? Adv. Mater. 34 (2022), 2201502 https://doi.org/10.1002/adma.202201502.

[51] R. Pazo-Llorente, C. Bravo-Díaz, E. González-Romero, Monitoring micelle breakdown by chemical trapping, Langmuir 19 (2003) 9142–9146, https://doi.org/10.1021/la034879t.

[52] J.M. Andrews, Determination of minimum inhibitory concentrations, J. Antimicrob. Chemother. 48 (2001) 5–16, https://doi.org/10.1093/jac/48.suppl_1.5.

Asier Rodriguez Muguruza – December 2023

5.6. References

1 D. Hawthorne, A. Pannala, S. Sandeman and A. Lloyd, *J. Drug Deliv. Sci. Technol.*, 2022, **78**, 103936.

2 M. Vallet-Regí, F. Schüth, D. Lozano, M. Colilla and M. Manzano, *Chem. Soc. Rev.*, 2022, **51**, 5365–5451.

3 L. C. Fonseca, A. J. De Paula, D. S. T. Martinez and O. L. Alves, *New J. Chem.*, 2016, **40**, 8060–8067.

4 Y. Feng, N. X. Li, H. L. Yin, T. Y. Chen, Q. Yang and M. Wu, *Mol. Pharm.*, 2019, **16**, 422–436.

5 C. H. Tsai, J. L. Vivero-Escoto, I. I. Slowing, I. J. Fang, B. G. Trewyn and V. S. Y. Lin, *Biomaterials*, 2011, **32**, 6234–6244.

6 J. Lu, M. Liong, J. I. Zink and F. Tamanoi, *Small*, 2007, **3**, 1341–1346.

7 D. P. Ferris, J. Lu, C. Gothard, R. Yanes, C. R. Thomas, J. C. Olsen, J. F. Stoddart, F. Tamanoi and J. I. Zink, *Small*, 2011, **7**, 1816–1826.

8 A. Bakhshian Nik, H. Zare, S. Razavi, H. Mohammadi, P. Torab Ahmadi, N. Yazdani, M. Bayandori, N. Rabiee and J. Izadi Mobarakeh, *Microporous Mesoporous Mater.*, 2020, **299**, 110115.

9 P. A. Bhat, A. A. Dar and G. M. Rather, *J. Chem. Eng. Data*, 2008, **53**, 1271–1277.

10 V. Suratkar and S. Mahapatra, *J. Colloid Interface Sci.*, 2000, **225**, 32–38.

11 M. Ghezzi, S. Pescina, C. Padula, P. Santi, E. Del Favero, L. Cantù and S. Nicoli, *J. Control. Release*, 2021, **332**, 312–336.

12 Y. Lu, E. Zhang, J. Yang and Z. Cao, *Nano Res.*, 2018, **11**, 4985–4998.

13 A. Srivastava and K. Ismail, *Colloids Surfaces A Physicochem. Eng. Asp.*, 2014, **462**, 115–123.

14 S. D. Choudhury, N. Barooah, V. K. Aswal, H. Pal, A. C. Bhasikuttan and J. Mohanty, *Soft Matter*, 2014, **10**, 3485–3493.

15 J. E. Morozova, V. V. Syakaev, Y. V. Shalaeva, A. M. Ermakova, I. R. Nizameev, M. K. Kadirov, A. D. Voloshina, V. V. Zobov, I. S. Antipin and A. I. Konovalov, *Soft Matter*, 2017, **13**, 2004–2013.

16 T. I. Janjua, Y. Cao, C. Yu and A. Popat, *Nat. Rev. Mater.*, 2021, **6**, 1072–1074.

17 J. M. V. Makabenta, A. Nabawy, C. H. Li, S. Schmidt-Malan, R. Patel and V. M. Rotello, *Nat. Rev. Microbiol.*, 2021, **19**, 23–36.

18 E. Ito, K. W. Yip, D. Katz, S. B. Fonseca, D. W. Hedley, S. Chow, G. W. Xu, T. E. Wood, C. Bastianutto, A. D. Schimmer, S. O. Kelley and F. F. Liu, *Mol. Pharmacol.*, 2009, **76**, 969–983.

19 T. Asefa and Z. Tao, *Chem. Res. Toxicol.*, 2012, **25**, 2265–2284.

20 C. A. Stewart, Y. Finer and B. D. Hatton, *Sci. Rep.*, 2018, **8**, 895–906.

21 D. Khushalani, A. Kuperman, N. Coombs and G. A. Ozin, *Chem. Mater.*, 1996, **8**, 2188–2193.

22 F. Testa, L. Pasqua, P. Frontera and R. Aiello, *Stud. Surf. Sci. Catal.*, 2004, **154 A**, 424–431.

23 C. A. Stewart, J. H. Hong, B. D. Hatton and Y. Finer, *Acta Biomater.*, 2018, **76**, 283–294.

24 M. Q. Marashdeh, C. A. Stewart, A. Kishen, C. Levesque and Y. Finer, *J. Endod.*, 2021, **47**, 1775–1782.

25 C. Stewart, A. Siu, C. Tsui, Y. Finer and B. Hatton, *J. Mater. Chem. B*, 2022, **10**, 6453–6463.

26 V. Dubovoy, A. Ganti, T. Zhang, H. Al-Tameemi, J. D. Cerezo, J. M. Boyd and T. Asefa, *J. Am. Chem. Soc.*, 2018, **140**, 13534–13537.

27 M. Zhang, J. Feng, Y. Zhong, J. Luo, Y. Zhao, Y. Yang, Y. Song, X. Lin, Y. Yang, H. Song and C. Yu, *Chem. Eng. J.*, 2022, **440**, 135837.

28 Y. He, Y. Zhang, M. Sun, C. Yang, X. Zheng, C. Shi, Z. Chang, Z. Wang, J. Chen, S. Pei, W. fei Dong, D. Shao and J. She, *Colloids Surfaces B Biointerfaces*, 2020, **187**, 110653.

29 O. V. Dement'eva, K. A. Naumova, E. M. Shishmakova, I. N. Senchikhin, S. K. Zhigletsova, M. V. Klykova, I. A. Dunaitsev, D. A. Kozlov and V. M. Rudoy, *Colloid J.*, 2021, **83**, 651–661.

30 K. A. Naumova, O. V. Dement'eva, I. N. Senchikhin and V. M. Rudoy, *Microporous Mesoporous Mater.*, 2021, **316**, 110911.

31 A. Brezhnev, F. K. Tang, C. S. Kwan, M. S. Basabrain, J. K. H. Tsoi, J. P. Matinlinna, P. Neelakantan and K. C. F. Leung, *ACS Appl. Bio Mater.*, 2022, **6**, 1221–1230.

32 X. Mao, D. L. Aue, W. Buchalla, K. A. Hiller, T. Maisch, E. Hellwig, A. Al-Ahmad and F. Cieplik, *Antimicrob. Agents Chemother.*, 2020, **64**, e00576-20.

33 P. Gilbert and L. E. Moore, *J. Appl. Microbiol.*, 2005, **99**, 703–715.

34 F. Cieplik, E. Kara, D. Muehler, J. Enax, K. A. Hiller, T. Maisch and W. Buchalla, *Microbiologyopen*, 2019, **8**, e695.

35 M. Vaara, *Microbiol. Rev.*, 1992, **56**, 395–411.

36 I. Molinero, M. L. Sierra, M. Valiente and E. Rodenas, *J. Chem. Soc. - Faraday Trans.*, 1996, **92**, 59–63.

37 D. Varade, T. Joshi, V. K. Aswal, P. S. Goyal, P. A. Hassan and P. Bahadur, *Colloids Surfaces A Physicochem. Eng. Asp.*, 2005, **259**, 95–101.

38 R. Verma, A. Mishra and K. R. Mitchell-Koch, *J. Chem. Theory Comput.*, 2015, **11**, 5415–5425.

39 K. Xu, H. qiang Ren, G. ming Zeng, L. li Ding and J. hui Huang, *Colloids*

Surfaces A Physicochem. Eng. Asp., 2010, **356**, 150–155.

40 J. Karayil, S. Kumar, Y. Talmon, P. A. Hassan, B. V. R. Tata and L. Sreejith, *J. Surfactants Deterg.*, 2016, **19**, 849–860.

41 J. Mirtič, A. Paudel, P. Laggner, S. Hudoklin, M. E. Kreft and J. Kristl, *Int. J. Pharm.*, 2020, **580**, 119199.

42 F. Hoffmann, M. Cornelius, J. Morell and M. Fröba, *Angew. Chemie - Int. Ed.*, 2006, **45**, 3216–3251.

43 H. Zou and Y. Ren, *Nanoscale*, 2023, **15**, 10484–10497.

44 H. Zhang, D. He, S. Niu and H. Qi, *Int. J. Hydrogen Energy*, 2021, **46**, 17221–17230.

45 M. Guo, M. Kanezashi, H. Nagasawa, L. Yu, K. Yamamoto, T. Gunji, J. Ohshita and T. Tsuru, *J. Memb. Sci.*, 2019, **584**, 56–65.

46 M. Guo, J. Qian, R. Xu, X. Ren, J. Zhong and M. Kanezashi, *J. Memb. Sci.*, 2022, **643**, 120018.

47 J. G. Croissant, Y. Fatieiev, A. Almalik and N. M. Khashab, *Adv. Healthc. Mater.*, 2018, **7**, 1700831.

48 J. Croissant, D. Salles, M. Maynadier, O. Mongin, V. Hugues, M. Blanchard-Desce, X. Cattoën, M. Wong Chi Man, A. Gallud, M. Garcia, M. Gary-Bobo, L. Raehm and J. O. Durand, *Chem. Mater.*, 2014, **26**, 7214–7220.

49 K. Okamoto, Y. Goto and S. Inagaki, *J. Mater. Chem.*, 2005, **15**, 4136–4140.

50 M. Jahns, D. P. Warwas, M. R. Krey, K. Nolte, S. König, M. Fröba and P. Behrens, *J. Mater. Chem. B*, 2020, **8**, 776–786.

51 J. Sebastián Manzano, D. Singappuli-Arachchige, B. L. Parikh and I. I. Slowing, *Chem. Eng. J.*, 2018, **340**, 73–80.

52 N. X. D. Mai, T. H. T. Nguyen, L. B. Vong, M. H. D. Dang, T. T. T. Nguyen, L. H. T. Nguyen, H. K. T. Ta, T. H. Nguyen, T. B. Phan and T. L. H. Doan, *Mater. Sci. Eng. C*, 2021, **127**, 112232.

53 Y. Chen, Q. Meng, M. Wu, S. Wang, P. Xu, H. Chen, Y. Li, L. Zhang, L. Wang and J. Shi, *J. Am. Chem. Soc.*, 2014, **136**, 16326–16334.

54 D. Zhang, Z. Wu, J. Xu, J. Liang, J. Li and W. Yang, *Langmuir*, 2010, **26**, 6657–6662.

55 U. Tehler, J. H. Fagerberg, R. Svensson, M. Larhed, P. Artursson and C. A. S. Bergström, *J. Med. Chem.*, 2013, **56**, 2690–2694.

56 A. Czyrski and J. Sznura, *Sci. Rep.*, 2019, **9**, 19458.

57 J. P. Mata, V. K. Aswal, P. A. Hassan and P. Bahadur, *J. Colloid Interface Sci.*, 2006, **299**, 910–915.

58 T. Mondol, P. Rajdev, A. Makhal and S. K. Pal, *J. Phys. Chem. B*, 2011, **115**, 2924–2930.

59 A. Barve, A. Jain, H. Liu, Z. Zhao and K. Cheng, *Acta Biomater.*, 2020, **113**, 501–511.

60 J. Mirtič, A. Paudel, P. Laggner, S. Hudoklin, M. E. Kreft and J. Kristl, *Int. J. Pharm.*, 2020, **580**, 119199.

61 Y. Wang, X. Ke, Z. X. Voo, S. S. L. Yap, C. Yang, S. Gao, S. Liu, S. Venkataraman, S. A. O. Obuobi, J. S. Khara, Y. Y. Yang and P. L. R. Ee, *Acta Biomater.*, 2016, **46**, 211–220.

62 D. L. Ross and C. M. Riley, *Int. J. Pharm.*, 1990, **63**, 237–250.

63 B. J. Kim, S. S. Im and S. G. Oh, *Langmuir*, 2001, **17**, 565–566.

64 N. Maurer, K. F. Wong, M. J. Hope and P. R. Cullis, *Biochim. Biophys. Acta - Biomembr.*, 1998, **1374**, 9–20.

65 C. M. Franzin, X. M. Gong, K. Thai, J. Yu and F. M. Marassi, *Methods*, 2007, **41**, 398–408.

66 W. Chen, S. A. Elfeky, Y. Nonne, L. Male, K. Ahmed, C. Amiable, P. Axe, S. Yamada, T. D. James, S. D. Bull and J. S. Fossey, *Chem. Commun.*, 2011, **47**, 253–255.

67 Y. J. Huang, Y. B. Jiang, S. D. Bull, J. S. Fossey and T. D. James, *Chem. Commun.*, 2010, **46**, 8180–8182.

68 Q. Zhao, S. Zhang, X. Zhang, L. Lei, W. Ma, C. Ma, L. Song, J. Chen, B. Pan and B. Xing, *Environ. Sci. Technol.*, 2017, **51**, 13659–13667.

69 G. De Guidi, G. Bracchitta and A. Catalfo, *Photochem. Photobiol.*, 2011, **87**, 1214–1229.

70 A. R. Soemo and J. E. Pemberton, *J. Fluoresc.*, 2014, **24**, 295–299.

71 L. Dalstein, E. Potapova and E. Tyrode, *Phys. Chem. Chem. Phys.*, 2017, **19**, 10343–10349.

72 M. Sulpizi, M. P. Gaigeot and M. Sprik, *J. Chem. Theory Comput.*, 2012, **8**, 1037–1047.

73 A. Méndez, E. Bosch, M. Rosés and U. D. Neue, *J. Chromatogr. A*, 2003, **986**, 33–44.

74 J. W. M. Osterrieth, J. Rampersad, D. Madden, N. Rampal, L. Skoric, B. Connolly, M. D. Allendorf, V. Stavila, J. L. Snider, R. Ameloot, J. Marreiros, C. Ania, D. Azevedo, E. Vilarrasa-Garcia, B. F. Santos, X. H. Bu, Z. Chang, H. Bunzen, N. R. Champness, S. L. Griffin, B. Chen, R. B. Lin, B. Coasne, S. Cohen, J. C. Moreton, Y. J. Colón, L. Chen, R. Clowes, F. X. Coudert, Y. Cui, B. Hou, D. M. D'Alessandro, P. W. Doheny, M. Dincă, C. Sun, C. Doonan, M. T. Huxley, J. D. Evans, P. Falcaro, R. Ricco, O. Farha, K. B. Idrees, T. Islamoglu, P. Feng, H. Yang, R. S. Forgan, D. Bara, S. Furukawa, E. Sanchez, J. Gascon, S. Telalović, S. K. Ghosh, S. Mukherjee, M. R. Hill, M. M. Sadiq, P. Horcajada, P. Salcedo-Abraira, K. Kaneko, R. Kukobat, J. Kenvin, S. Keskin, S. Kitagawa, K. ichi Otake, R. P. Lively, S. J. A. DeWitt, P. Llewellyn, B. V. Lotsch, S. T. Emmerling, A. M. Pütz, C. Martí-Gastaldo, N. M. Padial, J.

García-Martínez, N. Linares, D. Maspoch, J. A. Suárez del Pino, P. Moghadam, R. Oktavian, R. E. Morris, P. S. Wheatley, J. Navarro, C. Petit, D. Danaci, M. J. Rosseinsky, A. P. Katsoulidis, M. Schröder, X. Han, S. Yang, C. Serre, G. Mouchaham, D. S. Sholl, R. Thyagarajan, D. Siderius, R. Q. Snurr, R. B. Goncalves, S. Telfer, S. J. Lee, V. P. Ting, J. L. Rowlandson, T. Uemura, T. Iiyuka, M. A. van der Veen, D. Rega, V. Van Speybroeck, S. M. J. Rogge, A. Lamaire, K. S. Walton, L. W. Bingel, S. Wuttke, J. Andreo, O. Yaghi, B. Zhang, C. T. Yavuz, T. S. Nguyen, F. Zamora, C. Montoro, H. Zhou, A. Kirchon and D. Fairen-Jimenez, *Adv. Mater.*, 2022, **34**, 2201502.

75 S. Brunauer, P. H. Emmett and E. Teller, *J. Am.Chem.Soc.*, 1938, **60**, 309–319.

76 P. I. Ravikovitch, G. L. Haller and A. V. Neimark, *Adv. Colloid Interface Sci.*, 1998, **76**–**77**, 203–226.

77 J. Xu, W. Liu, Y. Yu, J. Du, N. Li and L. Xu, *RSC Adv.*, 2014, **4**, 37470–37478.

78 K. H. Ku, J. M. Shin, D. Klinger, S. G. Jang, R. C. Hayward, C. J. Hawker and B. J. Kim, *ACS Nano*, 2016, **10**, 5243–5251.

79 J. M. Andrews, *J. Antimicrob. Chemother.*, 2001, **48**, 5–16.

80 R. Pazo-Llorente, C. Bravo-Díaz and E. González-Romero, *Langmuir*, 2003, **19**, 9142–9146.

81 A. R. Muguruza, M. L. Odyniec, M. Manhota, Z. Habib, K. Rurack, J. M. A. Blair, S. A. Kuehne, A. D. Walmsley and Z. Pikramenou, *Microporous Mesoporous Mater.*, 2024, **363**, 112841.

82 J. Stetefeld, S. A. McKenna and T. R. Patel, *Biophys. Rev.*, 2016, **8**, 409–427.

83 F. J. Acebedo-Martínez, A. Domínguez-Martín, C. Alarcón-Payer, A. Sevillano-Páez, C. Verdugo-Escamilla, J. M. González-Pérez, F. Martínez-Checa and D. Choquesillo-Lazarte, *Int. J. Mol. Sci.*, 2023, **24**, 3305.

84 A. R. Muguruza, A. di Maio, N. J. Hodges, J. M. A. Blair and Z. Pikramenou, *Nanoscale Adv.*, , DOI:10.1039/d2na00884j.

85 K. S. W. Sing, D. H. Everett, R. A. W. Haul, L. Moscou, R. A. Pierotti, J. Rouquérol and T. Siemieniewska, *Pure Appl. Chem.*, 1985, **57**, 603–619.

86 T. Higuchi, *J. Pharm. Sci.*, 1963, **52**, 1145–149.

87 R. W. Korsmeyer, R. Gurny, E. Doelker, P. Buri and N. A. Peppas, *Int. J. Pharm.*, 1983, **15**, 25–35.

88 H. Kim, J. Yoo, Y. M. Lim, E. J. Kim, B. Il Yoon, P. Kim, S. Do Yu, I. C. Eom and I. Shim, *J. Appl. Toxicol.*, 2021, **41**, 470–482.

89 M. C. Jones, S. A. Jones, Y. Riffo-Vasquez, D. Spina, E. Hoffman, A. Morgan, A. Patel, C. Page, B. Forbes and L. A. Dailey, *J. Control. Release*, 2014, **183**, 94–104.

90 X. Huang, L. Li, T. Liu, N. Hao, H. Liu, D. Chen and F. Tang, *ACS Nano*, 2011, **5**, 5390–5399.

6. GENERAL CONCLUSIONS AND FUTURE WORK

In this thesis, we explored the chemical versatility of silica nanoparticles for the development of more efficient antibiotic delivery system through nanoparticle surface and framework modification.

Firstly, we developed an aminocarboxylate coated hybrid silica nanoparticle (**DTPA@SiO_2⊃Ru-Van**) *via* dual inclusion of a ruthenium(II) luminescent complex (**Ru**) and the glycopeptide antibiotic vancomycin (**Van**). Resulted nanoparticles displayed a continuous antibiotic release and optimal stable red-luminescence from the included **Ru**, ideal for imaging. The DTPA-coating was developed to enhance the internalization of nanoparticle into gram-negative bacterial cells, as the chosen antibiotic is not able to be internalised by itself due to the reduced membrane permeability of gram-negative bacterial cells. **DTPA@SiO_2⊃Ru-Van** nanoparticles displayed an excellent antibacterial activity, inhibiting bacterial growth with **Van** concentrations similar than those requited for inhibition of gram-positive bacterial cells. Structural Illumination Microscopy evidenced the importance of the coating as uncoated nanoparticles were not internalised into *E. coli* cells while coated particles displayed high internalization. Nevertheless, no change between uncoated and coated nanoparticles was observed for those bacterial species (*P. aeruginosa* and *B. cenocepacia*) that displayed protection of the structurally crucial membrane divalent cations.

Further modification of **DTPA@SiO_2⊃Ru-Van** coating by Fe(III) cation chelation resulted in the development of **Fe^{3+}DTPA@SiO_2⊃Ru-Van** nanoparticles with

enhanced activity compared with **DTPA@SiO_2⊃Ru-Van** even in case of *P. aeruginosa* and *B. cenocepacia*. The presence of the anchored metal complex onto nanoparticles surface was confirmed via a plethora of material chemistry characterization techniques. The present of the metal cation did not alter the release performance of the nanoparticles, neither their luminescent properties. Enhanced antibacterial properties of novel nanoparticles was confirmed against a range of different gram-negative bacterial cells. Their mechanism of action was elucidated which relied on nanoparticles uptake through siderophore-uptake systems, making those system the first silica nanoparticle whose uptake is driven by siderophore-uptake systems. Upon investigation of **Fe^{3+}DTPA@SiO_2⊃Ru-Van** activity with *S. aureus*, *E. coli* and *P. aeruginosa* strains with single siderophore-membrane receptor inactivation helped us to identified that those carboxylate- and hydroxamate-based receptors are involved in nanoparticles activity. These findings were further validated by Structural Illumination and Transmittance Electron Microscopy where nanoparticle internalization and interactions with bacterial cells was enhanced upon overexpression of receptors, and decreased upon inactivation of carboxylate- and hydroxamate-based receptors. Furthermore, we developed a molecular antibiotic-containing analogue (**Fe^{3+}DTPA-$Amox_2$**) and confirmed that shared same mechanism of action that **Fe^{3+}DTPA@SiO_2⊃Ru-Van.**

Moreover, a photoresponsive silica nanoparticle was developed containing novel silyl-modified spiropyran bridged within the framework (**SP-SiO_2**). The content of the photoswitch was optimized in order to achieved highest content possible and the effect of the hydrophilicity of the framework explored. Nanoparticles presented negative photochromism displaying the open form of the photoswitch due to H-bonding with the silica framework. Hydrophobicity increase by addition of DMDES resulted in a

decrease in the open forms of the photoswitch. Thereby, employed the described negative photochromism of the dye to lock the **TMP** antibiotic within the framework (**SP-SiO$_2$⊃TMP**), which was confirmed due to the disappearance of the protonated **H$^+$MC** form and based on the slower ***MC-to-SP*** upon irradiation and faster ***SP-to-MC*** dark conversion. **TMP**-loaded nanoparticles displayed light-triggered release alongside an on-off release mode. Their activity was confirmed against reference and clinical isolated of urinary tract infection *E. coli* strains with different susceptibilities against **TMP**. These results suppose the first evidence that developed nanoparticles could be employed for the functionalization of catheter surface for on-demand antibiotic release during long-term catheterization.

Finally, we explore different strategies for the effective encapsulation and release of the model hydrophobic **CPX** from silica-based nanoparticles. First approach was based on supramolecular interactions between **CPC** micelles and **CPX**, confirmed by NMR and optical spectroscopy, depicting **CPX** in the palisade regain of the **CPC** micelles. Formed supramolecular complex was encapsulated in silica nanoparticles (**SiO$_2$⊃CPC-CPX**) displaying higher porosity induced by micelle encapsulation and concomitant release of **CPC** and **CPX**. On the other hand, **PSQ** nanoparticles base don BTEB were synthetized and **CPX** encapsulated. Higher **CPX** encapsulation efficiency was obtained in **PSQ⊃CPX** nanoparticles compared with any other nanoparticle design alongside sustained **CPX** release. **PSQ** nanoparticles also displayed higher porosity as estimated by N_2 porosimetry analysis. Finally, quantitative analysis of **CPX** release profile from newly designed and controls nanoparticles (**SiO$_2$⊃CPX** and **MSN@CPX**) based on drug release kinetic models confirmed that **SiO$_2$⊃CPC-CPX** and **PSQ⊃CPX** nanoparticles exhibited sustained **CPX** release over time, while the control nanoparticles resulted in burst **CPX** release. These results

suppose a step forward for the development of more efficient silica-based nanoparticle for delivery of hydrophobic antibiotics.

Overall, each chapter presents a novel strategy for the design of more efficient antibiotic delivery systems by modification of the surface or framework composition of the traditional silica nanoparticles. This work could be understood as the development of a toolbox of elements for the *ex profeso* production of novel silica-based drug delivery systems combining the different surface modifications and framework compositions explored in this thesis. In this way, surface permeabilizer photoresponsive nanoparticles or polysilesquioxane nanoparticles with enhanced antibiotic release able to selectively interact with siderophore surface receptors would be investigated.

7. INSTRUMENTATION

^{1}H-NMR spectra were recorded on a Bunker AV300 (300 MHz), AV400 (400 MHz) and AV500 (500 MHz) spectrometers. ^{13}C-NMR spectra were recorded on a Bunker AV400 (400 MHz) spectrometers. All deuterated solvents were purchased from Sigma-Aldrich if the higher possible quality.

ESI-MS was recorded using a Thermo Scientific LCQ Fleet ion trap LC/MS mass spectrometer equipped with a Finningham Surveyor autosampler and controlled by XCalibur software. LC-MS analysis was performed in a Waters Xevo G2-XS chromatographer, Samples introduced using a Waters Acquity H-Class UPLC. Mass spectra acquired using a Waters Xevo G2-XS, operating in resolution mode, with a minimum resolution of 20,000 FWHM; Leucine Enkephalin used as the lockspray reference ion. ESI spectra obtained with a spray voltage of 2kV, operating at a temperature of 250°C.

FT-IR data was recorded with a Perkin Elmer 100FT-IR spectrometer fitted with ATR attachment; samples were dried overnight under vacuum prior the measurements.

DLS data was recorded by a Malvern Panalytical Zetasizer ZS instrument equipped with a H-Ne 633 nm laser at 25 ºC and with a back-scattering of 173 º using PBS buffer (0.1 M, pH = 7.4) as dispersant. The instrument was controlled with a Malvern DTS 7.03 software. All sizes were determined in based on 5 measurements containing 10 runs on each. ζ-potential was determined after measuring each sample at 25 °C in triplicate in MiliQ water or PBS buffer (0.1 M, pH = 7.4) as dispersant.

Solid-state UV-Vis spectra were recorded using a Cary 5000 Uv-Vis spectrophotometer equipped with a solid-state attachment. Steady state

luminescence measurements and time resolved studies were recorded on an Edinburgh Instruments FLS920 steady state and time-resolved spectrometer. The detection system used an incorporated R928 Hamamatsu photomultiplier tube. F980 spectrometer analysis software was used to record the data, and all spectra were corrected for photomultiplier and instrument response. Luminescent lifetimes were recorded with EPL-375 laser as an excitation source and fitted using Edinburgh Instruments FAST software with estimated error of ± 10%. Determination of released cargo was determined using a Horiba TCSPC Fluorolog spectrophotometer with Fluor Essence V3.8 software, corrected for lamp and instrument response or using a Cary 60 UV-Vis spectrometer.

Thermogravimetric analysis (TGA) was performed in a TGA 8000 PerkinElmer thermogravimetric analyser, controlled by a Pyris Software version 13.3.1.0019. Samples were loaded into ceramic sample crucibles, circa 6.6 mm in diameter and 1.95 mm in height. The temperature is held at 30 ºC for 1 min then increased from 30 to 120 ºC at 100 ºC min^{-1}, followed by an isothermal step at 120 ºC for 60 min. Then, temperature was raised from 100 to 800 ºC at 5ºC min^{-1}. Finally, samples were cooled down from 800 ºC to 30 ºC at a 30 ºC min-1 rate. All thermal decompositions are performed under airt flow.

Isothermal titration calorimetry (ITC) was performed using a Malvern MicroCal PEAQ-ITC instrument and the binding curve was fitted with the Malvern MicroCal PEAQ-ITC V1.41 using the ‘One Set of Sites’ model.

Structural illumination microscopy (SIM) was performed using a Zeiss Elyra 7 system equipped with 405 nm and 488 nm lattice lasers. Structural illumination images were processed using the Zeiss ZEN software and analysed using the ImageJ V1.51

software. Colocalization analysis between channels was carried out using the Fiji image software plugin Just Another Colocalization Plugin (JACoP), from which the Pearson and Manders' Overlapping correlation parameters were calculated over five different images per treatment.

The N_2 sorption analysis was performed at 77 K on a Nova porosimeter instrument in the relative pressure range 10−6–0.99 p/p_0 to avoid N_2 condensation on the micrometre scale. The samples (50–70 mg) were dried and degassed at 150°C overnight in the Nova instrument. The samples were analysed using 12 mm wide glass tubes. The pore size distribution was obtained using the 3Flex Software (v5.02) using the heterogeneous surface nonlinear DFT model (HS-NLDFT).

Scanning Electron Microscopy (SEM) images were recorded in a Zeiss EVO 10 electron microscope. Transmission Electron Microscopy (TEM) images were recorded in a JEOL1400 electron microscope.